PROCEEDINGS OF THE
INTERNATIONAL LINEAR COLLIDER WORKSHOP

LCWS 2007   ILC 2007

VOLUME 1

Edited by
ARIANE FREY
SABINE RIEMANN

Impressum

Proceedings of the International Linear Collider Workshop LCWS 2007 and ILC 2007

Committees

International Advisory Committee

S. Aronson (BNL), B. Barish (Caltech), J. Brau (Univ. Oregon), M. Calvetti (INFN-LNF), T. Camporesi (CERN), H.S. Chen (IHEP Beijing), J. Dainton (Cockcroft Inst.), M. Danilov (ITEP Moscow), J. Dorfan (SLAC), J. Engelen (CERN), A. Gurtu (Tata Inst.), R.D. Heuer (DESY/Univ. Hamburg), Y.B.Hsiung (Natl. Taiwan Univ.), P.W-Y. Hwang (Natl. Taiwan Univ.), J. Jaros (SLAC), A. Kakodkar (AEC & DAE India), J.S. Kang (Korea Univ.), D. Karlen (Univ. Victoria), S. Komamiya (Univ. Tokyo), A. Kronfeld (FNAL), F. LeDiberder (IN2P3), W.G. Li (IHEP Beijing), N. Lockyer (TRIUMF), K. Meier (Univ. Heidelberg), D. Miller (UCL), A. Miyamoto (KEK), P. Oddone (FNAL), M. Oreglia (Univ. Chicago), H. Park (Kyungpook Univ.), R. Patterson (Cornell Univ.), R. Petronzio (Univ. Rome), F. Richard (LAL), V. Rubakov (INR Moscow), A. Seiden (UCSC), R. Settles (MPI Munich), M. Shochet (Univ. Chicago), A. Shotter (TRIUMF), A. Skrinsky (Budker Inst.), A. Suzuki (KEK), F. Takasaki (KEK), G. Tayler (Univ. Melbourne), M. Tigner (Cornell Univ.), J. Timmermans (NIKHEF), A. Wagner (DESY), H. Yamamoto (Tohoku Univ.).

Programme Committee for ILC

J.-P. Delahaye (CERN), E. Elsen (DESY), B. Foster (Univ. Oxford), J. Gao (IHEP), M. Harrison (BNL), H. Hayano (KEK), M. Nozaki (KEK), T. Raubenheimer (SLAC), M. Ross (FNAL), N. Walker (DESY), B. Willis (Columbia Univ.), K. Yokoya (KEK).

Programme Committee for LCWS

U. Baur (Univ. Buffalo), T. Behnke (DESY), J. Brau (Univ. Oregon), T. Camporesi (CERN), M. Danilov (ITEP Moscow), R. Godbole (IISc), A. Gurtu (TIFR), R.-D. Heuer (DESY/ Univ. Hamburg), B. Hsiung (Natl. Taiwan Univ.), J. Jaros (SLAC), D. Karlen (Univ. Victoria), A. Kronfeld (FNAL), D. Miller (UCL), A. Miyamoto (KEK), Y. Okada (KEK), M. Oreglia (Univ. Chicago), H. Park (KNU), R. Patterson (Cornell Univ.), F. Richard (LAL), R. Settles (MPI Munich), J. Timmermanns (NIKHEF), G. Weiglein (Univ. Durham), L. Weiguo (IHEP Beijing), H. Yamamoto (Tohoku Univ.).

Local Organising Committee

T. Behnke (DESY, Chair), K. Büsser (DESY), E. Elsen (DESY), M. Fleischer (DESY), A. Frey (MPI Munich), B. Kniehl (Univ. Hamburg), F. Lehner (DESY), S. Riemann (DESY), N. Walker (DESY)

LCWS and ILC 2007 @ DESY
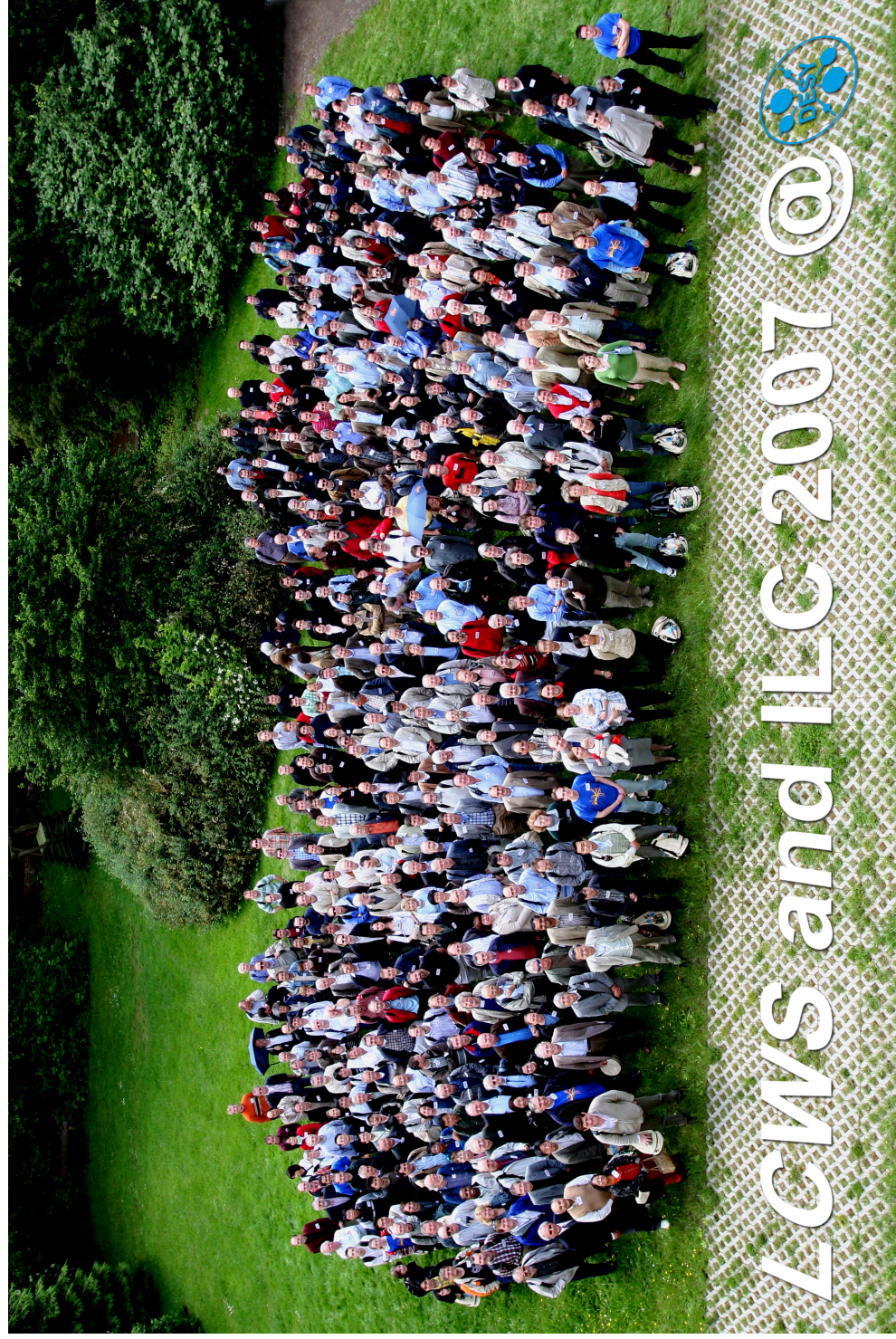
Table of Contents

Volume 1

Plenary Sessions

Higgs and Electroweak Symmetry Breaking
Conveners: H. Logan, T. Barklow, S. Heinemeyer, A. Raspereza, Y. Gao, Y. Okada

SUSY Particles

Conveners: H. Baer, G. Wilson, A. Djouadi, J. List, S. Youl Choi, K. Fujii

New Physics at TeV Scale and Precision Electroweak Studies
Conveners: J. Hewett, K. Mönig, G. Moreau, S. Raychaudhuri

Top and QCD
Conveners: A. Juste, T. Teubner, R. Godbole

$\gamma\gamma$, $e - \gamma$, e^-e^- Physics and Technology
Conveners: J. Gronberg, M. Velasco, M. Krawczyk, V. Telnov, E. Asakawa, K. Cheung

Loop Calculations
Conveners: D. Wackeroth, S. Dittmaier, Y. Yasui

Cosmological Connections

Conveners: M. Battaglia, Z. Zhang, N. Okada

Volume 2

Tracking and Vertexing

Conveners: T. Nelson, D. Peterson, J. Timmermans, M. Winter, H. Park, Y. Sugimoto

Calorimetry and Muons

Conveners: R. Frey, J. Blazey, F. Sefkow, T. Takeshita, B.G. Cheon

Simulation and Reconstruction

Conveners: N. Graf, M. Thomson, C. Gatto, A. Miyamoto

Machine Detector Interface

Conveners: T. Markiewicz, A. Seryi, E. Torrence, W. Lohmann, P. Bambade,
W. Kozanecki, K. Büßer, P. Burrows, T. Tauchi, T. Omori

Data Acquisition and Global Detector Network

Conveners: P. Le Du, D. Haas

Test Beam Contact

Conveners: M. Woods, J. Yu, F. Sefkow, K. Kawagoe

Beam Delivery System

Conveners: D. Angal-Kalinin, H. Yamamoto, A. Seryi

Main Linac

Conveners: L. Lilje, H. Hayano, C. Adolphsen, N. Solyak

Polarization

ATF2

Plenary Sessions

The Detector DCR

Akiya Miyamoto [*]

High Energy Accelerator Research Organization (KEK),
1-1 Oho, Tsukuba, Ibaraki 305-0801, Japan

The Detector Concept Report(DCR) consists of two parts, one for the physics and the other for ILC detectors. It has been prepared as the accompany document of the ILC Reference Design Report. The overview of the detector part of the DCR and the plan for the final release is presented in this talk.

1   Introduction

The preparation of the DCR has been started since LCWS2006 at Bangalore[1]. Four editors for the detector part, Ties Behnke, Chris Damerell, John Jaros and Akiya Miyamoto, have worked together with authors of sub-sections to prepare the document. The preliminary version has been open to the community after the workshop at Beijing (BILCW07)[2]. Taking into account comments from the community as well as those from the Review Panel, it is scheduled to be released in August this year[4].

The goal of the Detector DCR is to make the case that detectors can do the ILC physics, showing detector designs are within our reach, where we are in detector developments and where we are going. On the other hand, the DCR is neither a complete description of a detector nor a review of the ILC detector concepts. The detector DCR is based on Detector Outline Documents (DODs)[6, 7, 8, 9] prepared by four detector concept teams last year as well as new studies since then, but a little focus is put on concept specific issues.

Selected topics of the detector DCR is presented in the next section and the plan for the final release is described in the subsequent section.

2   Overview of the Detector DCR

The goal of the ILC physics includes understanding of the mechanism of mass generation and electroweak symmetry breaking, searching for and perhaps discovering supersymmetric particles and confirming the principle of supersymmetry, and hunting for signs of extra space-time dimensions and quantum gravity[5]. The ILC detectors have to be optimized for these ILC physics targets.

Experimental conditions at the ILC provide an ideal environment for the precision study of elementary particle interactions, thanks to the clean signal conditions and well-defined initial state. Events are recorded without a bias which might be caused by an event trigger. However, the physics poses challenges on detector performances, pushing the limits of jet energy resolution, tracker momentum resolution, and vertex impact parameter resolution, as well as full solid angle coverage. Although benign by LHC standards, the ILC environment poses some interesting challenges of its own.

The world-wide linear collider physics and detector community has worked on these challenges and made impressive progresses. Four teams, GLD[6], LDC[7], SiD[8] and 4th[9], have formed to study detector concepts for the ILC experiments. They have reported their

---

[*]Representing co-editors: Ties Behnke, Chris Damerell and John Jaros

studies as the Detector Outline Documents (DODs) last year, and have kept continuing concept studies. GLD, LDC, and SiD are equipped with a granular calorimeter for particle flow measurements, while 4th aims to achieve a good jet energy resolution by a dual-readout calorimeter. Key parameters of the four detector concepts are summarized in Table 1.

Table 1: *Some key parameters of the four detector concepts. See Table 3 for magnet parameters.*

	GLD	LDC	SiD	4th
VTX	pixel	pixel	pixel	pixel
R_{in}/R_{out} (cm)	2.0/5.0	1.6/6.0	1.4/6.1	1.5/6.1
Main Tracker	TPC[Si]	TPC[Si]	Si	TPC(drift)
R_{in}/R_{out}(TPC[Si]) (cm)	45/200[9/30]	30/158[16/27]	20/127	20/140
L_{half}(TPC[Si]) (cm)	230[62]	208[140]	168	150
# barrel points (TPC[Si])	200[4]	200[2]	5	200(120)
ECAL	Scinti.-W	Si-W	Si-W	Crystal
Barrel R_{in}/L_{half} (cm)	210/280	160/230	127/180	150/240
# X_0	27	23	29	27
HCAL	Scinti.-Fe	Scinti.-Fe	RPC/GEM-W	fiber Dream
Barrel R_{in}/L_{half} (cm)	229.8/280	180/230	141/277.2	180/280
Interaction length	5.8	4.6	4.0	9
Overall Detector				
R_{out}/L_{half} (cm)	720/750	600/620	645/589	550/650

In parallel to the concept studies, R&D on detector technologies have been pursued actively world-wide[10]. Inter-concept teams have been formed to address R&D issues common to concepts.

The detector DCR is based on these activities, but with a little emphasis on concept specific issues.

2.1 Challenges for Detector Design and Technologies

The relatively low radiation environment of the ILC allows detector designs and technologies not possible at the LHC, but the demanding physics goals still challenge the state of the art technologies.

Many of the interesting physics processes at the ILC appear in multi-jet final states, often accompanied by charged leptons or missing energy. The reconstruction of the invariant mass of two or more jets will provide an essential tool for identifying and distinguishing W's, Z's, H's, top and discovering new particles.To distinguish W's and Z's in their hadronic decay mode, the di-jet mass resolution should be comparable to their natural width, say a few GeV or less. The jet energy resolution of $\sigma_E/E < 3 \sim 4\%$ ($30\%/\sqrt{E}$ for jet energies below about 100 GeV), which is about a factor of two better than that achieved at LEP, will provide such di-jet mass resolution. A factor of two improvement in jet energy measurement improves the resolution of the Higgs mass measurement using the four-jet mode of the Higgsstrahlung process by about 20% as shown in Figure 1. It is equivalent to a luminosity gain of about 40%. A similar gain of performance is expected in measurements of such as $\Delta\mathrm{Br}(H \to WW^*)$ and the Higgs self-coupling.

The Higgs measurement from di-lepton recoil mass is important because it is measured without any assumption on its decay mode. In order to measure the Higgs mass at a precision close to the ultimate limit set by the initial beam energy spread, the momentum resolution of the tracking system $(\Delta p_t/p_t)$ has to be less than $1 \times 10^{-3} \oplus 5 \times 10^{-5} p_t (\text{GeV/c})$. Such a high-performance tracking device allows measurements of the center of mass energy

Figure 1: *Reconstructed Higgs di-jet invariant mass for different jet energy resolutions. The analysis has been performed for a center of mass energy of 350 GeV and a total integrated luminosity of 500 fb $^{-1}$*

at about 20 MeV precision by using the process, $e^+e^- \rightarrow \mu^+\mu^-(\gamma)$. In the measurement of the slepton mass using the end point of lepton momentum, a gain of about 40% in luminosity is expected if the momentum resolution improves from from $8 \times 10^{-5} p_t$ to $2 \times 10^{-5} p_t$.

Efficient and clean identification of bottom and charm quark jets are indispensable methods to carry out the ILC physics program. For example, the identification of b and c jets in Higgs decays are essential to measure Yukawa couplings of c and b quarks. b jets identification in the top quark decays are useful to reduce combinatorial background in finding a correct jet combination of their hadronic decay. Quark charge measurements of jets through an efficient reconstruction of secondary and thirdly vertices would be a key method for studies of forward-backword assymetries of b quark. The vertex detector which could measure the impact parameter at precision better than $5 \oplus 10/p\sin^{3/2}\theta$ (μm) will provide the performance to carry out these physics.

Sub-detector performances needed for key ILC physics measurements are summarized in Table 2.

Table 2: *Sub-Detector Performance Needed for Key ILC Physics Measurements.*

Physics Process	Measured Quantity	Critical System	Critical Detector Characteristic	Required Performance
ZHH $HZ \rightarrow q\bar{q}b\bar{b}$ $ZH \rightarrow ZWW^*$ $\nu\bar{\nu}W^+W^-$	Triple Higgs Coupling Higgs Mass $B(H \rightarrow WW^*)$ $\sigma(e^+e^- \rightarrow \nu\bar{\nu}W^+W^-)$	Tracker and Calorimeter	Jet Energy Resolution, $\Delta E/E$	$3 \sim 4$ %
$ZH \rightarrow \ell^+\ell^-X$ $\mu^+\mu^-(\gamma)$ $HX \rightarrow \mu^+\mu^-X$	Higgs Recoil Mass Luminosity Weighted E_{cm} $B(H \rightarrow \mu^+\mu^-)$	Tracker	Charged Particle Momentum Resolution, $\Delta p_t/p_t^2$	5×10^{-5}
$HZ, H \rightarrow b\bar{b}, c\bar{c}, gg$ $b\bar{b}$	Higgs Branching Fractions b quark charge asymmetry	Vertex Detector	Impact Parameter, δ_b	$5\mu\text{m} \oplus 10\mu\text{m}$ $/p(\text{GeV}/c)\sin^{3/2}\theta$

2.2 Machine Detector Interface

The ILC beam induces following backgrounds; disrupted beam, photons and low energy electron-positron pairs generated by beamstrahlung; synchrotron radiation created when beam pass through beam line magnets; muons created by interactions between beam halo and collimators; neutrons created by electron-positron pairs and disrupted beam hitting beam line components; hadrons and muons created by photon-photon interactions.

A careful design of shields against these backgrounds is crucial. Their impacts on detector performances have been studies based on Monte Carlo simulations and estimated background hit rates have been below critical level so far. For an example, a hit occupancy in TPC due to the electron-positron pair background has been estimated by a simulation. TPC takes 100 bunch crossing(BX) of time to readout an event. After superimposing 100 BX of background hits, the hit occupancy is less than 0.2%, which is well below the critical occupancy of 1%.

Concerning the detector integration, the baseline plan is to assemble most of the detectors on surface, then brought them down the underground experimental fall for final assembly. This is to minimize the size of the underground experimental hall and to save the detector construction time.

The baseline design of the ILC foresees one interaction region, equipped with two detectors. The two detectors are laid out in such a way that each can be moved quickly in and out the interaction region thus allowing the sharing of luminosity between both detectors (push-pull operation). Details such as switchover time and frequency are still under discussion and a system with two beam delivery lines will be kept as an option until the detailed engineering design study demonstrates the feasibility of such a push-pull scheme.

2.3 Subsystem Design and Technologies

Technologically oriented description of detector sub-systems for a ILC detector is described in this section, aiming to show what kind of technologies exists for them, their challenges, and required R&Ds to achieve goals.

2.3.1 Vertex Detector

Four to six layers of silicon pixel detectors are used for a vertex detector. In total there are about $10^9 \sim 10^{10}$ pixels of size of about 20 μm^2 or less. The beam pipe radius is 15 mm or less to place the vertex detector as close as to the interaction point. The thickness of each layer of the vertex detector is 0.1% X_0 or less. The vertex detector has to be reasonably hard against radiation and beam induced RF radiation (EMI). To keep background hits occupancy low, it has to be readout our fast or store locally and readout between the beam pulse. Due to a unique feature of the ILC beam structure, which has about 200 msec of quiet period after 1 msec of beam collisions, data of all collisions have to be read out without a front-end trigger for software filltering at later stages. To reach the performance goal, a calibration of internal alignment has to be carefully designed and an effect of powering and cooling to detector allignments should be minimum. There are no proven vertex detector technology to meet the performance goal under the ILC operational condition and R&Ds on more than 10 technologies are pursued worldwide extensively.

2.3.2 Silicon Strip Tracker

Silicon strip tracker is used as the main tracker of SiD concept and intermediate, forward or endcap trackers of other concepts. The silicon strip tracker is robust against unexpected radiation backgrounds; it is fast such that signal charges are collected before the next bunch crossing and an impact of beam backgrounds are minimum; it is precise such that point resolutions of $5 \sim 10\mu$m are achievable. While silicon strip detector has been used extensively in other experiments, large detector system has typically $2\%X_0$ of material per layer. The most of them is attributable to dead material needed for support, cooling and readout. This dead material is a source of a peformance deterioration. To significanly reduce these dead material while keeping the benefits of slicon strip detectors is one of the most significant challenges of R&Ds for silicon tracking at the ILC[4].

2.3.3 Gaseous Tracker

Time Projection Chamber (TPC) is considered as a main tracker by GLD, LDC and 4th concepts. The tracking of the TPC is robust because of many three-dimensional point measurements along the track. Material in the tracking volume is minimum and particle identification is possible. Detectors such as GEM[11] and MicroMegas[12] are candidates for the endplate detector, in order to meet the goal of the momentum resolution, Beam tests of a small test system suggest that the performance goal is within the technology in hand. Still a design to minimize a positive ion build up in the drift volume has to be developed and a gas with lowest diffusion and less contamination of Hydrogen atoms should be investigated. Operatability in non-uniform magnetic field caused by the anti-DID magnet and design of end-plate electronics with short radiation length is another challenge of the TPC R&D. International collaboration, LCTPC[13], is formed and pursing these studies.

2.3.4 Calorimeter

Calorimeter is a key device to achieve a good jet energy resolution. The GLD, LDC and SiD concepts are equipped with a particle flow calorimeter, which is characterized by a highly granular segmentation both in lateral and longitudinal directions. A sandwitch structure of absobers and small sensors are adopted. Both electromagnet and hadron calorimeters are placed in side the coil of the detector solenoid magnet. In the particle flow analysis, charged particle signals in the calorimeter are set aside by using tracker information, and calorimeter information is used only to measure neutral particle energies. Therefore, the high granularity in calorimeter segmentation and an excellent shower reconstruction alogirthm are crucial. On the other hand, 4th concept is equipped with a dual read out calorimeter: scintillating fibers for all charged particles in a shower and clear fibers for Cherenkov light induced by electrons and positrons. Despite it's few longitudinal sampling, it aims at a good jet energy resolution with a high resolution calorimeter.

A development of calorimeter technologies is one of the most active area of the ILC detector R&D[4] and many technologies are currently pursed, for example; for electromagnetic calorimeter, sandwiches of tungsten or lead absorber and silicon, MAPS, or scintillator and semiconductor photon sensor readout; for hadron calorimeter, lead or iron as absorber and scintillator and photon sensor readout, gas chamber and GEM or RPC readout.

Table 3: *Summary of the parameters of ILC detector magnet, compared with that of CMS.*

	unit	CMS	GLD	LDC	SiD	4th(In/Out)
Magnetic Field	Tesla	4	3	4	5	3.5/1.5
Coil Radius	m	3.25	4	3.16	2.65	3/4.5
Coil Half length	m	6.25	4.43	3.3	2.5	4/5.5
Stored Energy(E)	GJ	2.6	1.6	1.7	1.4	5.7
Cold mass (M)	ton	220	78	130	117	
E/M	kJ/kg	12.3	20	13	12	

2.3.5   Superconducting Magnet

A detector magnet is one of the major part of the detector cost. The GLD, LDC and SiD concepts use a large bore coil, while 4th concept use a dual coil system where the outer coil is used instead of iron flux return. Typical parameters of them are summarized in Table 3. As seen in the table, the parameters of the magnet for the ILC detector is similar to the CMS magnet and it's experience is useful.

2.3.6   Data Acquisition

The ILC RF system is operated at the frequency of 5Hz. During the beam period of 1 msec, the collision rate is about 3 MHz. A pipeline system is mandatory to record data of all collisions. The burst collision is followed by about 200 msec of a quiet time. Thus average event rate is about 15kHz, which is moderate compare to LHC. No hardware trigger is planned and event selection is done by software after readout data of all bunch collisions. On the other hand, zero suppression and data compression at detector front ends are importantl to minimize a load to the data acquisition system, because the ILC detectors are equipped with high granularity sensors.

2.3.7   Luminosity, Energy, and Polarization

The beam energy should be know to be less than 100 ppm precission for the precise Higgs recoil mass measurement. For physics at GigaZ or W threshold, it is required to be less than 50 ppm. About 200 ppm has been achieved at LEP and SLC. Several R&Ds[4] are in progress to achieve a factor of 2 or more improvement. These R&Ds include the studies on developments of a high precision beam position monitor to measure beam energy using upstream beam line magnets as a spectrometer; the beam energy measurement by detecting synchrotron lights emitted from downstream beam line bending magnets; and the measurement of the energy weighted luminosity from lepton's acollinearity of processes such as Bhabha and $\mu\bar{\mu}(\gamma)$.

Beam polarization should be measured at precision better than 0.5%. A gain in physics potential is anticipated if $\Delta P \sim 0.25\%$ or less. It is measured by Compton polarimeters at upstream and down stream of IP. Developments of the instruments for the Compton measurements is important.

Detector R&D requires supports by test beam resources. Resources are limited and optimal coordination world wide is necessary. Test Beams working group has been organized by WWS and the first report has been presented[14].

2.4   Sub detector performance

Each concept team has developed their own detector full simulator and reconstruction tools and pursued studies on performances of such as vertexing, tracking, jet reconstruction and so on. It is impossible to cover all results here and only typical ones are shown. Performances are more or less similar among the concepts.

The tracking performance has been studied for both TPC and Silicon main tracker. For the TPC main tracker, the track finding efficiency has been studied using Z pole events where Z decays to $d\bar{d}$. The obtained the efficiency exceeded 99%, though realistic effects such as those by a non-uniform magnetic field, space charges and background hits have yet to be taken into account. SiD adopts an inside-out tracking finding method, where the vertex detector is used to find a seed track. According to this method, the efficiency of about 99% is achived for a track whose origin is within 1 cm from the IP using a sample of $e^+e^- \to Z \to q\bar{q}$ events at 500 GeV center-of-mass energy. The momentum resolution of the tracking device has been studied by the GLD. Combining information of TPC, the intermediate tracker and the vertex detector, the momentum resolution is found to be consistent with the goal of $\Delta p_t/p_t \sim 10^{-3} \oplus 5 \times 10^{-5} p_t$ (GeV/c).

Impact parameter resolutions of the tracking system have also studied by each concept teams and found to be consistent with the performance goal.

As already pointed out in the sub-section 2.1, the pure and efficient tagging of b quark and c quark jets is important for the ILC physics. The topological vertexing as pioneered by SLD has the potential for sucha high performance tagging. The code has been ported for studies of ILC detectors. An initial result of its study is shown in Figure 2[15]. The obtained purity and efficiency using a realistic detector model is promising.

GLD, LDC and SiD all utilize sampling calorimeters, whose energy resolution is essentially determined by the sampling fraction. For single particles, the energy resolution of the electromagnetic calorimeters ranges from 14 to 17%/$\sqrt{E}$ for the stochastic term and

Figure 2: *Efficiency and purity for tagging a b-quark(red square) and c-quark(green triangle) jets in Z decays, using a full simulation. The blue-circle points indicate the further improvement in performance of the charm tagging in events with only bottom background is relevant.*

those for the hadron calorimeter ranges from 50 to 60%/$\sqrt{E}$. For jet energy measurements, the particle flow analysis (PFA) is crucial to achieve the required level of performance. At the ILC detectors, the trackers can measure charged particles better than the calorimeters.
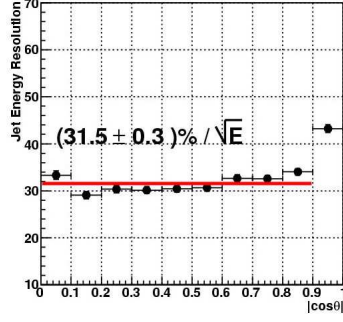
Figure 3: *The stochastic term of the jet energy resolution ($\sigma_{90}/\sqrt{E_{jet}}$) as a function of $|\cos\theta_{jet}|$ in the case of $e^+e^- \to q\bar{q}$ (light quarks only) events at Z pole energy. A result by GLD-PFA for the GLD detector.*
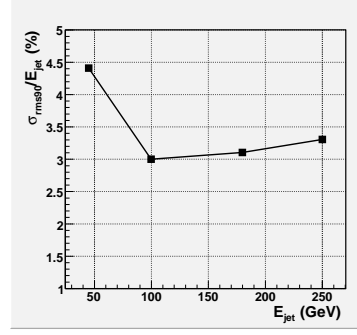
Figure 4: *The relative jet energy resolution, σ_{90}/E_{jet}, of PandoraPFA averaged in the region $|\cos\theta_{jet}| < 0.7$, as a function of the jet energy.*

Thus, in the PFA, tracker signals are used to get charged particle information and calorimeter signals are used only to reconstruct neutral particles. Since calorimeter is sensitive to charged particles as well, it is essential to develop a sophisticated algorithm to fully utilize the fine granularity of the calorimeters, identify and remove the calorimeter signals produced by charged particles.

To this end, PFA algorithm have been studied extensively by many groups. For an example, the algorithm such as WolfPFA[16] and GLD-PFA[17] consists of following steps; cluster calorimeter signal cells; discard clusters whose position and energy are matched with extrapolated charged tracks and use tracker information for such particles; consider remaining clusters as neutral partiles and use calorimeter information. The PandoraPFA[18] uses the similar approach but introduced algorithm of re-clustering to disconnect merged clusters or reconnect divided clusters, resulting better performance. Another approach includes the algorithm to use the charged track information as a seed of the calorimeter clustering[19].

The performance of the GLD-PFA has

Figure 5: *Jet energy resolution in terms of $\sigma_{90}/\sqrt{E}$ obtained with PandoraPFA and the Tesla TDR detector model plotted as a function of TPC outer radius and magnetic field.*

been studied using the Z pole events where Z decays to u, d or s quarks only. The distribution of the observed particle energy tends to have two-gaussian distribution, broader one being caused by a loss of particles due to imperfect acceptance. σ_{90} is introduced as a measure of the PFA performance. σ_{90} is defined as the RMS of samples containing 90% of all samples. The resultant performance is shown in Figure 3 as a function of the jet angle.

Figure 6: *Recoil mass spectrum reconstructed for a 120 GeV Higgs, with full background simulation.*
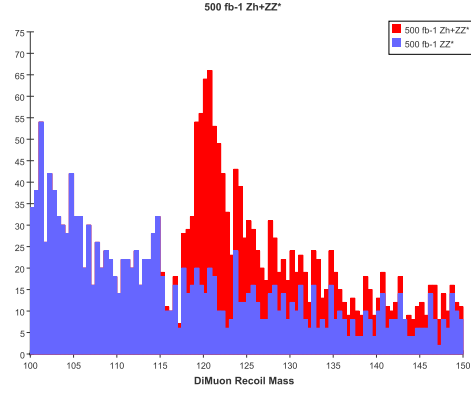
Figure 7: *Di-muon recoil mass for ZZ^* background (blue) and ZH signal plus background (red) for centrally produced muons.*

In the central region of $|\cos\theta_{jet}| < 0.9$, the obtained resolution is consistent with the goal.

However, for higher energy jets, the resolution of GLD-PFA gets worse and not satisfactory. On the otherhand, the PandoraPFA has successfully updated its algorithm recently and the resolution of about $30\%\sqrt{E}$ has been achieved for a jet of energy up to 100 GeV. The jet energy dependence of the energy resolution ($\Delta E/E$) of Pandora PFA is shown in Figure 4. Further improvements of the performance are anticipated because studies using a perfect PFA indicates that improvements in the resolution for high energy jets would be achievable.

The number of detector optimization studies have been performed with the PandoraPFA. For example, Figure 5 shows how the jet energy resolution depends on TPC radius (which is almost the same as the inner radius of calorimeter) and magnetic field. This study is suggesting that the resolution improves with increasing the magnetic field strength but the larger radius of the calorimeter is more important than the stronger magnetic field.

The dual readout calorimeter system of the 4th concept does not have longitudinal segmentation, thus the jet energy is determined mainly by the calorimeter after the jet clustering using the cone algorithm. The tracker information is used to correct low p_t tracks. The energy resolution of about $40\%\sqrt{E}$ has been reported[20].

2.5 Integrated Physics Performance

In this paper, studies on the Higgs recoil mass measurement and on the $\nu\bar{\nu}b\bar{b}$ chanel of the Higgsstrahlung process are presented. A few more physics studies are described in the DCR. The scope of the studies in this section is rather limited and does not cover the full physics potential of ILC. The purpose of this section is to illustrate the level of maturity of both the understanding of the detectors and of the reconstruction and analysis algorithms. Especially, development of the particle flow algorithms is still advancing rapidly. Therefore results presented in the following should be interpreted as a snapshot of an ongoing development, where significant further improvements can be expected in coming years.

The one of the most challenging reactions for the tracking system of the ILC detector is the measurement of the Higgs mass using the recoil mass technique. LDC has studied both $H\mu\mu$ and Hee final states of $e^+e^- \to ZH$ process near threshold ($\sqrt{s} \sim 250$ GeV), including background processes of 4 fermions and 2 fermions final states. Based on a data sample equivalent of 50 fb^{-1}, a signal from the Higgs has been reconstructed as shown in Figure 6. From a simple fit to the mass distribution, the error of Higgs mass measurement is estimated to about 70 MeV and the relative cross section error being 8%.

A similar analysis has been performed in the context of the SiD detector concept, at a center of mass energy of 350 GeV. The analysis fully simulated the machine background events as well. The background events have been combined with the signal events at the Monte Carlo hit level prior to digitization, then fed into a full track reconstruction code. Requiring two muons with momentum greater than 20 GeV, events whose invariant mass of the two-muon system is consisten with Z were selected. Figure 7 shows the recoil mass distribution for the ZZ^* background in blue and ZH signal plus background in red. The precision of the Higgs mass from this measurement, based on a comparison between the mass distribution reconstructed and template Monte Carlo distributions, is estimated to be 135 MeV. Taking in to account the larger center of mass energy of this analysis, the result is consistent with the previous analysis.

GLD has studied the process, $e^+e^- \to ZH$ at the center of mass energy of 350 GeV, where Z decays to invisibly and H decays to jets and the Higgs mass is 120 GeV/c^2. In this case, compared to the four-jet mode, a beam energy constraint does not work for improve measurements due to the missing particles. But there is no ambiguity in the mass measurement due to exchanges of colored particles in the final state because all of visible particles stem from the Higgs decay. Thus high-performance PFA measurements is crucial for a good measurement. $e^+e^- \to ZZ$ is the major background process and an excellent vertex detector is a key to reject them by discarding non-b quark jets.

The preliminary result of GLD is shown in Figure 8. The analysis was based on a Monte Carlo sample of 200 fb^{-1}. The effects of beamstrahlung as well as bremsstrahlung were included in the event generation. The Higgs signal is clearly seen above backgrounds, while further improvements of PFA performance is awaited to achieve the signal width consistent with $30\%\sqrt{E}$.
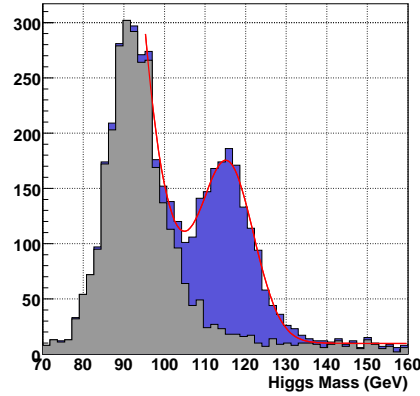
Figure 8: *Reconstructed mass spectrum for Higgs candidates in the $ZH \to \nu\bar{\nu}b\bar{b}$ decay.*

2.6 The case for two detectors

Two complementary detectors are crucial for ILC, because it offers competing experiments, cross checking of results and scientific redundancy for precision measurements at the level

which is not created by more than one analysis teams for one detector; significant increase of the scientific productivity, despite the spliting of the ILC luminosity; maximal participation of the global particle physics community; the backup if one detector needs significant down time. There are numerous historical examples where complementary experiments were critical. Further arguments will be find in Ref.[21].

2.7 Costs

The Costing Panel has been formed by WWS to estimate costs of each concept by a common approach. They have estimated the costs in light of the GDE costing rule and attempt to identify breakdown and cost drivers. The cost breakdowns are different among concepts depending on how to categorize items, for example, a separation or inclusion of M&S and man power costs. But, as naturally expected, calorimeters and magnets are the cost drivers. Overall, there is a reasonable agreement among estimates by GLD, LDC and SiD and the total cost lies in the range of $400 \sim 500$ M\$ with about 20% error.

2.8 Options

The one option is GigaZ, which aims to run at Z pole energy with a luminosity of $\sim 4 \times 10^{33}$cm^{-2}s^{-1} and accumulate 10^9 Z events in one year. Despite the high event rate, the event overlap probability is less than 1% and not a problem. Challenges are to run with a polarized positron beam with a frequent change of its polarity in order to reduce systematics and measure the beam energy at precision less than 3×10^{-5}.

The other is Photon Collider for experiments of $\gamma\gamma$ and $e\gamma$ collisions. It provides a novel opportunity of physics such as studies of $\Gamma(H \rightarrow \gamma\gamma)$ and CP properties of the Higgs. To make a $\gamma\gamma$ collision in the ILC, the beam lines have to be modified to change the crossing angle from 14 mrad to around 25 mrad. In addition, a $\gamma\gamma$ beam dump system has to be developed, to to deal with the γ energy after collision: the γ beam is collimated and has the energy of about 50% of the initial beam, but can not be steered or smeared out by magnets like e^+/e^- beams. For Photon Collider experiments, near beam line components of detectors has to be modified to open a space to inject a laser light and to extract γ beams. Additional space in a detector hall may be necessary for a laser optical cavity.

3 Comments

Editors appreciate for your patient reading of the draft and sending us valuable comments. We have received many technical comments, which will be included in the next version to be released after the workshop. There are another class of comments, where inputs from community are crucial.

One is regarding the goal of the jet energy measurement. It has been set as $\Delta E/E \sim 30\%/\sqrt{E} \oplus const.$, where the constant terms are usually neglected. This goal is to achieve a jet-pair invariant mass resolution $(\Delta M_{12}/M_{12})$ which is sufficient to separate W and Z in their hadronic decay modes. The mass resolution of the jet pair is approximated, in terms of the jet energy resolution$(\Delta E_i/E_i; i = 1, 2)$, as

$$\frac{\Delta M_{12}}{M_{12}} \sim \frac{1}{2}\left(\frac{\Delta E_1}{E_1} \oplus \frac{\Delta E_2}{E_2}\right), \tag{1}$$

where the mass of the jets and the error of the angle between the jets are neglected. For higher enrgy jets, the jet energy resolution is dominated by the constant term which would be mainly determined by a limitation of the PFA performance. Therefore, it would be more appropriate to express the goal of the jet energy resolution in terms of $\Delta E/E$ rather than the coefficient of the stocastic term. On the other hand, physics studies has been carried out assuming the formula, $\Delta E/E \sim \alpha/\sqrt{E}$ and studies assuming constant $\Delta E/E$ are yet to be done. The PFA performances will improve time to time and conservative opinions to keep the original arguments for the DCR have been made.

One another issue is regarding the momentum resolution: what do we gain by having the resolution which is significantly better than the original goal of $1 \times 10^{-3} \oplus 5 \times 10^{-5} p_t$? If the di-lepton recoil mass of the process, $e^+e^- \to ZH$, is measured at $\sqrt{s} = 350$ GeV for $M_h = 120$ GeV, the resolution improves with better momentum resolution. On the otherhand, as long as this measurement is concerned, much better performance is obtained if measured just above the threshold.

The statement in the draft DCR will be rephrased taking account these arguments.

4 Summary

The overview of the draft detector DCR is presented. The detector DCR describes detector designs, R&Ds on detector technologies, and expected performances, aiming to make the case for the ILC detectors.

The author of the DCR consists of those who have participated in the detector concept studies, linear collider detector R&D or have an interest in the physics and detectors for ILC. Those who are qualified are invited and encouraged to sign the DCR. The web page has been prepared for the sign up.

The draft is open to the public at `http://www.linearcollider.org/wiki` and comments from the community is welcomed. The DCR Review Panel has been formed by WWS. Preliminary comments from the panel is due by the end of LCWS2007 and the final report is expected by the beginning of July. Taking into accounts these comments, the DCR is scheduled to submit to ILCSC in August.

References

[1] LCWS2006, `http://www.tifr.res.in/~lcws06/`.

[2] Beijing Workshop, `http://bilcw07.ihep.ac.cn/`.

[3] See, `http://www.linearcollider.org/cms/?pid=1000025`.

[4] The Detector RDR is released as the detector volume of RDR this summer. It is now available at the RDR web site[3] together with other volumes on Executive Summary, Physics and Accelerator. Details on ILC detectors will be found in the detector volume of RDR.

[5] For example, see P. Zervas, in these proceedings; the physics volume of RDR[3].

[6] K. Abe *et al.*, *GLD Detector Outline Document*, arXiv:physics/0607154 (2006).

[7] D. Kiseilewska *et al.*, *Detector Outline Document for the Large Detector Group*, `http://www.ilcldc.org/documents/dod/` (2006).

[8] The SiD Concept Group, *SiD Detector Outline Document*, `http://hep.uchicago.edu/~oreglia/siddod.pdf` (2006).

[9] Patric Le Du *et al.*, *Detector Outline Document for the Fourth Concept Detector at the International Linear Collider*, `http://www.4thconcept.org/4doc.pdf` (2006).

[10] ILC Detector R&D Panel Website, `https://wiki.lepp.cornel.edu/ilc/bin/view/Public/WWS/`.

[11] F. Sauli, Nucl. Instr. & Methods, **A386** 531 (1997).

[12] Y. Giomataris *et al.*, Nucl. Instr. & Methods, **A376** 29 (1996).

[13] The LCTPC Collaboration, `http://www.lctpc.org/`.

[14] Road map for ILC Detector R&D Test Beams, KEK Report 2007-3, July 2007.

[15] H. Hillert, in these proceedings.

[16] V. Morgunov and A. Raspereza, arXiv:physics/0412108.

[17] T. Yoshioka, ECONF C0508141:ALCPG1711,2005.

[18] M.A. Thomson, arXiv:physics/060726.

[19] O. Wendt, in these proceedings.

[20] D. Barbareschi *et al.*, `//http://www.4thconcept.org/DCR.pdf`.

[21] See `http://physics.uoregon.edu/~lc/historical-examples.html`.

The ILC Physics Case

W. Kilian[1] and P. M. Zerwas[2]

1- Fachbereich Physik, Universität Siegen, D-57068 Siegen, Germany

2- Deutsches Elektronen-Synchrotron DESY, D-22603 Hamburg, Germany
Inst. Theor. Physik E, RWTH Aachen, D-52074 Aachen, Germany
Laboratoire de Physique Théorique, U. Paris-Sud, F-91405 Orsay, France

Experiments in the energy range from the scale of electroweak symmetry breaking to the TeV scale are expected to be crucial for unraveling the microscopic structure of matter and forces. The high precision which should be achieved in experiments at lepton colliders, is a necessary ingredient for providing a comprehensive picture of the mechanism breaking the electroweak symmetries and generating mass, the unification of forces, involving most likely supersymmetry, and the structure of space-time at small distances. In addition, clarifying the nature of the particles which build up cold dark matter in the universe, needs a lepton collider to match the high experimental precision which will be reached in cosmology experiments.
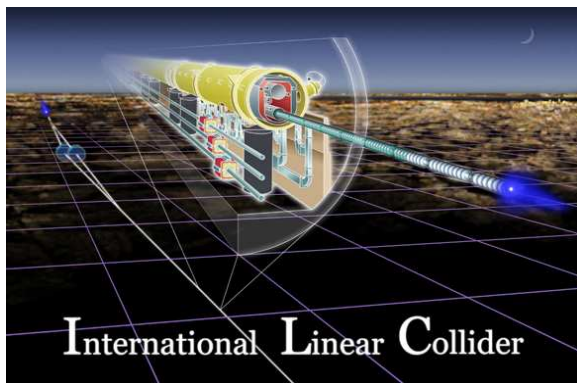
1   Introduction

High-energy physics has been tremendously successful in unraveling the basic laws of nature in the microcoscopic world. With the Standard Model of particle physics a picture has emerged which adequately describes the structure of matter and forces. However, this picture is still incomplete internally, and externally, driven by theoretical arguments and experimental observations, the model should be embedded in a more comprehensive theory which unifies the different degrees of freedom. These points lead us in a natural way to a set of crucial experimental questions. Answering these questions will unify our view of the microscopic world and thus deepen our understanding of the universe enormously.

Derived from our present knowledge of particle physics, solutions to the following problems, which are central to physics in general, must be approached experimentally:

 – the mechanism responsible for breaking the electroweak symmetries and generating mass;

- the unification of forces, including gravity in the end;

- the structure of space-time at small distances.

This set of fundamental problems is complemented by a new branch in the development of particle physics:

- the connection to cosmology.

Besides the nature of particles which may form components of cold dark matter in the universe, several other problems connect microscopic physics and cosmology, the baryon asymmetry in the universe being a prominent example.

Based on the present picture of physics, the scientific value of any new accelerator is determined by the unique contributions the facility can offer in approaching solutions to these problems.

We are in the fortunate position that the next generation of accelerators holds the promise of providing answers to these questions indeed. They will greatly advance the understanding of the microscopic world in particular and the universe as a whole. With the Large Hadron Collider LHC, soon starting at CERN, a first decisive step will be taken. From this machine which will operate at the TeV energy frontier, we expect breakthrough discoveries in the complex of electroweak symmetry breaking and in the physics area beyond the Standard Model. However, this hadron facility must be complemented with a lepton collider which will play a key role in drawing a comprehensive and high-resolution picture of electroweak symmetry breaking and of the physics layer underneath the Standard Model. Our present knowledge of physics is expected to converge to a unified picture in this layer.

The e^+e^- Linear Collider ILC, which is now in the design phase, would be the counterpart in a tandem with LHC, cf. Refs. [2, 3]. In analogy to the relation between LEP and Tevatron, the ILC energy of 1 TeV in the lepton sector is equivalent in many aspects to the higher LHC energy, effectively about 5 TeV in the quark sector. Moreover, by including the characteristic scale of electroweak symmetry breaking, the ILC covers one of the most crucial energy domains in particle physics. Discoveries at LHC may also point to physics scales beyond the reach of ILC; this area could be accessed by a multi-TeV e^+e^- facility [4].

1.1 Physics scenarios

Electroweak symmetry breaking and Higgs mechanism

The mechanism which breaks the electroweak symmetries, is the still missing cornerstone of the Standard Model. High-precision analyses strongly suggest the Higgs mechanism, including a light Higgs boson, to be responsible for the breaking of the electroweak symmetries and for generating the masses of the fundamental particles [5]. If the Higgs boson will be discovered at LHC, it must be established experimentally that this mechanism is indeed responsible for generating the masses of the particles. The precision with which this question can be answered at ILC, exceeds the LHC by an order of magnitude. In addition, in the most probable light mass range ILC provides the unique opportunity for establishing the Higgs self-energy potential, which is the essential *agens* for inducing the symmetry breaking.

In extensions of the Standard Model, like supersymmetric theories or Little Higgs theories, the Higgs sector is much more complex. A spectrum of Higgs particles will in general be realized, demanding precision studies of masses, mixing and couplings to explore the structure of the Higgs sector.

If the standard Higgs mechanism, including a set of Higgs particles, were not realized in nature, but alternatively a higgs-less theory as suggested, for example, in theories of electroweak symmetry breaking by new strong interactions at low scales, cf. Ref. [6], such a scenario could be explored in the scattering of electroweak bosons at LHC and ILC. However, taking advantage of the less complex final-state topology at the lepton collider ILC, experiments at this machine can cover the entire threshold region of the new strong interactions and open the door to an arena of novel interactions. Other higgs-less scenarios, as formulated in some theories of extra space dimensions, also give rise to new interactions between the standard electroweak gauge bosons mediated by novel TeV scale resonances.

Unification and supersymmetry

Progress in particle physics has opened the path to the truly unified understanding of nature. The unification of the electromagnetic, weak and strong interactions is strongly indicated by the evolution of the couplings merging at high energies, cf. Refs. [7] , and expected to be joined by gravity in the ultimate unification near the Planck scale. A key role in the evolution is played by supersymmetry, cf. Ref. [8]. LHC has the potential to discover supersymmetry in the next few years, and the theoretical concept can be verified in conjunction with ILC which is an essential instrument in this process.

Supersymmetry embraces several of the fundamental points introduced at the beginning – providing a stable bridge between the scale of electroweak symmetry breaking and the Planck scale; leading to the unification of the standard couplings and paving the path for including gravity in particle physics. In addition, the lightest supersymmetric particle is a compelling candidate for forming a component of the large amount of cold dark matter observed in the universe. Thus, this theory could not only play a fundamental role in particle physics but also links particle physics closely with cosmology.

In fact, high-precision measurements of electroweak observables, combined with constraints from the observation of the cold dark matter density by WMAP, allow for a large area of fairly low-scale supersymmetry parameters, though no firm conclusions can be drawn as yet. In the favorable case a significant fraction of the non-colored supersymmetric particles, i.e., partners of the photon, of the electron etc, should be observed at ILC operating in the first phase at 500 GeV, and more in the upgraded 1 TeV phase of the machine. LHC would play the complementary role for colored particles, the supersymmetric partners of the quarks and gluons.

Quite generally, apart from exceptional corners of parameter space, LHC experiments will discover supersymmetric particles if this symmetry is realized in nature not far above the electroweak scale. However, the spectrum of particles in this new world that can be detected at LHC will remain incomplete, particularly in the light non-colored sector. Moreover, the precision in the determination of their properties, like masses, mixings and couplings, remains limited. Operating ILC will, first, lead to a comprehensive view of the spectrum of light particles and, second, improve the accuracy in measuring their properties by one to two orders of magnitude.

Both points are very important for several reasons. Foremost, the completeness of the spectrum and the greatly improved accuracies will allow us to extrapolate the parameters to the unification scale where the fundamental supersymmetric theory and the microscopic picture of its breaking mechanism can be reconstructed.

This way we can study the structure of physics at scales close to the Planck scale. This

provides us with the unique opportunity to shed light on an energy domain where the roots of particle physics in particular, and physics quite generally, may be located. Information on this area from other branches of particle physics, potentially proton decay experiments etc, will remain very scarce so that the telescope character of high-precision high-energy experiments, in coherent LHC+ILC analyses, is of very high value.

High precision is also required in exploring the properties of the lightest supersymmetric particle which may contribute to the observed density of cold dark matter in the universe. Anticipating improved results from cold dark matter measurements in the near future, the accuracy of a lepton collider will be needed for masses, mixings and couplings to match eventually the accuracy of cosmology data. In addition, once the particle properties are determined accurately, observed fluxes in astroparticle search experiments can be exploited to map the distribution of cold dark matter in the universe. Thus ILC experimental results could reach far beyond the domain of particle physics.

Extra space dimensions

If extra space dimensions in the universe, cf. Refs. [9, 10, 11], are realized already at low energies, the experimental determination of the fundamental scale of gravity and the number of dimensions are of central interest. Starting these analyses with LHC, the picture can be refined considerably at ILC. By varying the energy of the collider, these two characteristics of gravity and space-time at short distances can be disentangled. By observing masses and widths of excited graviton states in other scenarios, the length scale and the curvature in an additional fifth dimension of space-time can be determined.

Many other measurements could be performed in this area, e.g., measurements of the spin of gravity fields, mixings of scalar fields etc, so that a large set of observables could be exploited at ILC which, joined with LHC results, would enable us to zoom in on the underlying theoretical picture.

1.2 Basic experimental parameters

It is generally assumed that the International Linear Collider ILC will be operated in two phases. In the first phase the cm energy will reach $\sqrt{s} = 500$ GeV, in the second phase 1 TeV. In each of the phases a total integrated luminosity of about 1 ab^{-1} is expected to be accumulated when the runs are completed. The first phase gives access to light Higgs bosons, the top quark, light supersymmetric particles, the second phase to strong electroweak symmetry breaking, heavy new particles in the Higgs and supersymmetric sectors, extra space dimensions and other high-scale phenomena. Some scenarios may suggest extensions of the linear collider program beyond the TeV energy.

Experiments at ILC will focus on high-precision analyses. If the electron and positron beams are polarized, typically $P_{e^-} \sim 90\%$ and $P_{e^+} \sim 60\%$, the experimental potential of the machine can truly be exhausted, cf. Ref. [12]. In addition to longitudinally polarized beams, spin rotators can generate transversely polarized electron/positron beams. The polarization of the electron beam is a necessary condition for many experimental analyses while the polarization of the positron beam is generally viewed as an auxiliary tool which however may turn out to be crucial in some special physics scenarios.

The luminosity in running the machine as an e^-e^- collider is significantly smaller as the electrons repel each other when the bunches of the two colliding beams traverse each other.

In addition to the high-energy electron-positron collider mode, the machine can be operated in the GigaZ mode. Running at low energies on top of the Z-boson resonance, some 1 billion events, i.e., a factor fifty more than at LEP, may be collected within a few months. Combined with W and *top* threshold analyses, this leads to the ultimate precision in the electroweak sector in the foreseeable future. Both electron and positron polarization is essential for these analyses.

Finally, by means of Compton back-scattering of laser light, the ILC can also be operated as an $e\gamma$ and $\gamma\gamma$ collider. A fraction of 80% of the incoming electron/positron energy can be transferred to the photon(s), cf. Ref. [13]. The spectrum is maximal at the upper edge if the incoming e^-/e^+ beam and the laser photon beam are longitudinally polarized with opposite helicities. In this way colliding $e\gamma$ and $\gamma\gamma$ experiments can be performed with 90% and 80% of the total e^+e^- energy, respectively, and about one third of the luminosity accumulating in a 20% margin below the maximum possible energy. In some scenarios these modes open up unique discovery channels for particles, in the Higgs and slepton sectors of supersymmetric theories, or in the particle towers of compositeness models, for example, cf. Ref. [14].

2 Electroweak symmetry breaking

Unraveling the mechanism which breaks the electroweak symmetries and generates the masses of the fundamental standard particles — electroweak gauge bosons, leptons and quarks — is one of the key problems of particle physics, cf. Refs. [15]. Theoretical realizations span a wide range of scenarios extending from weak to strong breaking mechanisms. Examples on one side are the Standard Model and its supersymmetric extension involving light fundamental Higgs fields, and new strong interaction models without a fundamental Higgs field on the other side. Symmetry breaking by specific boundary conditions for gauge fields in the compactification of extra space dimensions gives rise to higgs-less models. The forthcoming experiments at LHC will lead to a breakthrough in revealing the breaking mechanism and in making the first steps into this new territory while ILC should provide the comprehensive understanding of the theory underlying the breaking of the electroweak symmetries and the generation of mass. Thus the experimental solution of this problem at LHC and ILC will unravel one of the fundamental laws of nature.

2.1 Higgs mechanism in the Standard Model

The analysis of the precision electroweak data from LEP, SLC and elsewhere points clearly to a light mass value of the Higgs particle [17], if the electroweak symmetries are broken by the Higgs mechanism in the framework of the Standard Model:

$$M_H = 76^{+33}_{-24}\,\text{GeV} \ \text{ and } \ M_H < 144\,\text{GeV} \ \ (95\%\,\text{CL}). \tag{1}$$

The direct search for the SM Higgs boson at LEP has set a lower limit of 114 GeV on the Higgs mass [18].

The Higgs particle of the Standard Model is guaranteed to be discovered at LHC, cf. Ref. [19]. The combination of several channels in different mass ranges gives rise to a large significance for the detection, i.e., $> 5\sigma$ for an integrated luminosity of 30 fb^{-1}.

After the discovery of the Higgs particle, it must be established experimentally that the Higgs mechanism is responsible indeed for breaking the electroweak symmetries and for generating the masses of the fundamental particles. This requires the precise determination

of the profile of the Higgs particle. First steps in model-independent analyses of its properties can be taken at LHC by performing precision measurements of the Higgs mass, the ratios of some of the Higgs couplings, and bounds on couplings [20].

At ILC a clean sample of Higgs events can be generated in Higgs-strahlung, $e^+e^- \to ZH$, and WW fusion, $e^+e^- \to \bar{\nu}\nu H$. The clear signals above small backgrounds, cf. Fig. 1, allow the model-independent high-precision determination of the Higgs profile, besides the
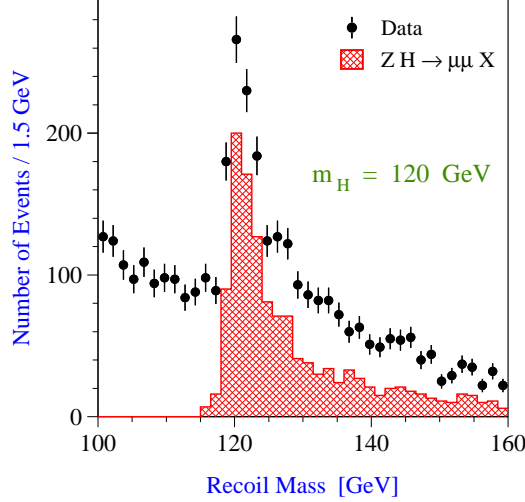
Figure 1: Signal and background of inclusive Higgs boson production in Higgs-strahlung; Ref. [21].

mass, the spin of the particle and, most important, its couplings, including the trilinear self-coupling in double-Higgs production. This information will be extracted from a set of production cross sections and angular distributions, and from decay branching ratios. Below a Higgs mass of 140 GeV a rich ensemble of final states can be studied; the ensemble of channels is reduced for heavier Higgs masses.

Higgs couplings

If the masses of the fundamental particles p are generated by the interaction with the Higgs field in the vacuum, the Higgs couplings must grow with the particle masses m_p:

$$g(Hpp) = (\sqrt{2}G_F)^{1/2}m_p. \qquad (2)$$

From the production cross sections for Higgs-strahlung and WW fusion the absolute values of the Higgs couplings to the electroweak gauge bosons Z and W can be determined in a model-independent way. Measuring the ratios of branching ratios involving quarks and leptons on one side, and the electroweak gauge bosons on the other side, also Higgs couplings to quarks and leptons can be determined in a model-independent way. A special case is the

Higgs-top coupling which can be measured in Higgs radiation off top-quark pairs produced in e^+e^- annihilation. The accuracy which can be achieved for various couplings is predicted at the per-cent level [22]. How well the Higgs coupling – mass relation can be tested, is apparent from Fig. 2 which clearly demonstrates the linear relation between the Higgs couplings and
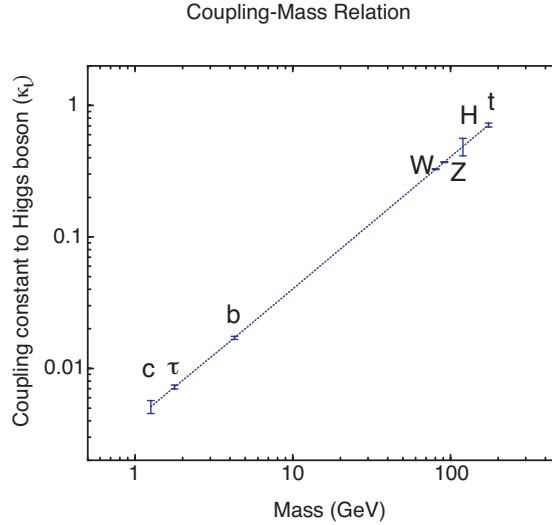
Figure 2: The relation between the Higgs coupling of a particle and its mass in the Standard Model; Ref. [23]. The error bars correspond to the accuracy expected from ILC data.

the masses for typical particle species in the Standard Model – electroweak gauge bosons, quarks and leptons, up and down types.

Higgs potential

The specific form of the Higgs potential, $V \sim [|\phi|^2 - v^2/2]^2$ shifts the ground state of the Higgs system to a non-zero field strength, $v/\sqrt{2}$. Specifying the direction of the field strength in charge space breaks the electroweak symmetries. The gauge and Yukawa interaction energy of other fields with the non-zero Higgs field in the vacuum can be reinterpreted as the mass of these particles. Expanding the potential about the minimum,

$$V = \frac{1}{2} M_H^2 \, H^2 + \frac{1}{2} \frac{M_H^2}{v} \, H^3 + \frac{1}{8} \frac{M_H^2}{v^2} \, H^4 \tag{3}$$

the trilinear coupling plays the crucial role for the non-trivial shape of the potential. This parameter can be measured in the process of double-Higgs production, $e^+e^- \to ZHH$ and $\bar{\nu}\nu HH$, as exemplified in Fig. 3. The product of small couplings and the large fraction of phase space absorbed by the masses render the production cross sections small. Nevertheless, the trilinear coupling is expected to be measured at ILC at a level of 12% for Higgs masses below about 140 GeV. The less crucial quartic coupling in the Standard Model seems out of reach for any collider in the foreseeable future. Thus the element in the Higgs potential which

is most crucial for generating the Higgs medium in the ground state, can be reconstructed at ILC. In the upper intermediate Higgs mass range access to the trilinear coupling could be given by SLHC [25].
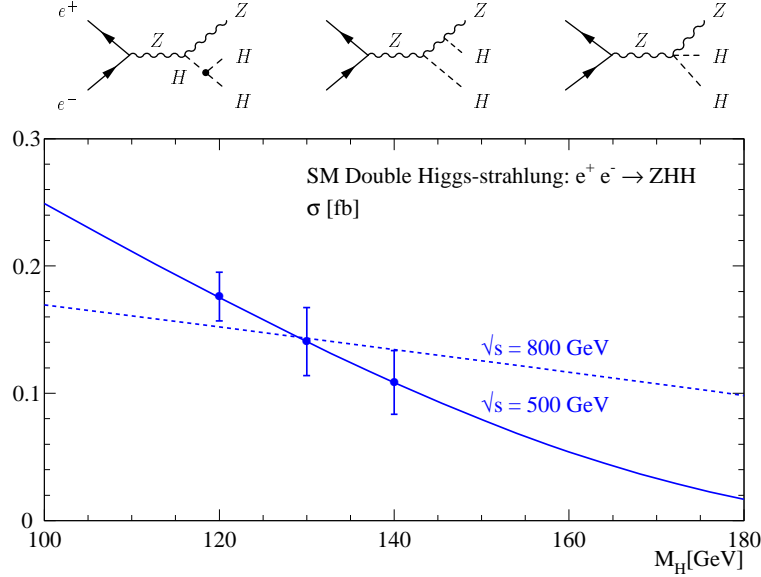
Figure 3: Cross section of Higgs pair production for measurements of the triple Higgs coupling; Ref. [24]. The error bars correspond to the accuracy expected from ILC data.

Direct measurements of the ZZH coupling to an accuracy of 1%, and of the HHH coupling to about 10%, give lower limits of about 3 and 1 TeV, respectively, for scales of new physics [26] . Since the microscopic dynamics of electroweak symmetry breaking is one of the central problems in particle physics, establishing these values would be a valuable and unique result of experiments at ILC — and even more so if deviations from the SM predictions would be discovered.

2.2 SUSY Higgs bosons

In supersymmetric theories the Higgs sector must be extended to at least two iso-doublet fields so that five or more physical Higgs particles are predicted. In the minimal extension the mass of the lightest neutral scalar Higgs particle h^0 is bounded from above to about 140 GeV, while the masses of the heavy neutral scalar and pseudoscalar Higgs bosons, H^0 and A^0, as well as the pair of charged Higgs bosons, $H^\pm$, may range from the electroweak scale to the (multi-)TeV region. The four heavy Higgs bosons tend to be nearly mass-degenerate. The upper bound on the lightest Higgs mass is relaxed to about 200 GeV in more general scenarios if the fields remain weakly interacting up to the Planck scale as naturally assumed in supersymmetric theories.

Minimal supersymmetric theory

While search and study of the light h^0 Higgs boson follows the pattern summarized above for the SM Higgs boson in most of the parameter space, the heavy scalar and pseudoscalar Higgs bosons are produced in mixed pairs, in the same way as the charged Higgs bosons:

$$e^+e^- \to H^0A^0 \ \text{ and } \ H^+H^- . \tag{4}$$

For masses of the heavy Higgs bosons beyond about 200 GeV they cannot be detected at LHC in a wedge in $M_A/\tan\beta$ parameter space that is centered around the medium mixing angle $\tan\beta \sim 7$ and opens up to high Higgs masses. The wedge can be covered by pair production in e^+e^- collisions for masses $M_{H,A} \le \sqrt{s}/2$, i.e., up to 500 GeV in the TeV phase of the machine. However, beyond this range, single production in photon-photon collisions,

$$\gamma\gamma \to H^0 \ \text{ and } \ A^0 \tag{5}$$

can cover the wedge up to Higgs masses of 800 GeV if a fraction of 80% of the total e^+e^- energy is transferred to the $\gamma\gamma$ system by Compton back-scattering of laser light [27]. Thus, a $\gamma\gamma$ collider may be the only facility in which, beyond the SM-type light Higgs boson, heavy Higgs bosons may be discovered before a multi-TeV linear collider can be operated. It is demonstrated in Fig. 4 how well the Higgs bosons can be detected in the two collider modes.
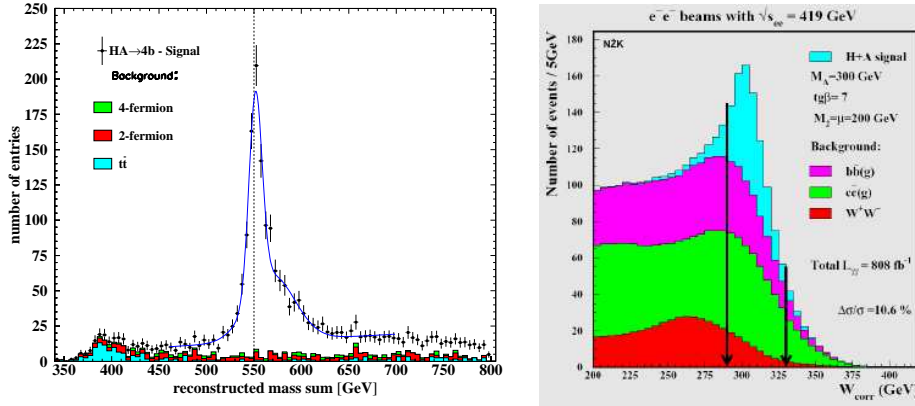
Figure 4: Left: Pair production of MSSM Higgs bosons HA in e^+e^- collisions; Ref. [28]; Right: Single Higgs production H and A in $\gamma\gamma$ fusion at a photon collider; Ref. [29].

High-precision measurements of the light Higgs mass can be exploited to determine parameters in the theory which are difficult to measure otherwise. By evaluating quantum corrections, the trilinear coupling A_t, for example, may be calculated from the Higgs mass, Fig. 5. For an error on the top mass of $\delta m_t = 100$ MeV, cf. Ref. [31], and an error on the Higgs mass of $\delta m_h = 50$ MeV, cf. Ref. [16], A_t can be determined at an accuracy of about 10%.
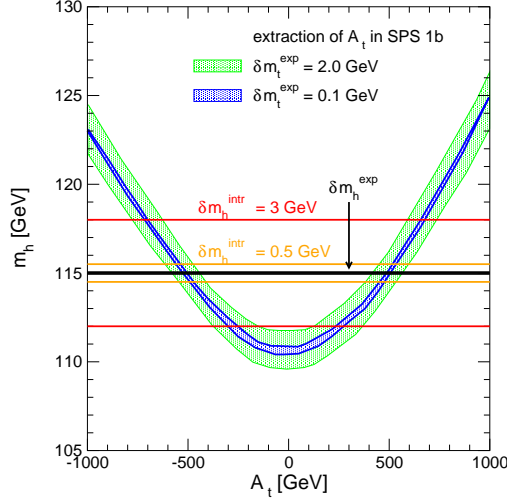
Figure 5: Extracting the trilinear coupling A_t from radiative corrections to the light MSSM Higgs mass; Ref. [30].

Extended supersymmetric theories

A large variety of theories, grand unified theories, string theories, etc., suggest additional Higgs fields beyond the minimal set in supersymmetric theories. Adding a complex iso-scalar to the iso-doublets, an additional pair of scalar and pseudoscalar Higgs particles is predicted. The axion-type character of the pseudoscalar boson renders this particle preferentially light. In general, the standard set of light and heavy Higgs bosons is expected in analogy to the MSSM, augmented however by a light scalar and a pseudoscalar Higgs boson, cf. Ref. [32], as illustrated in Fig. 6.

If the light pseudoscalar Higgs boson decays to b-quarks, a fan of b-jets is expected in Higgs-strahlung as the scalar Higgs bosons may decay to a pair of light pseudoscalar Higgs bosons, generating at least four b's in the final state [33, 34]. Nevertheless, a no-lose theorem for discovering at least one Higgs boson has been established for ILC while the situation is presently less clear for LHC.

2.3 Strong electroweak symmetry breaking

Within the Standard Model and its supersymmetric extensions, the Higgs field is introduced as a fundamental degree of freedom. Dynamical electroweak symmetry breaking is rooted in new strong interactions, not necessarily involving a Higgs boson. If global symmetries of these interactions are broken spontaneously, a set of Goldstone bosons will be generated, such as pions after breaking chiral symmetries in QCD. By absorbing these Goldstone bosons, longitudinal degrees of freedom and masses are generated for gauge bosons. Several scenarios have been developed along this path quite early [6, 35] as an alternative to the standard Higgs mechanism and more recently in a variant responding to the success of the light Higgs picture in accounting for the high-precision data in the electroweak sector.
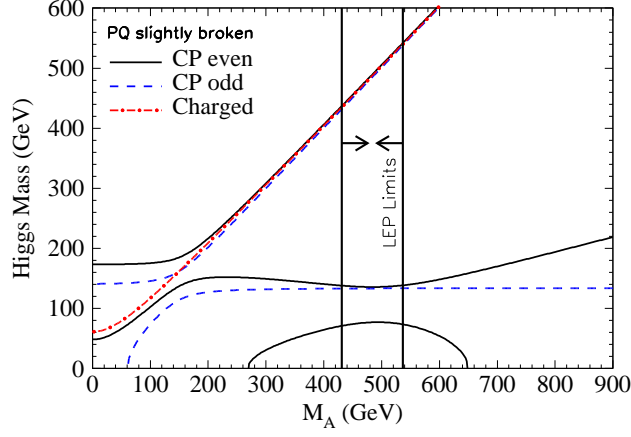
Figure 6: Typical Higgs mass spectrum in the non-minimal supersymmetric model NMSSM; Ref. [32].

Little-Higgs models

These models [36] are based on new unspecified interactions that are characterized by a scale Λ of order 10 TeV or more. The breaking of a huge global symmetry, e.g., SU(5) $\rightarrow$ SO(5), generates a set of [pseudo-]Goldstone bosons with properties characterized by the scale $F \sim \Lambda/4\pi$ which is close to a TeV. Collective breaking of the global symmetry retains a light mass at the level of $F/4\pi \sim v$ for some of the pseudo-Goldstone bosons, providing candidates for the SM-type Higgs boson.

While the new (multi-)TeV scalars and vectors may be searched for at LHC, at ILC their properties can be determined very precisely even if they remain virtual at the available energies [37, 38], cf. Fig. 7. Moreover, the entire parameter range of the model, as expected on general grounds, can be covered in searching for deviations from the Standard Model predictions in processes such as $e^+e^- \rightarrow f\bar{f}$, W^+W^-, ZH, and $\gamma\gamma \rightarrow H$.

Little-Higgs models predict a rich spectrum of new particles not only at the TeV scale, but new states may also be realized at low scales. Axion-type pseudoscalar bosons may be associated with the spontaneous breaking of $U(1)$ factors in the extra global symmetries. These particles have properties analogous to Higgs bosons [39]. They are produced parallel to Higgs bosons and their decay modes may be b-jet pairs:

$$e^+e^- \rightarrow t\bar{t}\eta \ \text{ with } \ \eta \rightarrow b\bar{b}. \tag{6}$$

Thus, instead of one Higgs resonance peak in the invariant $b\bar{b}$ mass in addition to the Z resonance, two peaks would be observed experimentally, Fig. 7. In $\gamma\gamma$ collisions the two states could be disentangled by using linearly polarized photon beams; scalars are generated in collisions of photons with parallel, pseudoscalars with perpendicular polarization vectors.
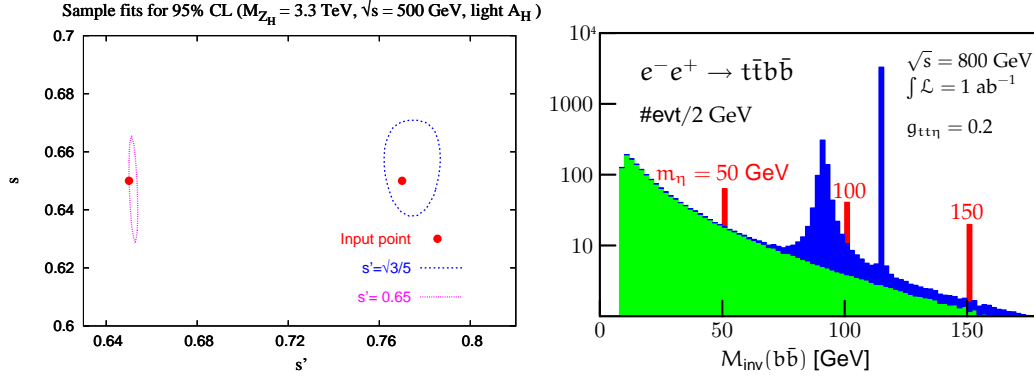
Figure 7: Little-Higgs models. Left: Sensitivity of SM processes to LH parameters; Ref. [38]. Right: Higgs and pseudoscalar boson production; Ref. [39].

Strongly interacting W, Z bosons

If no Higgs boson will be observed with mass below 1 TeV, quantum-mechanical unitarity demands strong interactions between the electroweak gauge bosons, becoming effective at energies $(4\sqrt{2}\pi/G_F)^{1/2} \simeq 1.2$ TeV to damp the growth of the amplitudes for (quasi-)elastic WW scattering processes. To achieve compatibility with the S, T parameters extracted from the precision electroweak data at low energies, the underlying theory must deviate from the QCD template as a strongly-interacting theory.

The new interactions between the electroweak bosons, generically called W, can be expanded in a series of effective interaction terms with rising dimensions [40]. Scattering amplitudes are expanded correspondingly in a series characterized by the energy coefficients s/Λ_*^2. Demanding CP-invariance and isospin-invariance, as suggested by the value of the ρ parameter very close to one, two new dimension-4 interaction terms must be included in the expansion, $\mathcal{L}_4 = \alpha_4 \langle W_\mu W_\mu \rangle^2$ and $\mathcal{L}_5 = \alpha_5 \langle W_\mu W_\nu \rangle^2$, with coefficients $\alpha_{4,5} = v^2/\Lambda_{*4,5}^2$ expressed in the new strong interaction scales Λ_*, cf. Ref. [41]. To compensate the growth of the scattering amplitudes in the perturbative expansion, the new contributions must match the perturbative loop factor $1/16\pi^2$, i.e., the scale parameters are bounded from above by the value $4\pi v$.

Quasi-elastic WW scattering,

$$WW \to WW \text{ and } ZZ \tag{7}$$

can be measured in the processes $e^+e^- \to \bar{\nu}\nu WW$ and $\bar{\nu}\nu ZZ$. The new interaction terms affect the total cross sections and the final-state distributions [41]. The reconstruction and separation of W and Z bosons in these analyses is a necessary condition, which can be fulfilled indeed in the clean environment of a lepton collider [42, 43]. Since the impact of the new interactions grows with the energy, ILC in the 1 TeV phase provides the most sensitive instrument for these studies. In fact, cf. Fig. 8, the entire range of Λ_* values can be covered experimentally:

$$\Lambda_* \leq 4\pi v \simeq 3\,\text{TeV} . \tag{8}$$
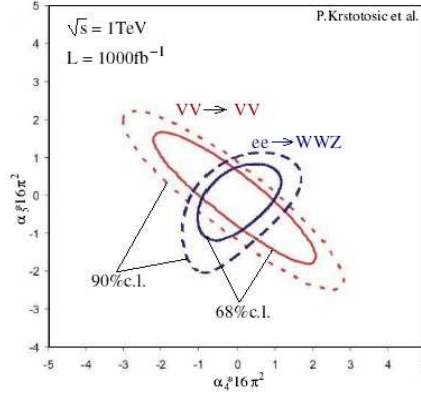
Figure 8: Measurement of parameters in new strong interactions of electroweak W bosons; Ref. [43].

The Λ_* values determine the masses of the resonances associated with the new interactions. The predictions can be helpful in the search for these resonances at LHC.

2.4 Extra space dimensions

A plethora of models have been constructed which can break the electroweak symmetries in scenarios of extra space dimensions. We will focus on a few characteristic aspects.

(i) In Randall-Sundrum models, a scalar *radion* field is introduced to stabilize the distance between the SM and the gravity brane. Carrying the same quantum numbers as the Higgs field, these two fields can mix and the properties of the Higgs boson will be altered [44]. In particular the branching ratio for Higgs decays to gluon jets may increase dramatically due to dominating radion decays to gluons, cf. [45].

(ii) Kaluza-Klein states can affect the $\gamma\gamma$ coupling and other loop-induced couplings of the Higgs field. Since the $\gamma\gamma$ width of the Higgs particle can be determined with an accuracy of 2% in the $\gamma\gamma$ fusion process at a photon-photon collider, the measurement provides the opportunity to study the particle sector associated with universal extra dimensions, for example, cf. Ref. [46].

(iii) Without introducing a scalar Higgs field, electroweak symmetries can be broken by choosing appropriate *boundary conditions* for the gauge fields in the compactified fifth dimension, with the fifth components of the gauge fields transformed to the longitudinal components of the massive gauge fields in $D = 4$ space-time dimensions. Cancellations which delay unitarity violations at high energies in WW scattering, are achieved by the exchange of Kaluza-Klein fields [47]. Sum rules connect the quartic couplings of the gauge fields with the couplings between gauge fields and Kaluza-Klein fields. The Kaluza-Klein states can be searched for at LHC and ILC [48]. At ILC the couplings are expected to be measured, even for the exchange of virtual Kaluza-Klein fields, quite accurately.

3   Supersymmetry and unification

If supersymmetry is realized in nature, cf. Ref. [49], this fundamental symmetry will have an impact across all areas in microscopic physics and cosmology. In the Higgs sector, supersymmetry would be crucial for generating a light Higgs boson and stabilizing the electroweak scale in the background of the grand unification and Planck scales. The contribution of the supersymmetric particle spectrum to the evolution is essential for the electromagnetic, weak and strong gauge couplings to approach each other at a high scale, a necessary condition for the unification of all three gauge interactions. In addition, local supersymmetry provides a rationale for gravity by demanding the existence of spin-2 gravitons.

No firm prediction is possible for the mass scale of supersymmetry. However, for moderate values of the Higgs mixing parameter $\tan\beta$ a fairly low mass spectrum is indicated in the constrained minimal supersymmetric model by combining results from radiative corrections to electroweak precision observables, $(g_\mu - 2)/2$ and $b \to s\gamma$, with the measurement of the cold dark matter density at WMAP, cf. Fig. 9. The spectrum corresponding to a parameter set with close to maximal probability is depicted in Fig. 9. This spectrum had been chosen as a benchmark set SPS1a$'$ for a minimal supergravity scenario in the SPA project [51]. For the large $\tan\beta$ range, the typical mass scale shifts to somewhat larger values but, when
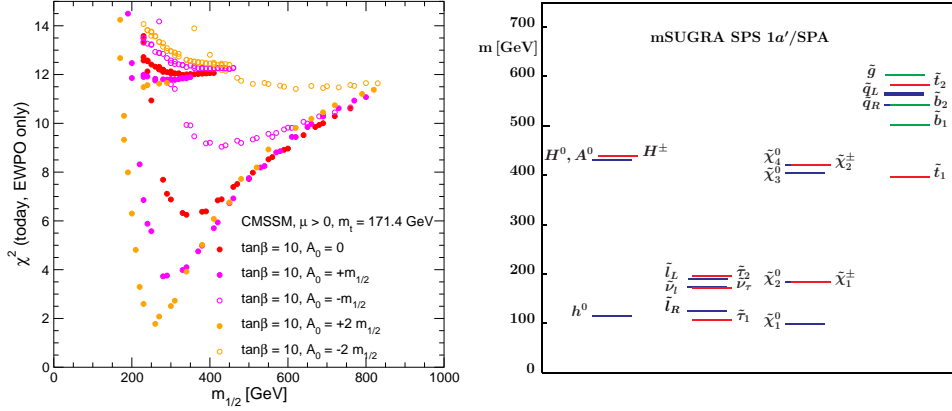
Figure 9: Left: Probability distribution of supersymmetry parameters (CMSSM/mSUGRA) from precision data for $\tan\beta = 10$; Ref. [50]. Right: The corresponding mass spectrum near the maximum, encoded in the benchmark point SPS1a$'$; Ref. [51].

using the approach of Ref. [50], the quality of the fit is worse.

The hadron collider LHC and an e^+e^- linear collider are a perfect tandem for exploring supersymmetry, cf. Ref. [52]. The heavy colored supersymmetric particles, squarks and gluinos, can be discovered for masses up to 3 TeV with large rates at LHC. Subsequent cascade decays give access to lower mass particles. The properties of the potentially lighter non-colored particles, charginos/neutralinos and sleptons, can be studied very precisely at an e^+e^- linear collider by exploiting in particular polarization phenomena at such a facility. After the properties of the light particles are determined precisely, the heavier particles can subsequently be studied in the cascade decays with similar precision.

Coherent hadron and lepton analyses will provide a comprehensive and high-precision picture of supersymmetry at the electroweak scale, cf. Refs. [53, 54]. Moreover, the emerging picture defines, on one side, a solid basis for the reconstruction of the fundamental supersymmetric theory near the Planck scale, and for the connection of particle physics with cosmology on the other side.

3.1 Properties of supersymmetric particles

For illustration the parameters of the mSUGRA reference point SPS1a$'$ [51], a derivative of the Snowmass point SPS1a [55], will be adopted. This point gives a comprehensive picture of the potential which is offered by coherent analyses at high energy hadron and e^+e^- colliders. It is characterized by the following values of the soft parameters at the grand unification scale:

$$
\begin{aligned}
&M_{1/2} = 250 \text{ GeV} \quad &M_0 = 70 \text{ GeV} \\
&A_0 = -300 \text{ GeV} \quad &\text{sign}(\mu) = + \\
&\tan\beta = 10
\end{aligned}
\tag{9}
$$

The universal gaugino mass is denoted by $M_{1/2}$, the scalar mass by M_0 and the trilinear coupling by A_0; the sign of the higgsino mass parameter μ is chosen positive and $\tan\beta$, the ratio of the vacuum-expectation values of the two Higgs fields, in the medium range. The modulus of the higgsino mass parameter is fixed by requiring radiative electroweak symmetry breaking so that $\mu = +396$ GeV. As shown by the supersymmetric particle spectrum in Fig. 9, the squarks and gluinos can be studied very well at the LHC while the non-colored gauginos and sleptons can be analyzed partly at LHC and in comprehensive and precise form at an e^+e^- linear collider operating at a total energy up to 1 TeV.

Masses

At LHC, the masses can best be obtained by analyzing edge effects in the cascade decay spectra, cf. Ref. [56]. The basic starting point is the identification of a sequence of two-body decays: $\tilde{q}_L \to \tilde{\chi}_2^0 q \to \tilde{\ell}_R \ell q \to \tilde{\chi}_1^0 \ell\ell q$. The kinematic edges and thresholds predicted in the invariant mass distributions of the two leptons and the jet determine the masses in a model-independent way. The four sparticle masses [$\tilde{q}_L$, $\tilde{\chi}_2^0$, $\tilde{\ell}_R$ and $\tilde{\chi}_1^0$] are used subsequently as input for additional decay chains like $\tilde{g} \to \tilde{b}_1 b \to \tilde{\chi}_2^0 bb$, and the shorter chains $\tilde{q}_R \to q\tilde{\chi}_1^0$ and $\tilde{\chi}_4^0 \to \tilde{\ell}\ell$, which all require the knowledge of the sparticle masses downstream of the cascades. Residual ambiguities and the strong correlations between the heavier masses and the LSP mass are resolved by adding the results from ILC measurements which improve the picture significantly.

At ILC, very precise mass values can be extracted from threshold scans and decay spectra. The excitation curves for chargino $\tilde{\chi}_{1,2}^\pm$ production in S-waves rise steeply with the velocity of the particles near the thresholds,

$$
\sigma \sim \sqrt{s - (\tilde{M}_i + \tilde{M}_j)^2}
\tag{10}
$$

and they are thus very sensitive to their mass values. The same holds true for mixed-chiral selectron pairs in $e^+e^- \to \tilde{e}_R^+ \tilde{e}_L^-$ and for diagonal pairs in $e^-e^- \to \tilde{e}_R^- \tilde{e}_R^-$, $\tilde{e}_L^- \tilde{e}_L^-$ collisions, cf. Fig. 10. Other sfermions, as well as neutralinos, are produced generally in P-waves, with
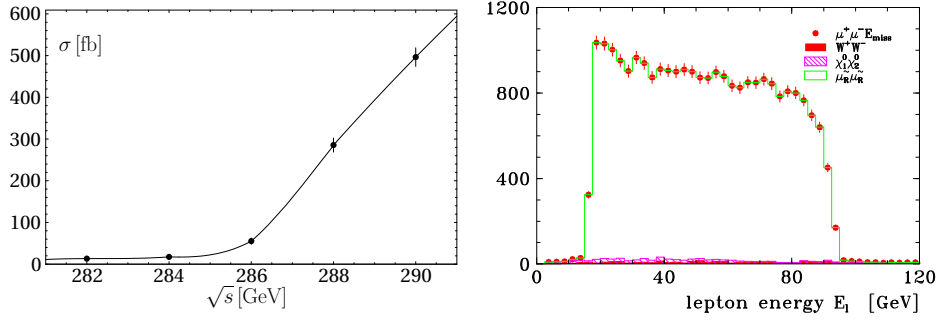
Figure 10: Left: Mass measurement in selectron $\tilde{e}^-\tilde{e}^-$ pair production; Ref. [57]; Right: Smuon and neutralino edges in smuon decays; Ref. [58].

a less steep threshold behavior proportional to the third power of the velocity. Additional information, in particular on the lightest neutralino $\tilde{\chi}_1^0$, can be obtained from the sharp edges of 2-body decay spectra, such as $\tilde{l}_R^- \to l^- \tilde{\chi}_1^0$. Denoting maximum and minimum edge of the decay lepton spectrum by $E_\pm$, cf. Fig. 10, slepton and $\tilde{\chi}_1^0$ masses can be derived from

$$
\begin{aligned}
m_{\tilde{\ell}} &= \sqrt{s}\,[E_+ E_-]^{\frac{1}{2}}/(E_+ + E_-) \\
m_{\tilde{\chi}_1^0} &= m_{\tilde{\ell}}\,[1 - 2(E_+ + E_-)/\sqrt{s}]^{\frac{1}{2}}
\end{aligned}
\tag{11}
$$

The accuracy in the measurement of the LSP $\tilde{\chi}_1^0$ mass can be improved at ILC by two orders of magnitude compared with LHC.

The values of typical mass parameters and their related measurement errors are presented in Tab. 1: "LHC" from LHC analyses and "ILC" from ILC analyses; the third column "LHC+ILC" presents the corresponding errors if the experimental analyses are performed coherently, i.e., the light particle spectrum, studied at ILC with high precision, is used as input set for the LHC analysis.

Spins

Determining the spin of new particles is an important measurement to clarify the nature of the particles and the underlying theory. This is necessary to discriminate the supersymmetric interpretation of new particles from other models. A well-known example is the distinction between supersymmetric theories and theories of universal extra space dimensions in which new Kaluza-Klein states carry spins different from supersymmetric particles.

The measurement of spins in particle cascades at LHC is an experimental challenge [59]. Spin measurements of sfermions at ILC, on the other hand, are quite easy. The polar angular distribution of smuon pairs, for example, approaches the characteristic $\sin^2\theta$ law for energies sufficiently above threshold. The smuons can be reconstructed up to a discrete ambiguity; false solutions in the reconstruction generate a flat background underneath the signal [60]. By contrast, the determination of $spin = 1/2$ for charginos and neutralinos requires the analysis of angular final-state distributions [60].

Particle	Mass	"LHC"	"ILC"	"LHC+ILC"
h^0	116.9	0.25	0.05	0.05
H^0	425.0		1.5	1.5
$\tilde{\chi}_1^0$	97.7	4.8	0.05	0.05
$\tilde{\chi}_2^0$	183.9	4.7	1.2	0.08
$\tilde{\chi}_4^0$	413.9	5.1	$3-5$	2.5
$\tilde{\chi}_1^\pm$	183.7		0.55	0.55
$\tilde{e}_R$	125.3	4.8	0.05	0.05
$\tilde{e}_L$	189.9	5.0	0.18	0.18
$\tilde{\tau}_1$	107.9	$5-8$	0.24	0.24
$\tilde{q}_R$	547.2	$7-12$	$-$	$5-11$
$\tilde{q}_L$	564.7	8.7	$-$	4.9
$\tilde{t}_1$	366.5		1.9	1.9
$\tilde{b}_1$	506.3	7.5	$-$	5.7
$\tilde{g}$	607.1	8.0	$-$	6.5

Table 1: Accuracies for representative mass measurements of SUSY particles in individual LHC, ILC and coherent "LHC+ILC" analyses for the reference point SPS1a$'$ [masses in GeV]. $\tilde{q}_R$ and $\tilde{q}_L$ represent the flavors $q = u, d, c, s$; cf. Ref. [53].

Mixings

Mixing parameters must be extracted from measurements of cross sections and polarization asymmetries. In the production of charginos and neutralinos, both diagonal or mixed pairs can be exploited: $e^+e^- \rightarrow \tilde{\chi}_i^+ \tilde{\chi}_j^-$ [$i,j = 1,2$] and $\tilde{\chi}_i^0 \tilde{\chi}_j^0$ [$i,j = 1,\ldots,4$]. The production cross sections for charginos are binomials in $\cos 2\phi_{L,R}$, the mixing angles rotating current to mass eigenstates. Using polarized electron and positron beams, the mixings can be determined in a model-independent way [61, 62].

The same methods can be applied to determine the mixings in the sfermion sector. The production cross sections for stop particle pairs, $e^+e^- \rightarrow \tilde{t}_i \tilde{t}_j^c$ [$i,j = 1,2$], depend on the mixing parameters $\cos/\sin 2\theta_{\tilde{t}}$ which can be determined with high accuracy by making use of polarized electron beams [63].

The measurement of the discrete quantum numbers of sfermions is another basic process. Using polarized electron and positron beams, the L/R quantum numbers of scalar electrons and positrons can be identified unambiguously even if the masses are nearly degenerate [12].

Couplings

Supersymmetry predicts the identity of Yukawa and gauge couplings among particle partners, in generic notation,

$$F\tilde{F}\tilde{V} = FFV \tag{12}$$

for gauge bosons V and gauginos $\tilde{V}$, and for fermions F and their scalar partners $\tilde{F}$. These fundamental relations can be studied experimentally in pair production of charginos and neutralinos which is partly mediated by the exchange of sneutrinos and selectrons in the t-channel, as well as selectron and sneutrino pair production which is partly mediated by neutralino and chargino t-channel exchanges.

An example is presented in Fig. 11 for the sensitivity which can be achieved at ILC in testing the identity of Yukawa and gauge couplings in selectron pair production. The
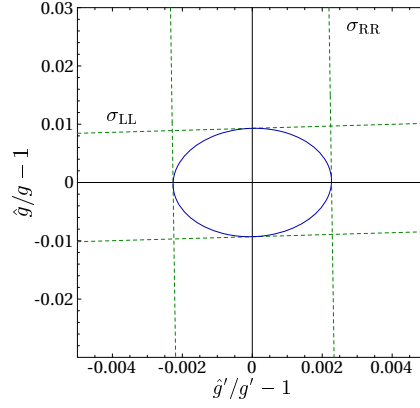
Figure 11: Relating the SU(2) and U(1) $\ell\tilde{\ell}\tilde{V}$ Yukawa couplings experimentally to the corresponding gauge couplings $\ell\ell V$ in selectron pair production; Ref. [57].

separation of the electroweak SU(2) and U(1) couplings is possible if polarized electron beams are available. At the end of course an overall analysis is required which takes into account the measurements of the masses and gaugino/higgsino mixing parameters of the neutralinos exchanged in the t-channel.

Same-sign dilepton production can be exploited at LHC to measure the identity $q\tilde{q}\tilde{g} = qqg$ for super-QCD Yukawa couplings [64]. Model-independent measurements of the couplings can be approached by making use of decay branching ratios determined in linear collider experiments.

3.2   Fundamental supersymmetric theory

The measurements described in the previous section provide the initial values for the evolution of the gauge couplings and the soft SUSY breaking parameters in the Lagrangian to the grand unification scale, cf. Ref. [65], where in many scenarios the fundamental supersymmetric theory is defined. The values at the electroweak scale are connected to the fundamental parameters at the GUT scale M_U by the renormalization group equations; to leading order,

$$
\begin{aligned}
&\text{gauge couplings} &&: \alpha_i = Z_i\,\alpha_U \\
&\text{gaugino masses} &&: M_i = Z_i\,M_{1/2} \\
&\text{scalar masses} &&: M_{\tilde{j}}^2 = M_0^2 + c_j M_{1/2}^2 + \textstyle\sum_{\beta=1}^{2} c'_{j\beta}\Delta M_\beta^2 \\
&\text{trilinear couplings} &&: A_k = d_k A_0 + d'_k M_{1/2}
\end{aligned}
$$

The index i runs over the gauge groups $i = $ SU(3), SU(2), U(1). To this order, the gauge couplings, and the gaugino and scalar mass parameters of soft supersymmetry breaking depend on the Z transporters $Z_i^{-1} = 1 + b_i \alpha_U/(4\pi) \log(M_U^2/M_Z^2)$. The scalar mass parameters $M_{\tilde{j}}^2$

	Present/"LHC"	GigaZ/"LHC+ILC"
M_U	$(2.36 \pm 0.06) \cdot 10^{16}\,\mathrm{GeV}$	$(2.360 \pm 0.016) \cdot 10^{16}\,\mathrm{GeV}$
α_U^{-1}	24.19 ± 0.10	24.19 ± 0.05
$\alpha_3^{-1} - \alpha_U^{-1}$	0.97 ± 0.45	0.95 ± 0.12

Table 2: Precision in extracting the unified gauge coupling α_U, derived from the meeting point of α_1 with α_2, and the strong coupling α_3 at the GUT scale M_U. The columns demonstrate the results for the expected precision from LEP and LHC data, as well as the improvement due to a GigaZ linear collider analysis, cf. Ref. [53].

depend also on the Yukawa couplings. Beyond these approximate solutions, the evolution equations have been solved numerically.

Gauge coupling unification

Measurements of the gauge couplings at the electroweak scale strongly support the unification of the couplings [66] at a scale $M_U \simeq 2 \times 10^{16}$ GeV, with a precision at the per-cent level. The couplings do not meet exactly, cf. Fig. 12 and Tab. 2, most evident after taking into
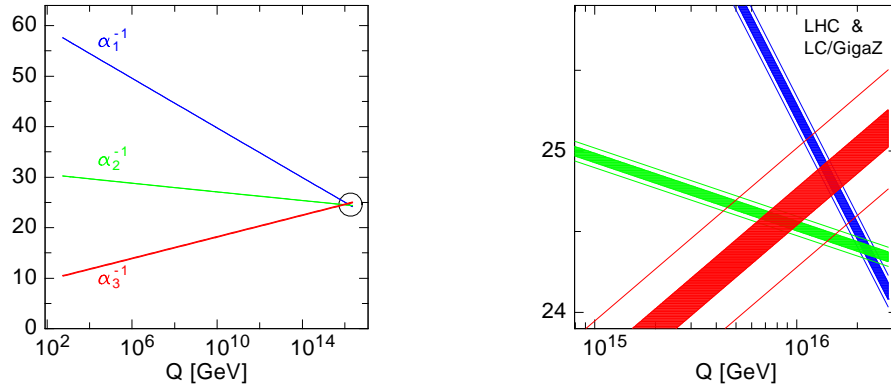
Figure 12: Gauge coupling unification at GigaZ; Ref. [53].

account results from GigaZ runs. The differences are to be attributed to threshold effects at the unification scale M_U. The quantitative evaluation implies important constraints on the particle content of the physics scenario in the grand unification / Planck region.

Gaugino and scalar mass parameters

The results for the evolution of the mass parameters from the electroweak scale to the GUT scale M_U are shown in Fig. 13. On the left of Fig. 13 the evolution is presented for the gaugino parameters M_i^{-1}. The model-independent reconstruction of the fundamental parameters and the test of universality in the SU(3)×SU(2)×U(1) group space are clearly under excellent control.
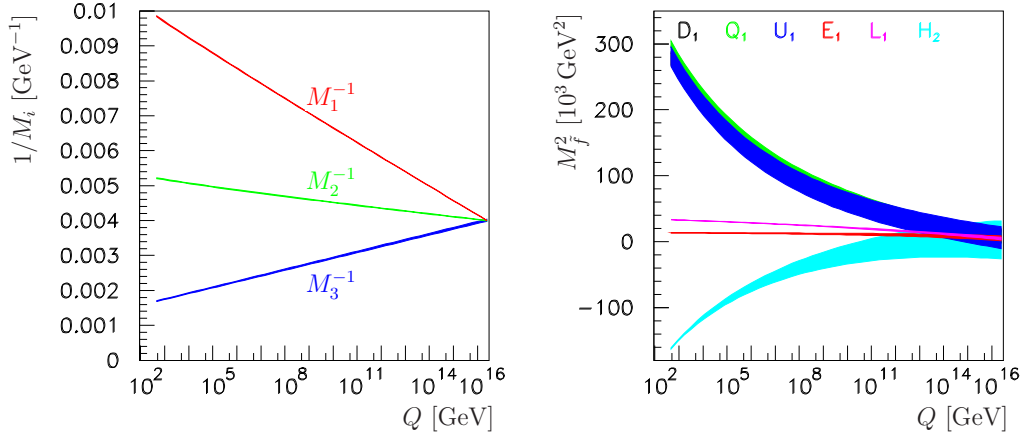
Figure 13: Unification of gaugino and scalar mass parameters; Ref. [53].

In the same way the evolution of the scalar mass parameters can be studied, presented on the right of Fig. 13 for the first/second generation. While the slepton parameters can be determined very precisely, the accuracy deteriorates for the squark parameters and the Higgs parameter $M_{H_2}^2$.

The evolution of the scalar mass parameters is quite distinct from scenarios in which supersymmetry is broken by a different mechanism. A typical example is gauge mediated supersymmetry breaking GMSB where regularities are predicted at an intermediate energy scale but extrapolations to Planck scale energies lead to markedly non-universal mass parameters [65]. Thus the microscopic picture of supersymmetry breaking can be explored this way experimentally.

These examples demonstrate that high-precision experiments at high-energy colliders allow us to reconstruct crucial elements of the physics scenario near the Planck scale. They shed light on a domain where in many theoretical approaches the roots of physics are located including gravity.

3.3   Left-right symmetric extension

The complex structure observed in the neutrino sector requires the extension of the minimal supersymmetric Standard Model MSSM, e.g., by a superfield including the right-handed neutrino field and its scalar partner. If the small neutrino masses are generated by the seesaw mechanism [67], a similar type of spectrum is induced in the scalar sneutrino sector, splitting into light TeV-scale and very heavy masses. The intermediate seesaw scales will affect the evolution of the soft mass terms which break the supersymmetry at the high (GUT) scale, particularly in the third generation with large Yukawa couplings. This will provide us with the opportunity to measure, indirectly, the intermediate seesaw scale of the third generation [68].

The measurement of the seesaw scale can be illustrated in an SO(10) model [69] in which the Yukawa couplings in the neutrino sector are proportional to the up-type quark

mass matrix. The masses of the physical right-handed Majorana neutrinos are hierarchical $\propto m_{\rm up}^2$, and the mass of the heaviest neutrino is roughly estimated by $M_{\rm R_3} \sim m_t^2/m_{\nu_3}$ which, for $m_{\nu_3} \sim 10^{-2}$ eV, amounts to $\sim 10^{15}$ GeV, i.e., a value close to the grand unification scale M_U.

Since the $\nu_{\rm R}$ is unfrozen only beyond $Q = M_{\nu_{\rm R}}$ the impact of the LR extension becomes visible in the evolution of the scalar mass parameters only at very high scales, but the effect of $\nu_{\rm R}$ can be manifest only in the third generation where the Yukawa coupling is large enough [65]. The evolution of the scalar mass parameters in the third generation and the Higgs mass parameter is sketched in Fig. 14. The kinks in the L3, H2 lines are induced by
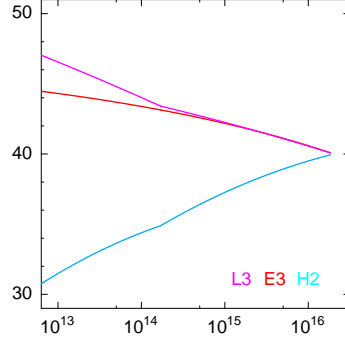
Figure 14: Impact of the heavy right-handed neutrino mass on the evolution of the scalar mass parameters in LR symmetric theories; Refs. [65, 68].

the right-handed neutrino. Only if $\nu_{\rm R}$, $\tilde{\nu}_{\rm R}$ are included, the picture is compatible with the assumption of universality.

The kinks in the evolution of $M_{\tilde{L}_3}^2$ shift the physical masses [squared] of the $\tilde{\tau}_{\rm L}$ and $\tilde{\nu}_{\tau \rm L}$ particles of the third generation by the amount $\Delta_\nu[M_{\rm R}]$ compared with the slepton masses of the first two generations. The measurement of

$$|m_{\tilde{\tau}}^2 - m_{\tilde{e}}^2|/m_{\tilde{e}}^2 \propto \log(M_{\rm GUT}^2/M_{\rm R_3}^2) \tag{13}$$

can be exploited to determine the neutrino seesaw scale of the third generation [70],

$$M_{\rm R_3} = 7.4^{+3.8}_{-2.8} \times 10^{14} \text{GeV} \tag{14}$$

in the LR extended SPS1a$'$ scenario. Thus, the analysis provides us with a unique estimate of the high-scale $\nu_{\rm R}$ seesaw mass parameter $M_{\rm R_3}$.

3.4 Split Supersymmetry

For a successful unification of forces at the GUT scale the size of the sfermion mass scale M_0 is irrelevant, since each generation of sfermions incorporates a complete representation of SU(5) [or SO(10)]. Likewise, the dark-matter prediction of the MSSM and its extensions does not rely on the value of M_0, but rather on the existence of a conserved discrete quantum number, R parity. These facts are compatible with the speculation that the sfermion mass scale may actually be much higher than the gaugino mass scale, effectively removing all

scalar partners of the matter fields and the extra heavy Higgs states of the MSSM from the low-energy spectrum [71].

In such a scenario sources of flavor violation besides CKM mixing are naturally absent, removing the requirement of sfermion-mass degeneracy from the mechanism of supersymmetry breaking. On the other hand, the Higgs potential is fine-tuned as in the non-supersymmetric SM.

With a sufficiently high sfermion mass scale, e.g., $M_0 \sim 10^9$ GeV, the gluino acquires a macroscopic lifetime and, for the purpose of collider experiments, behaves like a massive, stable color-octet parton. This leads to characteristic signatures at LHC. Detection of such a particle is possible up to $m_{\tilde{g}} = 1 - 2$ TeV [72, 73]. The Higgs boson mass is expected to be above the conventional MSSM mass range. Due to the absence of cascade decays, the production of the non-colored gauginos and higgsinos at LHC proceeds only via electroweak annihilation processes, and the production rates are thus considerably suppressed compared to conventional MSSM scenarios.

In this situation, the analysis of chargino and neutralino pair-production at ILC provides the information necessary to deduce the supersymmetric nature of the model. Extracting the values of chargino/neutralino Yukawa couplings, responsible for the mixing of gaugino and higgsino states, reveals the anomalous effects induced by the splitting of the gaugino and sfermion mass scales [72]. Furthermore, these parameters determine the higgsino content of the LSP and thus the relic dark-matter density predicted by the Split Supersymmetry Model [74].

3.5   String effective theories

Heterotic string theories give rise to a set of 4-dimensional dilaton S and moduli T superfields after compactification. The vacuum expectation values of S and T, generated by genuinely non–perturbative effects, determine the soft supersymmetry breaking parameters.

The properties of the supersymmetric theories are quite different for dilaton and moduli dominated scenarios, quantified by the mixing angle θ. This angle θ characterizes the $\tilde{S}$ and $\tilde{T}$ components of the wave function of the Goldstino, which is associated with the breaking of supersymmetry. The mass scale is set by the second parameter of the theory, the gravitino mass $m_{3/2}$.

In leading order, the masses [75] are given by

$$
\begin{aligned}
M_i &= -g_i^2 m_{3/2} \langle S \rangle \sqrt{3} \sin\theta + ... & (15) \\
M_{\tilde{j}}^2 &= m_{3/2}^2 \left(1 + n_j \cos^2\theta\right) + ... & (16)
\end{aligned}
$$

for the gaugino sector and the scalar sector, respectively. A dilaton dominated scenario, $\sin\theta \to 1$, leads to universal boundary conditions of the soft supersymmetry breaking parameters. On the other hand, in moduli dominated scenarios, $\cos\theta \to 1$, the gaugino mass parameters are universal, but universality is not realized for the scalar mass parameters. The breaking is characterized by integer modular weights n_j which quantify the couplings between the matter and the moduli fields. Within one generation significant differences between left and right field components and between sleptons and squarks can occur.

The results [65] for the analysis of a mixed dilaton/moduli superstring scenario with dominating dilaton component, $\sin^2\theta = 0.9$, and with different couplings of the moduli field to the (L,R) sleptons, the (L,R) squarks and to the Higgs fields corresponding to the O–I
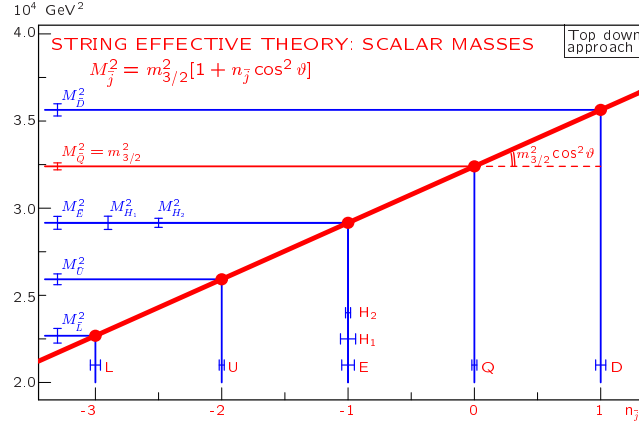
Figure 15: The linear relation between integer modular weights and scalar mass parameters in string effective theories; cf. Ref. [65].

representation $n_{L_i} = -3$, $n_{E_i} = -1$, $n_{H_1} = n_{H_2} = -1$, $n_{Q_i} = 0$, $n_{D_i} = 1$ and $n_{U_i} = -2$, are presented in Fig. 15. The gravitino mass is chosen to be 180 GeV in this analysis. Given this set of superstring induced parameters, the evolution of the gaugino and scalar mass parameters can be exploited to determine the modular weights n. Fig. 15 demonstrates how stringently this theory can be tested by analyzing the integer character of the entire set of modular weights.

Thus, high-precision measurements at high energy proton and lepton colliders may provide access to crucial derivative parameters in string theories.

3.6 Intermediate gauge bosons

Gauge bosons at the intermediate TeV scale are motivated by many theoretical approaches, cf. Ref. [76]. The breaking of GUT theories, based on SO(10) or E(6) symmetries for example, may leave one or several U(1) remnants unbroken down to TeV energies, before the symmetry is reduced finally to the SM symmetry:

$$
\begin{aligned}
\text{SO(10)} &\rightarrow \text{SM} \times \text{U(1)} & (17) \\
\text{E(6)} &\rightarrow \text{SO(10)} \times \text{U(1)} \rightarrow \text{SM} \times \text{U(1)} \times \text{U(1)} \\
&\rightarrow \text{SM} \times \text{U(1)} & (18)
\end{aligned}
$$

The final U(1) remnant of E(6) is a linear combination χ, ψ or η of the U(1)'s generated in the two-step symmetry breaking mechanism.

Such intermediate gauge bosons can be searched for at LHC for masses up to about 5 TeV. The role of ILC is twofold. First, by analyzing the effect of virtual Z' s-channel exchange on the cross sections and angular distributions of fermion pair production, $e^+e^- \rightarrow f\bar{f}$, the sensitivity to new gauge boson scales can be extended significantly, cf. Fig. 16, in SO(10) LR symmetric theories up to $\simeq 15$ TeV at ILC (and up to $\simeq 35$ TeV at CLIC [79]). Second, the couplings of the new Z' boson to SM fermions can be determined very precisely, Fig. 16. The
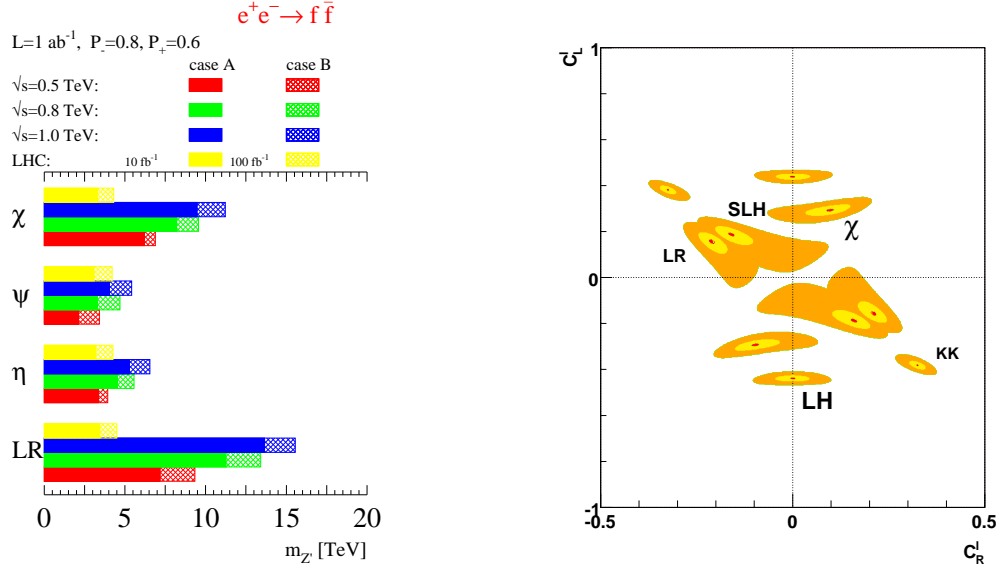
Figure 16: Z$'$ masses [77], and couplings [78], in extended SO(10), E(6) gauge theories.

various models can obviously be discriminated quite clearly and the nature of the underlying gauge symmetry can be identified.

4 Extra space dimensions

A large variety of models have been developed in which the ordinary 4-dimensional space-time is extended to higher dimensions already at energies of order 1 TeV. The ILC potential in analyzing such models, in which the extra dimensions are compactified at low scales, will be illustrated in two examples.

ADD scenario

In the ADD scenario [10] gravity extends from the brane on which the fields of the Standard Model are located, to the higher $D = 4 + \delta$ dimensions. It becomes strong in the extended space already at the fundamental Planck scale Λ_D of order TeV, much below the effective standard Planck scale Λ_{Pl} of order 10^{19} GeV, and it appears weak only if projected onto the 4-dimensional SM brane. The radii of the compactified higher dimensions are related to the Planck scale by $\Lambda_{Pl}^2 = R^\delta \Lambda_D^{2+\delta}$. The associated Kaluza-Klein states with masses $\sim n/R$ densely populate a tower with energy spacings of a small fraction of eV up to a few MeV, depending on the number of extra space dimensions.

At e^+e^- linear colliders the two crucial parameters of the ADD model, the fundamental Planck scale Λ_D and the number δ of extra space dimensions, can be disentangled by varying the cm energy of the collider. The cross section for the process of single γ production,

$$e^+e^- \rightarrow \gamma + G_{KK} \tag{19}$$

where G_{KK} denotes the sum over the invisible graviton states of the Kaluza-Klein tower, depends on these two parameters in the form [80]

$$\sigma(e^+e^- \to \gamma + \not{E}) = \frac{c_\delta}{\Lambda_{\mathrm{D}}^2} \left(\frac{\sqrt{s}}{\Lambda_{\mathrm{D}}}\right)^\delta . \tag{20}$$

Thus, the larger the number of extra dimensions the stronger would be the rise of the cross section for single isolated photons with the collider energy, Fig. 17.

RS scenario

While in the previous model space is flat in the standard and extra dimensions, it is curved in the RS(RS1) model [11]. The geometry is described by an exponential warp factor $\exp(-2kr_c\phi)$, characterized by the compactification radius r_c and the curvature k. The coordinate ϕ spans the distance between the gravity brane located at $\phi = 0$ and the SM brane located at $\phi = \pi$. Since the scale of physical processes on the SM brane is given by $\Lambda_{\mathrm{SM}} = \Lambda_{\mathrm{Pl}}\exp(-kr_c\pi) \sim 1$ TeV, the compactification radius r_c is estimated to be, roughly, one order of magnitude larger than the curvature radius k^{-1}, while k itself is of the order of the effective 4-dimensional Planck scale. The characteristics of our eigen-world on the 4-dimensional SM brane are described by the two parameters k and r_c, with the second parameter generally substituted by Λ_{SM}.

The Kaluza-Klein tower of the gravitons on the SM brane is characteristically different from towers associated with flat spaces, the sequence of masses [82] given by

$$M_n = x_n\, k\, \exp(-kr_c\pi) = x_n\Lambda_{\mathrm{SM}}\, k\,/\Lambda_{\mathrm{Pl}} \tag{21}$$

where x_n are the roots of the first-order Bessel functions. Such states can be searched for in fermion pair production $e^+e^- \to \mu^+\mu^-$, affecting this process by resonant s-channel exchanges. Fixing the lowest KK state to a mass of 600 GeV, the sequence of KK excitations is displayed in Fig. 17. The width of the KK states depends on the curvature $k \sim \Lambda_{\mathrm{Pl}}$ in the fifth dimension. The cross sections turn out to be very large if the parameters are such that the lowest KK states can be generated at the collider as an s-channel resonance.

If in addition to the gravity field SM fields are expanded to the extra space dimension, constraints derived from the SM precision measurements shift the mass scale of the Kaluza-Klein towers to considerably large values in the multi-TeV range and only virtual effects could be observed in SM processes at a TeV collider.

5   Cosmology connection

Collider physics programs focus in connection with cosmology presently on two fundamental problems, cf. Ref. [83]:

– the mechanism responsible for the baryon asymmetry: $\rho_{\mathrm{B}} = 4.0 \pm 0.4\%$

– the particle character of cold dark matter: $\rho_{\mathrm{CDM}} = 23 \pm 4\%$
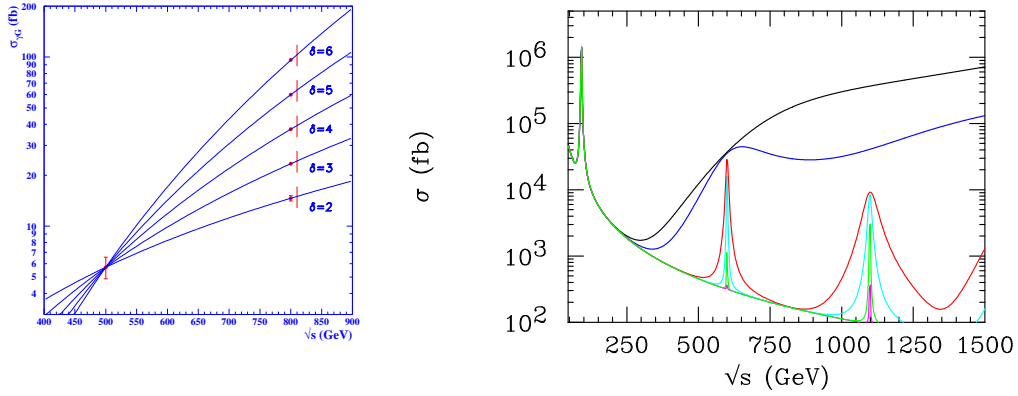
Figure 17: Left: Measuring the Planck scale and the number of dimensions in ADD scenarios; Ref. [81]. Right: Kaluza-Klein excitations in RS scenarios for various values of the curvature k; Ref. [82].

These central problems of physics cannot be solved within the framework of the Standard Model. Various solutions have been worked out which require experiments at high energy colliders to establish the proposed mechanism for generating the baryon asymmetry in the universe and for clarifying the nature of cold dark matter. Even if a single particle species were the main component of cold dark matter in the universe, the theoretical origin will in general be so complex that laboratory experiments are required to achieve the proper understanding of this phenomenon.

5.1 Baryon asymmetry

Two approaches for generating the baryon asymmetry are widely discussed in the literature: baryogenesis mediated by leptogenesis, and electroweak baryogenesis based on the supersymmetric extension of the Standard Model.

Leptogenesis

If leptogenesis [84] is the origin of the observed baryon asymmetry, the roots of this phenomenon are located near the Planck scale. CP-violating decays of heavy right-handed Majorana neutrinos generate a lepton asymmetry which is transferred to the quark/baryon sector by sphaleron processes. Heavy neutrino mass scales as introduced in the seesaw mechanism for generating light neutrino masses and the size of the light neutrino masses needed for leptogenesis define a self-consistent frame which is compatible with all experimental observations [85].

As shown in the preceding chapter, in some SUSY models the size of the heavy seesaw scales can be related to the values of the charged and neutral slepton masses [68]. A sum rule relates the difference between the slepton masses of the first two and the third generation to the mass of the heavy right-handed Majorana neutrino in the third generation within

SO(10) based supergravity theories. In this way the size of the seesaw scale can well be estimated.

Electroweak baryogenesis in supersymmetry

One of Sakharov's conditions for generating the baryon asymmetry of the universe requires a departure from thermal equilibrium. If triggered by sphaleron processes at the electroweak phase transition, the transition must be sufficiently strong of first order. Given the present bounds on the Higgs mass, this cannot be realized in the Standard Model. However, since top and stop fields modify the Higgs potential strongly through radiative corrections, supersymmetry scenarios can give rise to first-order transitions, cf. Ref. [86]. The parameter space of the MSSM is tightly constrained in this case: The mass of the light Higgs boson is bounded by 120 GeV from above, and the mass of the light stop quark is required to be smaller than the top quark mass, cf. Ref. [87].

This scenario suggests that the mass of the stop quark is only slightly larger than the lightest neutralino (LSP) mass. The correct density of cold dark matter is generated by stop-neutralino coannihilation in this region of parameter space, leading to tight constraints for the masses of the two particles.

While studies of the light stop quark are very difficult at hadron colliders if the main decay channel is the two-body decay $\tilde{t}_1 \to c\tilde{\chi}_1^0$ with a low-energy charm jet in the final state, the clean environment of an e^+e^- collider allows for precision studies of the system also in
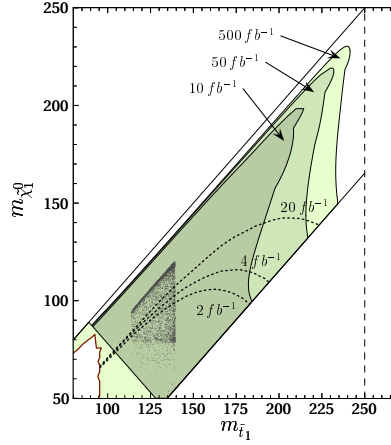
Figure 18: ILC coverage of stop/neutralino parameter space, dark grey points, in the MSSM based electroweak phase transition; Ref. [87].

such configurations. This is demonstrated in Fig. 18 which proves that a linear collider covers completely the region of dark gray points which are compatible with precision measurements of the cold dark matter density.

5.2 Cold dark matter

Cold dark matter (CDM) is the dominant component of matter in the universe. So far it has not been possible yet to reveal its microscopic nature. Attempts to solve this problem form an intimate link between cosmology and particle physics. CDM may be a complex structure and a mixture of several components. Theoretical particle physics offers hypothetical particle candidates which could be discovered in the next generation of accelerators. After determining the properties of candidate particles in laboratory experiments, their density in the universe can be predicted and the prediction can be confronted with cosmological precision measurements. In addition, compatibility with direct and indirect search experiments must be checked. In this way a closed circle may evolve which provides a self-consistent picture of the nature of cold dark matter and its distribution in the universe.

Theories which provide a CDM candidate must have a conserved parity quantum number. Examples are R parity in supersymmetric models, KK parity in extra-dimensional models, or T parity in Little-Higgs theories. The lightest particle with odd parity is then stable, must be charge- and color-neutral, and thus provides a CDM candidate. If this particle is in or below the TeV mass range and interacts with matter, it will be seen via missing-energy signatures at LHC. At ILC, a precise determination of its mass and interactions is possible due to kinematical hermeticity and low background, independently of the embedding theory.

Among the candidate theories, two specific examples will be summarized briefly to illuminate the ILC potential in clarifying the nature of cold dark matter particles. The examples chosen are the supersymmetric extension of the Standard Model embedded in minimal supergravity in which the lightest neutralino is the cold dark matter particle, and a supergravity theory in which the gravitino is identified with this particle. In the first example, the characteristic are the mass scale with a value near the electroweak scale, and the weak interactions of CDM. In the second example, CDM interacts only through gravity.

Neutralino cold dark matter

In the mSUGRA parameter range four characteristic areas have been identified in which the observed relic density [88] can be accommodated, cf. Fig. 19, and they have recently been studied systematically [89]-[92].

(i) In the *bulk region* the gaugino mass parameter $M_{1/2}$ and the scalar mass parameter M_0 are both in the area surrounding the electroweak scale. Neutralino pairs annihilate into fermion pairs. This area, including the benchmark point SPS1a′, has been studied very thoroughly for LHC as well as ILC experiments. From the ILC studies the CDM density is expected to be determined within an accuracy of about 2%, thus matching the precision expected from measurements of the Planck satellite in the near future.

(ii) In the *focus point region* the gaugino mass parameter remains moderate but the scalar mass parameter is very large. While the spectrum of charginos and neutralinos appears accessible at ILC, sleptons can be produced, if at all, only at a multi-TeV collider. Split Supersymmetry, where sleptons are completely inaccessible, is an extreme case of this scenario. Neutralino pairs annihilate primarily to gauge bosons. The prediction of the relic density is strongly correlated with the mass difference between the lightest chargino and neutralino as demonstrated in Fig. 19.

(iii) The *$\tilde{\tau}\tilde{\chi}$ coannihilation region* with moderate to large $M_{1/2}$ and moderate M_0 is difficult to explore experimentally as $\tilde{\tau} \to \tau\tilde{\chi}_1^0$ decays must be studied in which stau and
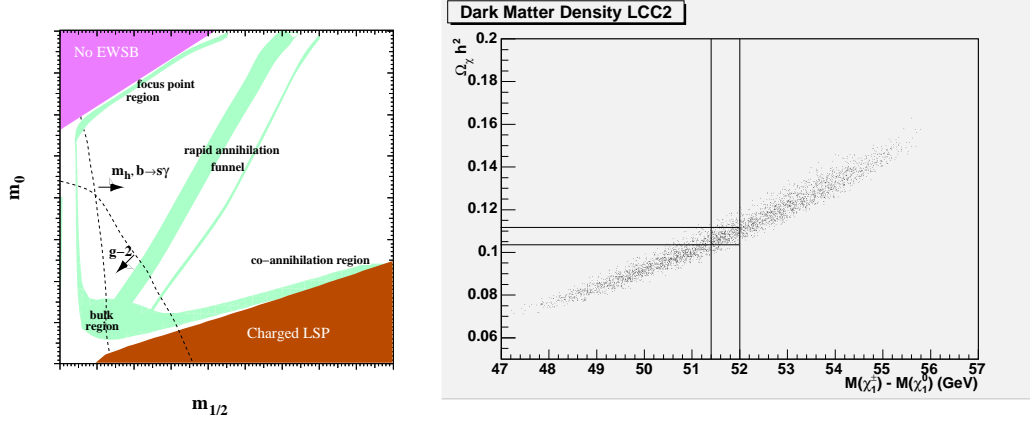
Figure 19: Left: Characteristics of mSUGRA parameter regions constrained by precision data on the relic density; cf. Ref. [83]. Right: Sensitivity of the prediction for the relic density from parameter measurements in the focus point region; Ref. [89], see also Refs. [90].

	character	channel	sensitivity	LHC	ILC
SPS1a$'$	bulk	$\tilde{\chi}\tilde{\chi} \to \tau\tau,\, bb$	$\tilde{\tau},\, \tilde{b}$	10%	2%
LCC2	focus point	$\tilde{\chi}\tilde{\chi} \to WW, ZZ$	$\tilde{V}\tilde{H}$ mix	82%	8%
LCC3	$\tilde{\tau}\tilde{\chi}$ co-ann.	$\tilde{\tau}\tilde{\chi} \to \tau\gamma$	$M[\tilde{\tau} - \tilde{\chi}_1^0]$	167%	18%
LCC4	A funnel	$\tilde{\chi}\tilde{\chi} \to A$	$M_A,\, \Gamma_A$	405%	19%

Table 3: Predictions of the relic density from measurements of supersymmetric particle properties at the LHC and the TeV linear collider; Ref. [92].

neutralino are close in mass so that the visible τ in the final state carries only a small amount of energy and is hard to detect.

(iv) In the *funnel region* neutralino annihilation is mediated by an s-channel Higgs boson. Predictions of the relic density in this region depend on the properties of the pseudoscalar Higgs boson A, the mass M_A and the width Γ_A; errors of the predictions are correspondingly large.

The accuracy of the relic density is presently set by thw WMAP analysis to

$$\Omega h^2 = 0.104^{+0.007}_{-0.013} \tag{22}$$

The accuracy is expected to be improved by the PLANCK satellite to 1.4%. Choosing a representative point for each of the characteristic regions, the predicted errors for the prediction of the relic density are collected in Tab. 3. Evidently, the accuracy expected in the analysis at the TeV linear collider analysis significantly improves expectations for LHC.

Gravitino cold dark matter

In supergravity models the gravitino $\tilde{G}$ itself may be the lightest supersymmetric particle, building up the dominant CDM component, cf. Ref. [93]. In such a scenario, with a gravitino

mass in the range of 100 GeV [in contrast to gauge-mediated supersymmetry breaking with very light gravitino mass], the lifetime of the next-to-lightest supersymmetric particle can become very long as the gravitino coupling is only of gravitational strength. The lifetime of the NLSP $\tilde{\tau}$ in the gravitino decay process,

$$\tau[\tilde{\tau} \to \tau + \tilde{G}] = const \times M_{\tilde{G}}^2 M_{\text{Pl}}^2 / M_{\tilde{\tau}}^5 \,, \tag{23}$$

can extend to macroscopic scales [94], suggesting special experimental efforts to catch the long-lived $\tilde{\tau}$'s and to measure their lifetime [95]. Production in $e^+ e^-$ annihilation determines the $\tilde{\tau}$ mass, the observation of the τ energy in the $\tilde{\tau}$ decay the gravitino mass. The measurement of the lifetime can subsequently be exploited to confirm the Planck scale M_{Pl} as the scale of the fundamental supergravity coupling.

6   Summary

The ILC can contribute to solutions of key questions in physics,

– *Electroweak Symmetry Breaking*: The Higgs mechanism *sui generis* can be established for breaking the electroweak symmetries and generating the masses of the fundamental particles.

– *Grand and Ultimate Unification*: A comprehensive and high-resolution picture of supersymmetry can be drawn by coherent analyses of hadron and lepton collider experiments. Thus the colliders may become telescopes to the physics scenario near the Planck scale where particle physics is linked with gravity and where the basic roots of physics are expected to be located.

– *Extra Space Dimensions*: The parameters of an extended space-time picture can be determined, the fundamental Planck scale and the number of extra dimensions. New Kaluza-Klein states can either be generated directly or their effect on Standard Model processes can be explored.

– *Cosmology Connection*: Drawing a microscopic picture of particles building up cold dark matter, the basis necessary for the understanding of matter in the universe can be provided by collider experiments. In addition, crucial elements for explaining the baryon asymmetry in the universe can be reconstructed.

Collider experiments will thus be essential instruments for unraveling the fundamental laws of nature.

References

[1] Slides: `http://ilcagenda.linearcollider.org/contributionDisplay.py?contribId=4&sessionId=0&confId=1296`

[2] J.A. Aguilar-Saavedra *et al.* [ECFA/DESY LC Physics Working Group Collaboration], arXiv:hep-ph/0106315; T. Abe *et al.* [American Linear Collider Working Group Collaboration], arXiv:hep-ex/0106055, hep-ex/0106056, hep-ex/0106057, and hep-ex/0106058; K. Abe *et al.* [ACFA Linear Collider Working Group Collaboration], arXiv:hep-ph/0109166.

[3] A. Djouadi, J. Lykken, K. Monig, Y. Okada, M. J. Oreglia and S. Yamashita, arXiv:0709.1893 [hep-ph].

[4] E. Accomando *et al.* [CLIC Physics Working Group Collaboration], arXiv:hep-ph/0412251.

[5] P. W. Higgs, Phys. Lett. **12** (1964) 132 and Phys. Rev. **145** (1966) 1156; F. Englert and R. Brout, Phys. Rev. Lett. **13** (1964) 321; G. S. Guralnik, C. R. Hagen and T. W. B. Kibble, Phys. Rev. Lett. **13** (1964) 585.

[6] S. Weinberg, Phys. Rev. D **13** (1976) 974 and Phys. Rev. D **19** (1979) 1277; L. Susskind, Phys. Rev. D **20** (1979) 2619.

[7] H. Georgi and S. L. Glashow, Phys. Rev. Lett. **32** (1974) 438; H. Georgi, H. R. Quinn and S. Weinberg, Phys. Rev. Lett. **33** (1974) 451.

[8] J. Wess and B. Zumino, Nucl. Phys. B **70** (1974) 39.

[9] I. Antoniadis and K. Benakli, Phys. Lett. B **326** (1994) 69 [arXiv:hep-th/9310151].

[10] N. Arkani-Hamed, S. Dimopoulos and G. R. Dvali, Phys. Rev. D **59** (1999) 086004 [arXiv:hep-ph/9807344].

[11] L. Randall and R. Sundrum, Phys. Rev. Lett. **83** (1999) 4690 [arXiv:hep-th/9906064].

[12] G. Moortgat-Pick *et al.*, arXiv:hep-ph/0507011.

[13] B. Badelek *et al.* [ECFA/DESY Photon Collider Working Group Collaboration], Int. J. Mod. Phys. A **19** (2004) 5097 [arXiv:hep-ex/0108012].

[14] M. M. Muhlleitner and P. M. Zerwas, Acta Phys. Polon. B **37** (2006) 1021 [arXiv:hep-ph/0511339].

[15] A. Djouadi, arXiv:hep-ph/0503172; M. Gomez-Bock, M. Mondragon, M. Muhlleitner, R. Noriega-Papaqui, I. Pedraza, M. Spira and P. M. Zerwas, J. Phys. Conf. Ser. **18** (2005) 74 [arXiv:hep-ph/0509077]; S. Dawson, arXiv:hep-ph/0510385.

[16] S. Heinemeyer *et al.*, 2005 Snowmass Workshop, arXiv:hep-ph/0511332.

[17] M. W. Grunewald, arXiv:0709.3744 [hep-ex].

[18] R. Barate *et al.* [LEP Working Group for Higgs boson searches], Phys. Lett. B **565** (2003) 61 [arXiv:hep-ex/0306033].

[19] F. Gianotti, Talk at the Lepton-Photon Symposium, Uppsala 2005.

[20] M. Duhrssen, S. Heinemeyer, H. Logan, D. Rainwater, G. Weiglein and D. Zeppenfeld, Phys. Rev. D **70** (2004) 113009 [arXiv:hep-ph/0406323].

[21] W. Lohmann, private communication, and P. Garcia-Abia and W. Lohmann, Eur. Phys. J. directC **2** (2000) 2 [arXiv:hep-ex/9908065].

[22] M. Battaglia and K. Desch, arXiv:hep-ph/0101165.

[23] S. Yamashita, Talk at LCWS 2005, Stanford CA.

[24] A. Djouadi, W. Kilian, M. Muhlleitner and P. M. Zerwas, Eur. Phys. J. C **10** (1999) 27 [arXiv:hep-ph/9903229].

[25] U. Baur, T. Plehn and D. L. Rainwater, Phys. Rev. D **67** (2003) 033003 [arXiv:hep-ph/0211224].

[26] V. Barger, T. Han, P. Langacker, B. McElrath and P. Zerwas, Phys. Rev. D **67** (2003) 115001 [arXiv:hep-ph/0301097].

[27] M. M. Muhlleitner, M. Kramer, M. Spira and P. M. Zerwas, Phys. Lett. B **508** (2001) 311 [arXiv:hep-ph/0101083].

[28] K. Desch, T. Klimkovich, T. Kuhl and A. Raspereza, arXiv:hep-ph/0406229.

[29] P. Niezurawski, A. F. Zarnecki and M. Krawczyk, arXiv:hep-ph/0507006.

[30] S. Heinemeyer, W. Hollik and G. Weiglein, arXiv:hep-ph/0412214.

[31] A. Juste *et al.*, 2005 Snowmass Workshop, arXiv:hep-ph/0601112.

[32] D. J. Miller, R. Nevzorov and P. M. Zerwas, Nucl. Phys. B **681** (2004) 3 [arXiv:hep-ph/0304049].

[33] J. F. Gunion and M. Szleper, arXiv:hep-ph/0409208.

[34] U. Ellwanger, J. F. Gunion, C. Hugonie and S. Moretti, arXiv:hep-ph/0401228.

[35] E. Farhi and L. Susskind, Phys. Rev. D **20** (1979) 3404; E. Eichten and K. D. Lane, Phys. Lett. B **90** (1980) 125; see also the reviews: C. T. Hill and E. H. Simmons, Phys. Rept. **381** (2003) 235 [Erratum-ibid. **390** (2004) 553] [arXiv:hep-ph/0203079]; W. Kilian, Springer tracts in modern physics **198** (2003).

[36] N. Arkani-Hamed, A. G. Cohen, H. Georgi, Phys. Lett. B **513** (2001) 232 [arXiv:hep-ph/0105239]; N. Arkani-Hamed, A. G. Cohen, T. Gregoire, and J. G. Wacker, JHEP **0208** (2002) 020. [arXiv:hep-ph/0202089]; N. Arkani-Hamed, A. G. Cohen, E. Katz, and A. E. Nelson, JHEP **0207** (2002) 034. [arXiv:hep-ph/0206021]; M. Schmaltz, JHEP **0408** (2004) 056; for reviews, see: M. Schmaltz and D. Tucker-Smith, arXiv:hep-ph/0502182; M. Perelstein, arXiv:hep-ph/0512128.

[37] T. Han, H. E. Logan, B. McElrath, and L.-T. Wang, Phys. Rev. D **67** (2003) 095004. [arXiv:hep-ph/0301040]; W. Kilian and J. Reuter, Phys. Rev. D **70** (2004) 015004 [arXiv:hep-ph/0311095]; T. Han, H. E. Logan, B. McElrath and L. T. Wang, Phys. Lett. B **563** (2003) 191 [Erratum-ibid. B **603** (2004) 257] [arXiv:hep-ph/0302188].

[38] J. A. Conley, J. Hewett and M. P. Le, Phys. Rev. D **72** (2005) 115014 [arXiv:hep-ph/0507198].

[39] W. Kilian, D. Rainwater and J. Reuter, Phys. Rev. D **71** (2005) 015008 [arXiv:hep-ph/0411213].

[40] T. Appelquist and C. Bernard, Phys. Rev. D22, 200 (1980); A. Longhitano, Phys. Rev. D22, 1166 (1980); Nucl. Phys. B188, 118 (1981); T. Appelquist and G. H. Wu, Phys. Rev. D **48** (1993) 3235 [arXiv:hep-ph/9304240].

[41] E. Boos, H. J. He, W. Kilian, A. Pukhov, C. P. Yuan and P. M. Zerwas, Phys. Rev. D **57** (1998) 1553 [arXiv:hep-ph/9708310], and Phys. Rev. D **61** (2000) 077901 [arXiv:hep-ph/9908409].

[42] R. Chierici, S. Rosati, and M. Kobel, LC-PHSM-2001-038.

[43] P. Krstonosic, K. Monig, M. Beyer, E. Schmidt and H. Schroder, arXiv:hep-ph/0508179.

[44] J. F. Gunion, arXiv:hep-ph/0410379.

[45] K. m. Cheung, Phys. Rev. D **63** (2001) 056007 [arXiv:hep-ph/0009232].

[46] F. J. Petriello, JHEP **0205** (2002) 003 [arXiv:hep-ph/0204067].

[47] C. Csaki, C. Grojean, H. Murayama, L. Pilo and J. Terning, Phys. Rev. D **69** (2004) 055006 [arXiv:hep-ph/0305237]; C. Csaki, C. Grojean, L. Pilo and J. Terning, Phys. Rev. Lett. **92** (2004) 101802 [arXiv:hep-ph/0308038]

[48] A. Birkedal, K. Matchev and M. Perelstein, Phys. Rev. Lett. **94** (2005) 191803 [arXiv:hep-ph/0412278], and arXiv:hep-ph/0508185.

[49] H. P. Nilles, Phys. Rept. **110** (1984) 1; H. E. Haber and G. L. Kane, Phys. Rept. **117** (1985) 75.

[50] J. R. Ellis, S. Heinemeyer, K. A. Olive, A. M. Weber and G. Weiglein, arXiv:0706.0652 [hep-ph].

[51] J. A. Aguilar-Saavedra *et al.* [SPA Project Collaboration], arXiv:hep-ph/0511344.

[52] G. Weiglein *et al.* [LHC/LC Study Group Collaboration], arXiv:hep-ph/0410364.

[53] B. C. Allanach, G. A. Blair, S. Kraml, H. U. Martyn, G. Polesello, W. Porod and P. M. Zerwas, arXiv:hep-ph/0403133 and arXiv:hep-ph/0512084.

[54] R. Lafaye, T. Plehn and D. Zerwas, arXiv:hep-ph/0404282; R. Lafaye, T. Plehn, M. Rauch and D. Zerwas, arXiv:0709.3985 [hep-ph]; P. Bechtle, K. Desch and P. Wienemann, Comput. Phys. Commun. **174** (2006) 47 [arXiv:hep-ph/0412012].

[55] B. C. Allanach *et al.*, Eur. Phys. J. C **25** (2002) 113 [arXiv:hep-ph/0202233].

[56] B. K. Gjelsten, D. J. Miller and P. Osland, JHEP **0412** (2004) 003 [arXiv:hep-ph/0410303]; JHEP **0506** (2005) 015 [arXiv:hep-ph/0501033]; and arXiv:hep-ph/0510356.

[57] A. Freitas, A. von Manteuffel and P. M. Zerwas, Eur. Phys. J. C **34** (2004) 487 [arXiv:hep-ph/0310182], and Eur. Phys. J. C **40** (2005) 435 [arXiv:hep-ph/0408341]; A. Freitas, D. J. Miller and P. M. Zerwas, Eur. Phys. J. C **21** (2001) 361 [arXiv:hep-ph/0106198]; see also J. L. Feng and M. E. Peskin, Phys. Rev. D **64** (2001) 115002 [arXiv:hep-ph/0105100].

[58] H. U. Martyn, arXiv:hep-ph/0406123.

[59] A. J. Barr, Phys. Lett. B **596** (2004) 205 [arXiv:hep-ph/0405052]; J. M. Smillie and B. R. Webber, JHEP **0510** (2005) 069 [arXiv:hep-ph/0507170]; A. J. Barr, arXiv:hep-ph/0511115.

[60] S. Y. Choi, K. Hagiwara, H. U. Martyn, K. Mawatari and P. M. Zerwas, Eur. Phys. J. C **51** (2007) 753 [arXiv:hep-ph/0612301].

[61] S. Y. Choi, A. Djouadi, M. Guchait, J. Kalinowski, H. S. Song and P. M. Zerwas, Eur. Phys. J. C **14** (2000) 535 [arXiv:hep-ph/0002033].

[62] S. Y. Choi, J. Kalinowski, G. Moortgat-Pick and P. M. Zerwas, Eur. Phys. J. C **22** (2001) 563 [Addendum-ibid. C **23** (2002) 769] [arXiv:hep-ph/0108117].

[63] A. Bartl, H. Eberl, S. Kraml, W. Majerotto and W. Porod, Eur. Phys. J. directC **2** (2000) 6 [arXiv:hep-ph/0002115]; A. Finch, A. Sopczak and H. Nowak, "A scalar top study with c-quark tagging at a linear e+ e- collider," LC-PHSM-2003-075 and Int. Europhysics Conference HEP(2003), Aachen.

[64] A. Freitas, P. Z. Skands, M. Spira and P. M. Zerwas, JHEP **0707** (2007) 025 [arXiv:hep-ph/0703160].

[65] G. A. Blair, W. Porod and P. M. Zerwas, Phys. Rev. D **63** (2001) 017703 [arXiv:hep-ph/0007107], and Eur. Phys. J. C **27** (2003) 263 [arXiv:hep-ph/0210058].

[66] J. R. Ellis, S. Kelley and D. V. Nanopoulos, Phys. Lett. B **260** (1991) 131; P. Langacker and M. x. Luo, Phys. Rev. D **44** (1991) 817; U. Amaldi, W. de Boer and H. Furstenau, Phys. Lett. B **260** (1991) 447.

[67] P. Minkowski, Phys. Lett. B **67** (1977) 421; T. Yanagida, *In Proceedings of the Workshop on the Baryon Number of the Universe and Unified Theories, Tsukuba, Japan, 1979*; M. Gell-Mann, P. Ramond and R. Slansky, *In Proceedings "Supergravity", North Holland, 1979*.

[68] A. Freitas, W. Porod and P. M. Zerwas, Phys. Rev. D **72** (2005) 115002 [arXiv:hep-ph/0509056].

[69] H. Baer, M. Brhlik, M. A. Diaz, J. Ferrandis, P. Mercadante, P. Quintana and X. Tata, Phys. Rev. D **63** (2001) 015007 [arXiv:hep-ph/0005027].

[70] F. Deppisch, A. Freitas, W. Porod and P. M. Zerwas, *in preparation*.

[71] N. Arkani-Hamed and S. Dimopoulos, JHEP **0506** (2005) 073 [arXiv:hep-th/0405159]; G. F. Giudice and A. Romanino, Nucl. Phys. B **699** (2004) 65 [Erratum-ibid. B **706** (2005) 65] [arXiv:hep-ph/0406088]; N. Arkani-Hamed, S. Dimopoulos, G. F. Giudice and A. Romanino, Nucl. Phys. B **709** (2005) 3 [arXiv:hep-ph/0409232].

[72] W. Kilian, T. Plehn, P. Richardson and E. Schmidt, Eur. Phys. J. C **39** (2005) 229 [arXiv:hep-ph/0408088].

[73] A. C. Kraan, J. B. Hansen and P. Nevski, arXiv:hep-ex/0511014.

[74] A. Pierce, Phys. Rev. D **70** (2004) 075006 [arXiv:hep-ph/0406144].

[75] P. Binetruy, M. K. Gaillard and B. D. Nelson, Nucl. Phys. B **604** (2001) 32 [arXiv:hep-ph/0011081].

[76] S. Godfrey, P. Kalyniak and A. Tomkins, 2005 Snowmass Workshop, arXiv:hep-ph/0511335, and *private communication*.

[77] S. Riemann, Note LC-TH-2001-007.

[78] S. Godfrey, P. Kalyniak and A. Tomkins, arXiv:hep-ph/0511335.

[79] M M. Battaglia, A. De Roeck, J. Ellis and D. Schulte (eds.), [CLIC Physics Working Group], CERN-2004-005.

[80] G. F. Giudice, R. Rattazzi and J. D. Wells, Nucl. Phys. B **544** (1999) 3 [arXiv:hep-ph/9811291].

[81] G. Wilson in Ref. [2].

[82] H. Davoudiasl, J. L. Hewett and T. G. Rizzo, Phys. Rev. Lett. **84** (2000) 2080 [arXiv:hep-ph/9909255].

[83] J. L. Feng, arXiv:hep-ph/0509309.

[84] M. Fukugita and T. Yanagida, Phys. Lett. B **174** (1986) 45.

[85] W. Buchmuller, P. Di Bari and M. Plumacher, Nucl. Phys. B **665** (2003) 445 [arXiv:hep-ph/0302092].

[86] M. Carena, M. Quiros and C. E. M. Wagner, Phys. Lett. B **380** (1996) 81 [arXiv:hep-ph/9603420].

[87] M. Carena, A. Finch, A. Freitas, C. Milstene, H. Nowak and A. Sopczak, Phys. Rev. D **72** (2005) 115008 [arXiv:hep-ph/0508152].

[88] D. N. Spergel *et al.* [WMAP Collaboration], Astrophys. J. Suppl. **148** (2003) 175 [arXiv:astro-ph/0302209].

[89] M. Battaglia, Talk at LCWS 2005, Stanford CA.

[90] P. Bambade, M. Berggren, F. Richard and Z. Zhang, arXiv:hep-ph/0406010; H. U. Martyn, arXiv:hep-ph/0408226; V. Khotilovich, R. Arnowitt, B. Dutta and T. Kamon, Phys. Lett. B **618** (2005) 182 [arXiv:hep-ph/0503165].

[91] G. Polesello and D. R. Tovey, JHEP **0405** (2004) 071 [arXiv:hep-ph/0403047]; M. M. Nojiri, G. Polesello and D. R. Tovey, arXiv:hep-ph/0512204.

[92] E. A. Baltz, M. Battaglia, M. E. Peskin and T. Wizansky, Phys. Rev. D **74** (2006) 103521 [arXiv:hep-ph/0602187].

[93] H. Pagels and J. R. Primack, Phys. Rev. Lett. **48** (1982) 223; M. Y. Khlopov and A. D. Linde, Phys. Lett. B **138** (1984) 265; J. R. Ellis, J. E. Kim and D. V. Nanopoulos, Phys. Lett. B **145** (1984) 181; M. Bolz, W. Buchmuller and M. Plumacher, Phys. Lett. B **443** (1998) 209 [arXiv:hep-ph/9809381].

[94] F. D. Steffen, AIP Conf. Proc. **903** (2007) 595 [arXiv:hep-ph/0611027].

[95] W. Buchmuller, K. Hamaguchi, M. Ratz and T. Yanagida, Phys. Lett. B **588** (2004) 90 [arXiv:hep-ph/0402179]; J. L. Feng, S. Su and F. Takayama, Phys. Rev. D **70** (2004) 075019 [arXiv:hep-ph/0404231]; A. De Roeck, J. R. Ellis, F. Gianotti, F. Moortgat, K. A. Olive and L. Pape, arXiv:hep-ph/0508198; H. U. Martyn, Eur. Phys. J. C **48** (2006) 15 [arXiv:hep-ph/0605257].

Physics and Detectors
for the International Linear Collider -
Charge to the 2007 Linear Collider Workshop
(LCWS07)

James E. Brau *

University of Oregon - Center for High Energy Physics
Eugene, OR USA 97403-1274

As the 2007 Linear Collider Workshop met at DESY, significant milestones had been achieved. The ILC Reference Design Report has been completed, the detector R&D is progressing, a detector roadmap is being defined, a Research Director is being appointed, and a call for Letters of Intent for ILC detectors to be engineered is being announced.

1   Introduction

We meet this year at DESY for the tenth workshop in the series that dates back to 1991. I remind you the previous workshops have been

1. Saariselka, Finland, 1991
2. Hawaii, USA, 1993
3. Morioka, Japan, 1995
4. Sitges, Spain, 1999
5. Fermilab, USA, 2000
6. Jeju Island, Korea, 2002
7. Paris, France, 2004
8. Stanford, USA, 2005
9. Bangalore, India, 2006

and now

10. DESY, Germany - May 30 - June 3, 2007

A compelling physics case has been established for the International Linear Collider, in part through the preparation and discussions of these workshops. The LHC will soon open Terascale physics. What is found in that initial exploration promises to reveal deep understanding of fundamental physics. The nature of Electroweak Symmetry Breaking should be more clear. We may even learn of new symmetries of space and time, hidden extra dimensions, or dark matter particles. Whatever the discoveries, the ILC will be needed to explore and elucidate the nature of the Terascale. In particular, the precision exploration that the ILC offers will further the understanding of Terascale physics.

The World Wide Study for Physics and Detectors at Future electron-positron Colliders (WWS) was formed in 1998 at the Vancouver International Conference on High Energy

Physics, and has organized this series of workshops ever since. The founding co-chairs were Charles Baltay (Yale), Sachio Komamiya (Tokyo), and David Miller (Univ. College London). The World Wide Study was recognized early by the International Committee on Future Accelerators (ICFA), and in 2004 its responsibility to organize and coordinate international activities on linear collider physics and detector studies was endorsed by ICFA and the International Linear Collider Steering Committee (ILCSC).

Specifically, the World Wide Study carries forward the following functions:

World Wide Study Functions
- Recognizes and coordinates studies on whole detector concepts, and works toward interregional detector engineering design reports;
- Interacts with the Global Design Effort (GDE), especially on machine detector interface (MDI) issues;
- Maintains a register of R&D relevant to the ILC experimental program, identifying those that are vital or missing, and ensuring peer review of R&D proposals;
- Organizes interregional meetings and workshops; and
- Reports to the ILCSC and ICFA on the matters above.

The efforts of the WWS are led by an organizing committee, consisting of 6 members from each of the three regions. These members are

Asia
Atul Gurtu, Tata Institute (India)
Yee Bob Hsiung, National Taiwan University (Taiwan)
Wei Guo Li, IHEP Beijing (China)
Akiya Miyamoto, KEK (Japan)
Hwanbae Park, Kyungpook National University (Korea)
Hitoshi Yamamoto, Tohoku University (Japan) - co-chair

Europe
Tiziano Camporesi, CERN
Michael Danilov, ITEP (Russia)
Rolf Heuer, U. Hamburg /DESY (Germany)
David Miller, U. C. London (UK)
Francois Richard, LAL/Orsay (France) - co-chair
Ron Settles, Munich (Germany)
Jan Timmermans, NIKHEF (Netherlands)

Americas
Jim Brau, University of Oregon (USA) - co-chair
John Jaros, SLAC (USA)
Dean Karlen, Victoria (Canada)
Andreas Kronfeld, Fermilab (USA)
Mark Oreglia, University of Chicago (USA)
Ritchie Patterson, Cornell (USA)

The World Wide Study web page is *http://physics.uoregon.edu/~lc/wwstudy*

2 ILC Reference Design Report

This year we have achieved a significant milestone toward realization of the ILC. In February, the ILC Reference Design[6], with costs, was released during the ACFA Linear Collider Workshop in Beijing. Among the features of the design are two 11 kilometer superconducting linacs operating at 31.5 MV/m for 500 GeV, a centralized injector, circular damping rings for electrons and positrons, an undulator-based positron source, a single IR for two detectors in a push-pull arrangement with a 14 mrad crossing angle, and a dual tunnel configuration for safety and availability. The layout is illustrated in Figure 1

The decision to design for a single IR in the push-pull configuration for the two detectors resulted from the large cost savings. A task force lead by Andrei Seryei, and including membership from both the WWS and the GDE has studied the push-pull configuration and concluded that there are no show-stoppers. However, very serious and thorough design efforts are needed to prove feasibility. A "quick" switch-over is needed to allow moving each of the two detectors onto the beamline a few times a year. The configuration envisioned allows access to the detector which is out of the beam, with shielding of about one-half meter of concrete on five sides. A platform which moves with the detector for electronics and services of about 10m by 8m by 8m should provide the needed ease of movement. It also provides vibration isolation. The two IR option should remain as a studied alternative.
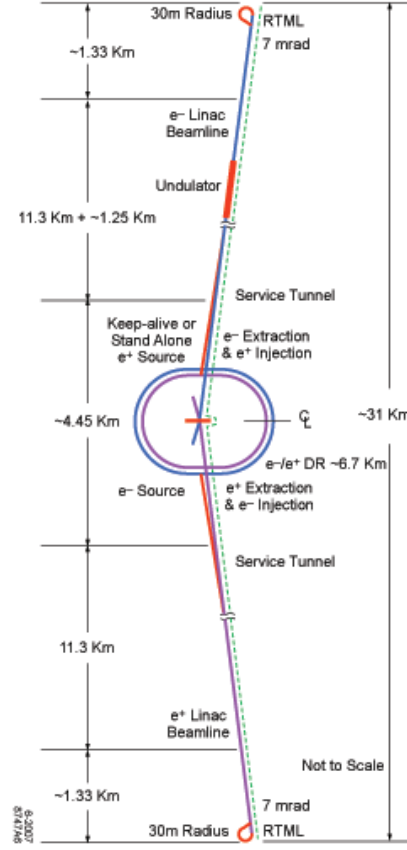
Figure 1: Layout of the ILC[6]

3 Detector R&D

Two years ago, beginning at the Snowmass ILC Workshop, an R&D Panel was created with the following charge:

WWS Detector R&D Panel Charge
- Surveys ILC detector R&D
- Maintains registry of ongoing ILC detector R&D
- Critically reviews the status of ILC detector R&D
- Registers the regional review processes

- Organizes global reviews of ILC detector R&D

The panel appointed by the WWS-OC in 2005 consists of three members from each region:

Asia: Tohru Takeshita, HonJoo Kim, Yasuhiro Sugimoto,
Europe: Chris Damerell (chair), Jean-Claude Brient, Wolfgang Lohmann,
Americas: Dean Karlen, Harry Weerts, Ray Frey.

Dean Karlen replaced Dan Peterson following the initial surveys, for which Dan devoted enormous effort in creating the web based registry.

The detector R&D program is motivated by the demanding detector performance requirements of ILC physics program. Advances beyond the state-of-the-art in detector technology are required. These include:

Detector R&D Goals

- Development of calorimeters with of the order of 100 million cells to achieve particle flow reconstruction of jets;

- Development of pixel vertex detectors with a billion pixels, sensitive to the full one millisecond bunchtrain of the ILC, without being overwhelmed by background hits, and achieving a better than four micron point resolution and an impact resolution of

$$5\mu\text{m} \oplus 10\mu\text{m/p } sin^{3/2}\theta \text{ ;}$$

- Tracking resolution, based on either a TPC tracker augmented by silicon, or a purely silicon tracker, of

$$\sigma(1/p) \leq 5 \times 10^{-5} GeV^{-1} \text{ ;}$$

- Development of high field solenoids of up to 5 Tesla field strength;

- Development of high quality forward tracking; and

- Development of triggerless readout.

These, and other requirements, will only be achieved with a strong R&D program. The discovery potential of the ILC is great, but it is limited by the detectors. The cross sections are small, and excellent discrimination between signals and backgrounds will yield scientific payoff.

This year the WWS initiated a series of R&D reviews, organized by the WWS R&D Panel. The first review was held during the February ACFA Linear Collider Workshop in Beijing. Tracking was reviewed. A committee of nineteen, including eight external reviews, conducted the review. The report for this review is posted on the WWS web page[2] and the ILC wiki. Calorimetry is being review during this workshop, and vertex detection will be reviewed in October during the ALCPG Workshop at Fermilab.[3] A fourth in this trial series of reviews will be held in Sendai (Tohoku University) during the ACFA Linear Collider Workshop (TILC08) in March, 2008.

	Tracker Tech.	Calorimeter Tech.	Solen'd Field (Tesla)	Solen'd Radius, Length (m)	Vertex Radius (mm)	ECAL Barrel Radius, Half-Length (m)	Overall Radius, Half-Length (m)
GLD	TPC	SiW ECal	3	4	20	2.1	7.65
		Pb/Scin Hcal		9.5		2.8	8.0
LDC	TPC	Scin/W ECal	4	3	15.5	1.58	5.98
		Dig. or Anlg. HCal		6.6		2.3	5.60
SiD	Silicon	SiW ECal	5	2.5	14	1.27	6.45
		Dig. HCal (RPC, .)		5.5		1.27	5.89
4th	TPC	Crystal EM	3.5	3	15	1.5	5.5
		dual-fiber Hcal		8		1.8	5.5

Table 1: Some key parameters of the four detector concepts.

4 ILC Detector Concepts

Progress in the development of the four[4] detector concepts has been good over the past year. Each concept (GLD, LDC, SiD, and 4th) published a Detector Outline Document in the Spring of 2007.[5] Some features of these three detectors are summarized in Table 1.

The WWS wrote a Physics Report and a Detector Concepts Report, which have been published along with the release of the Reference Design Report for the ILC accelerator.

The editors were:

Physics: A. Djouadi, J. Lykken, K. Moenig, Y. Okada, M. Oreglia, and S. Yamashita.

Detectors: J. Jaros, A. Miyamoto, T. Behnke, and C. Damerell.

A formal review has been conducted by a review team composed of K. Abe, J. Bagger, T. Camporesi, D. Marlow, T. Matsuda, J. Timmermans, R. Tschirhart, S. Y. Choi, and P. Zerwas. The detector cost estimates were reviewed by J.E. Augustin, P. Garbincius, and S. Yamada.

The community owes a great deal to the excellent efforts of the editors, and of the reviewers. The four volume set of documents (1. Executive Summary, 2. Physics, 3. Detectors, and 4. Accelerator) was published in August, 2007.[6]

5 Detector Roadmap

The Detector effort must keep pace with progress on the accelerator. Synchronization of the timelines is called for. With this in mind, the ILCSC and ICFA sent a message to the WWS co-chairs on February 28, 2007 asking the WWS to prepare a roadmap plan. Specifically, that message says:

a definite plan together with milestones is needed to have detector designs of a maturity similar to that of the accelerator by 2010. This needs an enhanced effort by the community. ILCSC will support the formation of an International

Detector Advisory Group to assist this effort. ICFA looks forward to receiving such a plan from WWS at the June 1, 2007 ILCSC meeting at DESY.

Responding to this request, the WWS co-chairs initiated a series of discussion via telephone with a *Roadmap Panel* consisting of two representatives from each of the four concepts, the WWS R&D Panel chair, and the WWS co-chairs. This request was also discussed by the WWS Organizing Committee. A web page was created to collect community comments, and a session was organized during LCWS08 to discuss the "roadmap."

The outcome of this discussion was to propose to the ILCSC that a Research Director, reporting to the ILCSC, be appointed to guide the enhanced effort by the community, and to serve as a single point of contact with the GDE management. It was also recommended that a call for Letters of Intent go out soon, for groups to present in about one year "proposals" to conduct engineering designs for detectors by 2010, and that two groups be recognized by the end of 2008 to carry through these engineering designs. It was recommended that an International Detector Advisory Group (IDAG) be formed to assist the Research Director in defining the process for the LOIs, and the review and recognition process. These recommendations were favorably received during LCWS08 by the ILCSC, and a search committee for the Research Director was created. Subsequently Sakue Yamada was nominated, and accepted an appointment by the ILCSC to serve as Research Director through the completion of the detector engineering design phase. At the time this is being written (October, 2007) a call for LOIs has been released to the community by ILCSC chair Shin-ichi Kurokawa, and the membership of the IDAG is being considered.

6   Conclusion

Significant progress continues on ILC physics and detector studies. By the time of LCWS08 in North America the Letters of Intent will have been submitted, and the process of beginning the detector engineering work will be underway. Much work is needed in the coming year to reach that important milestone. Judging from the pace of efforts over the past year, we will do well.

7   Acknowledgments

The World Wide Study is grateful to DESY for hosting the very well run LCWS07, and particularly to Ties Behnke, who coordinated all of our requests, and the many unseen aspects of such a large meeting.

References

[1] Slides: http://ilcagenda.linearcollider.org/contributionDisplay.py?contribId=6&sessionId=1&confId=1296

[2] http://physics.uoregon.edu/~lc/wwstudy/detrdrev.html

[3] Reports of the R&D Panel Reviews were given at LCWS07 by C. Damerell and W. Lohmann.

[4] GLD and LDC announced in the fall of 2007 that they are merging efforts, and call their new detector ILD.

[5] http://physics.uoregon.edu/~lc/wwstudy/concepts/

[6] Reference Design Report http://linearcollider.org

The LHC early phase for the ILC

Klaus Desch

Physikalisches Institut der Universität Bonn
Nussallee 12, 53115 Bonn - Germany

With the startup of the Large Hadron Collider LHC in 2008, exciting new phenomena at the TeV energy scale may be discovered. I describe first ideas concerning the implication of the potential discoveries for the planning of the International Linear Collider ILC. These ideas are based on the results of an initial workshop held at Fermilab in April 2007 [2].

1 LHC-ILC Interplay

High energy physics is entering a new era when, in 2008, the Large Hadron Collider LHC will provide access to particle collisions with 1 TeV partonic centre-of-mass energy an beyond. At this energy and with sufficient integrated luminosity, the important question how the electro-weak symmetry is broken can most likely be answered. Beyond that, the LHC experiments are sensitive to a broad spectrum of signatures that may indicate phenomena whose explanation lies beyond the Standard Model (SM). Such beyond-SM (BSM) models are generally motivated by fundamental theoretical questions: the apparent hierarchy of mass scales, the quest for a unification of forces and the absence of explanations for the observed dark matter and dark energy in our universe.

The predictions of BSM models which address the above questions often encompass new fundamental particles with masses in the TeV regime. The particles lead to signatures which involve jets and leptons with high transverse momenta p_t, in some cases accompanied by large missing transverse energy from high-p_t particles invisible to the detectors. The multi-purpose detectors ATLAS and CMS at the LHC are designed such, that they can discover any excess of high-p_t objects if they are produced with sufficient rate. In particular, signatures of the best-motivated BSM models, e.g. Supersymmetry, models with extra spatial dimensions, new heavy vector bosons, and excited fermions can be detected over large parts of the respective parameter spaces. We thus have any reason to be excited about the possible discoveries that ATLAS and CMS will make in the coming years.

In parallel to the preparations for the LHC and its detectors, a significant amount of work has gone into the preparation of tools which complement the LHC in the future. Most importantly, a new electron positron linear collider in the TeV energy regime has been shown in extensive studies to be the ideal tool to sharpen our view of the phenomena to be discovered at the LHC. Practically is has been shown that – independent of the findings of the LHC experiments – a Linear Collider with 500 GeV initial energy (and upgradeable to 1 TeV) will provide an important addition to the LHC's capabilities. This is mainly due to the fact that the SM without a Higgs boson violates unitarity at slightly above 1 TeV. Such a machine, the International Linear Collider ILC, based on superconducting acceleration technology is well advanced and according to a technically driven schedule can be realized by 2018 [3].

Over the past few years, the interplay of the LHC and the ILC has been studied in great detail [4]. The main focus of these studies was the question how the data from both machines together would yield a more complete picture of the realized new physics scenario compared

to that obtained from one machine alone. Also, it was studied how simultaneous analysis of the data may provide feedback and refine the single-machine analyses. Although no clear consensus was reached to which extent simultaneous running of LHC and ILC would be required, it remains evident that a timely construction of the ILC will significantly facilitate the successful interplay of LHC and ILC and thus the best possible exploration of TeV scale physics.

While the physics case for the ILC is to a large extent built on arguments which are independent of the results of the LHC experiments it is obvious that these results which will be available in the near future have to be taken into account, when a solid planning for the ILC's realisation, its initial configuration, and upgrade options is to be made. In this presentation I like to report on a workshop held at Fermilab in April 2007 which laid the ground for a more systematic study of the implications of early LHC physics results for the ILC.

Within the workshop, working groups are being formed around possible signatures seen in the early data of the LHC experiments. The term 'early' is not defined by running time of the LHC rather than by an integrated luminosity of $\mathcal{O}(10)$ fb^{-1} . The chosen signatures are

1. A SM-Higgs-like state at the LHC;

2. No Higgs boson state at the early stage of the LHC;

3. Leptonic resonances and multi-gauge-boson signals;

4. Missing energy signals (and everything else).

In the following, I will briefly sketch these four scenarios, the LHC prospects for early discoveries and possible implications for the ILC.

2   A SM-Higgs-like state at the early LHC

Both ATLAS and CMS have demonstrated that with approximately 10 fb^{-1} of understood data a significant signal from a SM-like Higgs boson can be extracted from the expected SM background. While for Higgs boson masses above 200 GeV, a discovery is relatively straight-forward due to the $H \to ZZ \to 4\ell$ decay mode, an early discovery for lower masses possibly needs the combination of several Higgs final states. For low masses below 140 GeV these are the inclusive $H \to \gamma\gamma$ mode, and the weak boson fusion mode $qqH \to qq\tau^+\tau^-$ [5].

While only a limited amount of information about the newly discovered particle will be available at this early stage, it will be probably enough to arrive at a solid decision for the ILC. Its mass will be known better than $\mathcal{O}(1$ GeV) and its observation in weak boson fusion or in its decay to ZZ will prove that the particle carries a gauge coupling and can thus be produced in the $e^+e^- \to HZ$ Higgs-strahlung process. With 30 fb^{-1} a rough estimate of the partial width ratios Z/W, γ/W, and τ/W will be possible [6].

What are the consequences of such a discovery for the ILC? The answer to this question depends to some extent on the observed mass of the new particle. If the Higgs boson mass is below approximately 160 GeV, the full program of precision measurements of the Higgs boson properties can be performed at the ILC. In particular, this program comprises precise measurements of the Higgs boson gauge and Yukawa (b,c,t,τ) couplings, its total decay width, and in particular its self-coupling in a completely model-independent way [7].

For a mass above 160 GeV, the phenomenology of a SM-like Higgs boson is less rich since the Yukawa decay modes are highly suppressed (except for $H \to t\bar{t}$ if $m_H > 340$ GeV). In this mass range, which with increasing Higgs mass is increasingly disfavoured by electro-weak precision measurements, the dominant decay modes can be observed at the LHC and furthermore, a model-independent measurement of the total width from the Higgs boson line-shape will be possible for masses beyond approximately 200 GeV.

It is one of the important goals of this working group to assess and compare the potential of the LHC and the ILC for measurements of Higgs boson properties in this mass range more quantitatively than previously done.

3   No Higgs (yet) at the LHC

If no Higgs-boson-like signal will be observed with approximately 10 fb^{-1} of well calibrated and understood data at the LHC experiments, there are two different roads of interpretation.

1. There is no Higgs mechanism at work, and thus there is really no Higgs boson.

2. The Higgs mechanism is at work, however its realisation is such that the corresponding Higgs boson(s) are not or not yet accessible with the LHC.

Since the implications of these two interpretations for the ILC are probably different, it is of major importance to study whether the LHC experiments can distinguish between these.

1. Models without Higgs mechanism require a mechanism to unitarize the amplitude for the elastic scattering of longitudinal gauge bosons. In general, the new phenomena associated with this mechanism modify the predictions for electro-weak precision observables. For Technicolor theories [8], this has been a long-standing problem. The more recently constructed Higgsless models [9] which require the existence of towers of new gauge bosons and heavy fermions (as predicted in theories with extra spatial-dimensions) are able to delay the unitarity problem to energy scales beyond those accessible with the LHC while at the same time avoiding too large electro-weak corrections.

In Higgsless models in general new particles should be observable at the LHC since they cannot be too heavy because they have to restore unitarity. The observation of a new Z'-like resonance at the LHC clearly calls for its exploration with the ILC as discussed in the next section.

2. The universal signature for the absence of a Higgs mechanism is a deviation of elastic gauge boson scattering. If the LHC could exclude strong vector boson scattering in absence of any Higgs-like signature, this could provide an indirect indication that a Higgs-like signature has been missed at the LHC. This clearly excludes the SM Higgs boson but also standard MSSM Higgs bosons. However, extended Higgs sectors may require higher luminosity at the LHC until at least one state can be observed, as it is the case e.g. in the NMSSM [10]. Also within little Higgs models [11], the discovery of the Higgs sector might be delayed at the LHC [12].

However, it might also be that the presence of the Higgs mechanism may only be revealed by the ILC. Viable models which implement this scenario are e.g. continua of Higgs bosons [13] and Higgs bosons with a very large width decaying into invisible particles [14]. Thus, contrary to some common wisdom, the absence of a Higgs-like state at the LHC may require an ILC to reveal the underlying physics.

4 Leptonic Resonances and Multi-Gauge-Boson Signals

New resonances which can be produced via the Drell-Yan process and which decay into e^+e^- and/or $\mu^+\mu^-$ can be seen rather fast by the LHC experiments. The required integrated luminosity to discover e.g. a sequential Z' boson with 1 TeV mass is below 100 pb^{-1} even with imperfect detector calibration [15]. The mass reach for discovery with 10 fb^{-1} is between 3 and 4 TeV, depending on the model.

The implications of such a discovery for the ILC depend on its mass. Given Tevatron exclusion bounds, a resonance within the reach of ILC phase 1 (500 GeV) is not very likely. Should a resonance below 1 TeV be observed, this would clearly call for a fast upgrade path of the ILC to study the new object in s-channel production. However in presence of a light SM-like Higgs boson, also ILC phase 1 remains well-motivated.

If the resonance should occur above the direct reach of the upgraded ILC a precise determination of its couplings structure can still be achieved at the ILC from interference effects with Z/γ in SM processes, provided its mass is known from the LHC [16]. Also, for W'-like objects, the ILC has sensitivity from the $e^+e^- \to \nu\bar{\nu}\gamma$ process [17].

5 Missing energy signals

Signals with an excess of missing transverse energy (MET) at the LHC have extensively been studied. The major motivation to do so are the predictions of low-energy Supersymmetry with R-parity conservation as implemented in the MSSM. However, also other theories which require or postulate the existence of a weakly interacting massive particle like Universal Extra Dimensions or some variants of Little Higgs models predict MET signals.

Understanding MET signals at the LHC experiments is particular difficult, since the proper measurement of MET is very sensitive to detector calibration and modeling. Furthermore, SM contributions to MET have to be simulated to high precision even in tails of distributions and have to be calibrated with real data. It is thus not very likely that a mere excess of events with large MET in the early LHC data can be claimed as a discovery of BSM physics immediately. On the other hand, often, in particular in parts of the MSSM parameter space, the expected excess of large-MET events is huge and furthermore accompanied by additional signatures like multi-jets and/or multi-leptons, which are much easier to control. It is very hard to predict when a clear and significant excess can be claimed.

In view of its implications for the ILC, it is important to infer from LHC data analysis if any signal in e^+e^- collisions is expected and at which centre-of-mass energy. For an MET-excess this questions is not easy to be answered without making too many model assumptions. The main reason for this is that with escaping WIMP-like particles, invariant masses of the decaying BSM particles cannot be reconstructed uniquely. The situation significantly improves if certain assumptions (like they are justified e.g. in mSugra models) about mass hierarchies etc. can be made.

Many different approaches towards mass reconstruction of SUSY-cascades have been worked out [18]. Furthermore global fits of the parameters of SUSY models [19, 20] and generic Monte Carlo tools [21] have been developed to approach this task. However in the course of the workshop new approaches and improvements are necessary.

6 Summary and conclusions

I gave a brief sketch of a new aspect of the relation of the LHC and ILC, namely the implications of early LHC data on ILC planning. While the physics motivation for the ILC is independent of the LHC findings, the early LHC data will have an impact on the decision when to build the ILC and on the choice of the parameters. In many possible scenarios, including the discovery of a Higgs boson, a timely construction of the ILC is clearly motivated. Some scenarios including e.g. the observation of an intermediate mass Higgs boson need further studies. A workshop which started in 2007 will study these questions in detail.

References

[1] Slides: `http://ilcagenda.linearcollider.org/contributionDisplay.py?contribId=7&sessionId=1&confId=1296`

[2] Workshop "The LHC Early Phase for the ILC", `http://conferences.fnal.gov/ilc-lhc07/`

[3] B. Barish, these procedings; slides:
`http://ilcagenda.linearcollider.org/contributionDisplay.py?contribId=2&sessionId=0&confId=1296`

[4] G. Weiglein *et al.* [LHC/LC Study Group], Phys. Rept. **426** (2006) 47 [arXiv:hep-ph/0410364].

[5] V. Buscher and K. Jakobs, Int. J. Mod. Phys. A **20** (2005) 2523 [arXiv:hep-ph/0504099].

[6] M. Duhrssen, S. Heinemeyer, H. Logan, D. Rainwater, G. Weiglein and D. Zeppenfeld, Phys. Rev. D **70** (2004) 113009 [arXiv:hep-ph/0406323].

[7] For a recent compilation see e.g. A. Djouadi, J. Lykken, K. Monig, Y. Okada, M. J. Oreglia and S. Yamashita, arXiv:0709.1893 [hep-ph].

[8] K. Lane, arXiv:hep-ph/0202255.

[9] C. Csaki, C. Grojean, L. Pilo and J. Terning, Phys. Rev. Lett. **92** (2004) 101802 [arXiv:hep-ph/0308038].

[10] R. Dermisek and J. F. Gunion, Phys. Rev. D **73** (2006) 111701 [arXiv:hep-ph/0510322].

[11] W. Kilian and J. Reuter, Phys. Rev. D **70** (2004) 015004 [arXiv:hep-ph/0311095].

[12] J. Reuter, these procedings and arXiv:0709.3816 [hep-ph].

[13] J. R. Espinosa and J. F. Gunion, Phys. Rev. Lett. **82** (1999) 1084 [arXiv:hep-ph/9807275].

[14] J. J. van der Bij, these procedings and arXiv:0707.0356 [hep-ph].

[15] The CMS Collaboration, J. Phys. **G 34** (2007) 995.

[16] S. Riemann, "Aspects Of New Gauge Bosons Searches At LHC/LC," in proceedings of LCWS 04, (2004).

[17] S. Godfrey, P. Kalyniak and A. Tomkins, arXiv:hep-ph/0511335.

[18] B. K. Gjelsten, D. J. Miller and P. Osland, JHEP **0412** (2004) 003 [arXiv:hep-ph/0410303];
B. K. Gjelsten, D. J. Miller, P. Osland and A. R. Raklev, AIP Conf. Proc. **903** (2007) 257 [arXiv:hep-ph/0611259];
K. Kawagoe, M. M. Nojiri and G. Polesello, Phys. Rev. D **71** (2005) 035008 [arXiv:hep-ph/0410160];
W. S. Cho, K. Choi, Y. G. Kim and C. B. Park, arXiv:0709.0288 [hep-ph];
S. Laplace [ATLAS Collaboration], Acta Phys. Polon. B **38** (2007) 617.

[19] R. Lafaye, T. Plehn and D. Zerwas, arXiv:hep-ph/0404282;
R. Lafaye, T. Plehn, M. Rauch and D. Zerwas, arXiv:0709.3985 [hep-ph].

[20] P. Bechtle, K. Desch and P. Wienemann, Comput. Phys. Commun. **174** (2006) 47 [arXiv:hep-ph/0412012];
P. Bechtle, K. Desch, W. Porod and P. Wienemann, Eur. Phys. J. C **46** (2006) 533 [arXiv:hep-ph/0511006].

[21] N. Arkani-Hamed, P. Schuster, N. Toro, J. Thaler, L. T. Wang, B. Knuteson and S. Mrenna, arXiv:hep-ph/0703088.

SOFTWARE TOOLS FOR ILC DETECTOR STUDIES

Roman Pöschl

Laboratoire de l'Accélérateur Linéaire (LAL)
B.P. 34 - F-91898 Orsay

This article presents a review on the main issues of the software and computing tools developed ILC Detector related studies. It works out common efforts but also differences among the efforts within the three different regions in which the detector R&D is pursued. It outlines the main features of the software packages and highlights results which were obtained by studies obtained within the frameworks. The grid is constantly evolving to be the computing environment for the studies.

1 Introduction

Software plays an important role in all aspects of the ILC detector development. Comprehensive software tools are essential to define the key parameters of a detector layout ready to achieve the goal of $30\%/\sqrt{E}$ of energy resolution. Currently, the R&D for the ILC detectors is performed within three regions comprising four different concepts for the detectors. These are namely the LDC, GLD, ALCPG and 4th Concept studies.

The computing environment as currently established for ILC Detectors comprises the core software, including the algorithms and the basic data models as well as the application of grid tools in order to perform the processing of Monte Carlo files and, in case of test beam efforts, real data [2]. In addition to that database services are provided to support the various efforts. Figure 1 shows a general overview of the ingredients of the ILC software and computing infrastructure.

Though the software frameworks differ among the three regions and four detector concepts there is a considerable effort in order to make the results interchangeable.

2 The Actual Software

The backbone of the ILC Software is the LCIO [3] package. It features a data model with well defined interfaces to common objects used in HEP studies. The application of such a data model clearly facilitates the exchange of results between different studies and therefore the comparison between detector models. Developed by SLAC and DESY IT groups, it is currently the de-facto standard for the ALCPG [4] and LDC [5] studies. Implementations of LCIO do exist for the java, C++ and Fortran programming language allowing therefore for a large community to benefit (and contribute) from (to) the existing algorithms. The SIO package is employed for data persistency and results are stored in so called 'lcio files'. The GLD study as well as the 4th concept have developed their own root' [6] based framework but envisage to provide their results in the LCIO format in order to facilitate the interchangeability of results [7, 8]. Being at a first stage developed and designed for full detector simulation studies, LCIO is increasingly applied in test beam studies such as within the CALICE collaboration. This strategy will permit to transport easily results from these test beam experiments into the full detector studies. Secondly, algorithms developed
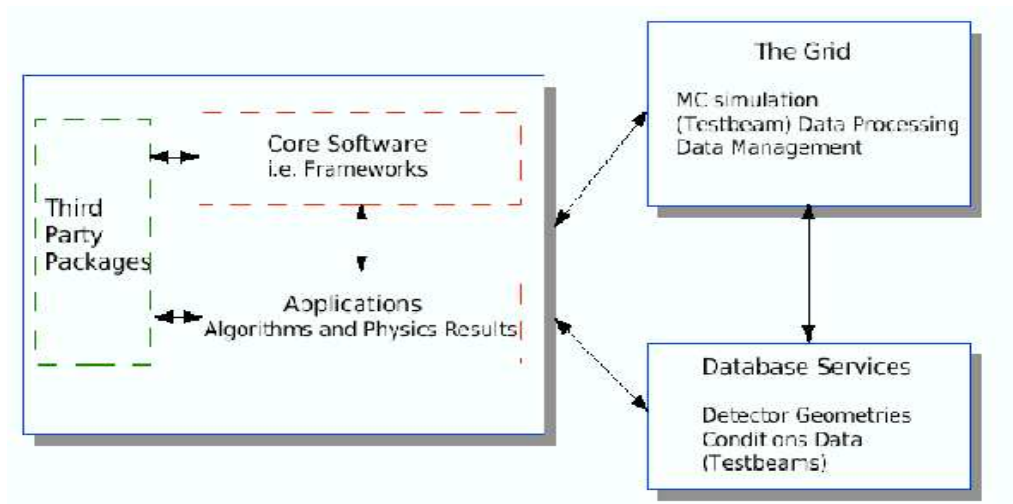
Figure 1: Ingredients of the ILC software and computing environment.

within the detector studies can be applied to 'real' data. The application of LCIO allows at an early stage the definition interfaces to DAQ systems, a project to be realized for the next generation of test beam efforts.

The simulation of the various detector proposals and prototypes employed in test beams is based on the GEANT4 [9] software package. In particular for several test beam efforts also GEANT3 implementations are maintained. These won't be described further here, The actual geometry is fed into GEANT4 by several methods. Within the MOKKA package [10] as used for the LDC study the descriptions are stored within a mysql data base. Within the ALCPG study the geometry is read via the package LCDD into SLIC which is the simulation package. The detailed detector description is defined within xml files. The framework allows for a rough or compact description of a given detector. The latter is transformed via a Geometry Converter into the needed xml files or other formats. Both approaches allow for a flexible adjustment of detector geometries as needed for detector optimization studies where the compact description facilitate the performance of quick studies in which the details of the detector geometry are of minor importance. Cross implementations, i.e. the implementation of one detector concept in the framework of the other concept, do exist, however on a still too low level.

The simulated files are subject to a reconstruction chain which exists for all concepts in a more or less complete form. The LDC concept uses the software package MARLIN. MARLIN provides a main program and users can implement their algorithms in form of so-called processors. The information is transported between the processors by means of an *LCEvent* object. Using MARLIN, the LDC study has developed a nearly complete event reconstruction, combining a first detector digitization, track reconstruction and vertex finding, calorimeter reconstruction jet finding and finally a particle reconstruction. Figure 2 shows the results of a recently published vertex finding suite [11] which is fully integrated into MARLIN. Table 2 gives an overview on the simulation packages and reconstruction packages used within the four concepts.
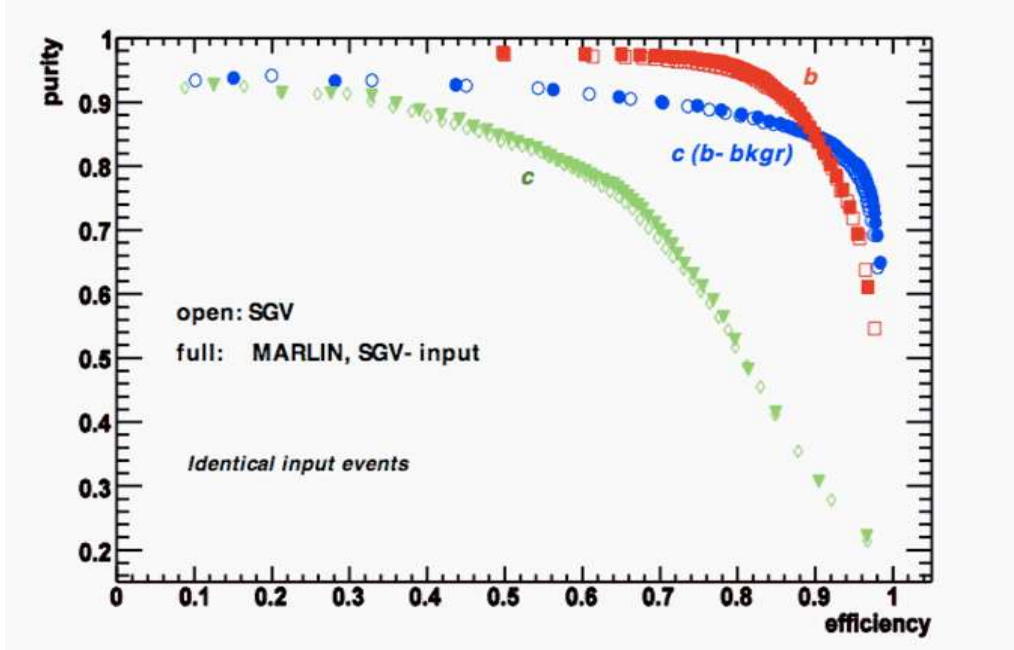
Figure 2: Flavor tagging efficiencies as obtained within the MARLIN reconstruction chain.

Concept	Simulation	Reconstruction	Webportal
LDC	MOKKA	MARLN	`http://ilcsoft.desy.de`
ALCPG	SLIC	org.lcsim	`http://www.lcsim.org`
GLD	JUPITER	URANUS	`http://ilcphys.kek.jp/soft`
4th Concept	ILCROOT	ILCROOT	`http://www.fisica.unile.it/~danieleb/IlcRoot/`

Table 1: Software frameworks used in the four concepts.

The ALCPG study assembles the reconstruction algorithms within the org.lcsim package. The GLD Study maintains the package URANUS which is a suite for reconstruction and analysis algorithms. An interesting approach is followed by the 4th Concept. In collaboration with the ALICE Experiment and others, the development and application of a generic reconstruction framework for HEP experiments, called HEPROOT, is under study. Such a framework would be largely based on the root system.

Having a full chain of reconstruction available allows for the application of recent Particle Flow Algorithms such as Pandora [12] and others [13, 14] under realistic conditions and hence for the optimization the of detector layout for the particle flow approach which is said to provide the precision needed for the physics studies envisaged at the ILC. Figure 3 shows the results of optimization studies done within the MARLIN framework and the URANUS framework. Both studies lead to the conclusion that a large inner calorimeter radius is more important for an optimal jet energy resolution than e.g. the magnetic field. The processor approach in MARLIN allows for an easy exchange of algorithms and therefore for detailed comparisons between different proposals.
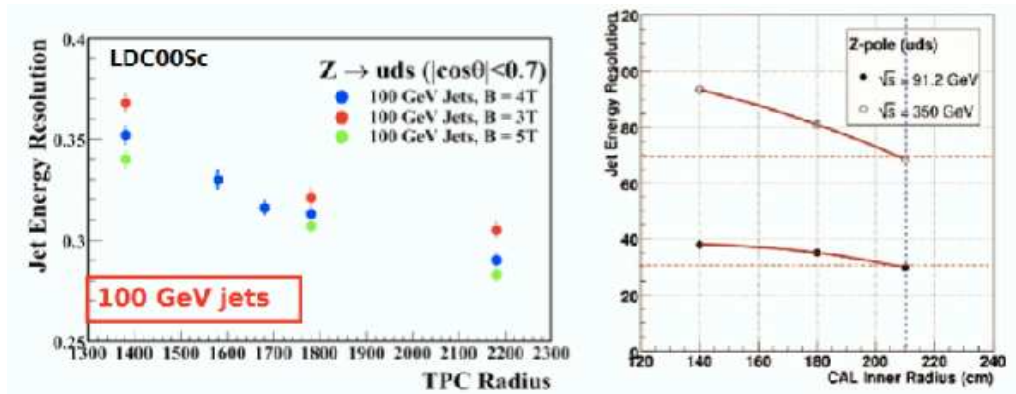
Figure 3: Examples of results of detector optimization studies within the MARLIN (left) and URANUS framework (right).

A problem which has not yet been solved so far is the access to a given detector geometry during the reconstruction. The GEAR package is one approach to remedy this short coming. Here the MOKKA simulation outputs an xml file which can be read into MAR-LIN using GEAR. Under development mainly by SLAC and DESY groups, the package LCGO is foreseen to provide an interface to detector geometries independent of the software framework.

The visualisation of the results is realized by event displays. The presumably most mature approach is the WIRED Event display within the JAS suite. This package has been written and is maintained by the ALCPG study. The WIRED event display reads the detector geometry by means of HEPREP files which is, loosely spoken, a flavor of the xml language. The JAS suite allows to read in directly LCIO files with the help of suited plug-ins. By this, the information stored within the LCIO files can be conveniently coupled to the given detector geometry. Both, HEPREP files and lcio files. can be produced by the simulation and reconstruction programs of the ALCPG and the LDC study thus facilitating the exchange of results.

3   The Infrastructure

Full detector studies of tentative ILC detectors do need a significant amount of computing power to be pursued. In addition, the data and results have to be shared among the community around the world. For the ILC, grid technologies have been identified to meet these requirement [15]. The exploitation of the grid by the ILC community naturally benefits largely from the efforts undertaken for LHC computing. The virtual organisation *ilc* has been established which is hosted by DESY. Using the grid, data can be stored in a virtual file system and are accessible to all members of the virtual organisation. The ILC is supported by IT divisions in all three regions leading to a total amount of several thousand CPUs and roughly 100-200 TByte of available disk space. Since the application of grid tools is still clearly at the beginning, there is so far no dedicated organization of the computing based on the grid as it is e.g. the case for the LHC with its subdivision into TIER centers. A

infrastructure like this may emerge with the forming of proto-collaborations as foreseen until the end of 2008.

Among the R&D projects for the ILC detectors the collaboration CALICE is using the grid extensively [16]. CALICE is performing R&D for the central calorimeters of the ILC detectors. For the data management and the processing of the data the vo *calice* has been established which counts currently 52 members. Up to now the collaboration has collected about 15 TByte of data. Together with reconstructed and simulated data, 30 TByte of disk space are occupied by the CALICE data.. The whole management and processing of the data is based on grid tools. The whole set of data is centrally stored at DESY but is or will be replicated to other major computing centers within the three regions. By this CALICE not only paves the way for an extended use of the grid by the ILC but delivered also important tests wrt. to a continous use of the grid for other experiments, in particular in terms of persistent data.

The rich set of parameters occurring in large scale data taking in test beam programs demands for an efficient handling of conditions data. The access to conditions data is realized by the LCCD package. It permits to store conditions data in different backends. One of these backends is a mysql database. In this case the LCCD package is itself interfaced to the CondDBMySQL [17] as written by the Lisbon Atlas group package which allows for a structured management of the conditions data. A layer and tagging tagging mechanism provides a full reproducibility of a given set of conditions data. It has to be pointed out that the current handling of conditions data is only a first attempt to establish such a software which is and will be of vital importance for any running experiment.

4   Conclusion and Outlook

All necessary parts of the software needed for ILC Detector and test beam studies do exist in a more or less mature form. Based on these tools, clear results which will influence the layout of the ILC detectors have been achieved. Emerging from different studies, the available software packages are still very heterogeneous. However, efforts are undergoing to enable the interchange of data among the studies. Here clearly the forming of proto-collaborations as foreseen until the end of 2008 will naturally lead to a larger homogenization of the software packages.

The grid has been identified as the environment for the processing and management of ILC related data. While already of vital importance for R&D projects like CALICE, it is expected that its importance for the ILC studies in general will grow considerably in the coming years.

In all fields of software the ILC community is short of manpower. This is in particular true for the development of a common and convenient event display but also for packages such as a common interface to detector geometries and for the handling of conditions data.

Acknowledgments

References

[1] Slides:
http://ilcagenda.linearcollider.org/contributionDisplay.py?contribId=8&sessionId=1&confId=1296

[2] For a comprehensive overview see:
http://ilcagenda.linearcollider.org/sessionDisplay.py?sessionId=76&slotId=0&confId=1296

[3] F. Gaede *et al.*, *"LCIO - A persistency framework for linear collider simulation studies"*
LC-TOOL-2003-053, see http://www-flc.desy.de/lcnotes
See also these proceedings for an update.

[4] N. Graf *"ALCPG Software Summary"*. These procedings.

[5] For an overview on the LDC software packages see http://ilcsoft.desy.de.

[6] For a reference see http://root.cern.ch.

[7] A. Miyamoto *"Software Tools in GLD study"*.
Talk given at the ILC Software Workshop Orsay (France) May 2007
http://events.lal.in2p3.fr/conferences/ILCSoftware/

[8] C. Gatto *"Tools in 4th Concept Study"*.
Talk given at the ILC Software Workshop Orsay (France) May 2007
http://events.lal.in2p3.fr/conferences/ILCSoftware/

[9] S. Agostinelli *et al.*, *"GEANT4 - A simulation toolkit"*, NIM **A 506** (2003) 250

[10] For a reference see http://polzope.in2p3.fr:8081/MOKKA.

[11] S. Hillert *et al.*, *"The LCFI Vertex Package"*, These proceedings.

[12] M. Thomson *et al.*, *"Status of Particle Flow Reconstruction with PandoraPFA"*, These proceedings.

[13] N. Graf *et al.*, *"PFA Development in the US"*, These proceedings.

[14] T. Yoshioka *et al.*, *"GLD PFA Studies"*, These proceedings.

[15] See for example A. Gellrich, *"ILC and the grid"*, These proceedings.

[16] R. Pöschl *Calice and the grid*.
Talk given at the ILC Software Workshop Orsay (France) May 2007
http://events.lal.in2p3.fr/conferences/ILCSoftware/

[17] For a reference see *http://savannah.cern.ch/projects/conddb-mysql*

Particle Flow Calorimetry at ILC Experiment

Tamaki Yoshioka

International Center for Elementary Particle Physics (ICEPP)
The University of Tokyo, 7-3-1 Bunkyo-ku, Hongo, Japan

Most of the important physics processes to be studied in the International Linear Collider (ILC) experiment have multi-jets in the final states. In order to achieve best attainable jet energy resolution, a so-called Particle Flow Algorithm (PFA) will be employed, and there is a rather wide consensus that PFA derives the overall ILC detector design. Three out of four are proposing a detector which is optimized for the PFA, though the technical realization is quite different. In this paper, the PFAs currently being developed and their performances are reviewed.

1   Introduction

The International Linear Collider (ILC) is a future energy-frontier electron-positron collider currently being designed by a world-wide collaboration[2]. The physics goal of the ILC experiment ranges over a wide variety of processes in a wide energy region of center of mass energy[3, 4]. Most of the important physics processes to be studied in the ILC experiment have multi-jets in the final states, and therefore precise jet energy reconstruction plays an important role to the ILC physics. One of the performance goal required to the ILC detector is that two-jets invariant mass resolution is comparable with the natural widths of W and Z (~ 2GeV) for their separation in hadronic final states. A jet energy resolution of $\sigma_E/E = \alpha/\sqrt{E}$ leads to a two-jets mass resolution of $\sigma_M/M = \alpha/\sqrt{E_{jet}}$ where E_{jet} is the energy of the two-jets system. At the ILC, the E_{jet} is typically ~ 150 GeV, suggesting the target resolution of $\sigma_E/E = 30\%/\sqrt{E(GeV)}$[2] which is a factor two better than the best jet energy resolution achieved at LEP, $\sigma_E/E = 60\%(1+|\cos\theta|)/\sqrt{E(GeV)}$[5]. Study on measurements of the Higgs mass in the four jet channel, $e^+e^- \to ZH \to q\bar{q}b\bar{b}$, shows significant benefit from such very high jet energy resolution[6]. Larger statistics than $e^+e^- \to ZH \to l^+l^-b\bar{b}$ channel can be expected for this channel as long as the Higgs mass is small enough that the branching ratio to b-quarks pairs is large enough. The study was performed by assuming a Standard Model Higgs with a mass of 120 GeV and an integrated luminosity of 500 fb^{-1}. Figure 1 shows the invariant mass of the two b-quark jets for $\sigma_E/E = 30\%/\sqrt{E(GeV)}$ (left) and $\sigma_E/E = 60\%/\sqrt{E(GeV)}$ (right). The error in the Higgs mass improves by a factor 1.2, corresponding to an equivalent 40% luminosity gain. The importance of achieving very high jet energy resolution in ILC detectors are also shown by studies on several other physics processes[2].

2   Particle Flow Algorithm

Achieving a jet energy resolution of $\sigma_E/E = 30\%/\sqrt{E(GeV)}$ is rather technical challenge for ILC detectors. Such energy resolution could be achieved by a combination of highly efficient and nearly hermetic tracking system with a very fine transverse and longitudinal segmented calorimeter. Since the momentum resolution for the charged particle measured by tracking system is much better than the energy resolution of calorimeters, the best jet
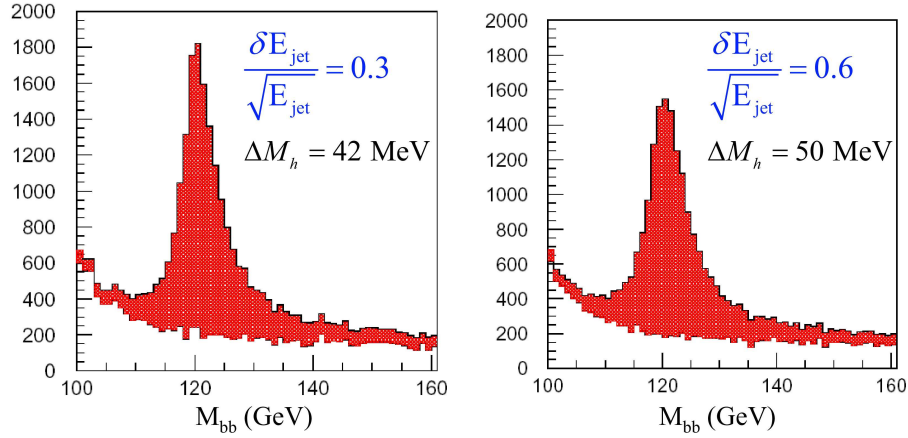
Figure 1: Higgs two-jet invariant mass for $e^+e^- \to ZH \to q\bar{q}b\bar{b}$ channel for $\sigma_E/E = 30\%/\sqrt{E(GeV)}$ (left) and $\sigma_E/E = 60\%/\sqrt{E(GeV)}$ (right). The error in the Higgs mass improves by a factor 1.2, corresponding to an equivalent 40% luminosity gain.

energy resolution is obtained by reconstructing momenta of individual particles avoiding double counting among trackers and calorimeters; charged particles, whose energy fraction in a jet is about 60%, are measured by trackers, photons, whose energy fraction is about 30%, are measured by electromagnetic calorimeter (ECAL) and neutral hadrons, which carry the rest of energy, are measured by both ECAL and hadron calorimeter (HCAL). To be more precisely, the total energy of an event E_{Total} is calculated as follows:

$$E_{Total} = P_e + P_\mu + P_{ChargedHadron} + E_\gamma + E_{NeutralHadron}, \qquad (1)$$

where P_e, P_μ and $P_{ChargedHadron}$ are momentum of the electron, muon and charged hadron measured by the tracking system, respectively, and, E_γ and $E_{NeutralHadron}$ are energy of the γ and neutral hadron measured by the calorimeters. This is known as a Particle Flow Algorithm (PFA) and it is widely believed that PFA is the most promising way to achieve a jet energy resolution of $\sigma_E/E = 30\%/\sqrt{E(GeV)}$. The crucial part of the PFA is that separation of particles in the calorimeter – i.e. reducing the density of charged and neutral particles at the calorimeter surface. Figure of merit is often quoted as $\frac{BR^2}{\sqrt{\sigma^2+R_M^2}}$, where B is the magnetic field, R is the ECAL inner radius, σ is the calorimeter granularity and R_M is the effective Moliere radius. As can be seen from the figure of merit, stronger magnetic field and large ECAL radius as well as the fine segmentation of the calorimeter are preferable for transverse separation of particles at the ECAL surface.

Four detector concepts for the ILC experiment have been proposed so far in the world[7]. Figure 2 shows an illustration of the four detector concepts. Three out of four (SiD, LDC and GLD) are proposing a detector which is optimized for the PFA, though the technical realization is quite different. The SiD detector has the highest magnetic field and the smallest ECAL inner radius, the GLD detector has the weakest field and the largest radius and the LDC detector is in between other two detectors. These values are summarized in Table 1. The 4th detector differs from the other three concepts; they utilizes a novel implementation
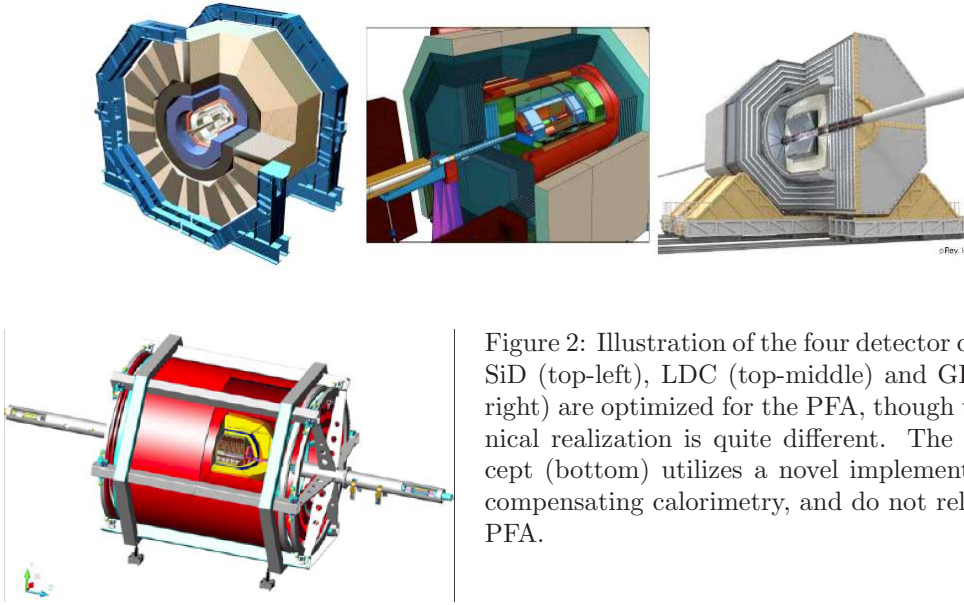
Figure 2: Illustration of the four detector concepts. SiD (top-left), LDC (top-middle) and GLD (top-right) are optimized for the PFA, though the technical realization is quite different. The 4th concept (bottom) utilizes a novel implementation of compensating calorimetry, and do not rely on the PFA.

of compensating calorimetry, and do not rely on the PFA. The magnetic field and ECAL inner radius for the 4th detector are also summarized in Table 1.

Concept	Magnetic Field Strength (Tesla)	ECAL Barrel Inner Radius (m)
SiD	5	1.3
LDC	4	1.6
GLD	3	2.1
4th	3.5	1.5

Table 1: Magnetic field strength and ECAL barrel inner radius of the four detector concepts.

3   Review of Current PFA

Each detector concept has their own full detector simulator based on Geant4[8] and reconstruction package[9]. Figure 3[10] shows $e^+e^- \to t\bar{t}$ event at center of mass energy 500 GeV generated by Geant4-based full simulator for the SiD detector, named SLIC. Dense jets are clearly seen in the event display, and main issues of PFA is to separate energy deposit in such high density environment. Several PFAs have been intensively developed in the framework of these software tools. While the algorithms are distinct, there are a number of features which are common. Basic features and current performance of the PFAs are shown in the following. Notice that study by the cheated/perfect PFA which use simulation information to connect a charged track and calorimeter signals is also on-going[11]. They are useful to understand factors which affect the jet energy resolution.

Figure 4 shows a structure of one of the PFA developed for SiD detector[12]. In the SiD-PFA, first of all, a clustering algorithm and track finding algorithm are applied to the
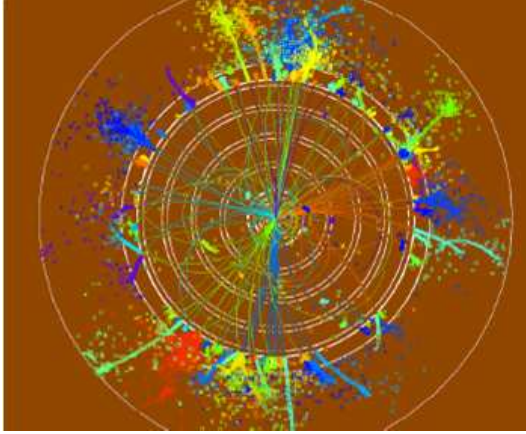
Figure 3: An event display of $e^+e- \to t\bar{t}$ event at center of mass energy 500 GeV generated by Geant4-based full simulator for the SiD detector, named SLIC. Main issues of PFA is to resolve such dense jets.
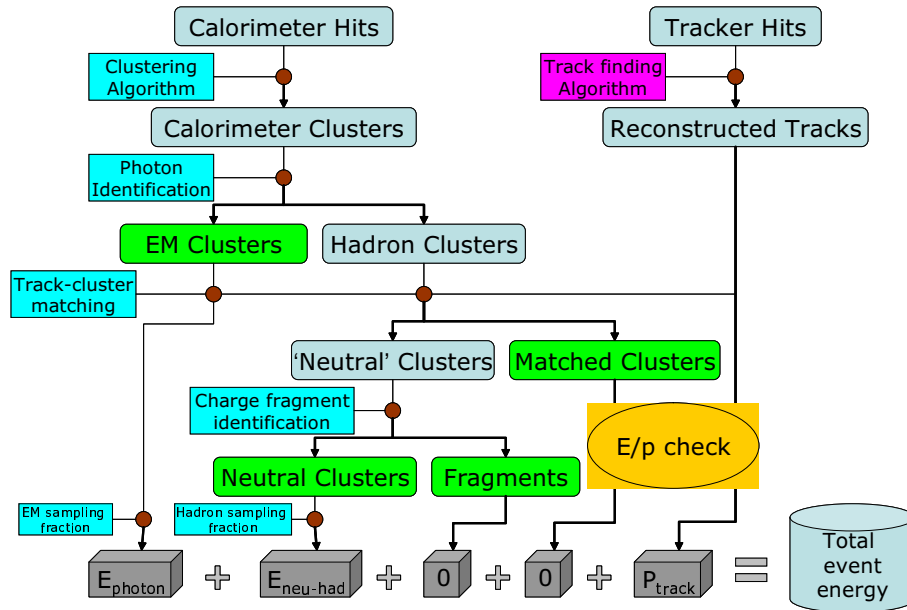
Figure 4: Flow of PFA for SiD detector. It consists of several methods: clustering algorithm, photon identification method, track-cluster matching method and fragment identification method. The total event energy is calculated by summing up E_{photon}, $E_{NeutralHadron}$ and P_{track} as it has already shown by eqn.(1). See text for more detail.
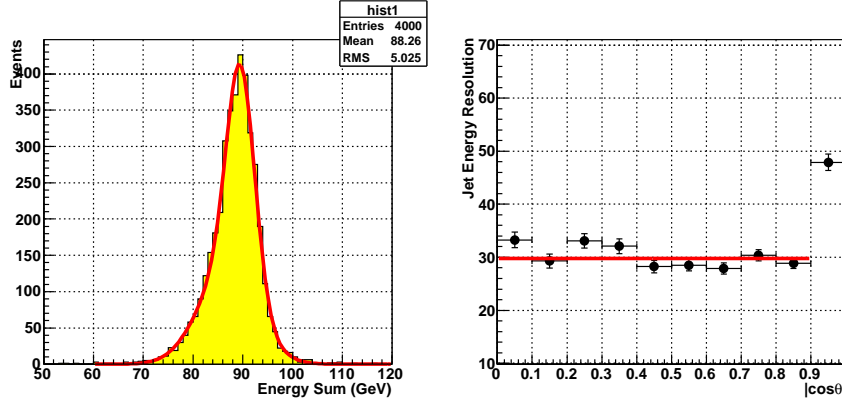
Figure 5: (left) The total reconstructed energy of $e^+e^- \to q\bar{q}$ events at center of mass energy of 91.18 GeV when the GLD-PFA is applied. (right) The jet energy resolution, defined as the α in $\sigma_E/E = \alpha/\sqrt{E}$, as a function of the initial quark direction.

calorimeter hits and tracker hits, respectively. In the next, the calorimeter clusters previously formed are classified according to the cluster type; EM clusters or Hadron clusters. Then, matching between the calorimeter clusters and the reconstructed tracks is examined (Track-Cluster matching). If there is no matched track for an EM cluster, they are considered to be a photon cluster, and the calorimeter energy is used in calculating the total event energy. The Track-Cluster matching is also performed to the Hadron clusters. If there is no matched track for a Hadron cluster, they are temporarily considered to be a neutral hadron cluster. Those clusters are further bifurcated, and classified to the neutral hadron clusters or fragments. The calorimeter energy is used for the neutral hadron clusters, while the energy of fragments are thrown away because they are considered to be the charged hadrons fragments. For the matched clusters among the hadron clusters, the charged track momentum is used instead of the calorimeter energy. Finally, the total event energy is calculated by summing up these quantities as it has already shown by eqn.(1).

The structure of the GLD-PFA is basically very similar to the SiD-PFA. It also consists of several methods: clustering algorithm, photon identification method, track-cluster matching method and fragmentation identification method. Figure 5 shows the current performance of the GLD-PFA. In this study, $e^+e^- \to q\bar{q}$ events at center of mass energy of 91.18 GeV (Z-pole) were generated by Jupiter, Geant4-based full simulator for the GLD detector. Only u, d, s quarks were generated by Pythia[13] without initial state radiation. Left figure shows the total reconstructed energy when the GLD-PFA is applied and right figure shows the jet energy resolution, defined as the α in $\sigma_E/E = \alpha/\sqrt{E}$, as a function of the initial quark direction. Each bin in the right figure was evaluated by the RMS90 method, which is the rms in the smallest range of reconstructed energy which contains 90% of the events. The ILC goal of $30\%\sqrt{E}$ has been achieved for the barrel region ($|\cos\theta| < 0.9$) of the Z-pole events ($E_{jet} \sim 45$ GeV) as shown in the right figure of Figure 5, but PFA becomes more challenging when considering higher energy jets. Figure 6 shows the event displays for 45 GeV jet (left) and 250 GeV jet (right). As clearly seen in the Figure 6, the opening angles between particles decreases due to the large Lorenz Boost for high energy jets, hence the
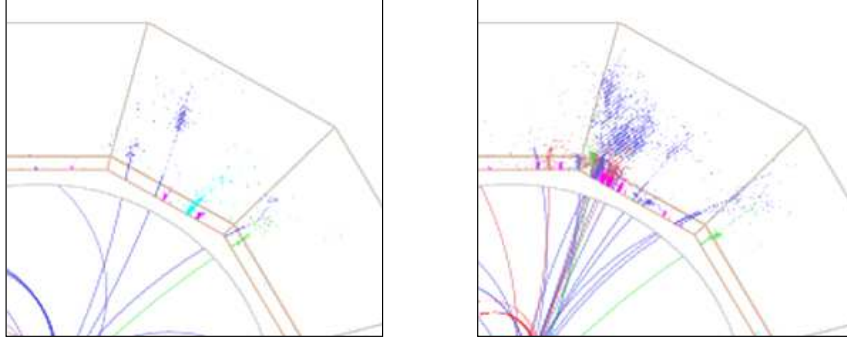
Figure 6: Event displays for 45 GeV jet (left) and 250 GeV jet (right). For high energy jets, the opening angles between particles decreases due to the large Lorenz Boost, hence the particle separation in PFA is more difficult.

particle separation in PFA is more difficult. In fact, the resolution with the current algorithm of the GLD-PFA degrades at higher energy, $\sim 45\%\sqrt{E}$ for $E_{jet} \sim 100$ GeV.

The PandoraPFA[14] has a special algorithm to take care of the high energy jets in addition to the basic methods as explained in the above. If track momentum and cluster energy are inconsistent, they perform reclustering; the clustering parameter is changed until the cluster splits and get sensible track-cluster match. Figure 7 shows the jet energy resolution, defined as the α in $\sigma_E/E = \alpha/\sqrt{E}$, as a function of the initial quark direction for different center of mass energies when the PandoraPFA is applied to $e^+e^- \to q\bar{q}$ event generated by Mokka, Geant4-based full simulator for the LDC detector. The jet energy resolutions in barrel region ($|\cos\theta| < 0.7$) are summarized in Table 2 and the ILC goal of $30\%\sqrt{E}$ has been achieved for even high energy jet ($E_{jet} \sim 100$ GeV). There are known flaws in the algorithm and the performance will become even better for more than 100 GeV jet.

E_{jet} (GeV)	α in $\sigma_E/E = \alpha/\sqrt{E}$ $|\cos\theta| < 0.7$
45	0.295
100	0.305
180	0.418
250	0.534

Table 2: The jet energy resolution in barrel region ($\cos\theta < 0.7$) for different four center of mass energies when the PandoraPFA is applied to $e^+e^- \to q\bar{q}$ event.

4   Detector Optimization Study

As shown in the previos section, the PandoraPFA performance is good enough to start the detector optimization and physics study using full detector simulator. A number of detector optimization studies have already been started by using the PandoraPFA[15]. Figure 8 shows jet energy resolution as a function of TPC radius with different magnetic field for 100 GeV jet. As can be seen from Figure 8, the jet energy resolution improves with increasing radius and increasing magnetic field as expected. Also, another studies shows higher granularity gives better jet energy resolution as expected.
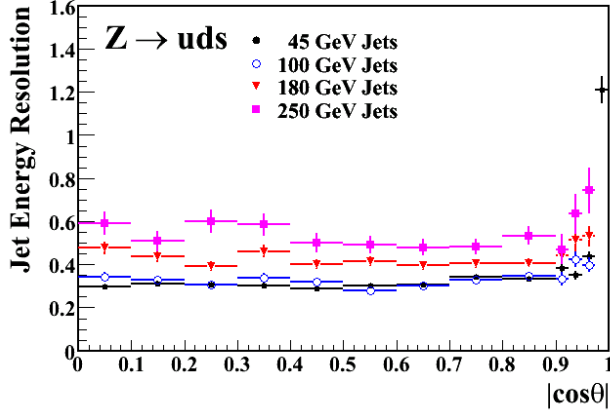
Figure 7: The jet energy resolution, defined as the α in $\sigma_E/E = \alpha/\sqrt{E}$, as a function of the initial quark direction for different center of mass energies when the PandoraPFA is applied to $e^+e^- \rightarrow q\bar{q}$ event.
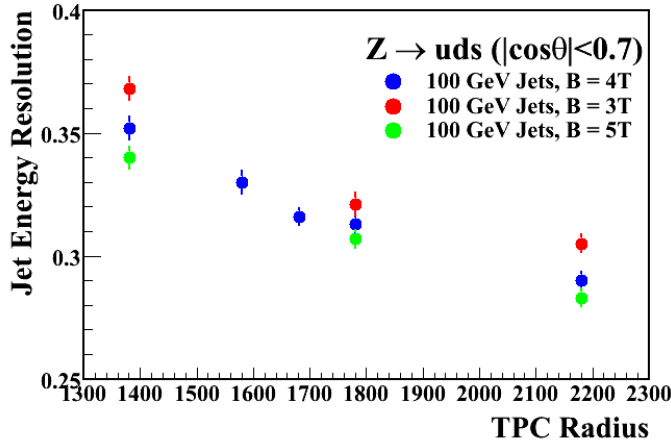
Figure 8: The jet energy resolution as a function of TPC radius with different magnetic field for 100 GeV jet. This result is obtained by using the PandoraPFA. The jet energy resolution improves with increasing radius and increasing magnetic field as expected.

5 Conclusion

Most of the interesting physics processes at the ILC experiment have multi-jets in the final state, and precise jet energy reconstruction, say $\sigma_E/E = 30\%/\sqrt{E(GeV)}$, is therefore the key to the ILC physics. Achieving such a high jet energy resolution is very challenging, and there is a rather wide consensus that PFA is the most promising way to realize it. As shown in this paper, it has already confirmed that we can certainly achieve such resolution by using the PFA for the jet energy of less than 100 GeV. Current PFA performance is good enough to start the detector optimization and physics study using full detector simulator.

References

[1] Slides: `http://ilcagenda.linearcollider.org/contributionDisplay.py?contribId=9&sessionId=1&confId=1296`

[2] `http://www.linearcollider.org/cms`
`http://ilc.kek.jp/RDR/`

[3] K. Abe *et al.* [ACFA Linear Collider Working Group], arXiv:hep-ph/0109166.

[4] "TESLA Technical Design Report", DESY 2001-011, ECFA 2001-209, March 2001.

[5] ALEPH Collaboration, D. Buskulic et al., Nucl. Inst. Meth. A360 (1995) 481.

[6] T. Barklow. Physics Impact of Detector Performance.
`http://www.slac.stanford.edu/lcws05/program/talks/18mar2005.ppt`, 2005.
presented at 2005 International Linear Collider Workshop.

[7] `http://physics.uoregon.edu/~lc/wwstudy/concepts/`.

[8] S. Agostinelli *et al.* [GEANT4 Collaboration], Nucl. Instrum. Meth. A **506**, 250 (2003).

[9] SiD : `http://www.lcsim.org/`
LDC : `http://ilcsoft.desy.de/portal/`
GLD : `http://ilcphys.kek.jp/soft/`.

[10] S. Magill, PFA Studies for SiD Concept
presented at ILC Software and Tools Workshop, 2-4 May 2007.

[11] S. Yamamoto, K. Fujii, A. Miyamoto, [arXiv:physics/0709.3147]

[12] L. Xia, PFA update.
presented at SiD Workshop, 9-11 April 2007.

[13] T. Sjostrand, S. Mrenna and P. Skands, JHEP **0605**, 026 (2006) [arXiv:hep-ph/0603175].

[14] M. A. Thomson, arXiv:physics/0607261.

[15] M. A. Thomson, Presentation at Linear Collider Workshop 2007 (LCWS2007), 29 May to 4 June 2007.

Progress Report from CALICE

José Repond[1]

1 – Argonne National Laboratory – High Energy Physics Division
9700 S. Cass Avenue, Argonne, IL 60439 – USA

ON BEHALF OF THE CALICE COLLABORATION

The CALICE collaboration develops calorimeters for the ILC detectors. This report summarizes recent progress with special emphasis on test beam results. The slides of the talk can be downloaded from [1].

1   The CALICE collaboration

The CALICE collaboration [2] currently counts over 200 physicists and engineers from twelve countries located in all three regions of the physics world. The collaboration formed with the aim of developing and testing various calorimeter technologies for use in ILC detectors. The CALICE calorimeters are optimized for the application of Particle Flow Algorithms (PFAs) [3] and so feature high segmentation of the readout, both longitudinally and laterally.

The collaboration builds so-called *physics prototypes* and *technical prototypes*. The physics prototypes are based on various technologies (silicon, scintillator, RPCs, etc.) and usually are large enough to contain most of the electromagnetic (in the case of electromagnetic calorimeters) and hadronic showers (in the case of hadronic calorimeters). They are not necessarily optimized for use in an ILC detector, but nevertheless undergo a detailed test program in particle beams. The major purpose of these physics prototypes is to provide a basis for choosing a viable calorimeter technology for the ILC detectors, to measure electromagnetic and hadronic showers with unprecedented spatial resolution (these measurements are needed to validate the simulation of hadronic showers, a crucial requirement for the development of a detector optimized for PFAs), and to advanced calorimeter technologies and understanding of calorimetry in general.

On the other hand technical prototypes, even though perhaps smaller or only partially equipped, are designed such that in principle they could be inserted into and operated within an ILC detector. Issues of the high/low voltage distributions, possibly the gas supply, and the data collection routes are being addressed with the boundary conditions of a real detector in mind.

Table I provides an overview of the various projects currently being pursued by the collaboration. Some projects, such as the silicon tungsten electromagnetic calorimeter (ECAL), are well advanced, others, such as the MAPS-tungsten effort, have only been initiated recently. The developments are tightly related to the three ILC detector concepts which are optimized for PFA performance, namely GLD, LDC and SiD. In the following we

will mainly concentrate on the projects which have already undergone tests in particle beams or are almost ready to do so.

The collaboration tested prototype modules in various test beams over the past 18 months:

- at DESY (electrons of 1 – 6 GeV)
- at CERN (electrons and pions of 6 – 120 GeV) and
- at FNAL (protons at 120 GeV).

At CERN alone the collaboration collected over 60 million events. Some of the results of this effort will be presented in the following. The protons at FNAL were used to test single layers of RPCs and GEMs.

Table I. Overview of current CALICE projects and their status

Calorimeter	Technology	Detector R&D	Physics Prototype	Technical Prototype
ECALs	Silicon - Tungsten	Well advanced	Exposed to beam	Design started
	MAPS - Tungsten	Started		
	Scintillator - Lead	Well advanced	Exposed to beam	
HCALs	Scintillator - Steel	Well advanced	Exposed to beam	Design started
	RPCs - Steel	Well advanced	Almost ready to be build	(Design started)
	GEMs- Steel	Ongoing		
	MicroMegas - Steel	Started		
TCMTs	Scintillator - Steel	Well advanced	Exposed to beam	

Being part of a larger collaboration, such as CALICE, offers significant advantages to the various efforts within the collaboration. For instance, different projects share the same readout system (such as the Si-tungsten ECAL and the scintillator-steel HCAL). All projects use the same data acquisition software, which facilitates combined tests of electromagnetic and hadronic calorimeter prototypes. The same test beam is often shared by different groups which results in mutual help with the setup of the equipment and the understanding of the beam lines. Last but not least, the CALICE collaboration offers a convenient forum to discuss ideas, present results and compare performances. Additional details on the collaboration and its various projects can be found in the CALICE report to the 2007 ILC calorimeter review [4].

2 Silicon-Tungsten electromagnetic calorimeter

A Silicon-tungsten ECAL offers the possibility of fine readout segmentation together with a

small Molière radius (of the order of 1.0 to 2.0 cm). Within the paradigm of PFAs, the latter is crucial for the identification and measurement of electromagnetic showers. A physics prototype consisting of 30 layers has been assembled. The tungsten plates vary in thickness from 1.4 mm (or 2/5 X_0) for the first 10 layers, to 2.8 mm (4/5 X_0) in the middle section and 4.2 mm (6/5 X_0) for the last 10 layers of the module. The readout area measured 12 x 18 cm^2 per plane and featured 1 x 1 cm^2 pads. The entire prototype module counted 6480 readout channels. The electronic front-end boards were placed on the side of the module, with digitization taking place in a VME-based system located off the detector.

Detailed measurements of the response to electrons were performed in the DESY and CERN test beams. Figure 1 shows the measured energy versus the nominal beam energy. The response is seen to be linear within the 1% level.
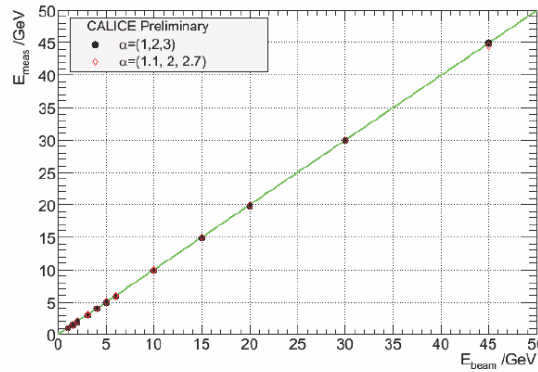
Figure 1: Silicon ECAL: Reconstructed energy versus beam energy

The energy resolution as function of $1/\sqrt{E_{beam}}$ energy is shown in Fig. 2. The open and closed circles correspond to different weighting schemes for the three sections of the calorimeter. The resolution can be parameterized as $17.1\%/\sqrt{E}$ with a small constant term of 0.5%. The results are very well reproduced by Monte Carlo simulations based on GEANT4.
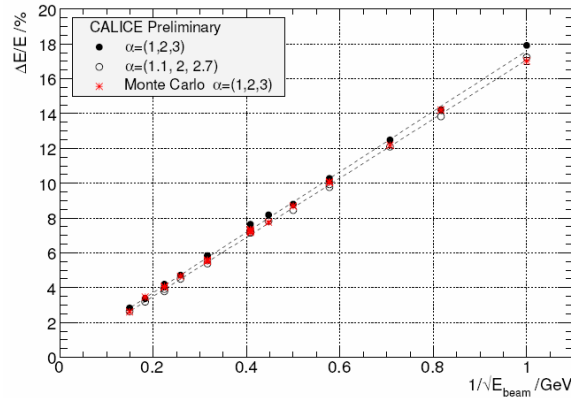
Figure 2: Silicon ECAL: Energy resolution versus $1/\sqrt{E_{beam}}$

Figure 3 shows the average radius for 90 and 95% energy containment as a function of beam energy. The Molière radius, defined as the radius corresponding to 90% energy containment, is of the order of 20 mm. This value is approximately a factor 2 larger than the Moliere radius of a solid block of tungsten without gaps for the active elements.
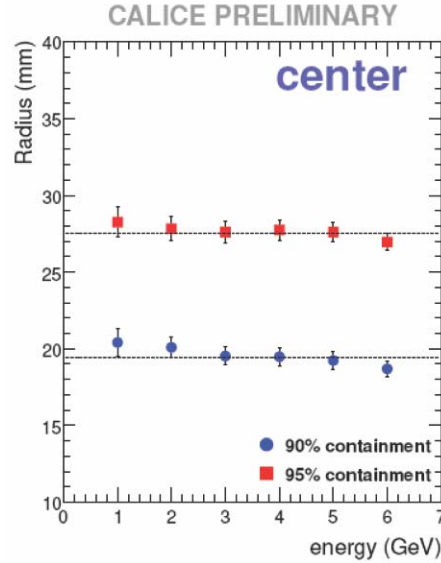
Figure 3: Silicon ECAL: Radius for 90% and 95% energy containment for electrons

3 Scintillator-Tungsten electromagnetic calorimeter

Scintillator as active element is being pursued by both an ECAL and an HCAL group. The advent of Silicon Photomultipliers [5] makes the development of a detector with small scintillator tiles to be operated in a strong magnetic field possible. The ECAL group built a prototype calorimeter with 26 active layers interleaved with 1 X_0 Tungsten plates. The scintillator tiles measure 4.5 x 1.0 x 0.3 cm^3 each. The setup tested different configurations for the light collection and tile separation: a) using wavelength shifting fibers imbedded in tiles separated by machined groves, b) using the same scintillator tiles without wavelength shifting fibers (direct coupling), and c) using wavelength shifting fibers imbedded in extruded scintillator tiles. The light was collected with Hamamatsu Multipixel Photon Counters (MPPCs).

The prototype calorimeter was tested in the DESY electron beam. Figure 4 shows the measured energy resolution versus $1/\sqrt{E_{beam}}$. The results can be parameterized as

$\sigma/E = 13.45\%/\sqrt{E} + 2.87\%$ (added in quadrature)
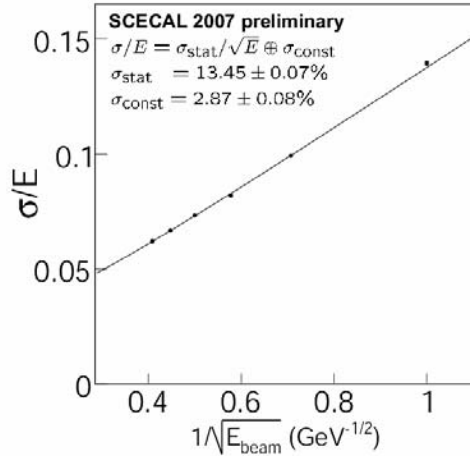
Figure 4: Scintillator ECAL: Energy resolution versus $1/\sqrt{E_{beam}}$ for electrons

4   The ultimate digital calorimeter: MAPS

The third ECAL project investigates the use of Monolithic Active Pixel Sensors (MAPS) as active elements. Here the comparator and logic is imbedded into the sensor structure. Due to the large number of channels (10^{12} pixels for the ECAL of an ILC detector), the readout resolution is reduced to a single bit (digital readout). A first prototype sensor with 50 x 50 μm^2 pixels has been designed and is being prototyped.

5   Scintillator-Steel hadron calorimeter

A (almost complete) physics prototype calorimeter using scintillator pads as active elements interleaved with 20 mm thick steel plates was exposed to both the DESY and CERN test beams in 2006. The tiles measure 3 x 3 cm^2 in the center of a given plane, increase to 6 x 6 cm^2 and finally 12 x 12 cm^2 at the edge of the planes, see Fig. 5 for a photograph of one of the layers. The area of each layer is approximately 1 m^2. The completed module with 38 layers will feature of the order of 8,000 readout channels, each individually equipped with a Silicon-Photomultiplier (SiPM). The readout utilizes a VME based data acquisition system, located off the detector, similarly to the system used by the Silicon-Tungsten ECAL. In the 2006 test beam run 23 of the planed 38 layers were fully equipped.

A detailed calibration procedure, involving LEDs and muon beams has been developed. Corrections for light-yield non-uniformities, SiPM gain variations, SiPM non-linearities in the response, and non-uniformities in the readout electronics are being applied. The light yield is found to be very satisfactory, with an average of 16 pixels per tile per minimum ionizing particle.

Standalone data (without ECAL in front of the module) have been collected with both

electrons and pions. The analysis of the electron data is particularly difficult due to the higher sensitivity to the non-linearity of SiPMs. In this case some deviations to Monte Carlo expectations are observed, possibly due to non-optimal corrections to the non-linearity and/or additional dead material in front of the module which has not yet been included in the simulation. This is work in progress.
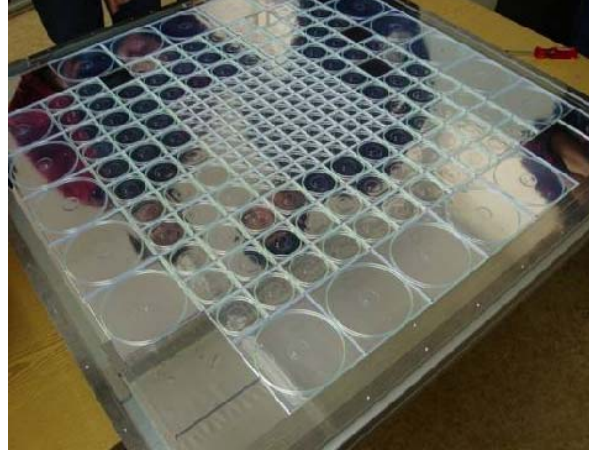
Figure 5: Scintillator HCAL: Photograph of one detector plane

Figure 6 shows the response and resolution as function of pion beam energy. The results are compared with two different predictions based on the GEANT3 simulation code, one based on GEISHA and the other one using FLUKA. Significant deviations to the measurements and among the predictions are observed. It should be noted that these measurements used an incompletely equipped module and that the final results using the complete module are expected to be significantly better.
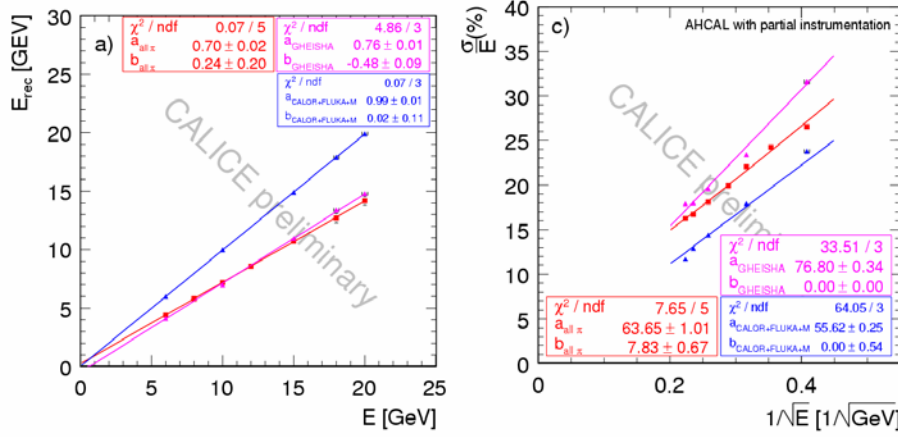
Figure 6: Scintillator HCAL: a) Reconstructed energy versus beam energy;
b) Energy resolution versus $1/\sqrt{E_{beam}}$

Figure 7 shows a first measurement of the transverse shower shape for different incident pion energies (between 6 and 20 GeV). Comparisons with simulations are forthcoming.
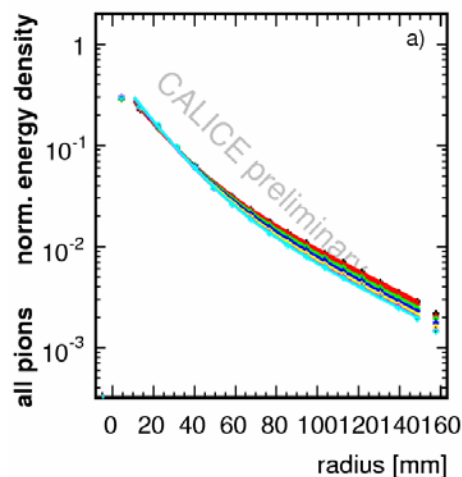
Figure 7: Scintillator HCAL: Measurement of the transverse shape of pion showers

6 Tail catcher and muon tracker

The purpose of the Tail Catcher and Muon Tracker (TCMT) is to provide a precision measurement of the longitudinal tails of hadronic showers. In the CERN test beam run it was located behind the ECAL and HCAL modules, as shown in Fig. 8. The TCMT consists of 16 active layers, each with an area of 1 m^2. The readout planes are subdivided into strips of scintillator with the dimensions of 5 x 100 x 0.5 cm^3. Each strip is read out individually by a Si-PM. The electronic readout system is identical to the one used for the other prototype calorimeters using scintillator as active element.

The TCMT was completed in 2006 and participated in all test beam runs at CERN. First results show a strong anti-correlation between the energy measured in the HCAL and the energy leaking into and measured by the TCMT. Adding the TCMT energy to the one measured in the calorimeter(s) located in front, significantly improves the overall energy resolution.

7 Digital hadron calorimeter

Last but not least, the CALICE collaboration investigates the use of gaseous detectors as active elements of a finely segmented hadron calorimeter. Within the collaboration different subgroups explore the use of Resistive Plate Chambers (R&D almost complete), Gas Electron

Multipliers (R&D ongoing) and Micromegas (R&D recently initiated). These detectors are being read out with 1 x 1 cm^2 pads, leading to a large overall number of readout channels. Equipping the same 38 layers of the scintillator HCAL with these devises results in a channel count of close to 400,000. To simplify the readout system, the resolution per pad has been degraded to a single-bit (digital) readout. Monte Carlo simulations indicate that such a digital readout of small pads is able to provide an adequate single-particle energy resolution.
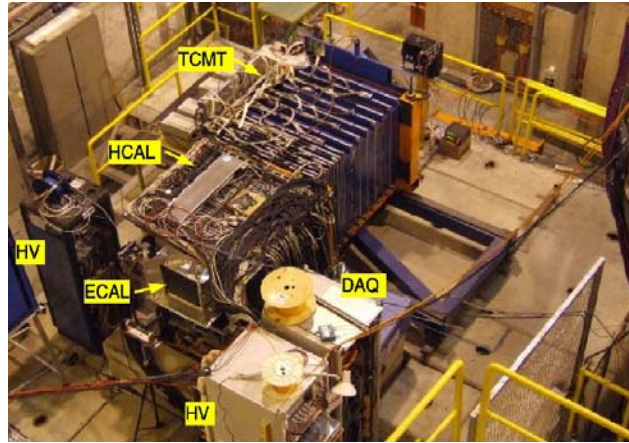
Figure 8: TCMT: Photograph of the setup in the CERN beam

A large effort has been deployed to develop an economical readout system capable of handling the inherently large number of channels of this type of calorimeter. The system is based on a front-end ASIC located directly on the pad-board and reading out 64 individual pads. The readout chain is completed with data concentrator (1 per 4 ASICs) and data collector (1 per 12 data concentrators) modules. A vertical slice of the readout system is being assembled as a proof of principle of the concept. Figure 9 shows the top of the prototype pad board, including four front-end ASICs.

At the time of the conference the first 1,000 cosmic ray events had been collected using the complete readout chain. The group is now preparing a larger test (involving up to 10 RPCs and 2 GEMs) in the Fermilab test beam.

8   Towards technical prototypes

In parallel to the construction and data taking with the various physics prototypes, the collaboration actively pursues the next steps towards 'realistic' calorimeter modules, the so-called technical prototypes. In the following we list a few selected topics of research.

The next step for the scintillator-tungsten ECAL features a compact design of the layer structure with imbedded front-end electronics. Particular care is devoted to keeping the active

gap size as small as possible, in an effort to retain the small Molière radius of Tungsten. A number of issues, such as electronics cooling, wafer gluing, and production techniques, are being addressed.
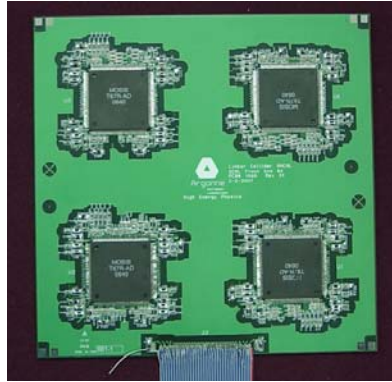
Figure 9: Gaseous HCAL: Photograph of a pad board equipped with 4 ASICs

The scintillator ECAL and HCAL are investigating the possibility of direct coupling to the SiPM or MPPC (omitting the wavelength shifting fiber). Ways to obtain a uniform response as function of the position on the tile are being developed. First designs of an integrated readout system, located inside the active gap, are being evaluated.

The next step in the development of the front-end electronics includes on-detector digitization (apart from the gaseous HCAL, which already includes this feature), token ring readout of the front-end ASICs, and possibly power pulsing. The latter will lead to a significant reduction in overall power consumption and therefore to a drastic simplification of the cooling system.

9 Conclusions

To conclude Table II summarizes the current plans for test beam activities until the end of 2009. The test beam program at CERN will conclude in 2007, after which the equipment will be moved to Fermilab in late 2007/early 2008.

10 Acknowledgements

The author likes to thank all members of the CALICE collaboration for their generous help in preparing the talk and this document.

Table II: CALICE test beam plans

Project		2007b	2008a	2008b	2009a	2009b
Si-W	ECAL	CERN test beam	FNAL test beam			
MAPS		1st prototype chip		2nd prototype chip	DESY test beam	
Scintillator				FNAL test beam		
Scintillator	HCAL	CERN test beam	FNAL test beam			
RPC		Vertical slice test in FNAL test beam	Physics prototype construction	FNAL test beam		
GEM		Vertical slice test in FNAL test beam	Further R&D on GEMs		Physics prototype construction	FNAL test beam
Micromegas			1 plane			
Scintillator	TCMT	CERN test beam	FNAL test beam			

11 References

[1] Slides:
http://ilcagenda.linearcollider.org/contributionDisplay.py?contribId=10&sessionId=1&confId=1296

[2] Web site of the CALICE collaboration:

http://polywww.in2p3.fr/activites/physique/flc/calice.html

[3] For more information on PFAs, consult talks given in the PFA session of this conference.

[4] http://www-flc.desy.de/lcnotes/notes/LC-DET-2007-007.pdf

[5] For more information on Silicon-Photomultipliers (Si-PMs) or Multipixel-Photoncounters (MPPCs), consult the talks given in the *Photosensor* session of the calorimeter parallel sessions.

Vertex Detector System Design

Ronald Lipton

Fermilab
P.O. Box 500, Batavia, Illinois - USA

We describe system design issues in vertex detector design for the iLC. Meeting ILC physics goals mandates a vertex detector of unprecedented precision. Machine characteristics define the range of operational parameters. We discuss how the ILC environment effects choices in mechanical design, cooling, power engineering, and how sensor technology is affected by and affects these choices.

1 Physics Requirements

The ILC is designed to explore precision physics produced with low cross sections. A flagship study at the ILC will be the measurements of Higgs couplings to quarks and bosons. These measurements, which will span more than two orders of magnitude in mass and coupling strength, require excellent separation of b, c, and light quark vertices. A related measurement is the self-coupling of the Higgs. Here the signal reaction, $e^+e^- \to Z^0 H^0 H^0 \to qqbbbb$ with four b-jets must be separated from backgrounds like $tt \to bbcscs, ZZZ$, and ZZH. Different constraints on the vertex detector come from measurements like heavy quark forward-backward asymmetry. Here the emphasis is on forward tracking with flavor tagging and determination of the charge of the parent b quark. Whether the ultimate focus is on Higgs, supersymmetry, or other new physics phenomena, it is likely that precise measurements of heavy quark jets and their decay vertices will play a crucial role [2].
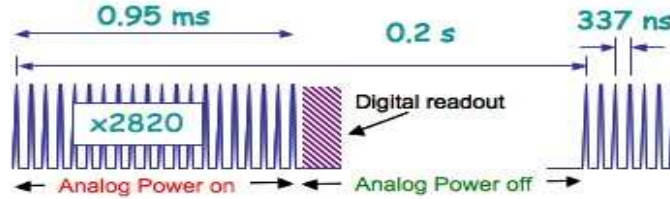
Figure 1: ILC bunch timing including possible readout and power cycling options.

2 The ILC Environment.

Figure 1 shows the bunch structure anticipated for the ILC, 2820 beam crossings, each separated by 337 ns are followed by a 199 ms inter-train gap. The low event rate and moderate background allow a variety of strategies to be considered to optimize the vertex detector. The long gap raises the possibility of detector readout during the gap, rather than in the train. The low duty factor means that the average power can be reduced by cycling power off between bunch trains, reducing mass needed for cooling.

The primary constraint on the geometrical design of the vertex detector is imposed by the electomagnetic background associated with the beam-beam interaction. Each crossing

produces a large flux of electrons and photons caused by pair production and bremstasslung in the intense fields at the interaction point. Charged particles fan out of the IR in a cone whose radius depends on the central magnetic field. The requirement that the inner layer of the vertex detector avoid this cone constrains both its inner radius and length [3]. The actual background flux will depend on machine operating parameters. The level of background that is tolerable in the inner layer defines the time resolution required for the readout.

3 Detector Goals.

The combination of requirement for precise vertex identification and the relatively low event yield motivates a detector that optimizes the vertex information for each event. This has to be done within the constraints imposed by beam backgrounds, ILC bunch structure and integration with other components of the detector. An informal set of goals has been formulated taking these opportunities and constraints into account:

- Good angular coverage with many layers close to the interaction point

- Excellent spacepoint precision ($< 5\mu m$)

- Superb impact parameter resolution ($5\mu m + 10\mu m/(psin^{3/2}\theta)$)

- Low mass ($\approx 0.1\% X_0$ per layer). This translates to a power constraint based on gas cooling of < 20 Watts in the barrel.

- Integration over < 150 bunch crossings ($45\mu sec$)

- Electromagnetic Interference (EMI) immunity

- Moderately radiation hard ($< 1MRad$)

Vertex detector performance is a function of inner radius, scattering material, and detector position resolution. Figure 2 shows the results of a parametric simulation of impact parameter resolution as a function of these variables for 1 GeV tracks. The inner radius is constrained by the beam background envelope and is likely to be about 1 to 1.5 cm. Point resolutions below 5 microns have been demonstrated in several detector technologies (DEPFET, CCD, MAPs). Minimal mass is crucial for good impact parameter resolution at low momentum and, coupled with power, is a driving constraint in most designs.

4 Time Resolution

The time resolution required for the vertex detector depends on the machine background rate as well as the pattern recognition ambiguity tolerable in the context of the overall experiment design. Early pattern recognition studies indicated that a $50\mu s$ integration time should be tolerable. Machine operating parameters can also play a role. For example, the first few hundred crossings in a train will be used to feedback the electron and positron beam positions to achieve head-on collisions. There is likely to be more background generated during this tuning process, which implies uneven occupancy during the train. In the absence of other constraints shorter integration times are better. We need to understand what the tradeoffs are and what level of background is really tolerable.
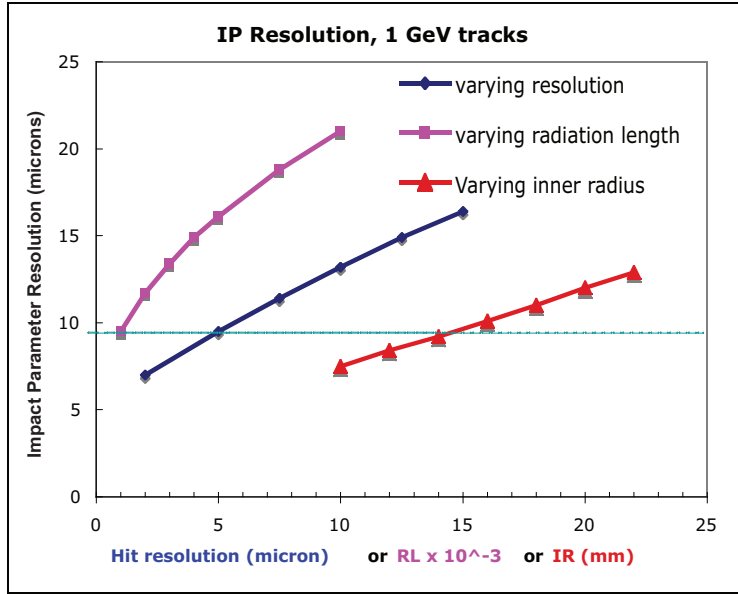
Figure 2: Parametric simulation of impact parameter resolution as a function of inner radius, detector resolution and mass using the SID geometry where the "nominal" detector (horizontal line) has $5\mu m$ resolution, 0.1% radiation length per layer, and a 1.4 cm inner radius.

There have been several approaches to achieving acceptable time resolution. For CCDs, the column parallel approach attempts to achieve 50 MHz clock rates with individual amplifiers on each column. Several CMOS MAPS devices and the DEPFET prototypes utilize a "rolling shutter" design, with a full frame readout every $\approx 50\mu sec$. The ISIS CCD and FAPS and CAPS CMOS MAPS devices sample charge, either in the silicon bulk or ISIS, or on external capacitors for the FAPS and CAPS devices [4] [5]. The Fermilab SOI and 3D devices [6], and the Chronopixel concept, utilize the fact that the per pixel occupancy is small during a train to store a time stamp in the pixel for each hit. This approach has the prospect of allowing crossing-level accuracy for the time stamp.

5   Technologies

The precision, low mass and low power required for an ILC vertex detector has driven extensive R&D on sensor technology. Each technology has features which affect any vertex detector system which utilizes them.

- CCDs - This technology was utilized for SLD, an application which bears the closest resemblance to an ILC vertex system. A standard serial readout CCD does not have sufficient time resolution to limit beam-related backgrounds. Alternative readout devices either using a column-parallel approach or in-pixel storage (ISIS) are being pursued [7].

- CMOS Active Pixels - This technology is based on collection of charge by diffusion in the high resistivity epitaxial layer utilized in several CMOS processes. Circuits are usually limited to NMOS transistors to avoid parasitic charge collection in PMOS implants [8].

- SOI - This is a new technology which utilizes the "handle wafer", which is the base of a handle/oxide($\approx 200nm$)/silicon($\approx 20nm$) sandwich where the sensor is formed in the handle and a full CMOS process is utilized for the top silicon. First prototypes are just becoming available from commercial vendors [9].

- 3D - This is also a new technology which utilizes vertical integration of several layers of electronics, each layer ≈ 7 microns thick, vertically integrated with micron-sized vias. This technology allows sophisticated processing within each pixel and the possibility of processing a field of pixels in higher tiers. The first chips utilizing this technology will be available this year [6].

- DEPFET - This technology utilizes a front-end transistor integrated into a fully depleted detector, providing both charge storage and amplification. This device can have very low noise and excellent position resolution. The current designs require readout and processing chips at the ends of columns [10].
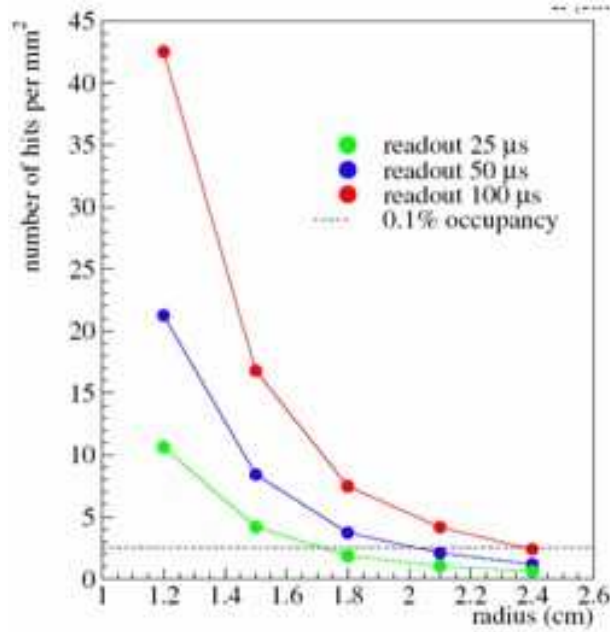
Figure 3: LDC simulation of hit density in the vertex detector as a function of radius for various integration times [11]

6   Mechanical design

The barrel section of the ILC vertex detector is about the size of a box of Quaker Oats (in the US), about 12 cm long with a 6 cm outer radius. To meet the goal of 0.1 % radiation length per layer both the sensors and support structures must be as thin as possible. Silicon wafer thinning technology is well developed by industry, but handling these devices and keeping them flat in the face of substantial internal stresses will be a challenge. Several options are being developed. A carbon-fiber support, based on a few layers of fiber with holes to reduce mass has been prototyped by a Fermilab/Wasington group. Several groups (LCFI, LBL) are experimenting with silicon carbide and reticulated vitreous carbon foam sandwich supports. Max Plank has developed a pure silicon "picture frame" support utilizing wafer bonding, thinning and etching technology.

In all of these cases a number of issues will need to be addressed before an optimal support design is available. The planarity of the sensors must be understood and whether the support structure is required to also flatten the sensors. Thermal bowing must be understood. This depends on the difference between assembly and operating temperature, which could be large for CCDs operated cryogenically. Another technology-dependent question is whether the ladder is composed of full sized single sensors (CCDs or DEPFETS) or a matrix of sensors whose size is limited to a typical CMOS optical reticle, about 2×2 cm (SOI, 3D, MAPS).

The interconnection problem is likely to be significant. There are a number of outstanding questions that require either more work or a technology decision. Can wirebonds can be made reliably to thinned silicon without fracturing the material? What services are needed by the sensors? How much bypass capacitance is needed and where is it located? How is power coupled to the sensor and routed among sensors? What support stiffness is needed to absorb cable torque? What independent position monitoring is needed? How would optical signals be coupled?

7   Power

Power considerations are likely to be the driving consideration in any vertex technology. Gas cooling is a necessity to minimize mass within the vertex detector. We can estimate the limit on total power that can be consumed by assuming laminar air flow to the vertex detector within a space that is limited by the outer tracking detectors and support structures. This has been estimated for the SiD barrel as a total of about 20 watts, or $131\mu W/mm^2$, with a maximum temperature rise of $6 - 8^oC$ [12]. This is a constraint on average power, and many schemes rely on power cycling, turning on the power only during the $1ms$ crossing period, as a way of meeting the average power constraint.

7.1   Technologies

Technologies are very different in their power requirements. The column parallel CCD must drive 50 MHz of capacitive clock phase lines at cryogenic temperatures. This corresponds to about 10 amps per CCD plane. The overall power can be reduced by minimizing gate electrode capacitance or reducing clock voltages, and both schemes are being explored. ISIS-style devices, which incorporate in-pixel charge storage, can spread the power consumption throughout the $200ms$ cycle, reducing peak currents with respect to the column parallel

design. Power for CMOS MAPS, 3D and SOI technologies are dominated by power in the front end transistors. The required power in these devices is a tradeoff between technology, speed, and noise. The thermal noise in such devices can be expressed as [13]:

$$ENC^2 = (C_{det} + C_{gate})^2 \frac{Kkt}{g_m t_s} \tag{1}$$

Where kt is the usual Boltzmann factor, C_{det} and C_{gate} are the detector load and input transistor gate capacitances, K is a constant which depends on the silicon technology (usually close to 1), g_m is the input transistor transductance, and t_s is the characteristic time of the amplifier. Pixel front end amplifiers usually operate in weak inversion where g_m is independent of device geometry and proportional to $\frac{I_d q_e}{kt}$, where I_d is the imput transistor drain current. Noise therefore scales as C_{load} and $\frac{1}{\sqrt{I_d}}$.

For a power constraint of $130\mu W/cm^2$, with 20 micron pitch pixels, assuming a duty factor of 100 for power cycling we have a constraint of $5.2\mu W/pixel$ or a drain current of $3.5\mu A$ at $1.5V$. For a more conservative $1\mu A$ drain current and $100ns$ shaping time, a C_d value of 100 femtofarads (ff) gives a 35-50 electron noise level. Load capacitances of 10 ff should be achievable in SOI-based technologies, and 25-50 ff might be achievable in CMOS MAPS. Signal levels for a MAPs device with a 10 micron epitaxial layer is about 800 electrons, while a fully depleted technology like SOI or DEPFET will collect 4000 electrons in a 50 micron thick device.

7.2 Power Distribution

Even if we are able to meet the average power constraint for the vertex detector, we must face the issue of power distribution. For a column parallel CCD-based system we will have ≈ 20 modules, each utilizing 20 amps, or 4000 amps of peak clock power. A MAPS or SOI detector which meets the 20 W average barrel power constraint using power cycling will require 1333 amps of peak current if the power is delivered at 1.5 volts with a duty factor of 100. If the required voltage stability is 50 mV a 3 cm diameter copper cable is required on each side. The mass of the supply cables is unacceptable unless something is done.

The most promising technology to address cable mass is serial powering. A serial powering scheme delivers power at higher voltage, thus reducing peak currents and IR drops, enabling much lower mass cables. Each module individually regulates it's voltage, passing current on to the next module at lower potential. Peak currents are reduced by a factor equal to the number of modules in series. This scheme has been tested with ATLAS strip and pixel modules and seems to work well, with no increase in overall system noise. A straw-man design for the SiD detector which includes a multiplex factor of between 9 and 15 would reduce the copper area by a factor of 12 (ignoring regulator overhead) for a given voltage drop in the supply line. The addition of the shunt/linear regulators would also relax constraints on the voltage drop allowed on the supply lines providing another large factor in the reduction of copper area.

Any power control system would have to address the rapid turn-on and off of a pulsed power system. A proper system design would probably include smart local regulation which could selectively depower the analog, digital, or both sections of a chip. Switching transients would have to be understood and the current supply properly synched to the detector modules to avoid overcurrent and local heating in the shunt regulator. Forces induced by the supply-return current loop have to be carefully balanced to avoid excessive torques on the
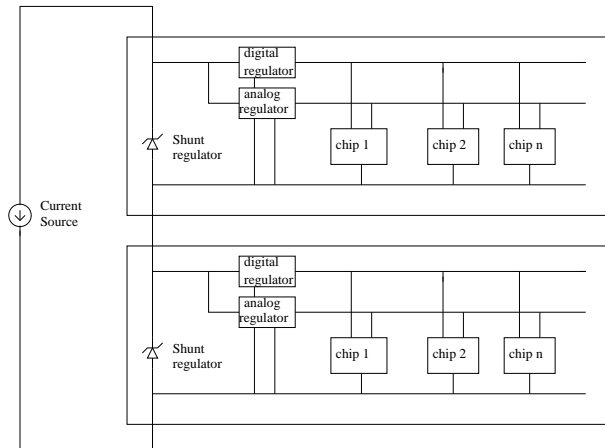
Figure 4: Schematic of a serial powering system.

low mass detector elements. Finally the mechanical and thermal effects of power switching at 5 Hz will need to be understood and carefully tested.

7.3 Readout Power

At the ILC essentially all hits during the bunch train will bed read out. Figure 5 shows an LDC simulation of the number of hits as a function of layer for various machine operation scenarios. If we take the 1 TeV high luminosity scenario, this corresponds to a data load of 1.4×10^7 hits per train. If we assume 30 bits per hit this corresponds to a data rate of 2 Gbit/sec. For a wire-based system the power needed would be frequency $\times$ cable capacitance $\times$ voltage^2, or about 30 watts for 15 nf cable capacitance, saturating the power budget. Optical drivers can use much less power, the ATLAS driver utilizes $\approx 10mW/line$, or about 1 Watt for 96 ladders.

8   Electromagnetic Interference

The electron and positron beams passing the interaction region can generate substantial image currents and wakefields. These are normally shielded by the beampipe. However, if beampipe penetrations are needed for instrumentation or control, a path is available for EMI to leak out and disrupt the vertex and tracker electronics. This occurred in SLD, where the phase lock loop controlling the CCD readout dropped out of synchronization during the beam crossing [15]. This experience has led to concern about the EMI environment at ILC, with much larger beam currents.

An experiment (reported at this conference) was performed at SLAC End Station A utilizing SLC vertex electronics [16]. Antennas were placed near gaps in the beam pipe and SLD vertex readout electronics boards were also studied. The antennas observed pulses of EMI in the high MHz range with strengths up to 20 V/m. EMI Pulse amplitudes varied in proportion to the bunch charge, and were found to be independent of the bunch length. A single layer of 5mil aluminum foil placed over the ceramic gap and clamped at both ends
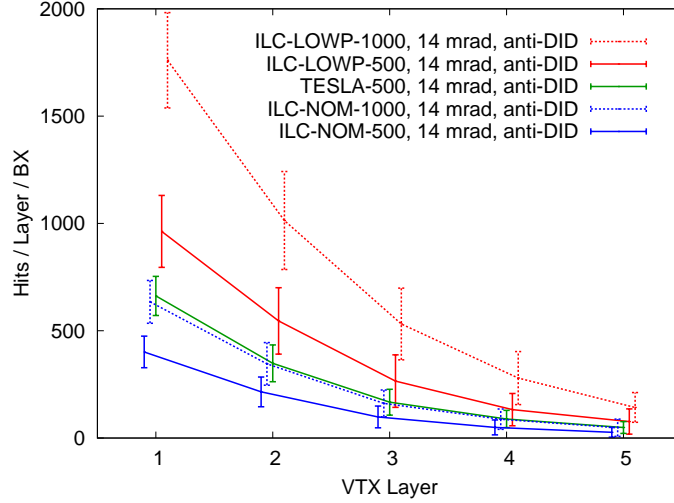
Figure 5: Vertex detector hits per beam crossing as a function of radius for various ILC operating scenarios. [14]

reduced the EMI by at least a factor of 10. A 1 cm hole in the aluminum was enough to cause the PLL to fail. These failures stopped when the hole size was reduced to .6 cm. This raises several interaction region design questions: Is there any need to have gaps in the pipe? How close to the IR would the gaps be? Can they be fully shielded? These issues need to be understood in order to understand how "EMI-hard" the vertex detector, and indeed all of the detector electronics, will have to be.

9   Conclusions

The ILC vertex detector presents a series of challenges to sensor technology, power control and distribution, and mechanical support. At the same time new technologies and tools are becoming available which will allow us to address the challenges. The electronics industry, in moving toward thinned wafers and 3D technology is just one example. Achieving the 0.1% layer radiation length goal will require a substantial engineering effort in understand thinned materials and supports, power cycling, power distribution, and interconnections. These items deserve a weight equal to sensor R&D.

References

[1] Slides: `http://ilcagenda.linearcollider.org/contributionDisplay.py?contribId=11&sessionId=1&confId=1296`

[2] M. Battaglia, T. Barklow, M. Peskin, Y. Okada, S. Yamashita and P. Zerwas, *In the Proceedings of 2005 International Linear Collider Workshop (LCWS 2005), Stanford, California, 18-22 Mar 2005, pp 1602* [arXiv:hep-ex/0603010].

[3] C. Rimbault, P. Bambade, K. Monig and D. Schulte, Phys. Rev. ST Accel. Beams **9**, 034402 (2006).

[4] R. Turchetta et al., Nucl. Instr. and Meth. A 560 (2006), p. 139.

[5] G. Varner, Nucl. Instr. and Meth. A 541 (2005) p. 166.

[6] R. Yarema, *In the Proceedings of 12th Workshop on Electronics For LHC and Future Experiments LECC 2006*, `http://doc.cern.ch/yellowrep/2007/2007-001/p71.pdf`

[7] K. Stefanov, this conference: `http://ilcagenda.linearcollider.org/getFile.py/access?contribId=297 &;sessionId=74&;resId=1&;materialId=slides&;confId=1296`

[8] G. Deptuch *et al.*, Nucl. Instrum. Meth. A **535**, 366 (2004).

[9] Y. Arai *et al.*, *In the Proceedings of International Symposium on Detector Development for Particle, Astroparticle and Synchrotron Radiation Experiments (SNIC 2006), Menlo Park, California, 3-6 Apr 2006, pp 0016.*

[10] J. Kemmer and G. Lutz, Nucl. Instr. and Meth. A 288 (1990), p. 92.

[11] LDC Detector Outline Document:
`http://www.ilcldc.org/documents/dod/`

[12] W. E. Cooper, *ILC VTX Workshop at Ringberg Castle May 28, 2006 - May 31, 2006*:
`http://www.hll.mpg.de/~lca/ringberg/Talks/1-Monday/3-1-cooper.ppt`

[13] P. OConnor, G. De Geronimo, Nucl. Instrum. Meth. A **480**, 713 (2006).

[14] Adrian Vogel, contribution to this conference:
`http://ilcagenda.linearcollider.org/conferenceOtherViews.py?view=standard&confId=1296`

[15] C. J. S. Damerell, "Vertex Detectors - How to Overcome Electromagnetic Interference,"
`www.slac.stanford.edu/econf/C0508141/proc/papers/ALCPG1418.PDF`.

[16] G. Bower, Y. Sugimoto, N. Sinev, R. Arnold and M. Woods, *Albuquerque 2007, Particle Accelerator, 3094-3096.*

Challenges for the ILC SCRF R&D

Maury Tigner

Cornell University – Laboratory for Accelerator-based Sciences and Education
Ithaca, New York, USA

The challenges for the ILC R&D program are noted and progress in meeting them described. Despite technical, organizational and resource difficulties the program results are positive. indicating that our goals are within reach.

1   Introduction

Good progress in meeting the goals set by the GDE Directorate is being made although there remains considerable work to do. The rate of progress is increasing through recently adapted infrastructures coming on line for ILC SCRF. Work is underway for a further, very significant speed up of that rate with additional infrastructure around the world being put into place.

The "high level" goals set by the GDE leadership are cast in terms of the groups defining the challenges. We adopt their nomenclature here for describing those goals: S0 – Demonstrate high yield of 35 MV/m cavities in vertical test; S1 – Assemble and test several cryomodules with average accelerating gradient > 31.5 MV/m; S2 – Demonstrate an RF Unit with ILC parameters, design gradient and ILC-like beam at full pulse rate. An RF unit is one klystron plus modulator, two cryomodules with 9 cavities and one cryomodule with 8 cavities plus a quadrupole. [1] Some results are already in hand

In the interests of meeting these global goals as well as various regional and national goals, infrastructures for manufacture, processing and test are being outfitted in the three regions. This effort will soon increase the pace at which results relevant to the S group goals are produced and put our community in a position to publish an EDR with confidence.

2   S0 - Where are We?

Proof of principle for 35 – 40 MV/m exists but the yield is low for 35 MV/m in 9 cell cavities. Single cell gradients of 40 - > 50 MV/m show that the baseline procedures being used are capable of good results. Controlled preparation and tests are underway at several labs in an effort to discover the sources of the poor reproducibility.   It is widely agreed that many coordinated tests will be required. Basic R&D with single cells is also underway to find even better treatments.

An idea of the reproducibility challenge can be gained from Fig. 1 showing that there are significant instances of good results but they had to be selected from a large number of tests on a large number of cavities. Fig. 2 shows the typical spread in results now being obtained. This relatively small yield implied by these figures is the focus on an increasingly coordinated international program to understand the sources of the scatter and devise methods to narrow it
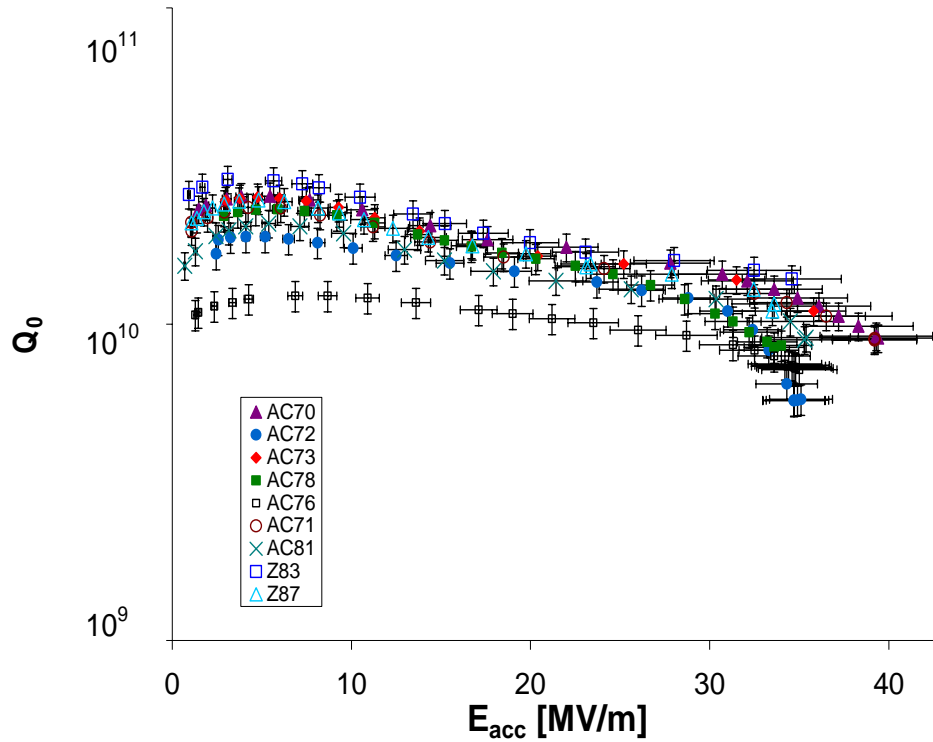
Fig. 1 TESLA 9 cells; best tests of 9 best cavities in vertical tests (courtesy Lutz Lilje)

significantly.

I am very pleased to report that there is already in indication of progress in this regard. Colleagues at KEK, using a limited sample of cavities to contrast with the usual processing results report a narrowing of the spread in single cells to less than 10 MV, centered at 46 MV. A key step in the improved process is believed to be a final, light, electropolish using freshly prepared acid. Of course, it is imperative to check these results using a commonly agreed upon protocol in the three regions and then, if good results are forth coming to begin applying the method to 9 cell cavities.

3   Upgraded and New Infrastructures

In order to make a significant increase in the rate at which cavities can be processed and tested as required by the S0 and other S activities, all three regions are bringing more infrastructure into operation.

In the Americas, JLAB has modified existing EP, HPR and Vertical test apparatus to deal with 9 cell 1.3 GHz cavities. Cornell has installed a vertical EP apparatus to see if this potentially more economical method of EP suffices. At FNAL/ANL vertical test capabilities
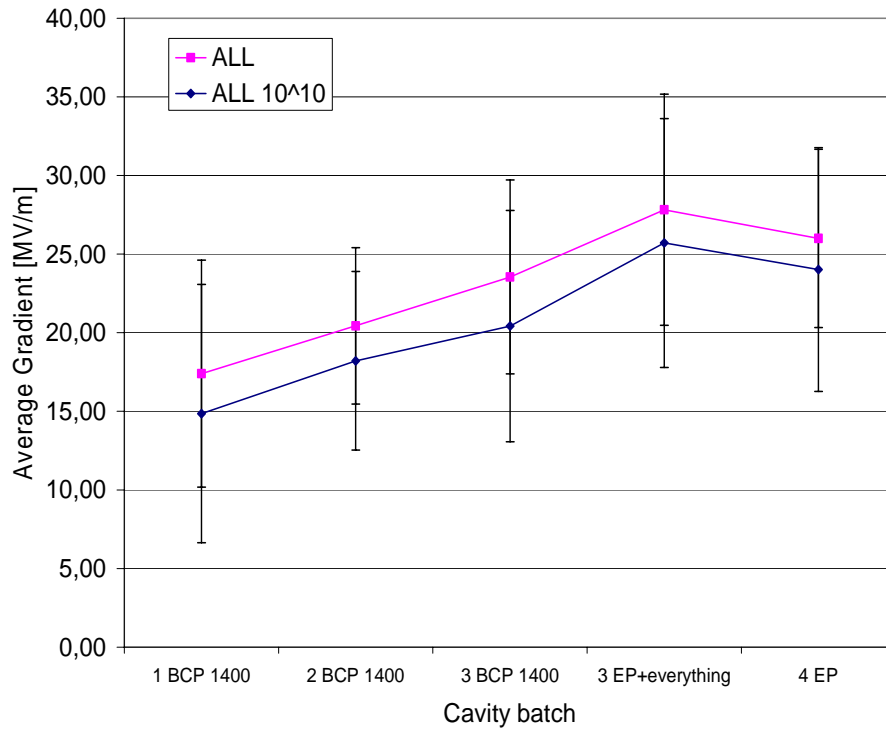
Fig. 2 Recording of all cavity tests prior to mid 2007. The notations along the bottom refer to processing methods: BCP – buffered chemical polish; EP – electropolish (courtesy Lutz Lilje)

for up to three pits and processing facilities are being installed for high test throughput. In Japan at KEK a new facility is also being constructed that will contain new processing apparatus and a clean room for assembly work.

Taking into account the existing facilities and the new ones coming on line, Table 1 shows the potential for processing and test throughput by year.

Year	Jlab	Cornell	ANL/FNAL	KEK	DESY	Total
2007	30	10	20	30	50	140
2008	40	10	50	40	50	190
2009	50	10	50	40	50	200

Table 1 The physical infrastructure limited number of cavity individual processing and test cycles that could be carried out in the three regions.

Whether the other resources required to fulfill this potential will be available remains to be seen. It is hopeful that the total of orders for new cavities from industry, needed for testing, is 60 in 2007.

4 S1 – Where are We?

In this area there is significant progress to report. A new module test stand has been completed at DESY and is now in operation. Modules 6 and 7 of the TESLA Test Facility/FLASH assembly have been successfully tested there. This is a big advance in that this facility is independent of the accelerator so that features of the cryomodules can be studied without interrupting beam operation of the accelerator. Fig. 3 shows the steady progress being made towards the ILC goal for S1.
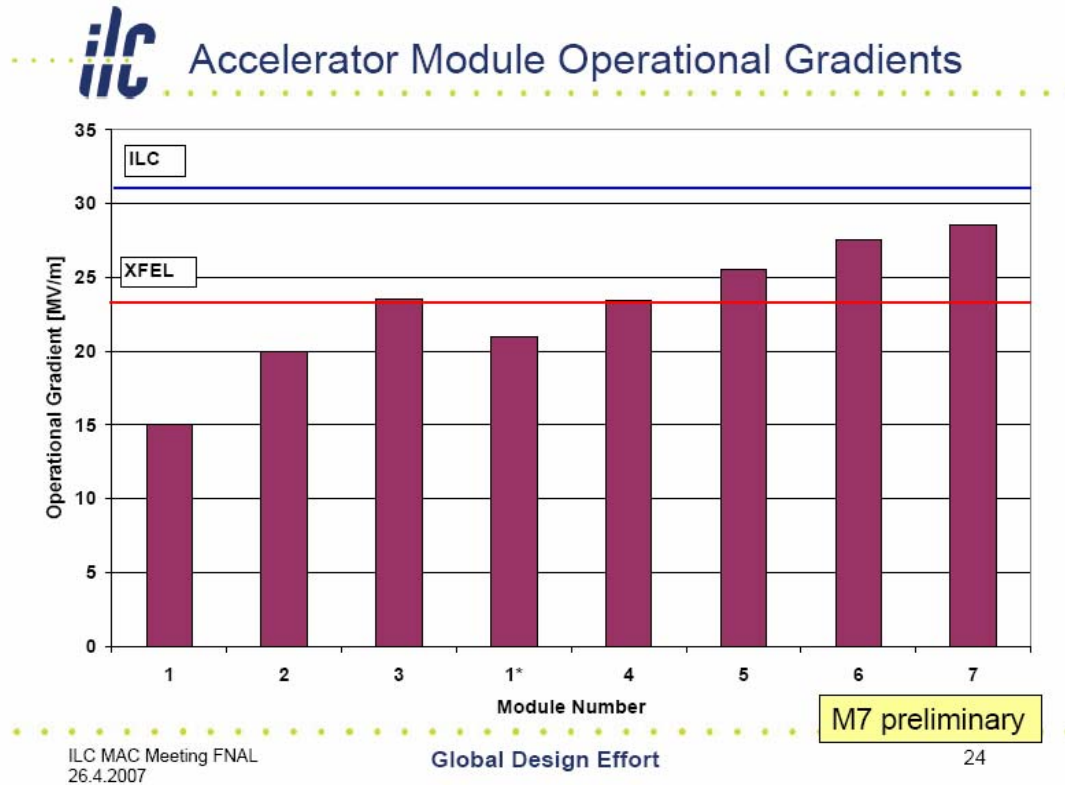
Fig. 3 Showing the improvement with module number of the achievable operating gradient

ILC module assembly and test facilities are being installed at KEK and Fermilab. When complete we will have powerful means for making rapid progress provided that we can arrange for coordinated programs – a challenge.

5 S2 – Where are We?

We anticipate that soon there will be three facilities capable of contributing to the carrying out of this charge. Currently the FLASH/TTF facility serves as the premier facility for this work and is

committed to test as many ideas and components as possible. A Superconducting Test Facility (STF) is under construction and early use at KEK. An ILC Test Facility is under construction at Fermilab too. As the S0 and S1 activities bear fruit we will have the means for making system tests of these sections of accelerator to solidify system requirements and introduce industry to the requirements. We hope that it will be possible to have significant enough participation from industries that ultimately we can depend on them for production of rf units meeting all requirements for the ILC.

While it is true that many issues for the ILC rf units have been addressed, at least partially, by TTF, many remain, particularly those having to do with operation at full ILC beam parameters and operation with those parameters for significant periods of time.

6 Alternate Concepts R&D – Long Range

While a number of suggestions have been made, three are receiving most of the attention: i) alternate cavity shapes; ii) alternate material form; iii) alternate fabrication methods.

6.1 Alternate shapes

The approach taken for the alternate cavity shapes is to minimize the ratio of surface magnetic field to accelerating gradient. This rests on the fact that the superconducting state is magnetic field limited. Shapes designed in somewhat different ways to achieve this end are referred to as the "low loss" shape, the "Ichiro" shape and the "reentrant" shape. Using the reentrant shape accelerating gradients in excess of 50 MV/m have been achieved in single cells. Implementing this achievement in 9 cell cavities with high yield remains for the future after we have been successful in this with the standard "Tesla" cavity shape.

6.2 Alternate Material Form

Here the idea is to use niobium material with large crystals to minimize the number of grain boundaries in a single cavity. An extension is to fabricate cavities from single crystals, grown large in the initial ingot formation and then sawed our and rolled into sheets large enough for drawing of cavity halves. Both of these approaches have been explored to some extent with encouraging results. Further tests are planned. The need for altering the manufacturing process at the niobium vendor should one of these approaches prove to be superior is an additional barrier to wide adoption on a short time scale.

6.3 Alternate Fabrication Methods

Electron beam welding is one of the most expensive steps in the currently employed manufacturing process. This has led to the trial of hydroforming or spinning for complete cavity shapes. Single cavities or groups of cavities can then be electron beam welded to the end groups where one 9 cell cavity is fastened to the next. Both of these methods have been developed to a significant extent. So far, however, the net simplification to the manufacture of 9 cell cavity unity has not warranted a switch to either of these approaches. Development continues.

7 Organizational Infrastructure for ILC SRF R&D

GDE R&D coordination in SRF has been progressing steadily. It is significantly strengthened by the existing, worldwide linkages of SRF workers as SRF applications expand, applications such as x-ray and neutron sources as well as heavy ion accelerator.

This broader perspective in encompassed by the Tesla Technology Collaboration (TTC) which comprises 52 member institutions in 12 countries. It holds meetings twice a year which deal will all aspects of SRF. This information exchange is of great benefit to ILC as well as to the other applications. A rich source of primary information on the subjects introduced above can be found in the proceedings of the most recent TTC meeting which was held at FNAL April 23-26, 2007 [2] In addition there are the triennial International SRF Workshops. The next TTC meeting will take place at DESY in January 2008; the next International Workshop in October 2007 in Beijing.

8 Acknowledgments

Grateful acknowledgment is hereby made of the information and illustrations furnished by many collaborators in the 3 regions. Much of the material was taken from the just completed TTC and ILC – MAC meetings. Particular thanks to Hasan Padamsee for his essential help in preparing the slides.

9 References

[1] ILC RDR Vol III, p. 80, www.linearcollider.org/cms/?pid=1000025
[2] TTC April 23 – 26 program, https://indico.desy.de/conferenceDisplay.py?confId=200

Loops for ILC

Matthias Steinhauser

Institut für Theoretische Teilchenphysik, Universität Karlsruhe (TH)
76128 Karlsruhe, Germany

This contribution summarizes the on-going activities connected to the evaluation of higher order radiative corrections in the context of a future international linear collider (ILC).

1   Introduction

The purpose of this contribution is two-fold. The primary task is to present a summary of the activities discussed in the parallel session "loops" of the Linear Collider Workshop (LCWS) 2007 at DESY in Hamburg. As a second aim we try to provide an overview of higher order corrections performed in the context of the ILC. It is clear that a brief review like the present one can not be complete and has to be restricted to the most important issues. For further related activities we want to refer to the summaries of the Top/QCD, Higgs, SUSY and extra dimensions parallel sessions which can also be found in these proceedings [1].

2   Bhabha scattering

Let us in a first step discuss the activities in the context of the next-to-next-to-leading order (NNLO) corrections to the Bhabha scattering which serves as an important luminosity monitor for basically all electron-positron colliders. The uncertainty in the luminosity enters into many observables and thus needs to be determined with the highest possible precision. This is in particular true for the Giga-Z option of the ILC.

In the recent years various groups have started the NNLO calculation to the Bhabha scattering which constitutes a highly non-trivial task since next to the kinematic variables s and t also the mass of the electron, m_e, has to be kept non-zero. As far as the dependence of the scattering cross section on m_e is concerned, it is only necessary to keep the logarithmic dependence and neglect the terms suppressed by m_e^2/s.

The calculation of the cross section $\sigma(e^+e^- \to e^+e^-)$ for $m_e = 0$ has been performed in Ref. [2]. In Ref. [3] this result has been used in order to perform a matching to the case where the infra-red singularities are regularized by a photon mass and the collinear ones by the electron mass. In this way the NNLO corrections for the purely photonic correction to the Bhabha scattering could be obtained. A similar approach has been elaborated in Ref. [4] where, however, the infrared divergences are still regularized dimensionally leading to more flexibility, in particular in view of applications within QCD (see also Ref. [5]).

The fermionic corrections which are defined by the presence of a closed lepton loop have been considered in Ref. [6] for the case of an electron loop. Recently, the results for a muon and tau have been obtained in Ref. [7]. In the approach used in this paper a reduction of the full multi-scale problem to master integrals is performed. Afterwards the latter are expanded in the desired kinematical limit. The results of Ref. [7] have been confirmed in Ref. [4].

There are various further contributions which are still missing to complete the NNLO corrections. Among them is the computation of the one-loop corrections where an additional

photon is radiated. Progress on the evaluation of the underlying five-point integrals have been presented at this workshop [8].

3 NLO corrections to multi-particle production

In the recent years there have been important developments concerning the techniques for one-loop calculations involving many external legs (see, e.g., Ref. [9] and references therein). However, many of the proposed methods still have to prove their applicability to real processes.

Up to date there are only two groups who performed a full one-loop calculation to a realistic $2 \to 4$ process. In Ref. [10] the process $e^+e^- \to 4f$ has been considered and in Ref. [11] electroweak corrections to $e^+e^- \to \nu\bar{\nu}HH$ have been obtained using the GRACE system (see, e.g., Ref. [12]).

In a contribution [13] to the present workshop an effective-theory approach has been introduced, based on a double-expansion in the fine structure constant and the ratio of width and mass of the W boson. In the threshold region, which is the validity range of the effective theory, good agreement with the results of Ref. [10] has been found for the cross section of the process $e^+e^- \to \mu^-\bar{\nu}_\mu u\bar{d}$.

In contribution [14] new developments for the GRACE system has been discussed. Among them there is an interface to FORM, the implementation of one-loop calculations in the MSSM and the proper treatment of infrared divergences in QCD processes. Furthermore, there is a new attempt to obtain octuple (or even a higher) precision in the numerical routines.

4 Sudakov logarithms

With the ILC it will be possible to consider the corrections of virtual W and Z bosons to exclusive reactions like the production of two quarks or two W bosons. Since the center-of-mass energy is significantly higher than the masses of the gauge bosons a conceptually new phenomenon occurs: in each loop-order quadratic logarithms of the form $\ln^2(s/M_{W/Z}^2)$ arise which can easily lead to corrections of order 30% at one and 5% at two loops. For recent papers dealing with this topic we refer to Refs. [15].

At LCWS07 a recent calculation has been presented [16] which deals with the complete two-loop NLL corrections to processes like $f_1 f_2 \to f_3 \ldots f_n$ involving n fermions. Furthermore, a new approach has been discussed which allows for the introduction of finite quark masses for the final state particles.

5 NNLO calculation to $e^+e^- \to 3$ jets

An accurate determination of the strong coupling can be obtained by the measurement of the 3-jet cross section in e^+e^- annihilation. Currently the error on α_s from this method is dominated by the theoretical uncertainties which is mainly due to the unknown NNLO corrections to $e^+e^- \to 3$ jets.

There are basically three ingredients contributing to $e^+e^- \to 3$ jets: (i) the two-loop virtual corrections, (ii) the one-loop corrections to the real radiation of a parton, and (iii) the double real radiation which involves five partons in the final state. The individual contributions are known since many years (see contribution [17] to this workshop). However,

up to very recently a proper combination of the individual pieces has not been achieved. The main reason for this are the infrared divergences inherent to the contributions (i), (ii) and (iii) which only cancel in the proper combination. In the recent years different approaches have been developed which are either based on the construction of appropriate subtraction terms or on direct numerical integration. The latter essentially relies on sector decomposition.

In Ref. [18] the first physical NNLO result has been presented for the thrust distribution defined through $T = \max_{\vec{n}} \frac{\sum_{i=1}^{n} |\vec{p}_i \cdot \vec{n}|}{\sum_{i=1}^{n} |\vec{p}_i|}$. The corrections turn out to be moderate leading to a significant reduction of the theoretical uncertainty on the thrust distribution.

6   Four-loop integrals

At the forefront of multi-loop calculations one also has to mention the contributions to four-loop vacuum integrals and four-loop massless two-point functions. The former integrals, often also denoted as "bubbles", are reduced with the help of the so-called Laporta-algorithm [19] to master integrals. The latter are evaluated with various methods based, e.g., on difference equations or on asymptotic expansion (see, e.g., Refs. [20, 21]).

Two applications have been presented at the LCWS07. In the first one the four-loop corrections to the ρ parameter have been studied [22, 23, 24, 25]. The new terms induce a shift in the W boson mass of about 2 MeV which is of the same order as the anticipated accuracy reached with the GIGA-Z option of the ILC. The latter is estimated to 6 MeV.

The second application [26] concerns the extraction of precise values for the charm and bottom quark masses which in the $\overline{\text{MS}}$ are given by [27] $m_c(m_c) = 1.286(13)$ GeV and $m_b(m_b) = 4.164(25)$ GeV. The analysis performed in Ref. [27] is based on improved experimental data to $\sigma(e^+e^- \rightarrow \text{hadrons})$ and new four-loop contributions to the photon polarization function [28, 29].

Also the four-loop massless two-point functions have various applications where the most important one is the order α_s^4 correction to the cross section $\sigma(e^+e^- \rightarrow \text{hadrons})$ (see, e.g., Ref. [30] for a recent publication). Their evaluation is based on Baikov's method [31] where the reduction to master integrals is established via an integral representation for the coefficients of the individual master integrals. The parameter integrals are solved in the limit of large space-time dimension, d. Due to the fact that the coefficients are rational functions of d it is possible to reconstruct the exact d dependence, provided sufficient expansion terms are available.

7   Further loops

There have been four further contributions which shall be mentioned in this Section.

New two-loop electroweak corrections to the partial decay width of the Higgs boson to bottom quarks have been presented in contribution [32] (see also Ref. [33]). Although the new terms are enhanced by a factor $(G_F m_t^2)^2$ the change of the partial decay rate is tiny and amounts to only 0.05%.

In contribution [34] new three-loop corrections to the relation between the $\overline{\text{MS}}$ and on-shell quark mass have been presented. In contrast to the previously known terms an additional mass scale from closed quark loop is allowed [35] where the main phenomenological

applications are charm quark corrections to the bottom quark mass. The reduction of all occurring integrals leads to 27 master integrals which involve two mass scales. They have been computed both with the help of the Mellin-Barnes and the differential equation technique.

The production of a Higgs boson at LHC in the so-called vector-boson fusion channel is very promising for its discovery. At LO in perturbation theory the gauge bosons are radiated off the quarks and combine in order to produce the Higgs boson. There is no colour exchange between the quarks and thus it is expected that two jets are observed at high rapidity whereas the decay products of the Higgs boson can be found at low rapidity. Thus, it is possible to apply cuts which allow for a huge suppression of the background. The exchange of colour between the quark lines occurs for the first time at NNLO. In contribution [36] the NNLO corrections originating from squared one-loop amplitudes with gluons in the initial state have been considered. Preliminary results have been presented which show that the numerical effect is small if the so-called "vector-boson fusion" cuts are applied.

In contribution [37] (see also Ref. [38]) a new method has been proposed to extract a precise top quark mass value from jet observables. It is based on a sequence of effective field theories which allows to derive a factorization theorem for the top quark invariant mass spectrum. The factorization theorem allows for a separation of perturbative and non-perturbative effects which in turn is the basis of the extraction of the so-called "jet mass".

For the evaluation of higher order quantum corrections it is crucial to have appropriate tools which facilitate the calculations [39]. As far as one-loop corrections are concerned one should mention `FeynArts` [40] and `FormCalc` [41] which have been applied to a variety of processes in the electroweak sector of the Standard Model but also in its extensions. Beyond one-loop the programs in general aim for specific tasks of the whole calculation. E.g., the program `AIR` [42] implements the Laporta algorithm, the `Mathematica` codes `AMBRE` [43] and `MB` [44] can be used to evaluate Feynman integrals with the Mellin-Barnes method, and the program `exp` [45] allows for the application of an Euclidian asymptotic expansion for a given hierarchy in the mass scales involved in the problem. A tool which nowadays is indispensable in higher order calculations is the algebra program `FORM` [46] enabling large computations in a quite effective way. Also its parallel versions, `ParFORM` [47] and `TFORM` [48], have proven to substantially extend the capability of `FORM`.

Acknowledgments

References

[1] J. Hewett, these proceedings; S. Kanemura, these proceedings.

[2] Z. Bern, L. J. Dixon and A. Ghinculov, Phys. Rev. D **63** (2001) 053007 [arXiv:hep-ph/0010075].

[3] A. A. Penin, Phys. Rev. Lett. **95** (2005) 010408 [arXiv:hep-ph/0501120]; Nucl. Phys. B **734** (2006) 185 [arXiv:hep-ph/0508127].

[4] T. Becher and K. Melnikov, JHEP **0706** (2007) 084 [arXiv:0704.3582 [hep-ph]].

[5] A. Mitov and S. Moch, JHEP **0705** (2007) 001 [arXiv:hep-ph/0612149].

[6] R. Bonciani, A. Ferroglia, P. Mastrolia, E. Remiddi and J. J. van der Bij, Nucl. Phys. B **701** (2004) 121 [arXiv:hep-ph/0405275]; Nucl. Phys. B **716** (2005) 280 [arXiv:hep-ph/0411321].

[7] S. Actis, M. Czakon, J. Gluza and T. Riemann, arXiv:0704.2400 [hep-ph].

[8] T. Riemann, these proceedings.

[9] R. K. Ellis, W. T. Giele and G. Zanderighi, JHEP **0605** (2006) 027 [arXiv:hep-ph/0602185].

[10] A. Denner, S. Dittmaier, M. Roth and L. H. Wieders, Phys. Lett. B **612** (2005) 223 [arXiv:hep-ph/0502063]; Nucl. Phys. B **724** (2005) 247 [arXiv:hep-ph/0505042].

[11] F. Boudjema *et al.*, [arXiv:hep-ph/0510184].

[12] G. Belanger, F. Boudjema, J. Fujimoto, T. Ishikawa, T. Kaneko, K. Kato and Y. Shimizu, Phys. Rept. **430** (2006) 117 [arXiv:hep-ph/0308080].

[13] C. Schwinn, these proceedings; arXiv:0708.0730 [hep-ph].

[14] Y. Yasui, these proceedings.

[15] B. Jantzen, J. H. Kühn, A. A. Penin and V. A. Smirnov, Nucl. Phys. B **731** (2005) 188 [Erratum-ibid. B **752** (2006) 327] [arXiv:hep-ph/0509157]; A. Denner, B. Jantzen and S. Pozzorini, Nucl. Phys. B **761** (2007) 1 [arXiv:hep-ph/0608326]; J. H. Kühn, F. Metzler and A. A. Penin, arXiv:0709.4055 [hep-ph].

[16] B. Jantzen, these proceedings; arXiv:0709.2311 [hep-ph].

[17] T. Gehrmann, these proceedings; arXiv:0709.0351 [hep-ph].

[18] A. Gehrmann-De Ridder, T. Gehrmann, E. W. N. Glover and G. Heinrich, arXiv:0707.1285 [hep-ph].

[19] S. Laporta and E. Remiddi, Phys. Lett. B **379** (1996) 283 [arXiv:hep-ph/9602417]; S. Laporta, Int. J. Mod. Phys. A **15** (2000) 5087 [arXiv:hep-ph/0102033].

[20] Y. Schroder and A. Vuorinen, JHEP **0506** (2005) 051 [arXiv:hep-ph/0503209].

[21] K. G. Chetyrkin, M. Faisst, C. Sturm and M. Tentyukov, Nucl. Phys. B **742** (2006) 208 [arXiv:hep-ph/0601165].

[22] C. Sturm, these proceedings.

[23] Y. Schroder and M. Steinhauser, Phys. Lett. B **622** (2005) 124 [arXiv:hep-ph/0504055].

[24] K. G. Chetyrkin, M. Faisst, J. H. Kuhn, P. Maierhofer and C. Sturm, Phys. Rev. Lett. **97** (2006) 102003 [arXiv:hep-ph/0605201].

[25] R. Boughezal and M. Czakon, Nucl. Phys. B **755** (2006) 221 [arXiv:hep-ph/0606232].

[26] M. Steinhauser, these proceedings; arXiv:0709.2020 [hep-ph].

[27] J. H. Kühn, M. Steinhauser and C. Sturm, Nucl. Phys. B **778** (2007) 192 [arXiv:hep-ph/0702103].

[28] K. G. Chetyrkin, J. H. Kühn and C. Sturm, Eur. Phys. J. C **48** (2006) 107 [arXiv:hep-ph/0604234].

[29] R. Boughezal, M. Czakon and T. Schutzmeier, Phys. Rev. D **74** (2006) 074006 [arXiv:hep-ph/0605023].

[30] P. A. Baikov, K. G. Chetyrkin and J. H. Kühn, Nucl. Phys. Proc. Suppl. **157** (2006) 27 [arXiv:hep-ph/0602126].

[31] P. A. Baikov, Nucl. Phys. Proc. Suppl. **116** (2003) 378.

[32] M. Butenschön, these proceedings.

[33] M. Butenschön, F. Fugel and B. A. Kniehl, Nucl. Phys. B **772** (2007) 25 [arXiv:hep-ph/0702215].

[34] S. Bekavac and D. Seidel, these proceedings.

[35] S. Bekavac, A. Grozin, D. Seidel and M. Steinhauser, arXiv:0708.1729 [hep-ph].

[36] M. Weber, these proceedings; arXiv:0709.2668 [hep-ph].

[37] A. Hoang, these proceedings.

[38] S. Fleming, A. H. Hoang, S. Mantry and I. W. Stewart, arXiv:hep-ph/0703207.

[39] R. Harlander and M. Steinhauser, Prog. Part. Nucl. Phys. **43** (1999) 167 [arXiv:hep-ph/9812357].

[40] T. Hahn, Comput. Phys. Commun. **140** (2001) 418 [arXiv:hep-ph/0012260].

[41] T. Hahn and M. Perez-Victoria, Comput. Phys. Commun. **118** (1999) 153 [arXiv:hep-ph/9807565].

[42] C. Anastasiou and A. Lazopoulos, JHEP **0407** (2004) 046 [arXiv:hep-ph/0404258].

[43] J. Gluza, K. Kajda and T. Riemann, Mellin-Barnes arXiv:0704.2423 [hep-ph].

[44] M. Czakon, Comput. Phys. Commun. **175** (2006) 559 [arXiv:hep-ph/0511200].

[45] R. Harlander, T. Seidensticker and M. Steinhauser, Phys. Lett. B **426** (1998) 125 [hep-ph/9712228]; T. Seidensticker, hep-ph/9905298.

[46] J. A. M. Vermaseren, arXiv:math-ph/0010025.

[47] M. Tentyukov, H. M. Staudenmaier and J. A. M. Vermaseren, Nucl. Instrum. Meth. A **559** (2006) 224.

[48] M. Tentyukov and J. A. M. Vermaseren, arXiv:hep-ph/0702279.

Summary of the data acquistion session for ILC detectors

Daniel Haas (`Daniel.Haas@cern.ch`)

Université de Genève - Département de Physique Nucléaire et Corpusculaire
24, quai Ernest-Ansermet, 1211 Genève 4 - Switzerland

Data acquisition is a key element for the ILC detectors. Current efforts in ongoing test-beam efforts are summarized together with future needs for the ILC. Promising new technologies like ATCA are presented as well. Please refer to the individual submissions of the DAQ session for more details and subjects that cannot be covered in this write-up.

1   Introduction

In the data acquisition session of the workshop, the presentations have been concentrated on two topics: DAQ systems used in current or upcoming test-beam campaigns and future needs for a 'final' ILC data acquisition system. This summary will concentrate on currently used DAQ systems by CALICE [2] and EUDET [3] and some selected topics for future DAQ systems. The expected data flow of different ILC subdetectors has been presented as well in the session, but will not be summarized in this write-up.

2   DAQ for current test-beam campaigns

In Europe, detector R&D efforts are currently concentrating on calorimetry, tracking and vertex detectors. The CALICE collaboration, who has recently also joined partly the EU-DET activities is concentrating on developments for electromagnetic and hadronic calorimeters. EUDET is a 6th framework programme of the European Union and includes developments for vertex and tracking detectors as well as calorimetry. Because each of the subsystems has different needs, a possible harmonization between the different data acquisition systems is currently feasible only at the trigger level and/or the data level, as will be shown later.

Each of the collaborations is putting its weight to different aspects of the DAQ system. CALICE wants to get a common readout hardware for the calorimeters, aiming already for a scalable solution for later ILC detectors. EUDET on the other hand has still individual, but usually lightweight solutions for the different subgroups, but proposes a combination of different subdetector groups via a newly designed trigger logic unit. Both collaborations write their data in the LCIO data format [4] and use the GRID as a backend for storage and analysis.

2.1   The CALICE DAQ

Figure 1 shows a schematic overview of the hardware of the calice data acquisition system. The detector interface (DIF) is a subdetector specific component, sending the data to the link data aggregator (LDA) and from there via optical links to off detector receivers (ODRs) housed in the acquisition PCs. The CALICE DAQ aims to use as many 'off-the-shelf'

components as possible, mainly for the LDAs and the ODRs, leaving only the very front end readout and part of the DIF detector specific.

The DIFs are fed by a low jitter clock (via the LDA) and offer a bi-directional link to the LDAs. They also offer a clock feadthrough and redundant data links to neighbouring DIFs and talk to the DAQ via a standardized firmware. The LDAs have to provide a fan out for clock and control signals and a fixed latency to the DIFs. They will be developed soon and may be based on commercial Spartan-3 development boards. Data transfer from the LDAs to the ODRs is done via a commercial 16x16 optical switch from Polatis. The current ODR prototype is based on a board from PLDApplications with a Xilinx Virtex4FX60 FPGA. This prototype has demonstrated already working functionality at gigabit ethernet speeds and could be upgraded to 10G ethernet via a small daughter card.

The CALICE collaboration is still working on the presented hardware solution and expects to have a full system in a time-scale of about one year together with a custom software framework for the readout.
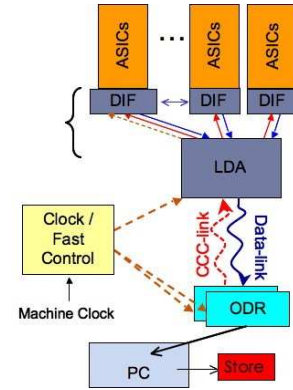
Figure 1: Schematic overview of the CALICE DAQ system

2.2 The DAQ for the EUDET pixel telescope

Within the EUDET collaboration, the pixel telescope working group has already performed their first test-beam activities in summer 2007. The data acquisition system of the pixel telescope is based on an adoptable readout card, the EUDRB [5], read either via VME (for test-beam activities) or USB2 (for bench-top systems). Synchronization of devices under test (DUTs) and the pixel telescope itself is achieved via a custom trigger logic unit, that has been developed by the University of Bristol [6].

Figure 2 shows an overview of the pixel telescope readout. The trigger logic unit receives inputs from the scintillators and provides a common trigger to the telescope and the DUT via LVDS signals. Optionally TTL or NIM signals are also available. DUT and telescope can synchronize either via a simple trigger/busy/reset logic or by clocking out a common event number from the TLU and attaching this number to the local events, thus avoiding any slipping of events during offline data analysis. The software framework for the pixel telescope is lightweight, platform independent (Linux, MacOSX and Windows using cygwin) and based on a minimum of open source libraries like POSIX for sockets and QT for the graphical user interface. Data is currently stored in a custom raw format for debugging reasons, but is then immediately converted to the LCIO data format and stored on the GRID for global access and analysis via 'standard' ILC software tools like Marlin etc.
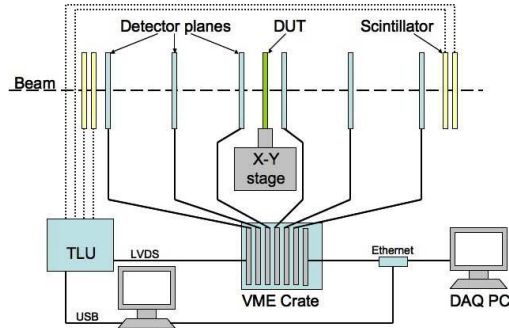
Figure 2: The EUDET pixel telescope DAQ

Within the scope of EUDET, harmonization of the DAQ will probably be done either at the trigger level, using the TLU or offline at the data level using the LCIO data format. The other subdetector groups of EUDET for tracking and calorimetry are currently evaluating the use of the TLU and external users have already successfully implemented the TLU in a combined test-beam. In the future, a common DAQ for all EUDET groups may be foreseen. Possible frameworks like ACE [7], EPICS [8] or DOOCS [9] are reviewed within EUDET, but may be implemented only in a successor program to EUDET.

3 ATCA, a new industry standard suitable also for ILC detectors

ATCA, or Advanced Telecom Computing Architecture is an open industry standard that has been introduced in 2005 and is supported by about 250 companies worldwide. Because of current modular standards using parallel backplanes are rapidly becoming obsolete, the HEP community needs to adapt to new platforms. ATCA is a possible candidate and first attempts to implement it are ongoing.

3.1 Some features of ATCA

ATCA provides a system building block which consists of crates or shelves and 12-14 modules with vital features, like:

- dual-redundant communications node with auto-failover,

- redundant 48 V power supplies and fans,

- serial power feeds to each module, serial I/O,

- an intelligent platform manager (IPM) to diagnose and isolate faulty modules etc.,

- all modules are hot-swappable,

- crate throughput of up to 2 Tb/s, offering unlimited scalability.

All these advantages result in an extremely high availability of the system of 99.999%, resulting in down-times of less than 5 minutes per year.

3.2 ATCA within the ILC scenario

The ILC will be an extremely complex machine with lots of systems and subsystems and needs a high overall availability of at least 85% [10]. As illustrated in Figure 3, this requires an availability of individual subsystems of at least 99.9%. Currently used and available technologies (VME etc.) are not able to provide this and ATCA is a valid candidate to be evaluated.
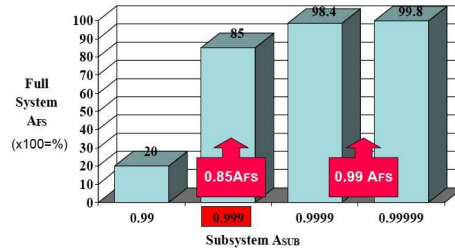
Figure 3: Required subsystem availability A_{sub} versus full system availability A_{FS}, comprising 16 systems with each 10 subsystems.

ATCA can provide off-the-shelf core components to the ILC community already today and the industry is developing the high availability software systems for the IPM etc. The offered module format is extremely versatile for custom applications, using small daughter cards on carrier boards or optional chassis sizes. Electrically, ATCA provides an excellent grounding and shielding scheme (grounding is connected in the 'right' order when hot-plugging modules) and robust connectors for multi gigabit per second serial transfer rates.

For the ILC machine, custom designs are needed. Highly precise timing and RF phase distribution modules must be built as well as specialized front-end modules for machine instrumentation. Interfaces to standard controlled machinery like movers etc. are needed and maybe also a connector system for rear transition modules (RTMs), similar to Fastbus.

Work in the ILC community has already started, with test systems at SLAC, FNAL, ANL and DESY, to evaluate the core system. DESY is currently investigating applications of ATCA for the XFEL facility and FNAL develops a 12 channel, 500 Mb/s 14 bit module for the SRF facilities. At SLAC, an ATCA to VME adaptor is under design, which will be extremely useful in the beginning for using existing readout solutions, and ANL is concentrating on system level software, interfacing to DAQ frameworks like EPICS or DOOCS.

ATCA could also be used for the ILC detectors, like for trigger systems and event building. The architecture is also valuable for inaccessible applications, but efforts

Figure 4: Evolution from a current LHC read-out scheme using multiple VME crates and PCs to a possible integrated solution at ILC with a single ATCA crate.

must be put for radiation hard device designs, and e.g. robotic replacement for buried applications. Figure 4 shows a possible evolution from a current readout system used at LHC to an ATCA based solution, reducing drastically the amount of crates, but it needs buffering of the data close to the subdetector front-ends to profit from the architectural advantages.

4 Future needs for the ILC DAQ

Figure 5 shows the current view of a possible uniform readout architecture for an ILC detector. Detector specific hardware and software/firmware should be integrated in the front-end of the detector and then transformed via a uniform interface. Treatment of the data should be done using commercial standards before making the data available to the worldwide global detector network (GDN). The whole is based on a 'software trigger' concept, taking into account the bunch train structure of the ILC beam. This requires up to 1 ms active pipelines for
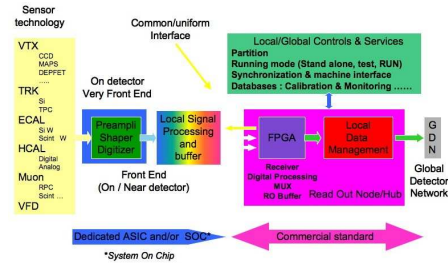
Figure 5: Current view of an uniform readout architecture for ILC detectors .

full bunch trains.

Of course, the detailed implementation still needs to be foreseen and there are remaining open questions. Do we need e.g. a trigger for cosmic rays? This has been proven extremely useful for LHC setups during installation. But because the ILC detectors will no longer be driven by external triggers, but more synchronized by a central clock, it may be difficult to implement such a scenario in individual front-end solutions. Also the details of the machine synchronization still must be worked out in the future.

5 Summary

The data acquisition for future detectors at the ILC is often considered to be a simple task, supposing that all the needed know-how and tools are already currently available. But already current test-beams often reach data throughputs well above recent LEP experiments and sometimes even close to LHC needs. The move from triggered machines like the LHC to a bunch-train concept like at the ILC also requires significant changes of existing DAQ schemes. Extremely high reliability of each subsystem becomes more and more important, and industrial solutions like ATCA will probably play a major role in the design of a future data acquisition system for the machine as well as the detectors at the future international linear collider.

References

[1] Slides:
http://ilcagenda.linearcollider.org/contributionDisplay.py?contribId=465&sessionId=148&confId=1296

[2] http://llr.in2p3.fr/activites/physique/flc/calice.html

[3] http://www.eudet.org

[4] http://lcio.desy.de/

[5] C. Bozzi, *The data reduction board of the EUDET pixel telescope*, in these proceedings.

[6] Eudet-Memo-2007-02: D. Cussans, *Description of the JRA1 Trigger Logic Unit*, see http://www.eudet.org

[7] http://www.cs.wustl.edu/~schmidt/ACE.html

[8] http://www.aps.anl.gov/epics/

[9] http://tesla.desy.de/doocs/doocs.html

[10] Larsen and Downing, in: Proceedings for the IEEE NSS conference, Rome, 2004.

ILC Project Tools:
ILCAgenda and ILCDoc

Maura Barone[1,2]

1- Fermi National Accelerator Laboratory (FNAL),
P.O.Box 500, Batavia, IL 60510-0500, USA

2- Global Design Effort

The International Linear Collider (ILC) Global Design Effort is now in the process of building an integrated set of project tools for communications, data archiving, engineering, costing, scheduling, and project management. In this article, we will focus on two project tools we adopted for meeting planning and document archiving: Indico and Invenio respectively.

1 Introduction: Indico and Invenio

One of the biggest challenges for the global and world-wide International Linear Collider (ILC) collaboration is to exchange information effectively. A key need is to ensure that the scientific and technical content can be archived for long-term preservation and easy retrieval. This requires the use of advanced electronic communication systems and Web applications. Figure 1 shows the three ILC/GDE project tools that will be used as Electronic Document Management Systems.

The adopted meeting planning tool is Indico [2], a conference management system.

Figure 1: The suite of Electronic Document Management Systems for the ILC Global Design Effort

For the document archival we selected Invenio [3], an integrated digital library system. Both tools are Web-based applications produced by the CERN Document Server Software Consortium [4]. Their Web interface follows the latest HTML standards and guarantees maximum compatibility with all browsers. Indico and Invenio are distributed under the GNU General Public License and the software is delivered as Open Source. Technically, they run on the Apache/Python Web application server. They use Zope Object Database (Indico) and MySQL (Invenio) to store conference and document metadata. They use the US Library of Congress standards for bibliographic information description and comply with the Open Archive Initiative metadata harvesting protocol (OAI-PMH). Both tools provide an advanced user delegation mechanism.

2 ILCAgenda

The ILC implementation of the digital conferencing software (Indico) is named ILCAgenda and it can be reached at `http://ilcagenda.linearcollider.org/`. Events in ILCAgenda

are organized in a hierarchical tree structure of categories reflecting the organization of the project and designed to insure the maximum flexibility and access to the information. Managers have been appointed for each category. Authorized users can submit talks and presentations through the easy-to-use Web interface.

ILCAgenda is in operation since March 2006. As of August 2007, it hosts about 8,000 talks and the average number of scheduled meetings per month is approximately 75.

3   ILCDoc

The ILC implementation of the digital library system (Invenio) is named ILCDoc and it can be reached at `http://ilcdoc.linearcollider.org/`. ILCDoc contains documents with textual or graphic information such as technical notes, preprints, schedules or images. Documents can be submitted by any authorized user via an intuitive Web interface and are organized in navigable collection trees. The tree structure in ILCDoc is very similar to the one in ILCAgenda and reflects the current organization of the project. ILCDoc features a search engine that allows searches across different collections and type of documents through customizable simple or advanced interfaces. In addition to searching in document metadata, such as title, author, keywords and date, it is possible to search the full-text. The ILCDoc search engine also allows searches through the public information submitted to ILCAgenda. This very important feature implies all the presentations and materials from the many ILC meetings are captured, archived and can be easily accessed.

ILCDoc was launched last February at the BILCW07 workshop at Beijing. In the following months it was extensively used for the archival of all the ILC Reference Design Report (RDR) volumes and the related documentation.

4   Conclusion

The implementation of ILCAgenda and ILCDoc is an essential step forward in developing the set of tools needed by the ILC collaboration to work together effectively. These tools provide easy retrieval of the electronic documents and guarantee their long-term availability.

5   Acknowledgments

We are grateful to the ILC EDMS Committee, for recommending the tools to adopt and helping in their ILC implementation: T. Markiewicz (SLAC) chair, J. Ferguson (CERN), L. Hagge (DESY), R. Stanek (Fermilab), N. Toge(KEK) and H. Weerts (Argonne). We also thanks the CERN Indico and Invenio teams, in particular T. Baron and D. Bourillot (CERN, Indico), J.-Y. Le Meur and T. Simko (CERN, Invenio), for hosting ILCAgenda and ILCDoc on CERN servers and for their extremely valuable advice and support.

References

[1] Slides:
   `http://ilcagenda.linearcollider.org/contributionDisplay.py?contribId=519&sessionId=30&confId=1296`

[2] CDS Indico `http://cdsware.cern.ch/indico/`

[3] CDS Invenio `http://cdsware.cern.ch/invenio/`

[4] CERN Document Server Software Consortium `http://cdsware.cern.ch/`

E-Document Systems at ILC, Part II: ILC EDMS

Jochen Bürger, Jasper A. Dammann, Silke Eucker, Lars Hagge[*], Andreas Herz, Jens Kreutzkamp,
Salvatore Pantó, Daniel Szepielak, Przemyslaw Tumidajewicz, Norbert Welle

Deutsches Elektronen-Synchrotron DESY, Hamburg, Germany

ILC EDMS is the central collaboration, documentation and configuration management platform for engineering design activities of the ILC. This paper gives a short introduction to the objectives and capabilities of ILC EDMS.

1   What is ILC EDMS?

The term Engineering Data Management (EDM), or synonymously Product Data Management (PDM) originates from the field of Computer-Aided Design and Manufacturing (CAD/CAM). EDM/PDM aims to integrate and organize product design and manufacturing information like e.g. specifications, CAD data, bills of materials, routing lists, change orders and inspection sheets. EDM/PDM has been superseeded by the term Product Lifecycle Management (PLM), which expands the data-centric PDM view to include methods, processes and people, and to cover the entire product lifecycle from first ideas over design, manufacturing, installation, operation and maintenance, remodeling and upgrades, to deconstruction.

An EDM or PLM System (EDMS) is an information system framework which contains functionality for e.g.

- Document Management;
- 3D CAD Data Management;
- Product Structure Management;
- Configuration, Version and Change Management;
- Workflow Management;
- Visualization, Digital Mock-Up and Mark-Up.

An EDMS has to be configured for its project prior to use. For example, document and relation types have to be defined and included into the data model, rules for access control have to be defined and implemented, workflows have to be created, user interface have to be customized, and external interfaces have to be provided. Configuring an EDMS is usually an ongoing effort through the project lifetime, as new requirements are continuously arising as the project progresses into new phases. DESY has introduced an EDMS for managing the complexity and optimizing the design and production processes in its next-generation accelerator projects. The DESY EDMS has been extended for the needs of the ILC collaboration and in that configuration is labelled ILC EDMS.

---

[*] Comunicating author, lars.hagge@desy.de

2 ILC EDMS Objectives

The ILC EDMS is the central collaboration and lifecycle management platform for the Global Design Effort of the ILC. It will:

- Enable members of the ILC collaboration to access and contribute project information independent of location;
- Enable engineers at the different laboratories to collaboratively design components using 3D CAD;
- Enable scientists to participate in design processes from the very beginning by viewing the evolving CAD models;
- Provide teams, committees, boards etc. with workspaces for work-in-progress document management;
- Support change control of the ILC baseline during the EDR phase;
- Protect confidential information and intellectual property against unauthorized access.

3 Basic EDMS Functionality
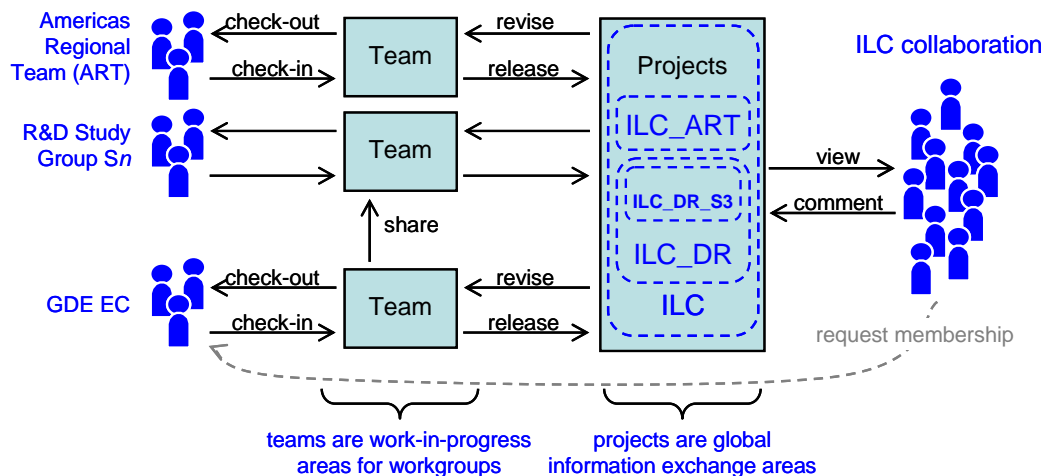
Figure 1. Basic EDMS operation principle

Figure 1 illustrates the basic ILC EDMS operation principle. The system offers local work-in-progress areas, so-called teams, for e.g. workgroups and boards. The teams interact with a web-like central information repository which is accessible for the entire ILC collaboration. The system offers a workflow engine for controlling reviewing, approval and change procedures.

4   Accessing 3D CAD Data

EDMS-ID	Name	Life Cycle State	Quantity
D00000000404473,A,1,85	3RD_HARMONIC_COMPLETE_ASSEMBLY	Working	
D00000000404269,A,1,2	COLD-MASS-SUPPORT_COVER_WELDMENT--426552	Working	2
D00000000404293,A,1,5	HARDWARE_COMPLETE_ASSY	Working	1
D00000000404299,A,1,5	COLDMASS_SUPT_SLIDING-WEL		
D00000000404302,A,1,5	COLDMASS_SUPT_FIXED-WELDM		
D00000000404428,A,1,8	STAND-ASSEMBLY		
D00000000404464,A,1,43	MAIN_COUPLER_WARM_ASSY		
D00000000404470,A,1,24	CRYO_3RD-HARM_VESSEL_ASSE		
D00000000404488,A,1,80	COLD_MASS_ASSEMBLY		
D00000000541513,A,1,1	HARDWARE_WARM_COUPLER		
D00000000541623,A,1,15	BELLOWS_TEST_1		
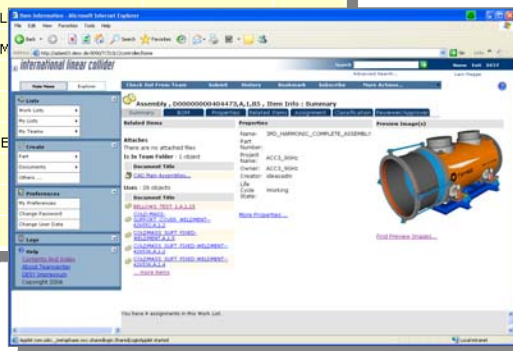
Figure 2. ILC EDMS screenshots showing example bill of materials and summary tab.

The ILC EDMS provides seamless integration of document and 3D CAD data management. CAD data items are treated like documents regarding e.g. storage and retrieval. They are organized using additional relations and hierarchies. Most important is the bill of materials (BOM), a hierarchical breakdown structure of a (sub-) system into its functional components. Defining a global ILC breakdown structure is one of the key success criteria for the ILC EDMS.

5   Putting ILC EDMS into Operation

ILC EDMS has been launched at LCWS/ILC 2007 workshop in Hamburg. The first groups who are adopting the system are the American Regional Team (ART) and the Beam Delivery System (BDS) group.

The ILC EDMS team is preparing training sessions which can be held by using Webex, and is organizing an ILC EDMS Power User Training to be held at DESY in November 2007. In addition, project management involvement is required for e.g. defining reference breakdown structures and policies for creating teams and projects. The team can be contacted at ilc-edms-support@desy.de.

6   References

[1] J. Bürger et al., "DESY and ILC EDMS : Engineering Data Management for Large Scientific Projects", PAC 2007, Albuquerque, May 2007.
[2] J. Bürger et al., "Towards Industrialization: Supporting the Manufacturing Processes of Superconducting Cavities at DESY", Phys C, 441(2006)268-271

Higgs and Electroweak Symmetry Breaking

Conveners: H. Logan, T. Barklow, S. Heinemeyer, A. Raspereza, Y. Gao, Y. Okada

Different vacua in 2HDM

I. F. Ginzburg, K.A. Kanishev [*]

Sobolev Institute of Mathematics and Novosibirsk State University,
Novosibirsk, Russia

The potential of Two Higgs Doublet Model (2HDM) can have extrema with different physical properties. We found explicit equations for extremum energies via parameters of potential if it has explicitly CP conserving form. These equations allow to pick out extremum with lower energy – vacuum state and to look for change of extrema (phase transitions) with the variation of parameters of potential. Our goal is to find general picture here to apply it for description of early Universe.

■ **Lagrangian**. The spontaneous electroweak symmetry breaking via the Higgs mechanism is described by the Lagrangian[a]

$$\mathcal{L} = \mathcal{L}_{gf}^{SM} + \mathcal{L}_H + \mathcal{L}_Y \quad with \quad \mathcal{L}_H = T - V, \quad \varphi_i = \begin{pmatrix} \varphi_i^+ \\ \varphi_i^0 \end{pmatrix}. \tag{1}$$

Here $\mathcal{L}_{gf}^{SM}$ describes the $SU(2) \times U(1)$ Standard Model interaction of gauge bosons and fermions, $\mathcal{L}_Y$ describes the Yukawa interactions of fermions with Higgs scalars and $\mathcal{L}_H$ is the Higgs scalar Lagrangian; T is the Higgs kinetic term and V is the Higgs potential.

The most general renormalizable Higgs potential is the sum of the operator $-V_2$ of dimension 2 and the operator V_4 of dimension 4. In the 2HDM

$$V = -V_2(x_i) + V_4(x_i); \quad V_2(x_i) = M_i x_i \equiv \left[m_{11}^2 x_1 + m_{22}^2 x_2 + \left(m_{12}^2 x_3 + h.c. \right) \right] /2,$$

$$V_4(x_i) = \frac{\Lambda_{ij} x_i x_j}{2} \equiv \frac{\lambda_1 x_1^2 + \lambda_2 x_2^2}{2} + \lambda_3 x_1 x_2 + \lambda_4 x_3 x_3^\dagger + \left[\frac{\lambda_5 x_3^2}{2} + \lambda_6 x_1 x_3 + \lambda_7 x_2 x_3 + h.c. \right], \tag{2}$$

$$x_1 = \varphi_1^\dagger \varphi_1, \quad x_2 = \varphi_2^\dagger \varphi_2, x_3 = \varphi_1^\dagger \varphi_2, \quad x_{3^*} \equiv x_3^\dagger = \varphi_2^\dagger \varphi_1 \ (i, j = 1, 2, 3, 3^*).$$

Here $\Lambda_{ij} = \Lambda_{ji}$, λ_{1-4} and m_{ii}^2 are real while λ_{5-7} and m_{12}^2 are generally complex.

■ **Extrema of potential**. The extrema of the potential define the values $\langle \varphi_{1,2} \rangle$ of the fields $\varphi_{1,2}$ via equations:

$$\partial V / \partial \varphi_i |_{\varphi_i = \langle \varphi_i \rangle} = 0, \qquad \partial V / \partial \varphi_i^\dagger |_{\varphi_i = \langle \varphi_i \rangle} = 0. \tag{3}$$

These equations have the electroweak symmetry conserving (EWc) solution $\langle \varphi_i \rangle = 0$ and could have several electroweak symmetry breaking (EWSB) solutions. Below e.g. $\langle F \rangle_N$ means numerical value of the operator F in N-th extremum.

We consider also the values y_i of operators x_i at the extremum points

$$y_{i,N} \equiv \langle x_i \rangle_N = \langle \varphi_a \rangle_N^\dagger \langle \varphi_b \rangle_N \qquad for \qquad x_i = \varphi_a^\dagger \varphi_b.$$

In each extremum point these values obey inequalities following from definition and Cauchy inequality, written for important auxiliary quantity Z:

$$y_1 > 0, \quad y_2 > 0, \qquad Z = y_1 y_2 - y_3^* y_3 \geq 0. \tag{4}$$

• **Classification of EWSB extrema**. It is useful to define quantities

$$T_a \equiv \langle \partial V / \partial x_a \rangle = \Lambda_{ai} y_i - M_a \quad (a = 1, 2, 3, 3^*), \quad T_{1,2} \quad are \quad real, \qquad T_{3^*} = T_3^*. \tag{5}$$

In these terms system (3) can be transformed to equations for y_i:

$$\langle \varphi_1 \rangle^\dagger \langle \partial V / \partial \varphi_1^\dagger \rangle = y_1 T_1 + y_3 T_3 = 0, \quad \langle \varphi_2 \rangle^\dagger \langle \partial V / \partial \varphi_1^\dagger \rangle = y_3^* T_1 + y_2 T_3 = 0,$$
$$\langle \varphi_2 \rangle^\dagger \langle \partial V / \partial \varphi_2^\dagger \rangle = y_2 T_2 + y_3^* T_{3^*} = 0, \quad \langle \varphi_1 \rangle^\dagger \langle \partial V / \partial \varphi_2^\dagger \rangle = y_3 T_2 + y_1 T_{3^*} = 0. \tag{6}$$

[a] Notations and main definitions follow [1], we use some equations from [2].

One can consider each pair of these equations as a system for calculation of quantities T_i via y_i. The determinant of these systems are precisely $Z = y_1 y_2 - y_3^* y_3$. Therefore, it is natural to distinguish two types of extrema, with $Z \neq 0$ (*charged extrema* with $T_i = 0$) and with $Z = 0$ (*neutral extrema* with $T_i \neq 0$).

• For each EWSB extremum one can choose the z axis in the weak isospin space so that the most general electroweak symmetry violating solution of (3) can be written in a form with real v_1 and complex v_2:

$$\langle \varphi_1 \rangle = \frac{1}{\sqrt{2}} \begin{pmatrix} 0 \\ v_1 \end{pmatrix}, \quad \langle \varphi_2 \rangle = \frac{1}{\sqrt{2}} \begin{pmatrix} u \\ v_2 \end{pmatrix} \qquad with \ v_1 = |v_1|, \ v_2 = |v_2| e^{i\xi} . \tag{7}$$

At $u \neq 0$ we have $Z > 0$ – charged extremum, at $u = 0$ we have $Z = 0$ – neutral extremum.

• **The distances from some extremum and between two extrema** are useful conceptions for discussions below, they are defined as

$$\mathcal{D}(\varphi, N) = (\varphi_1 \langle \varphi_2 \rangle_N - \varphi_2 \langle \varphi_1 \rangle_N)^\dagger (\varphi_1 \langle \varphi_2 \rangle_N - \varphi_2 \langle \varphi_1 \rangle_N) \equiv x_1 y_2 + x_2 y_1 - x_3 y_{3^*} - x_3^\dagger y_3 , \tag{8}$$

$$\mathcal{D}(I, II) = (\langle \varphi_1 \rangle_I \langle \varphi_2 \rangle_{II} - \langle \varphi_2 \rangle_I \langle \varphi_1 \rangle_{II})^\dagger (\langle \varphi_1 \rangle_I \langle \varphi_2 \rangle_{II} - \langle \varphi_2 \rangle_I \langle \varphi_1 \rangle_{II}) .$$

• **Decomposition around EWSB extremum**. Our potential can be rewritten as a sum of extremum energy and two polynomials in x_i of first ans second order. The form of second order polynomial is fixed by a quartic terms of potential, it can be only $V_4(x_i - y_i)$. The residuary first order polynomial in x_i must be proportional to $\mathcal{D}(\varphi, N)$. Therefore

$$V = \mathcal{E}_N^{ext} + V_4(x_i - y_{i,N}) + \mathcal{R} \cdot \mathcal{D}(\varphi, N) . \tag{9a}$$

Let us define $\mathcal{R}$. The differentiation of (9a) gives for T_i:

$$T_1 = y_2 \mathcal{R}, \quad T_2 = y_1 \mathcal{R}, \quad T_3 = -y_3^* \mathcal{R}, \quad T_{3^*} = -y_3 \mathcal{R} .$$

For the *charged extremum* $T_i = 0$, and we have from here $\mathcal{R}_{ch} = 0$.

For the *neutral extremum* the Higgs fields mass matrix $\partial^2 V / \partial \varphi_{i,a} \partial \varphi_{j,b}|_N$ for the upper $(\pm)$ components a, b can be written as

$$M_{++} = \begin{pmatrix} T_1 & T_3 \\ T_{3^*} & T_2 \end{pmatrix} \equiv \begin{pmatrix} y_2 & -y_3^* \\ -y_3 & y_1 \end{pmatrix} \mathcal{R} .$$

At $Z = 0$ determinant of this matrix equals to 0. Therefore, one eigenstate of this matrix equals to 0. This massless combination of charged Higgs fields form well known Goldstone state. The second eigenstate of above matrix describes the physical charged Higgs boson with mass $M_{H^\pm}^2 = Tr \ M_{++} = T_1 + T_2 = (y_1 + y_2) \mathcal{R}$. This quantity is positive for the minimum of the potential, it can be negative in other extremes. Finally, we obtain

$$\mathcal{R}_N = M_{H^\pm}^2 / (y_1 + y_2)|_N \ \ for \ neutral \ extremum \ N , \ \ and \ \mathcal{R}_{ch} = 0 . \tag{9b}$$

• **The extremum energy** in each extremum point can be expressed, using the theorem on homogeneous functions:

$$\mathcal{E}_N^{ext} = V(y_{i,N}) = -V_2(y_{i,N}) + V_4(y_{i,N}) = -V_4(y_{i,N}) = -V_2(y_{i,N})/2 . \tag{10}$$

The global minimum of potential realizes the vacuum state of the model. The direct comparison of extremum energies looks the best way for finding vacuum. More delicate but also important problem is possible existence minima of potential different from vacuum ("false vacuum" or "metastable state"). It can happen if only all eigenvalues of mass matrix near each extremum are positive.

■ **EW symmetry conserving (EWc) point**. The EWc point $\langle \varphi_1 \rangle = \langle \varphi_2 \rangle = 0$ is extremum of potential. Depending on m_{ij}^2 it has different nature: it is *minimum* if $det|m_{ij}^2| \geq 0$ and $m_{11}^2 < 0$, $m_{22}^2 < 0$, it is *maximum* if $det|m_{ij}^2| \geq 0$ and $m_{11}^2 > 0$, $m_{22}^2 > 0$,

or it is *saddle point* in any other case. According to [3] no other extremum can be a maximum of potential.

■ **Charged extremum.** In the case when $Z \neq 0$, eqs. (6) have form $T_i = 0$. This system of linear equations for y_i can have unique solution which is calculated easily. In accordance with (7), it describes an extremum of the original potential (2) if only the obtained values $y_{1,2}$ obey inequalities (4). These inequalities determine the range of possible values of λ_i and m_{ij}^2 where the charged extremum can exist. According to (9), the charged extremum is minimum of the potential if the quadratic form $V_4(x_i - y_{i,ch})$ is positively defined at each classical value of operators x_i, i.e. $V_4(z_i)$ must be positive at arbitrary real z_1, z_2 and complex z_3 (see also [3]). It is more strong condition for potential than positivity constraint ($V_4(z_i)$ must be positive in the corner of z_i space, limited by conditions of form (4)).

■ **Neutral extrema, general case**. Other solutions of the extremum condition (3) obey a condition for $U(1)$ symmetry of electromagnetism, that is solution with $Z = 0 \Rightarrow u = 0$. In the calculation of extremum condition it is essential that in case quantities y_i are not independent.

For the Higgs potential of general form we have no idea about classification of neutral extrema. However, if CP conserving extremum (with no scalar-pseudoscalar mixing) exists, there is a basis in (φ_1, φ_2) space in which potential has explicitly CP conserving form [4], [1] (with all real λ_i, m_{ij}^2). Below we use this very form of potential.

■ **Neutral extrema, case of explicit CP conservation (real λ_i, m_{ij}^2).**
In accordance with definitions (7), we have for each solution $y_3 = \sqrt{y_1 y_2}\, e^{i\xi}$. Now the extremum energy (10) is transformed to the form

$$\mathcal{E}^{ext} = -\frac{1}{2} \left\{ m_{11}^2 y_1 + m_{22}^2 y_2 + 2m_{12}^2 \sqrt{y_1 y_2}\, cos\xi \right\} + \frac{\lambda_1}{2} y_1^2 + \frac{\lambda_2}{2} y_2^2 + (\lambda_3 + \lambda_4) y_1 y_2 + \tag{11}$$
$$+ \lambda_5 y_1 y_2 cos 2\xi + 2 \left(\lambda_6 y_1 + \lambda_7 y_2 \right) \sqrt{y_1 y_2}\, cos\xi.$$

Now we find extrema in coordinates y_1, y_2, ξ. We start from the minimization in ξ at fixed y_i. It gives two types of solutions:

$$(A): \quad \cos\xi = \frac{m_{12}^2 - 2(\lambda_6 y_1 + \lambda_7 y_2)}{4\lambda_5 \sqrt{y_1 y_2}}, \quad (B): \quad \sin\xi = 0. \tag{12}$$

• **Spontaneously CP violating extremum**. The extremum point (12A) describes a solution with complex value v_2 at real parameters of the potential. In this case physical neutral Higgs states have no definite CP parity. So this extremum is called the **spontaneously CP violating (sCPv) extremum** [5, 6]. The substitution of $cos\xi$ from (12A) into (11) transform extremum energy to the second order polynomial in y_1, y_2. Minimum condition for this energy become system two linear equations for extremal values of y_1, y_2 with unique solution. Therefore, $\boldsymbol{y_1}$, $\boldsymbol{y_2}$ **and** $\boldsymbol{\cos\xi}$ **are described by parameters of the potential unambiguously**. Certainly, this extremum can be realized only in the range of parameters of the potential obeying inequalities $|\cos\xi| < 1$, $y_1 > 0$, $y_2 > 0$.

The energy (11) does not changes at the change $\xi \to -\xi$ (i. e. $\langle\varphi_2\rangle \to \langle\varphi_2\rangle^*$). Therefore

> If $\varphi_1 = \langle\varphi_1\rangle$, $\varphi_2 = \langle\varphi_2\rangle$ is the extremum of potential, then $\varphi_1 = \langle\varphi_1\rangle$, $\varphi_2 = \langle\varphi_2\rangle^*$ is also the extremum and these two extrema are degenerate in energy [5], $\qquad$ (13)

the sCPv extremum is doubly degenerated in the "direction" of CP violation.

Note that the potential (11) is a second order polynomial in $\cos\xi$. The sCPv extremum (if it exist) can be a minimum only if $\lambda_5 > 0$, in accordance with [7].

• **CP conserving extrema**. The solution (12B) describes extrema that correspond to $\xi = 0, \pi$. The case $\xi = \pi$ can be obtained from the case $\xi = 0$ if we allow v_2 (i.e. $\tan \beta$) to be negative. Therefore, without loss of generality we consider below the only case with $\xi = 0$. In these cases physical Higgs bosons have definite CP parity (**CP conserving – CPc – extrema**). The extremum condition , written for $v_i = \sqrt{2y_i}$, has form of the system of two cubic equations. Rewriting this system with parametrization $v_1 = v\cos\beta$, $v_2 = v\sin\beta$, we express the quantity v^2 via $t \equiv \tan\beta$ and obtain the equation for t similar to those presented in [9]. This equation can have up to 4 different solutions. Considering nearly degenerated example, one can state that in some cases system can have 2 different CPc minima.

■ **Case of soft Z_2 symmetry violation ($\lambda_6 = \lambda_7 = 0$) at real λ_5, m_{12}^2.** In the mentioned important case many equations become more transparent. We present explicit equations for extremum energy for the charged, sCPv and CPc extrema respectively

$$\mathcal{E}_{ch}^{ext} = -\frac{m_{11}^4\lambda_2 + m_{22}^4\lambda_1 - 2m_{11}^2 m_{22}^2\lambda_3}{8(\lambda_1\lambda_2 - \lambda_3^2)} - \frac{m_{12}^4}{4(\lambda_4 + \lambda_5)} \; ;$$

$$\mathcal{E}_{sCPv} = -\frac{m_{11}^4\lambda_2 + m_{22}^4\lambda_1 - 2m_{11}^2 m_{22}^2\tilde{\lambda}_{345}}{8(\lambda_1\lambda_2 - \tilde{\lambda}_{345}^2)} - \frac{m_{12}^4}{8\lambda_5} \;\; where \;\; \tilde{\lambda}_{345} = \lambda_3 + \lambda_4 - \lambda_5 \; ; \quad (14)$$

$$\mathcal{E}_{CPc} = -\frac{\left(m_{11}^2 + tm_{12}^2\right)\left(m_{11}^2 + 2tm_{12}^2 + t^2 m_{22}^2\right)}{8(\lambda_1 + \lambda_{345}t^2)}, \;\; where \; \lambda_{345} = \lambda_3 + \lambda_4 + \lambda_5 \;\; and$$

$$\lambda_2 m_{12}^2 t^4 + (\lambda_2 m_{11}^2 - \lambda_{345}m_{22}^2)t^3 + (\lambda_{345}m_{11}^2 - \lambda_1 m_{22}^2)t - \lambda_1 m_{12}^2 = 0 \,.$$

The results for general case with λ_6, $\lambda_7 \neq 0$ at real λ_i, m_{ij}^2 are presented in [8].

■ **Vacuum**. Now the using of decomposition (9) or direct comparison of general equations for extremum energy like (14) allow to obtain following conclusions.

1. If the EWc extremum ($\langle\varphi_1\rangle = \langle\varphi_2\rangle = 0$) realizes the vacuum state (it can happen only at m_{11}^2, $m_{22}^2 < 0$) all EWSB extrema are saddle points .

2. If the charged extremum realizes the minimum of the potential, all neutral extrema are saddle points.

3. For two neutral minima of potential or a minimum and a saddle point with $M_{H_{\pm,N}}^2 > 0$, the deeper (a candidate for the global minimum – the vacuum) is the extremum with the larger value of ratio $M_{H_{\pm,N}}^2/v_N^2$.

For **explicitly CP conserving potential** one can distinguish a CP conserving (CPc) extremum with zero phase difference between the values $\langle\varphi_i\rangle$ at the extremum point and spontaneously CP violating (sCPv) extrema, in which the phase difference between the values $\langle\varphi_i\rangle$ is nonzero, the latter generates neutral Higgs states without definite CP parity. Total number of extrema in this case can be up to 8 (0 or 1 charged extremum, up to 4 CPc extrema, 2 or 0 sCPv extrema, 1 EWc extremum).

4. At $\lambda_5 > 0$ and $\lambda_5 > \lambda_4$ system can have a sCPv minimum, and this minimum is vacuum. This vacuum is doubly degenerate in sign of phase difference between the values of fields at the extremum point. This degeneracy is broken by loop corrections to potential in correspondence with direction of *arrow of time*. In this case other EWSB extrema are saddle points, not minima.

5. System can have more than one CPc local minima, e. g. I and II. In this case the vacuum state is lowest among them. For the important case of softly broken Z_2 symmetry

(14) the state I is below state II and can describe vacuum if

$$m_{12}^2/(v_I^2 sin2\beta_I) - m_{12}^2/(v_{II}^2 sin2\beta_{Ii}) > 0 \,. \tag{15}$$

■ To illustrate our general discussion, we consider a simple toy potential with additional $\varphi_1 \leftrightarrow \varphi_2$ symmetry, where all the extrema can be calculated easily:

$$V_t = \frac{\lambda}{2} (x_1 + x_2)^2 + \frac{\lambda\varkappa}{2} \left(x_3^2 + x_3^{*2}\right) - \frac{m^2}{2} (x_1 + x_2) - \frac{m^2\varkappa r}{4} (x_3 + x_3^*) \,. \tag{16}$$

Below we present the map, representing change of vacuum states with the change of parameters of potential in the plane $(\varkappa r, \varkappa)$, where $\varkappa r = 2m_{12}^2/m^2$ – vertical axis and $\varkappa = \lambda_5/\lambda$ – horizontal axis. Left plot: $m^2 > 0$, right plot: $m^2 < 0$. Note that in this toy model potential has no minima except vacuum.
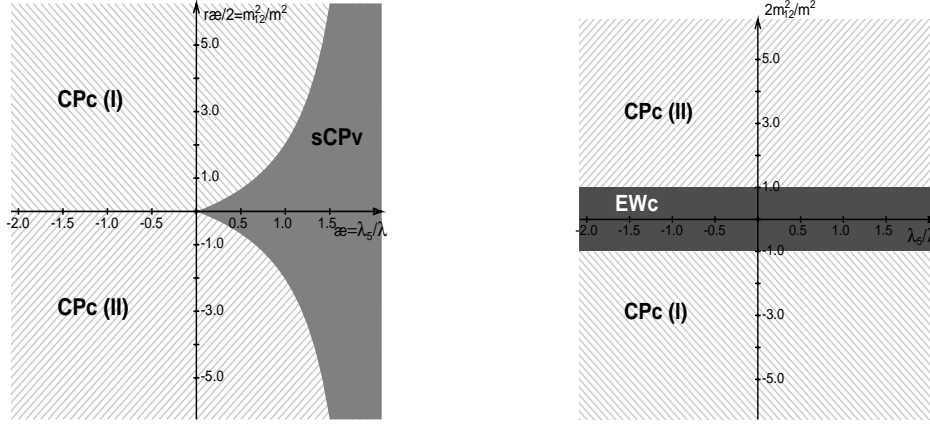
References

[1] I.F. Ginzburg, M. Krawczyk, *Phys. Rev.* **D 72** (2005) 115013; hep-ph/0408011

[2] I.F. Ginzburg, *Acta Phys. Polonica* **B37** (2006) 1161-1172 (preliminary version in hep-ph/0512102)

[3] I. P. Ivanov, Phys. Lett. **B 632** (2006) 360; Phys. Rev. **D75** (2007) 035001

[4] J. F. Gunion, H. E. Haber, *Phys. Rev.* **D72** (2005) 095002, hep-ph/0506227; S. Davidson, H. E. Haber, *Phys. Rev.* **D72** (2005) 035004, hep-ph/0504050.

[5] T. D. Lee. *Phys. Rev.* **D 8** 1226 (1973)

[6] A. Barroso, P.M. Ferreira, R. Santos, J.P. Silva, hep-ph/0507329, hep-ph/0608282 *Phys. Rev.* **D74** (2006) 085016, *and references there.*

[7] J. F. Gunion., H. E. Haber. *Phys. Rev.* **D 67** (2003) 075019.

[8] I.F. Ginzburg,K.A. Kanishev, hep-ph/0704.3664

[9] A. Barroso, P.M. Ferreira, R. Santos, hep-ph/0702098

The charged Higgs boson at LEP
Towards the final combination

Pierre LUTZ [*]

CEA Saclay - DAPNIA/Spp
91191 GIF SUR YVETTE CEDEX - France

The four LEP collaborations have searched for charged Higgs bosons in the framework of Two Higgs Doublet Models (2HDM). The data of the four experiments (still preliminary for OPAL) have been statistically combined. The results are interpreted within the 2HDM for Type I and Type II benchmark scenarios. No statistically significant excess has been observed when compared to the Standard Model background prediction, and the combined LEP data exclude large domains of the parameter space.

1 Introduction

The full presentation may be found in [1]. The four LEP collaborations have searched for charged Higgs bosons in the framework of Two Higgs Doublet Models (2HDM). Since the preliminary combination prepared for the summer 2001 conferences, three experiments have published their final results [2, 3, 4] and OPAL will soon do so. Thus the LEP working group for Higgs bosons searches has performed a preliminary statistical combination of the data taken at centre-of-mass energies from 183 GeV to 209 GeV.

The existence of a pair of charged Higgs bosons is predicted by several extensions of the Standard Model. In Two Higgs Doublet Models, the couplings are completely specified in terms of the electric charge and the weak mixing angle, θ_W, and therefore, at tree level, the production cross-section depends only on the charged Higgs boson mass. Higgs bosons couple to mass and therefore decay preferentially to heavy particles, but the precise branching ratios may vary significantly depending on the model. Two scenarios have been considered. The first one allows charged Higgs decays to fermions only, which is the case in the 2HDM of type II [5] for not too small m_A (section 2). The second scenario allows in addition the charged Higgs boson to decay into gauge and Higgs bosons (possibly off-shell). This situation is realized in the 2HDM of type I [6] over large parts of the $\tan\beta$ parameter space (section 3).

Pair-production of charged Higgs bosons occurs mainly via s-channel exchange of a photon or a Z^0 boson. The tree-level decay amplitude is independent of the model assumptions and depends only on the mass of the charged Higgs boson. Furthermore, the (electroweak) radiative corrections (which depend on the model) are small.

Each experiment has produced analyses for various decay channels which, combined with the different centre-of-mass energies, amounts to 122 samples of data.

The statistical procedure adopted for the combination of the data and the precise definitions of the confidence levels CL_b, CL_{s+b}, CL_s by which the search results are expressed, have been previously described [7]. The main sources of systematic error affecting the signal and background predictions are included, using an extension of the method of Cousins and Highland [8] where the confidence levels are the averages of a large ensemble of Monte Carlo experiments.

---

[*]On behalf of the LEP Higgs Working Group.

2 Combined searches in the 2HDM of type II

In type II 2HDM [5], one Higgs doublet couples to up-type fermions and the other to down-type fermions. The Higgs sector of the Minimal Supersymmetric Standard Model (MSSM) is a particular case of such models, where the $H^{\pm}$ is constrained to be heavier than the W boson at tree level. For the masses accessible at LEP energies, the $\tau^- \bar{\nu}_\tau$ and $\bar{c}s$ decays (and their charge conjugates) are expected to dominate, as can be seen on Figure 1 (left).
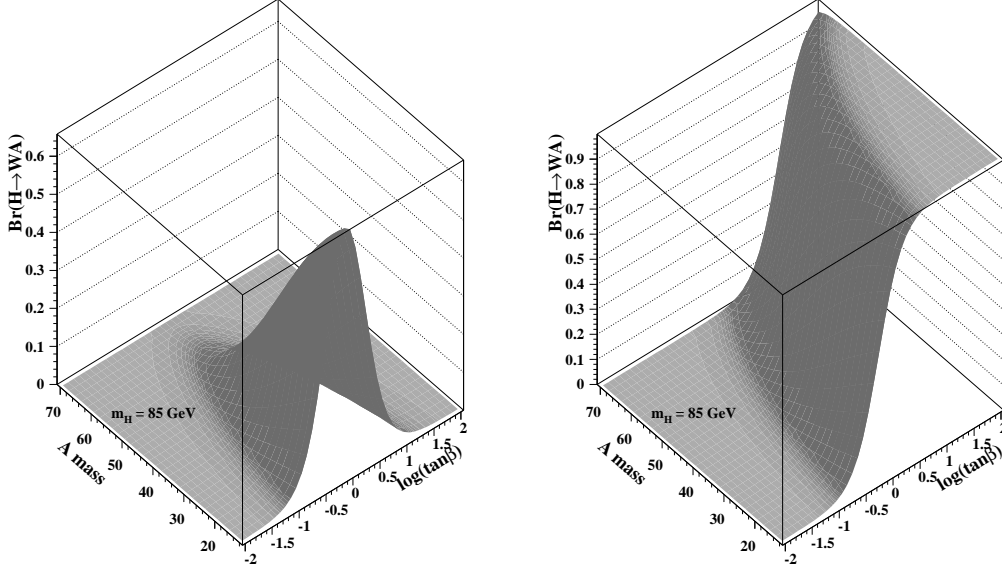
Figure 1: Bosonic Branching fraction in 2HDM Type II (left) and Type I (right)

The searches are carried out under the assumption that the two decays $H^+ \to c\bar{s}$ and $H^+ \to \tau^+\nu$ exhaust the H^+ decay width, but the relative branching ratio is free. This historical assumption is valid for the MSSM since the A mass is expected to be large. Combining the results from the four experiments, a scan has been done, in the plane Br = $B(H^+ \to \tau^+\nu)$ versus $m_{H^{\pm}}$. Figure 2 (left) shows the observed background confidence level CL_b. This observed confidence level is everywhere within the $\pm 2\sigma$ region of the background prediction, except for some small regions at low mass and high mass that slightly exceed the $2\,\sigma$ level. All three such regions are the superposition of small excesses compared to the expectation seen by two or three of the experiments, and are far from the expected limit. The expected median and observed mass limits are shown in Figure 2 (right).

3 Combined searches in the 2HDM of type I

An alternative set of models, type I models [6], assume that all fermions couple to the same Higgs doublet. In this case and if the neutral pseudo-scalar A is light enough (which is not excluded by direct searches for the general 2HDM [9]) the decay to W^*A can be predominant even in the range of masses of interest at LEP (W^* is an off-shell W boson).
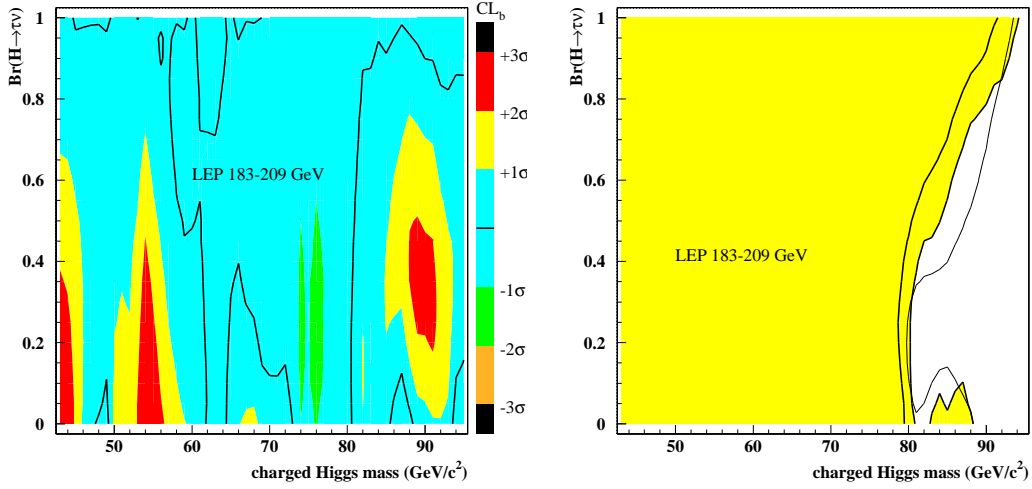
Figure 2: Type II 2HDM : Left : contours based on the observed p-values CL_b as a function of $m_{H^\pm}$ and Br, indicating the statistical significance of local departures from the expectation. Right : the bounds on $m_{H^\pm}$ as a function of Br. The shaded area is excluded at the 95% CL. The expected exclusion limit (at the 95% CL) is indicated by the thin solid line and the thick solid line inside the shaded area is the observed limit at the 99.7% CL.

Figure 1 (right) shows the branching ratio for this decay. Basically, for all boson masses, the possible charged Higgs boson decays are purely fermionic for low $\tan\beta$ (the ratio of the Higgs vacuum expectation values) and purely bosonic for high $\tan\beta$. Between these two extreme cases, the change is rapid in $\tan\beta$ (between typically 0.1 and 10.) and slower in A boson mass. Type I models are explored through the combination of all decay channels. The combination is performed according to the branching ratios predicted by the model as a function of $\tan\beta$ and the boson masses. When there was a possible overlap between two channels, the one providing less sensitivity was ignored to avoid double counting. This is the case in the intermediate region in $\tan\beta$ for purely hadronic channels (W^*AW^*A and $c\bar{s}\bar{c}s$) on one hand and the semi-leptonic channels ($W^*A\tau^-\bar{\nu}_\tau$ and $c\bar{s}\tau^-\bar{\nu}$) on the other hand. Furthermore, the scan is restricted to m_A above 12 GeV since the search was done only through its decay into two b-jets.

Figure 3 shows the observed confidence level in the backgound hypothesis CL_b, for three values of m_A, which exhibits a slight (always below the 3 σ level) excess for low and intermediate A masses in the region where the bosonic decays dominate (high $\tan\beta$). When proceeding to the limit computation, it happens that these limits are everywhere found in a region where an excess is observed, resulting in a shift of the order of 3 GeV between observed and expected limits, as can be seen on Figure 4. It is worth noting that the valley visible on Figure 4 corresponds to regions where the conservative approach of keeping only one channel when both contribute but may induce double counting is applied.
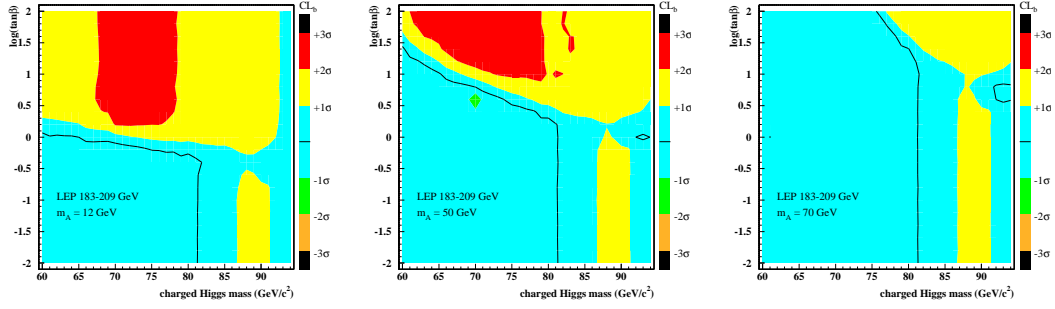
Figure 3: Type I 2HDM : Contours based on the observed p-values CL_b as a function of $m_{H\pm}$ and $\tan\beta$, indicating the statistical significance of local departures from the expectation, for 3 values of m_A (resp. 12, 50 and 70 GeV).

4 Conclusions

All results are still preliminary. In the scenario with fermionic decay channels alone, adapted for most of the 2HDM type II, the mass of the charged Higgs boson is greater than 80.1 GeV (95% CL), limited mainly by the WW background in that region. A new scenario has been explored, for 2HDM type 1, thanks to analyses by DELPHI and OPAL in the bosonic decay channels. In this case, the mass of the charged Higgs boson is greater than 76.0 GeV (95% CL), due mainly to a slight excess of observed events with respect to the expectation (79 GeV).

References

[1] http://ilcagenda.linearcollider.org/contributionDisplay.py?contribId=153&sessionId=71&confId=1296

[2] A. Heister *et al.* (ALEPH Collaboration), Phys. Lett. **B 543** (2002) 1-13;

[3] J. Abdallah *et al.* (DELPHI Collaboration), Eur. Phys. J. **C34** (2004) 399-418;

[4] P. Achard *et al.* (L3 Collaboration), Phys. Lett. **B 575** (2003) 208-220;

[5] H.E. Haber *et al.*, Nucl. Phys. **B 161** (1979) 493.

[6] S.L. Glashow and S. Weinberg, Phys. Rev. **D15** (1977) 1958;
E.A. Paschos, Phys. Rev. **D15** (1977) 1966;
A.G. Akeroyd Nucl. Phys. **B 544** (1999) 557.

[7] ALEPH, DELPHI, L3 and OPAL Collab., The LEP working group for Higgs boson searches, *Search for the Standard Model Higgs boson at LEP*, Phys. Lett. B **565** (2003) 61.

[8] R.D. Cousins and V.L. Highland, Nucl. Instr. Methods **A320** (1992) 331.

[9] J. Abdallah *et al.* (DELPHI Collaboration),"Searches for Neutral Higgs Bosons in Extended Models", Eur. Phys. J. **C38** (2004) 1-28.
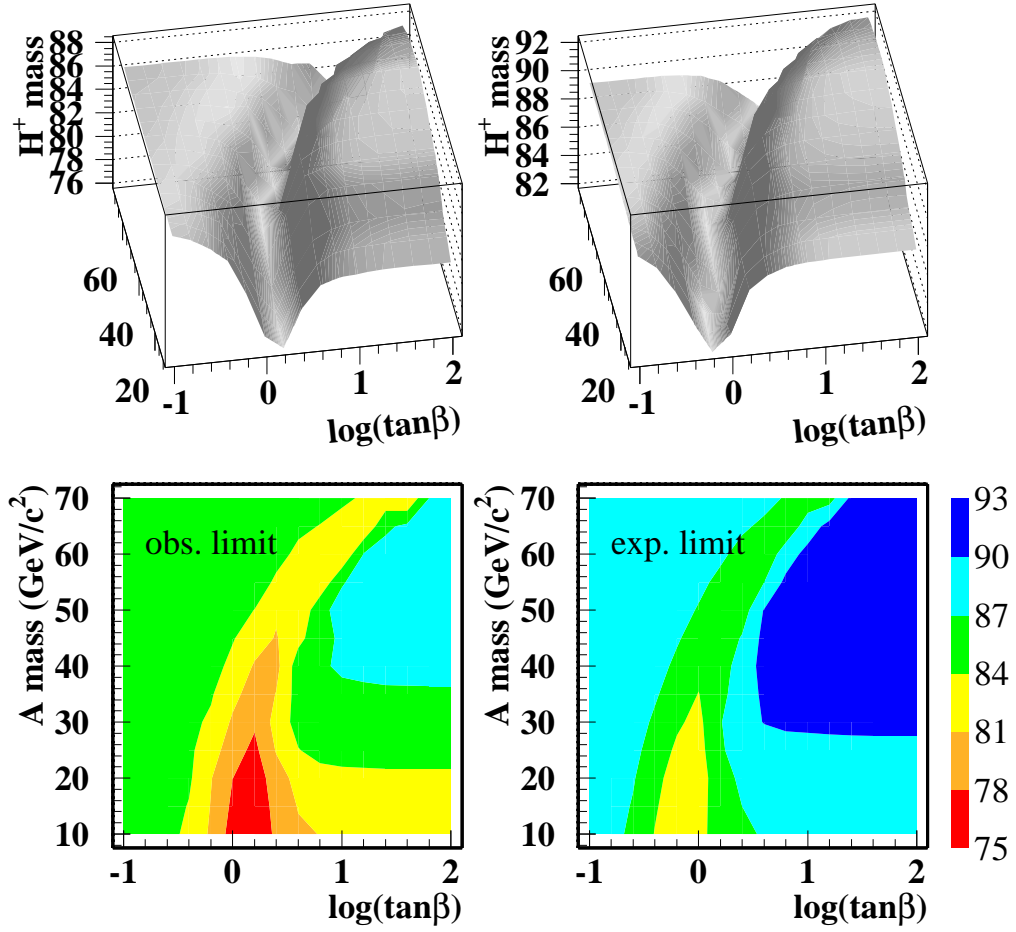
Figure 4: Type I 2HDM : Observed (left) and expected (right) 95% CL limits on the mass of the charged Higgs boson.

Higgs self coupling measurement

Djamel-Eddine BOUMEDIENE and Pascal GAY

Laboratoire de Physique Corpusculaire - Univ. B. Pascal/IN^{2}P^3-CNRS
24 Av. des Landais, F-63177 Aubière Cedex - France

A measurement of the Higgs self coupling from e^+e^- collisions in the International Linear Collider is presented. The impact of the detector performance in terms of b-tagging and particle flow is investigated.

1 Introduction

The trilinear Higgs self coupling, λ_{hhh}, is extracted from the measurement of the cross-section, σ_{hhZ}, of the Higgs-strahlung process $e^+e^- \rightarrow$ Zhh[2]. This study is performed in the standard model framework assuming $m_h = 120$ GeV/c^2 at $\sqrt{s} = 500$ GeV. At this centre-of-mass energy the W fusion process ($e^+e^- \rightarrow \nu\bar{\nu}$hh in t-channel) is negligible. It has been therefore established that $\frac{\Delta\lambda_{\mathrm{hhh}}}{\lambda_{\mathrm{hhh}}} \simeq 1.75\frac{\Delta\sigma_{\mathrm{hhZ}}}{\sigma_{\mathrm{hhZ}}}$. All the results are given for a luminosity of 2 ab^{-1}.

2 Monte Carlo simulation

The signal and background event samples have been generated with `Whizard`[3]. `PYTHIA`[4] has been used to perform the hadronisation of the primary partons. Table 1 summarizes the cross-section of the simulated processes. At $\sqrt{s} = 500$ GeV the dominant background processes involve top quarks. They are simulated, as well as final states with two and three bosons. 305 hhZ events are expected for an estimated background three orders of magnitude above.

The detector is simulated through a parametric Monte Carlo, [5] in which the sub-detectors are characterized by their acceptance angles, resolutions and energy thresholds. The intrinsic energy resolutions, $\frac{\Delta E}{\sqrt{E}}$, of the electromagnetic (ECAL) and hadronic (HCAL) calorimeters are respectively of 10.2% and 40.5%.

The b-tagging efficiency and c-jet contamination are parametrized according to the full reconstruction [6]. In this study, a b-tagging efficiency, ϵ_b, of 90% has been chosen, value which is not necessarily the best working point (cf. section 4.2)

Final state	hhZ	hZ	hZZ	ZZ	ZZZ	W$^+$W$^-$Z	e^+e^-ZZ	$e^\pm\nu$ZW$^\mp$
σ (fb)	0.1528	14.1	0.5	45.12	1.05	35.3	0.287	10.09
Nb. events	20k	110k	10k	110k	20k	130k	10k	60k

Final state	$t\bar{t}$	$\bar{t}b$W$^+$,$t\bar{b}$W$^-$	$t\bar{b}t\bar{b}$	$t\bar{t}$Z	$t\bar{t}$h	$t\bar{t}\nu\bar{\nu}$	$\nu\bar{\nu}$ZZ	$\nu\bar{\nu}$W$^+$W$^-$
σ (fb)	526.4	16.8	0.70	0.6975	0.175	0.141	1.083	3.627
Nb. events	1M	240k	20k	20k	20k	20k	20k	30k

Table 1: Cross sections of the simulated processes and number of generated events.

For each event the boson masses are reconstructed according to a final state hypothesis. The b-content of the event is obtained from an estimation of the number of the b-like jets in the event.

3 Event Selection and cross section measurement

The hhZ final state is sorted into three channels that correspond to the three Z decay modes $Z \to q\bar{q}$, $Z \to \nu\bar{\nu}$ and $Z \to \ell^-\ell^+$. In order to define the three samples representing these three channels, a preselection is applied on the signal and the background events, based on the following criteria:

- Global b content : only events with a minimal b-content are selected. The criteria value used to select hhq$\bar{q}$ events (six jets topology) is different from the one used to select hh$\nu\bar{\nu}$ or hh$\ell^-\ell^+$ events (four jets topology),

- the visible energy is used to define two exclusive samples which correspond to hh$\nu\bar{\nu}$ events (visible energy below $0.75\sqrt{s}$) and hhq$\bar{q}$ + hh$\ell^-\ell^+$ events (visible energy higher then $0.75\sqrt{s}$),

- the identification of two isolated leptons compatible with a Z boson mass allows to separate hh$\ell^-\ell^+$ from hhq$\bar{q}$ events.

Two variables are used to select the hhZ final state : a Neural Network (NN) [7] and the global event b-tag. Three kinds of inputs are used to feed the NN:

- event shape variables as, for instance, charged multiplicity, sphericity or thrust values,

- combinations of the different di-jet masses assuming a given final state,

- global b-flavor content of the event.

A Neural Network is designed for each of the hhq$\bar{q}$, hh$\nu\bar{\nu}$ and hh$\ell^-\ell^+$ final states. The neural networks are trained on large preselected samples of simulated events including all expected processes listed in Section 2. The output of the neural network for the hh$\nu\bar{\nu}$ selection is displayed on Figure 1.

For each channel, the cuts on NN and global b-tag are defined in order to maximize

Figure 1: Distribution of the Neural Network defined for the hh$\nu\bar{\nu}$ channel after preselection. The plain histogram represents the signal contribution while the line represents the background contribution.

the figure of merit $\delta = s/\sqrt{s+b}$. The combination of the three selections leads to 128 events expected from the background processes considered and 72 events from hhZ process corresponding to a δ value of 5.2.

In order to extract the cross section of the hhZ creation process, a Likelihood maximization method is used. It is based on the two dimensional NN $\times$ b-tag distribution. The expected precision on the cross-section measurement is 16%. Therefore, the expected precision on λ_{hhh} is 28%. This result is obtained for a particle flow resolution of $\frac{30\%}{\sqrt{E}}$ and a b-tag of 90%. A better working point for the b-tag efficiency may be found, as it will be shown in next section.

4 Scan of the detector performance parameters

Two parameters have been investigated : the particle flow resolution and the b-tagging . The full analysis described in section 3 has been performed and optimized for each hypothesis on the detector performance. The selection has been performed with different Neural Networks which combine the same input variables with adapted weights and re-optimized cuts.

4.1 Particle flow impact on the measurement

The particle flow uncertainty influences the jet pairing (based on di-jet masses) and propagates to the energies and momenta of the reconstructed bosons and then to the selection inputs. Then different efficiencies of the event selection are observed.

A fast simulation is used in order to determine the impact of the particle flow resolution on $\Delta\lambda_{\mathrm{hhh}}$.

For each event, the stable and visible particles (i.e. all stable except neutrinos) are considered with their generated energies and momenta with no detector simulation. They are clusterized in jets. A jet by jet smearing of the calorimeter cluster energies is then applied in order to simulate the combined effect of the detector resolution and the particle flow algorithms.

Figure 2: Expected resolution on λ_{hhh} as a function of the particle flow resolution. ϵ_b is fixed to 90%.

This study investigates the direct impact of the calorimetric resolution and the particle flow algorithms on the precision independently of its impact on the jet clusterisation. A $\frac{\Delta E}{\sqrt{E}}$ resolution range from 0% to 130% has been covered.

4.2 Event simulation with various b-tag efficiencies

The measurement performance depends also on the b-tag. For each jet as defined in section 4.1 consisting on b-fragmentation products, a b-tag is statistically defined assuming a given efficiency ϵ_b. For a given vertex detector (VDET) and a given jet energy, the values of ϵ_b is associated to a c flavored contamination (quantified by ϵ_c), namely the rate of c-jets identified as b-jets. Similary a rate of uds-jets identified as b-jets is associated to ϵ_b and it has also been taken into account. ϵ_b was varied in the range 40% to 95%.

4.3 Results

The dependence of the precision on the measurement of λ_{hhh}, with respect to the particle flow uncertainty is displayed on Figure 2.

For a given b-tag efficiency, the uncertainty on the λ_{hhh} measurement increases when $\frac{\Delta E}{\sqrt{E}}$ increases. For $\epsilon_b = 90\%$, the best measurement is 29% when a perfect particle flow is assumed while for higher resolution on particle flow the precision increases to 37%. The

improvement of the particle flow enhances the precision on the trilinear coupling by a factor 1.3. This gain is equivalent to a factor 1.7 on the required luminosity.

The dependence of the precision on the Higgs self coupling measurement with respect to the b-tag efficiency is displayed on Figure 3 where an optimum is observed around $\epsilon_b = 67\%$. This b-tag efficiency corresponds, for a typical jet energy of 45 GeV, to $\epsilon_c \simeq 3\%$ which means that the hhZ final state measurement is optimized for pure b-tagging .

5 Conclusion

The feasibility of the λ_{hhh} measurement was established. The expected statistical precision with a typical detector is about 28%. It was shown that an optimization of the b-tagging allows to reduce this uncertainty to 19%.
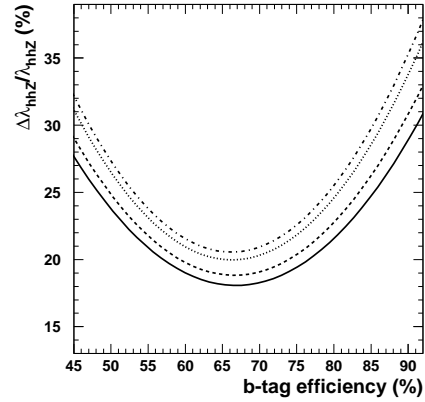
Figure 3: Expected resolution on the λ_{hhh} as a function of ϵ_b. From down to up $\frac{\Delta E}{\sqrt{E}}$=0%, 30%, 60% and 130%.

References

[1] Slides:
http://ilcagenda.linearcollider.org/contributionDisplay.py?contribId=155&sessionId=71&confId=1296

[2] A. Djouadi, W. Killian, M. Muhlleitner and P. Zerwas, Eur. Phys. J. **C10**

[3] W. Kilian, T. Ohl, J. Reuter, WHIZARD: Simulating Multi-Particle Processes at LHC and ILC, arXiv: 0708.4233 [hep-ph]

[4] T. Sjostrand, S. Mrenna and P. Skands JHEP05 (2006) 026.

[5] M. Pohl, H. J. Schreiber, SIMDET.3 A Parametric Monte Carlo for a TESLA Detector, DESY 99-030 (1999)

[6] R. Hawkings, Vertex detector and flavour tagging studies for the Tesla linear collider, LC-PHSM/2000-026

[7] J. Schwindling, MLPFit: A tool for Multi-Layer Perceptrons,
http://home.cern.ch/~schwind/MLPfit.html

Effects of polarisation on study of anomalous VVH interactions at a Linear Collider

Sudhansu S. Biswal[1], Debajyoti Choudhury[2], Rohini M. Godbole[1] and Mamta[3]

1- Centre for High Energy Physics, Indian Institute of Science, Bangalore 560 012, India

2- Department of Physics and Astrophysics, University of Delhi, Delhi 110 007, India

3- Department of Physics and Electronics, S.G.T.B. Khalsa College, University of Delhi, Delhi 110 007, India

We investigate the use of beam polarisation as well as final state τ polarisation effects in probing the interaction of the Higgs boson with a pair of heavy vector bosons in the process $e^+e^- \to f\bar{f}H$, where f is any light fermion. The sensitivity of the International Linear Collider (ILC) operating at $\sqrt{s} = 500$ GeV, to such $VVH(V = W/Z)$ couplings is examined in a model independent way. The effects of ISR and beamstrahlung are discussed.

1 Introduction

The particle physics community hopes that the LHC will soon present it with the signal for the Higgs; but, it is to the ILC that we will have to turn to for establishing it as *the* SM Higgs boson through a precision measurement of its properties. The dominant channel of Higgs production at the ILC, *viz.* $e^+e^- \to f\bar{f}H$ where f is any light fermion, proceeds via the VVH interaction with $V = Z(W)$. The most general form of the VVH vertex, consistent with Lorentz–invariance, can be written as:

$$\Gamma_{\mu\nu} = g_V^{SM} \left[a_V \ g_{\mu\nu} + \frac{b_V}{m_V^2}(k_{1\nu}k_{2\mu} - g_{\mu\nu} \ k_1 \cdot k_2) + \frac{\tilde{b}_V}{m_V^2} \ \epsilon_{\mu\nu\alpha\beta} \ k_1^\alpha k_2^\beta \right] \tag{1}$$

where k_i's denote the momenta of the two V's and, at the tree level in the SM, $a_V = 1$ and $b_V = \tilde{b}_V = 0$. In our analysis we assume a_V to be real and retain terms upto linear order in other anomalous parts. In an effective theory, the general structure of VVH coupling can be derived from dimension–six operators.

2 The Final State and Kinematical cuts

We choose to work with a Higgs boson of mass 120 GeV and consider its detection in the $b\bar{b}$ final state with a branching ratio 0.68. Furthermore, we assume the detection efficiency of b-quark to be 70%. We impose kinematical cuts designed to suppress dominant backgrounds. Cuts R_1 (R_2) on the invariant mass of the $f\bar{f}$ system: $\left| m_{f\bar{f}} - M_Z \right| \leq (\geq) 5\,\Gamma_Z$, can be used to enhance (suppress) the effect of the s–channel Z–exchange diagram.

Statistical fluctuations in the cross-section or in an asymmetry, for a given luminosity $\mathcal{L}$ and fractional systematic error ϵ , can be written as:

$$\Delta\sigma = \sqrt{\sigma_{SM}/\mathcal{L} + \epsilon^2\sigma_{SM}^2} \ \text{ and } \ (\Delta A)^2 = \frac{1 - A_{SM}^2}{\sigma_{SM}\mathcal{L}} + \frac{\epsilon^2}{2}(1 - A_{SM}^2)^2. \tag{2}$$

We demand that the contribution to the observable coming from the anomalous parts are less than the statistical fluctuation in these quantities at a chosen level of significance and study the sensitivity of a LC to probe them. We choose $\epsilon = 0.01$, $\mathcal{L} = 500$ fb^{-1} and look for a 3σ effect. Note that in the case of polarisation asymmetries the total luminosity of 500 fb^{-1} is divided equally among different polarisation states.

3 ZZH couplings

We construct observables ($\mathcal{O}_i$) whose behaviour (odd/even) under the discrete transformations C, P and $\tilde{T}$ (the pseudo time reversal operator which reverses particle momenta and spins without interchanging initial and final states) is the same as that for a particular operator in the effective Lagrangian. This is achieved by taking the expectation values of signs of various combinations of measured quantities such as particle momenta and spins ,C_i's, $i \neq 1$. Some of these combinations are listed in Table 1. The observables are cross-sections and various asymmetries with polarised beams and polarised final state τ's, which we discuss in the following sections and are also listed in the Table.

ID	C_i	C	P	CP	$\tilde{T}$	$CP\tilde{T}$	Observable($\mathcal{O}_i$)	Coupling
1		$+$	$+$	$+$	$+$	$+$	σ	$a_z, \Re(b_z)$
2a	$\vec{P}_e \cdot \vec{p}_H$	$-$	$+$	$-$	$+$	$-$	A_{FB}	$\Im(\tilde{b}_z)$
2b	$(\vec{P}_e \times \vec{p}_H) \cdot \vec{P}_f$	$+$	$-$	$-$	$-$	$+$	A_{UD}	$\Re(\tilde{b}_z)$
2c	$[\vec{P}_e \cdot \vec{p}_H] * [(\vec{P}_e \times \vec{p}_H) \cdot \vec{P}_f]$	$-$	$-$	$+$	$-$	$-$	A_{comb}	$\Im(b_z)$
2d	$[\vec{P}_e \cdot \vec{p}_f] * [(\vec{P}_e \times \vec{p}_H) \cdot \vec{P}_f]$	$\otimes$	$-$	$\otimes$	$-$	$\otimes$	A'_{comb}	$\Im(b_z), \Re(\tilde{b}_z)$

Table 1: *Various possible C_i's, their discrete transformation properties,the anomalous couplings on which they provide information along with observables $\mathcal{O}_i$. Symbol $\otimes$ indicates that the corresponding C_i's do not have any definite transformation property under CP or $\tilde{T}$. Here, $\vec{P}_e \equiv \vec{p}_{e^-} - \vec{p}_{e^+}$ and $\vec{P}_f \equiv \vec{p}_f - \vec{p}_{\bar{f}}$ with $\vec{p}_{e^-}$ ($\vec{p}_{e^+}$) is momentum of initial state electron (positron) and analogously $\vec{p}_f$ ($\vec{p}_{\bar{f}}$) is the momentum of final state fermions (anti-fermions).*

3.1 Use of Polarised Initial Beams

The preferentially axial coupling of the Z boson with the charged leptons indicate that initial beam polarisation may affect our observables strongly. A similar statement also holds for the W-contribution to $\nu_e \bar{\nu}_e H$ production. In our study, we take e^-/e^+ beam polarisations to be 80% and 60% respectively and denote $\mathcal{P} \equiv (-, +)$ for $\mathcal{P}_{e^-} = -0.8$ and $\mathcal{P}_{e^+} = 0.6$. The forward-backward (FB) asymmetry in the production of the Higgs boson with respect to (w.r.t.) the e^- direction ($\mathcal{O}_{2a}$) is odd under CP, even under $\tilde{T}$ and hence can be used to probe $\Im(\tilde{b}_Z)$. The up-down (UD) asymmetry ($\mathcal{O}_{2b}$) of the fermion w.r.t the H production plane, is odd under both CP and $\tilde{T}$ and hence can constrain $\Re(\tilde{b}_Z)$. In Table 2 we list the limits of sensitivity on $\Im(\tilde{b}_Z)$ and $\Re(\tilde{b}_Z)$ possible with polarised beams for $E_{cm} = 500$ GeV. We compare these limits with those obtained using unpolarised beams [2]. It is clear from Table 2 that use of longitudinally polarised beams improves the limit of $\Re(\tilde{b}_Z)$ and $\Im(\tilde{b}_Z)$ by a factor of upto 5 or 6. This improvement can be traced to the circumvention of the

vanishingly small vector coupling of electron to the Z boson. Our results agree with those of Ref. [3] if we remove the kinematical cuts as well as the use of finite b-tagging efficiency implemented in our analysis.

Polarised Beams		Unpolarised Beams	
Limits	Observables used	Limits	Observables used
$|\Re(\tilde{b}_z)| \le 0.070$	$\mathcal{O}_{2b}^{\mathcal{P}}$, R1-cut; $\mu^-\mu^+H$ final state	$|\Re(\tilde{b}_z)| \le 0.41$	A_{UD}, R1-cut; $\mu^-\mu^+H$ final state
$|\Im(\tilde{b}_z)| \le 0.0079$	$\mathcal{O}_{2a}^{\mathcal{P}}$, R1-cut; $\mu^-\mu^+H$, $q\bar{q}H$ final states	$|\Im(\tilde{b}_z)| \le 0.042$	A_{FB}, R1-cut; $\mu^-\mu^+H$, $q\bar{q}H$ final states

Table 2: *Limits on anomalous ZZH couplings from various observables at 3σ level with polarised and unpolarised beams, for values of different parameters as listed in the text.*

3.2 Use of Final state τ Polarization

Since τ polarisation can be measured [4, 5, 6] using the decay π energy distribution, one can also construct observables using the final state τ polarisation to probe ZZH couplings. To demonstrate this, we construct, various asymmetries for a sample of (as an example) left handed τ in the final state. Using the combination C_{2c} of Table 1 we construct a mixed polar-azimuthal asymmetry, given by $A_{\text{comb}} = (\sigma_{FU} - \sigma_{FD} - \sigma_{BU} + \sigma_{BD})/\sigma$.

Here σ is total cross section and σ_{FU} is the partial rate with H in the forward(F) hemi-sphere w.r.t. initial state e^- along with the τ^- above(U) the H production plane etc. It probes $\Im(b_Z)$. Similarly we use another combined asymmetry corresponding to combination C_{2d}, defined as $A'_{\text{comb}} = (\sigma_{F'U} - \sigma_{F'D} - \sigma_{B'U} + \sigma_{B'D})/\sigma$, where F' (B') corresponds to the production of τ^- in forward (backward) hemi-sphere w.r.t. initial state electron. U, D have the same meaning as above. One may use this asymmetry to constrain both $\Im(b_Z)$ and $\Re(\tilde{b}_z)$ simultaneously. The up-down (UD) azimuthal asymmetry for the τ^- can probe $\Re(\tilde{b}_z)$.

The important issue of efficiency of obtaining a sample enriched with τ's with a particular (say negative) helicity, which we use in the analysis, is beyond the scope of discussion here. Table 3 lists the limits of sensitivity to different anomalous couplings, assuming the net effect of having to isolate a negative helicity τ, to be just a scaling of asymmetries by 40% and 25% respectively. We also compare
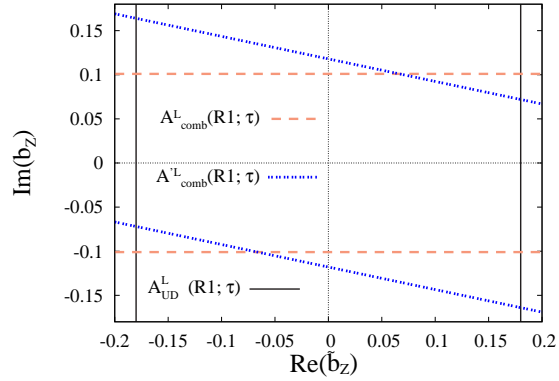
Figure 1: *Region in $\Re(\tilde{b}_Z) - \Im(b_Z)$ plane corresponding to the 3σ variation of asymmetries with an integrated luminosity of 500 fb^{-1}, corresponding to 40% scaling of the asymmetries as mentioned in the text. The horizontal lines are for 3σ variation in A_{comb}^L, whereas the vertical lines are for the variation in A_{UD}^L. The slant lines are corresponding to variation in A'^L_{comb}.*

Using Polarisation of final state τ				Unpolarised Beams	
Coupling		Limits	Observables used	Limits	Observables used
		40% eff. | 25% eff.			
$|\Im(b_z)|$	$\leq$	0.10 | 0.13	A^L_{1comb}	0.23	A_{1comb}
$|\Re(\tilde{b}_z)|$	$\leq$	0.18 | 0.23	A^L_{1UD}	0.41	A_{1UD}

Table 3: *Limits on anomalous ZZH couplings from various observables at 3σ level with/without using the information of final state τ polarisation.*

these with the limits possible without the use of τ polarisation information. The superscripts $L, 1$ in various asymmetries refer to the helicity of the τ, use of $R1$ cut etc. Table 3 shows that the use of the τ polarisation can improve the sensitivity to $\Im(b_z)$. Ref. [7] had also pointed out similar improvements on using the τ polarisation in the context of optimal observable analysis. Figure 1 shows the region in $\Re(\tilde{b}_Z) - \Im(b_Z)$ plane that can be probed using the above mentioned asymmetries for τ's in negative helicity state, scaling them by 40% as mentioned earlier.

4 WWH couplings

We study the process $e^+e^- \rightarrow \nu\bar{\nu}H$ with longitudinally polarised beams to constrain the anomalous WWH couplings. In this case, one can not use the momenta of ν's to construct any $\tilde{T}$-odd observables. We use polarised cross sections and FB-asymmetry w.r.t. polar angle of the Higgs boson to probe the anomalous parts of WWH vertex. Keeping only one anomalous coupling to be nonzero at a time, we obtain individual limits of sensitivity on these couplings. The values for the same for $\tilde{T}$-odd WWH couplings without/with beam polarisation are listed in Table 4. The simultaneous limits of sensitivity, obtained by letting all the anomalous couplings to be nonzero, for $\Im(b_W)$ and $\Re(\tilde{b}_W)$ with polarised and unpolarised beams are listed in Table 5. It may be noted from the limits given in Table 4 and 5 that although use of beam polarisation improves the sensitivity to $\Im(b_W)$ and $\Re(\tilde{b}_W)$ by upto a factor 2, there is little reduction in the contamination coming from the anomalous ZZH couplings.

Coupling		3σ limit with Polarized Beams	Observable used	3σ limit with Unpolarised Beams	Observable used
$|\Im(b_W)|$	$\leq$	0.31	$\sigma^{\mathcal{P}}_1$	0.62	σ_1
$|\Re(\tilde{b}_W)|$	$\leq$	0.76	$A^{\mathcal{P}}_{1FB}$	1.6	A_{1FB}

Table 4: *Individual limits on anomalous $\tilde{T}$-odd WWH couplings with polarised and unpolarised beams at 3σ level at an integrated luminosity of 500 fb^{-1}.*

Coupling		3σ limit with Polarized Beams	3σ limit with Unpolarised Beams
$|\Im(\tilde{b}_W)|$	$\leq$	0.71	1.6
$|\Re(\tilde{b}_W)|$	$\leq$	1.7	3.2

Table 5: *Simultaneous limits on anomalous $\tilde{T}$-odd WWH couplings with polarised and unpolarised beams at 3σ level at an integrated luminosity of 500 fb^{-1}.*

5   Sensitivity studies at higher c.m. energies.

The s and t channel behave differently with increasing energy. It is therefore interesting to study the energy dependence of the sensitivity of our observables to the anomalous couplings. We have also investigated the reach in sensitivity of CLIC to VVH couplings at five different c.m. energies, namely at 0.5, 0.8, 1, 1.5 and 3 TeV. We found that going to higher energy can improve the sensitivity and best possible sensitivity, for example, for $\Re(\tilde{b}_Z)$ is obtained at $\sqrt{s} = 1$ TeV, with R2-cut. This improvement is upto a factor of 2 as compared to the analysis made earlier for an ILC operating at 500 GeV c.m. energy [2]. At higher energies, however, both the initial state radiation (ISR) effect as well as the effect of beamstrahlung which causes energy loss of the incoming electron (or positron) due to its interaction with the electromagnetic field of the opposite bunch, have to be further taken into account. Corrections coming from both are sizable and change the rates. For example, at 500 GeV, the ISR effects change the SM contributions by $\lesssim 15\%$ whereas the contribution coming from (say) $\Re(b_Z)$ changes by about 9%; with Beamstrahlung at (say) 1 TeV these effects are $\sim 10\%$ and 20% respectively. However, the effect on the limits for sensitivity that may be obtained is less drastic as these affect both the SM as well as anomalous contribution similarly. At 1 TeV, for example, the above mentioned limit changes by 15%.

6   Summary

Thus we show that use of polarised initial beams can yield higher sensitivity to $\Re(\tilde{b}_Z)$, $\Im(\tilde{b}_Z)$ and to both the $\tilde{T}$-odd WWH couplings. The limit on $\Im(b_Z)$ can be improved by a factor of 2 to 3 using τ poalrisation as well, even with pessimistic assumptions on the efficiency of the polarisation measurement. We also study effect of increasing energy on the sensitivity. For example, at $\sqrt{s} = 1$TeV one obtains an improvement by a factor 2, which further changes by about 15% due to ISR and Beamstrahlung effects.

References

[1] Slides:
    http://ilcagenda.linearcollider.org/contributionDisplay.py?contribId=277&sessionId=71&confId=1296

[2] S. S. Biswal, R. M. Godbole, R. K. Singh and D. Choudhury, Phys. Rev. D **73**, 035001 (2006) [Erratum-ibid. D **74**, 039904 (2006)] [arXiv:hep-ph/0509070].

[3] T. Han and J. Jiang, Phys. Rev. D **63**, 096007 (2001) [arXiv:hep-ph/0011271].

[4] B. K. Bullock, K. Hagiwara and A. D. Martin, Nucl. Phys. B **395** (1993) 499.

[5] K. Hagiwara, A. D. Martin and D. Zeppenfeld, Phys. Lett. B **235**, 198 (1990).

[6] R. M. Godbole, M. Guchait and D. P. Roy, Phys. Lett. B **618**, 193 (2005) [arXiv:hep-ph/0411306].

[7] K. Hagiwara, S. Ishihara, J. Kamoshita and B. A. Kniehl, Eur. Phys. J. C **14**, 457 (2000) [arXiv:hep-ph/0002043].

Profile of Two-Higgs-Doublet-Model Parameter Space

Abdul Wahab El Kaffas[1], Odd Magne Ogreid[2] and Per Osland[1]

1- Department of Physics and Technology, University of Bergen
Postboks 7803, N-5020 Bergen, Norway

2- Bergen University College, Bergen, Norway

We review recent work on constraining the parameter space of the Two-Higgs-Doublet Model by theoretical and experimental results. Some characteristics of the model, in particular the distribution of masses in the surviving parameter space, are discussed.

1 Introduction

We report on recent work on constraining the multi-dimensional parameter space of the Two-Higgs-Doublet Model by theoretical and experimental results [1, 2].

As compared with the Standard Model (SM), the Two-Higgs-Doublet Model (2HDM) allows for an additional mechanism for CP violation [3]. This is one of the main reasons for continued strong interest in the model [4].

Several experimental constraints restrict its parameter space. The $B \to X_s \gamma$ rate excludes low values of the charged-Higgs mass, $M_{H^\pm}$ [5], whereas $B - \bar{B}$ oscillations and the branching ratio R_b for $Z \to b\bar{b}$ exclude low values of $\tan\beta$. The precise measurements at LEP of the ρ parameter constrain the mass splitting in the Higgs sector, and force the masses to be not far from the Z mass scale [6].

From the theoretical point of view, there are also consistency conditions. The potential has to be positive for large values of the fields [7, 8]. Furthermore, we require the tree-level Higgs–Higgs scattering amplitudes to be unitary [9]. Together, these constraints dramatically reduce the allowed parameter space of the model. In particular, the unitarity constrain excludes large values of $\tan\beta$, *unless* μ is reasonably large. This limit is basically the decoupling limit [10].

Our recent study [2], restricted to the so-called "Type II" version, where up-type and down-type quarks couple to different Higgs doublets, uses rather complete and up-to-date experimental results, as well as accurate theoretical predictions for the above quantities. We consider a model with the Z_2 symmetry respected by the quartic couplings, i.e., no λ_6 and λ_7 couplings. Otherwise, we allow for full generality. In particular, we allow for CP violation, taking λ_5 complex. (For a definition of the potential, see [2].) The neutral Higgs boson sector will thus contain three bosons, described by a 3×3 mixing matrix R. These three neutral Higgs bosons will in general all have CP-violating Yukawa couplings. A related study, focused more on large values of $\tan\beta$, was also presented at this Workshop [11].

2 Results

We parametrize the model in terms of the masses of the two lightest neutral Higgs bosons, together with the charged Higgs boson mass, $\tan\beta$, the soft parameter μ^2, and the rotation matrix R of the neutral sector. The third (heaviest) neutral mass is then calculable, as well as the quartic couplings, λ_i (see [12, 13]).

We establish allowed regions in the $\tan\beta$–$M_{H^\pm}$ plane by the following procedure: For each point in this plane, we scan over the parameters $\boldsymbol{\alpha} = \{\alpha_1, \alpha_2, \alpha_3\}$, defining the mixing matrix R in the neutral-Higgs sector, imposing the absolute theory constraints of positivity and unitarity. At each point, we evaluate a χ^2 penalty corresponding to the experimental constraints, adopting the "best" point (lowest χ^2) in $\boldsymbol{\alpha}$.

For two values of μ (200 and 500 GeV), we show in Fig. 1 the allowed regions in the $\tan\beta$–$M_{H^\pm}$ plane, taking into account the theoretical constraints mentioned above, the LEP2 non-discovery, the very precise $\Delta\rho$ measurements at LEP, as well as the B-physics constraints ($B \rightarrow X_s\gamma$, mainly), and R_b. The masses of the two lightest neutral Higgs bosons are here kept fixed, at $M_1 = 100$ GeV and $M_2 = 300$ GeV or 500 GeV.

Figure 1: Allowed regions in the $\tan\beta$–$M_{H^\pm}$ plane, taking into account theoretical and experimental constraints.

The over-all surviving regions of parameter space depend significantly on the "soft" parameter μ^2. At low or negative values, the unitarity constraint will cut off the allowed region already at moderate values of $\tan\beta$. We have therefore shown results for a couple of positive values of μ^2, the higher one approaching the so-called decoupling limit.

3 Distribution of Higgs masses

It turns out that, if μ is comparable with M_2, or smaller, the distribution of M_3-values will be very narrow, especially at large values of $\tan\beta$. This is illustrated in Fig. 2, for $M_1 = 100$ GeV, and two sets of (M_2, μ) values: $(300, 200)$ GeV and $(500, 500)$ GeV. Also, we note that for $M_2 = 500$ GeV and $\mu = 500$ GeV (lower panels), low values of $M_{H^\pm}$ are excluded. This is basically because of the $\Delta\rho$ constraint.

Figure 2: Distribution of M_3-values for fixed $M_1 = 100$ GeV. Top: $M_2 = 300$ GeV and $\mu = 200$ GeV; bottom: $M_2 = 500$ GeV and $\mu = 500$ GeV. Three slices of $\tan\beta$-values are shown.

On the other hand, if μ is larger than M_2, the distribution can be considerably wider, as is seen in Fig. 3.

4 Summary

We have shown that the constraints of positivity and tree-level unitarity of Higgs–Higgs scattering, B-physics results, together with the precise LEP measurements, in particular of the ρ-parameter at LEP, exclude large regions of the 2HDM (II) parameter space. High values of $\tan\beta$ are excluded unless μ is large, allowing M_2 and M_3 both to be heavy. Furthermore, M_2 and M_3 should be reasonably close to each other. Improved precision of the $\bar{B} \to X_s\gamma$ measurement could significantly reduce the remaining part of the parameter space, but it appears unlikely that the model could be excluded other than by a negative search at the LHC.
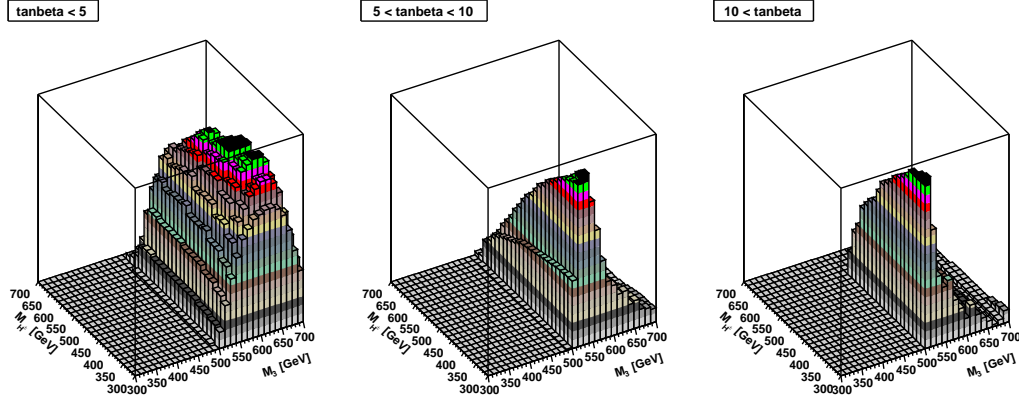
Figure 3: Distribution of M_3-values for $M_1 = 100$ GeV, $M_2 = 300$ GeV and $\mu = 500$ GeV. Three slices of $\tan\beta$-values are shown, increasing to the right.

Acknowledgments

References

[1] Slides:
http://ilcagenda.linearcollider.org/contributionDisplay.py?contribId=151&sessionId=71&confId=1296

[2] A. W. El Kaffas, P. Osland and O. Magne Ogreid, Phys. Rev. D, in print, arXiv:0706.2997 [hep-ph].

[3] T. D. Lee, Phys. Rev. D **8**, 1226 (1973); S. Weinberg, Phys. Rev. Lett. **37**, 657 (1976).

[4] E. Accomando *et al.*, "Workshop on CP studies and non-standard Higgs physics," arXiv:hep-ph/0608079.

[5] M. Misiak *et al.*, Phys. Rev. Lett. **98**, 022002 (2007) [arXiv:hep-ph/0609232].

[6] S. Bertolini, Nucl. Phys. B **272**, 77 (1986).

[7] N. G. Deshpande and E. Ma, Phys. Rev. D **18**, 2574 (1978); S. Nie and M. Sher, Phys. Lett. B **449**, 89 (1999) [arXiv:hep-ph/9811234]; S. Kanemura, T. Kasai and Y. Okada, Phys. Lett. B **471**, 182 (1999) [arXiv:hep-ph/9903289].

[8] A. W. El Kaffas, W. Khater, O. M. Ogreid and P. Osland, Nucl. Phys. B, **775**, 45 (2007) [arXiv:hep-ph/0605142].

[9] S. Kanemura, T. Kubota and E. Takasugi, Phys. Lett. B **313**, 155 (1993) [arXiv:hep-ph/9303263]; A. G. Akeroyd, A. Arhrib and E. M. Naimi, Phys. Lett. B **490**, 119 (2000) [arXiv:hep-ph/0006035]; A. Arhrib, arXiv:hep-ph/0012353; I. F. Ginzburg and I. P. Ivanov, arXiv:hep-ph/0312374; Phys. Rev. D **72**, 115010 (2005) [arXiv:hep-ph/0508020].

[10] J. F. Gunion and H. E. Haber, Phys. Rev. D **67**, 075019 (2003) [arXiv:hep-ph/0207010].

[11] M. Krawczyk, in:
http://ilcagenda.linearcollider.org/contributionDisplay.py?contribId=454&sessionId=71&confId=1296

[12] W. Khater and P. Osland, Nucl. Phys. B **661**, 209 (2003) [arXiv:hep-ph/0302004].

[13] A. W. E. Kaffas, O. M. Ogreid and P. Osland, Nonlinear Phenomena in Complex Systems, to appear [arXiv:hep-ph/0702097].

The charged Higgs boson mass in the 2HDM: decoupling and CP violation

Maria Krawczyk[1,2] * and Dorota Sokołowska[1]

1- Institute of Theoretical Physics, University of Warsaw
00-681 Warsaw, ul. Hoża 69, Poland

2- TH-Division, CERN, CH-1211 Genéve 23, Switzerland

Mass range of the charged Higgs boson in the 2HDM with explicit and spontaneous CP violation is discussed. Constraints on $M_{H^\pm}$ in the CP conserving 2HDM(II) are shown.

1 The 2HDM potential and spontaneous symmetries breaking

The most general, invariant under gauge group $SU(2)_L \times U(1)_Y$ and renormalizable potential of the Two Higgs Doublet Model (2HDM) [2, 3, 4] is given by

$$V = \frac{\lambda_1}{2}\left(\Phi_1^\dagger\Phi_1\right)^2 + \frac{\lambda_2}{2}\left(\Phi_2^\dagger\Phi_2\right)^2 + \lambda_3\left(\Phi_1^\dagger\Phi_1\right)\left(\Phi_2^\dagger\Phi_2\right) + \lambda_4\left(\Phi_1^\dagger\Phi_2\right)\left(\Phi_2^\dagger\Phi_1\right)$$
$$+ \left[\frac{1}{2}\lambda_5\left(\Phi_1^\dagger\Phi_2\right)\left(\Phi_1^\dagger\Phi_2\right) + \lambda_6\left(\Phi_1^\dagger\Phi_1\right)\left(\Phi_1^\dagger\Phi_2\right) + \lambda_7\left(\Phi_2^\dagger\Phi_2\right)\left(\Phi_1^\dagger\Phi_2\right) + h.c.\right] \quad (1)$$
$$- \frac{1}{2}m_{11}^2\left(\Phi_1^\dagger\Phi_1\right) - \frac{1}{2}m_{22}^2\left(\Phi_2^\dagger\Phi_2\right) - \left[\frac{1}{2}m_{12}^2\left(\Phi_1^\dagger\Phi_2\right) + h.c.\right],$$

where $\lambda_{1-4}, m_{11}^2, m_{22}^2 \in \mathbb{R}$ (by the hermicity of the potential), while in general $\lambda_{5-7}, m_{12}^2 \in \mathbb{C}$. In the most general CP breaking form it has 14 parameters, however only 11 are independent, see e.g. [5, 6]. In the model there are five Higgs particles: three neutral h_1, h_2, h_3 (for CP conservation - two CP-even h, H and one CP-odd A) and two charged Higgs bosons $H^\pm$.

1.1 Z_2 and CP symmetries

The Z_2 symmetry of the potential (1) is defined as the invariance of V under the following transformation of doublets: $\Phi_1 \to -\Phi_1, \Phi_2 \to \Phi_2$ or $\Phi_1 \to \Phi_1, \Phi_2 \to -\Phi_2$. If Z_2 (in either form) is a symmetry of the potential, then $m_{12}^2 = \lambda_6 = \lambda_7 = 0$. The Z_2 symmetry is *softly* broken by the terms proportional to m_{12}^2.

General 2HDM allows for CP violation both explicitly and spontaneously [7, 8, 2]. The CP violation can be naturally suppressed by imposing a Z_2 symmetry on the Higgs potential.

1.2 Reparametrization transformation

A global unitary transformation which mix two doublets and change their relative phase does not change the physical content of 2HDM as discussed recently in [9], see also [3, 4, 2]. It is given by

$$\left(\begin{array}{c} \Phi_1' \\ \Phi_2' \end{array}\right) = \mathcal{F}\left(\begin{array}{c} \Phi_1 \\ \Phi_2 \end{array}\right), \qquad \mathcal{F} = e^{-i\rho_0}\left(\begin{array}{cc} \cos\theta e^{i\rho/2} & \sin\theta e^{i(\tau-\rho/2)} \\ -\sin\theta e^{-i(\tau-\rho/2)} & \cos\theta e^{-i\rho/2} \end{array}\right). \quad (2)$$

There are three *reparametrization* parameters - ρ, θ, τ, and in addition ρ_0 parameter as an overall phase. If $\theta = 0$ there is no mixing of two dublets and the transformation becomes a global transformation of doublets with an independent phase rotations (*rephasing*):

$$k = 1, 2 : \Phi_k \rightarrow e^{-i\rho_i} \Phi_k, \quad \rho_1 = \rho_0 - \frac{\rho}{2}, \quad \rho_2 = \rho_0 + \frac{\rho}{2}, \quad \rho = \rho_2 - \rho_1. \tag{3}$$

The original form of the potential is recovered by the appropriate changes of phases of the following coefficients:

1.3 Explicit and spontaneous CP violation in 2HDM

CP violation may occur in 2HDM only if Z_2 symmetry is broken [8, 2, 3, 4, 9]. A necessary condition for an *explicit CP violation* in the Higgs potential V is an existence of complex parameters. However, if there exists a reparametrization leading to V with only real parameters (*real basis*), then there is no explicit CP violation in V. A spontaneous CP breaking, by the vacuum state, is still possible [7, 8, 2].

In the simply analysis [14], which results we present here, only the potential with exact and softly broken Z_2 symmetry was considered, i.e. $\lambda_{6,7} = 0$. In studying 2HDM with an *explicit* CP conservation or violation the *real vacuum representation* [4] was applied. A spontaneous CP violation was discussed assuming the *explicitly CP conserving V*.

1.4 Vacuum expectation values

The most general vacuum (extremum) state can be described by [8, 11, 12, 13, 14]

$$\langle \Phi_1 \rangle = \frac{1}{\sqrt{2}} \begin{pmatrix} 0 \\ v_1 \end{pmatrix}, \qquad \langle \Phi_2 \rangle = \frac{1}{\sqrt{2}} \begin{pmatrix} u \\ v_2 e^{i\xi} \end{pmatrix}, \tag{4}$$

where $v_1, v_2, \xi, u \in \mathbb{R}$. By gauge transformation one can always make $v_1 > 0$. Below we will assume that $v_2 \neq 0$, with $v^2 = v_1^2 + v_2^2 = (246 \text{ GeV})^2$, and $0 \leq \xi < 2\pi$.

For vacuum with $u \neq 0$ the electric charge is not conserved and the photon becomes a massive particle ("charged vacuum"). If $u = 0$ then a "neutral vacuum" are possible. Depending on the value of ξ there may or may not be a spontaneous CP violation [8, 3, 12, 13]. The useful quantity is $\nu = \frac{m_{12}^2}{2v_1 v_2}$ (or $\nu = \frac{\Re m_{12}^2}{2v_1 v_2}$) [4], which here is taken to be positive.

1.5 Extremum conditions

For the extremum states (4) the first derivatives of the considered potential lead to the following set of extremum conditions:

$$0 = u \left[v_1 v_2 \cos \xi \left(\lambda_4 + \lambda_5 \right) - m_{12}^2 \right], \ 0 = u \left[\lambda_2 \left(u^2 + v_2^2 \right) + \lambda_3 v_1^2 - m_{22}^2 \right] \tag{5}$$

$$0 = v_2 \sin \xi \left[2\lambda_5 v_1 v_2 \cos \xi - m_{12}^2 \right], \ 0 = v_2 \sin \xi \left[v_1^2 \left(\lambda_3 + \lambda_4 - \lambda_5 \right) + \lambda_2 \left(u^2 + v_2^2 \right) - m_{22}^2 \right] \tag{6}$$

$$0 = v_1 \left[v_2^2 \left(\lambda_5 \cos^2 2\xi + \lambda_4 \right) + \lambda_1 v_1^2 + \lambda_3 \left(u^2 + v_2^2 \right) - m_{11}^2 \right] - m_{12}^2 v_2 \cos \xi \tag{7}$$

$$0 = u v_1 v_2 \sin \xi \left(\lambda_4 - \lambda_5 \right), \ 0 = v_2 \cos \xi \left[v_1^2 \left(\lambda_3 + \lambda_4 + \lambda_5 \right) + \lambda_2 \left(u^2 + v_2^2 \right) - m_{22}^2 \right] - m_{12}^2 v_1 \tag{8}$$

If $u = 0$ then above conditions are satisfied for an exact Z_2 symmetry ($m_{12}^2 = 0$) when the only possible neutral vacuum state is the one which respects CP, i.e. with $\sin \xi = 0$, and for a broken Z_2 symmetry. In the latter case two neutral vacuum states are possible - without

and with CP violation, for $\sin\xi = 0$ and $\sin\xi \neq 0$, respectively. To get a real minimum of the potential the eigenvalues of the squared mass matrix have to be positive. We will assume in addition that positivity constraints hold guaranteeing stability of the vacuum [10].

1.6 Physical regions for CP conserving 2HDM

Expressions for masses of $H^\pm$ and A for 2HDM with an explicit or a spontaneous CP *conservation* are as follows.

Z_2 symmetry broken If Z_2 symmetry is softly broken ($\nu \neq 0$), then the masses squared of $H^\pm$ and A are given by:

$$M_{H^\pm}^2 = v^2 \left(\nu - \frac{1}{2} (\lambda_4 + \lambda_5) \right), \quad M_A^2 = v^2 (\nu - \lambda_5). \tag{9}$$

In order to have positive $M_{H^\pm}^2$ and M_A^2 inequalities $\lambda_5 + \lambda_4 < 2\nu$ and $\lambda_5 < \nu$ should hold.

Large masses for $H^\pm$ and A (9) can arise from large ν. In the limit $\nu \to \infty$ the decoupling is realized - h is like the Higgs boson in the Standard Model, while $H^\pm, A, H$ are heavy and almost degenerate [3, 4].

Exact Z_2 symmetry The results for an exact Z_2 symmetry can be obtained from above expressions in the limit $\nu \to 0$. Then $\lambda_5 < 0$. Masses cannot be too large, as here they can arise only due to $\lambda's$. However, large $\lambda's$ may violate tree-level unitarity constraints [15].

1.7 Physical regions for CP violating 2HDM

As it was mentioned above if the 2HDM potential breaks Z_2 symmetry then CP violation may be realized in the model. Note, that if CP is violated physical neutral Higgs states are h_1, h_2, h_3, without definite CP properties, while h, H, A are useful but only auxiliary states.

Explicit CP violation If there is explicit CP violation all formulae derived for the CP conservation case (9 and beyond) hold after the replacements: $\lambda_5 \to \Re\lambda_5$ and $m_{12}^2 \to \Re m_{12}^2$. Note, that the decoupling can be realized here as well, with large $M_{H^\pm}^2$ arising from large ν.

Spontaneous CP violation Spontaneous CP violation may appear if there is a CP breaking phase of the VEV, so $\sin\xi \neq 0$. From the extremum condition one gets that:

$$\cos\xi = \frac{m_{12}^2}{\lambda_5 2v_1 v_2} = \frac{\nu}{\lambda_5}, \tag{10}$$

from which it follows that $|\nu/\lambda_5| < 1$. The squared masses for $H^\pm$ and A are given by the following expressions, see also [13]:

$$M_{H^\pm}^2 = \frac{v^2}{2} (\lambda_5 - \lambda_4), \quad M_A^2 = \frac{v^2}{\lambda_5} (\lambda_5^2 - \nu^2) = v^2 \lambda_5 \sin^2\xi. \tag{11}$$

We see that they are quite different from the formulae for $M_{H^\pm}^2$ and M_A^2 discussed above. (Note, that although A is no longer a physical state, positivity of M_A^2 still provides a good constraint since it gives at the same time a condition for positivity of squared masses of physical particles.) From the last expression for M_A^2 (11) it is easy to see that λ_5 have to be positive. Furthermore, squared masses (11) are positive if $\lambda_5 > \lambda_4$ and $\lambda_5 > \nu > 0$.

It is worth mentioning that the squared mass of $H^\pm$ does not depend on ν at all. Therefore, $M_{H^\pm}$ cannot be too large in 2HDM with CP violated spontaneously, for the same reason as in the discussed above case of exact Z_2 symmetry.

1.8 Conclusion on possible vacuum states in 2HDM

Regions where various vacuum states (conserving or spontaneously violating CP) can be realized in 2HDM are mutually exclusive [10, 12, 13, 14]. The mass of charged Higgs boson may serve as a guide over various regimes of the 2HDM. Existence of heavy charged Higgs boson, with mass above 600-700 GeV [4, 14], would be a signal that in 2HDM Z_2 symmetry is violated, and CP can be violated only explicitly.

2 Experimental constraints on the 2HDM(II) with CP conservation

Here we consider the CP conserving 2HDM, assuming that Z_2 symmetry is extended also on the Yukawa interaction, which allows to suppress the FCNC [16]. We limit ourself to constraints on the Model II of the Yukawa interaction, as in MSSM, see e.g. [17]. There are 7 parameters for the potential with softly breaking Z_2 symmetry: masses $M_h, M_H, M_A, M_{H^\pm}$, mixing angles α and $\tan\beta = v_2/v_1$, and parameter ν.

Couplings (relative to the corresponding couplings of the SM Higgs) are as follows:

	$\boxed{h}$	$\boxed{A}$
to W/Z:	$\chi_V = \sin(\beta - \alpha)$	0
to down quarks/charged leptons:	$\chi_d = \chi_V - \sqrt{1 - \chi_V^2}\tan\beta$	$-i\gamma_5\tan\beta$
to up quarks:	$\chi_u = \chi_V + \sqrt{1 - \chi_V^2}/\tan\beta$	$-i\gamma_5/\tan\beta$

H couples like h with following replacements: $\sin(\beta - \alpha) \to \cos(\beta - \alpha)$ and $\tan\beta \to -\tan\beta$. For large $\tan\beta$ there are enhanced couplings to $d-$type fermions. Note, that coupling $\chi_{VH^+}^h = \cos(\beta - \alpha)$ is complementary to the χ_V^h.

Important constraints on mass of charged Higgs boson in 2HDM (II) are coming from the $b \to s\gamma$ and $B \to \tau\nu$ decays. The rate for the first process calculated at the NNLO accuracy in the SM [18], after a comparison with the precise data from BaBar and Belle, leads to the constraint: $M_{H^\pm} > 295$ GeV at 95 % CL for $\tan\beta > 2$. This limit together with the constraints from the tree-level analysis of $B \to \tau\nu$ [19] is presented in Fig.1 (Left).

The 2HDM analysis has been performed at the one-loop level for the leptonic tau decays [20]. The constraints are shown in Fig.1 (Right). Not only lower, but also in the non-decoupling scenario upper limits can be derived here. In contrast to the mentioned results from b decays here the (one-loop) constraints depend on masses of neutral Higgs bosons.

3 Acknowledgment

References

[1] Slides:
http://ilcagenda.linearcollider.org/contributionDisplay.py?contribId=454&sessionId=718&confId=1296

[2] G. C. Branco, L. Lavoura and J. P. Silva, 'CP violation," *Oxford, UK: Clarendon (1999) 511 p*

[3] J. F. Gunion and H. E. Haber, Phys. Rev. D **67** (2003) 075019, Phys. Rev. D **72** (2005) 095002.

[4] I. F. Ginzburg and M. Krawczyk, Phys. Rev. D **72**, 115013 (2005).

[5] L. Lavoura, Phys. Rev. D **50** (1994) 7089.

[6] E. Accomando *et al.*, arXiv:hep-ph/0608079.

[7] T. D. Lee, Phys. Rev. D **8** (1973) 1226.
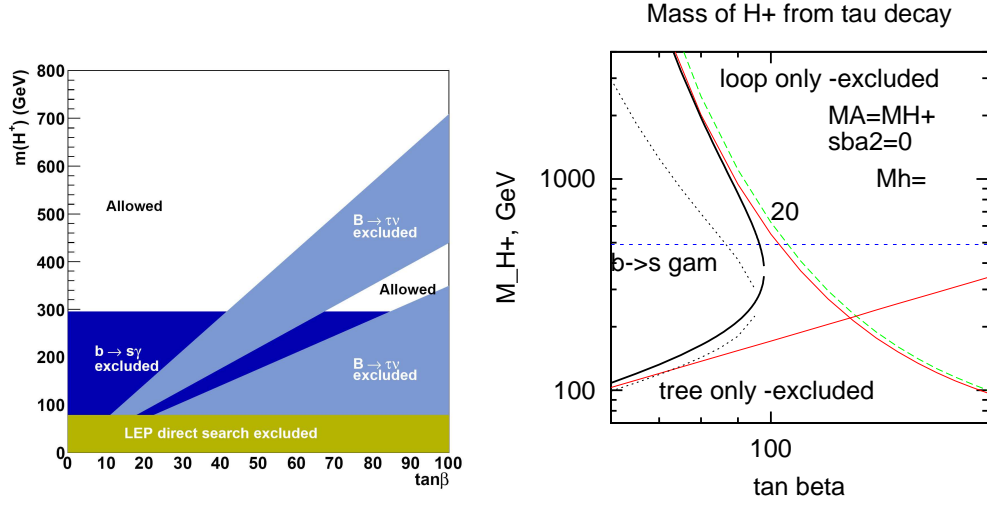
Figure 1: Left: Constraints from $B \to \tau\nu_\tau$ and $b \to s\gamma$ data on the charged Higgs boson mass as a function of $\tan\beta$ in 2HDM (II) [19]; Right: Limits from the leptonic τ decay for $M_h = 20$ GeV and $\chi_V^h = 0$ in 2HDM(II): tree-level exclusion of a region below the straight line $M_{H^\pm} \geq 1.71 \tan\beta$ GeV and one-loop exclusion of the region above the curve $\Delta \sim \tan\beta^2 [\ln \frac{M_h}{M_{H+}} + 1]$. The excluded region lies on the right on the curves: bold for $M_A = M_{H^\pm}$, dotted for $M_A = 100$ GeV. Exclusion from $\tau \to e\nu_\tau\bar{\nu}_e$ is represented by dashed line [20].

[8] G. C. Branco, Phys. Rev. Lett. **44** (1980) 504. G. C. Branco, Phys. Rev. D **22** (1980) 2901.

[9] I. P. Ivanov, Phys. Lett. B **632** (2006) 360, Phys. Rev. D **75**, 035001 (2007) [Erratum-ibid. D **76**, 039902 (2007)], arXiv:0710.3490 [hep-ph];
M. Maniatis, A. von Manteuffel and O. Nachtmann, arXiv:0707.3344 [hep-ph];
C. C. Nishi, Phys. Rev. D **76**, 055013 (2007), Phys. Rev. D **74**, 036003 (2006).

[10] N. G. Deshpande and E. Ma, Phys. Rev. D **18**, 2574 (1978).

[11] J. L. Diaz-Cruz and A. Mendez, Nucl. Phys. B **380**, 39 (1992).

[12] A. Barroso, P. M. Ferreira and R. Santos, Phys. Lett. B **652**, 181 (2007);
A. Barroso, P. M. Ferreira, R. Santos and J. P. Silva, Phys. Rev. D **74**, 085016 (2006);
A. Barroso, P. M. Ferreira and R. Santos, Phys. Lett. B **632**, 684 (2006), Phys. Lett. B **603**, 219 (2004) [Erratum-ibid. B **629**, 114 (2005)];
J. Velhinho, R. Santos and A. Barroso, Phys. Lett. B **322**, 213 (1994).

[13] I. F. Ginzburg and K. A. Kanishev, arXiv:0704.3664 [hep-ph].

[14] M. Krawczyk and D. Sokołowska - in preparation;
D. Sokołowska, Master Diploma, Dept. of Physics, U. of Warsaw, July 2007

[15] I. F. Ginzburg and I. P. Ivanov, Phys. Rev. D **72**, 115010 (2005);
A. G. Akeroyd, A. Arhrib and E. M. Naimi, Phys. Lett. B **490**, 119 (2000)

[16] S. L. Glashow and S. Weinberg, Phys. Rev. D **15** (1977) 1958;
E. A. Paschos, Phys. Rev. D **15** (1977) 1966.

[17] M. Krawczyk, Acta Phys. Polon. B **33**, 2621 (2002).

[18] M. Misiak *et al.*, Phys. Rev. Lett. **98**, 022002 (2007).

[19] D. s. Du, arXiv:0709.1315 [hep-ph], M. Nakao, talk given at LP2007, Korea.

[20] M. Krawczyk and D. Temes, Eur. Phys. J. C **44**, 435 (2005).

Searching for the Higgs at CDF

Victoria Martin, *on behalf of the CDF Collaboration*

School of Physics, University of Edinburgh,
Edinburgh, EH9 3JZ, UK.

The CDF experiment at the Fermilab Tevatron has performed direct searches for the Standard Model Higgs boson. There are two main search channels, each sensitive to different Higgs mass ranges. For a light mass Higgs boson ($m_H < 135$ GeV/c^2) we search for a Higgs decaying into two b-jets, produced in association with a vector boson. For heavier Higgs boson masses ($135 < m_H/\text{GeV}c^{-2} < 200$) we search for a Higgs decaying into two W-bosons. No evidence for Higgs production is found. At the most sensitive mass, the excluded cross section is a factor of 3.4 higher than the predicted Standard Model cross section.

1 Introduction

The Higgs boson (H) is the only Standard Model particle for which we have no direct evidence. Direct searches for the Higgs in the process $e^+e^- \to ZH$ at LEP provide a lower limit on the Standard Model Higgs boson mass of $m_H > 114.4$ GeV/c^2 at 95% confidence level (CL) [2]. An upper limit on m_H can be calculated through radiative corrections to various electroweak processes. Using the most recent measurement of the top quark mass from the Tevatron, $m_t = 170.9 \pm 1.1(\text{stat}) \pm 1.5(\text{syst})$ GeV/c^2 [3], and the improved accuracy of the mass W-boson, the upper limit on the Higgs boson mass is $m_H < 182$ GeV/c^2 at 95% CL [4].

2 Higgs production and decay at the Tevatron

This talk outlines searches at the CDF experiment for evidence of direct Higgs boson production.

The Fermilab Tevatron collides protons and antiproton at centre of mass energies of 1.96 TeV. The main mechanisms for producing Higgs bosons are through gluon-gluon fusion

Typical events in 1 fb^{-1} for m_H (GeV/c^2)	$ZH \to \ell^+\ell^- b\bar{b}$ 115	$ZH \to \nu\bar{\nu}b\bar{b}$ 115	$WH \to \ell\nu b\bar{b}$ 115	$H \to WW^{(*)} \to \ell\nu\ell\nu$ 160
Signal produced	5	15	30	20
Signal accepted	1	2	3	4
Backgrounds	100	300	500	300

Table 1: Number of signal and background events for main Higgs search channels. ℓ here refers to an electron or muon.

$gg \to H$ and associated production with a gauge boson: ZH or WH. The cross section for the associated production is roughly a factor of 10 smaller than for the gluon fusion. The cross sections decrease as m_H increases, from around 1 pb at $m_H = 115$ GeV/c^2 to around 0.2 pb at $m_H = 200$ GeV/c^2. For masses less than 135 GeV/c^2 the Higgs decays primarily as $H \to b\bar{b}$. For higher masses the dominant decay mode is into two W-bosons: $H \to WW^{(*)}$.

We therefore employ two different search strategies for the Higgs boson, each sensitive to a different range of m_H. For relatively low Higgs boson masses ($115 < m_H/\text{GeV}c^{-2} < 135$)

Figure 1: Left: From the $WH \to \ell\nu b\bar{b}$ search, the reconstructed di-jet mass for events where only one of the jets is tagged as a b-jet. Right: The output of the Neural Net tuned to find ZH events in the $ZH \to \ell^+\ell^- b\bar{b}$ analysis.

we search for a Higgs decaying into two b-jets produced in associated with a W or Z boson decaying leptonically. (The enormous background from di-jet production makes the search for non-associated production: $gg \to H \to b\bar{b}$ unfeasible.) For a higher Higgs boson masses ($135 < m_H/\mathrm{GeV}c^{-2} < 200$) we search for Higgs decaying into two W-boson, where both of the W-bosons decay into either an electron or muon plus associated neutrino. Table 1 shows the typical number of events expected in each 1 fb^{-1} of data.

3 Low-Mass Higgs Searches

For low mass Higgs searches b-jet tagging and the di-jet mass resolution are crucial for the Higgs search. CDF have made improvements to their b-jet tagging algorithms over the past year. For recent analyses, finding one b-tag improves the signal to background from 1:1000 to 1:100; finding two b-tag improves this to 1:50. The b-jet energy response is calibrated using simulated events. We cross check this calibration using reconstructed $Z \to b\bar{b}$ events.

To search for $WH \to \ell\nu b\bar{b}$, we select events with an isolated, high-p_T electron or muon, two high-E_T jets, with at least one tagged as a b-jet and large missing transverse energy ($\not{E}_T$) due to the unidentified neutrino. We plot the di-jet mass, as shown in Figure 1. The observed distribution of events can be accounted for by the backgrounds, which are dominated by top quark pair and direct W+heavy flavour production. We therefore set a limit on Higgs boson production. The observed limit and the expected limit are given in Table 2 [5].

The signature of $ZH \to \nu\bar{\nu} b\bar{b}$ is two high-E_T jets and large $\not{E}_T$ from the two neutrinos. We veto events containing an isolated charged lepton and we apply optimised kinematic cuts to reduce the huge background from QCD jet production. As before, we calculate the di-jet mass and compare this distribution expected from background events. No evidence for the Higgs is observed and we again set a limit on the Higgs cross section, given in Table 2 [6].
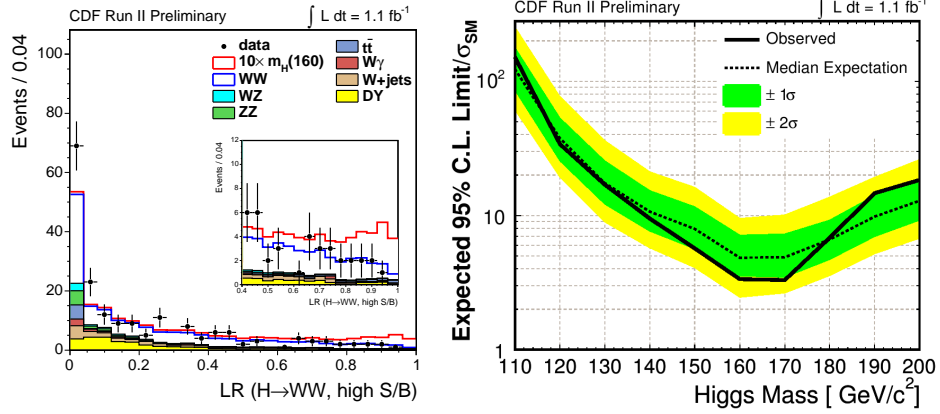
Figure 2: $H \to WW^{(*)}$ search using the likelihood ratio method. Left: The LR variable for the selected events. Right: Limit on the Higgs production cross section as a function of m_H.

The search for $ZH \to \ell^+\ell^- b\bar{b}$ begins by selecting events with two electrons or muons and two jets, of which at least one must be tagged as a b-jet. In the 1 fb^{-1} of data used for this search, these cuts selects around 100 events. One only of these events is expected to be from Higgs production. To improve the signal to background ratio we use a two-dimensional Neural Net (NN). Both NNs are each tuned to separate one background channel (either $t\bar{t}$ or $Zb\bar{b}$) from the signal. An illustation of the output is shown in Figure 1. Making

Low mass searches: $m_H = 115$ GeV/c^2	exp.	obs.
$\sigma(WH \to \ell\nu bb)/\sigma(\mathrm{SM})$	17	26
$\sigma(ZH \to \nu\bar{\nu}b\bar{b})/\sigma(\mathrm{SM})$	15	16
$\sigma(ZH \to \ell^+\ell^- b\bar{b})/\sigma(\mathrm{SM})$	16	16

Higgs mass searches: $m_H = 160$ GeV/c^2	exp.	obs.
$\Delta\phi$ anal: $\sigma(H \to WW \to \ell^+\ell^- \nu\bar{\nu})/\sigma(\mathrm{SM})$	6.0	9.2
LR anal: $\sigma(H \to WW \to \ell^+\ell^- \nu\bar{\nu})/\sigma(\mathrm{SM})$	4.8	3.4

Table 2: The expected (exp.) and observed (obs.) limits on Higgs production cross section at 95 % CL at two values of m_H. $\sigma(\mathrm{SM})$ is the Standard Model cross section.

appropriate cuts on the NN output improves the sensitivity of the search by a factor of 2.5. Again, no evidence for Higgs production is observed and limits are set as given in Table 2 [7].

4 High-Mass Higgs Searches

For Higgs boson masses above around 135 GeV/c^2 we search for $H \to WW^{(*)} \to \ell^+\ell^- \nu\bar{\nu}$ events. Through intensive study of the detector we have increased acceptances for electron and muons, mainly by incorporating regions of the detector not previously well understood [8]. The improvement in lepton acceptance increases the expected yield of $m_H = 160$ GeV/c^2 Higgs events from 2.5 to 4 events.

Due to the two neutrinos in the final state, it is impossible to reconstruct the Higgs mass directly. Instead, we exploit of the spinless nature of the Higgs boson and examine the polar angle difference between the two charged leptons, $\Delta\phi$. For Higgs production $\Delta\phi$ peaks at lower values than for direct WW production, the main background to this search. Again

we find no evidence for Higgs events contributing to the observed $\Delta\phi$ distribution and we set a limit on the Higgs production cross section, as given in Table 2.

A more sensitive search for $H \to WW^{(*)}$ events is performed using a matrix element technique. In terms of the probability, $P(\vec{x})$, to observe an event with kinematic properties $\vec{x}$, we define the likelihood ratio (LR) to observe a given event as:

$$\mathrm{LR}(\vec{x}_{\mathrm{obs}}) = \frac{P_H(\vec{x}_{\mathrm{obs}})}{P_H(\vec{x}_{\mathrm{obs}}) + \Sigma_{\mathrm{backg}} P_i(\vec{x}_{\mathrm{obs}})} \tag{1}$$

Where P_H is the probability to observe Higgs production and P_i is the probability to observe one of the backgrounds. LR gives the most discriminating power between the signal and background. Figure 2 shows the distribution of LR observed, along with the expectation for Higgs production and the backgrounds. The observed distribution is compatible with the expected backgrounds and therefore we set a limit on the Higgs cross section as a function of m_H, also shown in Figure 2 [9].

5   Conclusions

In conclusion, using 1 fb^{-1}, CDF sees no evidence for Standard Model Higgs production. Recent improvements in b-jet tagging, di-jet mass resolution, triggers and acceptances along with the use of more advanced analysis techniques have been critical in improving the sensitivity of the Higgs searches presented. Coupled with these searches, precision measurements from the Tevatron also constrain the mass of the Higgs boson within the Standard Model.

CDF has around two-and-a-half times more data on tape and the Tevatron is projected to deliver a total integrated luminosity of 4 fb^{-1} by the end of 2007. Further improvements to the analyses are also being incorporated, therefore we can expect substantial improvements compared to the limits presented in this talk. If the Tevatron continues to deliver improvements to the instantaneous luminosity, if the CDF and DØ experiments collaborate on combining analyses, and if the Higgs boson has a mass less than about 200 GeV/c^2 then the Tevatron does have a *chance* to observe direct evidence for the Higgs boson.

I thank the organisers of the workshop for a productive and interesting meeting and, in particular, for the opportunity to get up close and personal with a Nasenbär!

References

[1] Slides:
    http://ilcagenda.linearcollider.org/contributionDisplay.py?contribId=156&sessionId=71&confId=1296

[2] R. Barate *et al.* Phys. Lett. B **565** (2003) 61 [arXiv:hep-ex/0306033].

[3] CDF and D0 Collaborations, arXiv:hep-ex/0703034.

[4] LEP Electroweak Working Group, March 2007 results. http://lepewwg.web.cern.ch/LEPEWWG/

[5] CDF Collaboration, Public Note 8390, 2006
    http://fcdfwww.fnal.gov/physics/exotic/r2a/20060713.lmetbj_wh/cdf8390_WH_1fb_1.ps

[6] CDF Collaboration, Public Note 8442, 2006
    http://www-cdf.fnal.gov/~veszpv/Higgs_Public_Page/cdf8442_higgs_met_bjet_pub06.ps

[7] CDF Collaboration, Public Note 8742, 2007
    http://www-cdf.fnal.gov/~efron/ZHllbbMarch07/cdf8742.pdf

[8] A. Abulencia *et al.* [CDF Collaboration], Phys. Rev. Lett. **98** (2007) 161801 [arXiv:hep-ex/0702027].

[9] CDF Collaboration, Public Note 8774, 2007
    http://www-cdf.fnal.gov/physics/new/hdg/HWW_ME/cdf8774_WW_1fb_public_note.ps

Precision calculations for H → WW/ZZ → 4fermions with PROPHECY4F

A. Bredenstein[1], A. Denner[2], S. Dittmaier[3] and M.M. Weber[4] [*]

1- High Energy Accelerator Research Organization (KEK)
Tsukuba, Ibaraki 305-0801, Japan

2- Paul Scherrer Institut
Würenlingen und Villigen, CH-5232 Villigen PSI, Switzerland

3- Max-Planck-Institut für Physik (Werner-Heisenberg-Institut)
D-80805 München, Germany

4- Department of Physics, University at Buffalo
The State University of New York, Buffalo, NY 14260-1500, USA

PROPHECY4f is a Monte Carlo event generator for precise simulations of the Higgs-boson decay H → ZZ/WW → 4fermions, supporting leptonic, semileptonic, and four-quark final states. Both electroweak and QCD corrections are included. Treating the intermediate gauge bosons as resonances, the calculation covers the full Higgs-boson mass range above, near, and below the gauge-boson pair thresholds. In this article we pay particular attention to the recently implemented option of *PROPHECY4f* to generate unweighted events.

1 Introduction

The decay of a Standard Model Higgs boson into weak-boson pairs with a subsequent decay into four fermions, H → ZZ/WW → $4f$, plays an important role both in the Higgs search at the LHC [1] and in precision Higgs physics at the planned International e^+e^- Linear Collider (ILC). The spin and the CP properties of the Higgs boson could be verified upon studying angular and invariant-mass distributions [2] of the decay fermions. In order to match the estimated experimental precision in predictions, a Monte Carlo generator for H → ZZ/WW → $4f$ including radiative corrections is needed. In the past, only the electroweak $\mathcal{O}(\alpha)$ corrections to decays into on-shell gauge bosons H → ZZ/WW [3] and some leading higher-order corrections were known. However, in the threshold region the on-shell approximation becomes unreliable. Below the gauge-boson-pair thresholds only the leading order was known until recently.

PROPHECY4f [4] is a recently constructed Monte Carlo event generator for H → ZZ/WW → $4f$ that includes electroweak and QCD corrections as well as some higher-order improvements. Since the process with off-shell gauge bosons is consistently considered without any on-shell approximations, the obtained results are valid above, near, and below the gauge-boson pair thresholds. In this note we briefly describe the structure of the underlying calculations and illustrate the new option of *PROPHECY4f* to generate unweighted events by reproducing some of the numerical results presented in Ref. [4].

---

2 Calculational details

The calculation of the complete electroweak $\mathcal{O}(\alpha)$ and strong $\mathcal{O}(\alpha_s)$ corrections to the processes H $\to 4f$, which includes both the corrections to the decays H $\to$ ZZ $\to 4f$ and H $\to$ WW $\to 4f$ and their interference, is described in Ref. [4] in detail. Each ingredient of the calculation has been worked out twice, using independent approaches as far as possible.

For the implementation of the finite widths of the gauge bosons we use the "complex-mass scheme", which was introduced in Ref. [5] for lowest-order calculations and generalized to the one-loop level in Ref. [6]. In this approach the W- and Z-boson masses are consistently considered as complex quantities, defined as the locations of the propagator poles in the complex plane. The scheme fully respects all relations that follow from gauge invariance.

The one-loop amplitudes of the virtual corrections have been generated with *FeynArts*, using the two independent versions 1 [7] and 3 [8]. They have been generated and evaluated both in the conventional 't Hooft–Feynman gauge and in the background-field formalism using the conventions of Refs. [9] and [10], respectively. One version of the algebraic part of the calculation is based on an in-house program implemented in *Mathematica*, another has been completed with the help of *FormCalc* [11]. The one-loop tensor integrals are evaluated as in the calculation of the corrections to $e^+e^- \to 4$ fermions [6, 12]. They are recursively reduced to master integrals at the numerical level. The scalar master integrals are evaluated for complex masses using the methods and results of Refs. [13]. Tensor and scalar 5-point functions are directly expressed in terms of 4-point integrals [14]. Tensor 4-point and 3-point integrals are reduced to scalar integrals with the Passarino–Veltman algorithm [15] as long as no small Gram determinant appears in the reduction. If small Gram determinants occur, the alternative reduction schemes of Ref. [16] are applied.

Since corrections due to the self-interaction of the Higgs boson become important for large Higgs masses, we have included the dominant two-loop corrections to the decay H $\to VV$ proportional to $G_\mu^2 M_H^4$ in the large-Higgs-mass limit which were calculated in Ref. [17].

The soft and collinear singularities appearing in the real corrections are treated both in the dipole subtraction approach [18] and in the phase-space slicing method. For the calculation of non-collinear-safe observables we use the extension of the subtraction method introduced in Ref. [19]. Final-state radiation off charged leptons beyond $\mathcal{O}(\alpha)$, which is relevant if bare lepton momenta enter the event selection, is supported for weigthed events only. These corrections [4] are sizeable only in regions where the lowest-order prediction is relatively small and can amount to 4% for muons and up to about 10% for electrons.

3 Event generation

PROPHECY4f employs a multi-channel Monte Carlo generator similar to *RacoonWW* [5, 20] and *Coffer*$\gamma\gamma$ [19, 21]. The results obtained this way have been checked using the adaptive integration program *VEGAS* [22]. In its default version *PROPHECY4f* generates weighted events, which are not positive definite.

As a new option, the program now supports the generation of unweighted events in its "phase-space-slicing" branch, applying a hit-and-miss algorithm similar to the one used by *RacoonWW*. Each time an unweighted event is generated, a Fortran subroutine is called where information about the event is provided in the format of the Les Houches Accord [23] (Fortran common block `HEPEUP`). This subroutine can be modified by the user in order to read out the events.

In the unweighting procedure also negative events occur. Although their number is reduced by using only the sum of the tree-level, the virtual, and the soft endpoint contribution, they cannot be avoided completely. In *PROPHECY4f* the remaining negative events are treated in the same way as the positive events, i.e. they can be read out by the user in a subroutine. Their contribution ranges from less than a per mille to slightly more than one per cent of all events, depending on the Higgs-boson mass.

The price for generating unweighted events is an increase of CPU time by about a factor 10^2 up to some 10^3 w.r.t. weighted-event generation, depending on the chosen $4f$ final state and the Higgs-boson mass. The results compared below are obtained with 5×10^5 unweighted and 5×10^7 weighted events. The generation of these unweighted events requires about 2 days on a AMD Opteron 252 2.6GHz CPU. However, one should keep in mind that such unweighted decay events could be generated once for a chosen setup and stored in a database. Simulations of Higgs production at the LHC or ILC could then just randomly pick events for the Higgs decays from the database.

4 Numerical results

The input parameters and the details of the setup in our numerical evaluation are provided in Ref. [4], where a comprehensive survey of numerical results is presented. The results shown in the following are obtained without applying photon recombination, i.e. invariant masses and angles are derived from bare lepton momenta.

In this brief article we focus only on the decay $H \to e^-e^+\mu^-\mu^+$ and show the distributions in the invariant masses of the decay leptons and the angle between the Z-decay planes in Figs. 1 and 2, respectively. These distributions play an important role in the verification of the discrete quantum numbers of the Higgs boson [2]. Since the radiative corrections significantly distort the distributions, they have to be taken into account if these observables are used to set bounds on non-standard couplings. Neglecting the corrections could result in faking new-physics effects. A detailed discussion of the corrections to these distributions can be found in Ref. [4]. Here we merely emphasize the agreement between the results obtained with weighted and unweighted events generated with *PROPHECY4f*.

5 Conclusions

The generator *PROPHECY4f*, which simulates the Higgs decays $H \to ZZ/WW \to 4f$ including electroweak and QCD corrections at the state of the art, is extended by an option for the generation of unweighted events. The consistency of the new option is illustrated in invariant-mass and angular distributions.

References

[1] S. Asai *et al.*, Eur. Phys. J. C **32S2** (2004) 19 [hep-ph/0402254]; S. Abdullin *et al.*, Eur. Phys. J. C **39S2** (2005) 41.

[2] V.D. Barger, K.M. Cheung, A. Djouadi, B.A. Kniehl and P.M. Zerwas, Phys. Rev. D **49** (1994) 79 [hep-ph/9306270]; S.Y. Choi, D.J. Miller, M.M. Mühlleitner and P.M. Zerwas, Phys. Lett. B **553** (2003) 61 [hep-ph/0210077]; C. P. Buszello, I. Fleck, P. Marquard and J. J. van der Bij, Eur. Phys. J. C **32** (2004) 209 [arXiv:hep-ph/0212396].

[3] J. Fleischer and F. Jegerlehner, Phys. Rev. D **23** (1981) 2001; B.A. Kniehl, Nucl. Phys. B **352** (1991) 1 and Nucl. Phys. B **357** (1991) 439; D.Y. Bardin, P.K. Khristova and B.M. Vilensky, Sov. J. Nucl. Phys. **54** (1991) 833 [Yad. Fiz. **54** (1991) 1366].
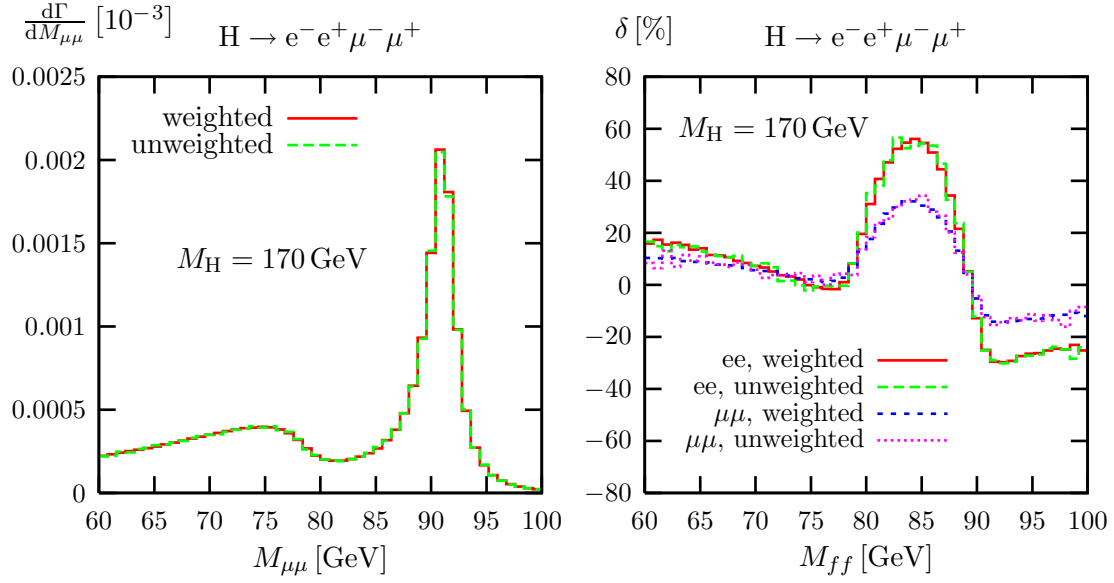
Figure 1: Corrected distribution in the invariant mass of the $\mu^-\mu^+$ pair (l.h.s.) and relative corrections for e^-e^+ and $\mu^-\mu^+$ pairs (r.h.s.) in the decay $H \to e^-e^+\mu^-\mu^+$, obtained with weighted and unweighted events.
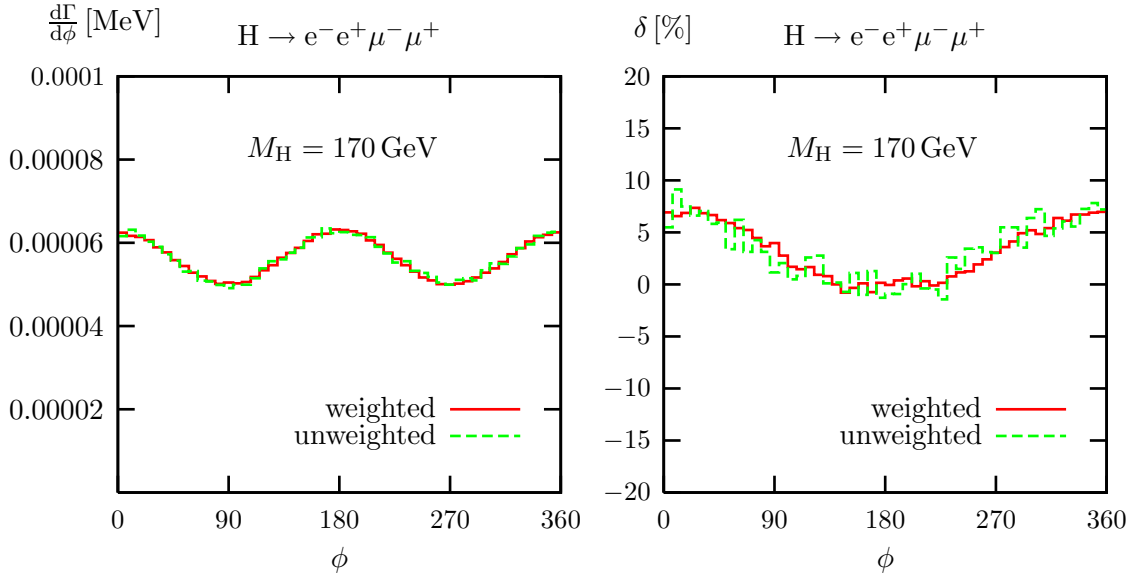
Figure 2: Corrected distribution in the angle between the $Z \to l^-l^+$ decay planes in the Higgs rest frame (l.h.s.) and relative corrections (r.h.s.) in the decay $H \to e^-e^+\mu^-\mu^+$, obtained with weighted and unweighted events.

[4] A. Bredenstein, A. Denner, S. Dittmaier and M. M. Weber, Phys. Rev. D **74** (2006) 013004 [hep-ph/0604011] and JHEP **0702** (2007) 080 [hep-ph/0611234].

[5] A. Denner, S. Dittmaier, M. Roth and D. Wackeroth, Nucl. Phys. B **560** (1999) 33 [hep-ph/9904472].

[6] A. Denner, S. Dittmaier, M. Roth and L. H. Wieders, Nucl. Phys. B **724** (2005) 247 [hep-ph/0505042].

[7] J. Küblbeck, M. Böhm and A. Denner, Comput. Phys. Commun. **60** (1990) 165; H. Eck and J. Küblbeck, *Guide to FeynArts 1.0*, University of Würzburg, 1992.

[8] T. Hahn, Comput. Phys. Commun. **140** (2001) 418 [hep-ph/0012260].

[9] A. Denner, Fortsch. Phys. **41** (1993) 307.

[10] A. Denner, G. Weiglein and S. Dittmaier, Nucl. Phys. B **440** (1995) 95 [hep-ph/9410338].

[11] T. Hahn and M. Perez-Victoria, Comput. Phys. Commun. **118** (1999) 153 [hep-ph/9807565]; T. Hahn, Nucl. Phys. Proc. Suppl. **89** (2000) 231 [hep-ph/0005029].

[12] A. Denner, S. Dittmaier, M. Roth and L.H. Wieders, Phys. Lett. B **612** (2005) 223 [hep-ph/0502063].

[13] G. 't Hooft and M. Veltman, Nucl. Phys. B **153** (1979) 365; W. Beenakker and A. Denner, Nucl. Phys. B **338** (1990) 349; A. Denner, U. Nierste and R. Scharf, Nucl. Phys. B **367** (1991) 637.

[14] A. Denner and S. Dittmaier, Nucl. Phys. B **658** (2003) 175 [hep-ph/0212259].

[15] G. Passarino and M. Veltman, Nucl. Phys. B **160** (1979) 151.

[16] A. Denner and S. Dittmaier, Nucl. Phys. B **734** (2006) 62 [hep-ph/0509141].

[17] A. Ghinculov, Nucl. Phys. B **455** (1995) 21 [hep-ph/9507240]; A. Frink, B.A. Kniehl, D. Kreimer and K. Riesselmann, Phys. Rev. D **54** (1996) 4548 [hep-ph/9606310].

[18] S. Dittmaier, Nucl. Phys. B **565** (2000) 69 [hep-ph/9904440].

[19] A. Bredenstein, S. Dittmaier and M. Roth, Eur. Phys. J. C **44** (2005) 27 [hep-ph/0506005].

[20] A. Denner, S. Dittmaier, M. Roth and D. Wackeroth, Comput. Phys. Commun. **153** (2003) 462 [hep-ph/0209330].

[21] A. Bredenstein, S. Dittmaier and M. Roth, Eur. Phys. J. C **36** (2004) 341 [hep-ph/0405169].

[22] G.P. Lepage, J. Comput. Phys. **27** (1978) 192.

[23] E. Boos *et al.*, arXiv:hep-ph/0109068.

Consistent Treatment of Imaginary Contributions to Higgs-Boson Masses in the MSSM

T. Hahn[1], S. Heinemeyer[2], W. Hollik[1], H. Rzehak[3] and G. Weiglein[4]

1- Max-Planck-Institut für Physik, Föhringer Ring 6, D–80805 Munich, Germany

2- Instituto de Fisica de Cantabria (CSIC-UC), Santander, Spain

3- Paul Scherrer Institut, Würenlingen und Villigen, CH–5232 Villigen PSI, Switzerland

4- IPPP, University of Durham, Durham DH1 3LE, UK

We show how the imaginary parts of the Higgs-Boson self-energies in the MSSM are consistenly taken into account in the Higgs-Boson mass determination. In a numerical example we find effects of 5 GeV in the mass difference of the two heavy neutral Higgs bosons. The imaginary contributions have been included into the code `FeynHiggs`.

1 Introduction

A striking prediction of models of supersymmetry (SUSY) [2] is a Higgs sector with at least one relatively light Higgs boson. In the Minimal Supersymmetric extension of the Standard Model (MSSM) two Higgs doublets are required, resulting in five physical Higgs bosons: the light and heavy $\mathcal{CP}$-even h and H, the $\mathcal{CP}$-odd A, and the charged Higgs bosons $H^{\pm}$. The Higgs sector of the MSSM can be expressed at lowest order in terms of M_Z, M_A and $\tan\beta \equiv v_2/v_1$, the ratio of the two vacuum expectation values. All other masses and mixing angles can therefore be predicted. Higher-order contributions give large corrections to the tree-level relations. The limits obtained from the Higgs search at LEP (the final LEP results can be found in Refs. [3, 4]), place important restrictions on the parameter space of the MSSM.

For the MSSM with real parameters (rMSSM) the status of higher-order corrections to the masses and mixing angles in the Higgs sector is quite advanced. The complete one-loop result within the rMSSM is known [5, 6, 7, 8]. The computation of the two-loop corrections has meanwhile reached a stage where all the presumably dominant contributions are available, see Refs. [9, 10] and references therein. Leading three-loop corrections have recently been obtained in Ref. [11]. The remaining theoretical uncertainty on the lightest $\mathcal{CP}$-even Higgs boson mass has been estimated to be below ~ 3 GeV [9, 12, 13]. The public code `FeynHiggs` [9, 14, 15, 16] is based on the results obtained in the Feynman-diagrammatic (FD) approach [9, 14, 17, 18]; it includes all available corrections in the FD approach. For the MSSM with complex parameters (cMSSM) the full one-loop result in the FD approach has been obtained in Ref. [16], and the corresponding leading $\mathcal{O}(\alpha_t \alpha_s)$ corrections can be found in Ref. [19].

2 Imaginary Contributions to Higgs-boson self-energies

The propagator matrix of the neutral Higgs bosons h, H, A can be written as a 3×3 matrix, $\Delta_{hHA}(p^2)$. The 3×3 propagator matrix is related to the 3×3 matrix of the irreducible vertex functions by

$$\Delta_{hHA}(p^2) = - \left(\hat{\Gamma}_{hHA}(p^2) \right)^{-1}, \tag{1}$$

where

$$\hat{\Gamma}_{hHA}(p^2) = i\left[p^2\mathbb{1} - \mathbf{M}_{\mathrm{n}}(p^2)\right],$$ (2)

$$\mathbf{M}_{\mathrm{n}}(p^2) = \begin{pmatrix} m_h^2 - \hat{\Sigma}_{hh}(p^2) & -\hat{\Sigma}_{hH}(p^2) & -\hat{\Sigma}_{hA}(p^2) \\ -\hat{\Sigma}_{hH}(p^2) & m_H^2 - \hat{\Sigma}_{HH}(p^2) & -\hat{\Sigma}_{HA}(p^2) \\ -\hat{\Sigma}_{hA}(p^2) & -\hat{\Sigma}_{HA}(p^2) & m_A^2 - \hat{\Sigma}_{AA}(p^2) \end{pmatrix}.$$ (3)

The three complex poles $\mathcal{M}^2$ of Δ_{hHA}, eq. (1), are determined as the solutions of

$$\mathcal{M}_i^2 - m_i^2 + \hat{\Sigma}_{ii}^{\mathrm{eff}}(\mathcal{M}_i^2) = 0 , \quad i = h, H, A .$$ (4)

The effective self-energy reads (no summation over i, j, k)

$$\hat{\Sigma}_{ii}^{\mathrm{eff}}(p^2) = \hat{\Sigma}_{ii}(p^2) - i\frac{2\hat{\Gamma}_{ij}(p^2)\hat{\Gamma}_{jk}(p^2)\hat{\Gamma}_{ki}(p^2) - \hat{\Gamma}_{ki}^2(p^2)\hat{\Gamma}_{jj}(p^2) - \hat{\Gamma}_{ij}^2(p^2)\hat{\Gamma}_{kk}(p^2)}{\hat{\Gamma}_{jj}(p^2)\hat{\Gamma}_{kk}(p^2) - \hat{\Gamma}_{jk}^2(p^2)},$$ (5)

where the $\hat{\Gamma}_{ij}(p^2)$ are the elements of the 3×3 matrix $\hat{\Gamma}_{hHA}(p^2)$ as specified in eq. (2). The complex pole is decomposed as

$$\mathcal{M}^2 = M^2 - iM\Gamma,$$ (6)

where M is the mass of the particle and Γ its width, We define the loop-corrected mass eigenvalues according to

$$M_{h_1} \leq M_{h_2} \leq M_{h_3}.$$ (7)

In our determination of the Higgs-boson masses we take into account all imaginary parts of the Higgs-boson self-energies (besides the term with imaginary parts appearing explicitly in eq. (4), there are also products of imaginary parts in $\mathrm{Re}\,\hat{\Sigma}_{ii}^{\mathrm{eff}}(M_i^2)$). The effects of the imaginary parts of the Higgs-boson self-energies on Higgs phenomenology can be especially relevant if the masses are close to each other. This has been analyzed in Ref. [20] taking into account the mixing between the two heavy neutral Higgs bosons, where the complex mass matrix has been diagonalized using a complex mixing angle, resulting in a non-unitary mixing matrix. The effects of imaginary parts of the Higgs-boson self-energies on physical processes with s-channel resonating Higgs bosons are discussed in Refs. [20, 21, 22]. In Ref. [20] only the one-loop corrections from the $t/\tilde{t}$ sector have been taken into account for the H–A mixing, analyzing the effects on resonant Higgs production at a photon collider. In Ref. [21] (using the code CPSuperH [23]) the full one-loop imaginary parts of the self-energies have been evaluated for the mixing of the three neutral MSSM Higgs bosons. The effects have been analyzed for resonant Higgs production at the LHC, the ILC and a photon collider (however, the corresponding effects on the Higgs-boson masses have been neglected). In Ref. [22] the $\tilde{t}/\tilde{b}$ one-loop contributions (neglecting the t/b corrections) on the H–A mixing for resonant Higgs production at a muon collider have been discussed. Our calculation [16, 24] incorporates for the first time the complete effects arising from the imaginary parts of the one-loop self-energies in the neutral Higgs-boson propagator matrix, including their effects on the Higgs masses and the Higgs couplings in a consistent way.

3   Numerical example

In order to study the impact of the imaginary parts of the Higgs-boson self-energies, it is useful to compare the full result with the "Im $\Sigma = 0$" approximation, which is defined by

performing the replacement

$$\text{Im}\,\Sigma = 0 \text{ approximation:} \qquad \Sigma(p^2) \quad \rightarrow \quad \text{Re}\,\Sigma(p^2) \tag{8}$$

for all Higgs-boson self-energies in eq. (3). The numerical example has been obtained for the following set of parameters:

$$M_{\text{SUSY}} = 500 \text{ GeV}, \ |A_t| = A_b = A_\tau = 1000 \text{ GeV},$$
$$\mu = 1000 \text{ GeV}, \ M_2 = 500 \text{ GeV}, \ M_1 = 250 \text{ GeV}, \ m_{\tilde{g}} = 500 \text{ GeV},$$
$$\mu_{\overline{\text{DR}}} = m_t = 171.4 \text{ GeV } [25]. \tag{9}$$
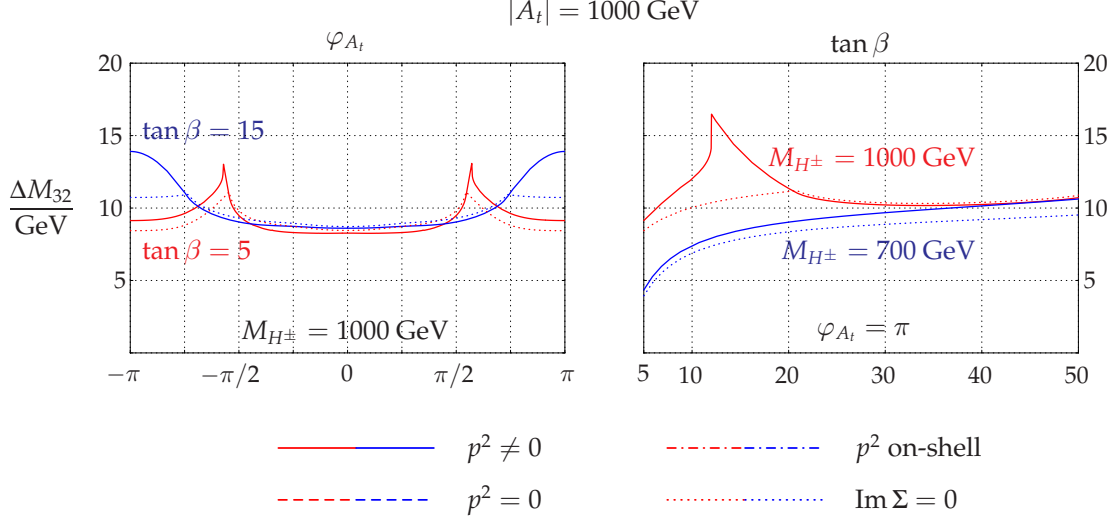
Figure 1: The mass difference $\Delta M_{32} := M_{h_3} - M_{h_2}$ is shown for $\tan\beta = 5, 15$ and $M_{H^\pm} = 1000$ GeV as a function of φ_{A_t} (left) and for $\varphi_{A_t} = \pi$, $M_{H^\pm} = 700, 1000$ GeV as a function of $\tan\beta$ (right). The solid line shows the full result, the dotted line the "$\text{Im}\,\Sigma = 0$" approximation. The other two lines correspond to other Higgs-boson self-energy approximations, see Ref. [16] for details.

In Fig. 1 we show an example of the effects of the imaginary parts of the Higgs-boson self-energies, i.e. the comparison of the full result with the "$\text{Im}\,\Sigma = 0$" approximation as defined in eq. (8). In the left plot we show $\Delta M_{32} := M_{h_3} - M_{h_2}$ as a function of φ_{A_t} for $\tan\beta = 5, 15$ and $m_{H^\pm} = 1000$ GeV. In the right plot we display ΔM_{32} as a function of $\tan\beta$ for $m_{H^\pm} = 700, 1000$ GeV and $\varphi_{A_t} = \pi$. Here φ_{A_t} denotes the angle of the complex valued trilinear coupling A_t. The other parameters are given in eq. (9). As one can see from the plot, the difference between the full result and the approximation with neglected imaginary parts is often ~ 1 GeV and can become as large as about 5 GeV.

4 Acknowledgments

tract MRTN-CT-2006-035505 'Tools and Precision Calculations for Physics Discoveries at Colliders'

References

[1] Slides:
   `http://ilcagenda.linearcollider.org/contributionDisplay.py?contribId=158&sessionId=71&confId=1296`

[2] H. Nilles, *Phys. Rept.* **110** (1984) 1; H. Haber and G. Kane, *Phys. Rept.* **117** (1985) 75; R. Barbieri, *Riv. Nuovo Cim.* **11** (1988) 1.

[3] [LEP Higgs working group], *Phys. Lett.* **B 565** (2003) 61 [arXiv:hep-ex/0306033].

[4] [LEP Higgs working group], *Eur. Phys. J.* **C 47** (2006) 547 [arXiv:hep-ex/0602042].

[5] J. Ellis, G. Ridolfi and F. Zwirner, *Phys. Lett.* **B 257** (1991) 83; Y. Okada, M. Yamaguchi and T. Yanagida, *Prog. Theor. Phys.* **85** (1991) 1; H. Haber and R. Hempfling, *Phys. Rev. Lett.* **66** (1991) 1815.

[6] A. Brignole, *Phys. Lett.* **B 281** (1992) 284.

[7] P. Chankowski, S. Pokorski and J. Rosiek, *Phys. Lett.* **B 286** (1992) 307; *Nucl. Phys.* **B 423** (1994) 437 [arXiv:hep-ph/9303309].

[8] A. Dabelstein, *Nucl. Phys.* **B 456** (1995) 25 [arXiv:hep-ph/9503443]; *Z. Phys.* **C 67** (1995) 495 [arXiv:hep-ph/9409375].

[9] G. Degrassi, S. Heinemeyer, W. Hollik, P. Slavich and G. Weiglein, *Eur. Phys. J.* **C 28** (2003) 133 [arXiv:hep-ph/0212020].

[10] S. Martin, *Phys. Rev.* **D 71** (2005) 016012 [arXiv:hep-ph/0405022]; *Phys. Rev.* **D 71** (2005) 116004 [arXiv:hep-ph/0502168].

[11] S. Martin, *Phys. Rev.* **D 75** (2007) 055005 [arXiv:hep-ph/0701051].

[12] S. Heinemeyer, W. Hollik and G. Weiglein, *Phys. Rept.* **425** (2006) 265 [arXiv:hep-ph/0412214].

[13] B. Allanach, A. Djouadi, J. Kneur, W. Porod and P. Slavich, *JHEP* **0409** (2004) 044 [arXiv:hep-ph/0406166].

[14] S. Heinemeyer, W. Hollik and G. Weiglein, *Eur. Phys. J.* **C 9** (1999) 343 [arXiv:hep-ph/9812472].

[15] S. Heinemeyer, W. Hollik and G. Weiglein, *Comput. Phys. Commun.* **124** (2000) 76 [arXiv:hep-ph/9812320]; see `www.feynhiggs.de` .

[16] M. Frank, T. Hahn, S. Heinemeyer, W. Hollik, R. Rzehak and G. Weiglein, *JHEP* **02** (2007) 047 [arXiv:hep-ph/0611326].

[17] S. Heinemeyer, W. Hollik and G. Weiglein, *Phys. Rev.* **D 58** (1998) 091701 [arXiv:hep-ph/9803277]; *Phys. Lett.* **B 440** (1998) 296 [arXiv:hep-ph/9807423].

[18] G. Degrassi, A. Dedes and P. Slavich, *Nucl. Phys.* **B 672** (2003) 144 [arXiv:hep-ph/0305127].

[19] S. Heinemeyer, W. Hollik, H. Rzehak and G. Weiglein, to appear in *Phys. Lett.* **B**, arXiv:0705.0746 [hep-ph].

[20] S. Choi, J. Kalinowski, Y. Liao and P. Zerwas, *Eur. Phys. J.* **C 40** (2005) 555 [arXiv:hep-ph/0407347].

[21] J. Ellis, J. Lee and A. Pilaftsis, *Phys. Rev.* **D 70** (2004) 075010 [arXiv:hep-ph/0404167]; *Nucl. Phys.* **B 718** (2005) 247 [arXiv:hep-ph/0411379]; *Phys. Rev.* **D 72** (2005) 095006 [arXiv:hep-ph/0507046].

[22] J. Bernabeu, D. Binosi and J. Papavassiliou, *JHEP* **0609** (2006) 023 [arXiv:hep-ph/0604046].

[23] J. Lee, A. Pilaftsis et al., *Comput. Phys. Commun.* **156** (2004) 283 [arXiv:hep-ph/0307377].

[24] T. Hahn, S. Heinemeyer, W. Hollik, H. Rzehak, G. Weiglein and K. Williams, arXiv:hep-ph/0611373.

[25] E. Brubaker et al. [Tevatron Electroweak Working Group], arXiv:hep-ex/0608032, see: `tevewwg.fnal.gov/top/` .

Prospects to Measure the Higgs Boson Mass and Cross Section in $e^+e^- \to ZH$ Using the Recoil Mass Spectrum

W. Lohmann[1], M. Ohlerich[1,2], A. Raspereza[3], and A. Schälicke[1]

1- DESY
Platanenallee 6, 15738 Zeuthen - Germany

2- BTU Cottbus
Konrad-Wachsmann-Allee 1, 03046 Cottbus - Germany

3- Max-Planck-Institut für Physik
Foehringer Ring 6, 80805 Muenchen - Germany

The process $e^+e^- \to ZH$ allows to measure the Higgs boson in the recoil mass spectrum against the Z boson without any assumptions on the Higgs boson decay. We performed a full simulation and reconstruction of $e^+e^- \to ZH$ using the MOKKA and MARLIN packages describing the LDC detector. The Z is reconstructed from its decays into electrons and muons. The mass of the Higgs boson is set to 120 GeV. Assuming a centre-of-mass energy of 250 GeV and an integrated luminosity of $50\,\mathrm{fb}^{-1}$ the Higgs boson mass and the Higgs-strahlung cross section can be measured with a precision of 120 MeV and 9%, respectively.

1 Introduction

The Standard Model (SM) [1] predicts one Higgs boson as a remnant from the spontaneous symmetry breaking mechanism [2]. This mechanism allows fermions and the W and Z bosons to acquire their masses by interaction with the Higgs field. To discover the Higgs boson, therefore, is of crucial interest to complete the SM. Electroweak precision measurements suggest the mass of the Higgs boson to be of the order $\mathcal{O}(100\,\mathrm{GeV})$. Direct searches at LEP have set a lower mass limit of 114 GeV. A Higgs boson with a mass above 114 GeV will be accessible in the experiments at the Large Hadron Collider (LHC). However, to be sure about the nature of the particle found, it is necessary to measure its properties such as mass, width, charge, spin, parity, couplings to other particles, and self-couplings to test the internal consistency of the SM, or to find hints for new physics.

For the determination of at least some of these quantities, LHC will not be sufficient. At the future International Linear Collider (ILC), we will have the chance to investigate the properties of new particles with high precision in all details. This e^+e^- collider with a center-of-mass energy up to 1 TeV provides a well known initial state, a very clear signature for events of $e^+e^- \to ZH$, and due to its high luminosity sufficient statistics for precision measurements.

In the Higgs-strahlung process $e^+e^- \to ZH$, we can investigate the coupling of the Higgs boson to the Z boson and determine the Higgs boson mass with high precision in a relatively model-independent way using the recoil mass spectrum against the Z,

$$m_{\mathrm{recoil}}^2 = s + m_{\mathrm{di-lepton}}^2 - 2 \cdot E_{\mathrm{di-lepton}} \cdot \sqrt{s}\,, \tag{1}$$

where s is the square of the centre-of-mass energy, and $m_{\mathrm{di-lepton}}$ and $E_{\mathrm{di-lepton}}$ are the mass and the energy of the leptons originating from the Z decay.

Previous studies using simplified parametric detector simulations have shown the potential of this technique [3].

Here, we study the prospects to measure the Higgs boson mass and cross section assuming its mass to be 120 GeV. At a centre-of-mass energy of 250 GeV, a full detector simulation of the process $e^+e^- \rightarrow ZH$ is performed using the MOKKA software package, which simulates events in the LDC detector. The response from the sub-detectors is digitised as in a real experiment and is processed using the MARLINRECO [4] reconstruction software. In addition, SM background processes are treated in the same way.

The Z is reconstructed from its decays into electrons and muons. Algorithms are developed to identify electrons and muons using the tracker and calorimeter information. A likelihood technique is used to separate signal events from the SM background processes with high efficiency.

2 Experimental Conditions

The study assumes a linear e^+e^- collider operating at a centre-of-mass energy of 250 GeV. This energy is chosen because the Higgs-strahlung cross section for the SM Higgs boson with a mass of 120 GeV reaches its maximal value.

The statistics for signal and background events corresponds to a luminosity of $50\,\mathrm{fb}^{-1}$. Signal events were generated using PYHTIA 6.4.11 [5]. Initial and final state bremsstrahlung and beamstrahlung are taken into account. To simulate beamstrahlung the GUINEAPIG 1.4.1 [6] program is used assuming ILC nominal beam parameters. Background events are produced using in addition the event generators BHWIDE 1.04 [7] and SHERPA 1.0.10 [8] as listed in Table 1.

Signal and background events are passed through a full detector simulation (MOKKA) and are processed in the full reconstruction scheme of MARLIN. A sketch of the simulation stages is shown in Figure 1. The LDC detector [9] is used for the simulation and reconstruc-

beamstrahlung:
GUINEAPIG

| event generator | MOKKA | MARLIN | post reconstruction analysis |

ISR, FSR
event generation

LDC Sc01,
full detector
simulation

full reconstruction of
isolated leptons, lepton
matching

signal background
separation
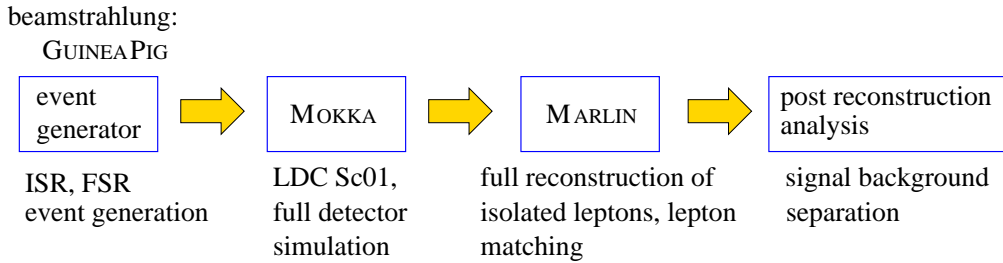
Figure 1: Scheme of simulation and analysis stages. Events of the different processes are generated using PYTHIA 6.4.11 , BHWIDE 1.04 and SHERPA 1.0.10. Beamstrahlung is treated by GUINEAPIG. MOKKA and MARLIN simulate and reconstruct events in the LDC detector. The analysis software is based on ROOT.

tion. The vertex detector (VTX) consists of five layers of silicon pixel detectors. The main tracker is a TPC of about 3 m diameter and 4 m length supplemented by cylindrical silicon strip detectors (SIT) and forward strip and pixel detectors (FTD). The TPC is surrounded by the electromagnetic (ECAL) and hadronic (HCAL) calorimeter, which in turn are enclosed by the 4 T magnet and the iron yoke. ECAL is a finely segmented silicon-tungsten

sandwich calorimeter. HCAL consists of a steel absorber structure with small scintillator tiles read out with silicon photomultipliers. When this analysis was performed no muon chamber was implemented in MOKKA. Thus the separation of muons and pions in the particle identification is done using the trackers and calorimeters only. The precision of the momentum measurement of the tracker system (TPC+VTX+SIT+FTD) is obtained to be $\sigma_{p_t}/p_t = 7 \cdot 10^{-5} \cdot p_t$ [GeV] using the FullLDCTracking processor in MARLINRECO.

	Process	σ [fb]	$N(50\text{ fb}^{-1})$	Generator
1.	$e^+e^- \to HZ \to X\ell^+\ell^-$	15.0	751	PYTHIA
2.	$e^+e^- \to e^+e^-$	4144.5	207223	BHWIDE
3.	$e^+e^- \to \mu^+\mu^-$	4281.0	214050	PYTHIA
4.	$e^+e^- \to \tau^+\tau^-$	4182.0	209100	PYTHIA
5.	$e^+e^- \to W^+W^- \to Xe, X\mu, Xe\mu$	5650.0	282277	PYTHIA
6.	$e^+e^- \to e^+e^-f\bar{f}$	475.7	23784	SHERPA
7.	$e^+e^- \to \mu^+\mu^-f\bar{f}$	359.4	17970	SHERPA
8.	$e^+e^- \to e^+e^-e^+e^-$	24.6	1231	SHERPA
9.	$e^+e^- \to \mu^+\mu^-\mu^+\mu^-$	7.2	360	SHERPA
10.	$e^+e^- \to e^+e^-\mu^+\mu^-$	177.0	8850	SHERPA

Table 1: The processes simulated for this study, their cross sections, the expected statistics for an integrated luminosity of 50 fb^{-1}, and the generators used. ℓ represents e, μ and f stands for τ, ν, q.

3 Simulation Details and Analysis

Signal and Background Processes

The signal and background processes considered in the analysis, their cross sections and expected statistics at $50\,\text{fb}^{-1}$, and the programs used to generate events are listed in Table 1. For the generation of e^+e^- events using BHWIDE, the following cuts are applied: the polar angle range is restricted to $|\cos\vartheta_{\text{lep}}| < 0.985$, the electron energy is required to be $E_e > 10$ GeV, the difference of the di-lepton mass and the Z mass is $|m_{ee} - m_Z| < 40\,\text{GeV}$, and the recoil mass against the Z is in the range $90\,\text{GeV} \le m_{\text{recoil}} \le 190\,\text{GeV}$. For event samples generated with SHERPA, cuts on the lepton polar angle, $|\cos\vartheta_{\text{lep}}| < 0.985$, the di-lepton and di-parton mass, $m_{ee,qq} > 10\,\text{GeV}$, and the energy of the final state fermions, $E_{\text{fermion}} > 5\,\text{GeV}$, are applied. These cuts avoid divergences in the cross sections, reduce computing time, and would have no influence on the results.

Analysis Strategy

The signature of events from $e^+e^- \to ZH$ are two leptons of the same kind and opposite charge. The invariant mass of the two leptons must be in the vicinity of the Z mass. The dominant background is expected from the process $e^+e^- \to ZZ \to \ell^+\ell^- X$, which is simulated within the four-fermion processes 6 - 10 in Table 1. Discriminating power is expected from the polar angle distribution of the Z. Processes 2 and 3 with two electrons or muons in the final state may be selected since initial state radiation leads to a radiative return and thus to an invariant mass near the Z. To distinguish them from the signal, the acoplanarity angle

can be used. The process 5 is a possible background due to its high cross section. The polar angle of the leptons can be used to distinguish the signal from this background.

In the fist step of the analysis, we look for isolated electrons and muons in each event using a likelihood method. An electron is identified as an electromagnetic shower in the ECAL that matches the position predicted from a track as impact point into the ECAL. A muon is identified as a track matching to deposits in the ECAL and HCAL compatible with the expectations from a minimum ionising particle.

For the second step, only events with a lepton pair of the same kind and with opposite charge are accepted. If there are several pairings possible, the one with an invariant mass closest to m_Z is chosen.

For further reduction of the background the following cuts are applied to:

- the polar angles of the leptons: $|\cos\vartheta_{\text{lep}}| < 0.95$,
- the difference between the invariant di-lepton mass and m_Z: $|m_{\text{di-lepton}} - m_Z| < 30\,\text{GeV}$,
- the lepton energy: $E_{\text{lep}} > 15\,\text{GeV}$,
- the recoil mass: $90\,\text{GeV} \leq m_{\text{recoil}} \leq 190\,\text{GeV}$,
- the polar angle of the di-electron system: $|\cos\vartheta_{\text{di-electron}}| < 0.90$.

The remaining events are analysed using likelihood density functions for the signal, the $e^+e^- \to 4f$, and the $e^+e^- \to 2f$ background channels in the variables: acoplanarity angle of the two leptons, acolinearity angle of the two leptons, the di-lepton mass, the polar angle of the di-lepton system, the polar angles of the two leptons and the transverse momentum of the Z.

For each event a likelihood is calculated characterising its compatibility with a signal event. A cut on this likelihood is set such that the quantity $\frac{\sqrt{S+B}}{S}$ is minimised in the mass range from 119 GeV to 125 GeV. Here, S and B are the numbers of signal and background events, respectively, in the final sample.

4 Results

In the final sample, the signal selection efficiency is obtained to be 43.1% for the $e^+e^- \to Zh \to e^+e^-X$ and 57.2% for the $e^+e^- \to Zh \to \mu^+\mu^-X$ channel, respectively. The recoil mass spectra are shown in Figure 2 for these processes. In both spectra a signal peak is seen on top of a moderate background. The signal has a smaller width in the di-muon channel, presumably because the muon track measurement is more precise due to less bremsstrahlung in the material of the detectors. This is confirmed by the resolution function for the transverse momentum, which has a pronounced tail to lower reconstructed momenta for electrons.

Cross Section Measurement

The recoil mass spectra in Figure 2 are used to determine the cross sections for the processes $e^+e^- \to Zh \to e^+e^-X$ and $e^+e^- \to Zh \to \mu^+\mu^-X$. The background originating from known SM processes is parametrised by a polynomial and kept constant in the fit to determine the
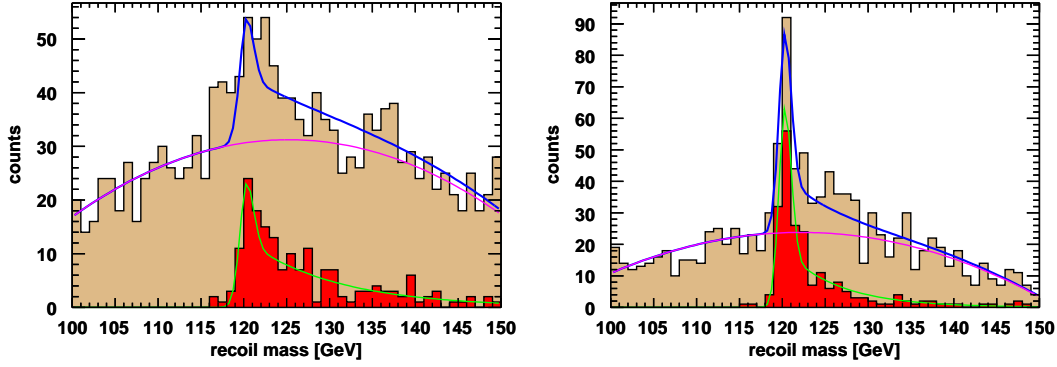
Figure 2: The recoil mass distributions of the selected $e^+e^- \to ZH$ events, left for $Z \to e^+e^-$ and right for $Z \to \mu^+\mu^-$ final states, respectively. The dark red distribution originates from the signal process and the light red distribution from the remaining background.

amount of the signal. The signal is described using the following parametrisation,

$$s(x) = \text{Norm}_{\text{GausExp}} \begin{cases} e^{-(x-m_0)^2/(2\sigma_{\text{gaus}}^2)} & : x < m_0 , \\ \beta e^{-(x-m_0)^2/(2\sigma_{\text{gaus}}^2)} + (1-\beta)e^{-(x-m_0)/\lambda} & : x > m_0 , \end{cases} \quad (2)$$

where m_0 is the central value of the peak, λ a constant to describe the tail to larger values in the signal mass distribution and $1 - \beta$ is the fraction of the tail. The tail to larger mass values in the signal is caused by bremsstrahlung and beamstrahlung. The former is well predicted from QED and the latter depends on the machine parameters. For known and reasonable stable machine parameters the shape and fraction of the tail can be determined, and we keep it constant in the fit, varying only m_0 and the number of events in the signal, N_{signal}. The cross section of the signal process is obtained from

$$\sigma(\text{process}) = N_{\text{signal}}/(\mathcal{L}\varepsilon), \quad (3)$$

where $\mathcal{L}$ is the integrated luminosity, and ε is the signal selection efficiency. The results obtained are $\sigma(e^+e^- \to ZH) = 216.0\,\text{fb}$ with an uncertainty of 20% using the di-electron final state and $\sigma(e^+e^- \to ZH) = 219.7\,\text{fb}$ with an uncertainty of 10% using the di-muon final state. Both results agree with the value of the cross section of $226.8\,\text{fb}$ obtained from Pythia.

An alternative method is to count all events, N, in the signal mass range from $119\,\text{GeV}$ to $125\,\text{GeV}$ and to subtract the background. The latter is obtained from a high statistics Monte Carlo simulation or from the integral over a parametrised background distribution in the same mass range, $\langle B \rangle$. The cross section is then given by

$$\sigma(\text{process}) = (N - \langle B \rangle)/(\mathcal{L}\varepsilon), \quad (4)$$

with an uncertainty of $(\pm \sqrt{N}/(N - \langle B \rangle))$ [%] . Using this method no assumption on the signal peak parametrisation is needed. The results obtained are compatible with the fit results given above.

Higgs boson mass

To determine the Higgs boson mass from the spectra shown in Figure 2 a likelihood method is used. Several signal samples of high statistics with Higgs boson masses between 119 and 121 GeV are generated and processed through the full simulation, reconstruction and analysis chain. The obtained spectra are parametrised using Formula (2). These parametrisations are then used in an unbinned likelihood fit to the simulated event samples shown in Figure 2 to determine the Higgs boson mass m_h. The results are $m_h = 119.78 \pm 0.42$ GeV and $m_h = 120.09 \pm 0.12$ GeV for the $Z \to e^+e^-$ and $Z \to \mu^+\mu^-$ decays, respectively.
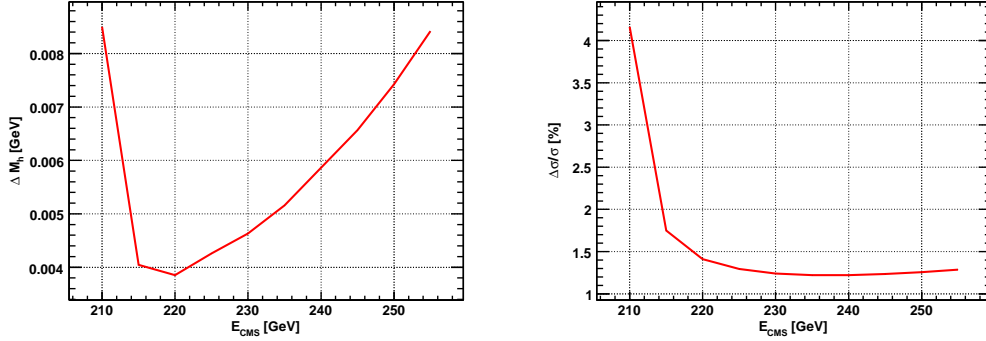
Figure 3: Uncertainties on the Higgs boson recoil mass measurement (left) and on the Higgs boson production cross section (right) as a function of the centre-of-mass energy. A Monte Carlo toy model with parametrised momentum resolution is used.

Estimate of the Optimal Centre-of-Mass Energy for the Measurements

A Monte Carlo toy model is used to estimate the optimal centre-of-mass energy for the measurement of the Higgs boson mass and cross section. The resolution of the track momentum measurement is parametrised as $\sigma_{p_t}/p_t = 10^{-4} \cdot p_t$ [GeV]. A lepton identification and pair matching is performed as described above. For a Higgs boson mass of 120 GeV the recoil mass spectra are used to determine the Higgs boson mass and cross section for centre-of-mass energies between 210 GeV and 250 GeV. The estimated accuracies for the mass and cross section measurements are shown in Figure 3 as a function of the centre-of-mass energy assuming an integrated luminosity of $500\,\text{fb}^{-1}$. The minimal uncertainty on the recoil mass occurs for $E_{\text{cms}} = 220$ GeV, in agreement with the results obtained in Ref.[10]. The cross section uncertainty is minimal for $E_{\text{cms}} = 240$ GeV, becoming worse by about 20% at $E_{\text{cms}} = 220$ GeV.

5   Conclusions

The recoil mass technique is a unique tool to determine the mass and cross section of the Higgs boson at the ILC. For the first time the prospects obtained from a full detector simulation and reconstruction are presented. Choosing the center-of-mass energy a few ten GeV above the kinematic threshold, here 250 GeV for $m_h = 120$ GeV, the Higgs boson mass

and cross section can be determined with an accuracy of 120 MeV and 9%, respectively, using only $50\,\mathrm{fb}^{-1}$. To reach a similar accuracy at a center-of-mass energy of $350\,\mathrm{GeV}$, an integrated luminosity $500\,\mathrm{fb}^{-1}$ is needed.

The talk held at the LCWS is available under Ref. [11].

References

[1] S.L. Glashow, Nucl. Phys. **22** (1961) 579; S. Weinberg, Phys. Rev. Lett. **19** (1967) 1264; A. Salam, *Elementary Particle Theory*, edited by N. Svartholm (Almqvist and Wiksell, Stockholm, 1968), p. 367.

[2] P.W. Higgs, Phys. Lett. **12** (1964) 132, Phys. Rev. Lett. **13** (1964) 508 and Phys. Rev. **145** (1966) 1156 ; F. Englert and R. Brout, Phys. Rev. Lett. **13** (1964) 321; G.S. Guralnik, C.R. Hagen and T.W.B. Kibble, Phys. Rev. Lett. **13** (1964) 585.

[3] P. Garcia-Abia and W. Lohmann, Eur. Phys. J. direct C **2** (2000) 2 [arXiv:hep-ex/9908065].

[4] ILC Software Portal: `http://www-flc.desy.de/ilcsoft`

[5] T. Sjostrand, S. Mrenna and P. Skands, JHEP **0605** (2006) 026 [arXiv:hep-ph/0603175].

[6] D. Schulte, Universität Hamburg (1996)

[7] S. Jadach, W. Placzek and B. F. L. Ward, Phys. Lett. B **390** (1997) 298 [arXiv:hep-ph/9608412].

[8] T. Gleisberg, S. Höche, F. Krauss, A. Schälicke, S. Schumann and J. C. Winter, JHEP **0402** (2004) 056 [arXiv:hep-ph/0311263].

[9] DOD, LDC Working Group: `http://www.ilcldc.org/documents/dod`

[10] F. Richard and P. Bambade, LAL-Orsay 07/03.

[11] Slides:
`http://ilcagenda.linearcollider.org/contributionDisplay.py?contribId=159&sessionId=71&confId=1296`

A Natural Nightmare for the LHC?

Thomas E.J. Underwood

Institute for Particle Physics Phenomenology (IPPP) - University of Durham
South Road, Durham, DH1 3LE - United Kingdom

A minimal lepton number conserving extension to the Standard Model is considered providing light Dirac neutrinos without resorting to tiny Yukawa couplings. Successful baryogenesis through leptogenesis is not only possible in this case, but even suggests an electroweak scale vacuum expectation value for a gauge singlet scalar in the model. The spectrum contains two massive Higgs bosons and a massless Nambu-Goldstone boson. The existence of the Nambu-Goldstone boson suppresses the Higgs to $b\bar{b}$ branching ratio and instead Higgs bosons will decay mainly into invisible Goldstone bosons. We consider the constraints on the potential and the implications for the LHC and ILC.

1   Introduction

It is (supposed to be) summer 2007. Physicists, the media and the general public are eagerly anticipating the start of LHC running. One of the primary aims of this immensely complex experiment is to uncover the mechanism underlying electroweak symmetry breaking – widely expected to be the Higgs mechanism. Central to this cause is the discovery of the Higgs boson, arguably the key to unravelling the reason why the $W^{\pm}$, the Z and indeed the other fundamental particles of the Standard Model have mass. But what if the LHC didn't see the Higgs? Not because it didn't exist, but because it decayed *invisibly* [1].

Nambu-Goldstone bosons, first considered in 1960 [2], have several special properties. In particular, they are massless and they couple to the divergence of the current j^{μ} associated with a spontaneously broken symmetry [3]. This coupling has a strength inversely proportional to the scale of the symmetry breaking F such that

$$\mathcal{L}_{\text{int}} \;=\; \frac{1}{2\,F}\,\mathcal{J}\,\partial_{\mu}j^{\mu}\,, \tag{1}$$

where $\mathcal{J}$ is the Nambu-Goldstone boson (NGB) field. Suzuki and Shrock [4] first proposed that if the Standard Model Higgs boson were to mix with a new scalar field that was charged under a spontaneously broken global symmetry, then it would decay into a pair of NGBs if the scale F was close to the electroweak scale, $F \approx 100$ GeV. Interestingly, such an invisible Higgs decay could actually be searched for at colliders, and the relatively clean environment of $e^{+}e^{-}$ machines makes them especially suited to this task [5].

This possibility seems less exotic when one considers that mixing between the SM Higgs H and a new complex scalar field Φ, $\mathcal{L}_{\text{int}} = H^{\dagger}H\Phi^{\dagger}\Phi$, is one of very few renormalizable operators allowed which could link the SM to a new gauge singlet sector i.e. Φ is charged under a new global symmetry G_P but singlet under the SM gauge group. In this way the Higgs provides a portal into a hidden, or "phantom" sector [6].

Another example of such a portal is the neutrino Yukawa coupling which links SM fields with a gauge singlet right-handed neutrino. This interaction is so commonly invoked that it is now normally considered as part of the SM. In this way, the usual (Majorana) see-saw mechanism is a very simple "phantom sector". The Majorana see-saw mechanism even

contains a broken global symmetry (lepton number) which in many extended models is spontaneously broken – leading to a NGB, the Majoron [7].

Stringent bounds can be placed on the coupling of massless particles to matter coming from considerations of energy loss in supernovae, stars and terrestrial collider experiments. For common NGBs such as Majorons, axions [8] and familions [9] these constraints generally mean that $F \gtrsim 10^9$ GeV. The underlying reason for such stringent bounds is that these NGBs couple to a current carried by quarks and/or charged leptons, e.g. lepton number in the case of the Majoron. If the NGB coupled to a current carried by gauge singlet matter (e.g. ν_R) then such stringent constraints on F would not apply.

2 Dirac neutrino masses and baryogenesis

Neutrinos are not necessarily Majorana particles. As yet, we have no firm evidence of neutrinoless double beta decay, a characteristic signature of the lepton number violation associated with Majorana neutrinos. Along the same lines as the Majorana see-saw mechanism, an operator generating naturally small, Dirac, neutrino masses is

$$\mathcal{L}_\nu = \frac{(\overline{L} \cdot \tilde{H})(\Phi \cdot \nu_R)}{\Lambda} , \qquad (2)$$

where L is the usual $SU(2)_L$ lepton doublet, $\tilde{H} \equiv i\,\sigma_2\,H$ is the SM Higgs doublet, ν_R is a gauge singlet right-handed neutrino and Φ is a new gauge singlet, complex scalar field.

In a model generating eq. (2), some global symmetry G_P carried by only by the gauge singlets Φ and ν_R prevents the neutrinos from acquiring masses via a $\overline{L} \cdot \tilde{H}\nu_R$ term in the Lagrangian. After the spontaneous breakdown of G_P and the electroweak symmetry, eq. (2) results in naturally small Dirac neutrino masses if the vacuum expectation values (VEVs) $\langle\Phi\rangle \approx \langle H\rangle \approx 100$ GeV provided that $\Lambda \sim 10^{16}$ GeV. A model generating the operator (2) was first considered by Roncadelli and Wyler [10].

Although lepton number is conserved in this model, it was recently shown [11] that the model could lead to successful baryogenesis via (Dirac) leptogenesis [12]. This is possible because the model of [10] contains heavy Dirac states, S and $\bar{S}$ much like the heavy, but Majorana, right-handed neutrinos of the usual see-saw. In the early Universe the S particles decay into neutrinos and Higgs scalars. Significantly, CP can be violated in this decay process. After the S have decayed, no reaction can take place quickly enough to bring the left and right-handed neutrinos into equilibrium – this is related to the smallness of the light neutrino masses. Matter/antimatter asymmetries in the left and right-handed neutrino sectors, produced during the CP-violating decays of the S, cannot equilibrate and a net lepton asymmetry remains amongst the left-handed $SU(2)_L$ doublet leptons. Rapid $B + L$ violating processes in the early Universe, which are insensitive to asymmetries in the gauge singlet ν_R, convert this lepton asymmetry into a baryon asymmetry.

Under reasonable assumptions, one can derive approximate limits on the VEV of the singlet scalar field Φ [11], 0.1 GeV $\lesssim \langle\Phi\rangle \lesssim \frac{2\,\text{TeV}}{T_{RH}}$, where T_{RH} is the reheating temperature of the Universe after inflation.

3 Higgs phenomenology

In models containing a singlet scalar Φ charged under a new global symmetry, e.g. $G_P = U(1)_P$, nothing prevents the term, $\mathcal{L}_{\text{link}} = \eta\,H^\dagger\,H\,\Phi^*\,\Phi$, from appearing in the Lagrangian,

where η is a new dimensionless coupling. After the spontaneous breakdown of U(1)$_P$ and electroweak symmetry the two massive Higgs bosons in the model mix. The spectrum also contains a massless NGB $\mathcal{J}$ associated with the breakdown of U(1)$_P$. The Higgs bosons will couple to this NGB [4] as

$$\mathcal{L}_{\text{int}} = \frac{1}{2\langle\Phi\rangle} \mathcal{J}\,\partial_\mu j^\mu \rightarrow -\frac{m_{H_i}}{\langle\Phi\rangle} O_{2i}\, H_i\, \mathcal{J}\mathcal{J}\,, \tag{3}$$

where O_{2i} is a mixing matrix element parameterizing the mixing of the massive H_i. Hence, the massive Higgs bosons H_i will decay into the massless and invisible $\mathcal{J}$ [13]. For Higgs masses $m_{H_i} \lesssim 130$ GeV the dominant decay mode of the Standard Model Higgs is $H \rightarrow b\bar{b}$. Comparing the rates $\Gamma(H_1 \rightarrow b\bar{b})$ and $\Gamma(H_1 \rightarrow \mathcal{J}\mathcal{J})$ it can be shown that for 20 GeV $\lesssim m_{H_1} \lesssim 130$ GeV the Higgs will dominantly decay into invisible $\mathcal{J}\mathcal{J}$.

LEP, LHC and ILC Higgs phenomenology is influenced by the number of visible Higgs decay events seen as compared to the SM expected value. This is quantified by the parameter $\mathcal{R}^2$ defined as

$$\mathcal{R}_i^2 \equiv \frac{\sigma(pp \rightarrow H_i\, X)\,\text{Br}(H_i \rightarrow YY)}{\sigma(pp \rightarrow h_{\text{SM}}\, X)\,\text{Br}(h_{\text{SM}} \rightarrow YY)}\,, \quad \mathcal{T}_i^2 \equiv \frac{\sigma(pp \rightarrow H_i\, X)}{\sigma(pp \rightarrow h_{\text{SM}}\, X)}\,\text{Br}(H_i \rightarrow \mathcal{J}\mathcal{J})\,, \tag{4}$$

where YY is a visible final state such as $b\bar{b}$ or $\gamma\gamma$, and $\mathcal{T}^2$ is the analogous parameter for invisible decays.

Looking to the future, both the ATLAS and CMS experiments have performed detailed studies exploring the discovery potential of their detectors in cases where Higgs bosons decay to visible final states [14] and also invisible final states [15]. Considering $\mathcal{L} = 30$ fb^{-1} of LHC integrated luminosity, it can be estimated that it would be difficult to discover a visibly decaying Higgs if $\mathcal{R}_i \lesssim 0.2$. Furthermore, ATLAS studies [15] indicate that with the same amount of integrated luminosity, invisible Higgs bosons with $m_{H_i} \lesssim 200$ GeV could be excluded only if $\mathcal{T}_i^2 \gtrsim 0.3$.

Figure 1 (left) shows the areas where either $\mathcal{R}_i^2 \geq 0.3$ or $\mathcal{T}_i^2 \geq 0.3$ in the m_{H_1} vs. $m_{H_2} - m_{H_1}$ plane. The plot assumes maximal mixing and $\langle\Phi\rangle = \langle H\rangle$. It is clear that a "nightmare" region remains where no Higgs bosons are accessible to the LHC if experiments do not have the sensitivity to see into areas where $\mathcal{R}_i^2 \leq 0.3$ and $\mathcal{T}_i^2 \leq 0.3$.

4 Triviality and vacuum stability

The potential of the model being considered reads

$$V = \mu_H^2 H^\dagger H + \mu_\Phi^2 \Phi^\dagger \Phi + \lambda_H (H^\dagger H)^2 + \lambda_\Phi (\Phi^* \Phi)^2 - \eta H^\dagger H \Phi^* \Phi\,. \tag{5}$$

There are two classic constraints regarding this potential; triviality and vacuum stability. The triviality constraint is essentially the requirement that the couplings λ_H, λ_Φ and η stay perturbative up to a certain scale $\Lambda_T \gg \langle H\rangle$. Demanding the vacuum is stable leads to the requirement that the potential is bounded from below, at least up to a scale $\Lambda_V \gg \langle H\rangle$. The vacuum stability bound can be reduced to the requirement that $4\lambda_H(Q)\,\lambda_\Phi(Q) > \eta(Q)^2$, at all scales $Q \lesssim \Lambda_V$.
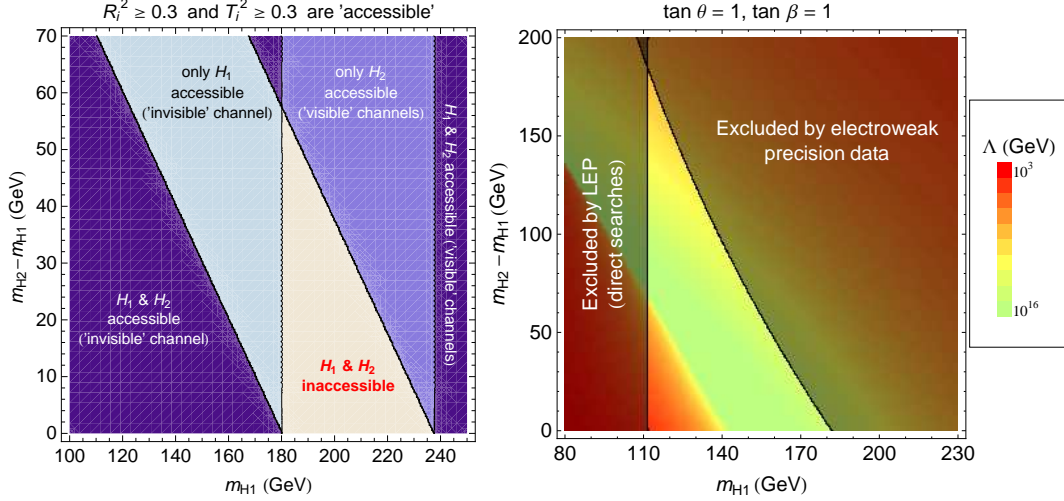
Figure 1: *The m_{H_1} vs. $m_{H_2} - m_{H_1}$ plane for $\tan\beta = 1$ and $\tan\theta = 1$. The left panel shows where different Higgs bosons are accessible. We define that a given H_i is accessible if either $\mathcal{R}_i^2 \geq 0.3$ or $\mathcal{T}_i^2 \geq 0.3$. In the dark (blue) regions both Higgs bosons are accessible. In the white (beige) region no Higgs bosons are accessible. The right panel shows the expected cut-off Λ, of the effective theory taking the triviality and positivity of the potential into account (the lower of either Λ_T or Λ_V is shown). The curved line shows the 95% C.L. upper limit on the Higgs masses coming from precision electroweak data (see [11]).*

The running parameters, defined at a scale $Q_0 = M_Z$ can be evolved up to higher scales with 1-loop renormalization group equations [16]

$$
\begin{aligned}
16\pi^2 \frac{d\lambda_H}{dt} &= \eta^2 + 24\,\lambda_H^2 + 12\,\lambda\,Y_t^2 - 6\,Y_t^4 - 3\lambda(3\,g_2^2 + g'^2) + \frac{3}{8}\left[2\,g_2^4 + (g_2^2 + g'^2)^2\right], \\
16\pi^2 \frac{d\eta}{dt} &= \eta\left[12\,\lambda_H + 8\,\lambda_\Phi - 4\,\eta + 6\,Y_t - \frac{3}{2}(3\,g_2^2 + g'^2)\right], \\
16\pi^2 \frac{d\lambda_\Phi}{dt} &= 2\,\eta^2 + 20\,\lambda_\Phi^2,
\end{aligned}
\tag{6}
$$

where $t \equiv \ln Q/Q_0$, g' and g_2 are respectively the U(1)$_Y$ and SU(2)$_L$ gauge couplings and Y_t is the top quark Yukawa coupling.

Figure 1 (right) shows the m_{H_1} vs. $m_{H_2} - m_{H_1}$ plane assuming $\langle\Phi\rangle = \langle H\rangle$ and maximal mixing, where the background colours show the scale of new physics Λ required either by positivity of the potential or triviality (whichever is lower). The plots can be compared to see that a region which is difficult to access at the LHC does in fact coincide with a potentially high effective theory cut-off. Furthermore, this region is compatible with constraints from LEP (using visible, invisible and model-independent Higgs searches [17]) and precision electroweak data (see ref. [11]).

Further investigation into the prospects for finding both potentially invisible Higgs bosons in this minimal model are currently underway, making use of the SHERPA event generator [18].

I would like to thank Sakis Dedes, Frank Krauss, Terrance Figy and David Cerdeno for collaboration.

References

[1] Slides:
http://ilcagenda.linearcollider.org/contributionDisplay.py?contribId=160&sessionId=71&confId=1296

[2] Y. Nambu, Phys. Rev. Lett. **4**, 380 (1960); J. Goldstone, Nuovo Cim. **19** (1961) 154.

[3] J. Goldstone, A. Salam and S. Weinberg, Phys. Rev. **127**, 965 (1962).

[4] R. E. Shrock and M. Suzuki, Phys. Lett. B **110**, 250 (1982).

[5] e.g. the previous talk:
http://ilcagenda.linearcollider.org/contributionDisplay.py?contribId=159&sessionId=71&confId=1296

[6] B. Patt and F. Wilczek, arXiv:hep-ph/0605188.

[7] Y. Chikashige, R. N. Mohapatra and R. D. Peccei, Phys. Lett. B **98**, 265 (1981); G. B. Gelmini and M. Roncadelli, Phys. Lett. B **99**, 411 (1981).

[8] S. Weinberg, Phys. Rev. Lett. **40**, 223 (1978); F. Wilczek, Phys. Rev. Lett. **40**, 279 (1978).

[9] F. Wilczek, Phys. Rev. Lett. **49**, 1549 (1982).

[10] M. Roncadelli and D. Wyler, Phys. Lett. B **133** (1983) 325.

[11] D. G. Cerdeno, A. Dedes and T. E. J. Underwood, JHEP **0609** (2006) 067.

[12] K. Dick, M. Lindner, M. Ratz and D. Wright, Phys. Rev. Lett. **84** (2000) 4039.

[13] A. S. Joshipura and S. D. Rindani, Phys. Rev. Lett. **69** (1992) 3269; A. S. Joshipura and J. W. F. Valle, Nucl. Phys. B **397** (1993) 105.

[14] e.g. F. Gianotti and M. L. Mangano, arXiv:hep-ph/0504221.

[15] F. Meisel, M. Dührssen, M. Heldmann, K. Jakobs, ATL-PHYS-PUB-2006-009; L. Neukermans, B. Di Girolamo, ATL-PHYS-2003-006.

[16] C. F. Kolda and H. Murayama, JHEP **0007**, 035 (2000); R. Schabinger and J. D. Wells, Phys. Rev. D **72**, 093007 (2005).

[17] S. Schael *et al.* [ALEPH Collaboration], Eur. Phys. J. C **47**, 547 (2006) [arXiv:hep-ex/0602042].
R. Barate *et al.* [ALEPH Collaboration], Phys. Lett. B **466**, 50 (1999); Phys. Lett. B **450**, 301 (1999); M. Acciarri *et al.* [L3 Collaboration], Phys. Lett. B **485**, 85 (2000) [arXiv:hep-ex/0004006]; [LEP Higgs Working for Higgs boson searches Collaboration], arXiv:hep-ex/0107032; G. Abbiendi [OPAL Collaboration], arXiv:0707.0373 [hep-ex].
G. Abbiendi *et al.* [OPAL Collaboration], Eur. Phys. J. C **18** (2001) 425 [arXiv:hep-ex/0007040].

[18] A. Dedes, T. Figy, F. Krauss, T. E. J. Underwood, *to appear*.

Light Pseudoscalars in Little Higgs Models at the ILC

Jürgen Reuter

Albert-Ludwigs-Universität Freiburg - Physikalisches Institut
Hermann-Herder-Str. 3, D-79104 Freiburg - Germany

We discuss the properties of light pseudoscalar particles, the so-called pseudoaxions, within Little Higgs models, focusing on their phenomenology at the ILC. We especially discuss a method of how to distinguish between the two basic classes of Little Higgs models, the product and simple group models, by a specific production channel and decay mode. These are strictly forbidden in the product group models.

1 Little Higgs Models

Little Higgs Models [2] provide a solution to the hierarchy problem, as they stabilize the Higgs boson against quadratic divergences at the one-loop level by the mechanism of collective symmetry breaking: the Higgs is charged under two global symmetry groups, which both need to be broken in order to lift the flat direction in the potential of the Higgs boson and make it a pseudo-Nambu-Goldstone boson (PNGB). During the last years a bewilderment of different models has been developed.
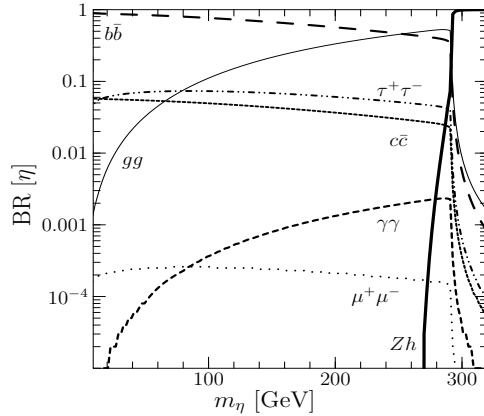
Figure 1: Branching ratios of the pseudoaxion in the Simplest Little Higgs as a function of its mass.

These models can be classified in three different categories, the so-called moose models with a moose diagram structure of links of global and local symmetry groups, the product-group models and the simple-group models. In the product-group models (the most-studied case is the Littlest Higgs) the electroweak gauge group is doubled, broken down to the group $SU(2)_L$, while the Higgs shares together with the other PNGBs an irreducible representation of the coset space of the global symmetry breaking. On the other hand, in simple-group models the electroweak gauge group is enlarged to a simple $SU(N)$ group, while the Higgs is distributed over several multiplets of the global symmetry group, which usually has a product group structure similar to chiral symmetries in QCD [3]. For an overview, see [4].

The two crucial scales in the Little Higgs set-up are the cut-off scale Λ where the models are embedded in a UV-complete theory (usually a strongly-interacting theory with a partonic substructure of the PNGBs) and the intermediate scale F which determines the masses and decay constants of the PNGBs (except for the Higgs which is down at v by the collective symmetry breaking mechanism). Electroweak precision observables and direct search limits [5] tell us that the scale F must be at least of the order of $1 - 2$ TeV. Paradoxically, the Higgs boson in Little Higgs models tends to be quite heavy compared to the Standard

Model or the MSSM, of the order of $200 - 600$ GeV [6]. For Little Higgs model scales that high most new particles will be produced close to the kinematical limit at the LHC, such that a precision determination of their parameters might be difficult. Furthermore, also the sensitivity of the ILC in indirect measurements might be limited, if the new phyics does couple to SM fermions only very weakly [7]. A method to distinguish between different models, especially at the LHC, is highly welcome. Such a method will be presented here.

2 Pseudoaxions in Little Higgs models

Little Higgs models generally have a huge global symmetry group, which contains not only products of simple groups but also a certain number of $U(1)$ factors. These Abelian groups can either be gauged, in which case they lead to a Z' boson, or they are only (approximate) global symmetries. In the latter case there is a pseudo-Goldstone boson attached to that spontaneously broken global $U(1)$ factor [8]. The number of pseudoaxions in a given model is determined by the mismatch between the rank reduction in the global and the local symmetry group, since it gives the number of uneaten bosons. In the Littlest Higgs, e.g., there is one such pseudoaxion, in the Simplest Little Higgs [9] there is one, in the original simple group model there are two, in the minimal moose model there are four, and so on.

These particles are electroweak singlets, hence all couplings to SM particles are sup-

Figure 2: Cross section for the $H\eta$ associated production at ILC, taking into account the destructive Z/Z' interference. The full, dashed and dotted lines correspond to $m_\eta = 309/200/50$ GeV, respectively.

pressed by the ratio of the electroweak over the Little Higgs scale, v/F. There mass lies in the range from several GeV to a few hundred GeV, being limited by a naturalness argument and the stability of the Coleman-Weinberg potential. For the Simplest Little Higgs, on whose phenomenology we will concentrate here, there is a seesaw between the Higgs and the pseudoscalar mass [8], determined by the explicit symmetry breaking parameter μ, where $m_\eta \approx \sqrt{2}\mu$. Since the pseudoaxions inherit the Yukawa coupling structure from the Higgs bosons, they decay predominantly to the heaviest available fermions in the SM, and because of the absence of the WW and ZZ modes, the anomaly-induced decays gg and $\gamma\gamma$ are sizable over a wide mass range, cf. Fig. 1. From this, one can see that as soon as the decay to HZ is kinematically allowed, it dominates completely. Such a ηHZ coupling, which is possible only after electroweak symmetry breaking and hence proportional to v/F, is only allowed in simple group models and is forbidden to all orders in product group models. One can factor out the $U(1)_\eta$ group from the matrix of pseudo-Goldstone bosons. We use $\xi = \exp[i\eta/F]$ for the pseudo-axion field and $\Sigma = \exp[i\Pi/F]$ for the non-linear representation of the remaining Goldstone multiplet Π of Higgs and other heavy scalars. Then, for product group models,

Figure 3: ILC cross section, left: small-mass η with final state Hbb, right intermediate mass with final state Hgg. The dotted line is without the Z/Z' interference, the dashed one the SM background.

the kinetic term may be expanded as

$$\mathcal{L}_{\text{kin.}} \sim F^2 \text{Tr}\left[(D^\mu(\xi\Sigma))^\dagger (D_\mu(\xi\Sigma))\right] = \ldots - 2F(\partial_\mu\eta)\,\text{Im}\text{Tr}\left[(D^\mu\Sigma)^\dagger\Sigma\right] + O(\eta^2), \qquad (1)$$

where we write only the term with one derivative acting on ξ and one derivative acting on Σ. This term, if nonzero, is the only one that can yield a $ZH\eta$ coupling.

We now use the special structure of the covariant derivatives in product group models, which is the key to the Little Higgs mechanism: $D_\mu\Sigma = \partial_\mu\Sigma + A_{1,\mu}^a\left(T_1^a\Sigma + \Sigma(T_1^a)^T\right) + A_{2,\mu}^a\left(T_2^a\Sigma + \Sigma(T_2^a)^T\right)$, where $T_i^a, i = 1, 2$ are the generators of the two independent $SU(2)$ groups, and $A_{i,\mu}^a = W_\mu^a +$ heavy fields. Neglecting the heavy gauge fields and extracting the electroweak gauge bosons, we have $\text{Tr}\left[(D^\mu\Sigma)^\dagger\Sigma\right] \sim W_\mu^a\text{Tr}\left[(T_1^a + T_2^a) + (T_1^a + T_2^a)^*\right] = 0$. This vanishes due to the zero trace of $SU(2)$ generators. The same is true when we include additional $U(1)$ gauge group generators such as hypercharge, since their embedding in the global simple group forces them to be traceless as well. We conclude that the coefficient of the $ZH\eta$ coupling vanishes to all orders in the $1/F$ expansion.

Next, we consider the simple group models, where we use the following notation for the nonlinear sigma fields: $\Phi\zeta$, where $\Phi = \exp[i\Sigma/F]$ and $\zeta = (0, \ldots 0, F)^T$ is the vev directing in the N direction for an $SU(N)$ simple gauge group extension of the weak group. Thus, in simple group models the result is the N, N component of a matrix:

$$\mathcal{L}_{\text{kin.}} \sim F^2 D^\mu(\zeta^\dagger\Phi^\dagger)D_\mu(\Phi\zeta) = \ldots + iF(\partial_\mu\eta)\left(\Phi^\dagger(D_\mu\Phi) - (D_\mu\Phi^\dagger)\Phi\right)_{N,N}. \qquad (2)$$

We separate the last row and column in the matrix representations of the Goldstone fields Σ and gauge boson fields $\mathbf{V}_\mu$: the Higgs boson in simple group models sits in the off-diagonal entries of Σ, while the electroweak gauge bosons reside in the upper left corner of $\mathbf{V}_\mu$. With the Baker-Campbell-Hausdorff identity, one gets for the term in parentheses in Eq. (2):

$$\mathbf{V}_\mu + \frac{i}{F}[\Sigma, \mathbf{V}_\mu] - \frac{1}{2F^2}[\Sigma, [\Sigma, \mathbf{V}_\mu]] + \ldots$$
$$= \begin{pmatrix} \mathbf{W}_\mu & 0 \\ 0 & 0 \end{pmatrix} + \frac{i}{F}\begin{pmatrix} 0 & -\mathbf{W}_\mu h \\ h^\dagger\mathbf{W}_\mu & 0 \end{pmatrix} - \frac{1}{2F^2}\begin{pmatrix} hh^\dagger\mathbf{W} + \mathbf{W}hh^\dagger & 0 \\ 0 & -2h^\dagger\mathbf{W}h \end{pmatrix} + \ldots \quad (3)$$

The N, N entry can only be nonzero from the third term on. The first term, would be a mixing between the η and the Goldstone boson(s) for the Z' state(s) and cancels with the help of the many-multiplet structure. If the N, N component of the second term were nonzero, it would induce a $ZH\eta$ coupling without insertion of a factor v. This is forbidden by electroweak symmetry. To see this, it is important to note that in simple group models the embedding of the Standard Model gauge group always works in such a way that hypercharge is a linear combination of the T_{N^2-1} and $U(1)$ generators. This has the effect of canceling the γ and Z from the diagonal elements beyond the first two positions, and preventing the diagonal part of $\mathbf{W}_\mu$ from being proportional to τ^3. The third term in the expansion yields a contribution to the $ZH\eta$ coupling, $(\partial^\mu\eta)h^\dagger\mathbf{W}_\mu h \sim vHZ_\mu\partial^\mu\eta$.

The crucial observation is that the matrix-representation embedding of the two non-Abelian $SU(2)$ gauge groups, and especially of the two $U(1)$ factors within the irreducible multiplet of the pseudo-Goldstone bosons of one simple group (e.g. $SU(5)$ in the Littlest Higgs), is responsible for the non-existence of this coupling in product group models. It is exactly the mechanism which cancels the quadratic one-loop divergences between the electroweak and heavy $SU(2)$ gauge bosons which cancels this coupling. In simple group models the Higgs mass term cancellation is taken over by enlarging $SU(2)$ to $SU(N)$, and the enlarged non-Abelian rank structure cancels the quadratic divergences in the gauge sector – but no longer forbids the $ZH\eta$ coupling. Hence, its serves as a discriminator between the classes of models.
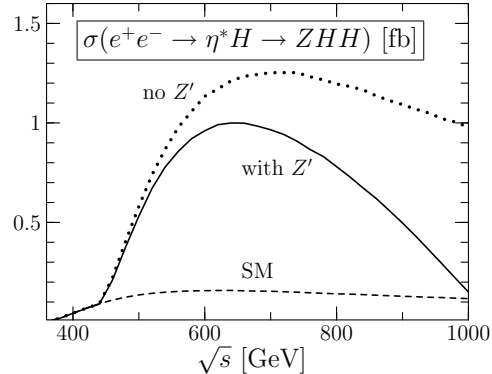
Figure 4: ILC cross section for a high-mass η with final state ZHH. The dotted line is without the Z/Z' interference, the dashed one the SM background.

3 ILC phenomenology

The pseudoaxion can be discovered at the LHC in gluon fusion and observed in the rare decay mode $\gamma\gamma$ [8]. But the ηHZ coupling can be observed at the LHC only if either one of the decays $H \to Z\eta$ or $\eta \to ZH$ is kinematically allowed. This leaves large holes in parameter space, which can be covered by a $500-1000$ GeV ILC, depending on the masses. Here, we focus on the discovery potential of the ILC for the pseudoaxions, assuming the presence of the $ZH\eta$ coupling. We focus on the Simplest Little Higgs with parameters chosen to fulfill the low-energy constraints. The production happens via an s-channel Z exchange, in association with a Higgs boson like in a two-Higgs-model. Fig. 2 shows the cross section as a function of $\sqrt{s}$ for three different values of the η mass. The simulations for the processes discussed here have been performed with the WHIZARD/OMEGA package [11, 12, 13], which is ideally suited for physics beyond the SM [14]. In the following, we assume that the Higgs properties are already known from LHC, and that the Higgs can be reconstructed. In Fig. 3 and 4 we show the three different possible final states, depending on the dominant branching ratio of the pseudoaxion: for low masses (up to approx. 150 GeV) this is $b\bar{b}$, in an interme-

diate range (between 150 GeV and 270 GeV) the gg (hence dijet) mode is largest, while ZH sets in above masses of 270 GeV. The figures show the effect of a destructive Z/Z' interference, which brings cross sections down by a factor of two at the peak, but never endangers visibility. SM backgrounds are nowhere an issue, from marginal for Hjj to negligible in the Hbb case. Interesting is the ZHH final state which is important for measuring the triple Higgs coupling [15]. In the SM the cross section is at the borderline of detectability, but Fig. 4 shows that rates are larger by factors two to six in the Simplest Little Higgs with the intermediate pseudoaxion. In conclusion, the ILC provides an ideal environment for discovering pseudoaxions and measuring their properties. The $ZH\eta$ coupling provides tool for the discrimination between simple and product group models.

4 Acknowledgments

5 Bibliography

References

[1] Slides:
http://ilcagenda.linearcollider.org/contributionDisplay.py?contribId=162&sessionId=71&confId=1296

[2] N. Arkani-Hamed *et al.*, JHEP **0208** (2002) 021; N. Arkani-Hamed, A. G. Cohen, H. Georgi, Phys. Lett. B **513** (2001) 232; N. Arkani-Hamed, A. G. Cohen, T. Gregoire, and J. G. Wacker, JHEP **0208** (2002) 020; N. Arkani-Hamed, A. G. Cohen, E. Katz, and A. E. Nelson, JHEP **0207** (2002) 034.

[3] D. E. Kaplan and M. Schmaltz, JHEP **0310** (2003) 039.

[4] M. Schmaltz and D. Tucker-Smith, Ann. Rev. Nucl. Part. Sci. **55**, 229 (2005); M. Perelstein, Prog. Part. Nucl. Phys. **58**, 247 (2007); S. Heinemeyer *et al.*, hep-ph/0511332; S. Kraml *et al.*, CPNSH report.

[5] C. Csáki *et al.*, Phys. Rev. D **67** (2003) 115002; Phys. Rev. D **68** (2003) 035009; J. L. Hewett, F. J. Petriello, and T. G. Rizzo, JHEP **0310** (2003) 062; M.-C. Chen and S. Dawson, Phys. Rev. D **70** (2004) 015003. T. Han, H. E. Logan, B. McElrath, and L.-T. Wang, Phys. Rev. D **67** (2003) 095004; G. Burdman, M. Perelstein, and A. Pierce, Phys. Rev. Lett. **90** (2003) 241802 M. Perelstein, M. E. Peskin, and A. Pierce, Phys. Rev. D **69** (2004) 075002; T. Han, H. E. Logan and L. T. Wang, JHEP **0601**, 099 (2006); A. J. Buras *et al.* JHEP **0611**,062 (2006); G. Azuelos *et al.*, Eur. Phys. J. C **39S2**, 13 (2005); B. C. Allanach *et al.*, hep-ph/0602198; K. Cheung *et al.*, hep-ph/0608259; J. Boersma, Phys. Rev. **D74**, 115008 (2006).

[6] W. Kilian and J. Reuter, Phys. Rev. D **70** (2004) 015004.

[7] M. Beyer *et al.*, Eur. Phys. J. C **48**, 353 (2006); W. Kilian and J. Reuter, hep-ph/0507099.

[8] W. Kilian, D. Rainwater and J. Reuter, Phys. Rev. D **71**, 015008 (2005); hep-ph/0507081.

[9] M. Schmaltz, JHEP **0408** (2004) 056.

[10] W. Kilian, D. Rainwater and J. Reuter, Phys. Rev. D **74**, 095003 (2006).

[11] T. Ohl, *O'Mega: An Optimizing Matrix Element Generator*, hep-ph/0011243; M. Moretti, T. Ohl, J. Reuter, hep-ph/0102195; J. Reuter, arXiv:hep-th/0212154.

[12] W. Kilian. *WHIZARD*, 2nd ECFA/DESY Study 1998-2001, 1924-1980, LC-TOOL-2001-039, Jan 2001.

[13] http://whizard.event-generator.org; W. Kilian, T. Ohl, J. Reuter, to appear in Comput. Phys. Commun., arXiv:0708.4233 [hep-ph].

[14] T. Ohl and J. Reuter, Eur. Phys. J. C **30**, 525 (2003); Phys. Rev. D **70**, 076007 (2004); K. Hagiwara *et al.*, Phys. Rev. D **73**, 055005 (2006); J. Reuter *et al.*, arXiv:hep-ph/0512012; W. Kilian, J. Reuter and T. Robens, Eur. Phys. J. C **48**, 389 (2006)

[15] A. Djouadi, W. Kilian, M. Mühlleitner and P. M. Zerwas, Eur. Phys. J. C **10**, 27 (1999).

New physics effect on the top-Yukawa coupling at ILC

Shinya Kanemura[1], Koichi Matsuda[2], Daisuke Nomura[3], and Koji Tsumura[3][*][†]

1- Department of Physics, University of Toyama
3190 Gofuku, Toyama 930-8555, Japan

2- Center for High Energy Physics, Tsinghua University
Beijing, 100084, China

3- Theory Group, KEK
1-1 Oho, Tsukuba 305-0801, Japan

Measurement of the top-Yukawa coupling is important to understand the fermion mass generation mechanism and dynamics of electroweak symmetry breaking. We discuss the top quark anomalous couplings which can be described by higher dimensional operators. We investigate the process $e^-e^+ \to W^-W^+\nu\bar{\nu} \to t\bar{t}\nu\bar{\nu}$ to study the contribution of the anomalous top-Higgs coupling to the cross section. The effect of the dimension-six top-Higgs interaction on the cross section can be a few hundred percent greater than the SM prediction. Such a large effect can be measured at the International Linear Collider.

1 Introduction

The mass of the top quark has been measured to be at the scale of the electroweak symmetry breaking, so that the top-Yukawa coupling has turned out to be of order one in the standard model (SM). It is a quite natural scale as compared to the other quarks. This fact would indicate a relation between the top quark physics and the dynamics of electroweak symmetry breaking. Top quark motivated models such as the top mode condensation, top color models, and top flavor models have been discussed in literature. These models generally predict rather strong dynamics for the electroweak symmetry breaking. Measuring the top-Yukawa coupling is essentially important not only to confirm the SM but also to test new physics models including them.

Information of Higgs coupling constants can be extracted at future experiments. However, measurement of the top-Yukawa coupling may be difficult because of the huge QCD backgrounds. Determination of the coupling constants can be performed at the International Linear Collider (ILC). At the ILC, the top-Yukawa interaction is expected to be measured through the process $e^-e^+ \to t\bar{t}H$[2] for a relatively light Higgs boson when it is kinematically allowed. For a heavier Higgs boson, it would be detectable via the vector boson fusion process $e^-e^+ \to W^-W^+\nu\bar{\nu} \to t\bar{t}\nu\bar{\nu}$[3] in Fig.1.

2 Dimension-six top quark operators

At low energies, the non-SM interaction can be expressed by using the higher dimensional operators. Such operators are introduced by integrating out the heavy new physics particles.
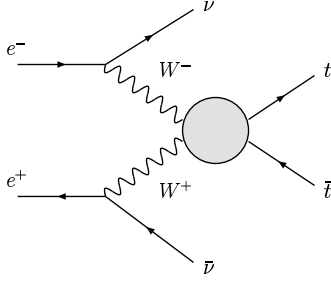
Figure 1: The top pair production via W boson fusion

In this section, we study the dimension-six operators which affect the top quark interaction.

Below the SM cutoff scale Λ, the new physics effect which is related to the top quark can be described by the effective Lagrangian as

$$\mathcal{L}_{\mathrm{eff}} = \mathcal{L}_{\mathrm{SM}} + \mathcal{L}_{\mathrm{dim.6}} + \mathcal{L}_{\mathrm{dim.8}} + \cdots , \qquad (1)$$

where $\mathcal{L}_{\mathrm{SM}}$ is the SM Lagrangian, and

$$\mathcal{L}_{\mathrm{dim.}n} = \frac{1}{\Lambda^{n-4}} \sum_i C_i \mathcal{O}_i^{(n)}, \quad (n \geq 6), \qquad (2)$$

where $\mathcal{O}_i^{(n)}$ are $SU(2)_L \times U(1)_Y$ gauge invariant dimension-n operators, and C_i are the coupling strength of $\mathcal{O}_i^{(n)}$. In this talk, we treat only the dimension-six operators because they should give the new physics interaction.

The dimension-six operators have been already discussed in literature. All the gauge invariant operators are given in Refs. [4, 5]. We concentrate on the CP-conserving top quark operators whose coefficients are real,

$$\begin{aligned}
\mathcal{O}_{t1} &= \left(\Phi^\dagger \Phi - \frac{v^2}{2} \right) \left(\bar{q}_L t_R \tilde{\Phi} + \mathrm{H.c.} \right), \\
\mathcal{O}_{t2} &= i \left(\Phi^\dagger D_\mu \Phi \right) \bar{t}_R \gamma^\mu t_R + \mathrm{H.c.}, \\
\mathcal{O}_{t3} &= i \left(\tilde{\Phi}^\dagger D_\mu \Phi \right) \bar{t}_R \gamma^\mu b_R + \mathrm{H.c.}, \\
\mathcal{O}_{Dt} &= \left(\bar{q}_L D_\mu t_R \right) \left(D^\mu \tilde{\Phi} \right) + \mathrm{H.c.}, \\
\mathcal{O}_{tW\Phi} &= \left(\bar{q}_L \sigma^{\mu\nu} \vec{\tau} t_R \right) \tilde{\Phi} \vec{W}_{\mu\nu} + \mathrm{H.c.}, \\
\mathcal{O}_{tB\Phi} &= \left(\bar{q}_L \sigma^{\mu\nu} t_R \right) \tilde{\Phi} B_{\mu\nu} + \mathrm{H.c.},
\end{aligned} \qquad (3)$$

where $q_L = (t_L, b_L)^T$, Φ is the scalar isospin doublet (the Higgs doublet) with hypercharge $Y = 1/2$, and $\tilde{\Phi} \equiv i\tau_2 \Phi^*$ with τ_i ($i = 1$–3) being the Pauli matrices. The dimension-six operators for the tau-Yukawa coupling have been discussed in Ref. [6].

Because we have not measured any Higgs coupling yet, the size of the anomalous coupling C_{t1} is completely free from constraints from the experimental data. The top quark gauge

C_i	Set A	Set B	Set C	Set D	Set E
C_{t1}	0	$-\frac{16\pi}{3\sqrt{2}}\frac{\Lambda}{v}$	$+\frac{16\pi}{3\sqrt{2}}\frac{\Lambda}{v}$	0	0
C_{Dt}	0	0	0	$+10.2$	-6.2

Table 1: Sets of the dimension-six couplings we used for the analyses.

interaction can be directly constrained by the Tevatron, but there are no severe bounds due to lower statistics. From the indirect measurement, the LEP precision results can give a stringent limit to the anomalous couplings C_i[7]. The coupling C_{Dt} is subject to weaker bound than the others. We here set the coupling strength of $\mathcal{O}_{t2}, \mathcal{O}_{t3}, \mathcal{O}_{tW\Phi}, \mathcal{O}_{tB\Phi}$ to be zero. The couplings C_i of the dimension-six operators can be constrained by perturbative unitarity[8]. Their bounds for C_{t1} and C_{Dt} are evaluated as[7]

$$|C_{t1}| \leq \frac{16\pi}{3\sqrt{2}}\left(\frac{\Lambda}{v}\right), \tag{4}$$

$$-6.2 \leq C_{Dt} \leq 10.2, \tag{5}$$

where $v \,(\simeq 246\text{GeV})$ is the vacuum expectation value of the Higgs boson.

3 New Physics effect on the top-Yukawa coupling

In this section, we study the phenomenology of the new physics effect in terms of the dimension-six operators. Han et al. have discussed those on the process of $e^-e^+ \to t\bar{t}H$[9]. Those effects on the W-boson fusion $e^-e^+ \to W^-W^+\nu\bar{\nu} \to t\bar{t}\nu\bar{\nu}$ are discussed in Ref. [10].

The W-boson fusion process has been studied in the SM[11, 12], and its QCD correction has also been studied in Ref. [13]. In the SM without the Higgs boson, instead of including the dimension-five operators, this process has been investigated in Ref. [14].

Since we have introduced the dimension-six top-Higgs interaction, the partial decay width for the process $H \to t\bar{t}$ is modified at tree level, which is obtained by using the effective top-Yukawa coupling

$$y_t^{\text{eff}}(q^2, \Lambda) = y_t^{\text{SM}} - v^2\frac{C_{t1}}{\Lambda^2} - q^2\frac{C_{Dt}}{2\Lambda^2}. \tag{6}$$

The loop induced decay widths of $H \to \gamma\gamma, Z\gamma, gg$ are also given by replacing y_t^{SM} by $y_t^{\text{eff}}(m_H^2)$ in the corresponding SM expressions. In Fig. 2, the values of the total width of the Higgs boson are shown for each set of the dimension-six couplings in Tab. 1 , according to the unitarity bounds. Set A corresponds to the SM case. The decay modes $H \to t\bar{t}$ (tree), $H \to \gamma\gamma$, $H \to \gamma Z$ and $H \to gg$ (one loop) are largely modified at the leading order by the inclusion of $\mathcal{O}_{t1}$ and $\mathcal{O}_{Dt}$.

We here evaluate the cross section of the full process $e^-e^+ \to W^-W^+\nu\bar{\nu} \to t\bar{t}\nu\bar{\nu}$ in the method of the effective W-boson approximation (EWA)[15] by combining the result of calculation of the subprocess. We also evaluated the cross section by the full matrix element calculation by using CalcHEP[16] (and LanHEP[17]), and compared the consistency with the EWA results. The EWA gives reasonable results for a large value of $\sqrt{\hat{s}}$ as compared to m_W. In order to keep the validity of the calculation based on the EWA, we need to make
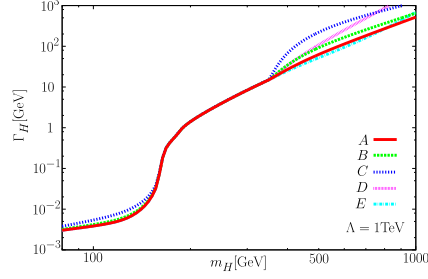
Figure 2: The total width of the Higgs boson for several cases of C_{t1} and C_{Dt} . Λ is set to be 1 TeV.

the kinematic cut at an appropriate value. Here we employ the cut $M_{tt} > 400$ GeV[12]. The accuracy of the EWA has been discussed in Ref. [18]. Our results agree with those in Ref. [14] where expected error is evaluated to be of the order of 10% for the cut $M_{tt} > 500$ GeV.

We add the dimension-six operators $\mathcal{O}_{t1}$ and $\mathcal{O}_{Dt}$ to the SM Lagrangian. In Figs. 3(a) and 3(b) cross sections for $e^- e^+ \to W_L^- W_L^+ \nu\bar{\nu} \to t\bar{t}\nu\bar{\nu}$ are shown as a function of m_H after the kinematic cut $M_{tt} \geq 400$ GeV. The collision energy is set to be $\sqrt{s} = 1$ TeV. The new physics scale Λ is assumed to be 1 TeV and 3 TeV. Fig. 3(a) shows the results for Set B and Set C, and Fig. 3(b) does those for Set D and Set E. In both figures, the result in the SM case [Set A] is also plotted.

The SM value of the cross section for $e^- e^+ \to W^- W^+ \nu\bar{\nu} \to t\bar{t}\nu\bar{\nu}$ is order 1fb for heavy Higgs bosons ($m_H \gtrsim 400$ GeV). At the ILC with an $e^- e^+$ energy of 1 TeV and the integrated luminosity of 500fb^{-1}, over several hundred events are produced. Naively, the statistic error of the cross section measurement can be less than about 10% level. The QCD corrections are evaluated to be the same order of magnitude[12]. Therefore, we can expect that the large correction of the cross section can easily be observed as long as it changes the cross section by a few times 10% or more. The effect of $\mathcal{O}_{Dt}$ under the constraint from the LEP data may also be observed when it changes the SM cross section by 10-20 %.

Background processes are also taken into account. Main background is $e^- e^+ \to \gamma t\bar{t}$ with γ to be missed. It can be reducible by making a kinematic cut for the transverse momentum of the final top quark. In Ref. [14], the simulation study for the background reduction has been performed in the SM, and the background can be sufficiently suppressed by the kinematic cuts. Another important background is the top pair production process via the photon fusion $\gamma\gamma \to t\bar{t}$. This mode can be suppressed by the cut $\not{E} > 50$ GeV[3], where $\not{E}$ is the missing energy. Finally, the direct top-pair production $e^- e^+ \to t\bar{t}$ can be suppressed by imposing the cut for the invariant mass M_{tt}.

4   Conclusions

In this talk, we have studied the new physics effect of the dimension-six top quark operators. Theoretical and experimental constraints on these operators have been discussed. We have evaluated the cross section of the process $e^- e^+ \to W^- W^+ \nu\bar{\nu} \to t\bar{t}\nu\bar{\nu}$ in the SM with the dimension-six top-Higgs interaction, and found that the deviation from the SM result can

be a few hundred percent greater than the SM one, which can easily be detected at a future linear collider including the ILC. Such a large deviation may also be detectable at the LHC via the process such as $pp \rightarrow W^-W^+X \rightarrow t\bar{t}X$ even though the QCD background is huge. Detailed simulation study should be necessary to clarify the significance.
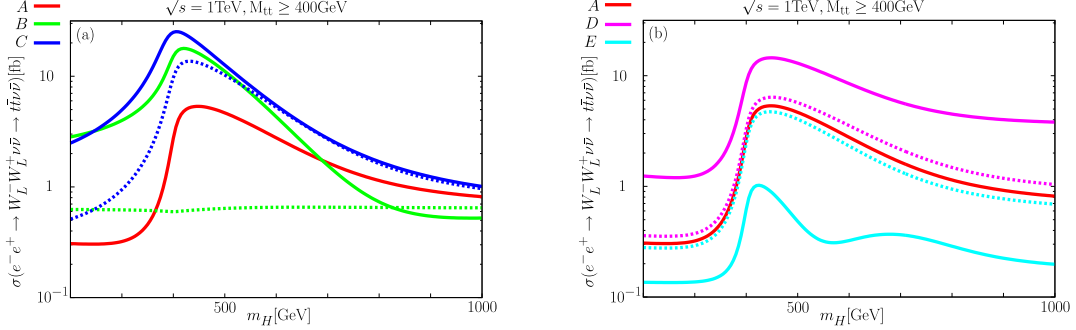
Figure 3: Cross sections of $e^-e^+ \rightarrow W_L^- W_L^+ \nu\bar{\nu} \rightarrow t\bar{t}\nu\bar{\nu}$ are shown as a function of Higgs boson mass for the cases of Set A, Set B and Set C [Fig. 3(a)], and for those of Set A, Set D and Set E [Fig. 3(b)] with $\Lambda = 1$ TeV (solid curves) and 3 TeV (dashed curves). The collider energy is taken to be $\sqrt{s} = 1$ TeV.

References

[1] Slides:
http://ilcagenda.linearcollider.org/contributionDisplay.py?contribId=163&sessionId=71&confId=1296

[2] A. Djouadi, J. Kalinowski and P. M. Zerwas, Z. Phys. C **54**, 255 (1992).

[3] D. R. T. Jones and S. T. Petcov, Phys. Lett. B **84**, 440 (1979); G. Altarelli, B. Mele and F. Pitolli, Nucl. Phys. B **287**, 205 (1987); R. P. Kauffman, Phys. Rev. D **41**, 3343 (1990); J. Alcaraz and E. Ruiz Morales, Phys. Rev. Lett. **86**, 3726 (2001).

[4] W. Buchmuller and D. Wyler, Nucl. Phys. B **268**, 621 (1986).

[5] G. J. Gounaris, D. T. Papadamou and F. M. Renard, Z. Phys. C **76**, 333 (1997).

[6] S. Mantry, M. J. Ramsey-Musolf and M. Trott, arXiv:0707.3152 [hep-ph].

[7] G. J. Gounaris, F. M. Renard and C. Verzegnassi, Phys. Rev. D **52**, 451 (1995).

[8] B. W. Lee, C. Quigg and H. B. Thacker, Phys. Rev. D **16**, 1519 (1977).

[9] T. Han, T. Huang, Z. H. Lin, J. X. Wang and X. Zhang, Phys. Rev. D **61**, 015006 (2000).

[10] S. Kanemura, D. Nomura and K. Tsumura, Phys. Rev. D **74**, 076007 (2006)

[11] C. P. Yuan, Nucl. Phys. B **310**, 1 (1988).

[12] M. Gintner and S. Godfrey, eConf **C960625**, STC130 (1996).

[13] S. Godfrey and S. h. Zhu, Phys. Rev. D **72**, 074011 (2005).

[14] F. Larios, T. Tait and C. P. Yuan, Phys. Rev. D **57**, 3106 (1998).

[15] S. Dawson, Nucl. Phys. B **249**, 42 (1985).

[16] A. Pukhov, arXiv:hep-ph/0412191.

[17] A. V. Semenov, arXiv:hep-ph/0208011.

[18] P. W. Johnson, F. I. Olness and W. K. Tung, Phys. Rev. D **36**, 291 (1987).

Higgs at CMS with 1, 10, 30 fb^{-1}

Sara Bolognesi

University of Torino - Dept of Experimental Physics
Via Giuria 1, Torino - Italy

The discovery strategies for the Standard Model Higgs boson at CMS are presented. The focus is on the results with 1, 10 and 30 fb^{-1} which should correspond respectively to about one year of data taking at the start-up luminosity and the first year and three years at low luminosity ($2 \times 10^{33} cm^{-2} s^{-1}$). [1]

1 Main Higgs channels studied at low luminosity

In Table 1 the accessible channels with less than 30 fb^{-1} are listed, the covered Higgs mass range and the order of magnitude of their cross sections are reported.

Between the early discovery channels, $H \to WW^{(*)} \to l\nu l\nu$ is the one with the biggest cross section and $H \to ZZ^{(*)} \to 4l$ is the cleanest one. Studying these decays, it is already possible to measure some Higgs properties (mass, width, cross section) with only 30 fb^{-1} [2] [3] [4] [5].

The Vector Boson Fusion (VBF) Higgs production process (qqH) can be studied with the Higgs decaying into $H \to \tau\tau$ or $H \to WW^{(*)}$ both in the fully leptonic ($l\nu l\nu$) and semileptonic final states ($jjl\nu$). These channels show a significance bigger than 3 or 5, respectively, with only 30 fb^{-1} but they requires a very good comprehension of the detector because of the complexity of the final states [6] [7] [8].

In the low Higgs mass region the $H \to \gamma\gamma$ decay is exploited: the preliminary results are encouraging but there are big uncertainties on the background because it strongly depends on the detector behavior and on the QCD physics at the LHC scale [9].

1.1 $H \to ZZ^{(*)} \to 4l$

These channels are very promising for the Higgs detection in the mass range 130 GeV-500 GeV, with the exception of a small interval near 160 GeV where the $H \to ZZ^{(*)}$ branching ratio (BR) has a big drop due to the opening of the WW on-shell production.

The main backgrounds are $t\bar{t}$ ($\sigma \simeq 840 \ pb$), $Zb\bar{b}$ ($\sigma \simeq 280 \ pb$) and $ZZ^{(*)}/\gamma^*$ ($\sigma \simeq 30 \ pb$), to be compared with the $H \to ZZ^{(*)}$ cross section of about 10-50 pb. Zcc has been found to be negligible.

channel	$\sigma \times BR$	studied $M(H)$
$H \to WW^{(*)} \to l\nu l\nu$	0.5-2.5 pb	120-200 GeV
$H \to ZZ^{(*)} \to 4l$	5-100 fb	130-500 GeV
$qqH \to WW^{(*)} \to jjl\nu$	200-900 fb	120-250 GeV
$qqH \to WW^{(*)} \to l\nu l\nu$	50-250 fb	120-200 GeV
$qqH \to \tau\tau$	50-160 fb	115-145 GeV
$H \to \gamma\gamma$	50-100 fb	115-150 GeV

Table 1: Accessible channels with less than 30 fb^{-1}

The trigger and the offline cuts applied in the analysis rely on the presence of isolated charged leptons coming from the primary vertex and with high transverse momentum. The Z mass peak is also a powerful feature: more than 50% (80%) of the events have at least one on-shell Z for $M(H) > 115$ (150) GeV.

The studied final states are $2e2\mu$, 4μ and $4e$. The first has the biggest BR while the second is the cleanest one. The main concern of the last channel is the presence, for low Higgs masses, of very soft electrons, well below the range for which the reconstruction will be best controlled in CMS via single Z and W measurements.

In Figure 1 the luminosity needed for a 5σ discovery and the significance achievable with $30\ fb^{-1}$, combining the three possible final states, is plotted as a function of the Higgs mass.

1.2 $H \to WW^{(*)} \to l\nu l\nu$

The leptonic decays of both the W in the ee, $e\mu$ and $\mu\mu$ combinations have been studied. The signal has a cross section of 0.5-2.3 pb with a peak at $M(H) = 160\ GeV$. The main backgrounds are single and double top production ($\sigma \simeq 90\ pb$) and double boson production ($\sigma \simeq 15\ pb$), considering only the fully leptonic decays. The Drell-Yan background after the full selection should be less than 2% of the total background. Figure 1 shows the luminosity needed for a 5σ discovery and the significance obtained with $30\ fb^{-1}$ as a function of the Higgs mass.

The final state selection relies mainly on the request of high missing energy ($> 50\ GeV$) and on a central jet veto. The main kinematic peculiarity of this channel is the closeness of the two charged leptons. The absence of the Higgs peak requires an high signal over background ratio and a good control of the background shape. Therefore a procedure to normalize the background from the data is necessary: a different signal free region for each background has been defined varying the analysis cuts. The uncertainties for the various backgrounds are between 15% and 20%, with the exception of single top and $gg \to WW$ processes for which it's not possible to find a good normalization region so that the systematics ($\simeq 30\%$) are dominated by MC theorethical errors.

1.3 qqH with $H \to WW$

The analysis of the fully leptonic decay channel ($qql\nu l\nu$ final state) is similar to that described in the previous section (Sec. 1.2). This process has a lower cross section (50-250 fb) but the presence of the two additional quarks from the VBF, with high energy and pseudorapidity, can be exploited to disentangle the signal from the background.

The semileptonic decay channel ($qqql\nu$ final state) has the advantage of a higher BR and it allows to reconstruct the Higgs mass peak. On the other hand it suffers from very high background: double top ($\sigma \simeq 840\ pb$), single top ($\sigma \simeq 100\ pb$), double boson plus jets ($\sigma \simeq 100\ pb$) and single boson plus jets (σ bigger than 1 mb), to be compared with the $qqH \to qqWW$ cross section of about 0.6-2.7 pb. Thus strong cuts are necessary and this implies a good knowledge of the physics involved. However the cross sections of the multiple jets processes at the LHC scale are not yet very well known and they will be measured precisely only from the LHC data themselves. Moreover many systematics about the jets detection and reconstruction are still quite uncertain, they can be understood and measured only from the data.

The preliminary estimation of the significance with $30\ fb^{-1}$ is shown in Figure 1 (left).

1.4 qqH with $H \to \tau\tau$

This channel has been analyzed with one τ decaying into leptons and the other τ into hadrons ($\sigma \simeq 50\text{-}160 \ pb$). The irreducible backgrounds are the QCD and EW production of two τ leptons from Z/γ^* with associated jets (QCD $2\tau+2/3$ jets $\sigma \simeq 1.6 \ pb$, EW $2\tau+2$ jets $\sigma \simeq 230$ fb). The reducible backgrounds considered are the $W+$ multi-jet production ($W+3/4$ jets $\sigma \simeq 14.5$ pb with $W \to \mu\nu$) and $t\bar{t}$ events ($\sigma \simeq 86$ pb with $W \to l\nu$), in which one of the jets can be misidentified as a τ-jet.

This analysis has to reconstruct a very complex final state. The hadronically decaying τ is reconstructed from a little ($\Delta R = 0.4$) isolated jet. A very low impurity (2.7%) is obtained thanks to the selection cuts, costing a low reconstruction efficiency (30%). The energy resolution on the reconstructed τ is 11.3%. The leptonically decaying τ is recognized from the electron or muon with highest transverse momentum, requiring $p_T > 15 \ GeV$. The τ energies are calculated using collinear approximation of visible part of τ decay products and neutrinos. A raw (not calibrated) missing transverse energy (MET) greater than $40 \ GeV$ is required. The MET resolution after all corrections is 20%, this is the largest contribution to the Higgs mass resolution. Finally the presence of the two quarks emitting the bosons in the VBF process can be exploited: they have very high energy and high rapidity gap because there is not color exchange between them, being produced trough an EW process. After having removed the τ jet and the two VBF jets, a central jet veto is applied using a Monte Carlo jet energy calibration.

The significance exceeds 3σ with $30 \ fb^{-1}$, as reported in Figure 1 (left). The number of events is measured directly from the data fitting the $M(\tau\tau)$ distribution. The uncertainty on the number of background events (7.8% with $30 \ fb^{-1}$) is computed from its spread in 10.000 toy Monte Carlo data distributions generated following the fit results.

1.5 Inclusive $H \to \gamma\gamma$

In this channel, because of the very low NLO BR ($\simeq 0.002$), the inclusive Higgs production is considered (mainly VBF and gg fusion).

The amount of background is very high: Drell-Yan e^+e^-, $pp \to \gamma\gamma$ (irreducible), $pp \to jets+\gamma$ and $pp \to jets$ where one or more jets are misidentified as γ (reducible). In particular this last kind of background has a big dependence on the detector performance and it involves not well known QCD physics. Therefore there is a great deal of uncertainty in the benchmark estimate of significance and of needed luminosity (shown in Figure 1). However this will not be a systematic error on real data since the background will be precisely measured from the data themselves, exploiting the big $M(\gamma\gamma)$ sidebands signal free. The analysis will be in fact based on a Neural Network trained on Monte Carlo for the signal and on the sidebands for the background: the systematic error achievable on the background interpolation under the Higgs peak with this method is very low ($\simeq 1\%$).

1.6 Conclusions

Figure 1 is a good summary of the CMS potential for the Higgs discovery with low luminosity. However it should be noticed that a careful preliminary work must be done in order get those results: the first data will be used to study the detector systematics (in particular the control of the jets response and of the MET resolution will be difficult at the beginning) and to
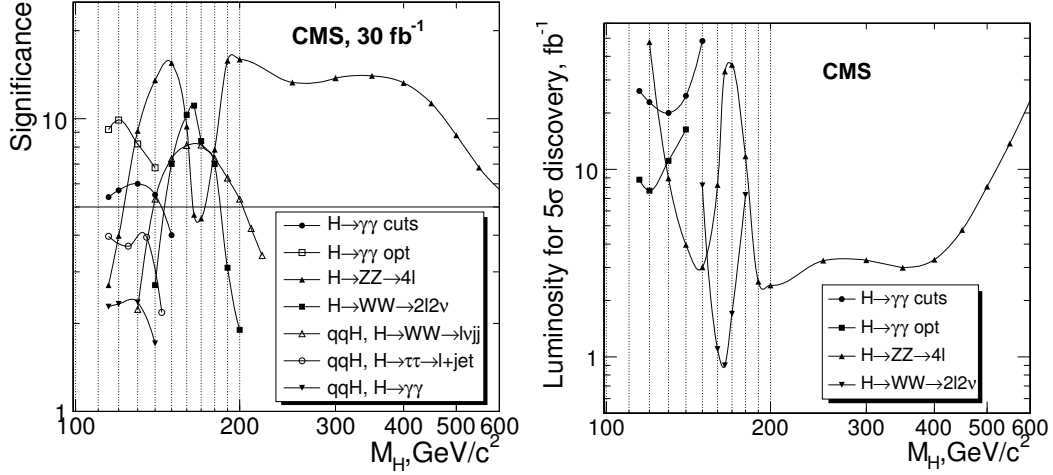
Figure 1: Significance achievable with 30 fb^{-1} (left) and luminosity needed for a 5σ discovery (right) in the various channels as a function of the Higgs mass.

measure the cross sections of multi-jets background processes (mainly $t\bar{t}$ and single and double boson production in association with jets).

References

[1] Slides:
http://ilcagenda.linearcollider.org/contributionDisplay.py?contribId=42&sessionId=8&confId=1296

[2] D. Futyan, D. Fortin and D. Giordano *Search for the Standard Model Higgs Boson in the Two-Electron and Two-Muon Final State with CMS*, CMS NOTE 2006/136

[3] S. Abdullin et al. *Search Strategy of the Standard Model Higgs Boson in the $H \to ZZ(*) \to 4\mu$ Decay Channel using $M(4\mu)$-Dependent Cuts*, CMS NOTE 2006/122

[4] S. Baffioni et al. *Discovery potential for the SM Higgs boson in the $H \to ZZ(*) \to e^+e^-e^+e^-$ decay channel*, CMS NOTE 2006/115

[5] G. Davatz, M. Dittmar and A.-S. Giolo-Nicollerat, *Standard Model Higgs discovery potential of CMS in the $H \to W^+W^- \to l\nu l\nu$ Channel*, CMS NOTE 2006/047

[6] , C. Foudas, A. Nikitenko and M. Takahashi *Observation of the Standard Model Higgs boson via $H \to \tau\tau \to lepton+jet$ Channel*, CMS NOTE 2006/088

[7] E. Yazgan, et al. *Search for a Standard Model Higgs Boson in CMS via Vector Boson Fusion in the $H \to WW \to l\nu l\nu$ Channel*, CMS NOTE 2007/011

[8] H. Pi et al. *Search for Standard Model Higgs Boson via Vector Boson Fusion in the $H \to W^+W^- \to l^\pm\nu jj$ with $120 < m_H < 250 GeV/c^2$*, CMS NOTE 2006/092

[9] M. Pieri et al. *Inclusive Search for the Higgs Boson in the $H \to \gamma\gamma$ Channel*, CMS NOTE 2006/112

$\mathcal{CP}$-violating Loop Effects in the
Higgs Sector of the MSSM

T. Hahn[1], S. Heinemeyer[2], W. Hollik[1], H. Rzehak[3], G. Weiglein[4] and K.E. Williams[4]

1- Max-Planck-Institut für Physik, Föhringer Ring 6, D–80805 Munich, Germany

2- Instituto de Fisica de Cantabria (CSIC-UC), Santander, Spain

3- Paul Scherrer Institut, Würenlingen und Villigen, CH–5232 Villigen PSI, Switzerland

4- IPPP, University of Durham, Durham DH1 3LE, UK

$\mathcal{CP}$-violating effects in the Higgs sector of the Minimal Supersymmetric Standard Model with complex parameters (cMSSM) are induced by potentially large higher-order corrections. As a consequence, all three neutral Higgs bosons can mix with each other. Recent results for loop corrections in the Higgs sector of the cMSSM are reviewed [1]. Results for propagator-type corrections of $\mathcal{O}(\alpha_t \alpha_s)$ and complete one-loop results for Higgs cascade decays of the kind $h_a \to h_b h_c$ are summarised, and the proper treatment of external Higgs bosons in Higgs-boson production and decay processes is discussed.

1 Introduction

A striking prediction of models of supersymmetry (SUSY) is a Higgs sector with at least one relatively light Higgs boson. In the Minimal Supersymmetric extension of the Standard Model (MSSM) two Higgs doublets are required, resulting in five physical Higgs bosons. In lowest order these are the light and heavy $\mathcal{CP}$-even h and H, the $\mathcal{CP}$-odd A, and the charged Higgs bosons $H^\pm$. The Higgs sector of the MSSM can be characterised at lowest order by the two parameters (besides the gauge couplings) $M_{H^\pm}$ and $\tan\beta \equiv v_2/v_1$, the ratio of the two vacuum expectation values. All other masses and mixing angles can be predicted in terms of these parameters. Higher-order contributions yield large corrections to the tree-level relations and, via complex phases, induce $\mathcal{CP}$-violating effects. In the MSSM with complex parameters (cMSSM) therefore all three neutral Higgs bosons can mix with each other. The corresponding mass eigenstates are denoted as h_1, h_2, h_3. If the mixing between the three neutral mass eigenstates is such that the coupling of the lightest Higgs boson to gauge bosons is significantly suppressed, this state can be very light without being in conflict with the exclusion bounds from the LEP Higgs searches [2, 3]. In this case the second-lightest Higgs boson, h_2, may predominantly decay into a pair of light Higgs bosons, $h_2 \to h_1 h_1$.

We report in this paper on recent progress on higher-order corrections in the Higgs sector of the cMSSM[a]. We briefly discuss propagator-type corrections of $\mathcal{O}(\alpha_t \alpha_s)$ [8] and complete one-loop results for Higgs cascade decays of the kind $h_a \to h_b h_c$ $(a, b, c = 1, 2, 3)$ [9]. In this context we put a particular emphasis on the treatment of external Higgs states in Higgs-boson production and decay process in the presence of $\mathcal{CP}$-violating mixing among all three neutral Higgs bosons.

---

[a]See e.g. Refs. [4–7] for recent reviews of the present status of higher-order corrections in the Higgs sector of the MSSM with and without complex phases.

2 External on-shell Higgs-bosons

The propagator matrix of the neutral Higgs bosons h, H, A can be written as a 3×3 matrix, $\Delta_{hHA}(p^2)$ (we neglect mixing with the Goldstone boson G and the Z boson in the propagator matrix since the corresponding contributions are of sub-leading two-loop order, see the discussion in Ref. [10]). This propagator matrix is related to the 3×3 matrix of the irreducible vertex functions by

$$\Delta_{hHA}(p^2) = -\left(\hat{\Gamma}_{hHA}(p^2)\right)^{-1}, \tag{1}$$

where $\hat{\Gamma}_{hHA}(p^2) = i\left[p^2 \mathbb{1} - \mathbf{M}_{\mathrm{n}}(p^2)\right]$,

$$\mathbf{M}_{\mathrm{n}}(p^2) = \begin{pmatrix} m_h^2 - \hat{\Sigma}_{hh}(p^2) & -\hat{\Sigma}_{hH}(p^2) & -\hat{\Sigma}_{hA}(p^2) \\ -\hat{\Sigma}_{hH}(p^2) & m_H^2 - \hat{\Sigma}_{HH}(p^2) & -\hat{\Sigma}_{HA}(p^2) \\ -\hat{\Sigma}_{hA}(p^2) & -\hat{\Sigma}_{HA}(p^2) & m_A^2 - \hat{\Sigma}_{AA}(p^2) \end{pmatrix}. \tag{2}$$

Here m_i $(i = h, H, A)$ denote the tree-level Higgs-boson masses, and $\hat{\Sigma}_{ij}$ are the renormalised self-energies. Inversion of $\hat{\Gamma}_{hHA}(p^2)$ yields for the diagonal Higgs propagators $(i = h, H, A)$

$$\Delta_{ii}(p^2) = \frac{i}{p^2 - m_i^2 + \hat{\Sigma}_{ii}^{\mathrm{eff}}(p^2)}, \tag{3}$$

where $\Delta_{hh}(p^2)$, $\Delta_{HH}(p^2)$, $\Delta_{AA}(p^2)$ are the (11), (22), (33) elements of the 3×3 matrix $\Delta_{hHA}(p^2)$, respectively. The structure of eq. (3) is formally the same as for the case without mixing, but the usual self-energy is replaced by the effective quantity $\hat{\Sigma}_{ii}^{\mathrm{eff}}(p^2)$ which contains mixing contributions of the three Higgs bosons. It reads (no summation over i, j, k)

$$\hat{\Sigma}_{ii}^{\mathrm{eff}}(p^2) = \hat{\Sigma}_{ii}(p^2) - i\frac{2\hat{\Gamma}_{ij}(p^2)\hat{\Gamma}_{jk}(p^2)\hat{\Gamma}_{ki}(p^2) - \hat{\Gamma}_{ki}^2(p^2)\hat{\Gamma}_{jj}(p^2) - \hat{\Gamma}_{ij}^2(p^2)\hat{\Gamma}_{kk}(p^2)}{\hat{\Gamma}_{jj}(p^2)\hat{\Gamma}_{kk}(p^2) - \hat{\Gamma}_{jk}^2(p^2)}, \tag{4}$$

where the $\hat{\Gamma}_{ij}(p^2)$ are the elements of the 3×3 matrix $\hat{\Gamma}_{hHA}(p^2)$ as specified above. The expressions for the off-diagonal Higgs propagators read $(i, j, k$ all different, no summation over $i, j, k)$

$$\Delta_{ij}(p^2) = \frac{\hat{\Gamma}_{ij}\hat{\Gamma}_{kk} - \hat{\Gamma}_{jk}\hat{\Gamma}_{ki}}{\hat{\Gamma}_{ii}\hat{\Gamma}_{jj}\hat{\Gamma}_{kk} + 2\hat{\Gamma}_{ij}\hat{\Gamma}_{jk}\hat{\Gamma}_{ki} - \hat{\Gamma}_{ii}\hat{\Gamma}_{jk}^2 - \hat{\Gamma}_{jj}\hat{\Gamma}_{ki}^2 - \hat{\Gamma}_{kk}\hat{\Gamma}_{ij}^2}, \tag{5}$$

where we have dropped the argument p^2 of the $\hat{\Gamma}_{ij}(p^2)$ appearing on the right-hand side for ease of notation. The three complex poles $\mathcal{M}^2$ of Δ_{hHA}, eq. (1), are defined as the solutions of

$$\mathcal{M}_i^2 - m_i^2 + \hat{\Sigma}_{ii}^{\mathrm{eff}}(\mathcal{M}_i^2) = 0, \; i = h, H, A, \tag{6}$$

with a decomposition of the complex pole as $\mathcal{M}^2 = M^2 - iM\Gamma$, where M is the mass of the particle and Γ its width. We define the loop-corrected mass eigenvalues according to $M_{h_1} \leq M_{h_2} \leq M_{h_3}$.

We now turn to the on-shell properties of an in- or out-going Higgs boson. In order to ensure the correct on-shell properties of S-matrix elements involving external Higgs it is

convenient to introduce finite wave function normalisation factors $\hat{Z}_i$, $\hat{Z}_{ij}$ ("Z-factors"). A vertex with an external Higgs boson, i, can be written as (with i, j, k all different, $i, j, k = h, H, A$, and no summation over indices)

$$\sqrt{\hat{Z}_i} \left(\Gamma_i \ + \ \hat{Z}_{ij}\Gamma_j \ + \ \hat{Z}_{ik}\Gamma_k + \dots \right) , \tag{7}$$

where the ellipsis represents contributions from the mixing with the Goldstone boson and the Z boson, see Refs. [9,10]. The Z-factors are given by:

$$\hat{Z}_i = \frac{1}{1 + \left(\hat{\Sigma}_{ii}^{\text{eff}}\right)' (\mathcal{M}_i^2)}, \quad \hat{Z}_{ij} = \frac{\Delta_{ij}(p^2)}{\Delta_{ii}(p^2)} \Big|_{p^2 = \mathcal{M}_i^2} \tag{8}$$

where the propagators $\Delta_{ii}(p^2)$, $\Delta_{ij}(p^2)$ have been given in eqs. (3) and (5), respectively. The Z-factors can be expressed in terms of a (non-unitary) matrix $\hat{\mathbf{Z}}$, whose elements take the form (with $\hat{Z}_{ii} = 1$, $i, j = h, H, A$, and no summation over i)

$$(\hat{\mathbf{Z}})_{ij} := \sqrt{\hat{Z}_i} \ \hat{Z}_{ij} . \tag{9}$$

A vertex with one external Higgs boson h_1, for instance, is then given by

$$(\hat{\mathbf{Z}})_{hh}\Gamma_h + (\hat{\mathbf{Z}})_{hH}\Gamma_H + (\hat{\mathbf{Z}})_{hA}\Gamma_A + \dots , \tag{10}$$

where the ellipsis again represents contributions from the mixing with the Goldstone boson and the Z boson.

It should be noted that the definition of the Z-factors used here and in Ref. [9] differs slightly from the one in Ref. [10]. The Higgs-boson self-energies in eq. (8) are evaluated at the complex pole, whereas in Ref. [10] the real part of the complex pole had been used. Furthermore, in the definition of $\hat{Z}_i$ in eq. (8) $\hat{\Sigma}_{ii}^{\text{eff}}$ appears, as compared to $\text{Re}\,\hat{\Sigma}_{ii}^{\text{eff}}$ in Ref. [10]. While the contributions of the imaginary parts in eq. (8) to Higgs-boson production and decay processes are formally of sub-leading two-loop order, it turns out that their inclusion in general improves the numerical stability of the results.

3 Propagator-type corrections of $\mathcal{O}(\alpha_t\alpha_s)$

The leading two-loop corrections of $\mathcal{O}(\alpha_t\alpha_s)$ have been recently been obtained [8] in the Feynman-diagrammatic approach for propagator-type corrections, which contribute to the predictions for the Higgs-boson masses, to wave function normalisation factors of external Higgs bosons and to effective couplings. The results are valid for arbitrary values of the complex parameters. The impact of the complex phases of the trilinear coupling A_t and the gluino mass parameter M_3 at the two-loop level turns out to be numerically sizable. As an example, in Fig. 1 the lightest Higgs-boson mass, M_{h_1}, is shown as a function of the phase φ_{A_t} of the trilinear coupling A_t. The one-loop result (dotted line) is compared with the new result that includes the $\mathcal{O}(\alpha_t\alpha_s)$ contributions (solid line). The dependence on the complex phase φ_{A_t} is much more pronounced in the two-loop result than in the one-loop case, which can easily be understood from the analytical structure of the corrections [8]. Thus, varying φ_{A_t} can give rise to shifts in the prediction for M_{h_1} of more than ± 5 GeV even in cases where the dependence on the complex phases in the one-loop result is very small. The new corrections have recently been implemented into the program `FeynHiggs` [10–12].
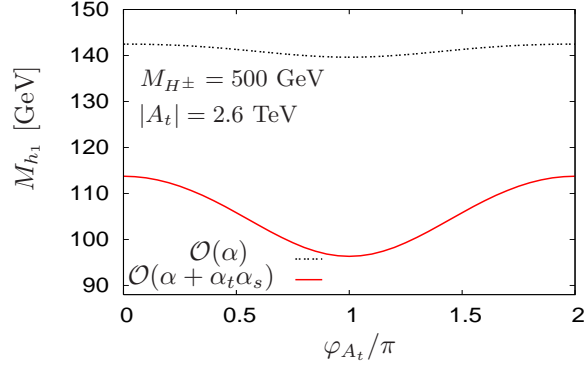
Figure 1: The lightest Higgs-boson mass, M_{h_1}, as a function of φ_{A_t} for $|A_t| = 2.6$ TeV and $M_{H^\pm} = 500$ GeV. The one-loop result (dashed line) is compared with the result including the $\mathcal{O}(\alpha_t \alpha_s)$ corrections (solid line). The other parameters are $M_{\mathrm{SUSY}} = 1000$ GeV, $\mu = 1000$ GeV, $M_2 = 500$ GeV, $m_{\tilde{g}} = 1000$ GeV, $\tan\beta = 10$.

4 Complete one-loop results for Higgs cascade decays

For Higgs cascade decays of the kind $h_a \to h_b h_c$, where $a, b, c = 1, 2, 3$, recently complete one-loop results have been obtained in the cMSSM [9]. They have been supplemented with the state-of-the-art propagator-type corrections (see above), yielding the currently most precise prediction for this class of processes. The genuine vertex corrections turn out to be very important, yielding a large increase of the decay width compared to a prediction based on only the tree-level vertex dressed with propagator-type corrections. This is demonstrated in Fig. 2, where the full result for $\Gamma(h_2 \to h_1 h_1)$ as a function of M_{h_1} in the CPX scenario [13] is compared with results based on various approximations for the genuine contributions to the $h_2 h_1 h_1$ vertex. The complete result (denoted as 'Full') differs by more than a factor of six in this example (for values of M_{h_1} sufficiently below the kinematic limit of $M_{h_1} = 0.5 M_{h_2}$ where the decay width goes to zero) from the result for the case where only wave-function normalisation factors but no genuine one-loop vertex contributions are taken into account ('Tree'). See Ref. [9] for a discussion of the other approximations shown in Fig. 2.

The new results for the Higgs cascade decays [9] have been used to analyse the impact of the limits on topological cross sections obtained from the LEP Higgs searches on the parameter space with a very light Higgs boson within the cMSSM. It has been found for the example of the CPX scenario [13] that, over a large part of the parameter space where the decay $h_2 \to h_1 h_1$ is kinematically possible, it is the dominant decay channel. A parameter region with $M_{h_1} \approx 45$ GeV and $\tan\beta \approx 6$ remains unexcluded by the limits on topological cross sections obtained from the LEP Higgs searches, confirming the results of the four LEP collaborations achieved in a dedicated analysis of the CPX benchmark scenario. The results of Ref. [9] will be incorporated into the public code `FeynHiggs`.

Acknowledgments
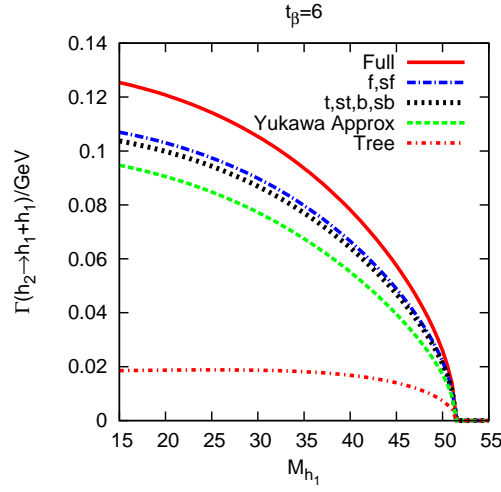
Figure 2: The full result for $\Gamma(h_2 \to h_1 h_1)$ as a function of M_{h_1} in the CPX scenario [13] for $\tan\beta = 6$ ($M_{H^\pm}$ is varied) is compared with various approximations, see text.

2006-035505 'Tools and Precision Calculations for Physics Discoveries at Colliders'.

References

[1] Slides:
http://ilcagenda.linearcollider.org/contributionDisplay.py?contribId=165&sessionId=71&confId=1296

[2] [LEP Higgs working group], *Phys. Lett.* **B 565** (2003) 61 [arXiv:hep-ex/0306033].

[3] [LEP Higgs working group], *Eur. Phys. J.* **C 47** (2006) 547 [arXiv:hep-ex/0602042].

[4] S. Heinemeyer, W. Hollik and G. Weiglein, *Phys. Rept.* **425** (2006) 265 [arXiv:hep-ph/0412214].

[5] B. Allanach, A. Djouadi, J. Kneur, W. Porod and P. Slavich, *JHEP* **0409** (2004) 044 [arXiv:hep-ph/0406166].

[6] A. Djouadi, arXiv:hep-ph/0503173.

[7] S. Heinemeyer, Int. J. Mod. Phys. **A 21**, 2659 (2006) [arXiv:hep-ph/0407244].

[8] S. Heinemeyer, W. Hollik, H. Rzehak and G. Weiglein, *Phys. Lett.* **B 652** (2007) 300, [arXiv:0705.0746 [hep-ph]].

[9] K.E. Williams and G. Weiglein, arXiv:0710.5320 [hep-ph]; arXiv:0710.5331 [hep-ph].

[10] M. Frank, T. Hahn, S. Heinemeyer, W. Hollik, R. Rzehak and G. Weiglein, *JHEP* **0702** (2007) 047 [arXiv:hep-ph/0611326].

[11] G. Degrassi, S. Heinemeyer, W. Hollik, P. Slavich and G. Weiglein, *Eur. Phys. J.* **C 28** (2003) 133 [arXiv:hep-ph/0212020].

[12] S. Heinemeyer, W. Hollik and G. Weiglein, *Comput. Phys. Commun.* **124** (2000) 76 [arXiv:hep-ph/9812320]; see www.feynhiggs.de ;
Eur. Phys. J. **C 9** (1999) 343 [arXiv:hep-ph/9812472];
T. Hahn, S. Heinemeyer, W. Hollik, H. Rzehak, G. Weiglein and K. Williams, arXiv:hep-ph/0611373;
T. Hahn, S. Heinemeyer, W. Hollik, H. Rzehak and G. Weiglein, arXiv:0710.4891 [hep-ph].

[13] M. Carena, J. Ellis, A. Pilaftsis and C. Wagner, *Phys. Lett.* **B 495** (2000) 155 [arXiv:hep-ph/0009212].

A Study of $e^+e^- \rightarrow H^0A^0$ Production at 1 TeV and the Constrain on Dark Matter Density

Marco Battaglia[1,2], Benjamin Hooberman[1], Nicole Kelley[1]

1- University of California - Dept of Physics, Berkeley, CA - USA

2- Lawrence Berkeley National Laboratory, Berkeley, CA - USA

1   Introduction

The connections between Cosmology and Particle Physics through Dark Matter (DM) have received special attention in the last few years for sharpening the physics case of collider physics at the TeV frontier. There are many extensions of the Standard Model (SM), which include a new, stable, weakly-interacting massive particle, possibly responsible for the observed relic DM in the Universe. The LHC will provide first important data to address the question whether one of these scenarios is indeed realised in nature. The ILC measurements of the properties of a DM candidate and of those other particles participating to its interactions in the early Universe may allow us to predict its relic density with an accuracy comparable to that currently achieved by CMB observations at satellites. With these data in hand, the comparison of the results would have striking consequences for our understanding of dark matter.

2   Neutralino Dark Matter Density in MSSM and the ILC

Supersymmetry emerges as the best motivated theory of new physics beyond the SM. It solves a number of problems, intrinsic to the SM and, most important to our discussion, the conservation of R-parity introduces a new stable, weakly interacting particle. The WMAP CMB data, and other astrophysical data, already set rather stringent bounds on Supersymmetry parameters, if the neutralino is responsible for saturating the amount of DM observed.

The potential of ILC data at 0.5 TeV and 1.0 TeV for determining the DM relic density, Ω_χ, in Supersymmetry has been investigated in detail in [1]. This study selected a set of benchmark points, the so-called LCC points, representative of various scenarios and determined the Ω_χ probability density function by a scan of the full MSSM parameter space and retaining those points compatible with the measurements available at the LHC and ILC within their accuracy.

3 $e^+e^- \rightarrow H^0A^0$ at LCC-4 with Full Simulation

We consider here a specific Supersymmetric scenarios, in which the DM candidate is the lightest neutralino, χ_1^0 and its relic density is controlled by the rate of neutralino annihilation through the CP-even heavy Higgs pole $\chi\chi \rightarrow A$. The LCC-4 benchmark point [1] is defined in the cMSSM, corresponding to the parameters m_0=380.00 GeV, $m_{1/2}$=420 GeV, $\tan\beta$=53, A=0, $Sgn(\mu)$=+1 and M_{top}=178 GeV. We use `Isasugra 7.69` [2] to compute the particle spectrum and we get M_{A^0}=419.4 GeV, $M_{\chi_1^0}$=169.1 GeV and $M_{\tilde{\tau}_1}$=195.5 GeV. The $e^+e^- \rightarrow$

$H^0 A^0 \to b\bar{b}b\bar{b}$ process at $\sqrt{s} = 1$ TeV ILC has already been studied for LCC4 [3]. That study, based on the parametric detector simulation program `Simdet 4.0`, showed that the A^0 boson mass can be determined to ± 0.8 GeV by imposing the natural width Γ_A or to ± 2.0 GeV by a simultaneous fit to mass and width. These results, when combined with other measurements to be peformed at 0.5 TeV, allow us to predict the neutralino contributoion to the dark matter density in the Universe, Ω_χ to a relative accuracy of 18 % in generic MSSM scenarios.

Here, we repeat the same study on `Geant-4`-based simulation [4] of the detector response and reconstruct the physics objects using processors developed in the `Marlin` framework [5]. This study adopts the LDC detector concept, which employs a large continuous gaseous tracker Time Projection Chamber surrounded by a highly granular calorimeter and complemented by a high resolution Vertex Tracker, for which we have chosen the option based on CMOS monolithic pixel sensors. The LDC detector is discussed in details elsewhere[6], the design is optimised for achieving excellent parton energy measurements, through the particle flow algorithm, and precise extrapolation of particle tracks to their production point. Both these features are important to the analysis, which aims to suppress backgrounds by exploiting its signature 4-b jet final state and requires good determinaton of energy and direction of hadronic jets to maximise the resolution on di-jet invariant masses. The jet energy resolution has been studied using a simulated sample of single b jets in the energy range from 10 GeV to 210 GeV over a polar angle, θ, range $0.4 < \theta < \pi/2$, we get $\delta E/E = (0.34 \pm 0.02)/\sqrt{E} \oplus (0.015 \pm 0.005)$, which is consistent with the particle flow performance specifications. Jet flavour tagging is based on three observables: the probability for all the particle tracks to originate at the event primary vertex, the fraction of the jet energy carried by secondary particles and the p_t-corrected mass of the secondary particles. These are combined to form a discriminant variable which peaks at one for b jets and peaks at zero for non-b jets.

At the chosen working point, an efficiency for b jets of 85 % is obtained with sufficient rejection of lighter quarks to effectively suppress the remaining non-b background. Signal events have been generated with `Pythia 6.205+Isajet 7.69`, including bremsstrahlung effects. These events have been passed through the full LDC simulation using the `Mokka 06-03` program [7] based on `Geant-4`. The `lcio` [8] collections produced by `Mokka` have been used as input for the `Marlin` reconstruction. At $\sqrt{s}$ = 1 TeV, the effective $e^+ e^- \to H^0 A^0$ production cross section, accounting for beamstrahlung, is 1.4 fb and the decay $\mathrm{BR}(A^0 \to b\bar{b})$ is 0.87. The main backgrounds are

Figure 1: Tranverse energy and thrust distributions for HA, $Z^0 Z^0$ and $W^+ W^-$. Generator level distributions are plotted as histograms, results of `Mokka + Marlin` simulation and reconstruction are given for the signal process as points with error bars.

$Z^0 Z^0$, $W^+ W^-$ production and the inclusive $b\bar{b}b\bar{b}$ production. Their cross sections are 0.2 pb,

3.2 fb and 5.1 fb respectively. We assume to operate the ILC at 1 TeV for a total integrated luminosity of 2 ab^{-1}. Backgrounds can be significantly suppressed using event shape and kinematic variables. We require events to fulfill the following criteria: total recorded energy in the event $E_{TOT} > 850$ GeV, total transverse energy $E_T > 350$ GeV, charged energy in the event $E_{CHA} > 350$ GeV, number or reconstructed particles $N_{TOT} > 50$, number of charged particles $N_{CHA} > 25$, event thrust $<.95$ and $Y_{34} < 0.0025$, where Y_{34} is the 3 to 4 jet crossover value of the jet clustering variable. The distributions of some of these variables is shown in Figure 1) for backgrounds and signal, for which a comparison of the generator-level and reconstructed values is also given.

After event selection, the di-jet pairing which minimises the di-jet mass difference has been chosen. The di-jet mass resolution has been improved by applying a 4-C fit. We
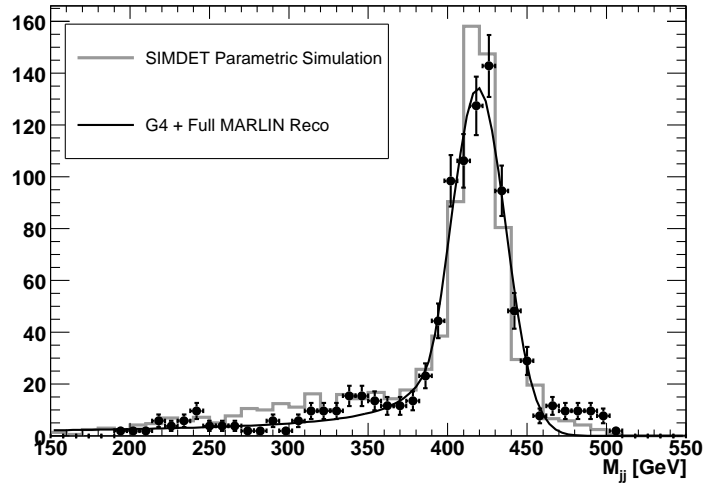
Figure 2: Dijet invariant mass distribution for $e^+e^- \rightarrow H^0 A^0$ events selected by the analysis cut. Mass constraint fit and jet flavour tagging has been applied. The distribution for fully simulated and reconstructed events (points with error bars) is compared to that obtained with parametric simulation (histogram).

have ported the `PUFITC` algorithm, developed for the DELPHI experiment at LEP, into a dedicated `Marlin` processor. The algorithm adjusts the momenta of the jets given by $\vec{p}_F = e^a \vec{p}_M + b\vec{p}_B + c\vec{p}_C$ where $\vec{p}_F$ is the fitted momentum, $\vec{p}_M$ is the measured momentum, $\vec{p}_B$ and $\vec{p}_C$ are unit vectors transverse to $\vec{p}_M$ and to each other, and a, b and c are the free parameters in the fit. The adjusted momenta satisfy a set of constraints while minimizing the fit χ^2, which is given by $\Sigma_i (a_i - a_0)^2/\sigma_a^2 + b_i^2/\sigma_b^2 + c_i^2/\sigma_c^2$, where a_0 is the expected energy loss parameter, σ_a is the energy spread parameter and σ_b, σ_c are the transverse momentum spread parameters. In this analysis we use the following constraints: $p_x = p_y = 0$ and $E \pm |p_z| = \sqrt{s}$, where the last condition accounts for beamstrahlung along the beam axis, z. We report here preliminary results from the analysis of a sample of 1050 fully simulated signal events. After applying final selection and mass constrained fit, the sample of events in the region 150 GeV$< M_{jj} <$550 GeV gives a selection efficiency of 23 % for signal $b\bar{b}b\bar{b}$

decays. The resulting mass distribution is shown in Figure 2. We describe the signal as a CRYSTAL BALL (CB) function [9] and extract the A^0 mass, M_A, and width, Γ_A have been by a multi-parameter fit leaving the CB parameters free. We determine the A^0 mass as (419.1 ± 0.9) GeV. This result is remarkably close to that obtained in the earlier analysis, based on parametric detector simulation. The production and analysis of fully simulated and reconstructed background samples is currently under way.

4 Further Constraints on Ω_χ

The constraints on LCC4 derived from mass measurements at the LHC and ILC, provide a prediction of the DM density in the Universe to a relative accuracy of 18 % with a generic MSSM model.

This accuracy is still far from that achieved by CMB study with satellites. The main contribution to the remaining uncertainty is the weak constrain which the data provide to MSSM solutions where Ω_χ is significantly lower than its reference for LCC4. A detailed study shows that these solutions are all characterised by large values of the stau trilinear coupling, A_{tau}. In the MSSM the $\tilde{\tau}$ coupling to the H^0 and A^0 bosons scales as $A_{tau}\frac{\cos\alpha}{\cos beta} + \mu\frac{\sin\alpha}{\cos\beta}$ and $A_{tau}\tan\beta+\mu$, respectively. In the funnel region the main annihilation mechanism is $\tilde{\chi}^0\tilde{\chi}^0 \to A^0 \to b\bar{b}$ and $M_A < M_{\tilde{\tau}_1}+M_{\tilde{\tau}_2}$. The only A^0 decay into $\tilde{\tau}$s, allowed by CP symmetry, $A^0 \to \tilde{\tau}_1\tilde{\tau}_2$ is kinematically forbidden. At large values of
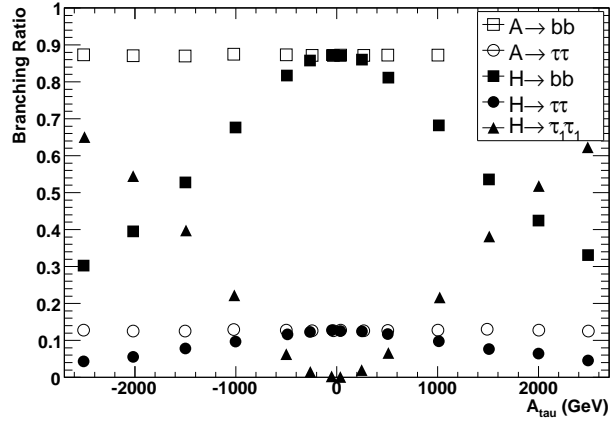
Figure 3: H^0 and A^0 decay branching fractions as a function of the stau trilinear coupling A_{tau} predicted by HDECAY. All the other MSSM parameters have been kept fixed to those corresponding to the LCC4 point.

$|A_{tau}|$, the stau decay process through the $H^0 \to \tilde{\tau}_1\tilde{\tau}_1$ gets a sizeable branching fraction. This channel contributes to the neutralino annihilation rate through $\tilde{\chi}^0\tilde{\chi}^0 \to H^0 \to \tilde{\tau}_1\tilde{\tau}_1$, bringing down the corresponding relic density, as observed in the MSSM scans. At the same time, a determination of the branching fraction of the decay $H^0 \to \tilde{\tau}_1\tilde{\tau}_1$, allows to constrain $|A_{tau}|$. Figure 3 shows the decay branching fractions of the A^0 and H^0 bosons computed using the HDECAY 2.0 program [10] as a function of A_{tau}. Now, a large $H^0 \to \tilde{\tau}_1\tilde{\tau}_1 \to \tau\tilde{\chi}^0\tau\tilde{\chi}^0$ yield can be detected by a standard $b\bar{b}\tau\tau$ analysis. A preliminary study shows that the A^0, $H^0 \to \tau\tau$ branching fraction can be determined to $\pm$ 15 % and A^0, $H^0 \to b\bar{b}$ to $\pm$ 7 %, from which a limit $|A_{tau}| < 250$ GeV can be derived. This constrain removes the tail at low values of Ω_χ and results in a prediction of the neutralino relic density with a relative accuracy of 8 %. A detailed study on full simulation to support this preliminary results is currently under way.

Acknowledgments

References

[1] E. A. Baltz, M. Battaglia, M. E. Peskin and T. Wizansky, Phys. Rev. D **74** (2006) 103521 [arXiv:hep-ph/0602187].

[2] F. E. Paige, S. D. Protopopescu, H. Baer and X. Tata, arXiv:hep-ph/0312045.

[3] M. Battaglia, arXiv:hep-ph/0410123.

[4] S. Agostinelli *et al.*, Nucl. Instrum. Meth. A **506** (2003), 250.

[5] F. Gaede, Nucl. Instrum. Meth. A **559** (2006) 177.

[6] Detector Outline Document for the Large Detector Concept, August 2006.

[7] G. Musat, *Prepared for International Conference on Linear Colliders (LCWS 04), Paris, France, 19-24 Apr 2004*

[8] F. Gaede, T. Behnke, N. Graf and T. Johnson, *In the Proceedings of 2003 Conference for Computing in High-Energy and Nuclear Physics (CHEP 03), La Jolla, California, 24-28 Mar 2003, pp TUKT001* [arXiv:physics/0306114].

[9] T. Skwarnicki, PhD thesis, DESY-F31-86-02 (1986).

[10] A. Djouadi, J. Kalinowski and M. Spira, Comput. Phys. Commun. **108** (1998) 56 [arXiv:hep-ph/9704448].

SUSY Particles

Conveners: H. Baer, G. Wilson, A. Djouadi, J. List, S. Youl Choi, K. Fujii

Determining Heavy Mass Parameters in SUSY SO(10)

F. Deppisch[1], A. Freitas[2], W. Porod[3] and P.M. Zerwas[4]

1- Deutsches Elektronen-Synchrotron DESY, D-22603 Hamburg, Germany

2- Inst. Theor. Physik, Universität Zürich, CH-8057 Zürich, Switzerland

3- Inst. Theor. Physik und Astrophysik, Universität Würzburg, D-97074 Würzburg, Germany

4- Inst. Theor. Physik E, RWTH Aachen, D-52056 Aachen, Germany

The high precision expected in e^+e^- collider experiments allows the reconstruction of the fundamental supersymmetric scalar mass parameters at the unification scale and the D-terms related to the breaking of GUT symmetries. We investigate the potential of this method in the lepton sector of SO(10) breaking directly to the SM gauge group. SO(10) naturally incorporates right-handed neutrino superfields in a seesaw scenario. The mass of the third generation heavy neutrino can also be estimated with our method.

The observation of neutrino oscillations has provided experimental proof for non-zero neutrino masses [2]. When right-handed neutrinos, not carrying any Standard Model gauge charges, are included in the set of leptons and quarks, the symmetry group SO(10) is naturally suggested as the grand unification group [3]. For theories formulated in a supersymmetric frame to build a stable bridge between the electroweak scale and the Planck scale, a scalar R-neutrino superfield is added to the spectrum of the minimal supersymmetric standard model. A natural explanation of the very light neutrino masses in relation to the electroweak scale is offered by the seesaw mechanism [4]. For right-handed Majorana neutrino masses $M_{\nu_{Ri}}$ in a range close to the GUT scale, small neutrino masses can be generated quite naturally by this mechanism: $m_{\nu_i} \sim m_{q_i}^2/M_{\nu_{Ri}}$, with m_{q_i} denoting up-type quark masses.

We investigate a one-step breaking scenario in which SO(10) is directly broken to the SM gauge group at the unification scale Λ_U. The SO(10) scalar soft SUSY breaking sector is parametrized by the gravity induced mass parameters m_{16} for the matter superfields and m_{10_1}, m_{10_2} for two Higgs superfields. Starting at Λ_U, the mass parameters evolve, following the renormalization group (RG), down to the electroweak scale. Once the masses of supersymmetric particles are measured, the RG evolution from the Tera-scale upwards will allow us to reconstruct the physics scenario at the GUT scale [5, 6]. The matter superfields of the three generations belong to 16-dimensional representations of SO(10) and the standard Higgs superfields to two 10-dimensional representations, while a Higgs superfield in the 126-dimensional representation generates the Majorana masses for the right-handed neutrinos. The couplings of this 126 Higgs to the other matter fields are assumed to be small. The Higgs sector of this model may be expanded to solve certain SO(10) GUT problems such as doublet-triplet splitting and proton decay, but such an expansion does not affect the present study significantly.

It follows from the Higgs-{10} SO(10) relation that $Y_\nu = Y_u$ between the neutrino and up-type Yukawa matrices at Λ_U. The effective mass matrix of the light neutrinos is constrained by the results of the oscillation experiments, $m_\nu = U_{MNS}^* \cdot diag(m_{\nu_1}, m_{\nu_2}, m_{\nu_3}) \cdot U_{MNS}^\dagger$. We assume the normal hierarchy for the light neutrino masses, and for the MNS mixing matrix the tri-bimaximal form. From the seesaw relation $M_{\nu_R} = Y_\nu m_\nu^{-1} Y_\nu^T \cdot v_u^2$, the heavy

Majorana R-neutrino mass matrix M_{ν_R} can finally be derived as

$$M_{\nu_R} \approx diag(m_u, m_c, m_t) m_\nu^{-1} diag(m_u, m_c, m_t). \tag{1}$$

For normal hierarchy, m_{ν_3} and m_{ν_2} are given by the squared mass differences measured in neutrino oscillation experiments. Solving Eq. (1) the $M_{\nu_{Ri}}$ spectrum is then predicted by the up-quark masses $m_{u,c,t}$ and the lightest neutrino mass m_{ν_1} at the GUT scale. Consequently, the mass spectrum of the R-neutrinos is strongly ordered in SO(10) with minimal Higgs content,

$$M_{\nu_{R3}} : M_{\nu_{R2}} : M_{\nu_{R1}} \sim m_t^2 : m_c^2 : m_u^2. \tag{2}$$

The Yukawa mass matrix squared, which determines the connection of the slepton masses in the third generation at low and high scales, is dominated by the 33 element, $\left(Y_\nu^\dagger Y_\nu\right)_{33} \approx m_t^2(\Lambda_U)/v_u^2 \approx 0.3$, while the other elements are suppressed to a level of 10^{-2} down to 10^{-5}.

The scalar mass parameters at the unification scale will be assumed universal for the SO(10) representations. However, the breaking of the rank-5 SO(10) symmetry group to the lower rank-4 SM group generates GUT D-terms D_U violating the scalar mass universality at Λ_U. To leading logarithmic order, the solutions of the RG equations, the masses of the selectrons and the L-type e-sneutrino, can be expressed in terms of the high scale parameter M_0, the universal gaugino mass parameter $M_{1/2}$ and the GUT and electroweak D-terms, D_U and $D_{EW} = 1/2 M_Z^2 \cos 2\beta$, respectively:

$$
\begin{aligned}
m_{\tilde{e}_R}^2 &= M_0^2 + D_U + \alpha_R M_{1/2}^2 - \tfrac{6}{5} S' - 2 s_W^2 D_{EW}, \\
m_{\tilde{e}_L}^2 &= M_0^2 - 3 D_U + \alpha_L M_{1/2}^2 + \tfrac{3}{5} S' - c_{2W} D_{EW}, \\
m_{\tilde{\nu}_{eL}}^2 &= M_0^2 - 3 D_U + \alpha_L M_{1/2}^2 - \tfrac{6}{5} S' + D_{EW}.
\end{aligned}
\tag{3}
$$

The coefficients α_L and α_R can be calculated from the gaugino/gauge boson loops, and a numerical integration yields $\alpha_R \approx 0.15$ and $\alpha_L \approx 0.5$. The universal gaugino mass parameter $M_{1/2}$ can be pre-determined in the chargino/neutralino sector. The non-universal initial conditions due to the D-terms generate the small generation-independent corrections $S' = -4 D_U \alpha_1(\tilde{M})/\alpha_1(\Lambda_U)$ from the GUT to the Tera-scale $\tilde{M}$.

Representations of the scalar masses in the *third generation* are complemented by $\nu_{R\tau}$ loops coupled by Yukawa interactions with the L and R fields. The masses of the third generation are shifted relative to the masses of the first two generations by two terms [5, 6]:

$$
\begin{aligned}
m_{\tilde{\tau}_R}^2 &= m_{\tilde{e}_R}^2 + m_\tau^2 - 2\Delta_\tau, \\
m_{\tilde{\tau}_L}^2 &= m_{\tilde{e}_L}^2 + m_\tau^2 - \Delta_\tau - \Delta_{\nu_\tau}, \\
m_{\tilde{\nu}_{\tau L}}^2 &= m_{\tilde{\nu}_{eL}}^2 - \Delta_\tau - \Delta_{\nu_\tau}.
\end{aligned}
\tag{4}
$$

The shifts Δ_τ and Δ_{ν_τ}, generated by loops involving charged lepton and neutrino superfields, respectively, are predicted by the renormalization group in the SO(10) scenario,

$$\Delta_\tau \approx \frac{m_\tau^2(\Lambda_U)}{8\pi^2 v_d^2} \left(3 M_0^2 + A_0^2\right) \log \frac{\Lambda_U^2}{M_Z^2}, \tag{5}$$

$$\Delta_{\nu_\tau} \approx \frac{m_t^2(\Lambda_U)}{8\pi^2 v_u^2} \left(3 M_0^2 + A_0^2\right) \log \frac{\Lambda_U^2}{M_{\nu_{R3}}^2}. \tag{6}$$

Anticipating measurements of high precision at the ILC, such an SO(10) scenario can be investigated in all its facets. As a concrete example, we study the following LR-extended scenario which is close to SPS1a/a′ [7, 8]:

$$
\begin{aligned}
M_0 &= 90 \text{ GeV} \\
M_{1/2} &= 250 \text{ GeV} \\
A_0 &= -640 \text{ GeV} \\
D_U &= (30 \text{ GeV})^2 \\
\tan\beta &= 10 \\
\text{sign}\mu &= + \\
M_{\nu_{R3}} &= 7.21 \cdot 10^{14} \text{ GeV}.
\end{aligned}
\tag{7}
$$

Figure 1: Evolution of scalar mass parameters between Λ_U and the Tera-scale for $D_U = 0$ with a r.h. neutrino mass $M_{\nu_{R3}} \approx 10^{15}$ GeV.

In this scenario, the masses of the charged sleptons can be measured with high precision in slepton pair production at ILC [9], while the sneutrino masses can be determined accurately from the decays of charginos [5]. Taking into account squark mass measurement at the LHC in addition, a global analysis leads to an accurate determination of A_0 [7, 11].

The measurement of the slepton and sneutrino masses of the first two generations allows us to extract the common scalar parameter M_0 as well as the D-term D_U. The approximate relations are given in Eq. (4). Including the complete one-loop and the leading two-loop corrections, the evolution of the scalar mass parameters is displayed in Figure 1. The right-handed neutrino mainly affects the evolution of the mass parameter m_{L3}^2 in the third generation. The characteristic kink in the evolution between m_{L3}^2 and m_{L1}^2 is exemplified in Figure 1 for a right-handed neutrino mass $M_{\nu_{R3}}$ of about 10^{15} GeV.

With the experimental measurement errors, the high-scale parameters can be calculated. With the RG evolution equations are evaluated to 2-loop order [12], a global analysis indicates that the high-scale parameters M_0 and $D_U^{1/2}$, can be reconstructed at per-mill to per-cent accuracy, $M_0 = (90 \pm 0.34)$ GeV, $D_U^{1/2} = 30 \pm 0.7$ GeV.

The right-handed neutrino mass is fixed by the intersection of the parameter Δ_{ν_τ}, Eq. (6), with the measured value $\Delta_{\nu_\tau}^{exp} = (4.7 \pm 0.4) \cdot 10^3$ GeV^2 extracted from the slepton masses. This is shown in Figure 2. The effect of the heavy ν_{R3} mass can indeed be traced back from measured slepton masses in universal supersymmetric theories. For the given scenario, the right-handed neutrino mass of the third generation is estimated in the margin $M_{\nu_{R3}} = 10^{14.9\pm0.2}$ GeV. Based on this estimate, the seesaw mechanism determines the value of lightest neutrino mass to $m_{\nu_1} = 10^{-2.5\pm0.3}$ eV.

Thus the combination of SO(10) symmetry, *i.e.* universal scalar masses and gauge couplings, and the seesaw mechanism leads, besides the high-scale SUSY parameters, to the determination of the heavy Majorana mass $M_{\nu_{R3}}$ of the third generation and, in a consecu-
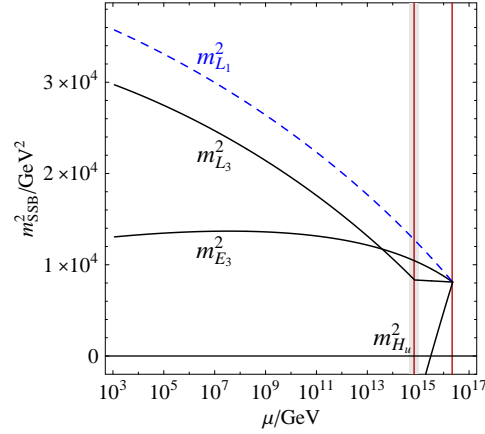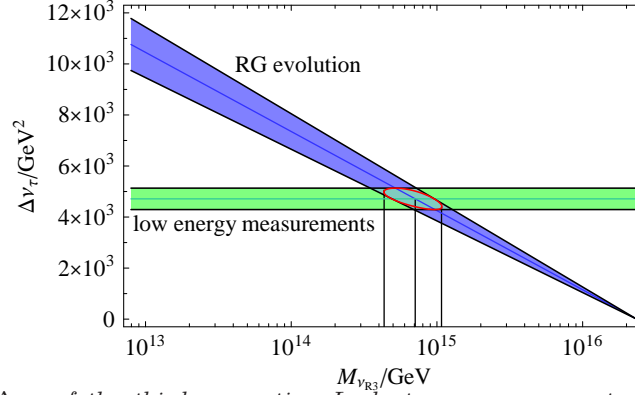
Figure 2: *Shift Δ_{ν_τ} of the third generation L slepton mass parameter generated by loops involving heavy r.h. neutrinos. The blue wedge corresponds to the prediction from the renormalization group, whereas the green band is determined by low-energy mass measurements.*

tive step, to an estimate value of the lightest neutrino mass m_{ν_1} in hierarchical theories.

References

[1] Slides:
    `http://ilcagenda.linearcollider.org/contributionDisplay.py?contribId=58&sessionId=69&confId=1296`

[2] Super-Kamiokande collaboration, Y. Fukuda *et al.*, Phys. Rev. Lett. **81**, 1562 (1998), [hep-ex/9807003]; SNO collaboration, Q. R. Ahmad *et al.*, Phys. Rev. Lett. **89**, 011301 (2002), [nucl-ex/0204008]; Kam-LAND collaboration, K. Eguchi *et al.*, Phys. Rev. Lett. **90**, 021802 (2003), [hep-ex/0212021].

[3] H. Georgi, AIP Conf. Proc. **23** (1975) 575; H. Fritzsch and P. Minkowski, Nucl. Phys. B **103** (1976) 61;

[4] P. Minkowski, Phys. Lett. B **67** (1977) 421; T. Yanagida, *Proceedings, Workshop on the Baryon Number of the Universe and Unified Theories (Tsukuba 1979)*; M. Gell-Mann, P. Ramond and R. Slansky, PRINT-80-0576-CERN; R. N. Mohapatra and G. Senjanovic, Phys. Rev. Lett. **44**, 912 (1980); J. Schechter and J. W. F. Valle, Phys. Rev. **D22**, 2227 (1980).

[5] A. Freitas, W. Porod and P. M. Zerwas, Phys. Rev. D **72** (2005) 115002 [arXiv:hep-ph/0509056].

[6] G. A. Blair, W. Porod and P. M. Zerwas, Phys. Rev. D **63** (2001) 017703 [arXiv:hep-ph/0007107]; G. A. Blair, W. Porod and P. M. Zerwas, Eur. Phys. J. C **27** (2003) 263 [arXiv:hep-ph/0210058].

[7] J. A. Aguilar-Saavedra *et al.*, Eur. Phys. J. C **46** (2006) 43 [arXiv:hep-ph/0511344].

[8] B. C. Allanach *et al.*, in *Proceedings, APS/DPF/DPB Summer Study on the Future of Particle Physics (Snowmass 2001),* and Eur. Phys. J. C **25** (2002) 113 [arXiv:hep-ph/0202233].

[9] A. Freitas, A. von Manteuffel and P. M. Zerwas, Eur. Phys. J. C **34** (2004) 487; A. Freitas, H. U. Martyn, U. Nauenberg and P. M. Zerwas, in *Proc. of the International Conference on Linear Colliders (LCWS 04), Paris, France, 19-24 Apr 2004* [hep-ph/0409129].

[10] K. Desch, J. Kalinowski, G. Moortgat-Pick, M. M. Nojiri and G. Polesello, JHEP **0402**, 035 (2004).

[11] P. Bechtle, K. Desch and P. Wienemann, Comput. Phys. Commun. **174** (2006) 47 [arXiv:hep-ph/0412012]; P. Bechtle, K. Desch, W. Porod and P. Wienemann, Eur. Phys. J. C **46** (2006) 533 [arXiv:hep-ph/0511006]; R. Lafaye, T. Plehn and D. Zerwas, arXiv:hep-ph/0512028 and R. Lafaye, T. Plehn and D. Zerwas, arXiv:hep-ph/0404282.

[12] W. Porod, Comput. Phys. Commun. **153**, 275 (2003) [arXiv:hep-ph/0301101].

Detection of long-lived staus and gravitinos at the ILC

Hans-Ulrich Martyn

RWTH Aachen, Aachen, and Deutsches Elektronen-Synchrotron DESY, Hamburg, Germany

A study is presented illustrating the excellent potential of future International Linear Collider (ILC) experiments to detect metastable staus $\tilde{\tau}$, measure precisely their mass and lifetime, and to determine the mass of the gravitino $\tilde{G}$ from the decay $\tilde{\tau} \to \tau\tilde{G}$, thus providing direct access to the gravitational coupling, respectively Planck scale.

1 Introduction

Supersymmetry (SUSY) provides an attractive scenario to account for the amount of dark matter in the universe. If R-parity is conserved, the lightest supersymmetric particle (LSP) is stable and an ideal dark matter candidate. A very interesting option is the spin $3/2$ gravitino $\tilde{G}$. The mass of the gravitino is set by the SUSY breaking scale F via $m_{3/2} = m_{\tilde{G}} = F/\sqrt{3}\,M_P$, with $M_P \simeq 2.4 \cdot 10^{18}$ GeV the reduced Planck scale. In general $m_{3/2}$ is a free parameter and may extend over a wide range of $\mathcal{O}(\text{eV} - \text{TeV})$ for gauge, gaugino and supergravity mediated symmetry breaking.

A gravitino LSP may be produced in decays of SUSY particles. If the next-to-lightest supersymmetric particle (NLSP) is the scalar tau $\tilde{\tau}$, the dominant process is $\tilde{\tau} \to \tau\tilde{G}$. Since the coupling is gravitational, the lifetime may be very long, ranging from seconds to years. The decay-width $\Gamma_{\tilde{\tau}}$, respectively lifetime $\tau = \Gamma_{\tilde{\tau}}^{-1}$, of the $\tilde{\tau}$ NLSP

$$\Gamma_{\tilde{\tau} \to \tau\tilde{G}} = \frac{1}{48\pi M_P^2} \frac{m_{\tilde{\tau}}^5}{m_{\tilde{G}}^2} \left[1 - \frac{m_{\tilde{G}}^2}{m_{\tilde{\tau}}^2} \right]^4 \tag{1}$$

depends only on the masses $m_{\tilde{\tau}}$ and $m_{\tilde{G}}$ as well as on the Planck scale M_P – no further SUSY parameters are required.

The cosmological production of gravitino dark matter proceeds essentially via thermal production and/or late decays of the NLSP. The big bang nucleosynthesis puts constraints on the $\tilde{\tau}$ lifetime [1], typically $\tau \lesssim 10^7$ s for $m_{\tilde{G}} \sim 100$ GeV. Bound states of $\mathcal{N}\tilde{\tau}^-$ may alter the production of light elements considerably, but possible consequences are controversial [2].

Experiments at the ILC offer a unique possibility to detect long-lived staus and to study the properties of gravitinos, which cannot be observed in astrophysical experiments. A variety of spectra and SUSY breaking scenarios have been investigated experimentally in detail [3]; here just two models, mSUGRA and GMSB scenarios, are presented.

2 $\tilde{\tau}$ detection & measurement principles

A typical ILC detector [4] is shown in Fig. 1. The main characteristics, relevant to the present study, are: a TPC with excellent tracking and dE/dx resolution to identify slow, heavy particles by ionisation; a highly segmented hadronic calorimeter (HCAL) with energy resolutions $\delta E_h/E = 0.5/\sqrt{E/\text{GeV}}$ for hadrons and $\delta E_{em}/E = 0.2/\sqrt{E/\text{GeV}}$ for electrons/photons; an instrumented iron yoke to allow for muon detection and coarse calorimetric measurements of hadrons. The amount of material available to absorb a heavy $\tilde{\tau}$ in the HCAL or yoke corresponds to an acceptance for scaled momenta of $p/m = \beta\gamma \lesssim 0.4-0.5$.

The stau detection and measurement principle consists of several steps: identify a $\tilde{\tau}$ and determine its mass from kinematics; follow the track until it is trapped inside the detector; observe the stopping point until a decay $\tilde{\tau} \to \tau \tilde{G}$ is triggered by a large energy release uncorrelated to beam collisions; record the decay time to determine the $\tilde{\tau}$ lifetime; finally, measure the τ recoil energy to get the gravitino mass

$$ E_\tau = \frac{m_{\tilde{\tau}}}{2} \left(1 - \frac{m_{\tilde{G}}^2 - m_\tau^2}{m_{\tilde{\tau}}^2} \right) . \quad (2) $$

Figure 1: Quadrant of a typical ILC detector [4], length units in mm; amount of material indicated by R [$\mathrm{g\,cm^{-2}}$]

The ILC provides a very favourable environment. The energy can be adjusted to optimise the number of observable staus. The e^+e^- beams collide in bunch trains of 1 ms duration repeated every 200 ms; the detector is inactive most of the time and ideally suited to measure long-lived particles. However, it is envisaged to operate the HCAL in a pulsed mode, switching on only during collisions. Clearly this concept has to be revised.

3   Experimental analyses – case studies

The analysis is based on a complete event simulation including QED radiation, beamstrahlung and detector resolutions. The experimental signature is very clean and distinct from Standard Model background. There are no missing particles (except $\nu's$ from decays), the observed particle momenta are balanced, $|\sum_i \vec{p}_i| \simeq 0$, but don't sum up to the cms energy $\sum_i p_i < \sqrt{s}$. These features allow the sparticle masses and decay chains to be reconstructed from the event kinematics. Each SUSY event contains two $\tilde{\tau}'s$, easily identified by ionisation in the TPC, and their passage through the detector can be accurately followed. Stopping $\tilde{\tau}'s$ can be located within a volume of a few cm^3.

The production of low momentum $\tilde{\tau}'s$ with a suitable $\beta\gamma$ factor to be trapped in the detector proceeds either directly or via cascade decays from light sleptons or neutralinos. These processes — $\tilde{\tau}_1\tilde{\tau}_1$, $\tilde{e}_R\tilde{e}_R$, $\tilde{\mu}_R\tilde{\mu}_R$ and $\tilde{\chi}_1^0\tilde{\chi}_1^0$ — rise only slowly above kinematic threshold with cross sections $\sigma \propto \beta^3$, thus providing relatively low rates. More efficient, if kinematically accessible, is associated selectron production $e^+e^- \to \tilde{e}_R\tilde{e}_L$, increasing as $\sigma \propto \beta$ near threshold. The event signatures are multi-lepton topologies: $2\tilde{\tau}_1$ from pair production, $2\tilde{\tau}_1 2\tau$ from neutralino production and $2\tilde{\tau}_1 2\tau 2\ell$ from selectron and smuon production.

3.1   mSUGRA scenario GDM ϵ

In *supergravity mediated symmetry breaking* (SUGRA) the gravitino mass $m_{3/2}$ is a free parameter of the same order as the other sparticle masses. In minimal versions with $\tilde{\tau}$ NLSP the common scalar mass m_0 has to be small and much lower than the common gaugino mass $M_{1/2}$. The mSUGRA scenario GDM ϵ [5] implies unified scalar and gravitino masses $m_0 = m_{3/2} = 20\,\mathrm{GeV}$, $M_{1/2} = 440\,\mathrm{GeV}$, $A_0 = 25\,\mathrm{GeV}$, $\tan\beta = 15$ and sign $\mu = +$. The corresponding sparticle spectrum is compiled in Table 1.
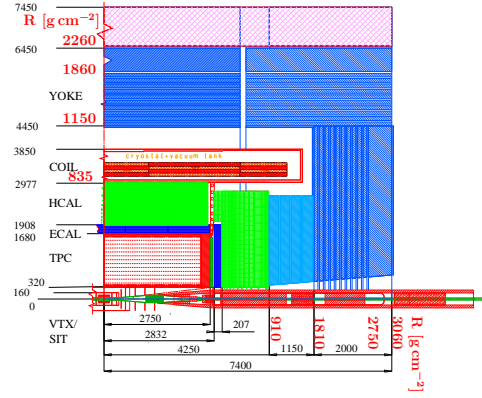
mSUGRA scenario GDM ϵ
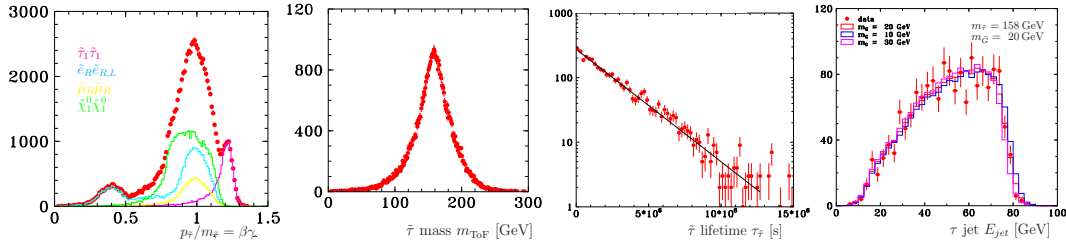
Figure 2: GDM ϵ scenario, assuming $\mathcal{L} = 100\,\mathrm{fb}^{-1}$ at $\sqrt{s} = 500\,\mathrm{GeV}$: (a) $\tilde{\tau}$ production spectra of scaled momentum $p/m = \beta\gamma$ with contributions from various processes; (b) $\tilde{\tau}$ mass m_{ToF} spectrum; (c) $\tilde{\tau}$ lifetime distribution; (d) τ jet energy spectrum of the decay $\tilde{\tau}_1 \to \tau\tilde{G}$ compared with simulations of $m_{\tilde{G}} = 20\,\mathrm{GeV}$, $10\,\mathrm{GeV}$ and $30\,\mathrm{GeV}$

	m [GeV]	$\mathcal{B}$		m [GeV]	$\mathcal{B}$
$\tilde{\tau}_1$	157.6	$\tau\tilde{G}$	$\tilde{\mu}_R$	175.1	$\mu\tau\tilde{\tau}$
$\tilde{e}_R$	175.1	$e\tau\tilde{\tau}$	$\tilde{e}_L$	303.0	$e\tilde{\chi}_1^0$
$\tilde{\chi}_1^0$	179.4	$\tau\tilde{\tau}$	$\tilde{G}$	20	

Table 1: Sparticle masses and decay modes of the mSUGRA scenario GDM ϵ accessible at $\sqrt{s} = 500\,\mathrm{GeV}$

The experimental assumptions for the case study are the canonical ILC energy $\sqrt{s} = 500\,\mathrm{GeV}$ and an integrated luminosity $\mathcal{L} = 100\,\mathrm{fb}^{-1}$ (< 1 year of data taking). The inclusive $\tilde{\tau}$ production cross section is $\sigma(\tilde{\tau}_1\tilde{\tau}_1 X) = 300\,\mathrm{fb}$.

The prolific *stau production* rate is characterised by the scaled momentum distribution $p/m = \beta\gamma$, shown in Fig. 2 a for the various reactions. The majority of particles come from diagonal slepton and neutralino pairs and leave the detector (peak around $\beta\gamma \simeq 1$). One observes, however, a second peak at low $\beta\gamma \lesssim 0.5$ from $\tilde{e}_R\tilde{e}_L$ decays, which will be stopped in the detector. The number of trapped $\tilde{\tau}'s$ are $N_{\tilde{\tau}}^{\mathrm{hcal}} = 4100$ and $N_{\tilde{\tau}}^{\mathrm{yoke}} = 1850$ in the hadron calorimeter and yoke, respectively.

The *stau mass* measurement is based on the kinematics of $e^+e^- \to \tilde{\tau}_1\tilde{\tau}_1$, see magenta curve in Fig. 2 a, to be identified as a pair of collinear, non-interacting particles with momenta $p_{\tilde{\tau}} < \sqrt{s}/2 = E_{\tilde{\tau}}$. A determination of the mean momentum $\langle p_{\tilde{\tau}} \rangle = 192.4 \pm 0.2$ GeV leads to a precise $\tilde{\tau}$ mass of $m_{\tilde{\tau}} = 157.6 \pm 0.2$ GeV.

Alternatively one may select all identified $\tilde{\tau}'s$ and perform a time-of-flight measurement using the calorimeter, having a resolution of $\delta t = 1\,\mathrm{ns}$. The reconstructed mass distribution $m_{\mathrm{ToF}} = \sqrt{(1/\beta^2 - 1)\,p^2}$, displayed in Fig. 2 b, provides an accuracy $\delta m_{\mathrm{ToF}} = 0.15$ GeV, similar to that of the momentum measurement.

The *stau lifetime* measurement is based on the decays of $\tilde{\tau}'s$ which have been stopped in the detector. Requiring an isolated energetic cluster or muon above a certain threshold originating somewhere inside the sensitive fiducial volume of the calorimeter or yoke, results in the decay time distribution shown in Fig. 2 c. A fit to the spectrum gives a $\tilde{\tau}$ lifetime of $\tau = (2.6 \pm 0.05) \cdot 10^6$ s, corresponding to roughly one month.

Note: The relative precision on the $\tilde{\tau}$ lifetime does not depend on the gravitino mass, should it be much lighter as for larger mass splittings or in gauge mediated supersymmetry models.

A *direct gravitino mass* measurement can be performed by exploiting the τ recoil of the decay $\tilde{\tau} \to \tau\tilde{G}$, see (2). The upper endpoints of the energy spectra which coincide with

GMSB scenario SPS 7

Figure 3: SPS 7 scenario, assuming $\mathcal{L} = 100\,\text{fb}^{-1}$ at $\sqrt{s} = 410\,\text{GeV}$: (a) $\tilde{\tau}$ production spectra of scaled momentum $p/m = \beta\gamma$ with contributions from various processes; (b) $\tilde{\tau}$ lifetime distribution; (c) τ jet energy spectrum of the decay $\tilde{\tau}_1 \to \tau\tilde{G}$ compared with simulations of $m_{\tilde{G}} = 0\,\text{GeV}$ and $10\,\text{GeV}$

the primary τ energy $E_\tau = 77.5\,\text{GeV}$, are directly related to the masses involved. Well defined upper edges are provided by the hadronic decays $\tau \to \rho\nu$ and $\tau \to \pi\pi\pi\nu$. The energy distribution of both decay modes, defined as 'τ jets', is shown in Fig. 2 d. In order to illustrate the sensitivity to the gravitino mass, simulations assuming the nominal value of $m_{\tilde{G}} = 20\,\text{GeV}$ and shifted by $\pm 10\,\text{GeV}$ are shown as well. A fit to the τ jet energy spectrum yields a gravitino mass $m_{\tilde{G}} = 20 \pm 4\,\text{GeV}$.

Combining all results one can test the gravitational coupling of the stau to the gravitino and access the Planck scale, respectively Newton's constant. Inserting the expected values and accuracies on $m_{\tilde{\tau}}$, τ and $m_{\tilde{G}}$ in (1) one finds for the supergravity Planck scale $M_P = (2.4 \pm 0.5) \cdot 10^{18}$ GeV, where the error is dominated by the gravitino mass measurement. It is a unique feature of gravitino LSP scenarios that the Planck scale can be directly measured in particle experiments by investigating the properties of the NLSP and its decay.

The *gravitino mass* can be deduced more precisely from the $\tilde{\tau}$ mass and lifetime, if the gravitational coupling is shown to be responsible for the decay or is *assumed* and the macroscopic value of M_P is taken in the decay-width of (1). The resulting gravitino mass is $m_{\tilde{G}} = 20 \pm 0.2\,\text{GeV}$. This value can be used to get the supersymmetry breaking scale $F = \sqrt{3}\,M_P\,m_{3/2} = (8.3 \pm 0.1) \cdot 10^{19}\,\text{GeV}^2$, which is an important parameter to unravel the supersymmetry breaking mechanism.

3.2 GMSB scenario SPS 7

Gauge mediated symmetry breaking (GMSB) usually occurs at rather low scales and a light gravitino is naturally the LSP. Typical masses are of order eV to keV which may be extended in the GeV range. The GMSB reference scenario SPS 7 [7] is described by the conventional parameters $\Lambda = 40\,\text{TeV}$, $M_m = 80\,\text{TeV}$, $N_m = 3$, $\tan\beta = 15$ and sign $\mu = +$, The sparticles are relatively light: $m_{\tilde{\tau}_1} = 123.4\,\text{GeV}$, $m_{\tilde{\ell}_R} = 130.9\,\text{GeV}$, $m_{\tilde{\ell}_L} = 262.8\,\text{GeV}$, $m_{\tilde{\chi}_1^0} = 163.7\,\text{GeV}$. The gravitino mass is set arbitrarily to $m_{\tilde{G}} = 0.1\,\text{GeV}$.

The SPS 7 model is investigated assuming $\sqrt{s} = 410\,\text{GeV}$ and $\mathcal{L} = 100\,\text{fb}^{-1}$, with a large inclusive $\tilde{\tau}$ cross section of $\sigma(\tilde{\tau}_1\tilde{\tau}_1 X) = 420\,\text{fb}$. As seen in the $\beta\gamma$ distribution of Fig. 3 a, most $\tilde{\tau}'s$ leave the detector. There is, however, a large signal at $\beta\gamma \simeq 0.4$ from $\tilde{e}_R\tilde{e}_L$ production, contributing to $N_{\tilde{\tau}}^{\text{hcal}} = 10000$ and $N_{\tilde{\tau}}^{\text{yoke}} = 4900$ trapped $\tilde{\tau}'s$ in the calorimeter and yoke.

The analysis of $\tilde{\tau}_1\tilde{\tau}_1$ pair production yields a mass of $m_{\tilde{\tau}_1} = 124.3 \pm 0.1\,\text{GeV}$. From a fit

to the decay time distribution, shown in Fig. 3 b, one obtains a lifetime of $\tau = 209.3 \pm 2.4$ s. These values can be used to derive a very accurate gravitino mass of $m_{\tilde{G}} = 100 \pm 1$ MeV *assuming* a gravitational coupling. To illustrate of the sensitivity to low gravitino masses as expected in many GMSB models: a gravitino mass of 0.5 MeV corresponds a $\tilde{\tau}$ lifetime of 5 ms, which should be easily measurable.

The τ recoil energy spectrum is displayed in Fig. 3 c. As can be seen from the simulation curves for 0 GeV and 10 GeV gravitinos, the measurement is not sensitive to such low masses and can only set an upper limit of $m_{\tilde{G}} < 9$ GeV (at 95% CL). The sensitivity to low gravitino masses decreases rapidly, see (2). A direct measurement of large $\tilde{\tau} - \tilde{G}$ mass splittings becomes extremely difficult, getting impossible for $m_{\tilde{G}}/m_{\tilde{\tau}} \lesssim 0.1$.

The nature of the LSP remains undetermined without knowing the gravitino mass. Further information can be gained from radiative decays $\tilde{\tau} \rightarrow \tau\gamma\tilde{G}$. The differential decay rates for a light spin 3/2 gravitino $\tilde{G}$ compared with a spin 1/2 neutralino $\tilde{\chi}$ [6] and a spin 1/2 axino $\tilde{a}$ [8] are found to exhibit detectable differences. Although experimentally ambitious – branching ratios suppressed by $\mathcal{O}(100)$, single $\gamma's$ to be disentangled from τ decays – the performance of the 'pictorial' calorimeter [4] and the large ILC data samples should allow one to discriminate between a light gravitino, a neutralino and an axino LSP.

4   Conclusions

Future ILC experiments have a rich potential to study Susy scenarios where the gravitino $\tilde{G}$ is the LSP and a charged stau $\tilde{\tau}$ is the long-lived, metastable NLSP. Precise determinations of the $\tilde{\tau}$ mass and lifetime and of the $\tilde{G}$ mass appear feasible already with moderate integrated luminosity. (More Susy scenarios can be found in [3].) A measurement of the gravitino mass from the τ recoil spectra of the decay $\tilde{\tau} \rightarrow \tau\tilde{G}$ gives access to the gravitational coupling, *i.e.* to the Planck scale, and provides a unique test of supergravity. Such observations will put stringent constraints on the gravitino as dark matter candidate.

References

[1] F. D. Steffen, AIP Conf. Proc. **903** (2007) 595.

[2] M. Pospelov, Phys. Rev. Lett. **98** (2007) 231301.
    K. Jedamzik, arXiv:0707.2070 [astro-ph].

[3] H.-U. Martyn, Eur. Phys. J. C **48** (2006) 15.

[4] Tesla Technical Design Report, DESY 2001-011, Part IV: *A Detector for TESLA*.

[5] A. De Roeck *et al.*, Eur. Phys. J. C **49** (2007) 1041.

[6] W. Buchmüller, K. Hamaguchi, M. Ratz, T. Yanagida, Phys. Lett. B **588** (2004) 90.

[7] B.C. Allanach *et al.*, Eur. Phys. J. C **25** (2002) 113.

[8] A. Brandenburg *et al.*, Phys. Lett. B **617** (2005) 99.

How light can the lightest neutralino be?

H. K. Dreiner[1], S. Heinemeyer[2], O. Kittel[*1], U. Langenfeld[1], A. M. Weber[3], and G. Weiglein[4]

1- Physikalisches Institut der Universität Bonn
Nußallee 12, 53115 Bonn - Germany

2- Instituto de Fisica de Cantabria (CSIC-UC),
Santander - Spain

3- Max-Planck-Institut für Physik (Werner-Heisenberg-Institut)
Föhringer Ring 6, 80805 München - Germany

4- University of Durham - IPPP
Durham DH1 3LE - UK

We show that in the Minimal Supersymmetric Standard Model, the mass of the lightest neutralino is experimentally unconstrained if the GUT relation between the gaugino mass parameters M_1 and M_2 is dropped. We discuss what the impact of light or massless neutralinos would be on their production at LEP, as well as on electroweak precision data and rare decays.

1 Introduction

In the Minimal Supersymmetric Standard Model (MSSM) [2], the masses and mixings of the neutralinos and charginos are given by their mass matrices [2,3]

$$
\mathcal{M}_0 = M_Z \begin{pmatrix} M_1/M_Z & 0 & -s_\theta c_\beta & s_\theta s_\beta \\ 0 & M_2/M_Z & c_\theta c_\beta & -c_\theta s_\beta \\ -s_\theta c_\beta & c_\theta c_\beta & 0 & -\mu/M_Z \\ s_\theta s_\beta & -c_\theta s_\beta & -\mu/M_Z & 0 \end{pmatrix}, \quad \mathcal{M}_\pm = M_W \begin{pmatrix} M_2/M_W & \sqrt{2}s_\beta \\ \sqrt{2}c_\beta & \mu/M_W \end{pmatrix},
$$

(1)

respectively, with $c_\beta = \cos\beta$, $s_\beta = \sin\beta$ and $c_\theta = \cos\theta_w$, $s_\theta = \sin\theta_w$, with the weak mixing angle θ_w. Besides the masses of the W and Z boson, M_W and M_Z, respectively, the neutralino and chargino sectors at tree level only depend on the $U(1)_Y$ and $SU(2)_L$ gaugino masses M_1 and M_2, respectively, the higgsino mass parameter μ, and the ratio $\tan\beta = v_2/v_1$ of the vacuum expectation values of the two Higgs fields. The neutralino (chargino) masses are the square roots of the eigenvalues of $\mathcal{M}_0\mathcal{M}_0^\dagger$ $(\mathcal{M}_\pm\mathcal{M}_\pm^\dagger)$ [3]. The LEP limit on the chargino mass is $m_{\tilde{\chi}_1^\pm} \gtrsim 100$ GeV [3], from which follows that $M_2, |\mu| \gtrsim 100$ GeV. If the GUT relation $M_1 = 5/3\tan^2(\theta_w)M_2 \approx 0.5\,M_2$ is assumed, then $M_1 \gtrsim 50$ GeV, such that the lightest neutralino mass is constrained to $m_{\tilde{\chi}_1^0} \gtrsim 50$ GeV [3]. However, if one drops the GUT relation, M_1 is an independent parameter, allowing to tune the neutralino mass determined from the lowest-order mass matrix $\mathcal{M}_0$ freely [4–8]. The neutralino mass is identically zero for [5]

$$
\det(\mathcal{M}_0) = 0 \quad \Rightarrow M_1 = \frac{M_Z^2 M_2 \sin^2\theta_w \sin(2\beta)}{\mu M_2 - M_Z^2 \cos^2\theta_w \sin(2\beta)} \approx 0.05\frac{M_Z^2}{\mu} = \mathcal{O}(1\,\text{GeV}).
$$

(2)

For $M_1 \ll M_2, |\mu|$, the neutralino $\tilde{\chi}_1^0$ is mainly a bino, i.e., it couples to hypercharge, and

---

*Speaker
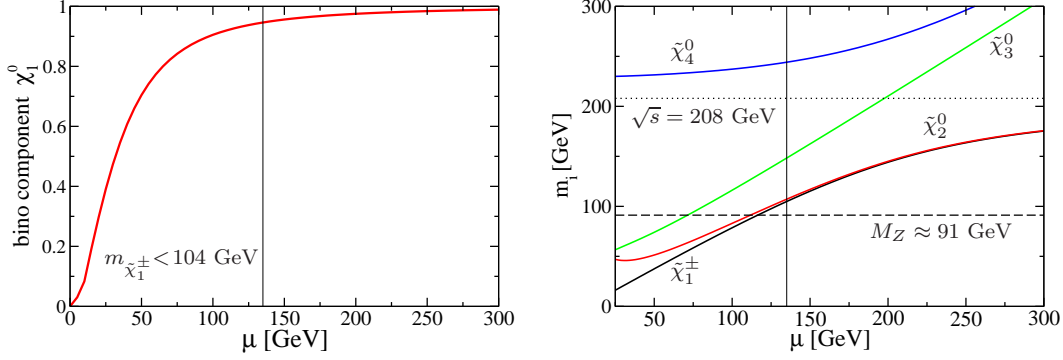
Figure 1: Bino admixture of $\tilde{\chi}_1^0$ (left plot) and masses of charginos and neutralinos (right plot) for $M_2 = 200$ GeV, $\tan\beta = 10$, and M_1 as given in Eq. (2), such that $m_{\tilde{\chi}_1^0} = 0$ GeV [7]. Left to the vertical lines at $\mu \approx 135$ GeV, the chargino mass is $m_{\tilde{\chi}_1^\pm} < 104$ GeV. In the right panel, the dotted line indicates the reach of LEP2 ($\sqrt{s} = 208$ GeV) for $e^+e^- \to \tilde{\chi}_1^0\tilde{\chi}_i^0$ production, and the dashed line indicates the mass of the Z boson, $M_Z \approx 91$ GeV.

the masses of the other neutralinos and charginos are of the order of M_2 and $|\mu|$, see Fig. 1. In the following, we discuss bounds on the neutralino mass from production at LEP and from precision observables [7,8], as well as bounds from rare meson decays [9]. Finally, we summarize bounds from cosmology and astrophysics [6–8].

2 Neutralino production at LEP

The OPAL collaboration [10] has derived upper bounds on the topological neutralino production cross section $\sigma(e^+e^- \to \tilde{\chi}_1^0\tilde{\chi}_2^0) \times \mathrm{BR}(\tilde{\chi}_2^0 \to Z\tilde{\chi}_1^0) \times \mathrm{BR}(Z \to q\bar{q})$ at LEP with $\sqrt{s} = 208$ GeV, normalized such that $\mathrm{BR}(\tilde{\chi}_2^0 \to Z\tilde{\chi}_1^0) = 1$. Their observed limit at 95% confidence level in the $m_{\tilde{\chi}_1^0}$–$m_{\tilde{\chi}_2^0}$ plane is shown in Fig. 2(a). For $m_{\tilde{\chi}_1^0} = 0$ GeV, one can roughly read off the upper limit $\sigma(e^+e^- \to \tilde{\chi}_1^0\tilde{\chi}_1^0 q\bar{q}) < 50$ fb, or equivalently, since $\mathrm{BR}(Z \to q\bar{q}) \approx 70\%$, $\sigma(e^+e^- \to \tilde{\chi}_1^0\tilde{\chi}_2^0) < 70$ fb. This is already a very tight bound, since typical neutralino production cross sections can be of the order of 100 fb. For bino-like neutralinos, the main contribution to the cross section is due to $\tilde{e}_R$ exchange. Thus one can translate the OPAL bound on the neutralino production cross section into lower bounds on the selectron mass $m_{\tilde{e}_R} = m_{\tilde{e}_L} = m_{\tilde{e}}$, for $m_{\tilde{\chi}_1^0} = 0$. In Fig. 2(b) we show the contours of $m_{\tilde{e}}$ in the μ–M_2 plane, such that along the contours $\sigma(e^+e^- \to \tilde{\chi}_1^0\tilde{\chi}_2^0) = 70$ fb. For example, for a fixed selectron mass of $m_{\tilde{e}} = 300$ GeV, the area below the 300 GeV contour in Fig. 2(b) is excluded by LEP.

Another search channel at LEP is radiative neutralino production, $e^+e^- \to \tilde{\chi}_1^0\tilde{\chi}_1^0\gamma$. Due to the large background from radiative neutrino production $e^+e^- \to \nu\bar{\nu}\gamma$, we find that the significance is always $S < 0.1$ for $\mathcal{L} = 100$ pb^{-1} and $\sqrt{s} = 208$ GeV [11, 12]. At the ILC however, radiative neutralino production will be measurable, due to the significant higher luminosity and the option of polarized beams [11–13].
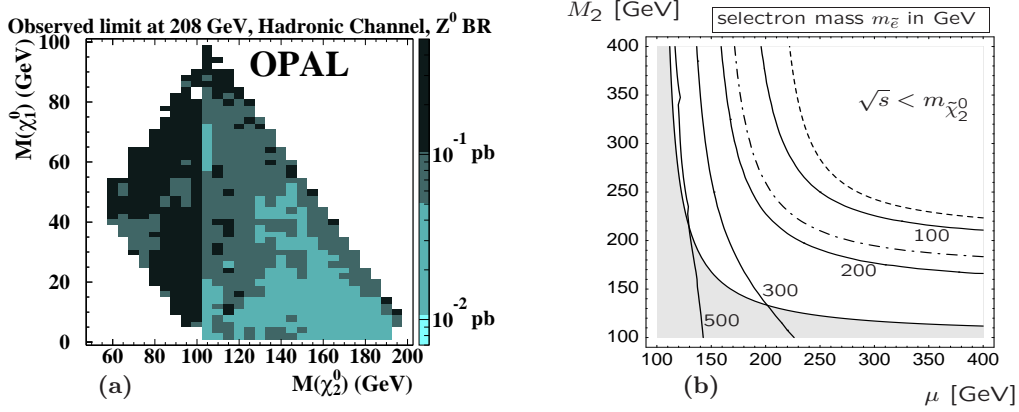
Figure 2: **(a)** 95% confidence limit on the cross section $\sigma(e^+e^- \to \tilde{\chi}_1^0\tilde{\chi}_2^0) \times \mathrm{BR}(\tilde{\chi}_2^0 \to Z\tilde{\chi}_1^0) \times$ $\mathrm{BR}(Z \to q\bar{q})$ with $\mathrm{BR}(\tilde{\chi}_2^0 \to Z\tilde{\chi}_1^0) = 1$ at $\sqrt{s} = 208$ GeV, OPAL collaboration [10]. **(b)** Contour lines in the μ–M_2 plane of the lower bounds on the selectron mass $m_{\tilde{e}_R} = m_{\tilde{e}_L} = m_{\tilde{e}}$, such that $\sigma(e^+e^- \to \tilde{\chi}_1^0\tilde{\chi}_2^0) = 70$ fb for $m_{\tilde{\chi}_1^0} = 0$ with $\tan\beta = 10$ [7]. The dashed line in **(b)** is the kinematical limit $m_{\tilde{\chi}_2^0} = \sqrt{s} = 208$ GeV, along the dot-dashed contour the relation $m_{\tilde{e}} = m_{\tilde{\chi}_2^0}$ holds.

3 Bounds from precision observables and rare decays

The invisible Z width Γ_{inv} is potentially very sensitive to a light or massless neutralino, due to the contribution from $Z \to \tilde{\chi}_1^0\tilde{\chi}_1^0$. However, a light neutralino is mainly bino-like for $|\mu| \gtrsim 125$ GeV, see Fig. 1. For a pure bino, the coupling to the Z boson vanishes at tree level. In Fig. 3, we show the difference $\delta\Gamma = (\Gamma_{\mathrm{inv}} - \Gamma_{\mathrm{inv}}^{\mathrm{exp}})/\Delta\Gamma$ from the measured invisible width $\Gamma_{\mathrm{inv}}^{\mathrm{exp}} = 499.0 \pm 1.5$ MeV [3, 14], in units of the experimental error $\Delta\Gamma = 1.5$ MeV, to the theoretical prediction Γ_{inv}. The calculations of Γ_{inv} include the full $\mathcal{O}(\alpha)$ SM and MSSM contributions, supplemented with leading higher-order terms [15]. The deviation from the measured width $\Gamma_{\mathrm{inv}}^{\mathrm{exp}}$ is larger than 5σ only for $|\mu| \lesssim 125$ GeV. For decreasing $|\mu|$, the increasing higgsino admixture leads to a non-negligible neutralino coupling to the Z boson. Note that already the SM contribution to Γ_{inv} is more than 1σ larger than the experimental value $\Gamma_{\mathrm{inv}}^{\mathrm{exp}}$ [14, 15].

We have also studied the impact of a massless or light neutralino on the W boson mass, the effective leptonic weak mixing angle $\sin^2\theta_{\mathrm{eff}}$, the electric dipole moments of the electron, neutron and mercury, and the anomalous magnetic moment of the muon $(g-2)_\mu$, but have found no significant constraints on the neutralino mass [7]. Also rare decays like $b \to s\gamma$, $\Upsilon(1S) \to \tilde{\chi}_1^0\tilde{\chi}_1^0$ [16], $J/\Psi(B^0) \to \tilde{\chi}_1^0\tilde{\chi}_1^0$, $K[D, B]^+ \to \pi^+\tilde{\chi}_1^0\tilde{\chi}_1^0$, do not constrain $m_{\tilde{\chi}_1^0}$ [9].

4 Bounds from cosmology and astrophysics

The impact of a light neutralino on its thermal relic density has previously been studied [6,8]. If the neutralino accounts for the dark matter, its mass has to be $m_{\tilde{\chi}_1^0} > 3 \ldots 20$ GeV, in order not to over-close the universe. However, this bound can be evaded by allowing a small amount of R parity violation [4]. One would thus assume that the neutralinos are stable on the time scale of collider experiments, but are not stable on cosmological time scales.

Light neutralinos could be thermally produced inside a Supernova. If their mean free
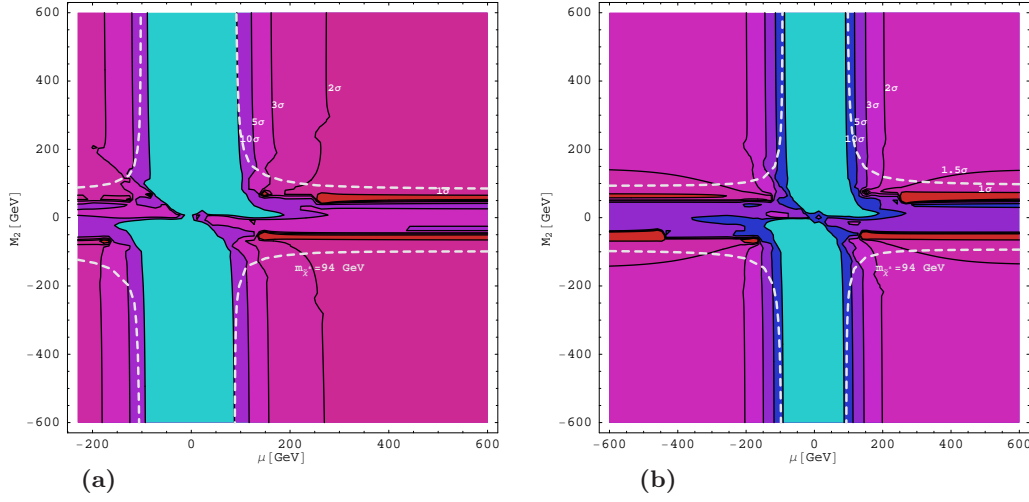
Figure 3: Contour lines in the μ–M_2 plane for the difference $\delta\Gamma = (\Gamma_{\text{inv}} - \Gamma_{\text{inv}}^{\text{exp}})/\Delta\Gamma$ of theory prediction and experimental value of the invisible Z width in units of the experimental error $\Delta\Gamma = 1.5$ MeV, for $m_{\tilde{\chi}_1^0} = 0$ GeV, $\tan\beta = 10$, and **(a)** $A_\tau = A_t = A_b = m_{\tilde{g}} = M_A = 2M_{\tilde{f}} = 500$ GeV, **(b)** $A_\tau = A_t = A_b = m_{\tilde{g}} = M_A = M_{\tilde{f}} = 600$ GeV. Along the dashed line $m_{\tilde{\chi}_1^\pm} = 94$ GeV.

path is of the order of the Supernova core size or lager, the neutralinos escape freely and lead to an additional cooling of the Supernova. To be in agreement with observations of the Kamiokande and IMB Collaborations from SN 1987A, see Ref. [17], the cooling must not shorten the neutrino signal. The energy that is emitted by the neutralinos is much smaller than that emitted by the neutrinos if $m_{\tilde{\chi}_1^0} \gtrsim 200$ MeV [17], with $m_{\tilde{e}} = 500$ GeV. For heavy sleptons, $m_{\tilde{e}} \gtrsim 1200$ GeV, however, no bound on the neutralino mass can be set [8, 17].

A very light neutralino would be a hot dark matter candidate. The Cowsik-McClelland bound [18] gives here $m_{\tilde{\chi}_1^0} \lesssim 1$ eV [8], such that a light relativistic neutralino does not disturb the formation of large structures in the universe. Thus, a light or even massless neutralino can be in agreement with constraints from cosmology and astrophysics.

References

[1] Slides:
    http://ilcagenda.linearcollider.org/contributionDisplay.py?contribId=77&sessionId=69&confId=1296

[2] H. E. Haber and G. L. Kane, Phys. Rept. **117**, 75 (1985).

[3] W. M. Yao *et al.* [Particle Data Group], J. Phys. G **33** (2006) 1.

[4] D. Choudhury, H. K. Dreiner, P. Richardson and S. Sarkar, Phys. Rev. D **61**, 095009 (2000).

[5] I. Gogoladze, J. D. Lykken, C. Macesanu and S. Nandi, Phys. Rev. D **68**, 073004 (2003).

[6] D. Hooper and T. Plehn, Phys. Lett. B **562**, 18 (2003) [arXiv:hep-ph/0212226]. A. Bottino, N. Fornengo and S. Scopel, Phys. Rev. D **67**, 063519 (2003) [arXiv:hep-ph/0212379]. A. Bottino, F. Donato, N. Fornengo and S. Scopel, Phys. Rev. D **68**, 043506 (2003) [arXiv:hep-ph/0304080]; Phys. Rev. D **70**, 015005 (2004) [arXiv:hep-ph/0401186]. G. Belanger, F. Boudjema, A. Cottrant, A. Pukhov and S. Rosier-Lees, JHEP **0403**, 012 (2004) [arXiv:hep-ph/0310037]; G. Belanger, F. Boudjema, A. Pukhov and S. Rosier-Lees, arXiv:hep-ph/0212227, J. S. Lee and S. Scopel, Phys. Rev. D **75**, 075001 (2007) [arXiv:hep-ph/0701221].

[7] H. K. Dreiner, S. Heinemeyer, O. Kittel, U. Langfeld, A. M. Weber, and G. Weiglein, in preparation.

[8] U. Langenfeld, PhD Thesis, University of Bonn, Germany, 2007.

[9] H. K. Dreiner, S. Grab, D. Koschade, M. Kramer, U. Langenfeld and B. Larry, in preparation.

[10] G. Abbiendi *et al.* [OPAL Collaboration], Eur. Phys. J. C **35** (2004) 1 [arXiv:hep-ex/0401026].

[11] H. K. Dreiner, O. Kittel and U. Langenfeld, Phys. Rev. D **74** (2006) 115010 [arXiv:hep-ph/0610020].

[12] H. K. Dreiner, O. Kittel and U. Langenfeld, arXiv:hep-ph/0703009.

[13] G. A. Moortgat-Pick *et al.*, arXiv:hep-ph/0507011.

[14] The ALEPH, DELPHI, L3, OPAL, SLD Collaborations, the LEP Electroweak Working Group, the SLD Electroweak and Heavy Flavour Groups, hep-ex/0509008; hep-ex/0612034; LEP Electroweak Working Group, see: `http://lepewwg.web.cern.ch/LEPEWWG/Welcome.html`.

[15] S. Heinemeyer, W. Hollik, A. M. Weber and G. Weiglein, MPP-2007-65, in preparation.

[16] B. McElrath, Phys. Rev. D **72**, 103508 (2005) [arXiv:hep-ph/0506151].

[17] H. K. Dreiner, C. Hanhart, U. Langenfeld and D. R. Phillips, Phys. Rev. D **68** (2003) 055004 [arXiv:hep-ph/0304289]; M. Kachelriess, JHEP **0002**, 010 (2000) [arXiv:hep-ph/0001160].

[18] R. Cowsik and J. McClelland, Phys. Rev. Lett. **29** (1972) 669.

Monte Carlo Simulations
for NLO Chargino Production at the ILC

Tania Robens [*]

RWTH Aachen - Institut für Theoretische Physik E
52056 Aachen - Germany

We present an extension of the Monte Carlo Event Generator `WHIZARD` which includes chargino production at the ILC at NLO. We include photons using both a fixed order and a resummation approach. In the latter, leading higher order corrections are automatically included. We present results for cross sections and event generation for both methods [1].This is an updated version of the results presented in [2].

1 Introduction

In many GUT models, the masses of charginos tend to be near the lower edge of the super-partner spectrum, and they can be pair-produced at a first-phase ILC with c.m. energy of 500 GeV. The precise measurement of their parameters (masses, mixings, and couplings) is a key for uncovering the fundamental properties of the MSSM [3]. Regarding the experimental precision at the ILC, off-shell kinematics for the signal process, the reducible and irreducible backgrounds [4], and NLO corrections need to be included. We here present the inclusion of NLO chargino production where corrections can be in the percent regime.

2 Chargino production at LO and NLO

The total fixed-order NLO cross section is given by

$$\sigma_{\mathrm{tot}}(s, m_e^2) = \sigma_{\mathrm{Born}}(s) + \sigma_{\mathrm{v+s}}(s, \Delta E_\gamma, m_e^2) + \sigma_{2\to3}(s, \Delta E_\gamma, m_e^2), \qquad (1)$$

where s is the cm energy, m_e the electron mass, and ΔE_γ the soft photon energy cut dividing the photon phase space. The 'virtual' contribution σ_{v} is the interference of the one-loop corrections [5] with the Born term. The collinear and infrared singularities are regulated by m_e and the photon mass λ, respectively. The dependence on λ is eliminated by adding the soft real photon contribution $\sigma_{\mathrm{s}} = f_{\mathrm{soft}}\,\sigma_{\mathrm{Born}}(s)$ with a universal soft factor $f_{\mathrm{soft}}(\frac{\Delta E_\gamma}{\lambda})$ [6]. We break the 'hard' contribution $\sigma_{2\to3}(s, \Delta E_\gamma, m_e^2)$, i.e., the real-radiation process $e^- e^+ \to \tilde{\chi}_i^- \tilde{\chi}_j^+ \gamma$, into a collinear and a non-collinear part, separated at a photon acollinearity angle $\Delta\theta_\gamma$ relative to the incoming electron or positron. The collinear part is approximated by convoluting the Born cross section with a structure function $f(x; \Delta\theta_\gamma, \frac{m_e^2}{s})$ [7]. The non-collinear part is generated explicitly.

The total fixed order cross section is implemented in the multi-purpose event generator `O'Mega`/`WHIZARD` [8, 9] using a 'user-defined' structure function and an effective matrix element $|\mathcal{M}_{\mathrm{eff}}|^2$ which contains the Born part, the soft-photon factor and the Born-1 loop interference term. In the soft-photon region this approach runs into the problem of negative
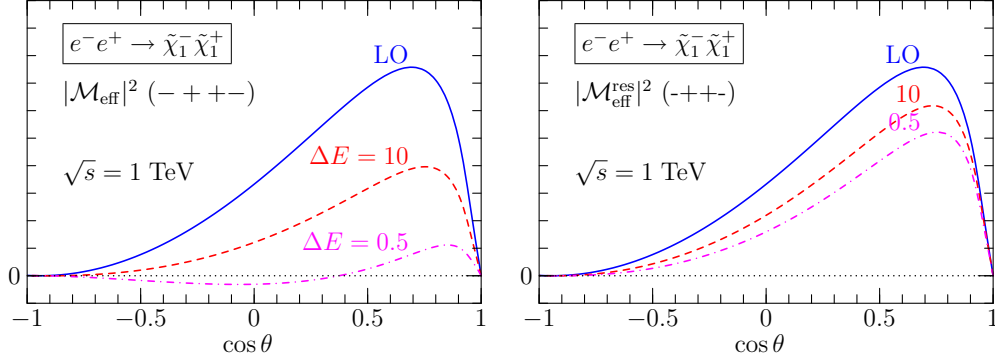
Figure 1: θ -dependence of effective squared matrix element ($\sqrt{s} = 1$ TeV).Left figure: fixed order effective matrix element; right figure: effective matrix element with the one-photon ISR part subtracted. Solid line: Born term; dashed: including virtual and soft contributions for $\Delta E_\gamma = 10$ GeV; dotted: same with $\Delta E_\gamma = 0.5$ GeV. $\Delta\theta_\gamma = 1°$.

event weights [10]: for some values of θ, the $2 \to 2$ part of the NLO-corrected squared matrix element is positive definite by itself only if ΔE_γ is sufficiently large, cf Fig. 1. To still obtain unweighted event samples, an ad-hoc approach is to simply drop events with negative events before proceeding further.

Negative event weights can be avoided by resumming higher-order initial radiation using an exponentiated structure function f_{ISR} [11]. In order to avoid double-counting in the combination of the ISR-resummed LO result with the additional NLO contributions [5], we have subtract from the effective squared matrix element the soft and virtual photonic contributions that have already been accounted for in $\sigma_{\text{s+v}}$. This defines $|\mathcal{M}_{\text{eff}}^{\text{res}}|^2 = |\mathcal{M}_{\text{eff}}|^2 - 2f_{\text{soft,ISR}}|\mathcal{M}_{\text{Born}}|^2$ which is positive for even low ΔE_γ cuts for all values of θ (cf Fig. 1), such that unweighting of generated events and realistic simulation at NLO are now possible in all regions of phase-space. Convoluting this with the resummed ISR structure function for each incoming beam, we obtain a modified $2 \to 2$ part of the total cross section which also includes soft and collinear photonic corrections to the Born/one-loop interference. This differs from the standard treatment in the literature (cf eg. [5]) where higher order photon contributions are combined with the Born term only ("Born+"). The complete result contains the hard non-collinear $2 \to 3$ part convoluted with the ISR structure function:

$$\sigma_{\text{res},+} = \int^{\Delta(E,\theta)} dx_i \, d\Gamma_2 \, f_{\text{ISR}}^{(e^+)}(x_1) f_{\text{ISR}}^{(e^-)}(x_2) |\mathcal{M}_{\text{eff}}^{\text{res}}|^2 + \int_{\Delta(E,\theta)} dx_i \, d\Gamma_3 \, f_{\text{ISR}}^{(e^+)}(x_1) f_{\text{ISR}}^{(e^-)}(x_2) |\mathcal{M}^{2\to 3}|^2$$

(2)

3   Results

Fig. 2 compares the ΔE_γ dependence of the numerical results from the semianalytic fixed-order calculation with the Monte-Carlo integration in the fixed-order and in the resummation schemes. The fixed-order Monte-Carlo result agrees with the semianalytic result as long as the cutoff is greater than a few GeV but departs from it for smaller cutoff values because here, in some parts of phase space, $|\mathcal{M}_{\text{eff}}|^2 < 0$ is set to zero. The semianalytic fixed-order
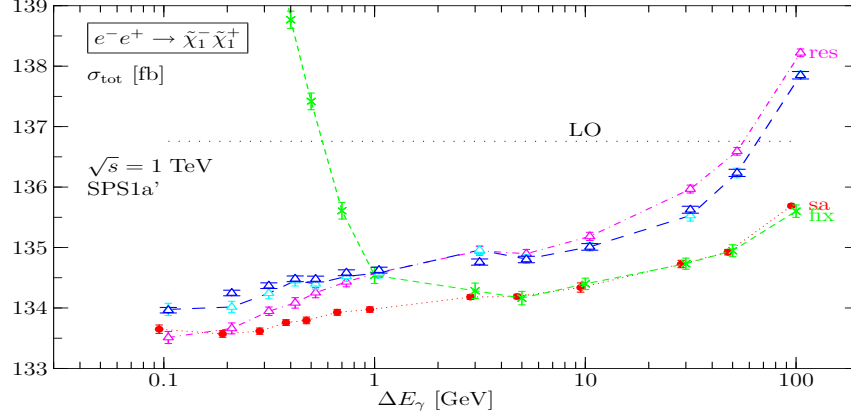
Figure 2: Total cross section dependence on ΔE_γ: 'sa' (dotted) = fixed-order semianalytic result; 'fix' (dashed) = fixed-order Monte-Carlo result; 'res' (long-dashed) = ISR-resummed Monte-Carlo result; (dash-dotted) = same but resummation applied only to the $2 \to 2$ part. $\Delta\theta_\gamma = 1°$. LO: Born cross section.

result is not exactly cutoff-independent, but exhibits a slight rise of the calculated cross section with increasing cutoff (breakdown of the soft approximation). For $\Delta E_\gamma = 1$ GeV (10 GeV) the shift is about 2 permil (5 permil) of the total cross section. The fully resummed result shows an increase of about 5 permil of the total cross section with respect to the fixed-order result which stays roughly constant until $\Delta E_\gamma > 10$ GeV. This is due to higher-order photon radiation.

In Fig. 3 we show the binned distribution of the chargino production angle obtained using a sample of unweighted events. It demonstrates that NLO corrections (which, for total cross sections, are in the percent regime and can reach 20% at the threshold) are important and cannot be accounted for by a constant K factor. Figure 4 shows the magnitude of second

and higher order photonic effects in different schemes. Resummation effects are clearly in the percent regime and cannot be neglected. For $\sqrt{s} > 500$GeV, the convolution of the interference term with f_{ISR} additionally changes the sign of the higher order corrections. For more details, cf. [12, 13].

4 Conclusions

We have implemented NLO corrections into the event generator WHIZARD for chargino pair-production at the ILC with several approaches for the inclusion of photon radiation. A careful analysis of the dependence on the cuts ΔE_γ, $\Delta\theta$ reveals uncertainties related to higher-order radiation and breakdown of the soft or collinear approximations. To carefully choose the resummation method and cutoffs will be critical for a truly precise analysis of real ILC data.The version of the program resumming photons allows to get rid of negative event weights, accounts for all yet known higher-order effects, allows for cutoffs small enough that soft- and collinear-approximation artefacts are negligible, and explicitly generates photons where they can be resolved experimentally. Corrections for the decays of charginos and non-factorizing corrections are in the line of future work.
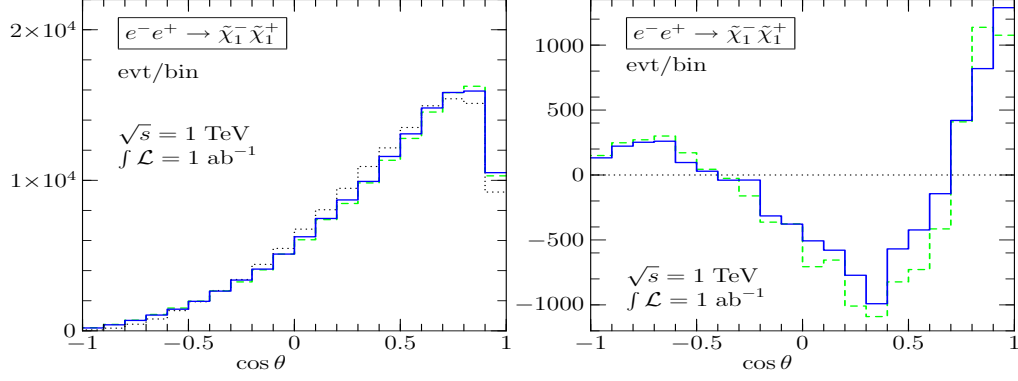
Figure 3: Polar scattering angle distribution for an integrated luminosity of 1 ab^{-1} at $\sqrt{s} = 1$ TeV. Left: total number of events per bin; right: difference w.r.t. the Born distribution. LO (dotted) = Born cross section without ISR; fix (dashed) = fixed-order approach; res (full) = resummation approach. Cutoffs: $\Delta E_\gamma = 3$ GeV and $\Delta\theta_\gamma = 1°$.
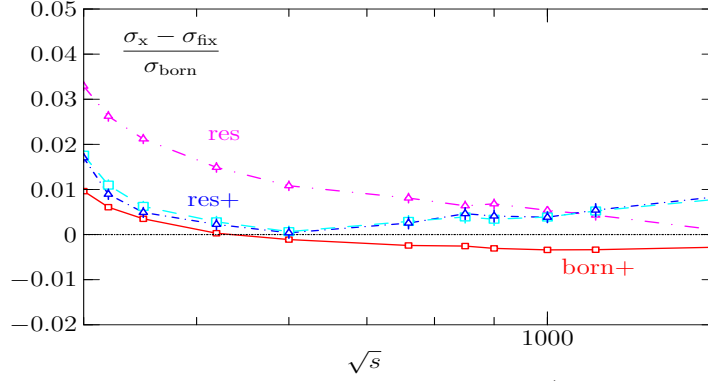
Figure 4: Relative higher-order effects for different methods: (magenta, long dash dotted) = σ_{res}, (blue/ cyan and dash-dotted/ dashed) = $\sigma_{\text{res}+}$, and (red, solid) = $\sigma_{\text{Born}+}$ vs σ_{Born}.

References

[1] http://ilcagenda.linearcollider.org/contributionDisplay.py?contribId=86&sessionId=69&confId=1296.

[2] W. Kilian, J. Reuter, and T. Robens. *AIP Conf. Proc.*, 903:177–180, 2007.

[3] J. A. Aguilar-Saavedra et al. *Eur. Phys. J.*, C46:43–60, 2006.

[4] K. Hagiwara et al. *Phys. Rev.*, D73:055005, 2006.

[5] T. Fritzsche and W. Hollik. *Nucl. Phys. Proc. Suppl.*, 135:102–106, 2004.

[6] A. Denner. *Fortschr. Phys.*, 41:307–420, 1993.

[7] M. Bohm and S. Dittmaier. *Nucl. Phys.*, B409:3–21, 1993.

[8] Mauro Moretti, Thorsten Ohl, and Jurgen Reuter, 2001. hep-ph/0102195.

[9] Wolfgang Kilian, Thorsten Ohl, and Jurgen Reuter. 2007. arXiv:0708.4233 [hep-ph].

[10] R. Kleiss et al. In *Proceedings, Z physics at LEP 1, vol. 3*, Geneva, 1989.

[11] Maciej Skrzypek and Stanislaw Jadach. *Z. Phys.*, C49:577–584, 1991.

[12] W. Kilian, J. Reuter, and T. Robens. *Eur. Phys. J.*, C48:389–400, 2006.

[13] Tania Robens. PhD thesis, 2006. DESY-THESIS-2006-029, hep-ph/0610401.

Polarization-independent CP-odd Observable in e^+e^- Chargino Production at One Loop

Per Osland[1], Jan Kalinowski[2], Krzysztof Rolbiecki[2] and Alexander Vereshagin[1]

1- Department of Physics and Technology - University of Bergen
Postboks 7803, N-5020 Bergen - Norway

2- Institute of Theoretical Physics - University of Warsaw
PL-00681 Warsaw - Poland

We discuss CP violation in the process $e^+e^- \to \tilde{\chi}_i^+ \tilde{\chi}_j^-$ with unpolarized beams. When the scalars are heavy, the box-diagram results constitute a major part of the full result. However, there are situations when the vertex and self-energy corrections dominate over the box diagrams. We also comment on CP violation in the final chargino decay.

1 Introduction

We review recent work on CP violation in unpolarized $e^+e^- \to \tilde{\chi}_i^+ \tilde{\chi}_j^-$ [1, 2, 3]. Let us consider the process with unpolarized initial beams:

$$e^+(p_1) + e^-(p_2) \to \tilde{\chi}_i^+(k_1) + \tilde{\chi}_j^-(k_2). \tag{1}$$

The crucial point here is that for $i \neq j$ the charginos do not form a particle-antiparticle pair. Hence, while the initial state is in the c.m. frame odd under charge conjugation, the final state has no such symmetry. This leads to the CP-violating effect we discuss here.

2 CP violating observable

Under CP conjugation the S-matrix element $\langle \tilde{\chi}_i^+(\boldsymbol{k}_1), \tilde{\chi}_j^-(\boldsymbol{k}_2)|S|e^+(\boldsymbol{p}_1), e^-(\boldsymbol{p}_2) \rangle$ of the process (1) gets transformed into (up to a phase which is irrelevant for us):

$$\text{CP:} \quad \langle \tilde{\chi}_j^+(-\boldsymbol{k}_2), \tilde{\chi}_i^-(-\boldsymbol{k}_1)|S|e^+(-\boldsymbol{p}_2), e^-(-\boldsymbol{p}_1) \rangle, \tag{2}$$

which amounts to the following change in the cross section[a]: $\boldsymbol{p}_1 \leftrightarrow -\boldsymbol{p}_2$, $\boldsymbol{k}_1 \leftrightarrow -\boldsymbol{k}_2$, $m_i \leftrightarrow m_j$. Due to Poincaré invariance the *unpolarized* cross section $d\sigma_0$ may depend only on the masses m_i, m_j and on two independent scalar variables, say, on Mandelstam's $s \equiv (p_1 + p_2)^2$ and $t \equiv (p_1 - k_1)^2$ which obviously do not change under C or P. Hence, if one sticks to the unpolarized part only, the CP transformation can be reduced to final-state chargino mass interchange: $m_i \leftrightarrow m_j$. Therefore, for equal-mass fermions in the final state ($i = j$) the unpolarized cross section is always P-, C- and CP-even[b]. In contrast, if the chargino species are different, CP-violating terms can arise even in the unpolarized cross-section. That is the effect we will consider, so unless otherwise stated the final-state chargino masses are taken

---

[a]Of course, the coupling constants at vertices with charginos should be considered as functions of the chargino masses m_i, m_j, or, better, the mass indices i, j.

[b]The famous forward-backward asymmetry term in the *unpolarized* cross-section of, say, $e^+e^- \to \mu^+\mu^-$ scattering, which is often referred to as parity violating, in fact only indicates the presence of a parity violating term in the interaction, the unpolarized cross-section itself being, of course, P-even.

non-equal. The polarization-dependent CP-violating observables at one-loop order require more involved analysis and will not be discussed here.

Calculations show that the tree-level cross section (polarized and unpolarized) of the process (1) is CP even [4], but CP-odd terms do arise in the one-loop contributions. Therefore, a natural experimental observable to consider is the ratio

$$\frac{d\sigma_0^{\mathrm{odd}}}{d\sigma_0} \ , \tag{3}$$

where $d\sigma^{\mathrm{odd}}$ is the CP-odd part of the corresponding cross-section:

$$d\sigma_0^{\mathrm{odd}} = \frac{1}{2}\Big[d\sigma_0 - d\sigma_0^{\mathrm{CP}}\Big], \quad d\sigma_0^{\mathrm{CP}} \equiv d\sigma_0\Big|_{m_i \leftrightarrow m_j}. \tag{4}$$

As just mentioned, the CP violation first enters at one loop, thus, to estimate the effect one should calculate $d\sigma_0^{\mathrm{odd}}$ at the one-loop level. On the other hand, in most of the kinematical regions far from any resonance, one can expect (see, e.g. [5, 6, 7, 8]) that the tree level gives a reasonable approximation to $d\sigma_0$ in the denominator of Eq. (3). So, we will deal only with the ratio

$$A_{\mathrm{CP}} = \frac{d\sigma_0^{\mathrm{odd}}\big|_{1\ \mathrm{loop}}}{d\sigma_0\big|_{\mathrm{tree}}} \ . \tag{5}$$

3   Box diagrams vs. full one loop contribution

In [2] partial one-loop calculations were provided for the case of complex higgsino mass parameter μ. A limitation of that analysis was that it was performed in the heavy slepton limit, and furthermore, all one-loop triangle vertex corrections to (5) were dropped. The observed effect turned out to be of the order of a couple of percent[c], depending on the chosen MSSM parameters and the kinematics. As explained in [2], this calculation was done just to make sure that the observable does not vanish, while its magnitude should be estimated from complete one-loop results.

A full calculation has recently been performed [3]. The full result turns out to be of the same order as the box-only estimates. In Fig. 1 the "box-only" and full one-loop values of the observable (5) are plotted as

Figure 1: Box-only contribution (dashed lines) vs. full one-loop result (full lines) in the heavy sfermions limit for $\tan\beta = 2$ and 10.

functions of the higgsino phase ϕ_μ for $\tan\beta = 2$ and 10. The other parameters are taken as: $\sqrt{s} = 600$ GeV, the polar scattering angle $\theta = \pi/3$, the Higgsino mass parameter $\mu = |\mu|e^{i\phi_\mu}$, $|\mu| = 300$ GeV, the SU(2) gaugino mass parameter $M_2 = 200$ GeV, the U(1) gaugino mass

[c]A factor of four was lost in the calculation.
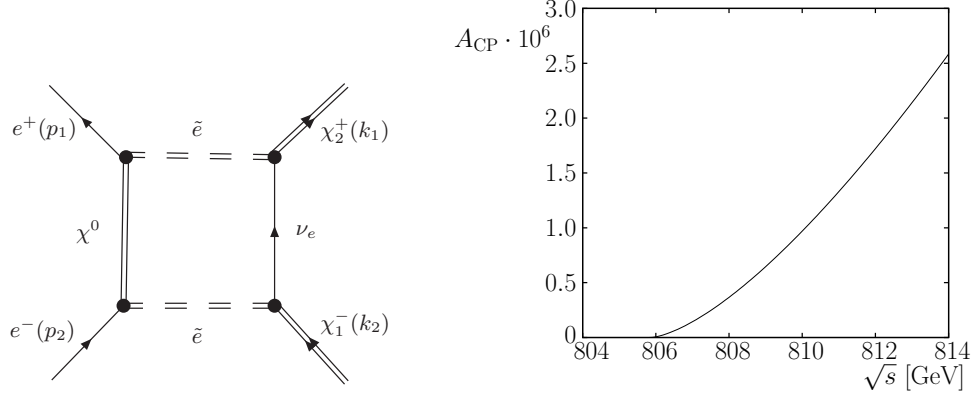
Figure 2: Selectron exchange box diagram and its contribution to (5). The selectron mass is 403 GeV.

parameter (taken to be real) $M_1 = 250$ GeV. The common SUSY breaking mass of the scalars (for the full one-loop calculation) is 1 TeV.

The qualitative agreement for the gauge box contribution alone can be (at least, partially) explained. Indeed, a closer look at the expression for the Z-boson exchange contribution (Eq. (4.1) in [2] gives the D-function part) shows, that only the imaginary part of the box integral can affect the observable. Since in the heavy slepton limit the position of the threshold singularity is high, the integral remains real in the kinematical region we consider. The selectron exchange box diagram provides a nice illustration: when we raise the c.m. energy above the selectron pair production threshold the selectron box diagram develops an absorptive part and its contribution to the asymmetry (5) is non-zero, see Fig. 3 (the selectron mass is 403 GeV). Similar statements can be made about most of the diagrams contributing to (5) at the one-loop order.

The above argument also indicates that in a scenario with lighter sparticles, other diagrams with vertex and self-energy corrections cannot be neglected, as demonstrated in [3]. It was also shown there that for the case of CP-violating origin in the top squark sector the box diagrams do not contribute and the CP asymmetry receives contributions only from vertex and self-energy diagrams.

4 Chargino decay: interference with CP violating effects

Since charginos are not stable particles and decay finally to leptons/quarks and the LSP, in a realistic experiment one has to take into account also chargino decays. On the other hand we know that also in chargino decays it is possible to obtain CP-violating effects at one-loop level [9]. Therefore one can worry if CP-violating effects in the decay would not cancel similar effects in the chargino production. However, a consideration similar to one presented in [2] helps here. As shown in that paper, at the one-loop level the observable (5) among other pieces contains the D-function integral.

To cancel such a contribution at any kinematical point, one needs a corresponding contribution from the final particle decay. So, the only way is the box diagram (e.g. the Z-exchange

box—see [2], Fig. 2) attached to one of the external legs. Even if the mass splitting between charginos is larger than $2m_Z$, the kinematic configuration of the box diagram in the decay is completely different from the one in the production, so the cancelation of different CP-odd contributions is in general not possible. This statement becomes trivial if the mass splitting is smaller than $2m_Z$ and no CP asymmetry arises in the decay due to double Z exchange diagram. Moreover it is even possible to arrange parameters in such a way that no 2-body decay channels remain open for charginos and therefore no CP-odd contribution due to chargino decays enter in the full production+decay process, but still allowing for such contributions in the chargino production. Therefore we conclude that in general CP-odd effects in the production process can not be canceled by CP-odd effects in the decays of charginos.

5 Summary

We have demonstrated that the CP asymmetry built from unpolarized cross sections for non-diagonal chargino pairs in e^+e^- annihilation can arise at the one-loop order.

Acknowledgements

References

[1] Slides:
http://ilcagenda.linearcollider.org/contributionDisplay.py?contribId=56&sessionId=69&confId=1296

[2] P. Osland and A. Vereshagin, Phys. Rev. D **76**, 036001 (2007) [arXiv:0704.2165 [hep-ph]].

[3] K. Rolbiecki and J. Kalinowski, arXiv:0709.2994 [hep-ph].

[4] S. Y. Choi, A. Djouadi, H. S. Song and P. M. Zerwas, Eur. Phys. J. C **8**, 669 (1999) [arXiv:hep-ph/9812236];
S. Y. Choi, A. Djouadi, M. Guchait, J. Kalinowski, H. S. Song and P. M. Zerwas, Eur. Phys. J. C **14**, 535 (2000) [arXiv:hep-ph/0002033];
A. Bartl, K. Hohenwarter-Sodek, T. Kernreiter and H. Rud, Eur. Phys. J. C **36**, 515 (2004) [arXiv:hep-ph/0403265].

[5] T. Blank and W. Hollik, in *2nd ECFA/DESY Study 1998–2001*; arXiv:hep-ph/0011092.

[6] M. A. Diaz and D. A. Ross, JHEP **0106**, 001 (2001) [arXiv:hep-ph/0103309].

[7] T. Fritzsche and W. Hollik, Nucl. Phys. Proc. Suppl. **135**, 102 (2004) [arXiv:hep-ph/0407095].

[8] W. Oller, H. Eberl and W. Majerotto, Phys. Rev. D **71**, 115002 (2005) [arXiv:hep-ph/0504109].

[9] H. Eberl, T. Gajdosik, W. Majerotto and B. Schrausser, Phys. Lett. B **618**, 171 (2005) [arXiv:hep-ph/0502112].

CP Violation in SUSY Particle Production and Decay

Stefan Hesselbach

University of Southampton - School of Physics & Astronomy
Highfield, Southampton SO17 1BJ - UK

Recent studies about CP violation in the Minimal Supersymmetric Standard Model (MSSM) with complex parameters are reviewed. In order to unambiguously identify the CP-violating phenomena it is necessary to study CP-odd or T-odd observables. In chargino and neutralino production and decay at the International Linear Collider (ILC) triple product asymmetries and asymmetries defined via transverse beam polarization have been analyzed. It has been found that these asymmetries can be measured at the ILC in a large region of the MSSM parameter space and are thus an important tool to establish CP violation in supersymmetry.

1 Introduction

In the Lagrangian of the Minimal Supersymmetric Standard Model (MSSM) many parameters can be complex which can give rise to new CP-violating phenomena [2] and may help to explain the baryon-antibaryon asymmetry of the universe [3]. After the elimination of unphysical phases two complex parameters remain in the neutralino and chargino sector, the U(1) gaugino mass parameter M_1 and the higgsino mass parameter μ, whereas the SU(2) gaugino mass parameter M_2 and the ratio $\tan\beta$ of the Higgs vacuum expectation values can be chosen real and positive. In addition the SU(3) gaugino (gluino) mass parameter M_3 and the trilinear scalar couplings A_f in the sfermion sector can be complex.

The new CP-violating phases are constrained by the experimental bounds on electric dipole moments (EDMs) of electron, neutron and Hg atom. However, these constraints are highly model-dependent. In constrained MSSM scenarios only small values of the phases are allowed, especially the phase of μ is strongly limited. In more general supersymmetric (SUSY) models larger phases may be possible due to cancellations between different SUSY contributions to the EDMs or in SUSY models with heavy sfermions in the first two generations [4]. For instance, it has been pointed out recently that for large A_f, phases $\phi_\mu \sim O(1)$ can be compatible with the EDM constraints [5]. Furthermore, the restrictions on the phases may also disappear if lepton flavor violating terms in the MSSM Lagrangian are included [6, 7]. In conclusion, large phases of SUSY parameters cannot be ruled out by present EDM experiments.

The precise determination of the underlying SUSY parameters including the phases is an important task of the International Linear Collider (ILC) [8]. The parameters M_1, M_2, μ and $\tan\beta$ of the neutralino and chargino sector are expected to be determined with very high precision which can be further enhanced by combining LHC and ILC analyses [9]. The impact of the SUSY CP phases on the MSSM Higgs sector is summarized in [10]. While CP-even observables like production cross sections and decay branching ratios may strongly depend on the new phases, CP-odd observables are necessary to unambiguously determine the phases and establish CP violation [11]. Concerning CP-even observables especially the decays of SUSY particles and Higgs bosons are a sensitive probe of the SUSY phases [12]. CP-odd observables can be constructed in form of rate asymmetries or with the help of triple products, transverse beam polarization or the polarization of final state

particles, for recent studies see e.g. [13]. In this contribution studies about CP-odd triple product asymmetries and asymmetries defined via transverse beam polarization in chargino and neutralino production and decay at the ILC are reviewed, focusing especially on their measurability.

2 Triple product asymmetries

T-odd triple product correlations between momenta and spins of the involved particles allow the definition of CP-odd asymmetries already at tree level [14]. For chargino and neutralino production and subsequent two-body decays CP-odd and T-odd asymmetries based on triple products and their measurability have been thoroughly studied in [15]. Decays involving W and Z bosons and those into sfermions and fermions have been analyzed and it has been found that especially in the latter case large asymmetries up to 30% are possible.

Here, I will focus on two studies about chargino and neutralino production and subsequent three-body decays [16, 17], $e^+e^- \rightarrow \tilde{\chi}_i + \tilde{\chi}_j \rightarrow \tilde{\chi}_i + \tilde{\chi}_1^0 f \bar{f}^{(\prime)}$. Including full spin correlations between production and decay products of the form $i\epsilon_{\mu\nu\rho\sigma} p_i^\mu p_j^\nu p_k^\rho p_l^\sigma$ (where the p_i^μ denote the momenta of the involved particles) appear in the amplitude squared in terms, which depend on the spin of the decaying chargino or neutralino [18]. Together with the complex parameters entering the couplings these terms can give real contributions to suitable observables at tree-level. Triple products $\mathcal{T}_1 = \vec{p}_{e^-} \cdot (\vec{p}_f \times \vec{p}_{\bar{f}^{(\prime)}})$ of the initial electron momentum $\vec{p}_{e^-}$ and the two final fermion momenta $\vec{p}_f$ and $\vec{p}_{\bar{f}^{(\prime)}}$ or $\mathcal{T}_2 = \vec{p}_{e^-} \cdot (\vec{p}_{\tilde{\chi}_j} \times \vec{p}_f)$ of the initial electron momentum $\vec{p}_{e^-}$, the momentum of the decaying neutralino or chargino $\vec{p}_{\tilde{\chi}_j}$ and one final fermion momentum $\vec{p}_f$ allow the definition of T-odd asymmetries

$$A_T = \frac{\sigma(\mathcal{T}_i > 0) - \sigma(\mathcal{T}_i < 0)}{\sigma(\mathcal{T}_i > 0) + \sigma(\mathcal{T}_i < 0)} = \frac{\int \mathrm{sign}(\mathcal{T}_i)|T|^2 d\mathrm{Lips}}{\int |T|^2 d\mathrm{Lips}}, \tag{1}$$

where $\int |T|^2 d\mathrm{Lips}$ is proportional to the cross section σ of the combined production and decay process. A_T is odd under naive time-reversal operation and hence CP-odd, if higher order final-state interactions and finite-widths effects can be neglected. In the case of chargino production and decay where the asymmetry $\bar{A}_T$ for the charge-conjugated process is accessible a genuine CP asymmetry

$$A_{\mathrm{CP}} = \frac{A_T - \bar{A}_T}{2} \tag{2}$$

can be defined.

The statistical significance S to which above asymmetries can be determined to be non-zero can be estimated in the following way: The absolute error of A_T is given by $\Delta A_T = S\sqrt{1 - A_T^2}/\sqrt{\sigma \mathcal{L}_{\mathrm{int}}}$, where S denotes the number of standard deviations, σ the cross section of the respective process and $\mathcal{L}_{\mathrm{int}}$ the integrated luminosity [19]. For $A_T \lesssim 10\%$ it is $\Delta A_T = S/\sqrt{\sigma \mathcal{L}_{\mathrm{int}}}$ in good approximation and requiring $A_T > \Delta A_T$ for A_T to be measurable one obtains

$$S = \sqrt{A_T^2 \sigma \mathcal{L}_{\mathrm{int}}} \qquad \text{and} \qquad S = \sqrt{2A_{\mathrm{CP}}^2 \sigma \mathcal{L}_{\mathrm{int}}}, \tag{3}$$

respectively, assuming that the statistical errors of A_T and $\bar{A}_T$ are independent of each other. S can be used as an estimation of the measurability of the asymmetries. However, in order to determine the final accuracy in the experiment also initial state radiation, beamstrahlung, backgrounds and detector effects have to be included. For neutralino production and decay
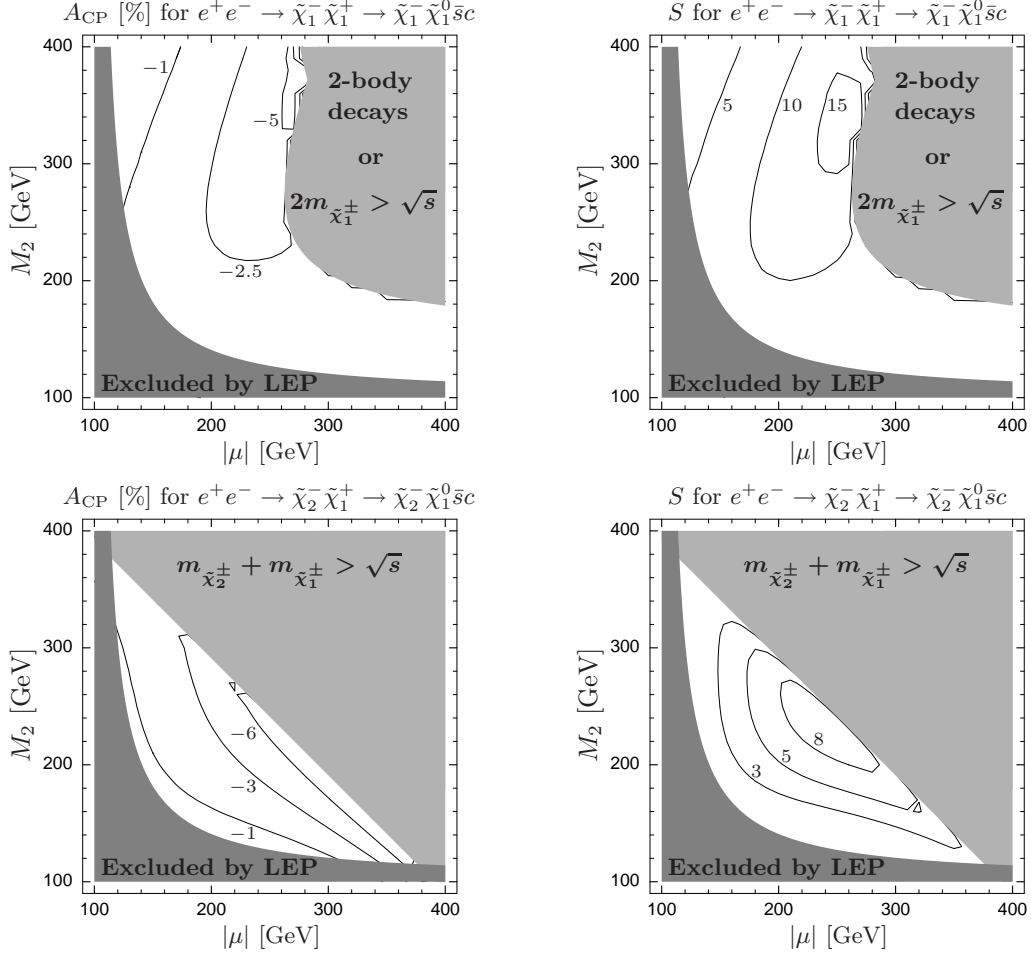
Figure 1: Contour lines of the CP-odd triple product asymmetry $A_{\rm CP}$, Eq. (2), and statistical significance S using $\mathcal{T}_1 = \vec{p}_{e^-} \cdot (\vec{p}_{\bar{s}} \times \vec{p}_c)$ for $|M_1|/M_2 = 5/3 \tan^2 \theta_W$, $\phi_{M_1} = 0.5\pi$, $\phi_\mu = 0$, $\tan\beta = 5$, $m_{\tilde{\nu}} = 250$ GeV, $m_{\tilde{c}} = 500$ GeV, $m_{\tilde{s}} = 505.9$ GeV, $\sqrt{s} = 500$ GeV, $\mathcal{L}_{\rm int} = 500$ fb^{-1} and longitudinal beam polarizations $(P_{e^-}, P_{e^+}) = (-80\%, +60\%)$. From [16].

this has been analyzed in [20] and it has been found that asymmetries $\mathcal{O}(10\,\%)$ are detectable after few years of running of the ILC.

In Figure 1 $A_{\rm CP}$ and S are shown for chargino production $e^+e^- \rightarrow \tilde{\chi}_j^- \tilde{\chi}_1^+$, $j = 1, 2$ and subsequent decay $\tilde{\chi}_1^+ \rightarrow \tilde{\chi}_1^0 \bar{s} c$ using the triple product $\mathcal{T}_1 = \vec{p}_{e^-} \cdot (\vec{p}_{\bar{s}} \times \vec{p}_c)$ [16]. Note that the statistical significance S is larger than 5 in large regions of the parameter space. However, in order to measure $A_{\rm CP}$ it is necessary to discriminate the two outgoing quark jets, i.e. to tag the c jet. The respective c tagging efficiency will decrease the final significance by about a factor 0.5 but nevertheless large regions of the parameter space can be covered. If instead the production plane is reconstructed by analyzing the decays of the $\tilde{\chi}_2^-$ in $e^+e^- \rightarrow \tilde{\chi}_2^- \tilde{\chi}_1^+$ also the leptonic decays $\tilde{\chi}_1^+ \rightarrow \tilde{\chi}_1^0 \ell^+ \nu$ can be used to define $A_{\rm CP}$ using $\mathcal{T}_2 = \vec{p}_{e^-} \cdot (\vec{p}_{\tilde{\chi}_1^+} \times \vec{p}_{\ell^+})$.

In this case, however, the cross sections are rather small, hence S is always smaller than about 5 despite potentially large asymmetries A_{CP}.

For neutralino production $e^+e^- \to \tilde{\chi}_i^0\tilde{\chi}_2^0$, $i = 1, \ldots, 4$, with subsequent leptonic three-body decay $\tilde{\chi}_2^0 \to \tilde{\chi}_1^0\ell^+\ell^-$, $\ell = e, \mu$, the triple product $\mathcal{T}_1 = \vec{p}_{e^-} \cdot (\vec{p}_{\ell^+} \times \vec{p}_{\ell^-})$ can be used to define the T-odd asymmetry A_T, which is directly measurable without reconstruction of the momentum of the decaying neutralino or further final-state analyses. It has been found in [17] that $A_T \gtrsim 10\%$ in large regions of the parameter space for $e^+e^- \to \tilde{\chi}_j^0 + \tilde{\chi}_2^0 \to \tilde{\chi}_j^0 + \tilde{\chi}_1^0\ell^+\ell^-$, $j = 1, 3$, yielding significances S larger than 5.

3 Asymmetries using transverse beam polarization

The use of transverse beam polarization offers further possibilities to define CP-sensitive observables. As all terms in the squared amplitude $|T|^2$ of respective processes which are sensitive to transverse beam polarization depend on the product of the degrees of transverse beam polarization of both beams the CP-sensitive observables are only accessible if both beams of the ILC can be polarized [21]. The respective terms in $|T|^2$ contain products of the form $i\epsilon_{\mu\nu\rho\sigma}t_\pm^\mu p_i^\nu p_j^\rho p_k^\sigma$ or $i\epsilon_{\mu\nu\rho\sigma}t_+^\mu t_-^\nu p_i^\rho p_j^\sigma$, where $t_\pm^\mu$ is the 4-vector of the transverse beam polarization of the positron and electron beam[a], respectively, and the p_i^ν denote the momenta of the involved particles. This in turn allows the definition of CP-odd asymmetries in suitable production and decay processes. In [23] such asymmetries and their measurability have been analyzed for selectron production at an e^-e^- collider. In [24, 25] CP-odd asymmetries using transverse beam polarization have been studied for neutralino production and subsequent two-body decays and their measurability has been compared with CP asymmetries accessible with unpolarized or longitudinally polarized beams.

In chargino production $e^+e^- \to \tilde{\chi}_i^+\tilde{\chi}_j^-$ all CP-odd terms in $|T|^2$ vanish because of CPT invariance and the fact that charginos are Dirac particles [26]. Due to the Majorana nature of the neutralinos the respective terms are allowed in neutralino production $e^+e^- \to \tilde{\chi}_i^0\tilde{\chi}_j^0$ and CP-odd asymmetries can be defined by analyzing the azimuthal distributions of the neutralinos [22]:

$$A_{\mathrm{CP}} = \left[\int_0^{\pi/2} - \int_{\pi/2}^\pi \right] A_{CP}(\theta)\, \mathrm{d}\theta\,, \tag{4}$$

$$A_{\mathrm{CP}}(\theta) = \frac{1}{\sigma} \left[\int_{\frac{\eta}{2}}^{\frac{\pi}{2}+\frac{\eta}{2}} - \int_{\frac{\pi}{2}+\frac{\eta}{2}}^{\pi+\frac{\eta}{2}} + \int_{\pi+\frac{\eta}{2}}^{\frac{3\pi}{2}+\frac{\eta}{2}} - \int_{\frac{3\pi}{2}+\frac{\eta}{2}}^{2\pi+\frac{\eta}{2}} \right] \frac{\mathrm{d}^2\sigma}{\mathrm{d}\phi\,\mathrm{d}\theta} \mathrm{d}\phi\,, \tag{5}$$

where ϕ denotes the azimuthal angle of the scattering plane and η the orientation of the transverse polarizations. The statistical significance is given by $S = \sqrt{A_{\mathrm{CP}}^2 \sigma \mathcal{L}_{\mathrm{int}}}$ or vice versa the necessary integrated luminosity to reach a certain significance by $\mathcal{L}_{\mathrm{int}} = S^2/(A_{\mathrm{CP}}^2\sigma)$.

In Figure 2 A_{CP} and $\mathcal{L}_{\mathrm{int}}$ necessary to reach $S = 5$ are shown for $e^+e^- \to \tilde{\chi}_1^0\tilde{\chi}_2^0$, where it can be seen that also the CP-odd asymmetry defined via transverse beam polarization can be measured in large regions of the SUSY parameter space at the ILC [22]. Similarly, the respective asymmetries for $e^+e^- \to \tilde{\chi}_1^0\tilde{\chi}_3^0$ are well measurable in large regions of the parameter space. However, in order to measure A_{CP} the production plane has to be reconstructed. This is not necessary if the subsequent decays of the neutralinos are included. It has been found in [22, 25] that respective asymmetries including two-body decays of the neutralinos are also measurable in large regions of the SUSY parameter space.

---

[a]For a detailed definition see e.g. [22].

(a) A_{CP} [%] for $e^+e^- \to \tilde\chi_1^0 \tilde\chi_2^0$

(b) $\mathcal{L}_{\mathrm{int}}$ [fb^{-1}] for $e^+e^- \to \tilde\chi_1^0 \tilde\chi_2^0$
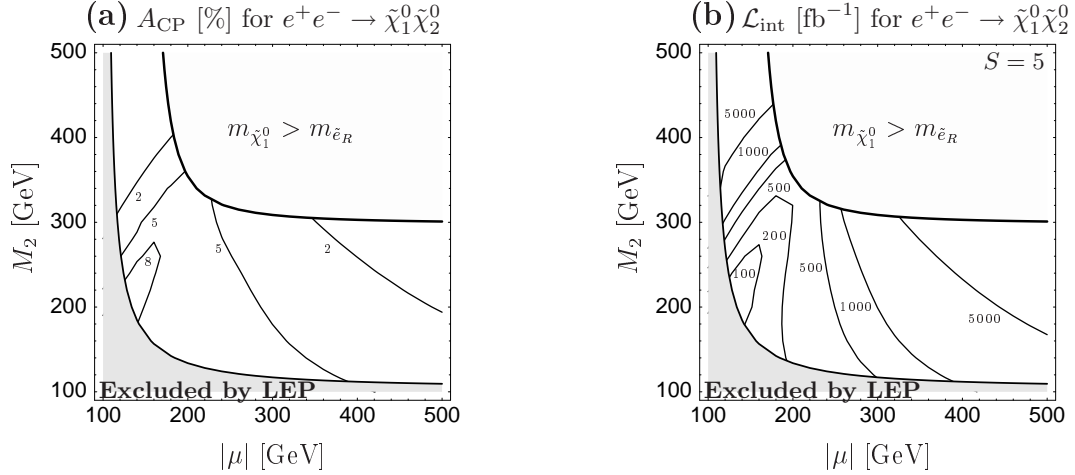
Figure 2: Contour lines of (a) the CP-odd asymmetry A_{CP}, Eq. (4), defined with help of transverse beam polarization and (b) the necessary integrated luminosity to reach a significance $S = 5$ for $|M_1|/M_2 = 5/3 \tan^2\theta_W$, $\phi_{M_1} = 0.5\pi$, $\phi_\mu = 0$, $\tan\beta = 5$, $m_{\tilde e_L} = 400$ GeV, $m_{\tilde e_R} = 150$ GeV, $\sqrt{s} = 500$ GeV and degrees of transverse beam polarizations of (a) $(P_{e^-}^T, P_{e^+}^T) = (100\%, 100\%)$ and (b) $(P_{e^-}^T, P_{e^+}^T) = (80\%, 60\%)$. From [22].

4 Conclusions

Recent studies analyzing CP-odd or T-odd triple product asymmetries or asymmetries defined via transverse beam polarization in chargino and neutralino production and decay have been reviewed. It has been found that these asymmetries are measurable in large regions of the SUSY parameter space and are thus an important tool to search for CP violation in SUSY and to unambiguously determine the SUSY phases.

References

[1] Slides:
http://ilcagenda.linearcollider.org/contributionDisplay.py?contribId=57&sessionId=69&confId=1296

[2] T. Ibrahim and P. Nath, arXiv:0705.2008 (2007).

[3] F. Csikor, Z. Fodor and J. Heitger, Phys. Rev. Lett. **82** 21 (1999);
M. Dine and A. Kusenko, Rev. Mod. Phys. **76** 1 (2004).

[4] For a review, see e.g. T. Ibrahim and P. Nath, hep-ph/0210251 (2002) and references therein;
S. Y. Choi, M. Drees and B. Gaissmaier, Phys. Rev. D **70** 014010 (2004);
M. Pospelov and A. Ritz, Annals Phys. **318** 119 (2005);
K. A. Olive, M. Pospelov, A. Ritz and Y. Santoso, Phys. Rev. D **72** 075001 (2005);
S. Abel and O. Lebedev, JHEP **0601** 133 (2006).

[5] S. Y. Ayazi and Y. Farzan, Phys. Rev. D **74** 055008 (2006).

[6] A. Bartl, W. Majerotto, W. Porod and D. Wyler, Phys. Rev. D **68** 053005 (2003).

[7] S. Y. Ayazi and Y. Farzan, JHEP **0706** 013 (2007).

[8] J. Brau *et al.*, *International Linear Collider Reference Design Report:*
http://www.linearcollider.org/cms/

[9] G. Weiglein *et al.* [LHC/LC Study Group], Phys. Rept. **426** 47 (2006).

[10] E. Accomando *et al.*, CERN-2006-009, arXiv:hep-ph/0608079 (2006).

[11] S. Hesselbach, Acta Phys. Polon. B **35** 2739 (2004) and references therein.

[12] A. Bartl, K. Hidaka, T. Kernreiter and W. Porod, Phys. Lett. B **538** 137 (2002); Phys. Rev. D **66** 115009 (2002);
A. Bartl, S. Hesselbach, K. Hidaka, T. Kernreiter and W. Porod, arXiv:hep-ph/0306281 (2003); Phys. Lett. B **573** 153 (2003); Phys. Rev. D **70** 035003 (2004);
T. Gajdosik, R. M. Godbole and S. Kraml, JHEP **0409** 051 (2004);
T. Ibrahim and P. Nath, Phys. Rev. D **71** 055007 (2005);
S. Heinemeyer and M. Velasco, arXiv:hep-ph/0506267 (2005);
A. Arhrib, R. Benbrik and M. Chabab, Phys. Lett. B **644** 248 (2007);
S. Moretti, S. Munir and P. Poulose, Phys. Lett. B **649** 206 (2007);
T. Ibrahim, arXiv:0704.1913 (2007);
S. Hesselbach, S. Moretti, S. Munir and P. Poulose, arXiv:0706.4269 (2007).

[13] J. A. Aguilar-Saavedra, Phys. Lett. B **596** 247 (2004); Nucl. Phys. B **717**, 119 (2005);
A. Bartl, E. Christova, K. Hohenwarter-Sodek and T. Kernreiter, Phys. Rev. D **70** 095007 (2004);
H. Eberl, T. Gajdosik, W. Majerotto and B. Schrausser, Phys. Lett. B **618** 171 (2005);
S. Y. Choi, B. C. Chung, J. Kalinowski, Y. G. Kim and K. Rolbiecki, Eur. Phys. J. C **46** 511 (2006);
J. R. Ellis, J. S. Lee and A. Pilaftsis, Phys. Rev. D **72** 095006 (2005); Mod. Phys. Lett. A **21** 1405 (2006);
K. Kiers, A. Szynkman and D. London, Phys. Rev. D **74** 035004 (2006);
A. Bartl, E. Christova, K. Hohenwarter-Sodek and T. Kernreiter, JHEP **0611** 076 (2006);
D. Eriksson, S. Hesselbach and J. Rathsman, arXiv:hep-ph/0612198 (2006);
E. Christova, H. Eberl, E. Ginina and W. Majerotto, JHEP **0702** 075 (2007);
A. Szynkman, K. Kiers and D. London, Phys. Rev. D **75** 075009 (2007);
P. Langacker, G. Paz, L. T. Wang and I. Yavin, JHEP **0707** 055 (2007);
M. Frank and I. Turan, Phys. Rev. D **76** 016001 (2007);
P. Osland and A. Vereshagin, Phys. Rev. D **76** 036001 (2007);
J. S. Lee, Mod. Phys. Lett. A **22** 1191 (2007);
A. Arhrib, R. Benbrik, M. Chabab, W. T. Chang and T. C. Yuan, arXiv:0708.1301 (2007).

[14] J. F. Donoghue, Phys. Rev. D **18** 1632 (1978);
Y. Kizukuri and N. Oshimo, Phys. Lett. B **249** 449 (1990);
G. Valencia, arXiv:hep-ph/9411441 (1994);
S. Y. Choi, H. S. Song and W. Y. Song, Phys. Rev. D **61** 075004 (2000).

[15] A. Bartl, H. Fraas, O. Kittel and W. Majerotto, Phys. Rev. D **69** 035007 (2004); Eur. Phys. J. C **36** 233 (2004); Phys. Lett. B **598** 76 (2004);
O. Kittel, A. Bartl, H. Fraas and W. Majerotto, Phys. Rev. D **70** 115005 (2004);
O. Kittel, arXiv:hep-ph/0504183 (2005).

[16] A. Bartl, H. Fraas, S. Hesselbach, K. Hohenwarter-Sodek, T. Kernreiter and G. Moortgat-Pick, Eur. Phys. J. C **51** 149 (2007).

[17] A. Bartl, H. Fraas, S. Hesselbach, K. Hohenwarter-Sodek and G. Moortgat-Pick, JHEP **0408** 038 (2004).

[18] G. Moortgat-Pick, H. Fraas, A. Bartl and W. Majerotto, Eur. Phys. J. C **7** 113 (1999); Eur. Phys. J. C **9** 521 (1999) [Erratum-ibid. C **9** 549 (1999)].

[19] K. Desch, J. Kalinowski, G. Moortgat-Pick, K. Rolbiecki and W. J. Stirling, JHEP **0612** 007 (2006).

[20] J. A. Aguilar-Saavedra, Nucl. Phys. B **697** 207 (2004).

[21] G. Moortgat-Pick *et al.*, arXiv:hep-ph/0507011 (2005).

[22] A. Bartl, H. Fraas, S. Hesselbach, K. Hohenwarter-Sodek, T. Kernreiter and G. Moortgat-Pick, JHEP **0601** 170 (2006).

[23] A. Bartl, H. Fraas, K. Hohenwarter-Sodek, T. Kernreiter, G. Moortgat-Pick and A. Wagner, Phys. Lett. B **644** 165 (2007).

[24] S. Y. Choi, M. Drees and J. Song, JHEP **0609** 064 (2006).

[25] A. Bartl, K. Hohenwarter-Sodek, T. Kernreiter and O. Kittel, arXiv:0706.3822 [hep-ph] (2007).

[26] A. Bartl, K. Hohenwarter-Sodek, T. Kernreiter and H. Rud, Eur. Phys. J. C **36** 515 (2004).

Interplay of Electroweak Precision Observables and B Physics Observables

S. Heinemeyer

Instituto de Fisica de Cantabria (CSIC-UC), Santander, Spain

Indirect information about the possible scale of supersymmetry (SUSY) breaking is provided by B-physics observables (BPO) as well as electroweak precision observables (EWPO). We review the combination of the constraints imposed by recent measurements of the BPO BR($b \to s\gamma$), BR($B_s \to \mu^+\mu^-$), BR($B_u \to \tau\nu_\tau$) and ΔM_{B_s} with those obtained from the experimental measurements of the EWPO M_W, $\sin^2\theta_{\text{eff}}$, Γ_Z, $(g-2)_\mu$ and M_h. We perform a χ^2 fit to the parameters of the constrained minimal supersymmetric extension of the Standard Model (CMSSM), in which the SUSY-breaking parameters are universal at the GUT scale. Assuming that the lightest supersymmetric particle (LSP) provides the cold dark matter density preferred by WMAP and other cosmological data, we confirm the preference found previously for a relatively low SUSY-breaking scale, though there is some slight tension between the EWPO and the BPO.

1   Introduction

In order to achieve a simplification of the plethora of soft SUSY-breaking parameters appearing in the general MSSM, one assumption that is frequently employed is that (at least some of) the soft SUSY-breaking parameters are universal at some high input scale, before renormalization. One model based on this simplification is the constrained MSSM (CMSSM), in which all the soft SUSY-breaking scalar masses m_0 are assumed to be universal at the GUT scale, as are the soft SUSY-breaking gaugino masses $m_{1/2}$ and trilinear couplings A_0. Further parameters are $\tan\beta$, the ratio of the two vacuum expectaion values, and the sign of the Higgs mixing parameter μ.

Within the CMSSM we perform a combined χ^2 analysis [2] of electroweak precision observables (EWPO) [3], going beyond previous such analyses [4, 5] (see also Ref. [6]), and of B-physics observables (BPO), including some that have not been included before in comprehensive analyses of the SUSY parameter space (see, however, Ref. [7]). The set of EWPO included in the analysis is the W boson mass M_W, the effective leptonic weak mixing angle $\sin^2\theta_{\text{eff}}$, the total Z boson width Γ_Z, the anomalous magnetic moment of the muon $(g-2)_\mu$, and the mass of the lightest MSSM Higgs boson mass M_h. In addition, we include four BPO: the branching ratios BR($b \to s\gamma$), BR($B_s \to \mu^+\mu^-$) and BR($B_u \to \tau\nu_\tau$), and the B_s mass mixing parameter ΔM_{B_s}. For the evaluation of the BPO we assume minimal flavor violation (MFV) at the electroweak scale.

2   The χ^2 evaluation

Assuming that the nine observables listed above are uncorrelated, a χ^2 fit has been performed with

$$\chi^2 \equiv \sum_{n=1}^{7} \left[\left(\frac{R_n^{\text{exp}} - R_n^{\text{theo}}}{\sigma_n} \right)^2 + 2\log\left(\frac{\sigma_n}{\sigma_n^{\text{min}}} \right) \right] + \chi^2_{M_h} + \chi^2_{B_s}. \tag{1}$$

Here R_n^{exp} denotes the experimental central value of the nth observable (M_W, $\sin^2\theta_{\text{eff}}$, Γ_Z, $(g-2)_\mu$ and BR($b \to s\gamma$), BR($B_u \to \tau\nu_\tau$), ΔM_{B_s}), R_n^{theo} is the corresponding MSSM prediction and σ_n denotes the combined error (intrinsic, parametric (from m_t, m_b, α_s, $\Delta\alpha_{\text{had}}$), and experimental). Additionally, σ_n^{min} is the minimum combined error over the parameter space of each data set as explained below, and $\chi^2_{M_h}$ and $\chi^2_{B_s}$ denote the χ^2 contribution coming from the experimental limits on the lightest MSSM Higgs boson mass and on BR($B_s \to \mu^+\mu^-$), respectively, see Ref. [2] for details.

In order to take the m_t and m_b parametric uncertainties correctly into account, we evaluate the SUSY spectrum and the observables for each data point first for the nominal values $m_t = 171.4$ GeV [8][a] and $m_b(m_b) = 4.25$ GeV, then for $m_t = (171.4 + 1.0)$ GeV and $m_b(m_b) = 4.25$ GeV, and finally for $m_t = 171.4$ GeV and $m_b(m_b) = (4.25 + 0.1)$ GeV. The latter two evaluations are used by appropriate rescaling to estimate the full parametric uncertainties induced by the experimental uncertainties $\delta m_t^{\text{exp}} = 2.1$ GeV [8] and $\delta m_b(m_b)^{\text{exp}} = 0.11$ GeV. These parametric uncertainties are then added to the other errors (intrinsic, parametric (α_s, $\Delta\alpha_{\text{had}}$), and experimental).

In regions that depend sensitively on the input values of m_t and $m_b(m_b)$, such as the focus-point region [10] in the CMSSM, the corresponding parametric uncertainty can become very large. In essence, the 'WMAP hypersurface' moves significantly as m_t varies (and to a lesser extent also $m_b(m_b)$), but remains thin. Incorporating this large parametric uncertainty naively in eq. (1) would artificially suppress the overall χ^2 value for such points. This artificial suppression is avoided by adding the second term in eq. (1), where σ_n^{min} is the value of the combined error evaluated for parameter choices which minimize χ^2_n over the full data set.

Throughout this analysis, we focus our attention on parameter points that yield the correct value of the cold dark matter density inferred from WMAP and other data, namely $0.094 < \Omega_{\text{CDM}}h^2 < 0.129$ [11]. The fact that the density is relatively well known restricts the SUSY parameter space to a thin, fuzzy 'WMAP hypersurface', effectively reducing its dimensionality by one. The variations in the EWPO and BPO across this hypersurface may in general be neglected, so that we may treat the cold dark matter constraint effectively as a δ function. We note, however, that for any given value of $m_{1/2}$ there may be more than one value of m_0 that yields a cold dark matter density within the allowed range, implying that there may be more than one WMAP line traversing the the $(m_{1/2}, m_0)$ plane. Specifically, in the CMSSM there is, in general, one WMAP line in the coannihilation/rapid-annihilation funnel region and another in the focus-point region, at higher m_0. Consequently, each EWPO and BPO may have more than one value for any given value of $m_{1/2}$. In the following, we restrict our study of the upper WMAP line to the part with $m_0 < 2000$ GeV for $\tan\beta = 10$ and $m_0 < 3000$ GeV for $\tan\beta = 50$, restricting in turn the range of $m_{1/2}$.

For our CMSSM analysis, the fact that the cold dark matter density is known from astrophysics and cosmology with an uncertainty smaller than 10 % fixes with proportional precision one combination of the SUSY parameters, enabling us to analyze the overall χ^2 value as a function of $m_{1/2}$ for fixed values of $\tan\beta$ and A_0. The value of $|\mu|$ is fixed by the electroweak vacuum conditions (and $\mu > 0$ due to $(g-2)_\mu$), the value of m_0 is fixed with a small error by the dark matter density, and the Higgs mass parameters are fixed by the universality assumption. As in previous analyses, we consider various representative values

---

[a]Using the most recent experimental value, $m_t = 170.9 \pm 2.1$ GeV [9] would have a minor impact on our analysis.

of $A_0 \propto m_{1/2}$ for the specific choices $\tan\beta = 10, 50$.

3 The χ^2 analyses for EWPO, BPO and combined

Here we show the χ^2 results as a function of $m_{1/2}$, using eq. (1). As a first step, Fig. 1 displays the χ^2 distribution for the EWPO alone. In the case $\tan\beta = 10$ (left panel), we see a well-defined minimum of χ^2 for $m_{1/2} \sim 300$ GeV when $A_0 > 0$, which disappears for large negative A_0 and is not present in the focus-point region. The rise at small $m_{1/2}$ is due both to the lower limit on M_h coming from the direct search at LEP [12] and to $(g-2)_\mu$, whilst the rise at large $m_{1/2}$ is mainly due to $(g-2)_\mu$. The measurement of M_W leads to a slightly lower minimal value of χ^2, but there are no substantial contributions from any of the other EWPO. The preference for $A_0 > 0$ in the coannihilation region is due to M_h, see the left plot in Fig. 4, and the relative disfavor for the focus-point regions is due to its mismatch with $(g-2)_\mu$. In the case $\tan\beta = 50$ (right panel), we again see a well-defined minimum of χ^2, this time for $m_{1/2} \sim 400$ to 500 GeV, which is similar for all the studied values of A_0. In this case, there is also a similar minimum of χ^2 for the focus-point region at $m_{1/2} \sim 200$ GeV. The increase in χ^2 at small $m_{1/2}$ is due to $(g-2)_\mu$ as well as M_h, whereas the increase at large $m_{1/2}$ is essentially due to $(g-2)_\mu$. Contrary to the $\tan\beta = 10$ case, M_h does not induce a large difference for the various A_0 values, see the right plot in Fig. 4. We note that the overall minimum of $\chi^2 \sim 2$ is similar for both values of $\tan\beta$, and represents an excellent fit in each case.

Fig. 2 shows the corresponding combined χ^2 for the BPO alone. For both values of $\tan\beta$, these prefer large values of $m_{1/2}$, reflecting the fact that there is no hint of any deviation from the SM, and the overall quality of the fit is good. Very small values of $m_{1/2}$ are disfavored, particularly in the coannihilation region with $A_0 > 0$, mainly due to $b \to s\gamma$. The focus-point region is generally in very good agreement with the BPO data, except at very low $m_{1/2} \lesssim 400$ GeV for $\tan\beta = 50$.

Finally, we show in Fig. 3 the combined χ^2 values for the EWPO and BPO, computed in accordance with eq. (1). We see that the global minimum of $\chi^2 \sim 4.5$ for both values of $\tan\beta$. This is quite a good fit for the number of experimental observables being fitted, and the $\chi^2/$d.o.f. is similar to the one for the EWPO alone. This increase in the total χ^2 reflects the fact that the BPO exhibit no tendency to reinforce the preference of the EWPO for small $m_{1/2}$. However, due to the relatively large experimental and theoretical errors for the BPO, no firm conclusion in any direction can be drawn yet. The focus-point region is disfavored for both values of $\tan\beta$ by comparison with the coannihilation region, though this effect is slightly less important for $\tan\beta = 50$. For $\tan\beta = 10$, $m_{1/2} \sim 300$ GeV and $A_0 > 0$ are preferred, whereas, for $\tan\beta = 50$, $m_{1/2} \sim 600$ GeV and $A_0 < 0$ are preferred. This change-over is largely due to the impact of the LEP M_h constraint for $\tan\beta = 10$ (see the left plot of Fig. 4) and the $b \to s\gamma$ constraint for $\tan\beta = 50$ (see Fig. 6 in Ref. [2]). Corresponding mass predictions for the SUSY particles can be found in Ref. [2].

4 Acknowledgments
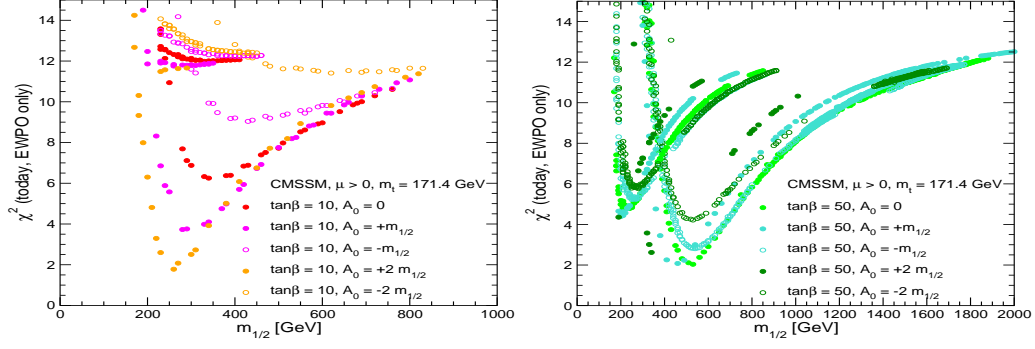
Figure 1: The combined χ^2 function for the electroweak observables M_W, $\sin^2\theta_{\text{eff}}$, Γ_Z, $(g-2)_\mu$ and M_h, evaluated in the CMSSM for $\tan\beta = 10$ (left) and $\tan\beta = 50$ (right) for various discrete values of A_0.
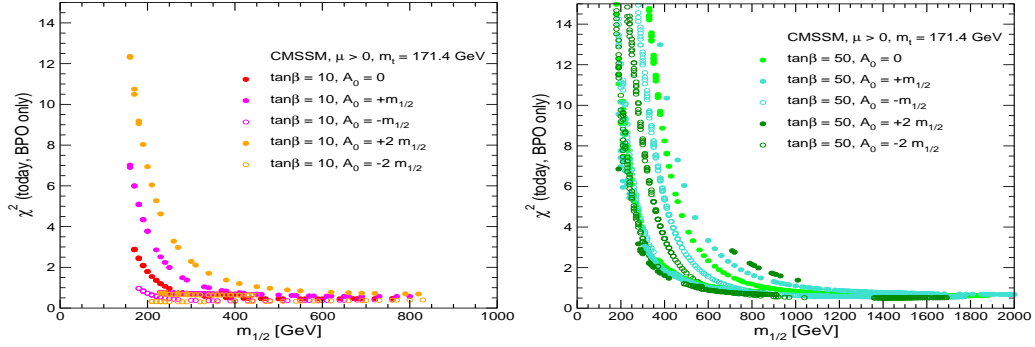
Figure 2: The combined χ^2 function for the B physics observables $\text{BR}(b \to s\gamma)$, $\text{BR}(B_s \to \mu^+\mu^-)$, $\text{BR}(B_u \to \tau\nu_\tau)$ and ΔM_{B_s}, evaluated in the CMSSM for $\tan\beta = 10$ (left) and $\tan\beta = 50$ (right) for various discrete values of A_0.
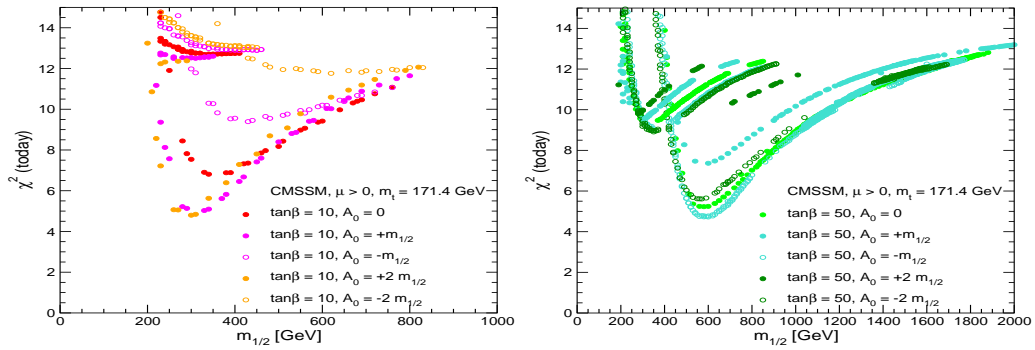
Figure 3: The combined χ^2 function for the EWPO and the BPO, evaluated in the CMSSM for $\tan\beta = 10$ (left) and $\tan\beta = 50$ (right) for various discrete values of A_0.
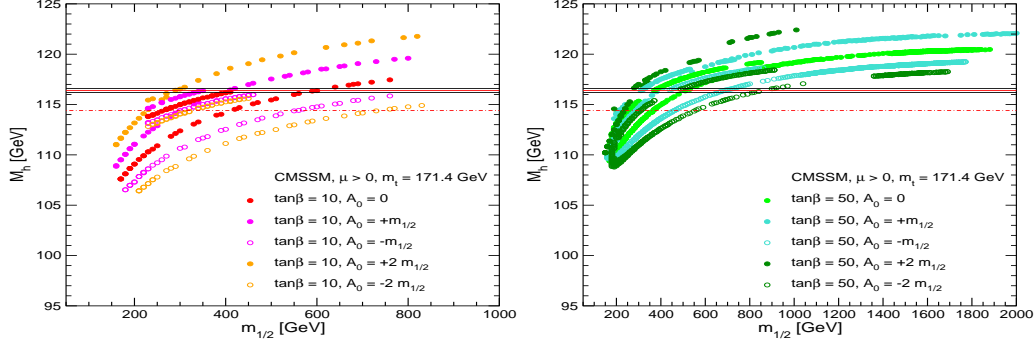
Figure 4: The CMSSM predictions for M_h as functions of $m_{1/2}$ with (a) $\tan\beta = 10$ and (b) $\tan\beta = 50$ for various A_0. We also show the present 95% C.L. exclusion limit of 114.4 GeV and a hypothetical LHC measurement of $M_h = 116.4 \pm 0.2$ GeV. The results have been obtained with `FeynHiggs` [13].

References

[1] Slides:
    `http://ilcagenda.linearcollider.org/contributionDisplay.py?contribId=52&sessionId=69&confId=1296`

[2] J. Ellis, S. Heinemeyer, K. Olive, A.M. Weber and G. Weiglein, *JHEP* **0708** (2007) 083 [arXiv:0706.0652 [hep-ph]].

[3] S. Heinemeyer, W. Hollik and G. Weiglein, *Phys. Rept.* **425** (2006) 265 [arXiv:hep-ph/0412214].

[4] J. Ellis, S. Heinemeyer, K. Olive and G. Weiglein, *JHEP* **0502** (2005) 013 [arXiv:hep-ph/0411216].

[5] J. Ellis, S. Heinemeyer, K. Olive and G. Weiglein, *JHEP* **0605** (2006) 005 [arXiv:hep-ph/0602220].

[6] J. Ellis, K. Olive, Y. Santoso and V. Spanos, *Phys. Rev.* **D 69** (2004) 095004 [arXiv:hep-ph/0310356];
    B. Allanach and C. Lester, *Phys. Rev.* **D 73** (2006) 015013 [arXiv:hep-ph/0507283]; B. Allanach, *Phys. Lett.* **B 635** (2006) 123 [arXiv:hep-ph/0601089]; R. de Austri, R. Trotta and L. Roszkowski, *JHEP* **0605** (2006) 002 [arXiv:hep-ph/0602028]; *JHEP* **0704** (2007) 084 [arXiv:hep-ph/0611173]; arXiv:0705.2012 [hep-ph]; B. Allanach, C. Lester and A. M. Weber, *JHEP* **0612** (2006) 065 [arXiv:hep-ph/0609295]; B. Allanach, K. Cranmer, C. Lester and A. M. Weber, arXiv:0705.0487 [hep-ph]; O. Buchmueller et al., arXiv:0707.3447 [hep-ph].

[7] G. Isidori, F. Mescia, P. Paradisi and D. Temes, *Phys. Rev.* **D 75** (2007) 115019 [arXiv:hep-ph/0703035]; M. Carena, A. Menon and C. Wagner, *Phys. Rev.* **D 76** (2007) 035004 [arXiv:0704.1143 [hep-ph]].

[8] E. Brubaker et al. [Tevatron Electroweak Working Group], arXiv:hep-ex/0608032, see:
    `tevewwg.fnal.gov/top/` .

[9] Tevatron Electroweak Working Group, arXiv:hep-ex/0703034.

[10] J. Feng, K. Matchev and T. Moroi, *Phys. Rev. Lett.* **84** (2000) 2322 [arXiv:hep-ph/9908309]; *Phys. Rev.* **D 61** (2000) 075005 [arXiv:hep-ph/9909334]; J. Feng, K. Matchev and F. Wilczek, *Phys. Lett.* **B 482** (2000) 388 [arXiv:hep-ph/0004043]; J. Feng and K. Matchev, *Phys. Rev.* **D 63** (2001) 095003 [arXiv:hep-ph/0011356].

[11] C. Bennett et al., *Astrophys. J. Suppl.* **148** (2003) 1 [arXiv:astro-ph/0302207]; D. Spergel et al. [WMAP Collaboration], *Astrophys. J. Suppl.* **148** (2003) 175 [arXiv:astro-ph/0302209]; D. Spergel et al. [WMAP Collaboration], arXiv:astro-ph/0603449.

[12] LEP Higgs working group, *Phys. Lett.* **B 565** (2003) 61 [arXiv:hep-ex/0306033]; *Eur. Phys. J.* **C 47** (2006) 547 [arXiv:hep-ex/0602042].

[13] S. Heinemeyer, W. Hollik and G. Weiglein, *Comp. Phys. Commun.* **124** 2000 76 [arXiv:hep-ph/9812320]; *Eur. Phys. J.* **C 9** (1999) 343 [arXiv:hep-ph/9812472]; G. Degrassi, S. Heinemeyer, W. Hollik, P. Slavich and G. Weiglein, *Eur. Phys. J.* **C 28** (2003) 133 [arXiv:hep-ph/0212020]; M. Frank, T. Hahn, S. Heinemeyer, W. Hollik, H. Rzehak and G. Weiglein, *JHEP* **0702** (2007) 047 [arXiv:hep-ph/0611326]; see:
    `www.feynhiggs.de` .

About the Running and Decoupling in the MSSM

L. Mihaila[1], R. V. Harlander[2] and M. Steinhauser[1] *

1- Institut für Theoretische Teilchenphysik - Universität Karlsruhe
76128 Karlsruhe - Germany

2- Fachbereich C Theoretische Physik - Universität Wuppertal
42097 Wuppertal - Germany

The evolution of the strong coupling constant α_s from M_Z to the GUT scale is presented, involving three-loop running and two-loop decoupling. Accordingly, the two-loop transition from the $\overline{\text{MS}}$- to the $\overline{\text{DR}}$-scheme is properly taken into account. We find that the three-loop effects are comparable to the experimental uncertainty for α_s.

1   Introduction

The observation that the gauge couplings of the strong, electromagnetic and weak interaction tend to unify in the Minimal Supersymmetric Standard Model (MSSM) at a high energy scale $\mu_{\text{GUT}} \simeq 10^{16}$ GeV and the consistent predictions made for SM parameters, such as the top quark mass and the ratio of the bottom quark to the tau lepton masses, using constraints on the Yukawa sector of SUSY-GUT models, brought SUSY in the center of the phenomenological studies.

Nevertheless, SUSY is only an approximate symmetry in nature and several scenarios for the mechanism of SUSY breaking have been proposed. A possibility to constrain the type and scale of SUSY breaking is to study, with very high precision, the relations between the MSSM parameters evaluated at the electroweak and the GUT scales. The extrapolation over many orders of magnitude requires high-precision experimental data at the low energy scale. A first set of precision measurements is expected from the CERN Large Hadron Collider (LHC) with an accuracy at the percent level. A comprehensive high-precision analysis can be performed at the International Linear Collider (ILC), for which the estimated experimental accuracy is at the per mill level. In this respect, it is necessary that the same precision is reached also on the theory side in order to match with the data [2]. Running analyses based on full two-loop renormalization group equations (RGEs) [3, 4] for all parameters and one-loop threshold corrections [5] are currently implemented in the public programs ISAJET [6], SOFTSUSY [7], SPHENO [8], SuSpect [9]. The agreement between the different codes is in general within one percent [10]. A first three-loop running analysis, based, however, only on one-loop threshold effects, was carried out in Ref. [11].

In this talk, we report on the evaluation of the strong coupling α_s in MSSM, based on three-loop RGEs [12] and two-loop threshold corrections [13]. On the one hand, the three-loop corrections reduce significantly the dependence on the scale at which heavy particles are integrated out [14] and on the other hand, they are essential for phenomenological studies, because they are as large as, or greater than, the effects induced by the current experimental accuracy of $\alpha_s(M_Z)$ [15]. Additionally, we compare the predictions obtained within the above mentioned approach with those based on the leading-logarithmic (LL) approximation suggested in Ref. [2].

---

2 Evaluation of $\alpha_s(\mu_{\mathrm{GUT}})$ from $\alpha_s(M_Z)$

The aim of this study is to compute α_s at a high-energy scale $\mu \simeq \mathcal{O}(\mu_{\mathrm{GUT}})$, starting from the strong coupling constant at the mass of the Z boson M_Z. We denote this parameter $\alpha_s^{\overline{\mathrm{MS}},(5)}(M_Z)$ to specify that the underlying theory is QCD with five active flavours and $\overline{\mathrm{MS}}$ is the renormalization scheme . The value of $\alpha_s(\mu_{\mathrm{GUT}})$ is the strong coupling constant in a supersymmetric theory, renormalized in the $\overline{\mathrm{DR}}$-scheme. The relation between the two parameters requires the consistent combination of the following ingredients.

- The renormalization group evolution of α_s.
  The energy dependence of the strong coupling constant is governed by the RGE. In QCD with n_f quark flavours, the β function is known through four loops both in the $\overline{\mathrm{MS}}$ [16, 17] and the $\overline{\mathrm{DR}}$-scheme [18]. In SUSY-QCD, the β function has been evaluated in the $\overline{\mathrm{DR}}$-scheme through three loops [12].

- The transition from the $\overline{\mathrm{MS}}$- to the $\overline{\mathrm{DR}}$-scheme.
  For the three-loop running analysis we are focusing on, one needs to evaluate the dependence of α_s values in the $\overline{\mathrm{DR}}$-scheme from those in $\overline{\mathrm{MS}}$-scheme through two loops [18]

$$\alpha_s^{\overline{\mathrm{MS}}} \;\; = \;\; \alpha_s^{\overline{\mathrm{DR}}}\left[1 - \frac{\alpha_s^{\overline{\mathrm{DR}}}}{4\pi} - \frac{5}{4}\left(\frac{\alpha_s^{\overline{\mathrm{DR}}}}{\pi}\right)^2 + \frac{\alpha_s^{\overline{\mathrm{DR}}}\alpha_e}{12\pi^2}\,n_f + \ldots\right], \qquad (1)$$

  where $\alpha_s^{\overline{\mathrm{DR}}} \equiv \alpha_s^{\overline{\mathrm{DR}},(n_f)}(\mu)$ and $\alpha_s^{\overline{\mathrm{MS}}} \equiv \alpha_s^{\overline{\mathrm{MS}},(n_f)}(\mu)$. $\alpha_e \equiv \alpha_e^{(n_f)}(\mu)$ is one of the so-called evanescent coupling constants that occur when $\overline{\mathrm{DR}}$ is applied to non-supersymmetric theories (QCD in this case). In particular, it describes the coupling of the 2ε-dimensional components (so-called ε-scalars) of the gluon to a quark.

- The transition from five-flavour QCD to the full SUSY theory.
  For mass independent renormalization schemes like $\overline{\mathrm{MS}}$ or $\overline{\mathrm{DR}}$, the decoupling of heavy particles has to be performed explicitly. In practice, this means that intermediate effective theories are introduced by integrating out the heavy degrees of freedom. One may separately integrate out every particle at its individual threshold ("step approximation"), a method suited for SUSY models with a severely split mass spectrum. But the intermediate effective theories with "smaller" symmetry raise the problem of introducing new couplings, each governed by its own RGE. To overcome this difficulty, for SUSY models with roughly degenerate mass spectrum at the scale $\tilde{M}$, one can consider the MSSM as the full theory that is valid from the GUT scale μ_{GUT} down to $\tilde{M}$, which we assume to be around $1\,\mathrm{TeV}$. Integrating out all SUSY particles at this common scale, one directly obtains the SM as the effective theory, valid at low energies. The transition between the two theories can be done at an arbitrary decoupling scale μ:

$$\alpha_s^{\overline{\mathrm{DR}},(n_f)}(\mu) \;\; = \;\; \zeta_s^{(n_f)}\,\alpha_s^{\overline{\mathrm{DR}},(\mathrm{full})}(\mu)\,, \quad \alpha_e^{(n_f)}(\mu) = \zeta_e^{(n_f)}\alpha_e^{(\mathrm{full})}(\mu)\,. \qquad (2)$$

  ζ_s and ζ_e depends logarithmically on the scale μ, which is why one generally chooses $\mu \sim \tilde{M}$. In Eq. (2), $n_f = 6$ means that only the SUSY particles are integrated out,

while for $n_f = 5$ at the same time the top quark is integrated out. This procedure, also known as "common scale approach" [19], is implemented in most of the present codes computing the SUSY spectrum [8, 7, 9] by applying the one-loop approximation of Eq. (2) and setting $n_f = 5$ and $\mu = M_Z$.

In the following, we will assume that QCD is obtained by integrating out the heavy degrees of freedom (squarks and gluinos) from SUSY-QCD. Due to SUSY, the evanescent couplings in SUSY-QCD can be related to the gauge coupling α_s as follows:

$$\alpha_e^{(\text{full})}(\mu) = \alpha_s^{\overline{\text{DR}},(\text{full})}(\mu). \tag{3}$$

The evanescent couplings in n_f-flavour QCD, i.e. $\alpha_e^{(n_f)}$ are then obtained by decoupling relations analogous to Eq. (2).

For the evaluation of $\alpha_s^{\overline{\text{DR}},(\text{full})}(\mu_{\text{GUT}})$ from $\alpha_s^{\overline{\text{MS}},(n_f)}(\mu_{M_Z})$ we propose the following method:

$$\alpha_s^{\overline{\text{MS}},(n_f)}(M_Z) \overset{(i)}{\to} \alpha_s^{\overline{\text{MS}},(n_f)}(\mu_{\text{dec}}) \overset{(ii)}{\to} \alpha_s^{\overline{\text{DR}},(n_f)}(\mu_{\text{dec}})$$
$$\overset{(iii)}{\to} \alpha_s^{\overline{\text{DR}},(\text{full})}(\mu_{\text{dec}}) \overset{(iv)}{\to} \alpha_s^{\overline{\text{DR}},(\text{full})}(\mu_{\text{GUT}}). \tag{4}$$

The individual steps require: (i) $\beta(\alpha_s)$ in QCD through three loops, (ii) the $\overline{\text{MS}}$–$\overline{\text{DR}}$ relation through order α_s^2, (iii) decoupling of the SUSY particles through order α_s^2, and (iv) $\beta(\alpha_s)$ through three loops in SUSY-QCD. The advantage of this procedure as compared to a multi-scale approach is that the RGEs are only one-dimensional and that for α_e one can apply Eq. (2).

2.1 Numerical results

The result for $\alpha_s^{\overline{\text{DR}}}(\mu_{\text{GUT}} = 10^{16}$ GeV), obtained using $M_Z = 91.1876$ GeV and $m_t = 170.9 \pm 1.9$ GeV, $\alpha_s^{\overline{\text{MS}}}(M_Z) = 0.1189$, $\tilde{M} = m_{\tilde{q}} = m_{\tilde{g}} = 1000$ GeV as input parameters is shown if Figure 1. The dotted, dashed and solid line are based on Eq. (4), where n-loop running is combined with $(n-1)$-loop decoupling, as it is required for consistency ($n = 1, 2, 3$, respectively). We find a nice convergence when going from one to three loops, with a very weakly μ_{dec}–dependent result at three-loop order. For comparison, we show the result (the dash-dotted line) obtained from the formula given in Eq. (21) of Ref [2]. It

Figure 1: $\alpha_s(\mu_{\text{GUT}})$ as a function of μ_{dec}.

corresponds to the resummed one-loop contributions originating from both the change of scheme and the decoupling of heavy particles. However, the difference between our three-loop result with two-loop decoupling (upper solid line) and the one-loop formula given in Ref. [2] exceeds the experimental uncertainty by almost a factor of four for sensible values of μ_{dec}. This uncertainty is indicated by the hatched band, derived from $\delta\alpha_s(M_Z) = \pm 0.001$ [15]. The formulae of Ref. [2] should therefore be taken only as rough estimates.

In Figure 2 we show $\alpha_s(\mu_{\mathrm{GUT}})$ as a function of $\tilde{M}$ where $\mu_{\mathrm{dec}} = \tilde{M}$ has been adopted. Dotted, dashed and full curve correspond again to the one-, two- and three-loop analysis and the uncertainty form $\alpha_s(M_Z)$ is indicated by the hatched band. One observes a variation of 10% as $\tilde{M}$ is varied between 100 GeV and 10 TeV. This shows that the actual SUSY scale can significantly influence the unification, respectively, the non-unification behaviour of the three couplings at the GUT scale.
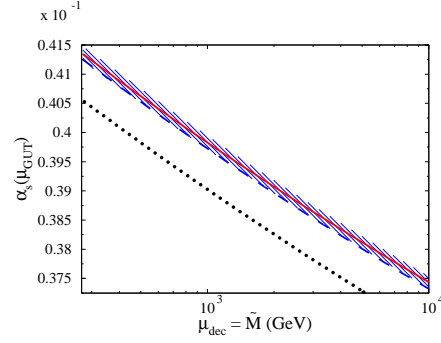
Figure 2: $\alpha_s(\mu_{\mathrm{GUT}})$ as a function of $\tilde{M}$.

3   Conclusions

We have used recent three- and four-loop results for the β functions, and the decoupling coefficients in order to derive $\alpha_s^{\overline{\mathrm{DR}}}(\mu_{\mathrm{GUT}})$ from $\alpha_s^{\overline{\mathrm{MS}}}(M_Z)$ at three- and four-loop level, respectively.

It turns out that the three-loop terms are numerically significant. The dependence on where the SUSY spectrum is decoupled becomes particularly flat in this case. The theoretical uncertainty is expected to be negligible w.r.t. the uncertainty induced by the experimental input values. In consequence, we recommend that phenomenological studies concerning the implications of low energy data on Grand Unification should be done at three-loop level.

References

[1] Slides:
    `http://ilcagenda.linearcollider.org/contributionDisplay.py?contribId=48&sessionId=69&confId=1296`

[2] J. A. Aguilar-Saavedra *et al.*, Eur. Phys. J. C **46** (2006) 43.

[3] S. P. Martin and M. T. Vaughn, Phys. Lett. B **318** (1993) 331.

[4] I. Jack and D. R. T. Jones, Phys. Lett. B **333** (1994) 372.

[5] D. M. Pierce, J. A. Bagger, K. T. Matchev and R. J. Zhang, Nucl. Phys. B **491** (1997) 3.

[6] F. E. Paige, S. D. Protopopescu, H. Baer and X. Tata, [arXiv:hep-ph/0312045].

[7] B. C. Allanach, Comput. Phys. Commun. **143** (2002) 305.

[8] W. Porod, Comput. Phys. Commun. **153** (2003) 275.

[9] A. Djouadi, J. L. Kneur and G. Moultaka, Comput. Phys. Commun. **176** (2007) 426.

[10] B. C. Allanach, S. Kraml and W. Porod, JHEP **0303** (2003) 016.

[11] P. M. Ferreira, I. Jack and D. R. T. Jones, Phys. Lett. B **387** (1996) 80.

[12] I. Jack, D. R. T. Jones and C. G. North, Phys. Lett. B **386** (1996) 138.

[13] R. Harlander, L. Mihaila and M. Steinhauser, Phys. Rev. D **72** (2005) 095009.

[14] R. V. Harlander, L. Mihaila and M. Steinhauser, JHEP **0612** (2007) 024.

[15] S. Bethke, Prog. Part. Nucl. Phys. **58** (2007) 351.

[16] T. van Ritbergen, J. A. M. Vermaseren and S. A. Larin, Phys. Lett. B **400** (1997) 379.

[17] M. Czakon, Nucl. Phys. B **710** (2005) 485.

[18] R. V. Harlander, D. R. T. Jones, P. Kant, L. Mihaila and M. Steinhauser, JHEP **0612** (2006) 024.

[19] H. Baer, J. Ferrandis, S. Kraml and W. Porod, Phys. Rev. D **73** (2006) 015010.

Off-Shell and Interference Effects for SUSY Particle Production

Jürgen Reuter

Albert-Ludwigs-Universität Freiburg - Physikalisches Institut
Hermann-Herder-Str. 3, D-79104 Freiburg - Germany

We show that the narrow-width approximation is insufficient for describing production of supersymmetric particles at the ILC. Especially when cuts are taken into account to extract signals using the narrow-width approximation can be wrong by an order of magnitude.

1 Precision SUSY measurements

Supersymmetry (SUSY) is the best-motivated solution to the hierarchy problem. If SUSY is realized in Nature, the LHC is likely to find sparticles during the next couple of years. The precision spectroscopy of the new particles will then be the major goal of future particle physics experiments. The aim is to perform mass measurements to get the spectrum (edges in decay chains), to access the spin of all new particles via angular/spin correlations, and finally to perform coupling measurements to verify SUSY by the relations among the couplings. Therefore, we need precise predictions SUSY processes: for their own determination as well as because they are background for (more difficult) SUSY processes. We need parameter values as precise as possible in order to reverse the renormalization-group evolution and get a handle on the GUT parameters [2, 3]. Corrections to (SUSY) processes (at the ILC) can be grouped into six categories [4]: 1) Loop corrections to SUSY production and decay processes; 2) nonfactorizable, maximally resonant photon exchange between production and decay; 3) real radiation of photons/gluons; 4) off-shell kinematics for the signal process (see also [5]); 5) irreducible background from all other SUSY processes; 6) reducible, experimentally indistinguishable SM background processes. Topics 1) and 3) are addressed in [6].

2 Complexity and Approximations

Generic SUSY processes have an incredible complexity: e.g. $e^+e^- \rightarrow b\bar{b}e^+e^-\tilde{\chi}_1^0\tilde{\chi}_1^0$ (which is just an exclusive final state for $\tilde{\chi}_2^0\tilde{\chi}_2^0$ production) has 66,478 diagrams already at tree level. Entangled in these amplitudes are different signal diagrams: $e^+e^- \rightarrow \tilde{\chi}_i^0\tilde{\chi}_j^0, \tilde{b}_i\tilde{b}_j, \tilde{e}_i\tilde{e}_j$. To disentangle them in simulations or a real data analysis, one has to use cuts and to consider SM backgrounds (here e.g. $e^+e^- \rightarrow b\bar{b}e^+e^-\nu_i\bar{\nu}_i$). There are much more complicated processes for LHC, and even for ILC. To deal with this complexity one needs to use multi-particle event generators [7].

There are three different levels of approximations used for describing such processes like $A_1A_2 \rightarrow P^{(*)} \rightarrow F_1F_2$: the narrow-width approximation $\sigma(A_1A_2 \rightarrow P) \times \mathrm{BR}(P \rightarrow F_1F_2)$ (on-shell production times branching ratio), the Breit-Wigner approximation $\sigma(A_1A_2 \rightarrow P) \times \frac{M_P^2\Gamma_P^2}{(s-M_P^2)^2+\Gamma_P^2M_P^2} \times \mathrm{BR}(P \rightarrow F_1F_2)$ (folding in a finite width propagator), and the full matrix elements: $\sigma(A_1A_2 \rightarrow F_1F_2)$. That last level is not featured by event generators like ISAJET, PYTHIA, HERWIG, SUSYGEN.
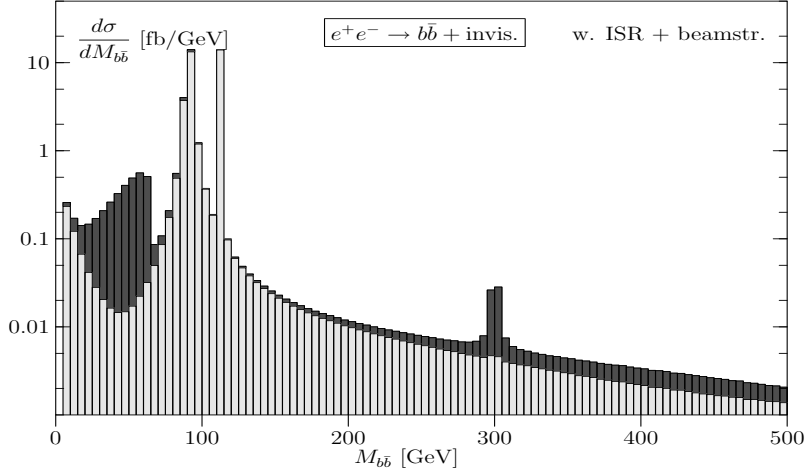
Figure 1: The $b\bar{b}$ invariant mass spectrum for the full process $e^+e^- \to b\bar{b} + \not{E}$ with ISR and beamstrahlung. The SM background ($Z \to \nu\bar{\nu}$) with the Z, h peaks is light gray. Dark gray represents all MSSM processes, with two peaks from heavy neutralino and heavy Higgs decays.

Channel	$\sigma_{2\to2}$	$\sigma \times \mathrm{BR}$	σ_{BW}
Zh	20.574	1.342	1.335
ZH	0.003	0.000	0.000
HA	5.653	0.320	0.314
$\tilde{\chi}_1^0\tilde{\chi}_2^0$	69.109	13.078	13.954
$\tilde{\chi}_1^0\tilde{\chi}_3^0$	24.268	3.675	4.828
$\tilde{\chi}_1^0\tilde{\chi}_4^0$	19.337	0.061	0.938
$\tilde{b}_1\tilde{b}_1$	4.209	0.759	0.757
$\tilde{b}_1\tilde{b}_2$	0.057	0.002	0.002
Sum		19.238	22.129
Exact			19.624
w/ISR			22.552
$Z\bar{\nu}\nu$	626.1	109.9	111.4
$h\bar{\nu}\nu$	170.5	76.5	76.4
$H\bar{\nu}\nu$	0.0	0.0	0.0
Sum		186.5	187.7
Exact			190.1
w/ISR			174.2

Channel	σ_{BW}	$\sigma_{\mathrm{BW}}^{\mathrm{cut}}$
Zh	1.335	0.009
HA	0.314	0.003
$\tilde{\chi}_1^0\tilde{\chi}_2^0$	13.954	0.458
$\tilde{\chi}_1^0\tilde{\chi}_3^0$	4.828	0.454
$\tilde{\chi}_1^0\tilde{\chi}_4^0$	0.938	0.937
$\tilde{b}_1\tilde{b}_1$	0.757	0.451
$\tilde{b}_1\tilde{b}_2$	0.002	0.001
Sum	22.129	**2.314**
Exact	19.624	**0.487**
w/ISR	22.552	**0.375**
$Z\bar{\nu}\nu$	111.4	2.114
$h\bar{\nu}\nu$	76.4	0.002
$H\bar{\nu}\nu$	0.0	0.000
Sum	187.7	2.117
Exact	190.1	1.765
w/ISR	174.2	1.609

Table 1: Main subprocesses for sbottom production at an 800 GeV ILC using the three level of complexity mentioned in the text. Left: before the cuts, right: after the cuts. Upper table is signal processes, lower one SM backgrounds. All processes in femtobarn.
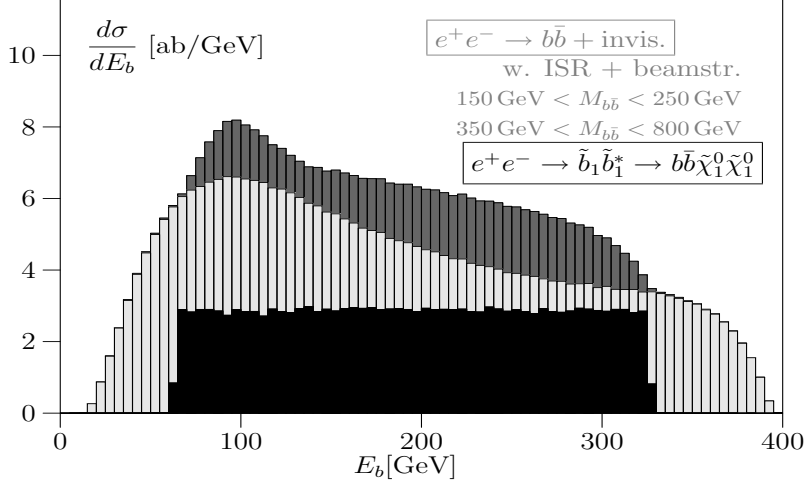
Figure 2: The E_b spectrum of $e^+e^- \rightarrow b\bar{b} + \not{E}$, including all interferences and off-shell effects, plus ISR and beamstrahlung. The light gray histogram is the SM background, dark gray the sum of SUSY processes, including the cuts. We also show the idealized case (red) of on-shell sbottom production without ISR or beamstrahlung.

The simulations presented here have been performed with the multi-purpose event generator WHIZARD [8], which is well-suited for physics beyond the SM [9]. Especially, the MSSM implementation has been thoroughly tested [4], e.g. in a comparison with the other two MSSM multi-particle generators, Madgraph and Sherpa. The reference data can be found at http://whizard.event-generator.org/susy_comparison.html.

3   Results

For our study [4] of off-shell and interference effects and to test the quality of the Breit-Wigner approximation, we took a SUGRA-inspired parameter point with non-universal right-handed scalar masses and $\tan\beta = 20$. Note, that the following does not depend on this special point, however. This point features a light Higgs, directly above LEP limit [10], large (47 %) invisible Higgs decays to the LSP, $m_{\tilde{q}} \sim 430$ GeV, light sbottoms accessible at the ILC, and is compatible with all low-energy data: $b \rightarrow s\gamma$, $B_s \rightarrow \mu^+\mu^-$, $\Delta\rho$, $g_\mu - 2$, CDM. The sbottoms have masses of 295.36 and 399.92 GeV and widths of 0.5295 and 3.4956 GeV, respectively. The neutralino masses are 46.84, 112.41, 148.09 and 236.77 GeV, their widths 0, 0.00005, 0.01162 and 1.0947 GeV, respectively. The focus lies on BR($\tilde{b}_1 \rightarrow b\tilde{\chi}_1^0$) = 43.2%, as we want to study sbottom production at an 800 GeV ILC.

In contrast to the LHC, at the ILC sbottoms are produced by electroweak interactions. Hence, much more channels contribute to the same exclusive final state, $e^+e^- \rightarrow b\bar{b}\tilde{\chi}_1^0\tilde{\chi}_1^0$: $e^+e^- \rightarrow Zh, ZH, Ah, HA, \tilde{\chi}_1^0\tilde{\chi}_2^0, \tilde{\chi}_1^0\tilde{\chi}_3^0, \tilde{\chi}_1^0\tilde{\chi}_4^0, \tilde{b}_1\tilde{b}_1^*, \tilde{b}_1\tilde{b}_2^*$, altogether 412 diagrams. The irreducible SM background is $e^+e^- \rightarrow b\bar{b}\nu_i\bar{\nu}_i$ (WW fusion, Zh, ZZ, 47 diagrams). Important is to use widths to the same order as your process, i.e. tree level in our case. The left of Tab. 1 shows the cross sections of the contributing subprocesses in the three levels of complexity

described above. The $b\bar{b}$ invariant mass spectrum (dark) including the SM background (light gray) is shown in Fig. 1. Light gray peaks stem from the Z and light Higgs resonance, while the dark gray peak comes from the heavy Higgses. The broad dark continuum at low energies results from heavy neutralinos. Hence, to isolate the SUSY signal it is mandatory to cut out the resonances, namely the two windows $M_{b\bar{b}} < 150$ GeV and $250\,\text{GeV} < M_{b\bar{b}} < 350$ GeV. The off-shell decay $\tilde{\chi}_3^0 \to (\tilde{b}_1)_{off}\bar{b} \to b\bar{b}\tilde{\chi}_1^0$ gives a broad continuum instead of a well-defined peak expected from subsequent 2-body decays; this causes some of the effects described below. ISR and beamstrahlung give corrections of the same order as off-shell effects and affect all p_{miss} observables. The corresponding plots can be found in [4]. The cross sections after application of the cuts are shown on the right of Tab. 1; note the difference between the exact result 0.487 fb and the Breit-Wigner approximation of 2.314 fb showing a deviation of an order of magnitude. Fig. 2 shows that the $\tilde{b}_1 \to b\tilde{\chi}_1^0$ decay kinematics is affected by the off-shell and interference effects, the SM backgrounds as well as ISR and beamstrahlung in a way that makes it much harder to precisely extract the sbottom mass as desired.

In summary, precision predictions for SUSY phenomenology are important, especially higher order virtual and real corrections. The factorization of processes into $2 \to 2$ production and decay is insufficient or even wrong. Off-shell effects and interferences affect the results, especially with cuts. Therefore one has to use full matrix elements (cf. [11]), available from multi-particle event generators where `WHIZARD` is especially well-suited for ILC.

4 Acknowledgments

5 Bibliography

References

[1] Slides:
   `http://ilcagenda.linearcollider.org/contributionDisplay.py?contribId=59&sessionId=69&confId=1296`

[2] P. Zerwas, these proceedings.

[3] `http://spa.desy.de/spa`; J. A. Aguilar-Saavedra *et al.*, Eur. Phys. J. C **46**, 43 (2006).

[4] K. Hagiwara *et al.*, Phys. Rev. D **73**, 055005 (2006).

[5] D. Berdine, N. Kauer and D. Rainwater, arXiv:hep-ph/0703058.

[6] T. Robens, these proceedings; W. Kilian, J. Reuter and T. Robens, Eur. Phys. J. C **48**, 389 (2006); AIP Conf. Proc. **903**, 177 (2007)

[7] J. Reuter *et al.*, arXiv:hep-ph/0512012;

[8] `http://whizard.event-generator.org`; W. Kilian, T. Ohl, J. Reuter, to appear in Comput. Phys. Commun.; hep-ph/0708.4233; M. Moretti, T. Ohl, J. Reuter, hep-ph/0102195; J. Reuter, arXiv:hep-th/0212154.

[9] T. Ohl and J. Reuter, Eur. Phys. J. C **30**, 525 (2003); Phys. Rev. D **70**, 076007 (2004); J. Reuter, these proceedings, arXiv: 0708.4241 [hep-ph]; arXiv: 0708.4383 [hep-ph]; W. Kilian and J. Reuter, Phys. Rev. D **70** (2004) 015004; W. Kilian, D. Rainwater and J. Reuter, Phys. Rev. D **71**, 015008 (2005); hep-ph/0507081; Phys. Rev. D **74**, 095003 (2006). M. Beyer *et al.*, Eur. Phys. J. C **48**, 353 (2006); W. Kilian and J. Reuter, hep-ph/0507099.

[10] S. Heinemeyer *et al.*, hep-ph/0511332; S. Kraml *et al.*, arXiv:hep-ph/0608079.

[11] J. Hewett, these proceedings.

Dark Matter in the U(1) Extended SUSY

D. Jarecka[1], J. Kalinowski[1]*, S.F. King[2] and J.P. Roberts[1]

1- Physics Department, University of Warsaw
Hoza 69, 00-681 Warsaw, Poland

2- Department of Physics and Astronomy, University of Southampton
Highfield, Souhtampton, SO17 1BJ, United Kingdom

The neutralino sector of the U(1) extended SUSY is presented and some collider and cosmology-related phenomenology discussed.

1 Introduction

Supersymmetry (SUSY) has been considered to be the best candidate beyond the standard model (SM) from a viewpoint of both the hierarchy problem and the gauge coupling unification. Recent astrophysical observations showing the existence of a substantial amount of non-relativistic and non-baryonic dark matter seem to make SUSY even more promising. The lightest SUSY particle (LSP) of R-parity conserving models, in most cases the lightest neutralino, can serve as a good candidate for Dark Matter (DM).

The parameter space of the constrained MSSM, however, is strongly restricted by the requirement of matching the precise measurement of the DM relic density as measured by the WMAP. The MSSM also suffers from a naturalness problem (the so-called μ problem): why the dimensionful parameter μ of the supersymmetric Higgs mass term $\mu \hat{H}_1 \hat{H}_2$ has to be of EW scale. This problem can be solved in the next-to-MSSM (NMSSM) by promoting the μ parameter to a new singlet superfield S coupled to Higgs doublets, $\lambda \hat{S} \hat{H}_1 \hat{H}_2$ [1]. This triple-Higgs coupling term also helps to push up the mass of the lightest CP-even Higgs boson, relaxing the fine-tuning necessary to comply with the LEP bounds. Postulating an additional $U_X(1)$ gauge symmetry [2] avoids a massless axion, or domain wall problems of the NMSSM. Such a U(1)-extended MSSM (USSM) can be considered as an effective low-energy approximation of a more complete E_6SSM model [3], with other E_6SSM fields assumed heavy.

In addition to the MSSM superfields, the USSM contains a chiral superfield $\hat{S}$ and an Abelian gauge superfield B'. Thus the MSSM particle spectrum is extended by a new CP-even Higgs boson S, a gauge bozon Z' and two neutral –inos: a singlino $\tilde{S}$ and a bino' $\tilde{B}'$; other sectors are not enlarged. As a result the phenomenology of the neutralino sector can be significantly modified both at colliders [4] and in cosmology-related processes [5, 6]. To illustrate this we consider a physically interesting scenario with higgsino and gaugino mass parameters of the order $M_{\text{SUSY}} \sim \mathcal{O}(10^3$ GeV), and we take the interaction between the singlino and the MSSM fields to be of the order of the EW scale, $v \sim \mathcal{O}(10^2$ GeV).

---

*Presented at the International Linear Collider Workshop 2007: LCWS2007 and ILC2007, DESY, Hamburg.

2 The neutralino sector of the USSM

We assume the MSSM gaugino unification relation $M_1 = (5/3)\tan^2\theta_W M_2 \approx 0.5M_2$ and unified couplings $g_X = g_Y$, but M_1' will be taken as independent[a] to investigate the impact of new states as a function of M_1'. For the numerical values we take $M_2 = 1.5$ TeV, $\mu = \lambda v_s/\sqrt{2} = 0.3$ TeV, $m_s = g_X v_s = 1.2$ TeV, $\tan\beta = 5$, $M_A = 0.5$ TeV, neglect (small) $\tilde{B}$-$\tilde{B}'$ mixing, and adopt the E$_6$SSM assignment for the U$_X$(1) charges [4].

Unlike the 4x4 MSSM case, the full 6x6 neutralino mass matrix cannot be diagonalised analytically. However, since the mixing between the new and MSSM states is small $\mathcal{O}(v)$ compared to $M_{\rm SUSY}$, one can perform first the diagonalisation of the 4x4 MSSM and the 2x2 $\tilde{S}$-$\tilde{B}'$ submatrices separately. Then the perturbative expansion of the block-diagonalisation in $v/M_{\rm SUSY}$ provides an excellent approximation to masses and mixings [4].

The mass spectrum is shown in Fig.1 (left) as a function of M_1'. For small M_1' the eigenstates (denoted by numbers with primes) are almost pure MSSM U(1) and SU(2) gauginos $\tilde{\chi}_{1'}^0, \tilde{\chi}_{2'}^0$, MSSM higgsinos $\tilde{\chi}_{3'}^0, \tilde{\chi}_{4'}^0$, and maximally mixed U$_X$(1) gaugino and singlino states, $\tilde{\chi}_{5'}^0, \tilde{\chi}_{6'}^0$. When M_1' is shifted to higher values, the mass eigenvalues in the new sector move apart, generating strong cross–over patterns whenever a (signed) mass from the new block comes close to one of the (signed) MSSM masses. This happens at $M_1' \approx 0.91$ TeV for $\tilde{\chi}_{6'}^0$ and $\tilde{\chi}_{2'}^0$ states, and at $M_1' \approx 2.68$ TeV for $\tilde{\chi}_{4'}^0$ and $\tilde{\chi}_{5'}^0$. For higher M_1' the $\tilde{\chi}_{5'}^0$ approaches the singlino state and becomes the LSP.
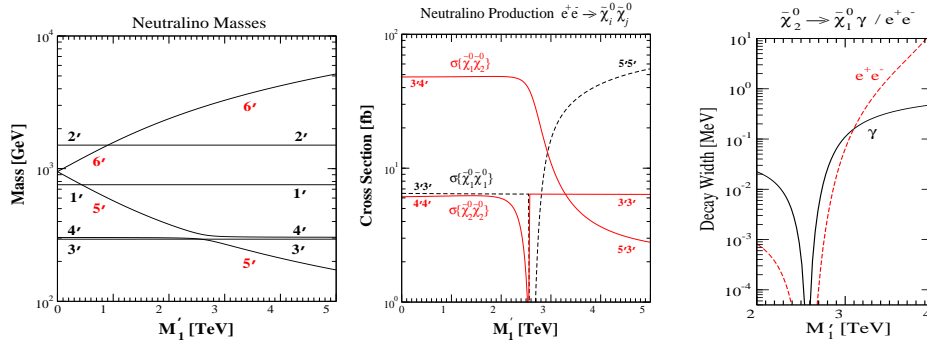
Figure 1: *The M_1' evolution of (left) neutralino masses, (center) production cross sections for $\tilde{\chi}_1^0\tilde{\chi}_1^0$, $\tilde{\chi}_1^0\tilde{\chi}_2^0$ and $\tilde{\chi}_2^0\tilde{\chi}_2^0$ pairs in e^+e^- collisions, and (right) partial decay widths of $\tilde{\chi}_2^0$ (from [4]).*

At an e^+e^- collider the production processes $e^+e^- \to \tilde{\chi}_i^0\tilde{\chi}_j^0$ are generated by s–channel Z_1 and Z_2 exchanges (mass-eigenstates of Z and Z'), and t– and u–channel $\tilde{e}_{L,R}$ exchanges.[b] In our scenario $M_{Z_2} = 949$ GeV, the ZZ' mixing angle $\theta_{ZZ'} = 3.3 \times 10^{-3}$, and $m_{\tilde{e}_{R,L}} = 701$ GeV. The M_1' dependence of the production cross sections for the three pairings of the two lightest neutralinos, {11}, {12} and {22}, is shown in Fig.1 (center) for $\sqrt{s} = 800$ GeV. For small M_1' the presence of Z_2 has little influence on $\sigma\{\tilde{\chi}_1^0\tilde{\chi}_2^0\}$ which is of similar size as in the MSSM for mixed higgsino pairs. However it significantly enhances diagonal higgsino pairs $\sigma\{\tilde{\chi}_1^0\tilde{\chi}_1^0\}$ and $\sigma\{\tilde{\chi}_2^0\tilde{\chi}_2^0\}$ compared with the MSSM, even though the light neutralino

---

[a]For a mechanism of generating non-universal U(1) gaugino masses, see e.g. [7].

[b]The numbering without primes refers to mass eigenstates ordered according to ascending masses.

masses are nearly identical in the two models. At and beyond the cross–over with singlino, $M_1' \approx 2.68$ TeV, dramatic changes set in for pairs involving the lightest neutralino.

At the LHC the neutralinos will be analyzed primarily in cascade decays of squarks or gluinos. In the USSM the cascade chains may be extended compared with the MSSM by an additional step due to the presence of two new neutralino states, for example, $\tilde{u}_R \to u\tilde{\chi}_6^0 \to uZ_1\tilde{\chi}_5^0 \to uZ_1\ell\tilde{\ell}_R \to uZ_1\ell\ell\tilde{\chi}_1^0$, with partial decay widths significantly modified by the singlino and bino' admixtures. Also the presence of additional Higgs boson will influence the decay chains. Moreover, in the cross–over zones the gaps between the masses of the eigenstates become very small suppressing standard decay channels and, as a result, enhancing radiative decays of neutralinos. These decays are particularly important in the cross–over at $M_1' \simeq 2.6$, where the radiative modes $\tilde{\chi}_2^0, \tilde{\chi}_3^0 \to \tilde{\chi}_1^0 + \gamma$, $\tilde{\chi}_3^0 \to \tilde{\chi}_2^0 + \gamma$ become non–negligible, see Fig.1 (right). Since the photon will be very soft, these decays will be invisible making the decay chains apparently shorter.

3   USSM implications for dark matter
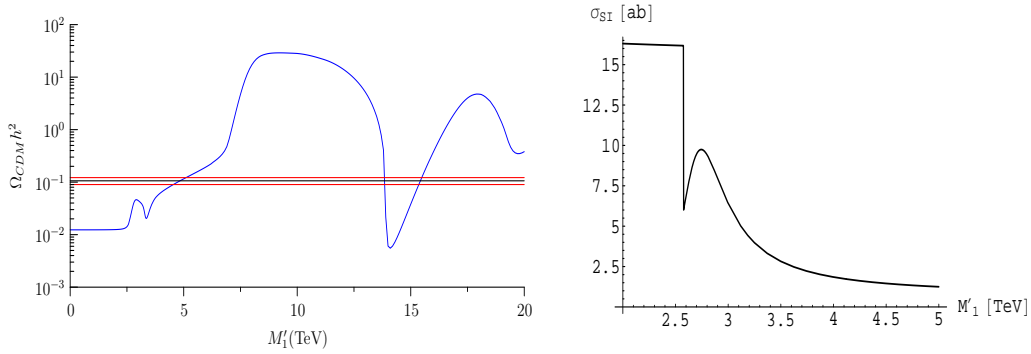
Figure 2: *The M_1' dependence of (left) the predicted relic density of DM, and (right) the elastic spin-independent LSP-^{73}Ge cross section. We restrict the right hand plot to 5 TeV as there are no new features above this energy.*

If the lightest neutralino (LSP) is expected to be the source of the relic abundance of dark matter in the universe, the predicted relic density depends on the LSP composition. In the left panel of Fig.2 it is shown as a function of M_1' [6]. For small M_1' the LSP is almost an MSSM higgsino and for a mass ~ 300 GeV the predicted value falls below the WMAP result. As M_1' increases, the singlino admixture increases suppressing the LSP annihilation cross section and the predicted relic density increases. The singlino LSP predominantly annihilates via an off-shell s-channel singlet Higgs, which decays to two light Higgs bosons. As M_1' increases, the LSP mass decreases and at $M_1' \approx 3.3$ TeV it reaches $m_{\tilde{\chi}_1^0} \approx 250$ GeV making the resonant annihilation via the heavy Higgs boson efficient enough to lower the relic density. Further increase of M_1' switches off the heavy Higgs resonance and eventually the WMAP value is met (shown as a horizontal band in Fig.2 (left) [6]). Around $M_1' = 7.5$ TeV the LSP becomes lighter than the light Higgs. This switches off the annihilation via an off-shell singlet Higgs, $\tilde{\chi}_1^0\tilde{\chi}_1^0 \to h_1h_1$, normally the dominant annihilation mode of a singlino

LSP. As a result the relic density rises sharply. Further increasing M_1' decreases the LSP mass until it matches the resonant annihilation channels of the light Higgs (at around 14 TeV) and Z boson (at around 20 TeV). In both cases this results in a significant dip in the relic density.

The singlino nature of the LSP is also of importance for direct DM searches. It has a strong impact on the elastic spin-independent scattering off the nuclei, e.g. as shown in Fig.2 (right) [6] for the ^{73}Ge nucleus (the numerical codes have been developed in [8]). For small M_1' the two lightest neutralinos (3' and 4' in Fig.1) are almost pure maximally mixed MSSM higgsinos. When M_1' increases, the mixing with singlino lowers $m_{4'}$ so that at $M_1' \approx 2.6$ TeV the state 4' becomes the LSP. Since the higgsino mixing angles are such that the elastic scattering of the state 4' is almost two orders of magnitude smaller than for the state 3', it explains a sudden drop seen in Fig.2 (right). At the same time the singlino and bino' admixture of the LSP increases, which explains a local maximum around 2.8 TeV. As the singlino component (the state 5') of the LSP becomes dominant for higher M_1' values, the elastic cross section becomes smaller and smaller.

4 Summary

The U(1) extended MSSM provides an elegant way of solving the μ problem. As the neutralino sector is extended, the collider phenomenology can significantly be altered and new scenarios for matching the WMAP constraint can be realised. One example, in contrast to the NMSSM, is that the USSM contains regions in which predominantly singlino dark matter can fit the WMAP relic density measurement without the need for coannihilation, or resonant s-channel annihilation processes, where the LSP annihilates via $\tilde{S}\tilde{B}' \to S^* \to hh$.

Acknowledgements

References

[1] For a recent summary and references, see D.J. Miller, R. Nevzorov and P.M. Zerwas, Nucl. Phys. B **681** (2004) 3.

[2] D. Suematsu and Y. Yamagishi, Int. J. Mod. Phys. A **10** (1995) 4521; M. Cvetič, D.A. Demir, J.R. Espinosa, L.L. Everett and P. Langacker, Phys. Rev. D **56** (1997) 2861; **58** (1997) 119905(E).

[3] S. F. King, S. Moretti and R. Nevzorov, Phys. Rev. D **73** (2006) 035009 [arXiv:hep-ph/0510419], and references therein.

[4] S. Y. Choi, H. E. Haber, J. Kalinowski and P. M. Zerwas, Nucl. Phys. B **778** (2007) 85 [arXiv:hep-ph/0612218], and references therein.

[5] V. Barger, P. Langacker, I. Lewis, M. McCaskey, G. Shaughnessy and B. Yencho, Phys. Rev. D **75** (2007) 115002 [arXiv:hep-ph/0702036], and references therein.

[6] D. Jarecka, J. Kalinowski, S.F.King and J. Roberts, in preparation.

[7] D. Suematsu, JHEP **0611** (2006) 029 [arXiv:hep-ph/0606125].

[8] D. Jarecka, MSc thesis, `http://www.fuw.edu.pl/~djarecka/praca/praca11508dz.pdf` (in Polish).

Precision Measurement of a Particle Mass at the Linear Collider

C. Milsténe[1], A. Freitas [2], M. Schmitt[3], A. Sopczak4 [*]

1-Fermi National Laboratory- Batavia-Il-60510 -USA.

2-Institut für Theoretische Physik,Universität Zürich,
Winterthurerstrasse 190, CH-8057, Zürich, Switzerland.

3- Northwestern University, Evanston, USA.

4- Lancaster University, Lancaster LA1 4YB, United Kingdom.

Precision measurement of the stop mass at the ILC is done in a method based on cross-sections measurements at two different center-of-mass energies. This allows to minimize both the statistical and systematic errors. We obtain a much better stop mass precision than in previous studies In the framework of the MSSM, a light stop is studied in its decay into a charm jet and a neutralino, the Lightest Supersymmetric Particle, as a candidate of dark matter. This takes place in the co-annihilation region, namely, for a small stop-neutralino mass difference.

1 Introduction

In this study we are aiming at the minimisation of the systematic uncertainties as well as the statistical error [1]. This is achieved by using a method which allows to increase the precision in two ways. We will deal with a ratio of cross-sections at two energy points. This will take care of the systematic uncertainties by cancelations and then, we choose one of the energies to be at the threshold were the sensitivity to mass is maximale. We will show that even though we are dealing with more realistic data than in [2], we improve substantially the precision in the mass measurement. As in [2], we are considering the MSSM with R Parity conservation and a scenario in which a light stop co-annihilates with the Lightest Supersymetric Particle (LSP), the neutralino, to produce the right amount of dark matter relic density,namely, within the experimental precision of WMAP and the Sloan digital sky survey [3]. Together with a light Higgs, a light right-handed stop also supports electroweak baryogenesis. Our data now include hadronization and fragmentation of the stop before its decay as well as fragmentation of the charm of the decay. This provides a rather big smearing of the particles produced and increases the number of jets. We will use two different approaches. First we will optimize a set of sequential cuts as in [2], then we will be using a multi-variable optimization, of the neural-network type IDA. We do take also advantage of the polarization since we deal with an almost right-handed stop as required for E.W. baryogenesis. This allow us to enhance the signal while getting rid of a big part of the main background.

2 Mass Precision Measurement:the Method

- The production cross-section of stop pairs $e^+e^- \rightarrow \tilde{t}_1 \bar{\tilde{t}}_1$ is represented to next to leading order (NLO), as a function of the energy for two hypothetical values of the stop mass,122.5 GeV and 123.5 GeV, shown in Figure 1.

---

[*]presented by A. Sopczak
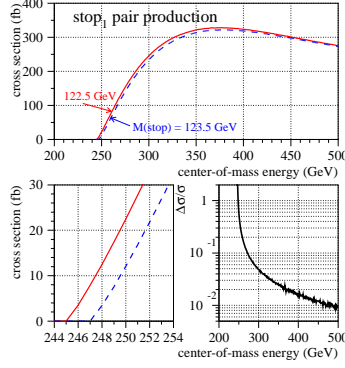
Figure 1: Precision in Pair Production Cross-Section

- In the lower left figure the scale has been blown up and one can see that the sensitivity to small mass difference is high at or close to threshold while in the lower right figure one sees that it is not the case at peak value.

- We will define a parameter Y, as a ratio of production cross-sections at two energy points. This will reduce the systematic uncertainties in Y from the efficiencies as well as from the beam luminosity measurements between the two energy points.

- One of the energy points is chosen at or close to the production energy threshold. This provides an increased sensitivity of Y to mass changes.

$$Y(M_X, \sqrt{s_{\text{th}}}) \equiv \frac{N_{\text{th}} - B_{\text{th}}}{N_{\text{pk}} - N_{\text{pk}}} = \frac{\sigma(\sqrt{s_{\text{th}}})\epsilon_{th}L_{th}}{\sigma(\sqrt{s_{\text{pk}}})\epsilon_{pk}L_{pk}} \tag{1}$$

σ is the cross-section in [fb], N the number of detected data, B is the number of estimated background events, s is the square of the center of mass energy, ϵ the total efficiency and acceptance and L is the integrated luminosity. The suffix (th) is used for the point at energy threshold and (pk) for the energy peak. M_x is the mass to be determined with high precision.

In the method, we determine the stop mass by comparing Y with the theoretical calculation of the cross-sections to next to the leading order (NLO) for both QCD and QED.It has been done for +80% polarizations for the e^- beam and −60% polarization for the e^+.

3 The Channel Studied $e^+e^- \to \tilde{t}_1 \bar{\tilde{t}}_1 \to cX^0\bar{c}\bar{X}^0$

A scan in the super-symmetry parameter space [5] has shown that a stop mass of 122.5 GeV and a neutralino mass of 107.2 GeV are consistent with baryogenesis and dark matter. The process and the background channels are listed below with their cross-sections with and without polarisation.

3.1 Simulations Characteristics

The signal and background channels were generated with Pythia(6.129), the simulator Simdet(4.03) and for the beamstrahlung Circe(1.0)[6]. They were generated in proportion

Process	Cross-section [pb] at $\sqrt{s} = 260$ GeV			Cross-section [pb] at $\sqrt{s} = 500$ GeV		
$P(e^-)/P(e^+)$	0/0	$-80\%/+60\%$	$+80\%/-60\%$	0/0	$-80\%/+60\%$	$+80\%/-60\%$
$t_1 t_1^*$	0.032	0.017	0.077	0.118	0.072	0.276
W^+W^-	16.9	48.6	1.77	8.6	24.5	0.77
ZZ	1.12	2.28	0.99	0.49	1.02	0.44
$We\nu$	1.73	3.04	0.50	6.14	10.6	1.82
eeZ	5.1	6.0	4.3	7.5	8.5	6.2
$q\bar{q}, q \neq t$	49.5	92.7	53.1	13.1	25.4	14.9
$t\bar{t}$	0.0	0.0	0.0	0.55	1.13	0.50
2-photon $p_t > 5$ GeV	786			936		

Table 1: *The Cross-sections at $\sqrt{s} = 260$ GeV and $\sqrt{s} = 500$ GeV for the signal and Standard Model background are given for different polarization combinations. The signal is given for a stop mixing angle of 0.01 and for a stop of $m_{\tilde{t}} = 122.5$ Gev,consistant with E.W. baryogenesis. The e^- negative polarization values refer to left-handed polarization and positive values to right-handed polarization.*

with their cross-sections.

- Hadronization of the $\tilde{t}_1$ quark and the fragmentation of the charm quark come from the Lund string fragmentation model. We use Peterson fragmentation [7].

- The stop fragmentation is simulated using T. Sjostrands code [6]. The stop quark is set stable until after fragmentation, then it is allowed to decay as described in detail by A.C.Kraan[7]. The stop fragmentation parameter is set relative to the bottom fragmentation parameter $\epsilon_{\tilde{t}} = \epsilon_b m_b^2/m_{\tilde{t}}^2$ and $\epsilon_b = -0.0050 \pm 0.0015$. The charm fragmentation is set from LEP to $\epsilon_c = -0.031 \pm 0.011$.

- The mean jet multiplicity increased for the data with fragmentation included.

4 The Analysis

The ntuple analysis code [8] which incorporates the Durham jet algorithm is used. The pre-selection and selection cuts are discribed in detail at both energies in [9].

4.1 The sequential cuts

Were made as similar as possible at the two energies to aim at the cancellation in Y of the systematics. The cuts and their detailed results are given in [9].

After performing the cuts and assuming for the beam e^- +80% polarisation and for e^+-60% polarization we have at 260 GeV with 34% signal efficiency 1309 events for a beam luminosity of 50 fb$^-$1, with a background of 60 Weν, 53 two-photons, 45 $q\bar{q}$ and a score of WW, ZZ, eeZ.

At 500 GeV, with the same beam polarizations and a luminosity of 500 fb$^-$1, the signal efficiency is 22% with 29270 events and a background including 5495 Weν, 81 ZZ, 43 $q\bar{q}$, 31 two-photons, and a score of $t\bar{t}$.

4.2 Iterative Discriminant Analysis (IDA)

Combines the kinematic variables in parallel. The same variables and simulated events are used than in the cut-based analysis. A non-linear discriminant function followed by iterations enhances the separation signal-background. Both signal and background have
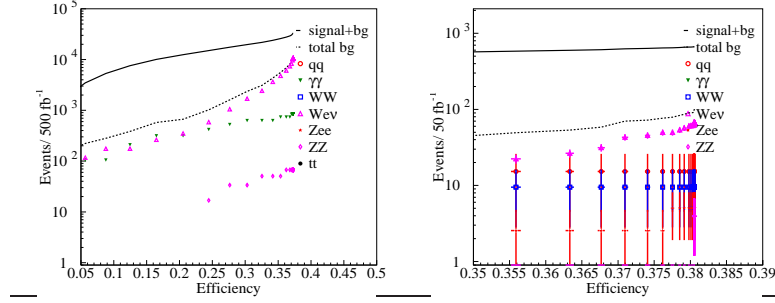
Figure 2: Detection Efficiency and Background Events at 500 GeV(left) and 260 GeV (right).

been divided in equally sized samples, one used for the training, the other as data. We will make two IDA iterations in our final analysis [9]. The results are shown after a first IDA iteration for which one keeps 99% of the signal efficiency followed by a second iteration. We assume the same luminosities and polarizarions than for the sequential based analysis.

With a similar background the efficiency reached is 41.6% at 500 GeV (22% sequential cut) and 38.7% at 260 GeV (34% with sequential cuts).

Error source for Y	Cut-based analysis	Iterative Discriminant Analysis
Statistical	3.1%(0.19GeV)	2.7%(0.17GeV)
Detector effects(systematics)	1.0%	2.1%
Jet mumber (systematics)	1%	1%
Charm fragmentation (systematics)	0.5%	0.5%
Stop fragmentation(systematics)	2.7%	2.8%
Charm tagging algorithm (systematics)	< 0.5%	< 0.5%
Sum of experimental systematics	3%(0.18 GeV)	3.6%(0.22 GeV)
Sum of experimental errors	4.3%(0.26 GeV)	4.5%(0.28 GeV)
Theory for signal cross-section	5.5%	5.5%
Theory for background cross-section	2.0%	1.1%
Total error δY	7.3% (0.44 GeV)	7.2%(0.45 GeV)

Table 2: *Combination of statistical and systematic errors for the determination of the stop mass from a threshold-continuum cross-section measurement. In parenthesis is given the overall error on the measured mass.*

The next to next to leading order (NNLO) QCD corrections are expected to be of the same order than the NLO. This is based on the top quark results. Assuming a factor two improvement in the calculations by the time ILC is running (A 1% NNLO correction is assumed for the EW componant). The relic dark matter density is shown below
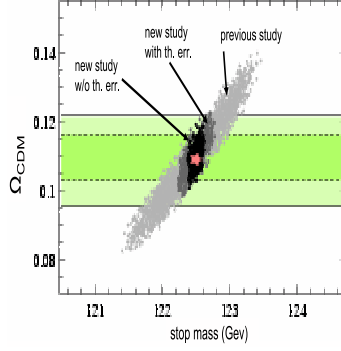
Figure 3: Dark matter Relic Density

5 Conclusions

We deal with more realistic data, including quarks hadronization and fragmentation but still manage to improve the stop mass precision by a factor three comparatively to [2]. The results for the mass precision are shown together with the dark Matter relic density in three cases for $\delta m_{\tilde{t}_1} = 0.44$ GeV, $\Omega_{CDM} h^2 = 0.109 + 0.0015 - 0.013$, it includes both experimetal and theoretical errors. For $\delta m_{\tilde{t}_1} = 0.26$ GeV $\Omega_{CDM} h^2 = 0.109 + 0.0013 - 0.0010$, for experimental errors and sequential cuts and for $\delta m_{\tilde{t}_1} = 0.28$ GeV, $\Omega_{CDM} h^2 = 0.109 + 0.0013 - 0.0010$ as well for the IDA and experimental errors. The evolution in the precision of the dark matter relic density evaluation due to improvements in $\delta m_{\tilde{t}_1}$ is shown in the last figure.

References

[1] Slides:
http://ilcagenda.linearcollider.org/contributionDisplay.py?contribId=49&sessionId=69&confId=1296

[2] M. Carena, A. Finch, A. Freitas, C. Milstene, H. Nowak, A. Sopczak, Phys. Rev.**D72** 115008 (2005).
C. Milsténe, M. Carena, A. Finch, A. Freitas, H. Nowak and A. Sopczak, in *Proc. of International Linear Collider Physics and Detector Workshop, Snowmass, Colorado, 14-27 Aug 2005*, eConf C0508141.

[3] D. N. Spergel *et al.* [WMAP Collaboration], astro-ph/0603449. M. Tegmark *et al.* [SDSS Collaboration], Astrophys. J. **606**, 702 (2004).

[4] G. Feldman,R. Cousins, Phys. Rev.**D57**3873 (1998).

[5] C. Balazs, M. Carena, C. Wagner) hep-ph/0403224v2-(2004).

[6] T. Sjöstrand, P. Eden, C. Friberg, L. Lönnblad, G. Miu, S. Mrenna and E. Norrbin, Comput. Phys. Commun. **135**, 238 (2001); see also T. Sjöstrand, L. Lönnblad and S. Mrenna, hep-ph/0108264.(Pythia).
M. Pohl and H. J. Schreiber, hep-ex/0206009,(Simdet).
T. Ohl,Comput. Phys. Commun. **101**, 269 (1997),(Circe).

[7] Peterson *et al.* Phys. Rev.**D27** 105 (1983),(Petersen). A. C. Kraan, Eur. Phys. J. C **37**, 91 (2004).

[8] T. Kuhl, *N-Tuple working on Simdet DST structure*,
http://www.desy.de/ kuhl/ntuple/ntuple.html.

[9] A. Freitas, C. Milstene, M. Schmitt, A. Sopczak. Publication with a complete description of the method and the analysis(in preparation).

LHC/ILC interplay for challenging SUSY scenarios

Klaus Desch[1], Jan Kalinowski[2], Gudrid Moortgat-Pick[3]*, Krzysztof Rolbiecki[2], W.J. Stirling[3]

1- Physikalisches Institut, Universität Bonn
D-53115 Bonn, Germany

2- Instytut Fizyki Teoretycznej, Uniwersytet Warszawski
PL-00681 Warsaw, Poland

3- IPPP, Institute for Particle Physics Phenomenology, University of Durham
South Road, Durham DH1 3LE, UK

Combined analyses at the Large Hadron Collider and at the International Linear Collider are important to unravel a difficult region of supersymmetry that is characterized by scalar SUSY particles with masses around 2 TeV. Precision measurements of masses, cross sections and forward-backward asymmetries allow to determine the fundamental supersymmetric parameters even if only a small part of the spectrum is accessible. Mass constraints for the heavy particles can be derived.

1   Introduction

Supersymmetry (SUSY) is one of the best-motivated candidates for physics beyond the Standard Model (SM). If experiments at future accelerators, the Large Hadron Collider (LHC) and the International Linear Collider (ILC), discover SUSY they will also have to determine precisely the underlying SUSY-breaking scenario. Scenarios where the squark and slepton masses are very heavy (multi-TeV range) as required, for instance, in focus-point scenarios (FP) [2], are particularly challenging. It is therefore of particular interest to verify whether the interplay of an LHC/ILC analysis [3] could unravel such models with very heavy sfermions. Here we combine only results from the LHC with results from the 1$^{\rm st}$ stage of the ILC with $\sqrt{s} \leq 500$ GeV.

Methods to derive the SUSY parameters at collider experiments have been worked out, for instance in [4, 5]. In [6, 7, 8] the chargino and neutralino sectors have been exploited at the ILC to determine the MSSM parameters. However, in most cases only the production processes have been studied. Furthermore, it has been assumed that the masses of the virtual scalar particles are already known. Exploiting spin effects in the whole production-and-decay process in the chargino/neutralino sector [9], it has been shown in [10] that, once the chargino parameters are known, useful indirect bounds for the mass of the heavy virtual particles could be derived from forward–backward asymmetries of the final lepton $A_{\rm FB}(\ell)$.

Here a FP-inspired scenario is discussed that is characterized by a ~ 2 TeV scalar particles sector [11]. The analysis is performed entirely at the EW scale, without any reference to the underlying SUSY-breaking mechanism.

2   Case study at LHC and ILC

We study chargino production $e^- + e^+ \to \tilde{\chi}_1^+ + \tilde{\chi}_1^-$ with subsequent leptonic $\tilde{\chi}_1^\pm \to \tilde{\chi}_1^0 + \ell^\pm + \nu$ and hadronic decays $\tilde{\chi}_1^\pm \to \tilde{\chi}_1^0 + \bar{q}_d + q_u$, where $\ell = e, \mu$, $q_u = u, c$, $q_d = d, s$. The production process contains contributions from γ- and Z^0-exchange in the s-channel and

---

*g.a.moortgat-pick@durham.ac.uk, speaker [1].

$m_{\tilde{\chi}^{\pm}_{1,2}}$	$m_{\tilde{\chi}^0_{1,2,3,4}}$	$m_{\tilde{\nu}_e, \tilde{e}_{R,L}}$	$m_{\tilde{q}_{R,L}}$	$m_{\tilde{t}_{1,2}}$	$m_{\tilde{g}}$
117, 552	59, 117, 545, 550	1994, 1996, 1998	2002, 2008	1093, 1584	416

Table 1: Masses of the SUSY particles [in GeV].

from $\tilde{\nu}$-exchange in the t-channel. The decay processes are mediated by $W^{\pm}$, $\tilde{\ell}_L$, $\tilde{\nu}$ or by $\tilde{q}_{dL}$, $\tilde{q}_{uL}$ exchange. The masses and eigenstates of the neutralinos and charginos are determined by the fundamental SUSY parameters: the $U(1)$, $SU(2)$ gaugino mass parameters M_1, M_2, the Higgs mass parameter μ and the ratio of the vacuum expectation values of the two neutral Higgs fields, $\tan\beta = \frac{v_2}{v_1}$. In our case study the MSSM parameters at the EW scale are given by: $M_1 = 60$ GeV, $M_2 = 121$ GeV, $M_3 = 322$ GeV, $\mu = 540$ GeV, $\tan\beta = 20$. The derived masses of the SUSY particles are listed in Table 1.

2.1 Expectations at the LHC

All squarks in this scenario are kinematically accessible at the LHC. The largest squark production cross section is for $\tilde{t}_{1,2}$. However, with stops decaying mainly to $\tilde{g}t$ (with $BR(\tilde{t}_{1,2} \to \tilde{g}t) \sim 66\%$), where background from top production will be large, no new interesting channels are open in their decays.

Since the gluino is rather light in this scenario, several gluino decay channels can be exploited. The largest branching ratio for the gluino decay in our scenario is a three-body decay into neutralinos, $BR(\tilde{g} \to \tilde{\chi}^0_2 b\bar{b}) \sim 14\%$, followed by a subsequent three-body leptonic neutralino decay $BR(\tilde{\chi}^0_2 \to \tilde{\chi}^0_1 \ell^+\ell^-)$, $\ell = e, \mu$ of about 6%. In this channel the dilepton edge will be clearly visible [3]. The mass difference between the two light neutralino masses can be measured from the dilepton edge with an uncertainty of about $\delta(m_{\tilde{\chi}^0_2} - m_{\tilde{\chi}^0_1}) \sim 0.5$ GeV [12]. The gluino mass can be reconstructed in a manner similar to the one proposed in [13] and a relative uncertainty of $\sim 2\%$ can be expected.

2.2 Expectations at the ILC

At the first stage of the ILC, $\sqrt{s} \le 500$ GeV, only light charginos and neutralinos are kinematically accessible. However, in this scenario the neutralino sector is characterized by very low production cross sections, below 1 fb, so that it might not be fully exploitable [11]. Only the chargino pair production process has high rates and we use $\sqrt{s} = 350$ and 500 GeV. The chargino mass can be measured in the continuum, with an error of about 0.5 GeV [14]. This can serve to optimize the ILC scan at the threshold which, can be used to determine the light chargino mass very precisely, to about [14]:

$$m_{\tilde{\chi}^{\pm}_1} = 117.1 \pm 0.1 \text{ GeV}. \tag{1}$$

The mass of the lightest neutralino $m_{\tilde{\chi}^0_1}$ can be derived, either from the lepton energy distribution ($BR(\tilde{\chi}^-_1 \to \tilde{\chi}^0_1 \ell^- \bar{\nu}_\ell) \sim 11\%$) or from the invariant mass distribution of the two jets ($BR(\tilde{\chi}^-_1 \to \tilde{\chi}^0_1 q_d \bar{q}_u) \sim 33\%$). We take [14]

$$m_{\tilde{\chi}^0_1} = 59.2 \pm 0.2 \text{ GeV}. \tag{2}$$

Together with the information from the LHC a mass uncertainty for the second light neutralino of about

$$m_{\tilde{\chi}_2^0} = 117.1 \pm 0.5 \text{ GeV} \tag{3}$$

can be assumed.

We identify the chargino pair production process in the fully leptonic and semileptonic final states and estimate an overall selection efficiency of 50%. The W^+W^- production is the dominant SM background. For the semileptonic (slc) final state, this background can be efficiently reduced from the reconstruction of the hadronic invariant mass. In Table 2, we list cross sections multiplied by the branching fraction $B_{slc} = 2 \times BR(\tilde{\chi}_1^+ \rightarrow \tilde{\chi}_1^0 \bar{q}_d q_u) \times BR(\tilde{\chi}_1^- \rightarrow \tilde{\chi}_1^0 \ell^- \bar{\nu}) + [BR(\tilde{\chi}_1^- \rightarrow \tilde{\chi}_1^0 \ell^- \bar{\nu})]^2 \sim 0.34$ (first two families) including a selection efficiency of $e_{slc} = 50\%$. The error includes the statistical uncertainty of the cross section and $A_{\rm FB}$ (see [11]) based on $\mathcal{L} = 200 \text{ fb}^{-1}$ in each polarization configuration, $(P_{e^-}, P_{e^+}) = (-90\%, +60\%)$ and $(+90\%, -60\%)$, and a relative uncertainty in the polarization of $\Delta P_{e^\pm}/P_{e^\pm} = 0.5\%$ [15].
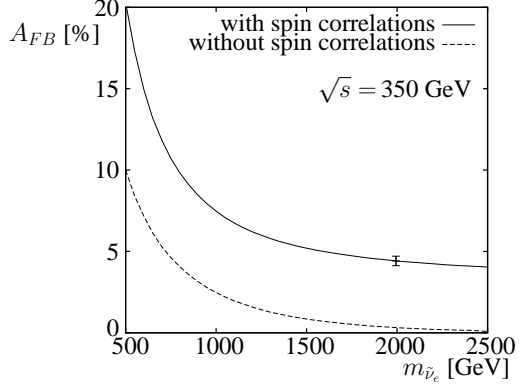
Figure 1: Forward–backward asymmetry of the final e^- [11] as a function of $m_{\tilde{\nu}_e}$. For nominal value of $m_{\tilde{\nu}_e} = 1994$ GeV the expected experimental errors are shown.

3 Parameter determination

We determine the underlying SUSY parameters in several steps:

3.1 Analysis without $A_{\rm FB}$

Only the masses of $\tilde{\chi}_1^\pm$, $\tilde{\chi}_1^0$, $\tilde{\chi}_2^0$ and the chargino pair production cross section, including the fully leptonic and the semileptonic decays have been used as observables. A four-parameter fit for the parameters M_1, M_2, μ and $m_{\tilde{\nu}}$ has been applied, for fixed values of $\tan\beta = 5, 10, 15, 20, 25, 30, 50$ and 100. Due to the strong correlations among parameters [11], fixing of $\tan\beta$ is necessary. We perform a χ^2 test and obtain the following 1σ bounds for the SUSY parameters:

$$59.4 \leq M_1 \leq 62.2 \text{ GeV}, \quad 118.7 \leq M_2 \leq 127.5 \text{ GeV},$$
$$450 \leq \mu \leq 750 \text{ GeV}, \quad 1800 \leq m_{\tilde{\nu}_e} \leq 2210 \text{ GeV}.$$

3.2 Analysis including leptonic $A_{\rm FB}$

We now extend the fit by using as an additional observable the leptonic forward–backward asymmetry, which is sensitive to $m_{\tilde{\nu}}$. Proper account of spin correlations is crucial, see Fig. 1. The $SU(2)$ relation between the two virtual masses $m_{\tilde{\nu}}$ and $m_{\tilde{e}_{\rm L}}$ has been assumed.

	$\sqrt{s} = 350$ GeV		$\sqrt{s} = 500$ GeV	
(P_{e^-}, P_{e^+})	$(-90\%, +60\%)$	$(+90\%, -60\%)$	$(-90\%, +60\%)$	$(+90\%, -60\%)$
$\sigma(\tilde{\chi}_1^+ \tilde{\chi}_1^-)$	6195.5	85.0	3041.5	40.3
$\sigma(\tilde{\chi}_1^+ \tilde{\chi}_1^-) \, B_{slc} \, e_{slc}$	1062.5±4.0	14.6±0.7	521.6±2.3	6.9±0.4
$A_{\mathrm{FB}}(\ell^-)/\%$	4.42±0.29	–	4.62±0.41	–
$A_{\mathrm{FB}}(\bar{c})/\%$	4.18±0.74	–	4.48±1.05	–

Table 2: Cross sections for the process $e^+ e^- \to \tilde{\chi}_1^+ \tilde{\chi}_1^-$ [in fb] and forward–backward asymmetries A_{FB} in the leptonic $\tilde{\chi}_1^- \to \tilde{\chi}_1^0 \ell^- \bar{\nu}$ and hadronic $\tilde{\chi}_1^- \to \tilde{\chi}_1^0 s\bar{c}$ decay modes, for different beam polarization P_{e^-}, P_{e^+}. Concerning the errors, see text and [11].

The multiparameter fit strongly improves the results. No assumption on $\tan\beta$ has to be made. We find

$$59.7 \leq M_1 \leq 60.35 \text{ GeV}, \quad 119.9 \leq M_2 \leq 122.0 \text{ GeV}, \quad 500 \leq \mu \leq 610 \text{ GeV},$$
$$14 \leq \tan\beta \leq 31, \quad 1900 \leq m_{\tilde{\nu}_e} \leq 2100 \text{ GeV}.$$

The constraints for the mass $m_{\tilde{\nu}_e}$ are improved by a factor of about 2 and for gaugino mass parameters M_1 and M_2 by a factor of about 5. The masses of heavy chargino and neutralinos are predicted to be within the ranges

$$506 < m_{\tilde{\chi}_3^0} < 615 \text{ GeV}, \quad 512 < m_{\tilde{\chi}_4^0} < 619 \text{ GeV}, \quad 514 < m_{\tilde{\chi}_2^\pm} < 621 \text{ GeV}.$$

3.3 Analysis including hadronic and leptonic A_{FB}: test of $SU(2)$

In the last step both the leptonic and hadronic forward–backward asymmetries have been used. With the constraints for the squark masses from the LHC, the hadronic forward–backward asymmetry could be used to control the sneutrino mass. The leptonic forward–backward asymmetry provides constraints on the selectron mass and the $SU(2)$ relation between selectron and sneutrino masses could be tested. A six-parameter fit for the parameters M_1, M_2, μ, $m_{\tilde{\nu}}$, $m_{\tilde{e}_{\mathrm{L}}}$ and $\tan\beta$ has been applied, resulting in the following constraints:

$$59.45 \leq M_1 \leq 60.80 \text{ GeV}, \quad 118.6 \leq M_2 \leq 124.2 \text{ GeV}, \quad 420 \leq \mu \leq 770 \text{ GeV},$$
$$11 \leq \tan\beta \leq 60, \quad 1900 \leq m_{\tilde{\nu}_e} \leq 2120 \text{ GeV}, \quad 1500 \text{ GeV} \leq m_{\tilde{e}_{\mathrm{L}}}.$$

The limits are somewhat weaker comparing to the previous case, but we get now constraints for one additional parameter: the selectron mass.

4 Conclusions and outlook

Scenarios with heavy scalar particles are challenging for determining the MSSM parameters. A very powerful tool in this kind of analysis turns out to be the forward–backward asymmetry. This asymmetry is strongly dependent on the mass of the exchanged heavy particle. If the $SU(2)$ constraint is applied, the slepton masses can be determined to a precision of about 5% for masses around 2 TeV at the ILC running at 500 GeV. In addition powerful predictions for the heavier charginos/neutralinos can be made.

In future developments it will be crucial to add radiative corrections which are so far available separately for the production [16] and decays [17]. Full simulations of the whole production-and-decay process will be necessary for precision physics at the ILC.

Acknowledgements

References

[1] Slides:
    http://ilcagenda.linearcollider.org/contributionDisplay.py?contribId=55&sessionId=69&confId=1296

[2] J. L. Feng, K. T. Matchev and T. Moroi, Phys. Rev. D **61** (2000) 075005 [arXiv:hep-ph/9909334]; J. L. Feng and F. Wilczek, arXiv:hep-ph/0507032.

[3] G. Weiglein *et al.* [LHC/LC Study Group], Phys. Rept. 426 (2006) 47 [arXiv:hep-ph/0410364].

[4] T. Tsukamoto, K. Fujii, H. Murayama, M. Yamaguchi and Y. Okada, Phys. Rev. D **51** (1995) 3153; J. L. Feng, M. E. Peskin, H. Murayama and X. Tata, Phys. Rev. D **52** (1995) 1418; H. Baer *et al.*, arXiv:hep-ph/9503479.

[5] P. Bechtle, K. Desch and P. Wienemann, Comput. Phys. Commun. **174** (2006) 47 [arXiv:hep-ph/0412012]; R. Lafaye, T. Plehn and D. Zerwas, arXiv:hep-ph/0404282.

[6] S. Y. Choi, A. Djouadi, H. K. Dreiner, J. Kalinowski and P. M. Zerwas, Eur. Phys. J. C **7** (1999) 123; S. Y. Choi, A. Djouadi, M. Guchait, J. Kalinowski, H. S. Song and P. M. Zerwas, Eur. Phys. J. C **14** (2000) 535 [arXiv:hep-ph/0002033]; J. L. Kneur and G. Moultaka, Phys. Rev. D **61** (2000) 095003 [arXiv:hep-ph/9907360].

[7] S. Y. Choi, J. Kalinowski, G. Moortgat-Pick and P. M. Zerwas, Eur. Phys. J. C **22** (2001) 563 [Addendum, *ibid.* C **23** (2002) 769] [arXiv:hep-ph/0108117]; S. Y. Choi, J. Kalinowski, G. Moortgat-Pick and P. M. Zerwas, arXiv:hep-ph/0202039; E. Boos, H. U. Martyn, G. A. Moortgat-Pick, M. Sachwitz, A. Sherstnev and P. M. Zerwas, Eur. Phys. J. C **30** (2003) 395 [arXiv:hep-ph/0303110]; K. Rolbiecki, Acta Phys. Polon. B **36** (2005) 3477; S. Y. Choi, B. C. Chung, J. Kalinowski, Y. G. Kim and K. Rolbiecki, Eur. Phys. J. C **46** (2006) 511 [arXiv:hep-ph/0504122].

[8] K. Desch, J. Kalinowski, G. Moortgat-Pick, M. M. Nojiri and G. Polesello, JHEP **0402** (2004) 035 [arXiv:hep-ph/0312069].

[9] G. Moortgat-Pick, H. Fraas, A. Bartl and W. Majerotto, Eur. Phys. J. C **7** (1999) 113 [arXiv:hep-ph/9804306]; G. Moortgat-Pick and H. Fraas, Phys. Rev. D **59** (1999) 015016 [arXiv:hep-ph/9708481].

[10] G. Moortgat-Pick and H. Fraas, Acta Phys. Polon. B **30** (1999) 1999 [arXiv:hep-ph/9904209]; G. Moortgat-Pick, A. Bartl, H. Fraas and W. Majerotto, Eur. Phys. J. C **18** (2000) 379 [arXiv:hep-ph/0007222].

[11] K. Desch, J. Kalinowski, G. Moortgat-Pick, K. Rolbiecki and W. J. Stirling, JHEP **0612** (2006) 007 [arXiv:hep-ph/0607104]; K. Rolbiecki, K. Desch, J. Kalinowski and G. Moortgat-Pick, arXiv:hep-ph/0605168.

[12] K. Kawagoe, M. M. Nojiri and G. Polesello, Phys. Rev. D **71** (2005) 035008 [arXiv:hep-ph/0410160].

[13] B. K. Gjelsten, D. J. Miller and P. Osland, JHEP **0506** (2005) 015 [arXiv:hep-ph/0501033].

[14] H. U. Martyn and G. A. Blair, arXiv:hep-ph/9910416; J. A. Aguilar-Saavedra *et al.*, arXiv:hep-ph/0106315; K. Abe *et al.*, arXiv:hep-ph/0109166; T. Abe *et al.*, hep-ex/0106056.

[15] G. A. Moortgat-Pick *et al.*, arXiv:hep-ph/0507011.

[16] T. Fritzsche and W. Hollik, Nucl. Phys. Proc. Suppl. **135** (2004) 102 [arXiv:hep-ph/0407095]; W. Oeller, H. Eberl and W. Majerotto, Phys. Rev. D **71** (2005) 115002 [arXiv:hep-ph/0504109]; W. Kilian, J. Reuter and T. Robens, Eur. Phys. J. C **48** (2006) 389 [arXiv:hep-ph/0607127].

[17] J. Fujimoto, T. Ishikawa, Y. Kurihara, M. Jimbo, T. Kon and M. Kuroda, Phys. Rev. D **75** (2007) 113002; K. Rolbiecki, arXiv:0710.1748 [hep-ph].

Distinguishing SUSY scenarios using τ polarisation and $\tilde{\chi}_1^0$ Dark Matter.

L. Calibbi[1], R. Godbole[2], Y. Mambrini[3] and S. K. Vempati[2].

1- Departament de Física Teòrica, Universitat de València-CSIC, E-46100, Burjassot, Spain.

2- Centre for High Energy Physics, Indian Institute of Science, Bangalore, 560012, India.

3- Laboratoire de Physique Theorique, Universite Paris Sud, F-91405 Orsay, France

We discuss first a method of measuring τ polarisation at the ILC using the 1–prong hadronic decays of the τ. We then show in this contribution how a study of the $\tilde{\tau}$ sector and particularly use of decay τ polarisation can offer a very good handle for distinguishing between mSUGRA and a SUSY-GUTs scenario, both of which can give rise to appropriate Dark Matter.

1 Introduction

Supersymmetry (SUSY) [2] at the TeV scale provides one of the most attractive solution to the problem of instability of the Higgs mass under radiative correction. In fact SUSY forms the template of the physics beyond the Standard Model (BSM physics) that one wishes to probe at the coming colliders like the LHC and the ILC [3]. In the R–parity conserving version of the theory, SUSY also provides a natural dark matter candidate, the lightest neutralino $\tilde{\chi}_1^0$. However, a consistent TeV scale supersymmetry is possible with quite different theoretical realisations at the high scale. For example, mSUGRA [2] and SUSY-GUTs with/without seesaw mechanism [4] are two models embodying SUSY with quite different high scale physics, both of which in turn provide a satisfactory explanation of the Dark Matter (DM) in the Universe. The high scale physics of course leaves its imprints on the properties of the sparticles at the electroweak (EW) scale. The issue of being able to distinguish between such different scenarios using collider experiments has been a matter of great interest to the community. ILC with the possibilities of the high precision measurements offers itself as a natural candidate for the job in hand. In this contribution we show how a study of $\tilde{\tau}$ sector can offer a good possibility of distinguishing the above mentioned specific scenarios in the $\tilde{\tau} - \tilde{\chi}_1^0$ co-annihilation region.

2 τ polarisation: measurement and use as a SUSY probe.

Recall that the mass eigenstates $\tilde{\tau}_i, i = 1, 2$ and $\tilde{\chi}_j^0, j = 1, 4$ are mixtures of $\tilde{\tau}_L, \tilde{\tau}_R$ and gauginos, higgsinos respectively. The couplings of a sfermion with a gaugino does not involve a helicity flip whereas that with a higgsino does. As a result the net helicity of the τ produced in the decay $\tilde{\tau}_i \to \tilde{\chi}_j^0 \tau$, can carry information about L–R mixing in the $\tilde{\tau}$ sector as well as that in the $\tilde{\chi}_j^0$ sector [5]. In collinear approximation for the $\tilde{\tau}$ decay; i.e. $m_\tau \ll m_{\tilde{\tau}_1}$, the polarisation of the τ produced, for example, in $\tilde{\tau}_1 \to \tau \tilde{\chi}_1^0$ is given by,

$$\mathcal{P}_\tau = \frac{\left(a_{11}^R\right)^2 - \left(a_{11}^L\right)^2}{\left(a_{11}^R\right)^2 + \left(a_{11}^L\right)^2};$$

$$a_{11}^R = -\frac{2g}{\sqrt{2}} N_{11} \tan\theta_W \sin\theta_\tau - \frac{gm_\tau}{\sqrt{2}m_W \cos\beta} N_{13} \cos\theta_\tau,$$

$$a_{11}^L = \frac{g}{\sqrt{2}} \left[N_{12} + N_{11} \tan\theta_W\right] \cos\theta_\tau - \frac{gm_\tau}{\sqrt{2}m_W \cos\beta} N_{13} \sin\theta_\tau, \tag{1}$$

where we have used the standard notation [2] with the matrix N representing the diagonalising matrix of the neutralino mass matrix with the notation $\tilde{\chi}_1 = N_{11}\tilde{B} + N_{12}\tilde{W} + N_{13}\tilde{H}_1 + N_{14}\tilde{H}_2$. $\mathcal{P}_\tau$ depends on the mixing in the slepton sector as well as that in the neutralino sector which are determined by the SUSY model parameters; thus giving a good handle of the measurement of SUSY parameters.

Even more importantly, τ polarisation can be also measured well at the colliders. The energy distribution of the π produced in the decay, $\tau \to \nu_\tau \pi$ as well as those in $\tau \to \rho\nu_\tau, \tau \to a_1\nu_\tau$ depends on the handedness of the τ. In fact the angular distribution of the decay meson depends on τ polarisation and is different for longitudinal and transverse states of the vector meson v. The transverse (longitudinal) vector mesons share the energy of parent meson evenly (unevenly) among the decay pions. For the τ decay the only measurable momentum is τ-jet momentum and its value relative to p_τ is determined by the meson decay angle. Hence the energy distribution of decay pions can be used then to measure the τ polarisation [6, 7, 8]. As a matter of fact a lot of nice analysis of τ polarisation and hence of the MSSM parameter determination at a Linear Collider, making use of the $\tau \to \rho/a_1\nu_\tau$ (multi-prong) mode exist [9, 10].

In this note we first discuss a method to determine the P_τ using 1–prong π final state [11]. If we consider the inclusive distributions of the 1–prong π final state and define $R = p_{\pi^\pm}/p_{\tau-jet}$, one finds that for $\mathcal{P}_\tau = 1$ the distribution in R is peaked at $R < 0.2$ and $R > 0.8$, whereas for $\mathcal{P}_\tau = -1$ it is peaked in the middle. The observable R can be simply determined by measuring the energies of the τ in the tracker and the calorimeter. Further, the fraction

$$f = \frac{\sigma(0.2 < R < 0.8)}{\sigma_{total}},$$

can be shown to be very nicely correlated with the τ–polarisation [11] and hence can be used as its measure. Note that full reconstruction of the a_1 and ρ as needed in the mutli-prong analysis is also not needed.

The left panel in Fig.1 (taken from [11] shows distribution in R for different values of polarisations $\mathcal{P}_\tau$ as indicated on the figure for specific choice of $\sqrt{s}$, $\tilde{\tau}_1$, $\tilde{\chi}_1^0$ masses and kinematical cuts on τ mentioned therein. The right panel shows f as a function of $\mathcal{P}_\tau$. Uncertainty due to the different parameterisations of the a_1 and non-resonant contributions to the π, give rise to the slight spread of the lines. One can see from the Figure that $\Delta\mathcal{P}_\tau = \pm0.03(\pm0.05)$ for $\mathcal{P}_\tau = -1(+1)$. Even if an additional error were to come from the experimental measurement of f, still a measurement of $\mathcal{P}_\tau$ with less than 10% error, i.e. $\Delta\mathcal{P}_\tau < 0.1$ is sure to be possible. There is some dependence of the slope on the kinematics of the τ, but it is clear from the figure that the use of inclusive 1-prong channel, is a robust method of determining τ polarisation. If the aim is only to determine τ polarisation, then
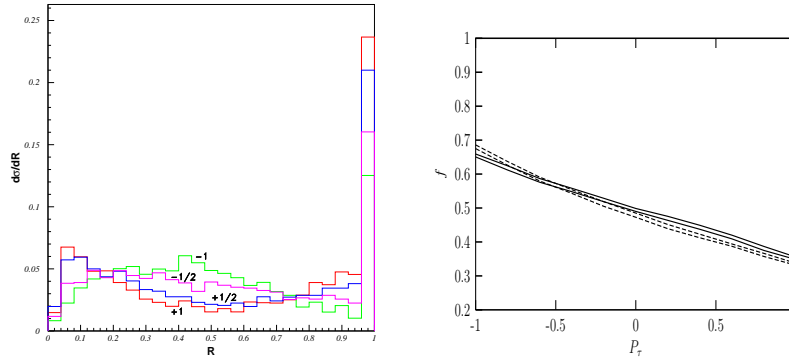
Figure 1: Left panel shows R distribution for τ produced in $\tilde{\tau}_1 \rightarrow \tau\tilde{\chi}_1^0$ for different values of $\mathcal{P}_\tau$ and right panel shows f, defined in text, as a measure of the polarisation. For details see [11]

the 1–prong method has the advantage of higher statistics and smaller systematic errors, compared to the exclusive channel.

3 SUSY-GUTs, mSUGRA and τ polarisation

Let us now see how the properties of the $\tilde{\tau}$ sector and particularly the τ poalrisation can be used to distinguish between various SUSY models. In the present case, we will choose mSUGRA model and a SUSY $SU(5)$ with seesaw mechanism $(SU(5)_{\mathrm{RN}})$ [4]. Requiring neutralino DM relic density to be consistent with the recent WMAP measurements significantly reduces the degeneracies present in the parameter space between these two models. In fact, the effect is quite dramatic; in contrast to mSUGRA, the SUSY-GUT model has only two "allowed" regions: (a) the *stau* coannihilation channel, whose shape is quite different to the corresponding one in mSUGRA[a]; (b) the A-pole funnel region which does exist for large value of $\tan\beta$ whereas a focus point region is not present at least up to 5 TeV in the SUSY masses [4]. From the above it's clear that probing the $\tilde{\tau}$-neutralino sector could give a handle in distinguishing both the models as long as SUSY spectrum is determined by the coannihilation region, where the masses of $\tilde{\tau}_1$ and $\tilde{\chi}_1^0$ are very close. In fact, in our analysis [12], we find that the two models can be clearly distinguished from measuring $\mathcal{P}_\tau$ in the decays of $\tilde{\tau}_2 \rightarrow \tau\tilde{\chi}_1^0$ (Fig. 2 right panel). Here for most of the parameter space, the $\mathcal{P}_\tau$ has different signs. In the small overlap region, $|\Delta\mathcal{P}_\tau| \gtrsim 0.2$, which make them distinguishable at the ILC. In the decay, $\tilde{\tau}_1 \rightarrow \tau\tilde{\chi}_1^0$, the tau polarisation cannot be really used to distinguish between both the models as we see from the left panel of Fig. 2. In our analysis, we have assumed that $\tilde{\tau}_1$ and $\tilde{\tau}_2$ can be distinguished from the kinematics (as $\tilde{\tau}_1$ is closer to mass of $\tilde{\chi}_1^0$ in the coannihilation region).

The behaviour of $\mathcal{P}_\tau$ from $\tilde{\tau}_2 \rightarrow \tau\tilde{\chi}_1^0$ in the two frameworks can be understood as follows. In the approximation of $\tilde{\chi}_1^0 \approx \tilde{B}$, very well satisfied in the $\tilde{\tau}$ coannihilation region, $\mathcal{P}_\tau$ just depends on the L–R mixing for $\tilde{\tau}$ and is simply related to the parameters entering the $\tilde{\tau}$

---
[a]And further predicts an upper bound on the $\tilde{\chi}_1^0$ mass for a given $\tan\beta$.
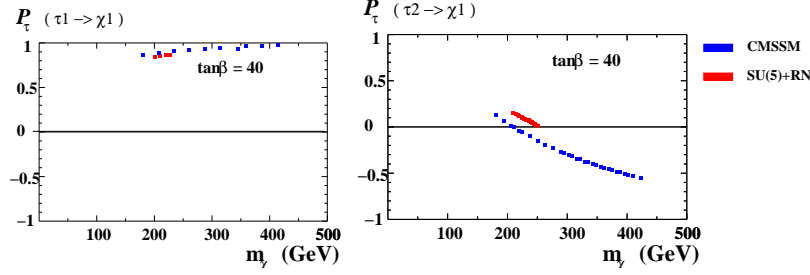
Figure 2: Left panel shows $\mathcal{P}_\tau$ for mSUGRA and $SU(5)_{\mathrm{RN}}$ model in $\tilde{\tau}_1 \to \tilde{\chi}_1^0$ decay as a function of the $\tilde{\chi}_1^0$ mass. The blue(dark) points are for mSUGRA whereas the red(grey) points are for $SU(5)_{\mathrm{RN}}$ model. The right panel shows the same for $\tilde{\tau}_2 \to \tilde{\chi}_1^0$.

mass matrix [5]; given by:

$$\mathcal{P}_\tau = \frac{4m_{\mathrm{LR}}^4 - (m_{\mathrm{LL}}^2 - m_{\tilde{\tau}_1}^2)^2}{4m_{\mathrm{LR}}^4 + (m_{\mathrm{LL}}^2 - m_{\tilde{\tau}_1}^2)^2}.$$

Here m_{LL}^2 is the soft SUSY-breaking mass of $\tilde{\tau}_{\mathrm{L}}$, $m_{\tilde{\tau}_1}^2$ the lightest $\tilde{\tau}$ mass eigenvalue and $m_{\mathrm{LR}}^2 \simeq -m_\tau \mu \tan\beta$ the L–R mixing term. From this expression, we can see that the condition for a positive polarization reads:

$$\mathcal{P}_\tau > 0 \;\Leftrightarrow\; 2\left|m_{\mathrm{LR}}^2\right| > \left|m_{\mathrm{LL}}^2 - m_{\tilde{\tau}_1}^2\right| \tag{2}$$

In mSUGRA, such condition can be satisfied for a small region of the paramater space. The factor 2 on the l.h.s. of Eq. 2 plays a crucial role. In $SU(5)_{\mathrm{RN}}$, the mixing term $\left|m_{\mathrm{LR}}^2\right|$ is enhanced as an effect of RH neutrinos and GUT [4], and this tends to make $\mathcal{P}_\tau$ larger. Moreover there is an upper bound on the $\tilde{\chi}_1^0$ mass in the coannihilation region: these two effects conspire to keep $\mathcal{P}_\tau$ always positive (right panel of Fig. 2).

Thus in this contribution we show how, using τ polarisation and $\tilde{\chi}_1^0$ DM constraints, we can go a long way in distinguishing various SUSY models at the ILC.

References

[1] Slides:
    http://ilcagenda.linearcollider.org/contributionDisplay.py?contribId=343&sessionId=69&confId=1296

[2] See for example, M. Drees, R. Godbole and P. Roy, "Theory and phenomenology of sparticles: An account of four-dimensional N=1 supersymmetry in high energy physics," *Hackensack, USA: World Scientific (2004) 555 p*

[3] G. Weiglein *et al.* [LHC/LC Study Group], Phys. Rept. **426** (2006) 47 [arXiv:hep-ph/0410364].

[4] L. Calibbi, Y. Mambrini and S. K. Vempati, JHEP **0709** (2009) 081 [arXiv:0704.3518 [hep-ph]].

[5] M. M. Nojiri, Phys. Rev. D **51** (1995) 6281 [arXiv:hep-ph/9412374].

[6] K. Hagiwara, A. D. Martin and D. Zeppenfeld, Phys. Lett. B **235** (1990) 198.

[7] D. P. Roy, Phys. Lett. B **277** (1992) 183.

[8] B. K. Bullock, K. Hagiwara and A. D. Martin, Nucl. Phys. B **395** (1993) 499.

[9] M. M. Nojiri, K. Fujii and T. Tsukamoto, Phys. Rev. D **54** (1996) 6756 [arXiv:hep-ph/9606370].

[10] E. Boos, H. U. Martyn, G. A. Moortgat-Pick, M. Sachwitz, A. Sherstnev and P. M. Zerwas, Eur. Phys. J. C **30** (2003) 395 [arXiv:hep-ph/0303110].

[11] R. M. Godbole, M. Guchait and D. P. Roy, Phys. Lett. B **618** (2005) 193 [arXiv:hep-ph/0411306].

[12] L. Calibbi, R. Godbole, Y. Mambrini and S. K. Vempati, *to appear*.

New Physics at TeV Scale and Precision Electroweak Studies

Conveners: J. Hewett, K. Mönig, G. Moreau, S. Raychaudhuri

Two-loop Heavy Fermion Corrections to Bhabha Scattering

S. Actis[1], M. Czakon[2], J. Gluza[3] and T. Riemann[1] *

1 – Deutsches Elektronen-Synchrotron DESY
Platanenallee 6, D–15738 Zeuthen, Germany

2 – Institut für Theoretische Physik und Astrophysik, Universität Würzburg
Am Hubland, D-97074 Würzburg, Germany

3 – Institute of Physics, Univ. of Silesia, Universytecka 4, 40007 Katowice, Poland

We derive the two-loop corrections to Bhabha scattering from heavy fermions in the limit $m_e^2 << m_f^2 << s, t, u$. These $n_f = 2$ contributions arise from self-energies, vertices and box topologies. The numerical effects are estimated for small and large angle scattering at 10, 91, 500 GeV and are at the level of per mille or less. The corrections for $m_f^2 \sim s, t, u$ and those due to hadronic insertions remain to be studied by another technique.

1 Introduction

The Bhabha cross-section has to be determined with an NNLO accuracy.[a] The production of W^+W^- or of fermion pairs, including wide angle Bhabha scattering, at the ILC is anticipated with 10^6 events, and at the GigaZ (or MegaW) option with rates being up to two orders of magnitude higher. Further, it is planned to measure the luminosity with small angle Bhabha scattering. Thus, the cross-section for Bhabha scattering has to be predicted to better than few permille, preferably at the 10^{-4} level; see the talk [3]. The kinematics is compatible with $m_e^2 << s, t, u$, so that the NNLO virtual corrections may be determined in the limit of vanishing electron mass, even for very small scattering angles.

Existing Monte Carlo packages don't cover these corrections completely, see e.g. the review [4] and the reports on small angle Bhabha scattering [5–9], as well as the talks [10–13]. The Monte Carlo programs use small but non-vanishing electron and photon masses as infrared regulators.

Quite recently, the photonic two-loop corrections for massive Bhabha scattering have been determined in a series of papers [14–16], using the analytically known result for the massless case [17]. Together with NNLO contributions from diagrams with electron loop insertions [18–21], the $n_f = 1$ two-loop Bhabha cross-section evaluation was completed [22–24].

An additional class of diagrams with one more scale, the $n_f = 2$ contributions, with heavy fermion loops was calculated quite recently with two different methods; by a direct

---

SE3l2M1m   SE3l2M1md   V4l2M2m

V4l2M2md   V4l2M1m   V4l2M1md

B5l2M2md   B5l2M2m
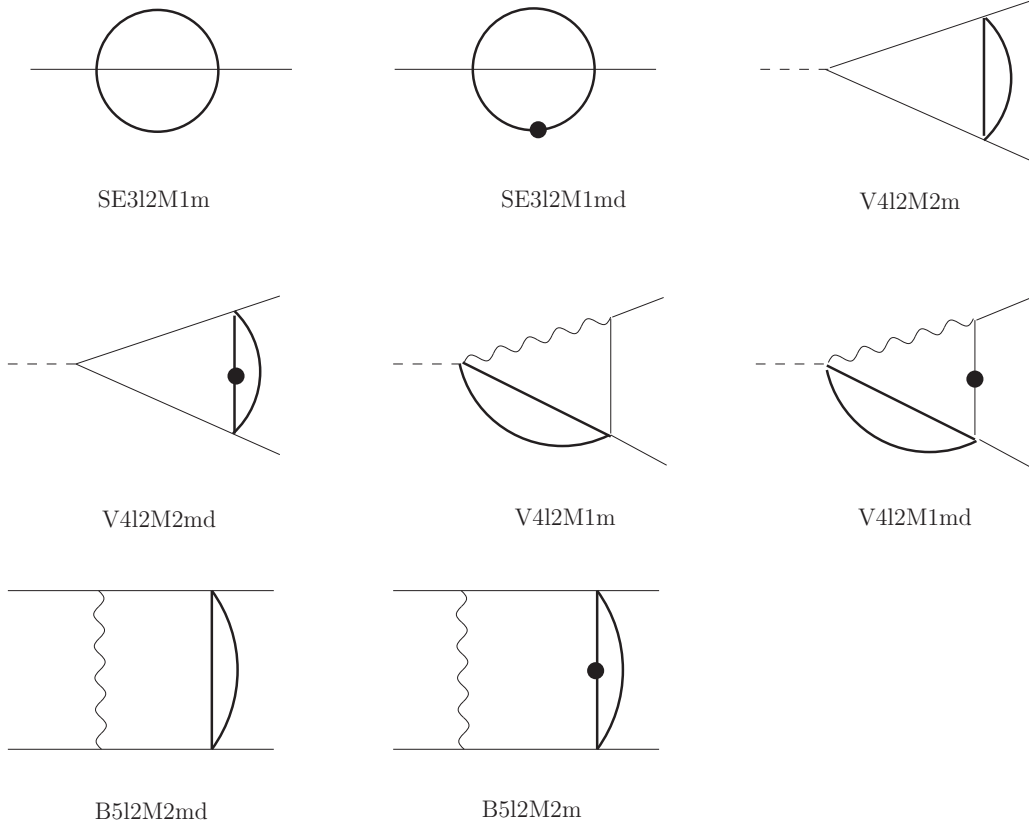
Figure 1: The $n_f = 2$ master integrals

Feynman diagram calculation in [25] and by relating massless and massive diagrams in [26] (see for the method also [27]). In this contribution, we report on our determination of the $n_f = 2$ contributions by evaluation of Feynman diagrams with Mellin-Barnes representations of master integrals and their subsequent expansion first in m_e^2/s, and then in m_f^2/s, at $s \sim t \sim u$.

2 Master integrals

The eight master integrals for the $n_f = 2$ Feynman diagrams for massive Bhabha scattering have been identified in [21] with the Laporta algorithm [28], using the package `IdSolver`. They are shown in Figure 1. These diagrams depend on three different scales: $s/m_e^2, t/m_e^2, M^2/m_e^2$. We evaluated them with the Mellin-Barnes technique (with the algorithm introduced in [29] and realized in the Mathematica packages `ambre` [30]) and `MB` [31], expanding in two steps in the mass scales, $m_e^2 << M^2 << s, t, u$ [25,32]. Let us reproduce here the two double box masters ($m_e = m$):

$$\texttt{B5l2M2m[x,y]} = \frac{m^{-4\epsilon}}{x} \left\{ \frac{1}{\epsilon^2} L_m(x) + \frac{1}{\epsilon} \left(-\zeta_2 + 2L_m(x) + \frac{1}{2}L_m^2(x) + L_m(x)L_m(y) \right) \right.$$
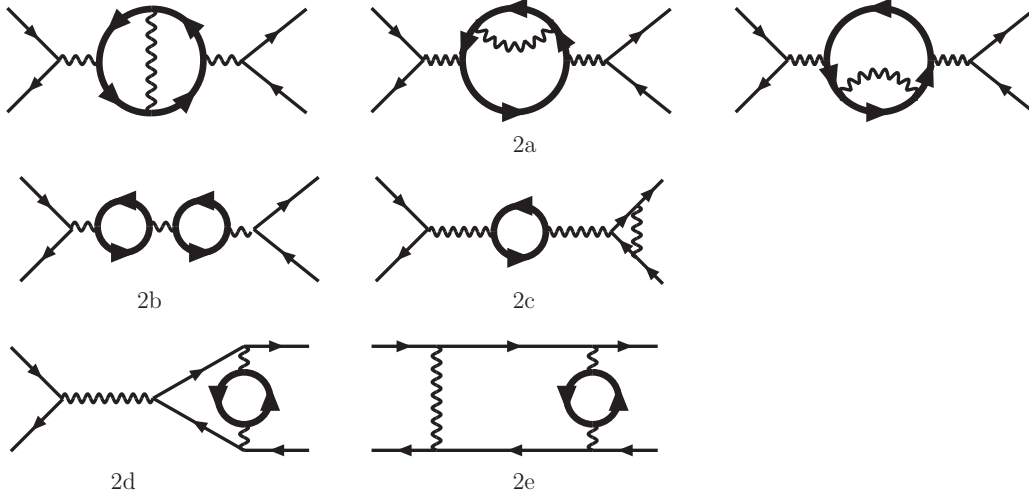
Figure 2: Two-loop diagrams with heavy fermion insertions

$$
\begin{aligned}
- \quad & 2\zeta_2 - 2\zeta_3 + 4L_m(x) + L_m^2(x) + \frac{1}{3}L_m^3(x) - 4\zeta_2 L_m(y) \\
+ \quad & 2L_m(x)L_m(y) + L_m(x)L_m^2(y) - \frac{1}{6}L_m^3(y) \\
- \quad & \left(3\zeta_2 + \frac{1}{2}L_m^2(x) - L_m(x)L_m(y) + \frac{1}{2}L_m^2(y)\right)\ln\left(1 + \frac{y}{x}\right) \\
- \quad & \left(L_m(x) - L_m(y)\right)\mathrm{Li}_2\left(-\frac{y}{x}\right) + \mathrm{Li}_3\left(-\frac{y}{x}\right)\Big\},
\end{aligned}
\tag{1}
$$

$$
\begin{aligned}
\texttt{B512M2md[x,y]} \quad = \quad & \frac{m^{-4\epsilon}}{xy}\Big\{\frac{1}{\epsilon}\Big[-L_m(x)L_m(y) + L_m(x)L(R)\Big] - 2\zeta_3 + \zeta_2 L_m(x) + 4\zeta_2 L_m(y) \\
- \quad & 2L_m(x)L_m^2(y) + \frac{1}{6}L_m^3(y) - 2\zeta_2 L(R) + 2L_m(x)L_m(y)L(R) - \frac{1}{6}L^3(R) \\
+ \quad & \left(3\zeta_2 + \frac{1}{2}L_m^2(x) - L_m(x)L_m(y) + \frac{1}{2}L_m^2(y)\right)\ln\left(1 + \frac{y}{x}\right) \\
+ \quad & \left(L_m(x) - L_m(y)\right)\mathrm{Li}_2\left(-\frac{y}{x}\right) - \mathrm{Li}_3\left(-\frac{y}{x}\right)\Big\}.
\end{aligned}
\tag{2}
$$

We use $L(R) = \ln(m^2/M^2)$, $L_m(x) = \ln(-m^2/x)$, and $L_M(x) = \ln(-M^2/x)$.

3 Cross-sections

The two-loop diagrams to be evaluated are shown in Figure 2. Their interference with the Born diagrams has to be combined with loop-by-loop corrections and soft real bremsstrahlung in order to get an infrared finite cross-section:

$$
\frac{d\sigma^{\mathrm{NNLO}}}{d\Omega} + \frac{d\sigma_\gamma^{\mathrm{NLO}}}{d\Omega} \quad = \quad \frac{d\sigma^{\mathrm{NNLO,e}}}{d\Omega} + \sum_{f\neq e} Q_f^2 \frac{d\sigma^{\mathrm{NNLO,f^2}}}{d\Omega} + \sum_{f\neq e} Q_f^4 \frac{d\sigma^{\mathrm{NNLO,f^4}}}{d\Omega}
$$

$$+ \sum_{f_1, f_2 \neq e} Q_{f_1}^2 Q_{f_2}^2 \frac{d\sigma^{\text{NNLO,2f}}}{d\Omega}. \tag{3}$$

The most complicated part is due to the double box diagrams, it is contained in $d\sigma^{\text{NNLO,f}^2}/d\Omega$:

$$\frac{d\sigma^{\text{NNLO,f}^2}}{d\Omega} = \frac{\alpha^2}{s} \left\{ \sigma_1^{\text{NNLO,f}^2} + \sigma_2^{\text{NNLO,f}^2} \ln\left(\frac{2\omega}{\sqrt{s}}\right) \right\}$$

The virtual part of the contribution is (with $x = -t/s$):

$$
\begin{aligned}
\sigma_1^{\text{NNLO,f}^2} =\ & \frac{\left(1 - x + x^2\right)^2}{3x^2} \Big\{ -\frac{1}{3}\Big[\ln^3\left(\frac{s}{m_e^2}\right) + \ln^3\left(R_f\right)\Big] + \ln^2\left(\frac{s}{m_e^2}\right)\Big[\frac{55}{6} - \ln\left(R_f\right) \\
& + \ln\left(1 - x\right) - \ln\left(x\right)\Big] + \ln\left(\frac{s}{m_e^2}\right)\Big[-\frac{589}{18} + \frac{37}{3}\ln\left(R_f\right) - \ln^2\left(R_f\right) \\
& - 2\ln\left(R_f\right)\Big(\ln\left(x\right) - \ln\left(1 - x\right)\Big) - 8\text{Li}_2\left(x\right)\Big] + \frac{4795}{108} - \frac{409}{18}\ln\left(R_f\right) + \frac{19}{6}\ln^2\left(R_f\right) \\
& - \ln^2\left(R_f\right)\Big(\ln\left(x\right) - \ln\left(1 - x\right)\Big) - 8\ln\left(R_f\right)\text{Li}_2\left(x\right) + \frac{40}{3}\text{Li}_2\left(x\right)\Big\} \\
& + \ln\left(\frac{s}{m_e^2}\right)\Big[\zeta_2\Big(-\frac{2}{3x^2} + \frac{4}{3x} + \frac{11}{2} - \frac{23}{3}x + \frac{16}{3}x^2\Big) + \ln^2\left(x\right)\Big(-\frac{1}{3x^2} + \frac{17}{12x} \\
& - \frac{5}{4} - \frac{x}{12} + \frac{2}{3}x^2\Big) + \ln^2\left(1 - x\right)\Big(-\frac{2}{3x^2} + \frac{11}{6x} - \frac{5}{2} + \frac{11}{6}x - \frac{2}{3}x^2\Big) \\
& + \ln\left(x\right)\ln\left(1 - x\right)\Big(\frac{2}{3x^2} - \frac{4}{3x} - \frac{1}{2} + \frac{5}{3}x - \frac{4}{3}x^2\Big) + \ln\left(x\right)\Big(\frac{55}{9x^2} - \frac{83}{9x} + \frac{65}{6} \\
& - \frac{85}{18}x + \frac{10}{9}x^2\Big) + \frac{1}{3}\ln\left(1 - x\right)\Big(-\frac{10}{3x^2} + \frac{31}{6x} - 10 + \frac{31}{6}x - \frac{10}{3}x^2\Big)\Big] \\
& + \frac{1}{3}\ln^3\left(x\right)\Big(-\frac{1}{3x^2} + \frac{31}{12x} - \frac{11}{6} - \frac{x}{6} + \frac{x^2}{3}\Big) + \frac{1}{3}\ln^3\left(1 - x\right)\Big(-\frac{1}{3x^2} + \frac{1}{x} \\
& - \frac{4}{3} + x - \frac{x^2}{3}\Big) + \ln^2\left(x\right)\ln\left(1 - x\right)\Big(-\frac{1}{3x^2} + \frac{1}{3x} - \frac{4}{3} + x - \frac{x^2}{3}\Big) \\
& + \frac{1}{3}\ln\left(x\right)\ln^2\left(1 - x\right)\Big(-\frac{1}{x^2} + \frac{2}{x} - \frac{7}{4} + \frac{x}{2}\Big) + \ln^2\left(x\right)\Big[\frac{55}{18x^2} - \frac{46}{9x} \\
& + \frac{14}{3} - \frac{4}{9}x - \frac{10}{9}x^2 + \ln\left(R_f\right)\Big(-\frac{1}{3x^2} + \frac{17}{12x} - \frac{5}{4} - \frac{x}{12} + \frac{2}{3}x^2\Big)\Big] \\
& + \ln^2\left(1 - x\right)\Big[\frac{10}{9x^2} - \frac{29}{9x} + \frac{9}{2} - \frac{29}{9}x + \frac{10}{9}x^2 + \ln\left(R_f\right)\Big(-\frac{2}{3x^2} + \frac{11}{6x} \\
& - \frac{5}{2} + \frac{11}{6}x - \frac{2}{3}x^2\Big)\Big] + \ln\left(x\right)\ln\left(1 - x\right)\Big[-\frac{10}{9x^2} + \frac{37}{18x} + \frac{1}{2} - \frac{25}{9}x \\
& + \frac{20}{9}x^2 + \ln\left(R_f\right)\Big(\frac{2}{3x^2} - \frac{4}{3x} - \frac{1}{2} + \frac{5}{3}x - \frac{4}{3}x^2\Big)\Big] + \ln\left(x\right)\Big[-\frac{589}{54x^2} + \frac{1753}{108x} \\
& - \frac{701}{36} + \frac{925}{108}x - \frac{56}{27}x^2 + \text{Li}_2\left(x\right)\Big(-\frac{4}{x^2} + \frac{19}{3x} - 7 + 3x - \frac{2}{3}x^2\Big) \\
& + \ln\left(R_f\right)\Big(\frac{37}{9x^2} - \frac{56}{9x} + \frac{47}{6} - \frac{67}{18}x + \frac{10}{9}x^2\Big) + \zeta_2\Big(-\frac{2}{3x^2} + \frac{4}{x} - \frac{1}{6} \\
& - \frac{10}{3}x + 2x^2\Big)\Big] + \ln\left(1 - x\right)\Big[\frac{56}{27x^2} - \frac{161}{54x} + \frac{56}{9} - \frac{161}{54}x + \frac{56}{27}x^2 \\
& + \ln\left(R_f\right)\Big(-\frac{10}{9x^2} + \frac{31}{18x} - \frac{10}{3} + \frac{31}{18}x - \frac{10}{9}x^2\Big) + \zeta_2\Big(-\frac{2}{x^2} + \frac{20}{3x} - \frac{32}{3} + \frac{20}{3}x \\
& - 2x^2\Big)\Big] + \text{Li}_3\left(x\right)\Big(\frac{4}{3x^2} - \frac{7}{3x} + 3 - \frac{5}{3}x + \frac{2}{3}x^2\Big) + \frac{2}{3}S_{1,2}\left(x\right)\Big(-\frac{1}{x^2} + \frac{1}{x}
\end{aligned}
$$

$$
\begin{aligned}
- \quad & x + x^2 \Big) + \zeta_2 \Big[\frac{19}{9x^2} - \frac{13}{18x} - \frac{43}{3} + \frac{311}{18}x - \frac{98}{9}x^2 + \ln{(R_f)}\Big(-\frac{2}{3x^2} + \frac{4}{3x} \\
+ \quad & \frac{11}{2} - \frac{23}{3}x + \frac{16}{3}x^2 \Big) \Big] + \zeta_3 \Big(-\frac{4}{3x^2} + \frac{3}{x} - 5 + \frac{11}{3}x - 2x^2 \Big).
\end{aligned} \tag{4}
$$

4   Numerical results

The numerical results are summarized in Table 1 for small angle scattering and in Table 2 for large angle scattering.   The net $n_f = 2$ corrections are small compared to the photonic

dσ / dΩ [nb] $\mid \sqrt{s}$ [GeV]	10	91	500
QED Born	440873	5323.91	176.349
full Born	440875	5331.5	176.283
NNLO (e)	-1397.35	-35.8374	-1.88151
NNLO $(e + \mu)$	-1394.74	-43.1888	-2.41643
NNLO $(e + \mu + \tau)$			-2.55179
NNLO photonic	9564.09	251.661	12.7943

Table 1: Numerical values for the NNLO corrections to the differential cross section. Results are expressed in nanobarns for a scattering angle $\theta = 3°$. Empty entries are related to cases where the high-energy approximation cannot be applied. For comparison, we show also the QED and the full electroweak Born cross sections.

dσ / dΩ [nb] $\mid \sqrt{s}$ [GeV]	10	91	500
QED Born	0.466409	0.00563228	0.000186564
full Born	0.468499	0.127292	0.0000854731
NNLO (e)	-0.00453987	-0.0000919387	$-4.28105 \cdot 10^{-6}$
NNLO $(e + \mu)$	-0.00570942	-0.000122796	$-5.90469 \cdot 10^{-6}$
NNLO $(e + \mu + \tau)$	-0.00586082	-0.000135449	$-6.7059 \cdot 10^{-6}$
NNLO $(e + \mu + \tau + t)$			$-6.6927 \cdot 10^{-6}$
NNLO photonic	0.0358755	0.000655126	0.0000284063

Table 2: Same as Table 1, but for a scattering angle $\theta = 90°$.

corrections or to those with an electron loop ($n_f = 1$ corrections). Nevertheless, they reach the level of few permille in certain kinematical regions, and for an accuracy of 10^{-4} one definitely has to take them into account. Thus, at several of the ILC instances, they will be needed. We have not combined them with unresolved real fermion pair emission, which might diminish the numerical effects further due to a compensation of the leading logarithmic terms.

Note added. After this conference, a longer write-up of the material presented here was published [25]. Later, the dispersion technique was applied to the $n_f = 2$ contributions with

semi-analytical predictions for the cross-sections, and relaxing the scale conditions applied here, to $m_e^2 << M^2, s, t, u$ [33]. Another approach was applied to these $n_f = 2$ contributions in [34].

References

[1] Slides:
http://ilcagenda.linearcollider.org/contributionDisplay.py?contribId=231&sessionId=72&confId=1296

[2] DESY, webpage http://www-zeuthen.desy.de/theory/research/bhabha/bhabha.html.

[3] K. Mönig, "Bhabha scattering at the ILC", talk at Bhabha Workshop of SFB/TRR 9, Karlsruhe, April 2005,
http://sfb-tr9.particle.uni-karlsruhe.de/veranstaltungen/bhabha-talks/moenig.pdf.

[4] S. Jadach, "Theoretical error of luminosity cross section at LEP", hep-ph/0306083.

[5] S. Jadach, W. Placzek, E. Richter-Was, B. Ward, Z. Was, "Upgrade of the Monte Carlo program BHLUMI for Bhabha scattering at low angles to version 4.04", *Comput. Phys. Commun.* **102** (1997) 229–251.

[6] S. Jadach, M. Melles, B. F. L. Ward, and S. A. Yost, "Bhabha process at LEP: Theoretical calculations", *Nucl. Phys. Proc. Suppl.* **51C** (1996) 164–173, hep-ph/9607358.

[7] N. P. Merenkov, A. B. Arbuzov, V. S. Fadin, E. A. Kuraev, L. N. Lipatov, and L. Trentadue, "Analytical calculation of small angle Bhabha cross-section at LEP-1", *Acta Phys. Polon.* **B28** (1997) 491–507.

[8] A. Arbuzov *et al.*, "Small-angle Bhabha scattering", *Nucl. Phys. Proc. Suppl.* **51C** (1996) 154–163, hep-ph/9607228.

[9] A. Arbuzov, D. Haidt, C. Matteuzzi, M. Paganoni, and L. Trentadue, "The running of the electromagnetic coupling α in small-angle Bhabha scattering", *Eur. Phys. J.* **C34** (2004) 267–275, hep-ph/0402211.

[10] S. Jadach, "Theoretical calculations for LEP luminosity measurements", talk at Bhabha Workshop of SFB/TRR 9, Karlsruhe, April 2005,
http://sfb-tr9.particle.uni-karlsruhe.de/veranstaltungen/bhabha-talks/jadach.pdf.

[11] A. Denig, "Bhabha scattering at Dafne: The Kloe luminosity measurement", talk at Bhabha Workshop of SFB/TRR 9, Karlsruhe, April 2005,
http://sfb-tr9.particle.uni-karlsruhe.de/veranstaltungen/bhabha-talks/denig.pdf.

[12] L. Trentadue, "Measurement of α_{QED}: An alternative approach", talk at Bhabha Workshop of SFB/TRR 9, Karlsruhe, April 2005,
http://sfb-tr9.particle.uni-karlsruhe.de/veranstaltungen/bhabha-talks/trentadue.pdf.

[13] G. Montagna, "Status of precision MC tools for luminosity monitoring at meson factories", talk at XXXI Conference of Theoretical Physics "Matter to the Deepest: Recent Developments In Physics of Fundamental Interactions", Ustroń, Poland, 5-11 September 2007, http://prac.us.edu.pl/~us2007/talks.htm.

[14] N. Glover, B. Tausk, and J. van der Bij, "Second order contributions to elastic large-angle Bhabha scattering", *Phys. Lett.* **B516** (2001) 33–38, hep-ph/0106052.

[15] A. Penin, "Two-loop corrections to Bhabha scattering", *Phys. Rev. Lett.* **95** (2005) 010408, hep-ph/0501120.

[16] A. Penin, "Two-loop photonic corrections to massive Bhabha scattering", *Nucl. Phys.* **B734** (2006) 185–202, hep-ph/0508127.

[17] Z. Bern, L. Dixon, and A. Ghinculov, "Two-loop correction to Bhabha scattering", *Phys. Rev.* **D63** (2001) 053007, hep-ph/0010075.

[18] R. Bonciani, P. Mastrolia, and E. Remiddi, "Vertex diagrams for the QED form factors at the 2-loop level", *Nucl. Phys.* **B661** (2003) 289–343, hep-ph/0301170.

[19] R. Bonciani, P. Mastrolia, and E. Remiddi, "QED vertex form factors at two loops", *Nucl. Phys.* **B676** (2004) 399–452, hep-ph/0307295.

[20] R. Bonciani, A. Ferroglia, P. Mastrolia, E. Remiddi, and J. van der Bij, "Planar box diagram for the $n_f = 1$ 2-loop QED virtual corrections to Bhabha scattering", *Nucl. Phys.* **B681** (2004) 261–291, hep-ph/0310333.

[21] M. Czakon, J. Gluza, and T. Riemann, "Master integrals for massive two-loop Bhabha scattering in QED", *Phys. Rev.* **D71** (2005) 073009, hep-ph/0412164.

[22] R. Bonciani, A. Ferroglia, P. Mastrolia, E. Remiddi, and J. van der Bij, "Two-loop $n_f = 1$ QED Bhabha scattering differential cross section", *Nucl. Phys.* **B701** (2004) 121–179, hep-ph/0405275.

[23] R. Bonciani, A. Ferroglia, P. Mastrolia, E. Remiddi, and J. van der Bij, "Two-loop $n_f = 1$ QED Bhabha scattering: Soft emission and numerical evaluation of the differential cross-section", *Nucl. Phys.* **B716** (2005) 280–302, hep-ph/0411321.

[24] R. Bonciani and A. Ferroglia, "Two-loop Bhabha scattering in QED", *Phys. Rev.* **D72** (2005) 056004, hep-ph/0507047.

[25] S. Actis, M. Czakon, J. Gluza, and T. Riemann, "Two-loop fermionic corrections to massive Bhabha scattering", *Nucl. Phys.* **B786** (2007) 26–51, arXiv:0704.2400v.2 [hep-ph].

[26] T. Becher and K. Melnikov, "Two-loop QED corrections to Bhabha scattering", *JHEP* **06** (2007) 084, arXiv:0704.3582 [hep-ph].

[27] A. Mitov and S. Moch, "The singular behavior of massive QCD amplitudes", *JHEP* **05** (2007) 001, hep-ph/0612149.

[28] S. Laporta, "High-precision calculation of multi-loop Feynman integrals by difference equations", *Int. J. Mod. Phys.* **A15** (2000) 5087–5159, hep-ph/0102033.

[29] B. Tausk, "Non-planar massless two-loop Feynman diagrams with four on- shell legs", *Phys. Lett.* **B469** (1999) 225–234, hep-ph/9909506.

[30] J. Gluza, K. Kajda, and T. Riemann, "AMBRE - a Mathematica package for the construction of Mellin-Barnes representations for Feynman integrals", *Comput. Phys. Commun.* **177** (2007) 879–893, arXiv:0704.2423 [hep-ph].

[31] M. Czakon, "Automatized analytic continuation of Mellin-Barnes integrals", *Comput. Phys. Commun.* **175** (2006) 559–571, hep-ph/0511200.

[32] S. Actis, M. Czakon, J. Gluza, T. Riemann, "Planar two-loop master integrals for massive bhabha scattering: $n_f = 1$ and $n_f = 2$", *Nucl. Phys. Proc. Suppl.* **160** (2006) 91–100, hep-ph/0609051.

[33] S. Actis, M. Czakon, J. Gluza, and T. Riemann, "Two-loop fermionic corrections to massive Bhabha scattering", Contribution to the XXXI Conference of Theoretical Physics "Matter to the Deepest: Recent Developments in Physics of Fundamental Interactions", Ustroń, Poland, 5-11 September 2007, to appear in Acta Phys. Polonica; http://prac.us.edu.pl/∼us2007/talks.htm, arXiv:0704.2400 [hep-ph].

[34] R. Bonciani, A. Ferroglia, and A. A. Penin, "Two-loop heavy-flavor contribution to Bhabha scattering", arXiv:0710.4775 [hep-ph].

High-Precision Tests of the MSSM with GigaZ

S. Heinemeyer[1], W. Hollik[2], A.M. Weber[2] and G. Weiglein[3] *

1- Instituto de Fisica de Cantabria (CSIC-UC), Santander, Spain

2- Max-Planck-Institut für Physik, Föhringer Ring 6, D–80805 Munich, Germany

3- IPPP, University of Durham, Durham DH1 3LE, UK

We review the physics potential of the GigaZ option of the International Linear Collider (ILC) for probing the Minimal Supersymmetric Standard Model (MSSM) via the sensitivity of the electroweak precision observables measured at the ILC to quantum corrections [1]. A particular focus is put on the effective leptonic weak mixing angle, $\sin^2 \theta_{\text{eff}}$. The MSSM predictions take into account the complete one-loop results including the full complex phase dependence, all available MSSM two-loop corrections as well as the full Standard Model (SM) results. We find that the anticipated experimental accuracy at the ILC with GigaZ option may resolve the virtual effects of SUSY particles even in scenarios where the SUSY particles are so heavy that they escape direct detection at the LHC and the first phase of the ILC.

1 Introduction

Electroweak precision observables (EWPO) are very powerful for testing the Standard Model (SM) and extensions of it. A particularly attractive extension is the Minimal Supersymmetric Standard Model (MSSM), see Ref. [2] for a review of electroweak precision physics in the MSSM. In this context the Z-pole observables (and also the relation between the W- and Z-boson masses obtained from muon decay) play an important role. They comprise in particular the effective leptonic weak mixing angle, $\sin^2 \theta_{\text{eff}}$, the total Z-boson width, Γ_Z, the ratio of the hadronic to leptonic decay width of the Z, R_l, the ratio of the partial decay width for $Z \to b\bar{b}$ to the hadronic width, R_b, and the hadronic peak cross section, σ^0_{had}. Performing fits in constrained SUSY models a certain preference for not too heavy SUSY particles has been found [3–7]. The prospective improvements in the experimental accuracies, in particular at the ILC with GigaZ option, will provide a high sensitivity to deviations both from the SM and the MSSM. In Tab. 1 we summarize the current experimental results [8–10] together with the anticipated improvements at the LHC and the ILC with GigaZ option, see Refs. [2, 11–13] for details.

In order to confront the predictions of supersymmetry (SUSY) with the electroweak precision data and to derive constraints on the supersymmetric parameters, it is desirable to achieve the same level of accuracy for the SUSY predictions as for the SM. In Refs. [14, 15] an new evaluation of M_W and the Z-pole observables in the MSSM has been presented. It includes the full one-loop result (for the first time with the full complex phase dependence), all available MSSM two-loop corrections (entering via the ρ parameter [16–18]), as well as the full SM results, see Refs. [14, 15] for details. The Higgs-boson sector has been implemented including higher-order corrections (as evaluated with `FeynHiggs` [19–21]). These corrections, being formally of higher-order, can give sizable contributions to the EWPO. The remaining theory uncertainties have been estimated to be $\delta M_W^{\text{theo}} \lesssim 10$ MeV [14] and $\delta \sin^2 \theta_{\text{eff}}^{\text{theo}} \lesssim 7 \times 10^{-5}$ [15]. It has furthermore been shown in Ref. [15] that M_W, $\sin^2 \theta_{\text{eff}}$ and Γ_Z show

---

*email: Georg.Weiglein@durham.ac.uk

observable	central exp. value	$\sigma \equiv \sigma^{\text{today}}$	σ^{LHC}	$\sigma^{\text{ILC/GigaZ}}$
M_W [GeV]	80.398	0.025	0.015	0.007
$\sin^2 \theta_{\text{eff}}$	0.23153	0.00016	0.00020–0.00014	0.000013
Γ_Z [GeV]	2.4952	0.0023	—	0.001
R_l	20.767	0.025	—	0.01
R_b	0.21629	0.00066	—	0.00014
σ^0_{had}	41.540	0.037	—	0.025
m_t [GeV]	170.9	1.8	1.0	0.1

Table 1: Summary of the electroweak precision observables, including the top-quark mass, their current experimental central values and experimental errors, $\sigma \equiv \sigma^{\text{today}}$ [8–10]. Also shown are the anticipated experimental accuracies at the LHC, σ^{LHC}, and the ILC (including the GigaZ option), σ^{ILC}. Each number represents the combined results of all detectors and channels at a given collider, taking into account correlated systematic uncertainties, see Refs. [2, 11–13] for details. Non-existing analyses are referred to as "—".

a pronounced sensitivity to the SUSY parameters, while the other EWPO exhibit only a small variation over the MSSM parameter space. In view of the extraordinary anticipated accuracy of $\delta \sin^2 \theta_{\text{eff}}^{\text{ILC/GigaZ}} = 1.3 \times 10^{-5}$ [13], the effective leptonic weak mixing angle will be a highly sensitive probe of electroweak physics.

2 $\sin^2 \theta_{\text{eff}}$ in a global MSSM scan

We first analyse the sensitivity of $\sin^2 \theta_{\text{eff}}$ to higher-order effects in the MSSM by scanning over a broad range of the SUSY parameter space. The following SUSY parameters are varied independently of each other in a random parameter scan within the given range:

$$
\begin{aligned}
\text{sleptons} \quad &: \quad M_{\tilde{F}, \tilde{F}'} = 100 \dots 2000 \text{ GeV}, \\
\text{light squarks} \quad &: \quad M_{\tilde{F}, \tilde{F}'_{\text{up/down}}} = 100 \dots 2000 \text{ GeV}, \\
\tilde{t}/\tilde{b} \text{ doublet} \quad &: \quad M_{\tilde{F}, \tilde{F}'_{\text{up/down}}} = 100 \dots 2000 \text{ GeV}, \quad A_{\tau,t,b} = -2000 \dots 2000 \text{ GeV}, \\
\text{gauginos} \quad &: \quad M_{1,2} = 100 \dots 2000 \text{ GeV}, \quad m_{\tilde{g}} = 195 \dots 1500 \text{ GeV}, \\
&\qquad \mu = -2000 \dots 2000 \text{ GeV}, \\
\text{Higgs} \quad &: \quad M_A = 90 \dots 1000 \text{ GeV}, \quad \tan \beta = 1.1 \dots 60.
\end{aligned}
\tag{1}
$$

Here $M_{\tilde{F}, \tilde{F}'}$ are the diagonal soft SUSY-breaking parameters in the sfermion sector, A_f denote the trilinear couplings, $M_{1,2}$ are the soft SUSY-breaking parameters in the chargino and neutralino sectors, $m_{\tilde{g}}$ is the gluino mass, μ the Higgs mixing parameter, M_A the $\mathcal{CP}$-odd Higgs boson mass, and $\tan \beta$ is the ratio of the two vacuum expectation values. Only the constraints on the MSSM parameter space from the LEP Higgs searches [22, 23] and the lower bounds on the SUSY particle masses from direct searches as given in Ref. [24] were taken into account. Apart from these constraints no other restrictions on the MSSM parameter space were made.

In Fig. 1 we compare the SM and the MSSM predictions for $\sin^2 \theta_{\text{eff}}$ as a function of m_t as obtained from the scatter data. The predictions within the two models give rise to
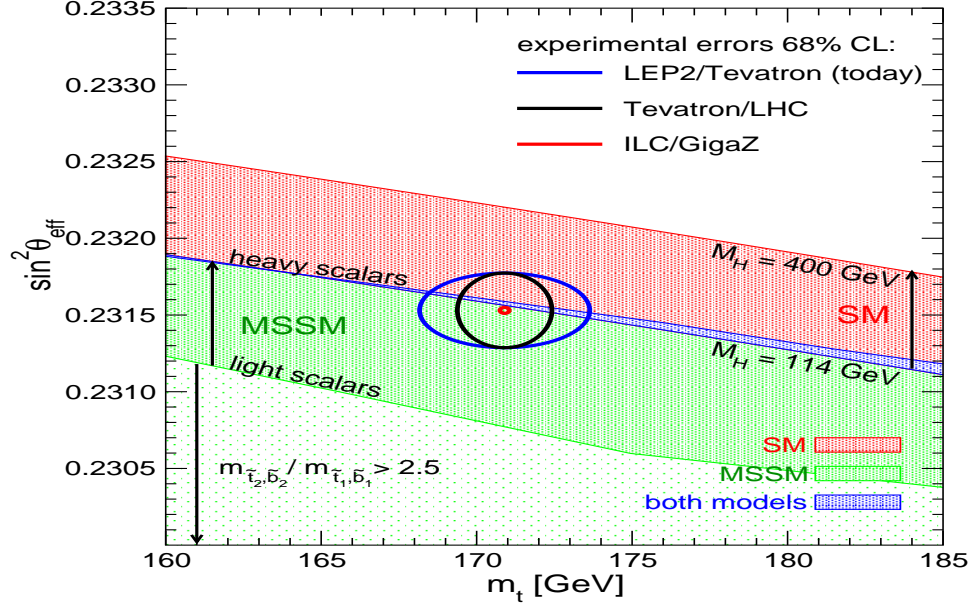
Figure 1: MSSM parameter scan for $\sin^2\theta_{\text{eff}}$ as a function of m_t over the ranges given in eq. (1). Todays 68% C.L. ellipses as well as future precisions, drawn around todays central value, are indicated in the plot.

two bands in the m_t–$\sin^2\theta_{\text{eff}}$ plane with only a relatively small overlap region (indicated by a dark-shaded (blue) area). The allowed parameter region in the SM (the medium-shaded (red) and dark-shaded (blue) bands) arises from varying the only free parameter of the model, the mass of the SM Higgs boson, from $M_H^{\text{SM}} = 114$ GeV, the LEP exclusion bound [23] (lower edge of the dark-shaded (blue) area), to 400 GeV (upper edge of the medium-shaded (red) area). The very light-shaded (green), the light shaded (green) and the dark-shaded (blue) areas indicate allowed regions for the unconstrained MSSM. In the very light-shaded region at least one of the ratios $m_{\tilde{t}_2}/m_{\tilde{t}_1}$ or $m_{\tilde{b}_2}/m_{\tilde{b}_1}$ exceeds 2.5 (with the convention that $m_{\tilde{f}_1} \leq m_{\tilde{f}_2}$), while the decoupling limit with SUSY masses of $\mathcal{O}(2 \text{ TeV})$ yields the upper edge of the dark-shaded (blue) area. Thus, the overlap region between the predictions of the two models corresponds in the SM to the region where the Higgs boson is light, i.e., in the MSSM allowed region ($M_h \lesssim 130$ GeV [19, 20]). In the MSSM it corresponds to the case where all superpartners are heavy, i.e., the decoupling region of the MSSM. The 68% C.L. experimental results for m_t and $\sin^2\theta_{\text{eff}}$ are indicated in the plot. As can be seen from Fig. 1, the current experimental 68% C.L. region for m_t and $\sin^2\theta_{\text{eff}}$ is in good agreement with both models and does not indicate a preference for one of the two models. The prospective accuracies for the Tevatron/LHC and the ILC with GigaZ option, see Tab. 1, are also shown in the plot (using the current central values). Especially the ILC/GigaZ precision indicates the strong potential for a significant improvement of the sensitivity of the electroweak precision tests [12]. A comparison of the MSSM parameter space preferred by $\sin^2\theta_{\text{eff}}$ and the directly measured values will constitute a highly sensitive test of the model.

3 Scenario where no SUSY particles are observed at the LHC

It is interesting to investigate whether the high accuracy achievable at the GigaZ option of the ILC would provide sensitivity to indirect effects of SUSY particles even in a scenario where the (strongly interacting) superpartners are so heavy that they escape detection at the LHC.
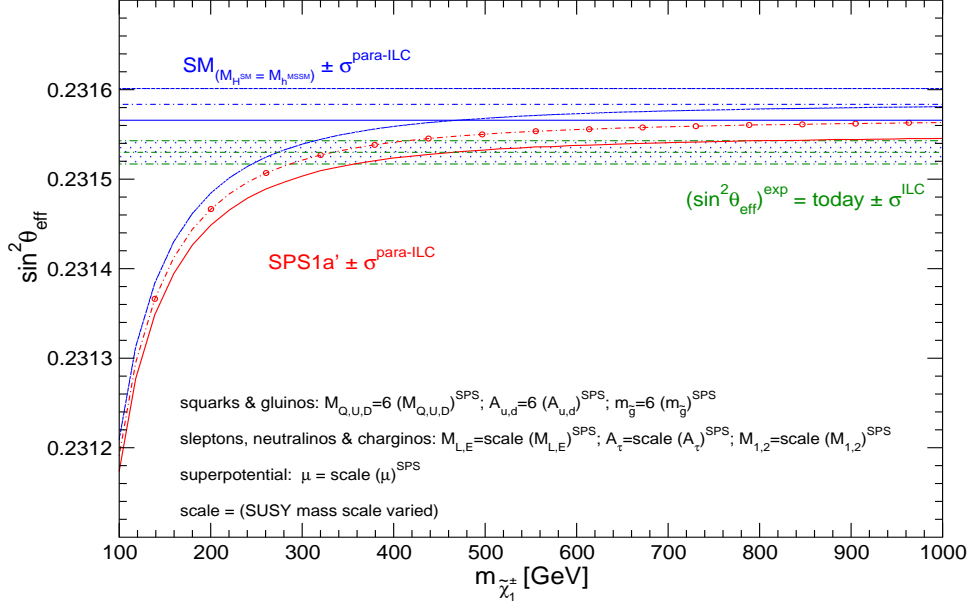
Figure 2: Theoretical prediction for $\sin^2\theta_{\text{eff}}$ in the SM and the MSSM (including prospective parametric theoretical uncertainties) compared to the experimental precision at the ILC with GigaZ option. An SPS1a$'$ inspired scenario is used, where the squark and gluino mass parameters are fixed to 6 times their SPS 1a$'$ values. The other mass parameters are varied with a common scalefactor.

We consider in this context a scenario with very heavy squarks and a very heavy gluino. It is based on the values of the SPS 1a$'$ benchmark scenario [25], but the squark and gluino mass parameters are fixed to 6 times their SPS 1a$'$ values. The other masses are scaled with a common scale factor except M_A which we keep fixed at its SPS 1a$'$ value. In this scenario the strongly interacting particles are too heavy to be detected at the LHC, while, depending on the scale-factor, some colour-neutral particles may be in the ILC reach. In Fig. 2 we show the prediction for $\sin^2\theta_{\text{eff}}$ in this SPS 1a$'$ inspired scenario as a function of the lighter chargino mass, $m_{\tilde{\chi}_1^\pm}$. The prediction includes the parametric uncertainty, $\sigma^{\text{para-ILC}}$, induced by the ILC measurement of m_t, $\delta m_t = 100$ MeV [26], and the numerically more relevant prospective future uncertainty on $\Delta\alpha_{\text{had}}^{(5)}$, $\delta(\Delta\alpha_{\text{had}}^{(5)}) = 5 \times 10^{-5}$ [27]. The MSSM prediction for $\sin^2\theta_{\text{eff}}$ is compared with the experimental resolution with GigaZ precision, $\sigma^{\text{ILC}} = 0.000013$, using for simplicity the current experimental central value. The SM prediction (with $M_H^{\text{SM}} = M_h^{\text{MSSM}}$) is also shown, applying again the parametric uncertainty $\sigma^{\text{para-ILC}}$.

Despite the fact that no coloured SUSY particles would be observed at the LHC in this scenario, the ILC with its high-precision measurement of $\sin^2\theta_{\text{eff}}$ in the GigaZ mode could resolve indirect effects of SUSY up to $m_{\tilde{\chi}_1^\pm} \lesssim 500$ GeV. This means that the high-precision measurements at the ILC with GigaZ option could be sensitive to indirect effects of SUSY even in a scenario where SUSY particles have *neither* been directly detected at the LHC nor the first phase of the ILC with a centre of mass energy of up to 500 GeV.

4 Conclusions

EWPO provide a very powerful test of the SM and the MSSM. We have reviewed results for M_W and Z boson observables such as $\sin^2\theta_{\text{eff}}$, Γ_Z, R_{l}, R_{b}, σ_{had}^0. Within the MSSM new results for the EWPO containing the complete one-loop results with complex parameters and all available higher-order corrections in the SM and the MSSM have recently become available. The sensitivity to higher-order effects will drastically improve with the ILC precision (including the GigaZ option) on the EWPO and m_t. This has been illustrated in two examples. A general scan over the MSSM parameter space for $\sin^2\theta_{\text{eff}}$ and m_t currently does not prefer the SM or the MSSM over the other. However, the anticipated GigaZ precision indicates the high potential for a significant improvement of the sensitivity of the electroweak precision tests. In a second example we have assumed a scenario with very heavy SUSY particles, outside the reach of the LHC and the first stage of the ILC with $\sqrt{s} = 500$ GeV. It has been shown that even in such a scenario the GigaZ precision on $\sin^2\theta_{\text{eff}}$ may resolve virtual effects of SUSY particles, providing a possible hint to the existence of new physics.

References

[1] Slides:
http://ilcagenda.linearcollider.org/contributionDisplay.py?contribId=234&sessionId=72&confId=1296

[2] S. Heinemeyer, W. Hollik and G. Weiglein, *Phys. Rept.* **425** (2006) 265.

[3] J. Ellis, S. Heinemeyer, K. Olive and G. Weiglein, *JHEP* **0502** (2005) 013; *JHEP* **0605** (2006) 005.

[4] J. Ellis, S. Heinemeyer, K. Olive, A.M. Weber and G. Weiglein, *JHEP* **0708** (2007) 083.

[5] B. Allanach and C. Lester, *Phys. Rev.* **D 73** (2006) 015013; B. Allanach, C. Lester and A.M. Weber, *JHEP* **0612** (2006) 065; C. Allanach, K. Cranmer, C. Lester and A.M. Weber, *JHEP* **0708** (2007) 023.

[6] R. de Austri, R. Trotta and L. Roszkowski, *JHEP* **0605** (2006) 002; *JHEP* **0704** (2007) 084.

[7] O. Buchmueller et al., to appear in *Phys. Lett.* **B**, arXiv:0707.3447 [hep-ph].

[8] [The ALEPH, DELPHI, L3, OPAL, SLD Collaborations, the LEP Electroweak Working Group, the SLD Electroweak and Heavy Flavour Groups], *Phys. Rept.* **427** (2006) 257; hep-ex/0511027.

[9] M. Grünewald, arXiv:0709.3744 [hep-ph]; see also: lepewwg.web.cern.ch/LEPEWWG.

[10] [Tevatron Electroweak Working Group], see tevewwg.fnal.gov .

[11] U. Baur, R. Clare, J. Erler, S. Heinemeyer, D. Wackeroth, G. Weiglein and D. Wood, hep-ph/0111314.

[12] S. Heinemeyer, T. Mannel and G. Weiglein, hep-ph/9909538; J. Erler, S. Heinemeyer, W. Hollik, G. Weiglein and P. Zerwas, *Phys. Lett.* **B 486** (2000) 125.

[13] R. Hawkings and K. Mönig, *EPJdirect* **C 8** (1999) 1.

[14] S. Heinemeyer, W. Hollik, D. Stöckinger, A.M. Weber and G. Weiglein, *JHEP* **0608** (2006) 052.

[15] S. Heinemeyer, W. Hollik, A.M. Weber and G. Weiglein, arXiv:0710.2972 [hep-ph].

[16] A. Djouadi, P. Gambino, S. Heinemeyer, W. Hollik, C. Jünger and G. Weiglein, *Phys. Rev. Lett.* **78** (1997) 3626; *Phys. Rev.* **D 57** (1998) 4179.

[17] S. Heinemeyer and G. Weiglein, *JHEP* **0210** (2002) 072.

[18] J. Haestier, S. Heinemeyer, D. Stöckinger and G. Weiglein, *JHEP* **0512** (2005) 027.

[19] S. Heinemeyer, W. Hollik and G. Weiglein, *Comput. Phys. Commun.* **124** 2000 76; *Eur. Phys. J.* **C 9** (1999) 343; see: `www.feynhiggs.de` .

[20] G. Degrassi, S. Heinemeyer, W. Hollik, P. Slavich and G. Weiglein, *Eur. Phys. J.* **C 28** (2003) 133.

[21] M. Frank, T. Hahn, S. Heinemeyer, W. Hollik, H. Rzehak and G. Weiglein, *JHEP* **0702** (2007) 047.

[22] S. Schael et al. [ALEPH, DELPHI, L3, OPAL Collaborations and LEP Working Group for Higgs boson searches], *Eur. Phys. J.* **C 47** (2006) 547.

[23] G. Abbiendi et al. [ALEPH, DELPHI, L3, OPAL Collaborations and LEP Working Group for Higgs boson searches], *Phys. Lett.* **B 565** (2003) 61.

[24] W. Yao et al. [Particle Data Group Collaboration], *J. Phys.* **G 33** (2006) 1.

[25] B. Allanach et al., *Eur. Phys. J.* **C 25** (2002) 113; the definition of the MSSM parameter for the SPS points can be found at `www.ippp.dur.ac.uk/∼georg/sps/` ;
J. Aguilar-Saavedra et al., *Eur. Phys. J.* **C 46** (2006) 43.

[26] A. Hoang et al., *Eur. Phys. J. direct* **C 2** (2000) 1; M. Martinez and R. Miquel, *Eur. Phys. J.* **C 27** (2003) 49.

[27] F. Jegerlehner, talk presented at the LNF Spring School, Frascati, Italy, 1999; hep-ph/0105283.

ILC Sensitivity on Generic New Physics in Quartic Gauge Couplings

Jürgen Reuter

Albert-Ludwigs-Universität Freiburg - Physikalisches Institut
Hermann-Herder-Str. 3, D-79104 Freiburg - Germany

We investigate the potential of the ILC for measuring anomalous quartic gauge couplings, both in production of three electroweak gauge bosons as well as in vector boson scattering. Any new physics that could possibly couple to the electroweak gauge bosons is classified according to its spin and isospin quantum numbers and parameterized in terms of resonance parameters like masses, widths, magnetic moment form factors etc. By a maximum log-likelihood fit, the discovery reach of a 1 TeV ILC for scalar, vector and tensor resonances is examined.

1 Parameterization of new physics in terms of resonances

The Standard Model (SM) with all yet discovered particles (fermions and gauge bosons) can be described by a non-linear sigma model for the electroweak (EW) interactions, dictated by the invariance under $SU(2)_L \times U(1)$ transformations (see e.g. [2, 3]. In this EW chiral Lagrangian the Higgs boson is absent, and the model has to be renormalized order by order, adding new higher-dimensional operators. Any new physics beyond the SM can then be parameterized in terms of these operators in a quite generic way. The building blocks of this (bottom-up) approach are the SM fermions, ψ, the $SU(2)_L$ gauge bosons, W_μ^a, the hypercharge gauge boson, B_μ, and the nonlinear representation of the Goldstone bosons: $\Sigma = \exp\left[\frac{-i}{v} w^a \tau^a\right]$. The longitudinal vector bosons are built from the Goldstone bosons within the vector $\mathbf{V} = \Sigma(\mathbf{D}\Sigma)^\dagger$. To describe isospin-breaking effects, one singles out the neutral component: $\mathbf{T} = \Sigma \tau^3 \Sigma^\dagger$. With these prerequisites we can write the minimal SM Lagrangian (without the yet unobserved Higgs boson) including all the EW gauge interactions as

$$\mathcal{L}_{\min} = \sum_\psi \overline{\psi}(i\gamma^\mu D_\mu)\psi - \frac{1}{2g^2}\operatorname{tr}\left\{\mathbf{W}_{\mu\nu}\mathbf{W}^{\mu\nu}\right\} - \frac{1}{2g'^2}\operatorname{tr}\left\{\mathbf{B}_{\mu\nu}\mathbf{B}^{\mu\nu}\right\} + \frac{v^2}{4}\operatorname{tr}\left\{(vD_\mu\Sigma)(vD^\mu\Sigma)\right\}$$

The complete Lagrangian, since non-renormalizable, contains infinitely many higher-dimensional operators and, hence, infinitely many parameters:

$$\mathcal{L}_{\mathrm{eff}} = \mathcal{L}_{\min} - \sum_\psi \overline{\psi}_L \Sigma M \psi_R + \beta_1 \mathcal{L}_0' + \sum_i \alpha_i \mathcal{L}_i + \frac{1}{v}\sum_i \alpha_i^{(5)} \mathcal{L}^{(5)} + \frac{1}{v^2}\sum_i \alpha_i^{(6)} \mathcal{L}^{(6)} + \ldots$$

All of flavor physics is contained in the fermion mass matrix M, but is ignored for the rest of the paper, since we are interested mainly in the bosonic EW structure. Indirect information on new physics is encoded in the ρ (or T) parameter β_1, the α parameters and higher-dimensional coefficients. The parameters above can be expressed in terms of the fundamental building blocks (for more details cf. [4]):
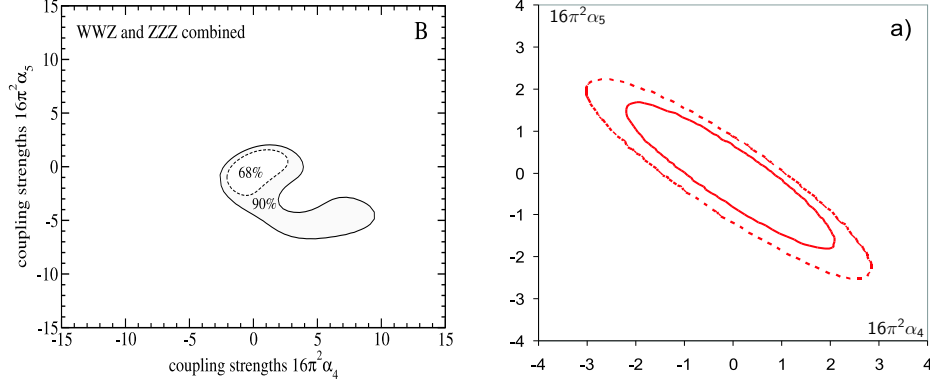
Figure 1: Left: Combined fit for WWZ/ZZZ production at $\sqrt{s} = 1$ TeV, 1 ab^{-1}, both beams polarized. Right: Expected sensitivity (combined fit for all processes) to quartic anomalous couplings for a 1 ab^{-1} e^+e^- sample in the conserved $SU(2)_c$ case. Solid lines represent 90% CL, dashed ones 68%.

	$J = 0$	$J = 1$	$J = 2$
$I = 0$	σ^0 (Higgs ?)	ω^0 (γ'/Z' ?)	f^0 (Graviton ?)
$I = 1$	$\pi^\pm, \pi^0$ (2HDM ?)	$\rho^\pm, \rho^0$ (W'/Z' ?)	$a^\pm, a^0$
$I = 2$	$\phi^{\pm\pm}, \phi^\pm, \phi^0$ (Higgs triplet ?)	—	$t^{\pm\pm}, t^\pm, t^0$

Table 1: Classification of resonances that could possibly couple to the sector of EW bosons according to their spin and isospin quantum numbers, together with some simple examples for them.

$$\mathcal{L}_0' = \frac{v^2}{4} \operatorname{tr}\{\mathbf{T V}_\mu\} \operatorname{tr}\{\mathbf{T V}^\mu\}$$

$$\mathcal{L}_1 = \operatorname{tr}\{\mathbf{B}_{\mu\nu}\mathbf{W}^{\mu\nu}\} \qquad \mathcal{L}_6 = \operatorname{tr}\{\mathbf{V}_\mu\mathbf{V}_\nu\} \operatorname{tr}\{\mathbf{T V}^\mu\} \operatorname{tr}\{\mathbf{T V}^\nu\}$$

$$\mathcal{L}_2 = i \operatorname{tr}\{\mathbf{B}_{\mu\nu}[\mathbf{V}^\mu, \mathbf{V}^\nu]\} \qquad \mathcal{L}_7 = \operatorname{tr}\{\mathbf{V}_\mu\mathbf{V}^\mu\} \operatorname{tr}\{\mathbf{T V}_\nu\} \operatorname{tr}\{\mathbf{T V}^\nu\}$$

$$\mathcal{L}_3 = i \operatorname{tr}\{\mathbf{W}_{\mu\nu}[\mathbf{V}^\mu, \mathbf{V}^\nu]\} \qquad \mathcal{L}_8 = \tfrac{1}{4} \operatorname{tr}\{\mathbf{T W}_{\mu\nu}\} \operatorname{tr}\{\mathbf{T W}^{\mu\nu}\}$$

$$\mathcal{L}_4 = \operatorname{tr}\{\mathbf{V}_\mu\mathbf{V}_\nu\} \operatorname{tr}\{\mathbf{V}^\mu\mathbf{V}^\nu\} \qquad \mathcal{L}_9 = \tfrac{i}{2} \operatorname{tr}\{\mathbf{T W}_{\mu\nu}\} \operatorname{tr}\{\mathbf{T}[\mathbf{V}^\mu, \mathbf{V}^\nu]\}$$

$$\mathcal{L}_5 = \operatorname{tr}\{\mathbf{V}_\mu\mathbf{V}^\mu\} \operatorname{tr}\{\mathbf{V}_\nu\mathbf{V}^\nu\} \qquad \mathcal{L}_{10} = \tfrac{1}{2} \left(\operatorname{tr}\{\mathbf{T V}_\mu\} \operatorname{tr}\{\mathbf{T V}^\mu\}\right)^2$$

The α parameters can be measured at ILC with an expected accuracy at least an order of magnitude better than at LEP, which allows to access new physics scales that lie outside the kinematical range of LHC. One of the tasks of this paper is to study the sensitivity of ILC for new physics scales in the bosonic EW sector, parameterized by the α_i. From the LEP experiments we already know that the α parameters must be quite small, $\alpha_i \ll 1$. If new physics coupled to the EW sector is present, we expect the parameters to be of the order of $\alpha_i \gtrsim 1/16\pi^2 \approx 0.006$, because the higher-dimensional operators renormalize divergences which appear with $\mathcal{O}(1)$ coefficients, $16\pi^2\alpha_i \gtrsim 1$.

$e^+e^- \rightarrow$	Subproc.	σ [fb]
$\nu_e \bar{\nu}_e q \bar{q} q \bar{q}$	$WW \rightarrow WW$	23.19
$\nu_e \bar{\nu}_e q \bar{q} q \bar{q}$	$WW \rightarrow ZZ$	7.624
$\nu \bar{\nu} q \bar{q} q \bar{q}$	$V \rightarrow VVV$	9.344
$\nu e q \bar{q} q \bar{q}$	$WZ \rightarrow WZ$	132.3
$ee q \bar{q} q \bar{q}$	$ZZ \rightarrow ZZ$	2.09
$ee q \bar{q} q \bar{q}$	$ZZ \rightarrow WW$	414.
$b\bar{b}X$	$e^+e^- \rightarrow t\bar{t}$	331.768
$q\bar{q}q\bar{q}$	$e^+e^- \rightarrow WW$	3560.108
$q\bar{q}q\bar{q}$	$e^+e^- \rightarrow ZZ$	173.221
$e\nu q\bar{q}$	$e^+e^- \rightarrow e\nu W$	279.588
$e^+e^- q\bar{q}$	$e^+e^- \rightarrow eeZ$	134.935
X	$e^+e^- \rightarrow q\bar{q}$	1637.405

$SU(2)_c$ conserved		
coupl.	$\sigma-$	$\sigma+$
α_4	-1.41	1.38
α_5	-1.16	1.09
$SU(2)_c$ broken		
coupl.	$\sigma-$	$\sigma+$
α_4	-2.72	2.37
α_5	-2.46	2.35
α_6	-3.93	5.53
α_7	-3.22	3.31
α_{10}	-5.55	4.55

Table 2: Left: Generated processes and cross sections for signal and background for $\sqrt{s} = 1$ TeV, polarization 80% left for electron and 40% right for positron beam. For each process, those final-state flavor combinations are included that correspond to the indicated signal or background subprocess. Right: The expected sensitivity from 1 ab^{-1} e^+e^- sample at 1 TeV, asymmetric 1 sigma errors.

A single new physics scale, Λ or Λ^*, by which the higher-dimensional operators are suppressed in the form of $\alpha_i \sim v^2/\Lambda^2$, is in itself not a very meaningful quantity. Furthermore, it cannot be unambiguously extracted, since the operator normalization is arbitrary as long as the full theory is unknown. And, as we will demonstrate below, the power counting can be quite intricate, such that there is no simple one-to-one correspondence between new physics and chiral Lagrangian parameters.

To be specific: we consider resonances that couple to the EW symmetry breaking sector of the SM. The resonance masses will give detectable shifts in the α_i parameters. These resonances could either be quite narrow in which case we would call them "particles" or rather wide where they would be accounted for as a "continuum". In that sense, the approach we are using here accounts for both weakly and strongly interacting models. In Tab. 1 we classified all possibilities of resonances that can couple to the EW sector according to their spin and isospin quantum numbers. A special case is the parameter β_1 ("ρ" parameter) being much smaller than the others as it expresses the $SU(2)_c$ custodial symmetry almost respected by the SM Lagrangian. The custodial symmetry is broken by the hypercharge gauge interactions $g' \neq 0$ and the fermion masses.

The most reliable way to take the effects of heavy resonances on the EW Lagrangian into account is to integrate them out in the path integral by completing the square in the Gaussian integration. Considering the leading order effects of resonances on the EW sector, integrating out a resonance Φ generates higher-dimensional current-current interactions:

$$\mathcal{L}_\Phi = z \left[\Phi \left(M_\Phi^2 + DD \right) \Phi + 2\Phi J \right] \quad \Rightarrow \quad \mathcal{L}_\Phi^{\text{eff}} = -\frac{z}{M^2} JJ + \frac{z}{M^4} J(DD)J + \mathcal{O}(M^{-6})$$

Here, D is the covariant derivative with respect to $SU(2)_L \times U(1)$, J is the current of the bosonic sector of the SM and z is a normalization constant. The simplest example is a scalar singlet σ with Lagrangian $\mathcal{L}_\sigma = -\frac{1}{2}\sigma(M_\sigma^2 + \partial^2)\sigma - \frac{g_\sigma}{2}v\sigma \, \text{tr} \{\mathbf{V}_\mu \mathbf{V}^\mu\} - \frac{h_\sigma}{2} \, \text{tr} \{\mathbf{TV}_\mu\} \, \text{tr} \{\mathbf{TV}^\mu\}$,
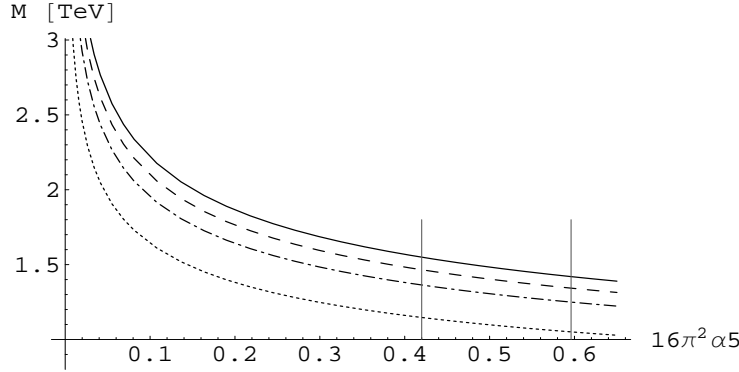
Figure 2: Mass of the scalar singlet resonance in the isospin-conserving case as a function of α_5, with the resonance's width to mass ratio f_σ equal to 1.0 as full, 0.8 as dashed, 0.6 as dot-dashed, and 0.3 as dotted line, respectively. The left vertical line in the plot is the $1\,\sigma$ limit on α_5, the right one the $2\,\sigma$ limit.

which leads to an effective Lagrangian with the following anomalous quartic couplings $\alpha_5 = g_\sigma^2 \cdot v^2/(8M_\sigma^2)$, $\alpha_7 = 2g_\sigma h_\sigma \cdot v^2/(8M_\sigma^2)$, $\alpha_{10} = 2h_\sigma^2 \cdot v^2/(8M_\sigma^2)$. A special case of this would be the SM Higgs with $g_\sigma = 1$ and $h_\sigma = 0$. (Another example for such states would be the light pseudoscalars present in Little Higgs models [5]).

Assuming that this scalar resonance is much heavier than the EW gauge bosons ($M_\sigma \gg M_W, M_Z$) we can neglect mass effects and calculate its width:

$$\Gamma_\sigma = \frac{g_\sigma^2 + \frac{1}{2}(g_\sigma^2 + 2h_\sigma^2)^2}{16\pi} \left(\frac{M_\sigma^3}{v^2}\right) + \Gamma(\text{non} - WW, ZZ)$$

For a broad continuum the largest allowed coupling would result in a width that equals the resonance's mass, $\Gamma \sim M \gg \Gamma(\text{non} - WW, ZZ) \sim 0$. This limiting case translates into bounds for the effective Lagrangian (e.g. in the case of a scalar singlet with no isospin violation):

$$\alpha_5 \leq \frac{4\pi}{3} \left(\frac{v^4}{M_\sigma^4}\right) \approx \frac{0.015}{(M_\sigma \text{ in TeV})^4} \quad \Rightarrow \quad 16\pi^2\alpha_5 \leq \frac{2.42}{(M_\sigma \text{ in TeV})^4}$$

In performing the power counting in a similar manner for other resonances one would naively conclude the following dependence of the anomalous couplings on the resonance masses:

Scalar:	$\Gamma \sim g^2 M^3$,	$\alpha \sim g^2/M^2$	$\Rightarrow$	$\alpha_{\max} \sim 1/M^4$
Vector:	$\Gamma \sim g^2 M$,	$\alpha \sim g^2/M^2$	$\Rightarrow$	$\alpha_{\max} \sim 1/M^2$
Tensor:	$\Gamma \sim g^2 M^3$,	$\alpha \sim g^2/M^2$	$\Rightarrow$	$\alpha_{\max} \sim 1/M^4$

This naive power counting fails in providing the correct answer (for the technical details see [4]). Here the $1/M^2$ term only renormalizes the kinetic energy (i.e. v), and hence is unobservable.

So for vector resonances, all $\alpha_i \sim 1/M_\rho^4$, except for the ρ parameter $\beta_1 \sim \Delta\rho \sim T \sim h_\rho^2/M_\rho^2$. Of course, if new physics resonances couple with non-negligible parameters to the SM fermions, there will be 4-fermion contact interactions that scale like $j_\mu j^\mu \sim 1/M_\rho^2$ and constitute effective T and U parameters. Since these are the most constrained cases (and those most investigated in the literature) we focus here on physics where these interactions can be neglected compared to those to the bosonic EW sector. As a remark of caution we mention that there is also the possibility of a coupling of the EW current due to new resonances to the longitudinal EW bosons which also leads to an effective S parameter $j_\mu V^\mu \sim 1/M_\rho^2$. It induces a mismatch between the measured fermionic and bosonic couplings g [6, 7]. The presence of heavy vector resonances leads to the following effects: for the triple gauge couplings at $\mathcal{O}(1/M^2)$ to a renormalization of the ZWW coupling, at $\mathcal{O}(1/M^4)$ to shifts in Δg_1^Z, $\Delta\kappa^\gamma$, $\Delta\kappa^Z$, λ^γ, λ^Z; for the quartic gauge couplings at order $\mathcal{O}(1/M^4)$ to shifts in the α parameters that are orthogonal to the scalar case in the α_4–α_5 space.

2   Results and Interpretation

There are two ways to study quartic gauge couplings at the ILC, namely triple boson production and vector boson scattering. Concerning the first case, we consider the processes $e^+e^- \to WWZ/ZZZ$, which depend on the combinations $(\alpha_4 + \alpha_6)$, $(\alpha_5 + \alpha_7)$, $\alpha_4 + \alpha_5 + 2(\alpha_6 + \alpha_7 + \alpha_{10})$, respectively. Polarization populates the longitudinal modes and drastically suppresses the SM background. The simulations for the processes discussed here have been performed with the WHIZARD package [8, 9, 10], which is ideally suited for physics beyond the SM [11].

For the triple boson production we assumed a 1 TeV ILC with $1\,\mathrm{ab}^{-1}$ integrated luminosity. The complete six-fermion final states generated with WHIZARD have been piped through the SIMDET fast simulation. As observables we used M_{WW}^2, M_{WZ}^2, and the angle between the incoming electron and the Z. We considered the three cases A) unpolarized, B) 80% e_R^-, C) 80% e_R^-, 60% e_L^+. One has a branching ratio of 32 % hadronic decays, for which we used the Durham jet algorithm. The most severe SM background is $t\bar{t} \to 6$ jets being vetoed against by a missing energy variable cut, $E_{\mathrm{mis}}^2 + p_{\perp,\mathrm{mis}}^2$. So far, no angular correlations have been used in this analysis yet. The result is shown for the combined WWZ/ZZZ case in the left of Fig. 1.

$SU(2)_c$ conserved			
Spin	$I = 0$	$I = 1$	$I = 2$
0	1.55	–	1.95
1	–	2.49	–
2	3.29	–	4.30
$SU(2)_c$ broken			
Spin	$I = 0$	$I = 1$	$I = 2$
0	1.39	1.55	1.95
1	1.74	2.67	–
2	3.00	3.01	5.84

Table 3: Accessible scale Λ in TeV for all possible spin/isospin channels, derived from the analysis of vector-boson scattering at the ILC.

Vector boson scattering – as the second process where quartic gauge couplings could be measured – has been studied for a 1 TeV ILC with $1\,\mathrm{ab}^{-1}$, full six-fermion final states, 80 % e_R^- and 60 % e_L^+ polarization. The contributing channels are mainly $WW \to WW$, $WW \to ZZ$, $WZ \to WZ$, $ZZ \to ZZ$, in more detail in the left of Tab. 2. We performed a binned log-likelihood analysis for all different spin-/isospin combinations listed in Tab. 1. To interpret the ILC reach as limits

on resonances, we consider the width to mass ratio, $f = \Gamma/M$, by which we can trade the unknown parameters (i.e. coupling constants) by experimentally accessible resonance parameters like the position and shape of the resonance.

As the simplest example, we show the $SU(2)$ conserving scalar singlet in Fig. 2. Here the relation between the resonance mass, the α parameters and the width-to-mass ratio, $M_\sigma = v \left((4\pi f_\sigma)/(3\alpha_5)\right)^{\frac{1}{4}}$, can easily be solved. Extracting limits for resonances with $SU(2)$ breaking or higher isospin gets more and more complicated. The most complex case is the $SU(2)$ broken vector triplet: since the effects from the presence of the vector resonance enter only at $\mathcal{O}(1/M^4)$ one has to consider all operators at this order. This includes also magnetic moments of the vector resonances. Assuming also $SU(2)_c$ breaking the system contains too many unknown parameters. The missing information can be gained from the investigation of the triple gauge couplings: we used the covariance matrix from this measurement [12] to find the minimum in the multi-dimensional parameter space for these cases.

ILC has the ability to detect new physics in the EW sector even if it is kinematically out of reach. Our results are summarized in Tab. 3. For the case of a scalar singlet with conserved $SU(2)$ we combined triple boson production and boson scattering, shown on the right of Fig. 1 and Tab. 2. The limits are translated into resonance masses from the 1σ limits on the αs. In general, the limit lies in the range from $1 - 6$ TeV, getting better the more internal degrees of freedom are contributing (higher spin and isospin). It is important to note that these limits apply for narrow resonances as well as broad continua.

3 Acknowledgments

4 Bibliography

References

[1] Slides:
http://ilcagenda.linearcollider.org/contributionDisplay.py?contribId=235&sessionId=72&confId=1296

[2] W. Kilian, Springer Tracts Mod. Phys. **198**, 1 (2003).

[3] S. Heinemeyer *et al.*, hep-ph/0511332; S. Kraml *et al.*, arXiv:hep-ph/0608079.

[4] M. Beyer *et al.*, Eur. Phys. J. C **48**, 353 (2006); W. Kilian and J. Reuter, hep-ph/0507099.

[5] J. Reuter, these proceedings, arXiv:0708.4241 [hep-ph]; W. Kilian, D. Rainwater and J. Reuter, Phys. Rev. D **71**, 015008 (2005); hep-ph/0507081; Phys. Rev. D **74**, 095003 (2006).

[6] A. Nyffeler and A. Schenk, Phys. Rev. D **62**, 113006 (2000).

[7] W. Kilian and J. Reuter, Phys. Rev. D **70** (2004) 015004.

[8] T. Ohl, *O'Mega: An Optimizing Matrix Element Generator*, hep-ph/0011243; M. Moretti, T. Ohl, J. Reuter, hep-ph/0102195; J. Reuter, arXiv:hep-th/0212154.

[9] W. Kilian, LC-TOOL-2001-039, Jan 2001.

[10] http://whizard.event-generator.org; W. Kilian, T. Ohl, J. Reuter, to appear in Comput. Phys. Commun., arXiv:0708.4233 [hep-ph].

[11] T. Ohl and J. Reuter, Eur. Phys. J. C **30**, 525 (2003); Phys. Rev. D **70**, 076007 (2004); K. Hagiwara *et al.*, Phys. Rev. D **73**, 055005 (2006); J. Reuter *et al.*, arXiv:hep-ph/0512012; W. Kilian, J. Reuter and T. Robens, Eur. Phys. J. C **48**, 389 (2006)

[12] W. Menges, LC-PHSM-2001-022.

The Noncommutative Standard Model at the ILC

Ana Alboteanu,[*] Thorsten Ohl, and Reinhold Rückl

Universität Würzburg, Institut für Theoretische Physik und Astrophysik
Am Hubland, 97074 Würzburg, Germany

We study phenomenological consequences of a noncommutative extension of the standard model in the θ-expanded approach at the ILC. We estimate the sensitivity of the ILC for the noncommutative scale Λ_{NC}. Comparing with earlier estimates for the LHC, we demonstrate the complementarity of the experiments at the two colliders.

1 The Model

A noncommutative (NC) structure of space-time

$$[\hat{x}^\mu, \hat{x}^\nu] = \mathrm{i}\theta^{\mu\nu} = \mathrm{i}\frac{C^{\mu\nu}}{\Lambda_{\mathrm{NC}}^2} \tag{1}$$

introduces a new energy scale Λ_{NC}. The motivations of (1) that are provided by string theory and quantum gravity place this scale in the vicinity of the corresponding Planck scale: $\Lambda_{\mathrm{NC}} \approx M_{\mathrm{Pl}}$. If $M_{\mathrm{Pl}} \approx 10^{19}\,\mathrm{GeV}$, (1) is unlikely to be ever probed directly by collider experiments. However, in models with additional space dimensions M_{Pl} can be as low as the Terascale and, as a result, Λ_{NC} can be in the reach of future TeV scale colliders, like LHC and ILC. Therefore, quantum field theories on NC space-time (NCQFT), in particular NC extensions of the standard model (SM), are interesting objects for collider phenomenology. Using methods developed for studying NCQFT at the LHC [2], we have estimated the discovery potential of the ILC and its sensitivity to the NC parameters (1).

In this study, we assume a canonical structure of NC space-time, i.e. a constant antisymmetric 4×4 matrix $C^{\mu\nu}$ in (1) that commutes with all the $\hat{x}_\mu$. For convenience, we parametrize $C^{\mu\nu}$ in analogy to the electromagnetic field-strength tensor and denote the time-like components C^{0i} by $\vec{E}$ and the space-like components C^{ij} by $\vec{B}$. Instead of constructing NCQFT directly in terms of the operators $\hat{x}$, we encode the NC structure (1) of space-time by means of a deformed product of functions on an ordinary commuting space-time, the so called Moyal-Weyl $\star$-product:

$$f(x) \star g(x) = f(x)\mathrm{e}^{\frac{\mathrm{i}}{2}\overleftarrow{\partial^\mu}\theta_{\mu\nu}\overrightarrow{\partial^\nu}}g(x)\,. \tag{2}$$

For the implementation of the gauge structure of the SM, we use the framework introduced in [3], where the Lie algebra valued gauge and matter fields A_ξ and ψ are mapped to universal enveloping algebra valued fields $\hat{A}_\xi[A,\theta]$ and $\hat{\psi}[A,\psi,\theta]$, allowing the $SU(N)$ gauge groups and fractional $U(1)$-charges of the SM on NC space-time. These so called Seiberg Witten Maps (SWM) are defined as solutions of so called gauge equivalence equations, that express the requirement that the NC gauge transformations are realized by ordinary gauge transformations:

$$\hat{\delta}_\alpha \hat{A}_\mu(A,\theta) = \delta_\alpha \hat{A}_\mu(A,\theta) \tag{3a}$$

$$\hat{\delta}_\alpha \hat{\psi}(\psi,A,\theta) = \delta_\alpha \hat{\psi}(\psi,A,\theta)\,. \tag{3b}$$

---

[*]Speaker [1]

The solutions of (3) can be obtained as an expansion in powers of θ. While we have constructed the most general second order expressions recently [4], we will restrict ourselves here to the first order in θ, to be consistent with the existing LHC study [2].

The construction sketched in the previous paragraph introduces momentum dependent corrections to the SM vertices, as well as new vertices that are absent in the SM, e.g. $f\bar{f}VV$ contact interactions among fermions and gauge bosons. In addition, the gauge boson sector of the NCSM shows a new feature, characteristic to the universal algebra valued approach [3]: the action depends on the choice of the representation, resulting in different versions of the model: the minimal NCSM containing no triple couplings among neutral gauge bosons and the nonminimal NCSM, where such triple gauge boson (TGB) couplings, that are forbidden in the SM, appear. The coupling strength of TGB interactions are not uniquely fixed in the nonminimal NCSM, but constrained to a finite domain (see Figure 1, left). An important aspect of our phenomenological analysis is probing different values of these couplings at the ILC and derive the corresponding sensitivity on the NC scale Λ_{NC}. This will reveal a complementarity with measurements at the LHC.

2 Phenomenology

We perform a phenomenological analysis of the unpolarized scattering process $e^+e^- \to Z\gamma$ in the minimal as well as in the nonminimal NCSM. The final state was selected to contain a Z-boson, since the axial coupling of the Z is crucial for a non-cancellation of the NC effects after summing over polarizations [5, 2].

In the minimal NCSM, the $\mathcal{O}(\theta)$ contribution to the $e^+e^- \to Z\gamma$ scattering amplitude is given by the diagrams
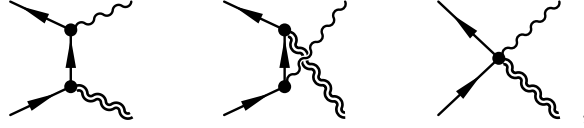
whereas in the nonminimal NCSM two additional s-channel diagrams
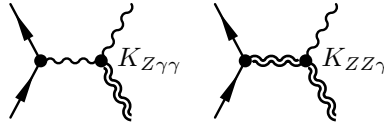
have to be added, introducing a dependence on $K_{Z\gamma\gamma}$ and $K_{ZZ\gamma}$.

2.1 Dependence on the Azimuthal Angle

A NC structure of space-time as introduced in (1), breaks Lorentz invariance, including rotational invariance around the beam axis. This leads to a dependence of the cross section on the azimuthal angle, that is otherwise absent in the SM, as well as in most other other models of physics beyond the SM (see Figure 1, right). In principle, we can distinguish $\vec{E}$-type and $\vec{B}$-type NC contributions by their different dependence on the polar scattering angle: the differential cross section is antisymmetric in $\cos\vartheta$ for $\vec{E} \neq 0$ and it is symmetric for $\vec{B} \neq 0$. However, the dependence of the cross section on $\vec{E}$ is much larger than the one on $\vec{B}$, which will make it very hard to discover the latter at the LHC [2].
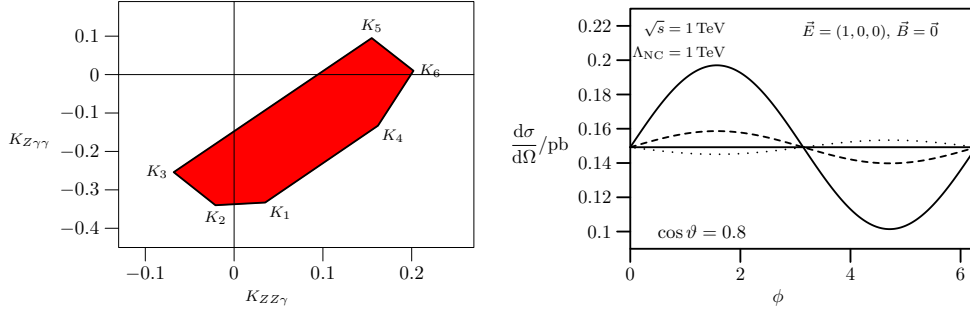
Figure 1: Left: The allowed region for the values of the couplings $K_{Z\gamma\gamma}$ and $K_{ZZ\gamma}$. Right: Azimuthal dependence of the cross section, with different values for the TGB couplings: $K_1 = (-0.333, 0.035)$ (solid) , $K_5 = (0.095, 0.155)$ (dotted) and $K_0 = (0.0, 0.0)$ (dashed).

2.2 Dependence on the Coupling Constants

Since the t-, u- and c-channel diagrams are always proportional to Q^2, the cross section of the minimal NCSM depends only on the modulus $|Q|$ of the charge of the particle in the initial state. In contrast, in the nonminimal NCSM, the interference with the s-channel diagrams adds a Q^3 term to the cross section and the cross section also depends on $\text{sgn}(Q)$. As a result, NC effects in $e^+e^- \to Z\gamma$ are maximally enhanced by the s-channel contribution for the pairs of couplings K_1 and K_2 corresponding to the lower edge of the polygon in Figure 1, left. However, the same couplings lead to cancellations of the NC effects for $u\bar{u}$ scattering resulting in minimal deviations of the NCSM with respect to the SM. In this sense, the ILC will nicely complement the LHC. On the other hand, the pair of couplings K_5, which produces maximal effects at the LHC, will lead to an NCSM cross section comparable to the one where the TGB couplings vanish.

2.3 Monte Carlo Simulations for the ILC

In order to estimate the sensitivity of the ILC on the NC scale Λ_{NC}, we have performed Monte Carlo simulations using the event generator WHIZARD [6]. In the analysis we used a center of mass energy of $\sqrt{s} = 500\,\text{GeV}$ and an integrated luminosity of $\mathcal{L} = 500\,\text{fb}^{-1}$.

A typical signature for new physics is a modified p_T-distribution. Previously, we have studied $pp \to Z\gamma \to e^+e^-\gamma$ at the LHC and the deviation from the SM $p_T(\gamma)$ distribution could not be resolved due to the poor statistics and complicated cuts [2]. However, the high statistics and the clean initial state of the ILC, allows deviations of the NCSM from the SM to be seen also in the p_T distribution for reasonable values of Λ_{NC} (see Figure 2, left). Of course, cuts with respect to the azimuthal angle ϕ have to be applied, because otherwise all $\mathcal{O}(\theta)$ interference effects will cancel, since the events "missing" in one hemisphere (e. g. for $\pi < \phi < 2\pi$) are compensated by the "excess" of events in the other. Figure 2, right, shows this distribution exemplarily, where for the TGB couplings we have chosen the set of values for which we expect the largest deviation from the SM distribution in electron-positron scattering, i. e. K_1.

Nevertheless, we have used the azimuthal dependence (Figure 2) of the cross section in
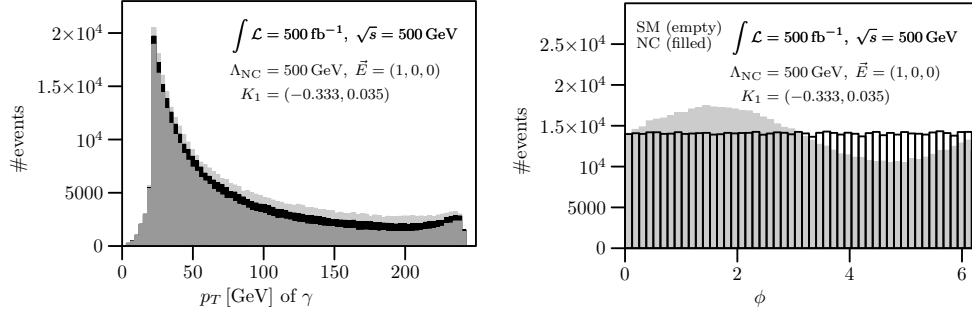
Figure 2: Left: Monte Carlo simulation for the photon p_T distribution of the process $e^+e^- \rightarrow Z\gamma$ at the ILC showing above the black SM histogramm the NCSM distribution for $0.0 < \phi < \pi$ and beneath the NCSM distribution for $\pi < \phi < 2\pi$. Right: Monte Carlo simulation for the azimuthal dependence of the process $e^+e^- \rightarrow Z\gamma$ at the ILC.

order to derive the bounds on Λ_{NC} from the ILC.

As shown in [2], the strong boost along the beam axis from the partonic to the hadronic CMS at the LHC induces kinematical correlations between (E_1, B_2) and (E_2, B_1), respectively. Therefore, in the laboratory frame we always deal with an entanglement of time- and space-like noncommutativity. Fortunately, the different properties of the $\vec{E}$ and $\vec{B}$ parameters with respect to the partonic scattering angle discussed in section 2.1 allows separate measurements of the time- and space-like components of θ. Integrating just over one hemisphere (i. e. $-0.9 < \cos\vartheta^* < 0$ or $0 < \cos\vartheta^* < 0.9$) we can perform a measurement of $\vec{E}$, since the $\vec{B}$ dependence is negligibly small. On the other hand, an integration over the whole sphere (i. e. $-0.9 < \cos\vartheta^* < 0.9$) in principle provides a pure measurement of $\vec{B}$, since the effect of $\vec{E}$ will completely cancel out, due to its antisymmetry.

One advantage of the ILC compared to the LHC is the only mildly boosted initial state. In the e^+e^- initial state, we only have to account for beamstrahlung, which we have done, using CIRCE [7] inside WHIZARD [6]. This will lead to a boost of the CMS of the electrons to the laboratory frame. Yet, compared to the LHC, this boost is negligibly small: $\beta_{\mathrm{ILC}} = 0.14$ versus $\beta_{\mathrm{LHC}} = 0.8$. We therefore have negligible correlations between E_1 and B_2 or E_2 and B_1, respectively, and we can derive the bounds on Λ_{NC} separately for the case of purely $\vec{E}$ or purely $\vec{B}$ noncommutativity.

3 Results and Conclusions

We have performed likelihood fits similar to the ones described in [2] in order to derive bounds on the NC scale Λ_{NC}. The results are summarized in Table 1. In contrast to the LHC case, the ILC is sensitive on all noncommutative parameters, time-like and space-like, as well as on all values of the TGB couplings. The ILC is especially sensitive on the couplings lying in the lower region of the polygon of Figure 1. These are exactly the set of TGB couplings for which the LHC is less sensitive, while the TGB couplings leading to maximal deviations at the LHC, lead to minimal effects at the ILC. Thus, we have shown the complementarity of the ILC to the LHC regarding the different values of the TGB. If

$(K_{Z\gamma\gamma}, K_{ZZ\gamma})$	$|\vec{E}|^2 = 1, \vec{B} = 0$	$\vec{E} = 0, |\vec{B}|^2 = 1$
$K_0 \equiv (0,0)$	$\Lambda_{\rm NC} \gtrsim 2\,{\rm TeV}$	$\Lambda_{\rm NC} \gtrsim 0.4\,{\rm TeV}$
$K_1 \equiv (-0.333, 0.035)$	$\Lambda_{\rm NC} \gtrsim 5.9\,{\rm TeV}$	$\Lambda_{\rm NC} \gtrsim 0.9\,{\rm TeV}$
$K_5 \equiv (0.095, 0.155)$	$\Lambda_{\rm NC} \gtrsim 2.6\,{\rm TeV}$	$\Lambda_{\rm NC} \gtrsim 0.25\,{\rm TeV}$
$K_3 \equiv (-0.254, -0.048)$	$\Lambda_{\rm NC} \gtrsim 5.4\,{\rm TeV}$	$\Lambda_{\rm NC} \gtrsim 0.9\,{\rm TeV}$

Table 1: Bounds on $\Lambda_{\rm NC}$ from $pp \to Z\gamma \to e^+e^-\gamma$ at the LHC, for the minimal (first row) and nonminimal NCSM

a noncommutative structure of space-time is indeed realized at scale of the order of 1 TeV but LHC data will not find any sign of noncommutativity due to an unfavorable realization of the TGB in nature (i. e. in the upper part of the polygon in Figure 1), then the ILC will see it.

4 Acknowledgments

References

[1] Slides:
http://ilcagenda.linearcollider.org/contributionDisplay.py?contribId=237&sessionId=72&confId=1296

[2] A. Alboteanu, T. Ohl and R. Rückl, Phys. Rev. **D74**, 096004 (2006) [arXiv:hep-ph/0608155]; PoS **HEP2005** (2006), 322 [arXiv:hep-ph/0511188].

[3] X. Calmet, B. Jurčo, P. Schupp, J. Wess and M. Wohlgenannt, Eur. Phys. J. **C23**, 363 (2002) [arXiv:hep-ph/0111115]; B. Melic, K. Passek-Kumericki, J. Trampetic, P. Schupp and M. Wohlgenannt, Eur. Phys. J. C **42**, 483 (2005) [arXiv:hep-ph/0502249]; B. Melic, K. Passek-Kumericki, J. Trampetic, P. Schupp and M. Wohlgenannt, Eur. Phys. J. C **42**, 499 (2005) [arXiv:hep-ph/0503064].

[4] A. Alboteanu, T. Ohl and R. Rückl, arXiv:0707.3595 [hep-ph].

[5] T. Ohl and J. Reuter, Phys. Rev. **D70**, 076007 (2004) [arXiv:hep-ph/0406098]; T. Ohl and J. Reuter [arXiv:hep-ph/0407337].

[6] W. Kilian, T. Ohl and J. Reuter, arXiv:0708.4233 [hep-ph]; M. Moretti, T. Ohl and J. Reuter, [arXiv:hep-ph/0102195]; W. Kilian, LC-TOOL-2001-039.

[7] T. Ohl, Comput. Phys. Commun. **101**, 269 (1997) [arXiv:hep-ph/9607454].

Prospects of Discovering a New Massless Neutral Gauge Boson at the ILC

E. Boos[1], V. Bunichev[1] and H.J. Schreiber[2]

1- Skobeltsyn Institute of Nuclear Physics, MSU, 119992 Moscow, Russia

2- DESY, Deutsches Elektronen-Synchrotron, D-15738 Zeuthen, Germany

Prospects to search for a new massless neutral gauge boson, the paraphoton, in e^+e^- collisions at center-of-mass energies of 0.5 and 1 TeV are studied. The paraphoton naturally appears in models with abelian kinetic mixing. Interactions of the paraphoton with Standard Model fermion fields are proportional to the fermion mass and grow with energy, with however negligible couplings to ordinary matter. At the ILC, a potentially process to search for the paraphoton is its radiation off top quarks. Hence, the event topology of interest is a pair of acoplanar top quark jets with missing energy. Applying a multivariate method for signal selection limits for the top-paraphoton coupling could be derived. Arguments in favor of the missing energy as the paraphoton with spin 1 are shortly discussed.

1 Introduction

Modern elementary particle field theories are based on principe of the gauge invariance. It means that the Lagrangian of the theory should be invariant with respect to group transformation of the local symmetry which leads to a corresponding number of massless vector gauge boson fields. In the Standard Model (SM), based on the $U_Y(1) \times SU_L(2) \times SU_C(3)$ gauge symmetry group, 12 gauge vector bosons exist. Three of them, the electroweak bosons $W^{\pm}$ and Z^0, get masses due to the Higgs mechanism of spontaneous symmetry breaking. The eight massless strongly interacting gauge bosons, the gluons, are confined in hadrons and only one directly observed massless neutral vector boson, the well known photon, exists within the SM.

Although the Standard Model does not require any additional gauge fields it is possible to introduce gauge invariant operators in the Lagrangian which involve new gauge fields not forbidden by basic principe of gauge invariance. An example is given in [2] by the abelian kinetic mixing of the SM $U_Y(1)$ field with a new $U_P(1)$ field in a gauge invariant manner. The mixing term of the two $U(1)$ fields can be diagonalized and canonically normalized by an $SL(2,R)$ transformation in a way that one linear combination of the fields corresponds to the ordinary photon which couples in the usual manner to all electrically charged particles within the SM. The other linear combination appears as a massless spin-1 neutral particle, referred to as the "paraphoton" in [3] and denoted by γ' in this paper. The paraphoton couples only indirectly to the SM fields via higher mass-dimension operators.

In this study we follow an approach proposed in [4] where the effective Lagrangian of the interaction of the paraphoton with the SM fermion fields was proposed by considering higher dimensional operators. A possible lowest order Lagrangian which preserves both the new $U_P(1)$ and the SM gauge symmetries with the SM fermion cirality structure has the following form:

$$\frac{1}{M^2} P_{\mu\nu} \left(\bar{q}_L \sigma^{\mu\nu} C_u \tilde{H} u_R + \bar{q}_L \sigma^{\mu\nu} C_d H d_R + \bar{l}_L \sigma^{\mu\nu} C_e H e_R + h.c \right) , \tag{1}$$

where q_L, l_L are the quark and lepton doublets, u_R, d_R the up and down-type $SU(2)$ singlet quarks, e_R the electrically-charged $SU(2)$-singlet leptons, and H is the Higgs doublet. An index labeling the three fermions generations is implicit here. The 3×3 matrices in flavor space, C_u, C_d, C_e, have dimensionless complex elements, and M is the mass scale where the operators are generated.

One can see that the interactions of the paraphoton with Standard Model fermions are suppressed by two powers of the mass scale M, but are directly proportional to the fermion mass m_f and the dimensionless coupling strength parameter C_f, with $f = u, d, e$. The coefficients C_f are unknown, but various phenomenological constraints exist. Discussions on possible lower limits on γ' interactions with fermions can be found in ref. [4].

From the Lagrangian, eq.(1), follows that γ' interaction with SM particles is strongest with the top quark, and small or negligible with light fermions. Therefore, the most interesting process to search for the paraphoton will be γ' radiation off the top. Since so far no constraint on c_t exists, access to $M/\sqrt{c_t}$ seems possible or corresponding limits might be set for the first time.

It seems a priori very difficult to perform γ' searches at hadron colliders because of copious $t\bar{t}$ + multi-jet background production. The next generation e^+e^- linear collider (ILC) is ideally suited to evaluate prospects of a search for the paraphoton via the channel

$$e^+e^- \to t\,\bar{t}\,\gamma' \ . \tag{2}$$

The search strategy relies on the property of the γ' to interact weakly with ordinary matter and its favored emission from top quarks. Hence, the signal signature consists of a pair of acoplanar top quark jets with missing transverse energy, $\not{E}_T$, carried away by the paraphoton. The rate of such events if noticed should clearly exceed the expected SM background.

Simulations of $t\bar{t}\gamma'$ signal events with a 'reasonable' value of the coupling parameter $M/\sqrt{c_t}$ and SM background reactions were performed at $\sqrt{s} = 0.5$ and 1.0 TeV and an integrated luminosity of 0.5, respectively, 1 ab^{-1}. These assumptions are in accord with the present design for the ILC, initially producing collisions at 0.5 TeV and in a second stage at 1 TeV [5].

2   The signal reaction $e^+e^- \to t\,\bar{t}\,\gamma'$

The characteristics of the signal reaction were computed and partonic events were generated by means of the program package CompHEP [8]. The Feynman rules for the fermion-fermion-γ' vertices following from the effective Lagrangian (1)

$$\frac{c_f}{M^2} \cdot m_f \cdot p_3^\nu \delta_{pq} \left(\gamma_{ac}^\nu \gamma_{cb}^\mu - \gamma_{ac}^\mu \gamma_{cb}^\nu \right) \ . \tag{3}$$

have been implemented into CompHEP. An interface with PYTHIA 6.202 [9] allows to simulate initial and final state radiation and jet hadronization, needed at a later stage of the study. Also, beamstrahlung effects [10] are taken into account.

Table 1 shows the number of signal events expected at $\sqrt{s} = 0.5$ and 1 TeV as a function of

$M/\sqrt{c_t}$ $[TeV]$	$\sqrt{s} = 0.5\ TeV$	$\sqrt{s} = 1\ TeV$
0.2	5700	42500
0.3	1100	8500
0.5	40	1100
1	10	70

Table 1: $t\bar{t}\gamma'$ event rates for several values of $M/\sqrt{c_t}$ at $\sqrt{s} = 0.5$ and 1 TeV and an integrated luminosity of 0.5, respectively, 1 ab^{-1}.

$M/\sqrt{c_t}$ for an accumulated luminosity of 0.5, respectively, 1 ab^{-1}. The event rates become rapidly smaller with increasing $M/\sqrt{c_t}$, so that simulations were only performed for $M/\sqrt{c_t} = 0.2$ TeV.

In order to establish a search strategy for the paraphoton in $t\bar{t}$ events it is advantageous to know whether an off-shell or on-shell top quark radiates the γ'. Fig. 1 (left) shows the invariant mass of the $\gamma'Wb$ system of that top which radiates the paraphoton. Clearly, in most cases the paraphoton is radiated off a top being off-shell, and γ' search strategies should be based on on-shell top with $t \to Wb$ decays in association with the γ'. The energy of the γ' shown in Fig. 1 (right) at 1 TeV reveales that substantial energy is carried away by the paraphoton, so that large missing energy, $E\!\!\!/$, will tag signal events.
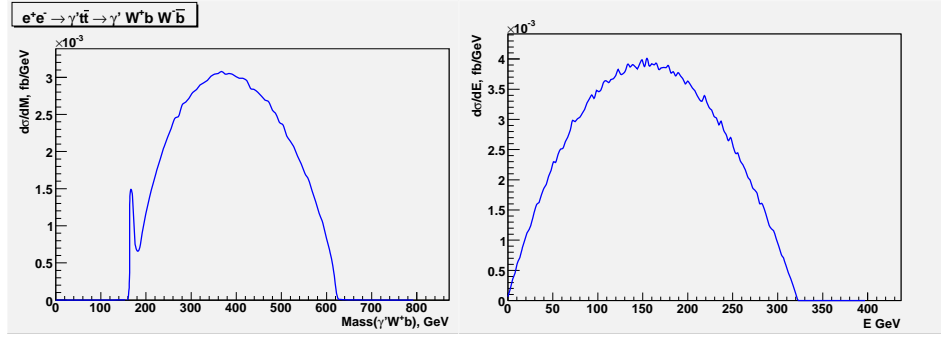
Figure 1: Left: Invariant mass of the $\gamma'Wb$ system. Right: γ' energy distributions at $\sqrt{s} = 1$ TeV.

3 Signal event selection

After event generation using CompHEP, PYTHIA and the CompHEP-PYTHIA interface packages [12] an approximate response of an ILC detector was simulated by means of SIMDET_v4 [13]. Including a simple particle flow algorithm, the output of SIMDET denoted as 'energy flow objects' was subject to our search studies.

Basic properties of the signal process as discussed in the previous section may suggest that a reasonable separation of signal events from large SM background should be possible. The most important background consists of $t\bar{t} + (\gamma)$ events, where the γ from initial state radiation (ISR) is very often not detected. The number of events expected for both energies are given in Table 2. They exceed substantially the number of signal events for interesting $M/\sqrt{c_t}$ values.

The next significant background to consider is the channel $e^+e^- \to t\bar{t} + \nu\bar{\nu}$, with a signature similar to that of the signal due to escaping neutrinos in the final state. The corresponding event numbers also given in Table 2 are comparable to the signal event rates

for not too small $M/\sqrt{c_t}$ values. An invariant mass cut of e.g. $M_{\nu\bar{\nu}} < 80$ GeV, i.e. a cut on the event missing mass, removes most of these events. Additional SM background with a topology of a pair of acoplanar top quark jets and large $\not{E}_T$ is not needed to be addressed.

In a first attempt for signal event selection, a conventional method was applied by using consecutive cuts on kinematical variables based on either the energy flow objects or, utilizing a jet finder, the 4-momenta of jets consistent with the $t\bar{t} \to (Wb)(Wb) \to (q\bar{q})b\,(q\bar{q})b$ decay chain. Jets were reconstructed by means of the routine PUCLUS from PYTHIA which relies on a cluster analysis method using particle momenta. The 'jet-resolution-power' was adjusted to provide 7- and 8-jet event rates in accord with expectations from gluon radiation. The method of consecutive cuts, however, was found to be inefficient to select signal from background because of the failure of distinct properties between signal and background events.

background	$\sqrt{s} = 0.5\ TeV$	$\sqrt{s} = 1\ TeV$
$t\bar{t}(\gamma)$	276675	200310
$t\bar{t}\nu\bar{\nu}$	75	930

Table 2: Background events at $\sqrt{s} = 0.5$ and 1 TeV for an integrated luminosity of 0.5, respectively, 1 ab^{-1}.

Under such circumstances one needs to pursue more sophisticated strategies to extract the signal. Out of several powerful multivariate selection methods we used the following. Kinematical variables as discussed above were combined into a global discriminant variable P_P, designed to give a measure of the 'Paraphoton-likeness' of any particular event. This quantity was constructed from large statistics signal and background event samples, and for each event, signal and background probabilities were then calculated, and by multiplication of all signal probabilities the sensitivity for an event to be a paraphoton candidate was maximized. The quantity so obtained was constraint to lie in the region [0;1]. Background events are preferentially distributed at low P_P values while for signal events P_P is close to unity. The distributions of P_P for both energies considered are shown in Fig. 2. Clear accumulations of γ' candidate events can be recognized near P_P
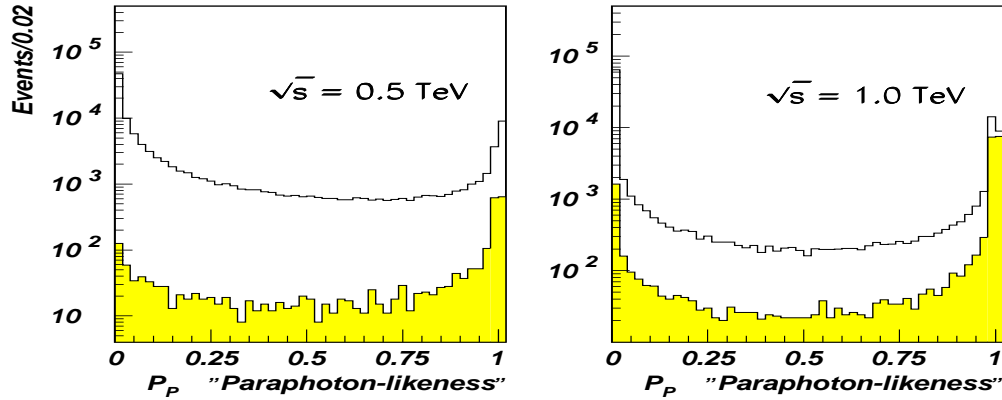
Figure 2: Distributions of the discriminant variable P_P for $t\bar{t}\gamma'$ signal events (shaded) and the sum of signal and background events at $\sqrt{s} = 0.5$ (left) and 1 TeV (right).

$= 1$, with some non-negligible background in particular at 0.5 TeV. A cut of $P_P > 0.98$ was applied to select signal events. This method resulted in a γ' selection efficiency of 49%

(76%) at $\sqrt{s} = 0.5$ (1) TeV, while only 9% of background events survived. In the following, we rely on the results of this method and demand $P_P > 0.98$ as the principal cut in the study.

At $\sqrt{s} = 0.5$ TeV, S/$\sqrt{B} = 11.96$ for $M/\sqrt{c_t} = 0.2$ TeV, while S/$\sqrt{B} = 162.6$ at 1 TeV, i.e. the chance of measuring the signal event rates as a result of a background fluctuation is $0.5 \cdot 10^{-12}$ and $< 10^{-15}$ at 0.5, respectively, 1 TeV, using Gaussian sampling of uncertainties.

Fig. 3 shows the $\not{E}_T$ and $\not{p}_T$ distributions at 0.5 and 1 TeV for the signal events (shaded) and the sum of signal and background events, surviving the cut $P_P > 0.98$. As apparent from Fig. 3, convincing excess of γ' events is evident in both distributions at 1 TeV and the ratio $S/\sqrt{B}$ can be further enhanced by demanding, for example, $\not{E}_T > 330$ GeV or $\not{p}_T > 100$ GeV. In this way, an almost background-free signal event sample can be extracted for further measurements. The situation is much less convenient at 0.5 TeV.
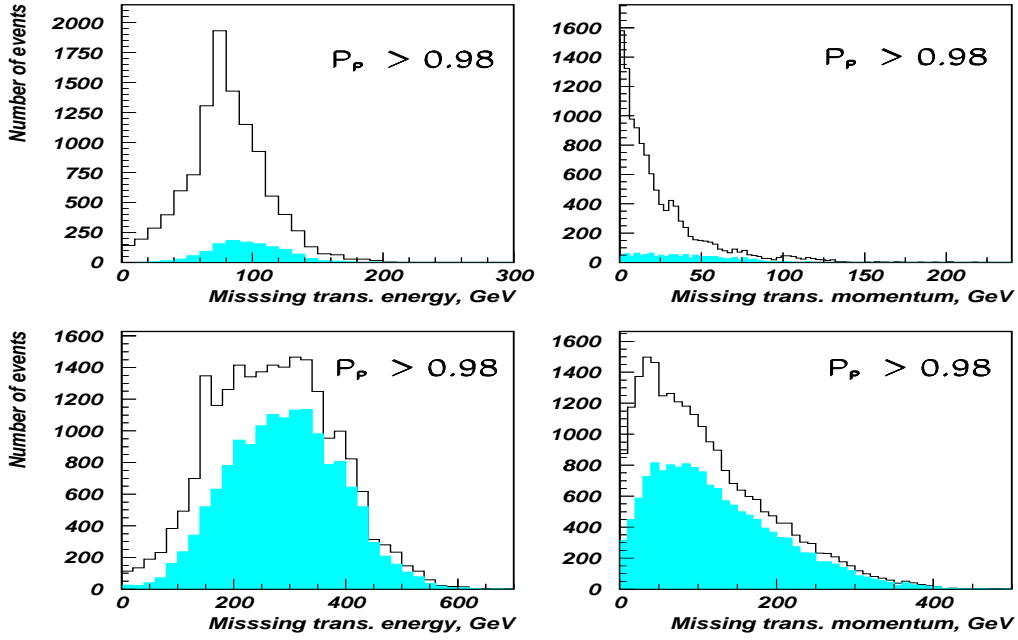
Figure 3: $\not{E}_T$ and $\not{p}_T$ distributions of $t\bar{t}\gamma'$ signal events (shaded) and the sum of signal and background events at $\sqrt{s} = 0.5$ (top) and 1 TeV (bottom).

4   Discussion of the results

If an excess of signal events over the SM background has been established, limits on $M/\sqrt{c_t}$ accessible for a significance[a] of $S/\sqrt{B} = 5$ can be derived. We consider this figure as sufficient for discovery the paraphoton. The number of surviving γ' events for 5σ discovery amounts to 508 (450) at 0.5 (1) TeV for an integrated luminosity of 0.5 (1.0) ab^{-1}. These numbers

---

[a]We quantify the discovery potential of the γ' in the usual way of $significance = signal/\sqrt{background}$, where signal and background imply the number of corresponding events passing all cuts.

can be converted into a limit for the 'coupling' parameter $M/\sqrt{c_t}$ of 0.33 (0.61) TeV, with the 1 TeV value of 0.61 TeV as the most stringent limit accessible at the ILC.

We will also discuss the signal-to-background ratio, S/B, as it will be important for attempting to understand the nature of the excess events. At $\sqrt{s} = 0.5$ TeV, S/B of 0.11 does not favor such studies, while at 1 TeV S/B of 1.79 is sufficiently large so that background contamination should not be a major worry. If we require in addition $\not{E}_T > 330$ GeV, S/B results to $5231/2654 = 1.97$.

In order to demonstrate the spin-1 nature of the γ', we follow studies performed to establish the vector nature of the gluon in 3-jet e^+e^- annihilation events at PETRA [14–17] and LEP [18–20] energies, based on predictions that a spin-$\frac{1}{2}$ quark radiates the spin-1 gluon.

In a first step, we calculated the Ellis-Karliner angle [21] for each accepted event at 1 TeV. Distinction between the vector and scalar particle interpretations is made only on the basis of the shape of the distribution. We found that spin-1 assignment for the paraphoton is highly favored over spin 0.

Alternatively, after interpreting a signal candidate event as a 3-jet event, the polar angle distribution of the normal to the three-jet plane, θ_N, was proposed to distinguish between the vector and scalar hypothesis of the emitted particle [26, 27]. The θ_N distributions for various thrust cut-off values, corrected for background and detector effects, were fitted to the expression predicted for vector particle emission [28]. Good agreement between the data and the theoretical expectation was found.

5   Conclusions

Some realistic extensions of the Standard Model of elementary particle physics suggest the existence of a new massless neutral gauge boson, denoted as the paraphoton γ' in this study. This particle is similar to the ordinary photon, but the couplings of the γ' are very distinct: interactions with Standard Model fermions are negligible except those to the top quark. Hence, if the paraphoton is radiated off the top the signature of γ' events in the channel $e^+e^- \to t\,\bar{t}\,\gamma'$ consists of a pair of acoplanar top quark jets with missing transverse energy, $\not{E}_T$, carried away by the paraphoton. Only the all-hadronic top decay mode was selected to ensure a high signal-to-background ratio and to avoid complications due to final state neutrinos in leptonic W decays.

Based on a multivariate search strategy[b] prospects to discover the γ' at the ILC are studied. Maximizing the probability of each event to be a γ' candidate the method selected 49% (76%) of the signal (S) at 0.5 (1) TeV and strongly suppressed the background (B), resulting to a $S/\sqrt{B}$ larger than 150 at $\sqrt{s} = 1$ TeV. Allowing for a 5σ paraphoton discovery significance, e^+e^- collisions at 1 TeV will bound the γ'-top quark 'coupling' to $M/\sqrt{c_t} \lesssim 0.61$ TeV, which seems to be the most stringent limit accessible at the next generation colliders.

For the sake of demonstration two angular variables, the Ellis-Karliner angle and the polar angle of the normal to the $t\,\bar{t}\,\gamma'$ plane as a function of a thrust cut-off, were studied to establish the vector nature of the γ'. Both angular distributions are in accord with the spin-1 assignment of the paraphoton and inconsistent with e.g. a scalar hypothesis.

---

[b]This method was necessary to pursue because of large $t\bar{t}(\gamma)$ SM background, small signal event rates and little discrimination power of variables.

6 Acknowledgments

References

[1] Slides:
http://ilcagenda.linearcollider.org/contributionDisplay.py?contribId=238&sessionId=72&confId=1296

[2] B. Holdom, Phys. Lett. **B166** 196 (1986) and Phys. Lett. **B178** 65 (1986).

[3] L. B. Okun, Sov. Phys. JETP **56** 502 (1982), [Zh. Eksp. Teor. Fiz. **83** 8921 (1982);
L. B. Okun, M. B. Voloshin and V. I. Zakharov, Phys. Lett. **B138** 115 (1984);
A. Y. Ignatiev, V. A. Kuzmin and M. E. Shaposhnikov, Phys. Lett. **B84** 315 (1979).

[4] B. A. Dobrescu, Phys. Rev. Lett. **94**, 151802 (2005), arXiv:hep-ph/0411004.

[5] The ILC reference report (RDR) is available from *http://www.linearcollider.org/cms/*.

[6] S. Hoffmann, Phys. Lett. **B193**, 117 (1987).

[7] M. Pospelov and A. Ritz, Phys. Rev. **D63**, 073015 (2001), arXiv:hep-ph/0010037.

[8] A. Pukhov et al., Report INP-MSU 98-41/542, arXiv:hep-ph/9908288;
E. Boos et al., Nucl. Instrum. Meth. **A534**, 250 (2004), arXiv:hep-ph/0403113.

[9] T. Sjostrand, L. Lonnblad, S. Mrenna and P. Skands, *PYTHIA 6.3: Physics and manual*, arXiv:hep-ph/0308153.

[10] J. A. Aguilar-Saavedra et al., *TESLA Technical Design Report Part III: Physics at an e^+e^- Linear Collider*, arXiv:hep-ph/0106315.

[11] A. S. Belyaev et al., *CompHEP-PYTHIA interface: Integrated package for the collision event generation based on exact matrix elements*, arXiv:hep-ph/0101232.

[12] E. Boos et al., *Generic user process interface for event generators*, arXiv:hep-ph/0109068.

[13] M. Pohl and H. J. Schreiber, *SIMDET - Version 4: A parametric Monte Carlo for a TESLA Detector*, arXiv:hep-ex/0206009.

[14] R. Brandelik et al., Phys. Lett. **B97** 453 (1980): S. Wu, Phys. Rep. **107** 162 (1984).

[15] H.J. Behrend et al., Phys. Lett. **B110** 329 (1982).

[16] Ch. Berger et al., Phys. Lett. **B97** 459 (1980).

[17] D. Burger et al., *Proceedings of the 21st Internationale Conference on High Energy Physics*, Paris 1982, J. Phys. (Paris) **43**, C3-C6.

[18] G. Alexander et al., Z. Phys. **C52** 543 (1991).

[19] B. Adeva et al., Phys. Lett. **B263** 551 (1991).

[20] P. Abreu et al., Phys. Lett. **B274** 498 (1992).

[21] J. Ellis and I. Karliner, Nucl. Phys. **B148** 141 (1997).

[22] W. Braunschweig et al., Z. Phys. **C36** 349 (1987).

[23] J.del Peso, Ph.D. Thesis, Universad Autonoma de Madrid, FTUAM-EP-89-02, unpublished.

[24] M. Althoff et al., Z. Phys. **C29** 29 (1985).

[25] W. Braunschweig et al., Phys. Lett. **B214** 216 (1988).

[26] G. Kramer, G.Schierholz and J. Willrodt, Phys. Lett. **B79** 249 (1978); Phys. Lett. **B80** 433 (1978) and Z. Phys. **C4** 149 (1980).

[27] K. Koller et al., Z. Phys. **C6** 131 (1980).

[28] J. Koerner, G.A. Schuler and F. Barreiro, Phys. Lett **B188** 272 (1987).

LCFI Vertex Package: Precision Physics Opportunities with Heavy Flavour

Ben Jeffery on behalf of the LCFI Collaboration

University Of Oxford - Department of Physics
Denys Wilkinson Building, Keble Road, Oxford OX1 3RH - UK

The LCFI collaboration has recently released LCFIVertex, a software package for reconstructing heavy quark flavour and charge using vertex detector information at the International Linear Collider. This contribution reviews the content of the package and some of the precision physics opportunities arising from its use. These include Higgs branching ratios and self coupling, anomalous top couplings and top polarisation, and asymmetry measurements.

1 Introduction

One of the key features of the International Linear Collider (ILC) will be the ability to reconstruct events at the parton level with unprecedented accuracy. Part of this accuracy comes from the ability to determine the quark flavour and charge of heavy flavour hadronic jets with excellent purity and efficiency. This results in exciting prospects in many interesting processes, such as: high precision unfolded asymmetry measurements giving access to physics beyond the centre of mass energy; Higgs branching ratios and self coupling; anomalous top couplings; top polarisation; and background rejection in other channels. The key questions under current research include what the best methods for this reconstruction are, what accuracy is acheviable with a given detector and what sensitivity this brings to key benchmark channels. LCFI are conducting a program of tool development and benchmark studies to answer these questions in a realistic full MC and reconstruction framework.

The key to flavour and charge identification of heavy quarks is information from the vertex detector. This is in the form of precise impact parameter measurements. An expected track point resolution of $\sim 3\mu$m gives an impact parameter of[2]:

$$\sigma_{rz} \approx \sigma_{r\phi} \approx 4.2\mu\text{m} \oplus \frac{4\mu\text{m}}{p\sin^{\frac{3}{2}}\theta}$$

(Where θ is the polar angle of the track) These precise impact parameters are used to locate particles produced a distance from the interaction point by the decay of short lived B or D hadrons. By intersection with other tracks the decay vertices and decay products are identified and the properties of the decaying hadron inferred.

To enable initial benchmark studies LCFI have implemented a reconstruction package in the C++ based MARLIN framework. The package is based on algorithms used in previous ILC studies (but not available in a flexible modern framework) thereby allowing effective comparison and providing a solid benchmark. The package consists of three distinct parts: vertexing, flavour and charge tagging, and utilities such as cuts and MC information.

2 Tracks To Flavour

The vertexing within the LCFI vertex package is performed by ZVTOP[3]. a vertexing algorithm initially developed by D. Jackson for use on the SLD experiment. ZVTOP consists

of two complementary branches, ZVRES and ZVKIN

ZVRES employs a heuristic vertex function (based on track probability density) in the detector space to identify likely points of true vertices. Tracks are assigned by proximity to maxima in the vertex function and ambiguities resolved by χ^2 considerations and the magnitude of the vertex function. ZVRES serves as a good benchmark algorithm due to its performance and previous use both in SLD and ILC studies. During development detailed comparisons were conducted against the previous FORTRAN based SGV version.[4]

ZVKIN uses a kinematic approach to reconstruct the unseen decaying hadron. The sum of χ^2s of vertices of all possible pairs of input tracks and a line projecting outwards from the interaction point is minimised in the line's angular degrees of freedom. The vertices are then combined by considering the fit probability of the combined vertices until no combinations are probable. Note that this enables vertices with only one detected track to be reconstructed. This is particularly useful for neutral vertex charge as disscussed later. Although used at SLD, this branch has not been studied for use at the ILC and the implementation has had minimal testing. It is therefore the default and recommended behaviour that only the ZVRES branch is used in non-experimental studies. Once any secondary vertices in a given jet have been reconstructed, flavour tagging can be performed using the vertex information. The algorithm implemented follows that of R. Hawkins[5]. The method defines a set of discriminating variables calculated from the jet and from secondary vertices (if any are found). For classification of jet flavour from the set of discriminating variables, a simple linear perceptron neural net is used. The LCFI package uses a neural net toolkit developed by D. Bailey to perform this classification.

3 Vertex Charge

Vertex charge is performed by a method developed at SLD and improved in an ILC study by S. Hillert[6]. The charges of all secondary tracks found by vertexing and tracks passing a cut (based on distance from the jet axis) are summed to give a measure of charge of the decaying hadron. The charge of the initial parton can thus be inferred in most cases (see Figure 1). Neutral vertices require a further technique developed at SLD[7]. The charge
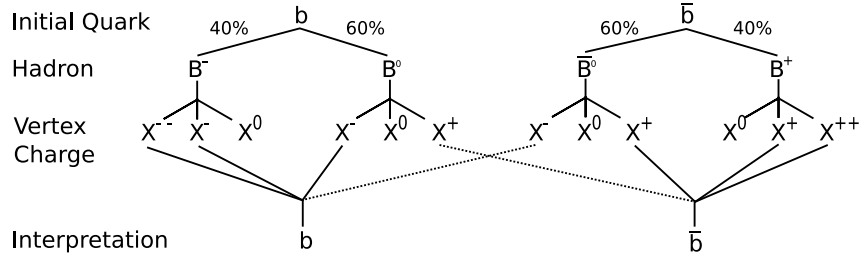
Figure 1: How quark charge is inferred from vertex charge - the dashed line are the only cases where assignment is incorrect.

dipole of a jet is the distance between B and D vertices multiplied by their charge difference: $\delta Q = L_{B \to D} \times SIGN (Q_D - Q_B)$ This gives good separation of b and $\bar{b}$ for neutral vertices: as shown in Figure 2, the mistag probability is $\sim 20\%$. A study into the usage of this technique at the ILC is planned, it requires the ZVKIN branch of ZVTOP as both B and D

vertices need to be identified - many of which have only one seen track and would therefore be missed by ZVRES.
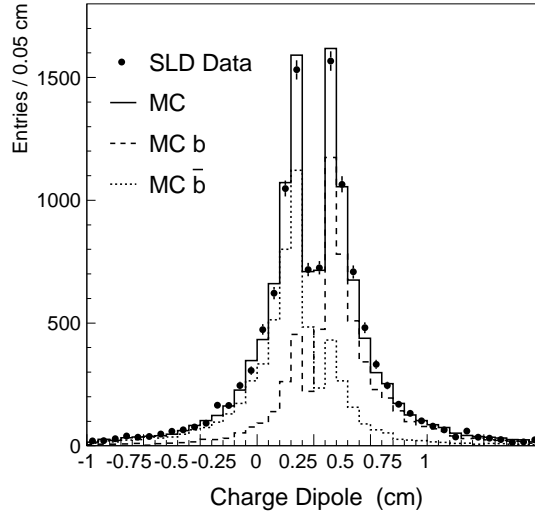
Figure 2: Charge dipole distribution and separation at SLD[7]

4   LCFIVertex Package

The software package LCFIVertex contains the above algorithms implemented in C++ and interfaced to the European software framework MARLIN. Input is in LCIO[8] format, by default from the MARLINReco[9] package. An interface to the US Java based org.lcsim [10] framework is also planned. During development, extensive testing and comparison with the previous SGV-based FORTRAN code was performed using identical input events[4]. Comparisons with previous full reconstruction studies[11] are favorable[12], as shown in Figure 3, However, there are technical differences between the two studies such as tracks produced by the decays of K_S or Λ particles are suppressed at the MC truth level in the LCFIVertex result. See [12] for details. The package is available for download at the ILC Software portal[13].

5   Applications

LCFI are currently starting to use the newly released package to study several processes where accurate flavour tagging is crucial to separate out decays to different quark flavours. Measurement of the hadronic branching ratios of the Higgs boson has been previously studied for the ILC, using a fast parametric simulation (SIMDET)[14]. In this case the use of realistic track-wise flavour tagging (as opposed to a parameterisation of well separated jets) resulted in a 50% increase in production rate error for $H \to c\bar{c}$ and $H \to gg$, highlighting the need for realistic flavour tagging. A full study considering the impact of detector options and material budget is planned.
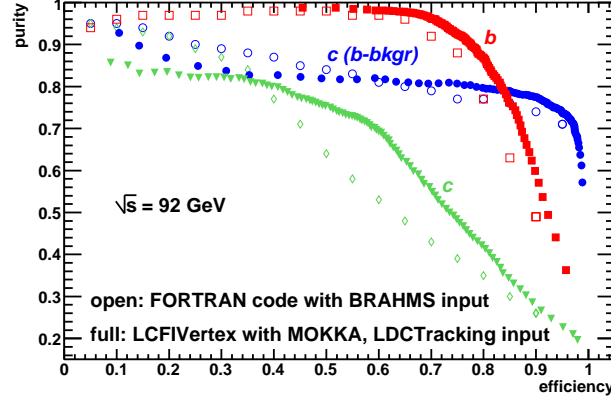
Figure 3: Purity vs. Efficiency for the newly released LCFIVertex code and a previous FORTRAN based study[11] The discrepancy is likely due to technical differences discussed in [12]

The reconstruction of vertex charge enables the measurement of top polarisation[15]. For the other heavy quarks, depolarisation effects during fragmentation wash out the quark helicities. However for the top, its short lifetime preserves its spin. In $t \to bW^+, W^+ \to c\bar{s}$ if the b and c jet are correctly tagged the $\bar{s}$ can be inferred by knowing the vertex charge of either the b or c jet. The $\bar{s}$ jet then has a $1 - \cos\theta$ angular dependence on the polarisation of the top (θ being the polar angle of the jet). Measurement of top polarization in scalar top and scalar bottom decays can be used to determine the fundamental SUSY parameters $\tan\beta$ and the trilinear couplings A_t, A_b[16].

Another interesting top measurement is that of the coupling W_{tb} which is sensitive to anomalous magnetic couplings[17]. Measurement of the coupling can be performed by the forward-backward asymmetry of b quarks in the process $e^+e^- \to t\bar{t} \to W^+bW^-\bar{b}$ If one wishes to use spin-spin correlations to boost the sensitivity, then a double b tag increases the need for high tagging efficiency. Currently, the t and W identification methods are being optimised in preparation for a full study.

An obvious application of accurate flavour and charge determination is the measurement of asymmetries in simple two-jet production. The measurement of A_{LR} in $e^+e^- \to q\bar{q}$ is sensitive to many phenomena beyond the standard model, including leptoquarks, Z' and extra spacial dimensions[18]. The possibility of polarised beams at the ILC, combined with high statistics and efficient flavour and charge tagging, allow a very precise measurement which is sensitive to effects far beyond the centre of mass energy. The analysis is expected to be sensitive to the material budget of the vertex detector, as the region of interest is at small θ (see Figure 4). It is therefore be a good benchmark for detector optimisation.

6 Summary

Flavour and charge tagging are essential to many of the benchmarking processes needed to optimise ILC detector design. LCFI are conducting studies of several physics channels
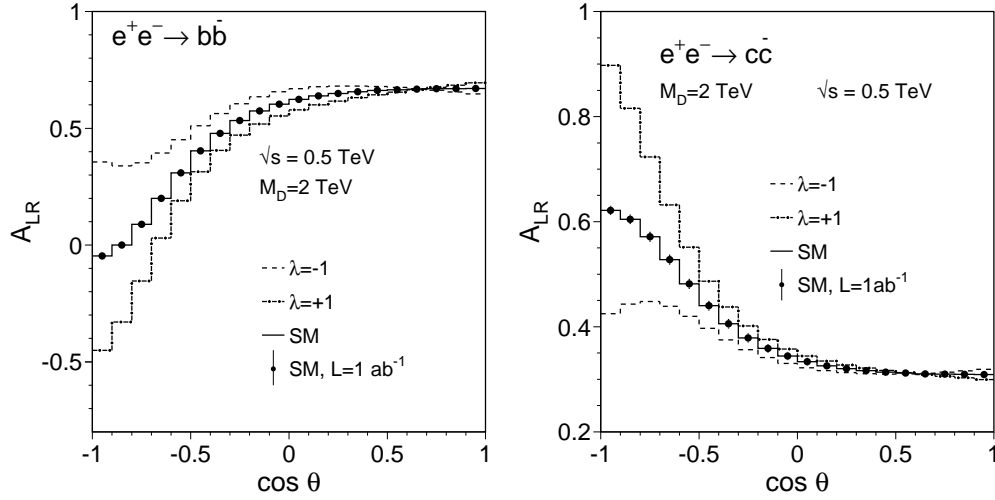
Figure 4: Expected signature in A_{LR} from extra spacial dimensions for both b and c pair production. Note that the sensitive region is at small θ (λ is a model parameter)[18]

using the newly developed LCFIVertex package. The package provides vertexing by two complementary algorithms, a flavour tag and a charge tag, all within a flexible framework. It is actively maintained and supported, and has a growing user base. Several comprehensive studies are already in progress.

References

[1] Slides:
   http://ilcagenda.linearcollider.org/contributionDisplay.py?contribId=242&sessionId=72&confId=1296

[2] C. J. S. Damerell, LC-DET-2001-023;

[3] D. J. Jackson, Nucl. Instrum. Meth. A **388** (1997) 247;

[4] B. Jeffery, *Contribution to International Linear Collider Workshop (ILC-ECFA and GDE Joint Meeting), Valencia, 6-10 November 2006*, slides:
   http://ilcagenda.linearcollider.org/contributionDisplay.py?contribId=72&sessionId=7&confId=1049

[5] S. M. Xella Hansen, C. Damerell, D. J. Jackson and R. Hawkings,
   Prepared for 5th International Linear Collider Workshop (LCWS 2000), Fermilab, Batavia, Illinois, 24-28 Oct 2000, LC-PHSM-2001-024;

[6] S. Hillert [LCFI Collaboration], *In the Proceedings of 2005 International Linear Collider Workshop (LCWS 2005), Stanford, California, 18-22 Mar 2005, pp 0313*, ECONF,C050318,0313;

[7] K. Abe *et al.* [SLD Collaboration], Phys. Rev. D **67** (2003) 012006 [arXiv:hep-ex/0209002].

[8] F. Gaede, T. Behnke, N. Graf and T. Johnson, *In the Proceedings of 2003 Conference for Computing in High-Energy and Nuclear Physics (CHEP 03), La Jolla, California, 24-28 Mar 2003, pp TUKT001* [arXiv:physics/0306114];

[9] O. Wendt, F. Gaede and T. Kramer, LC-DET-2007-001;

[10] org.lcsim web page at http://www.lcsim.org/software/lcsim/;

[11] S. M. Xella Hansen, M. Wing, D. J. Jackson, N. De Groot and C. J. S. Damerell, "Update on flavour tagging studies for the future linear collider using the BRAHMS simulation", LC-PHSM-2003-061.

[12] S. Hillert [LCFI Collaboration], *In the Proceedings of 2007 International Linear Collider Workshop (LCWS 2007, DESY, Hamburg, Germany 30 May-03 June 2007)*, [arXiv:0708.2622v1];

[13] ILC software portal at `http://ilcsoft.desy.de/portal`;

[14] T. Kuhl, K. Desch, LC-PHSM-2007-002;

[15] E. Ruiz Morales and M. E. Peskin, [arXiv:hep-ph/9909383];

[16] E. Boos, H. U. Martyn, G. A. Moortgat-Pick, M. Sachwitz, A. Sherstnev and P. M. Zerwas, Eur. Phys. J. C **30** (2003) 395 [arXiv:hep-ph/0303110];

[17] E. Boos, M. Dubinin, M. Sachwitz and H. J. Schreiber, Eur. Phys. J. C **16** (2000) 269 [arXiv:hep-ph/0001048];

[18] S. Riemann, LC-TH-2001-007;

The ILC Energy Requirements from the Constraints on New Boson Production at the Tevatron

Mihail Chizhov[1,2] *

1- Sofia University, Physics Department
BG-1164 Sofia, Bulgaria

2- H1 Collaboration at DESY
Notkestr. 85, D-22607 Hamburg, Germany

Direct constraints on the masses of new heavy bosons by the Tevatron data are discussed. Some excesses in the experimental data are interpreted as a resonance production of new charged and 'leptophobic' neutral chiral bosons with masses 500 GeV and 700 GeV, respectively. The interpretation was provided on the basis of the theoretical model, proposed by the author about 15 years ago. New Tevatron data and the LHC results will definitely confirm or reject this interpretation. The ILC with an energy above 1 TeV would be an ideal place to produce and to study the properties of these particles.

1 Introduction

The hadron colliders, due to the biggest center-of-mass energy and their relatively compact sizes, still remain a main tool for discoveries of very heavy particles. Thus, in 1983 the two dedicated experiments UA1 [1] and UA2 [2] discovered the intermediate vector bosons at the CERN SPS Collider. One faces, however, a very large background from the strong interactions.

In any case, besides the simple manifestation of the existence of the weak bosons, one needs a precise study of their properties following from the Standard Model (SM). This task has been excellently fulfilled by the Large Electron-Positron (LEP) storage ring at CERN and the Stanford Linear Collider (SLC) at SLAC. However, the masses of the t quark and the undiscovered yet Higgs boson happened to be too high to be discovered at these colliders.

I remember the words by Samuel Ting at one of the LEP meetings in defence of continuation of the LEP running: "Each collision at the lepton colliders is an event, while it is a background at the hadron colliders". So, the precision of the electroweak measurements at the lepton colliders was so high, that the predicted from the radiative loop corrections mass of the top-quark $m_t = 180 \, ^{+8}_{-9} \, ^{+17}_{-20}$ GeV [3] has been found in agreement and with a comparable accuracy of its first direct measurements at the Fermilab Tevatron by the CDF [4] $m_t = 176 \pm 8 \pm 10$ GeV and the D0 [5] $m_t = 199 \, ^{+19}_{-21} \pm 22$ GeV collaborations.

Nevertheless, in spite of the overwhelming background for the top-quark pair production by the strong interactions at the hadron collider, the uncertainty of the top-quark mass $m_t = 170.9 \pm 1.1 \pm 1.5$ GeV [6] is considerably reduced at present. Moreover, recently, the evidence for a single top-quark production [7] through the weak interactions and the direct measurement of $|V_{tb}|$ at the Fermilab Tevatron hadron collider became possible. Another achievement in precise measurements at the hadron collider is the W-mass measurement $m_W = 80.413 \pm 0.048$ GeV [8] by the CDF collaboration at a comparable with the LEP

experiments accuracy, which represents the single most precise measurement to date. All these measurements will allow to constrain further the mass of the Higgs particle, which discovery is a priority task of the running Tevatron and the Large Hadron Collider (LHC).

The discovery of the theoretically predicted heavy particles and the establishment of the SM without any surprises are characteristic for the experimental high energy physics during the last thirty years. Therefore, the LHC construction is connected not only with the Higgs discovery, but with the hope to find the physics beyond the SM. Up to now it is not clear what kind of physics it will be. Therefore, any inputs like constraints on the new physics from low-energy precise experiments or from the presently most powerful Tevatron collider at FNAL are badly needed when discussing the properties of future colliders, in particular, the International Linear Collider (ILC).

This talk is dedicated to the energy requirements for the future lepton colliders, which follow from the constraints on the new boson production at the Tevatron. In order to investigate the properties of the new bosons and eventually to distinguish among different models of the new physics, the energy of the future ICL should be enough to produce them. Although it is still possible to investigate some properties of the new bosons at low-energy, we will consider the case of their resonance or threshold production, as an optimal possibility.

In the second part of the talk we will consider one of the possible scenarios of new physics in the boson sector, for which some confirmation from the Tevatron data already exists. A quantitative model of such a new physics will be very valuable in interpreting the data from the hadron colliders, Tevatron and LHC, that presents concrete requirements for the ILC energy design.

2 Tevatron constraints

Let us start with the case of new neutral massive bosons, Z', which can be produced at the lepton colliders as resonances. Such a type of bosons is very difficult to detect in the low-energy experiments due to the huge background from the electromagnetic interactions. Some guiding principle is necessary to distinguish them from the known interactions. For example, the neutral weak currents were detected in the deep-inelastic electron scattering through the measurements of P-odd quantities. Therefore, we expect that direct constraints from the high-energy hadron colliders should be more restrictive.

Moreover, up to now, the Drell-Yan process with high-energy invariant mass of the lepton pairs remains the most clear indication of the heavy boson production at the hadron colliders. Therefore, the constraints from these investigations can be directly applied to the resonance boson production at the lepton colliders. So, using only a modest integrated luminosity of 200 pb^{-1} collected during RUN II, the D0 Collaboration puts tight restrictions on the Z' masses for the different models from the di-electron events [9]: $M_{Z'_{SM}} < 780$ GeV, $M_{Z'_{\eta}} < 680$ GeV, $M_{Z'_{\psi}} < 650$ GeV, $M_{Z'_{\chi}} < 640$ GeV and $M_{Z'_{I}} < 575$ GeV. A comparable statistics in the di-muon channel leads approximately to the same constraint $M_{Z'_{SM}} < 680$ GeV [10]. The CDF constraints from the di-electron channel are based on more data, 1.3 fb^{-1}, which lead to tighter restrictions [11]: $M_{Z'_{SM}} < 923$ GeV, $M_{Z'_{\eta}} < 891$ GeV, $M_{Z'_{\psi}} < 822$ GeV, $M_{Z'_{\chi}} < 822$ GeV and $M_{Z'_{I}} < 729$ GeV.

Another possible channel, which can indicate the production of the neutral heavy bosons, is their hadronic decay into $t\bar{t}$ pairs. While the light quark decay channels are swamped by multijet background, the $t\bar{t}$ pairs can be detected, for example, through their decays

into two energetic b-jets and two W's, where one W boson decays hadronically and one leptonically. Although the constraints from this channel cannot be applied directly to the energy requirements for the lepton collider due to the possible leptophobic character of the bosons, it is interesting to detect the eventual peaks in the Tevatron data. So the latest results both of the D0 [12] and of the CDF [13] Collaborations show some excess in the invariant mass distributions around 700 GeV (Fig. 1). A possible explanation of this excess will be discussed in the next section.
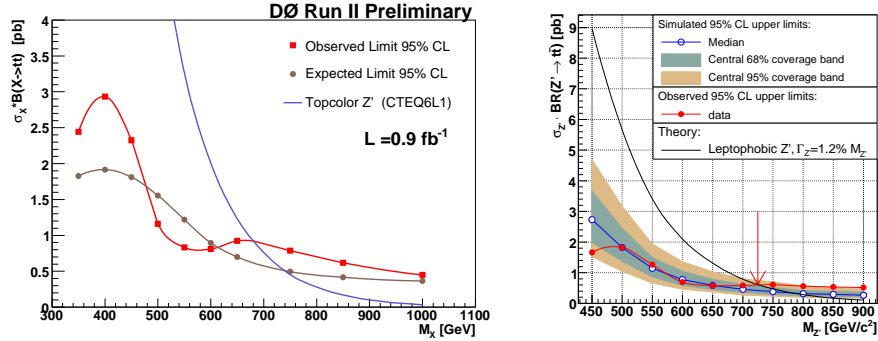
Figure 1: Expected and observed 95% C.L. upper limits on $\sigma_X \times \mathcal{B}(X \to t\bar{t})$ in comparison with the predicted leptophobic topcolor Z' cross section (left panel from [12] – D0 data, right panel from [13] – CDF data of 680 pb^{-1}).

Let us consider the case of the new heavy charged bosons, generically noted by W'. They could be produced at the lepton colliders only in pairs or in association with other charged boson, like W. Therefore, restrictions on their masses lead to the following energy requirements for their threshold production $E > M_{W'} + M_W$ at the lepton colliders. Here again we will consider leptonic and hadronic channels of their decays.

The leptonic decay of the new heavy charged boson into high-energy pair of a lepton and a corresponding antineutrino is the most clear signature of its production at the hadron colliders. So, already from 205 pb^{-1} of RUN II data, the CDF Collaboration obtained a tight constraint on possible W' mass $M_{W'} > 788$ GeV [14]. The most rigid constraint comes from the D0 Collaboration [15] $M_{W'} > 965$ GeV, based on bigger statistics, 900 pb^{-1}, and better calorimetry than the CDF detector.

The hadronic decay of the new heavy charged boson into a $t\bar{b}$ pair of a heavy b quark and a short living t quark with its subsequent decay to Wb pair allows to make jet b-tagging, where one of the jets must have a displaced secondary vertex. A search for the intermediate heavy bosons in this channel has been fulfilled by both the D0 and CDF collaborations, and for this purpose the part of the same data sets of the single top production analysis has been used. Owing to boson high masses this analysis is even simpler than the single top production searches, because at such energies the background is considerably reduced.

So the D0 Collaboration, based on 230 pb^{-1} of integrated luminosity, puts the following constraints on the W' mass depending on the model: $M_{W'_{SM}} > 610$ GeV, $M_{W'_R(\to \ell \text{ and } q)} > 630$ GeV, and $M_{W'_R(\to q \text{ only})} > 670$ GeV [16]. The CDF constraints are tighter (Fig. 2): $M_{W'} > 760$ GeV for $M_{W'} > M_{\nu_R}$ and $M_{W'} > 790$ GeV for $M_{W'} < M_{\nu_R}$, since they are

based on 955 pb^{-1} [17].

Taking into account the most stringent constraints from the Tevatron data, we can conclude, that in order to produce the heavy charged boson in association with the W boson or the heavy neutral boson a lepton collider with energy above 1 TeV is necessary. Also it is interesting to note the presence of some excesses in the observed data in Figs. 1 and 2, which we will discuss in the next section.
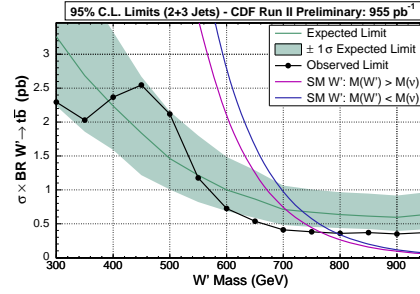
Figure 2: Observed limits from [17].

3　New spin-1 chiral bosons

Additional chiral bosons, which have anomalous interactions with fermions, were proposed in [18]. An exchange through these bosons leads to effective tensor interactions with the coupling constant by two orders of magnitude smaller than G_F. This follows from the precise low-energy experiments of the radiative pion decay [19]. Assuming the universality of these interactions we can explain the long standing discrepancy between the two pion production in the e^+e^- annihilation and the τ decay [20], which now reaches $4.5\,\sigma$ [21].

The universality of the interactions of the new bosons and the hypothesis about a dynamical generation of their kinetic terms allow to predict their masses [22]. Due to the mixing between two charged chiral bosons the lightest state corresponds to $U^\pm$-boson with a mass $M_L \approx 509$ GeV and the heaviest one is $T^\pm$-boson with a mass $M_H \approx 1137$ GeV. The neutral physical states come as CP-even U^R and CP-odd U^I bosons with approximately the same masses $M_U \approx 719$ GeV, which couple only to the up fermions, and analogous but heavier bosons T^R and T^I with a common mass $M_T \approx 1017$ GeV, coupling to the down fermions.

Due to the anomalous interactions the angular distribution of the chiral boson decays differs drastically from the analogous distribution of the gauge bosons. This leads to a specific transverse momentum distribution [23], which has a broad smooth bump with a maximum below the kinematical endpoint $p_T = M/2$, instead of a sharp Jacobian peak (Fig. 3). The form of the decay distribution for the chiral bosons resembles the bump anomalies in the inclusive jet E_T distribution (Fig. 4), reported by the CDF Collaboration [24] many years ago.

Analysing the bumps in the jet transverse energy distribution in Fig. 4, we can find the endpoint of the first bump at 250 GeV and guess about the second bump endpoint from the minimum around 350 GeV. If we assign
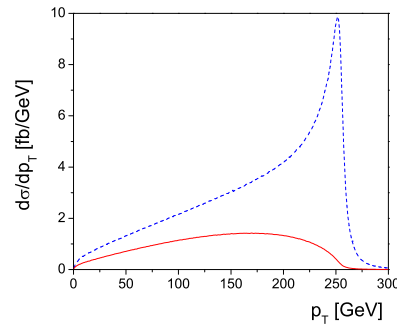
Figure 3: The distributions for the gauge W' (dashed) and for the chiral $U^\pm$ (solid) bosons as functions of the lepton transfers momentum.

the first bump to the hadron decay products of the lightest charged bosons, which exactly corresponds to the estimated mass, the second endpoint hints to a mass around 700 GeV, which is also in a quantitative agreement with our estimations for the mass of the lightest neutral boson. However, taking into account the large systematic uncertainties in jet production, these conclusions may be premature, unless they are confirmed in other channels.

Indeed, an excess about 2σ in the lepton channel has been pointed out recently by the CDF Collaboraion [14] in the region 350 GeV $< M_T \simeq 2p_T <$ 500 GeV. At the same time the same collaboration, however, denies the peak in the quark channel in the same region (Fig. 2), claiming that "since the predictions in *the neighboring bins* agree with the observation, and since *the three jet bin* does not show a similar excess, we anticipate that the excess in this region is a statistical fluctuation". But this signature means just a resonance and this excess is in some sense a confirmation of the excess in the leptonic channel!

Therefore, the independent result from the D0 collaboration is very important. Their published result [16] is based on 230 pb^{-1} of integrated luminosity and does not

Figure 4: The Fig. 1 from [24]

show any excess in the histogram with the bin's width of 50 GeV. However, it should always be taken into account that the narrow peak could be missed due to the smearing effect of the detector resolution or an insufficient statistics. Indeed, the right histogram in the Fig. 3 of the conference paper [25] of the same collaboration with the bin's width of the 45 GeV reveals, nevertheless, the weak peak in the same region of the 500 GeV. All these not statistically significant results for the separated analyses may give a more conclusive answer after their combination and an additional investigation of the angular distributions of the events in this region.

The small excess in the $t\bar{t}$ channel around 700 GeV (Fig. 1) can be explained in the framework of our model by the production and the decay of the lightest neutral chiral boson. The latter shows 'leptophobic' property, since it decays to 'invisible' $\nu\bar{\nu}$ leptonic channel, and can be detected only through its decay into a pair of up quarks. The D0 Collaboration even superimposed its plot of the $t\bar{t}$ invariant mass distribution with the expected signal for a topcolor-assisted technicolor Z' with $M_{Z'} =$ 750 GeV, which perfectly agrees with the data.

4   Conclusions

There are some hints for the existence of a lightest charged chiral boson with a mass around 500 GeV and a lightest neutral 'leptophobic' chiral boson with a mass around 700 GeV in the Tevatron data. In the positive case the LHC would be able to discover all predicted charged and neutral chiral bosons spanning in mass up to around 1 TeV (see their leptonic decay distributions in the Fig. 5). The ILC with such energy would be an ideal place to
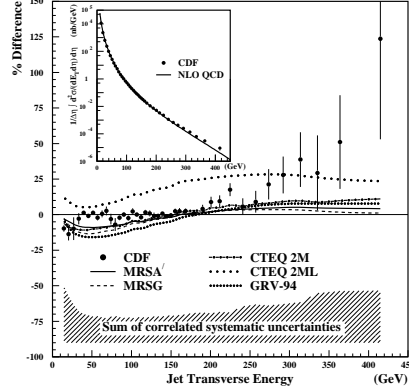
produce and to study these particles.
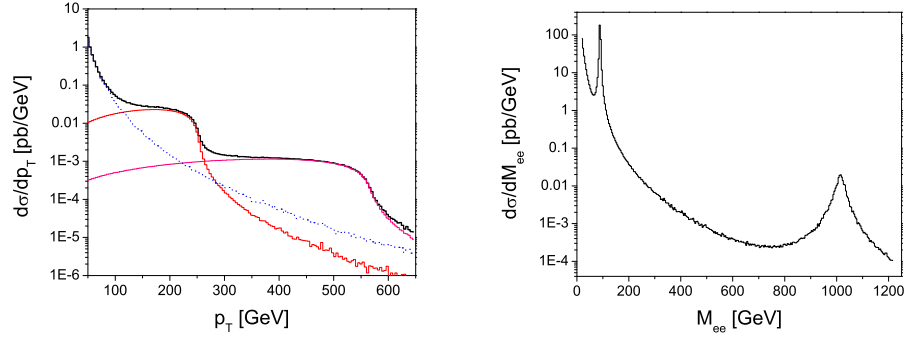
Figure 5: The distributions in the lepton channels at the LHC, namely $pp \to e \not{E}_T$ (left) and $pp \to e^+ e^-$ (right).

References

[1] G. Arnison *et al.* (UA1 Collaboration), Phys. Lett. **B122** 103 (1983); Phys. Lett. **B126** 398 (1983).

[2] M. Banner *et al.* (UA2 Collaboration), Phys. Lett. **B122** 476 (1983); P. Bagnaia *et al.* (UA2 Collaboration), Phys. Lett. **B129** 130 (1983).

[3] P. Antilogus *et al.* (LEP Collaborations and LEP Electroweak Working Group), CERN-PPE/95-172 (1995).

[4] F. Abe *et al.* (CDF Collaboration), Phys. Rev. Lett. **74** 2626 (1995).

[5] S. Abachi *et al.* (D0 Collaboration), Phys. Rev. Lett. **74** 2632 (1995).

[6] Tevatron Electroweak Working Group, arXiv:hep-ex/0703034 (2007).

[7] V.M. Abazov *et al.* (D0 Collaboration), Phys. Rev. Lett. **98** 181802 (2007).

[8] T. Aaltonen *et al.* (CDF Collaboration), arXiv:0708.3642 [hep-ex] (2007).

[9] D0 Collaboration, D0 note 4375-CONF (2004).

[10] D0 Collaboration, D0 note 4375-CONF (2004).

[11] T. Aaltonen *et al.* (CDF Collaboration), arXiv:0707.2524[hep-ex] (2007).

[12] D0 Collaboration, D0 note 5443-CONF (2007).

[13] T. Aaltonen *et al.* (CDF Collaboration), arXiv:0709.0705[hep-ex] (2007).

[14] A. Abulencia *et al.* (CDF Collaboration), Phys. Rev. **D75** 091101 (2007).

[15] D0 Collaboration, D0 note 5191-CONF (2006).

[16] V. M. Abazov *et al.* (D0 Collaboration), Phys. Lett. **B641** 423 (2006).

[17] CDF Collaboration, CDF Note 8747 (2007).

[18] M. V. Chizhov, Mod. Phys. Lett. **A8** 2753 (1993) [arXiv:hep-ph/0401217 (2004)].

[19] V.N. Bolotov *et al.*, Phys. Lett. **B243** 308 (1990); E. Frlež *et al.*. Phys. Rev. Lett. **93** 181804 (2004).

[20] M.V. Chizhov, arXiv:hep-ph/0311360 (2003).

[21] M. Davier, Nucl. Phys. Proc. Suppl. **169**, 288 (2007).

[22] M.V. Chizhov, arXiv:hep-ph/0609141 (2006).

[23] M.V. Chizhov, arXiv:0705.3944 (2007).

[24] F. Abe *et al.*, Phys. Rev. Lett. **77** 438 (1996).

[25] D0 Collaboration, D0 Note 5024-CONF (2006).

No Higgs at the LHC ?! A case for the ILC.

J. J. van der Bij [*]

Albert-Ludwigs Universität Freiburg - Institut für Physik
H. Herderstr. 3, 79104 Freiburg i.B. - Deutschland

I discuss the question whether it is possible that the LHC will find no signal for the Higgs particle. It is argued that in this case singlet scalars should be present that could play an important role in astroparticle physics. A critical view at the existing electroweak data shows that this possibility might be favored over the simplest standard model. In this case one needs the ILC in order to study the Higgs sector.

1   Introduction

The standard model gives a good description of the bulk of the electroweak data. Only a sign of the Higgs particle is missing at the moment. The Higgs field is necessary in order to make the theory renormalizable, so that predictions are possible and one can really speak of a theory. A complete absence of the Higgs field would make the theory non-renormalizable, implying the existence of new strong interactions at the TeV scale. Therefore one is naively led to the so-called no-lose theorem [2]. This theorem says that when one builds a large energy hadron collider, formerly the SSC now the LHC, one will find new phyics, either the Higgs particle or otherwise new strong interactions. Since historically no-theorems have a bad record in physics one is naturally tempted to try to evade this theorem. So in the following I will try to find ways by which the LHC can avoid seeing any sign of new physics.

At the time of the introduction of the no-lose theorem very little was known about the Higgs particle. Since then there have been experiments at LEP, SLAC and the Tevatron, that give information on the Higgs mass. Through precise measurements of the W-boson mass and various asymmetries one can get constraints on the Higgs mass. The Higgs mass enters into the prediction of these quantities via radiative corrections containing a virtual Higgs exchange. Moreover at LEP-200 the direct search gives a lower limit of $114.4\,\text{GeV}$. The situation regarding the precision tests is not fully satisfactory. The reason is that the Higgs mass implied by the forward-backward asymmetry $A_{FB}(b)$ from the bottom quarks is far away from the mass implied by the other measurements, that agree very well with each other. No model of new physics appears to be able to explain the difference. From $A_{FB}(b)$ one finds $m_H = 488^{+426}_{-219}\,\text{GeV}$ with a 95% lower bound of $m_H = 181\,\text{GeV}$. Combining the other experiments one finds $m_H = 51^{+37}_{-22}\,\text{GeV}$ with a 95% upper bound of $m_H = 109\,\text{GeV}$. The χ^2 of the latter fit is essentially zero. Combining all measurements gives a bad fit. One therefore has a dilemma. Keeping all data one has a bad fit. Ignoring the b-data the standard model is ruled out. In the last case one is largely forced towards the extended models that appear in the following. Accepting a bad fit one has somewhat more leeway, but the extended models are still a distinct possibility.

2   Is a very heavy Higgs boson possible?

One way to avoid seeing the Higgs boson would be if it is too heavy to be produced at the LHC. At first sight this possibility appears to be absurd given the precision data. Even if one

---

takes all data into account there is an upper limit of $m_H = 190\,\text{GeV}$. However the question is surprisingly difficult to answer in detail. The reason is that the Higgs mass is not a free parameter in the Lagrangian. Because of the spontaneous symmetry breaking the Higgs mass is determined by its self-coupling λ and the vacuum expectation value f: $m_H^2 = \lambda f^2$. This means that a heavy Higgs boson is strongly interacting. Therefore higher-loop effects can become important. These effects give corrections to the precision measurements with a behaviour $m_H^{2.(loop-1)}$. These effects can in principle cancel the one-loop $log(m_H)$ corrections, on which the limits are based. Therefore one could have the following situation: the strong interactions compensate for the loop effects, so that from the precision measurements the Higgs appears to have a mass of $50\,\text{GeV}$. At the same time the Higgs is so heavy that one does not see it at the LHC. For this to happen the Higgs mass would have to be about $3\,\text{TeV}$. Detailed two-loop [3, 4, 5, 6, 7] and non-perturbative $1/N$ calculations [8, 9] have shown that the first important effects are expected at the three-loop level. The important quantity is the sign of the three-loop correction compared to the one-loop correction. This question was settled in a large calculation that involved of the order of half a million Feynman diagrams [10, 11]. The conclusion is that the strong interactions enhance the effects of a heavy Higgs boson. This conclusion is confirmed by somewhat qualitative non-perturbative estimates [12, 13]. Therefore the Higgs boson cannot be too heavy to be seen at the LHC.

3 Singlet scalars

3.1 Introduction

If the Higgs boson is not too heavy to be seen the next try to make it invisible at the LHC is to let it decay into particles that cannot be detected. For this a slight extension of the standard model is needed. In order not to effect the otherwise good description of the electroweak data by the standard model one introduces singlet scalars. The presence of singlets will not affect present electroweak phenomenology in a significant way, since their effects in precision tests appear first at the two-loop level and are too small to be seen [14]. These singlet scalars will not couple to ordinary matter in a direct way, but only to the Higgs sector. It is acually quite natural to expect singlet scalars to be present in nature. After all we know there also exist singlet fermions, namely the right handed neutrino's. The introduction of singlet scalars affects the phenomenology of the Higgs boson in two ways. On the one hand one creates the possibility for the Higgs boson to decay into said singlets, on the other hand there is the possibility of singlet-doublet mixing, which will lead to the presence of more Higgs bosons however with reduced couplings to ordinary matter. In the precision tests this only leads to the replacement of the single Higgs mass by a weighted Higgs mass and one cannot tell the difference between the two cases. Mixing and invisible decay can appear simultaneously. For didactical purpose I show in the following simple models consisting of pure invisible decay or pure mixing. For a mini-review of the general class of models see ref. [26].

3.2 Invisible decay

When singlet scalars are present it is possible that the Higgs boson decays into these scalars if they are light enough. Such an invisible decay is rather natural, when one introduces the Higgs singlets S_i as multiplets of a symmetry group [15, 16, 17, 18, 19, 20], for instance

$O(N)$. When the $O(N)$ symmetry group stays unbroken this leads to an invisibly decaying Higgs boson through the interaction $\Phi^\dagger \Phi S_i S_i$, after spontaneous breaking of the standard model gauge symmetry. When the $O(N)$ symmetry stays unbroken the singlets S_i are stable and are suitable as candidates for the dark matter in the universe [21, 22, 23, 24, 25].

To be more concrete let us discuss the Lagrangian of the model, containing the standard model Higgs boson plus an O(N)-symmetric sigma model. The Lagrangian density is the following:

$$L_{Scalar} = L_{Higgs} + L_S + L_{Interaction} \tag{1}$$

$$L_{Higgs} = -\frac{1}{2} D_\mu \Phi^\dagger D_\mu \Phi - \frac{\lambda}{8} (\Phi^\dagger \Phi - f^2)^2 \tag{2}$$

$$L_S = -\frac{1}{2} \partial_\mu \vec{S} \partial_\mu \vec{S} - \frac{1}{2} m_S^2 \vec{S}^2 - \frac{\lambda_S}{8N} (\vec{S}^2)^2 \tag{3}$$

$$L_{Interaction} = -\frac{\omega}{4\sqrt{N}} \vec{S}^2 \Phi^\dagger \Phi \tag{4}$$

The field $\Phi = (\sigma + f + i\pi_1, \pi_2 + i\pi_3)$ is the complex Higgs doublet of the standard model with the vacuum expectation value $< 0|\Phi|0 >= (f, 0)$, $f = 246$ GeV. Here, σ is the physical Higgs boson and $\pi_{i=1,2,3}$ are the three Goldstone bosons. $\vec{S} = (S_1, \ldots, S_N)$ is a real vector with $< 0|\vec{S}|0 >= \vec{0}$. We consider the case, where the $O(N)$ symmetry stays unbroken, because we want to concentrate on the effects of a finite width of the Higgs particle. Breaking the $O(N)$ symmetry would lead to more than one Higgs particle, through mixing. After the spontaneous breaking of the standard model gauge symmetry the π fields become the longitudinal polarizations of the vector bosons. In the unitary gauge one can simply put them to zero. One is then left with an additional interaction in the Lagrangian of the form:

$$L_{Interaction} = -\frac{\omega f}{2\sqrt{N}} \vec{S}^2 \sigma \tag{5}$$

This interaction leads to a decay into the $\vec{S}$ particles, that do not couple to other fields of the standard model Lagrangian. On has therefore an invisible width:

$$\Gamma_{Higgs}(invisible) = \frac{\omega^2}{32\pi} \frac{f^2}{m_{Higgs}} (1 - 4m_S^2/m_{Higgs}^2)^{1/2} \tag{6}$$

This width is larger than the standard model width even for moderate values of ω, because the standard model width is strongly suppresed by the Yukawa coupings of the fermions. Therefore the Higgs boson decays predominantly invisibly with a branching ratio approximating 100%. Moreover one cannot exclude a large value of ω. In this case the Higgs is wide and decaying invisibly. This explains the name stealth model for this kind of Higgs sector.

However, is this Higgs boson undetectable at the LHC? Its production mechanisms are exactly the same as the standard model ones, only its decay is in undetectable particles. One therefore has to study associated production with an extra Z-boson or one must consider the vector-boson fusion channel with jet-tagging. Assuming the invisible branching ratio to be large and assuming the Higgs boson not to be heavy, as indicated by the precision tests, one still finds a significant signal [27]. Of course one cannot study this Higgs boson in great detail at the LHC. For this the ILC would be needed, where precise measurements are possible in the channel $e^+e^- \rightarrow ZH$.

3.3 Mixing: fractional Higgses

Somewhat surprisingly it is possible to have a model that has basically only singlet-doublet mixing even if all the scalars are light. If one starts with an interaction of the form $H\Phi^\dagger\Phi$, where H is the new singlet Higgs field and Φ the standard model Higgs field, no interaction of the form H^3, H^4 or $H^2\Phi^\dagger\Phi$ is generated with an infinite coefficient [28]. At the same time the scalar potential stays bounded from below. This means that one can indeed leave these dimension four interactions out of the Lagrangian without violating renormalizability. This is similar to the non-renormalization theorem in supersymmetry that says that the superpotential does not get renormalized. However in general it only works with singlet extensions. As far as the counting of parameters is concerned this is the most minimal extension of the standard model, having only two extra parameters.

The simplest model is the Hill model:

$$L = -\frac{1}{2}(D_\mu\Phi)^\dagger(D_\mu\Phi) - \frac{1}{2}(\partial_\mu H)^2 - \frac{\lambda_0}{8}(\Phi^\dagger\Phi - f_0^2)^2 - \frac{\lambda_1}{8}(2f_1 H - \Phi^\dagger\Phi)^2 \qquad (7)$$

Working in the unitary gauge one writes $\Phi^\dagger = (\sigma, 0)$, where the σ-field is the physical standard model Higgs field. Both the standard model Higgs field σ and the Hill field H receive vacuum expectation values and one ends up with a two-by-two mass matrix to diagonalize, thereby ending with two masses m_- and m_+ and a mixing angle α. There are two equivalent ways to describe this situation. One is to say that one has two Higgs fields with reduced couplings g to standard model particles:

$$g_- = g_{SM}\cos(\alpha), \qquad g_+ = g_{SM}\sin(\alpha) \qquad (8)$$

Because these two particles have the quantum numbers of the Higgs particle, but only reduced couplings to standard model particles one can call them fractional Higgs particles. The other description, which has some practical advantages is not to diagonalize the propagator, but simply keep the $\sigma - \sigma$ propagator explicitely. One can ignore the $H - \sigma$ and $H - H$ propagators, since the H field does not couple to ordinary matter. One simply replaces in all experimental cross section calculations the standard model Higgs propagator by:

$$D_{\sigma\sigma}(k^2) = \cos^2(\alpha)/(k^2 + m_-^2) + \sin^2(\alpha)/(k^2 + m_+^2) \qquad (9)$$

The generalization to an arbitrary set of fields H_k is straightforward, one simply replaces the singlet-doublet interaction term by:

$$L_{H\Phi} = -\sum \frac{\lambda_k}{8}(2f_k H_k - \Phi^\dagger\Phi)^2 \qquad (10)$$

This will lead to a number of (fractional) Higgs bosons H_i with reduced couplings g_i to the standard model particles such that

$$\sum_i g_i^2 = g_{SM}^2 \qquad (11)$$

3.4 A higher dimensional Higgs boson

The mechanism described above can be generalized to an infinite number of Higgses. The physical Higgs propagator is then given by an infinite number of very small Higgs peaks,

that cannot be resolved by the detector. Ultimately one can take a continuum limit, so as to produce an arbitray line shape for the Higgs boson, satisfying the Källén-Lehmann representation.

$$D_{\sigma\sigma}(k^2) = \int ds\, \rho(s)/(k^2 + \rho(s) - i\epsilon) \tag{12}$$

One has the sum rule [13, 29] $\int \rho(s)\, ds = 1$, while otherwise the theory is not renormalizable and would lead to infinite effects for instance on the LEP precision variables. Moreover, combining mixing with invisible decay, one can vary the invisible decay branching ratio as a function of the invariant mass inside the Higgs propagator. There is then no Higgs peak to be found any more. The general Higgs propagator for the Higgs boson in the presence of singlet fields is therefore determined by two function, the Källén-Lehmann spectral density and the s-dependent invisible branching ratio. Unchanged compared to the standard model are the relative branching ratio's to standard model particles.

Given the fact that the search for the Higgs boson in the low mass range heavily depends on the presence of a sharp mass peak, this is a promising way to hide the Higgs boson at the LHC. However the general case is rather arbitrary and unelegant and ultimately involves an infinite number of coupling constants. The question is therefore whether there is a more esthetic way to generate such a spread-out Higgs signal, without the need of a large number of parameters. Actually this is possible. Because the $H\Phi^\dagger\Phi$ interaction is superrenormalizable one can let the H field move in more dimensions than four, without violating renormalizability. One can go up to six dimensions. The precise form of the propagator will in general depend on the size and shape of the higher dimensions. The exact formulas can be quite complicated. However it is possible that these higher dimensions are simply open and flat. In this case one finds simple formulas. One has for the generic case a propagator of the form:

$$D_{\sigma\sigma}(q^2) = \left[q^2 + M^2 - \mu_{lhd}^{8-d}(q^2 + m^2)^{\frac{d-6}{2}} \right]^{-1}. \tag{13}$$

For six dimensions one needs a limiting procedure and finds:

$$D_{\sigma\sigma}(q^2) = \left[q^2 + M^2 + \mu_{lhd}^2 \log\left(\frac{q^2 + m^2}{\mu_{lhd}^2}\right) \right]^{-1}. \tag{14}$$

The parameter M is a four-dimensional mass, m a higher-dimensional mass and μ_{lhd} a higher-to-lower dimensional mixing mass scale. When one calculates the corresponding Källén-Lehmann spectral densities one finds a low mass peak and a continuum that starts a bit higher in the mass. The location of the peak is given by the zero of the inverse propagator. Because this peak should not be a tachyon, there is a constraint on M, m, μ_{lhd}, that can be interpreted as the condition that there is a stable vacuum.

Explicitely one finds for $d = 5$ the Källén-Lehmann spectral density:

$$\begin{aligned}
\rho(s) = \quad & \theta(m^2 - s)\, \frac{2(m^2 - s_{peak})^{3/2}}{2(m^2 - s_{peak})^{3/2} + \mu_{lhd}^3}\, \delta(s - s_{peak}) \\
+ \quad & \frac{\theta(s - m^2)}{\pi}\, \frac{\mu_{lhd}^3\, (s - m^2)^{1/2}}{(s - m^2)(s - M^2)^2 + \mu_{lhd}^6},
\end{aligned} \tag{15}$$

For $d = 6$ one finds:

$$\rho(s) = \qquad \theta(m^2 - s)\ \frac{m^2 - s_{peak}}{m^2 + \mu_{lhd}^2 - s_{peak}}\ \delta(s - s_{peak})$$
$$+ \quad \theta(s - m^2)\ \frac{\mu_{lhd}^2}{[\,s - M^2 - \mu_{lhd}^2\,\log((s - m^2)/\mu_{lhd}^2)\,]^2 + \pi^2\,\mu_{lhd}^4}. \tag{16}$$

If one does not introduce further fields no invisible decay is present. If the delta peak is small enough it will be too insignificant for the LHC search. The continuum is in any case difficult to see. There might possibly be a few sigma signal in the τ-sector. However if one adds to this model some scalars to account for the dark matter, this will water down any remnant signal to insignificance.

4   Comparison with the LEP-200 data

We now confront the higher dimensional models with the results from the direct Higgs search at LEP-200 [30]. Within the pure standard model the absence of a clear signal has led to a lower limit on the Higgs boson mass of 114.4 GeV at the 95% confidence level. Although no clear signal was found the data have some intriguing features, that can be interpreted as evidence for Higgs bosons beyond the standard model. There is a $2.3\,\sigma$ effect seen by all experiments at around 98 GeV. A somewhat less significant $1.7\,\sigma$ excess is seen around 115 GeV. Finally over the whole range $s^{1/2} > 100$ GeV the confidence level is less than expected from background. We will interpet these features as evidence for a spread-out Higgs-boson [31]. The peak at 98 GeV will be taken to correspond to the delta peak in the Källén-Lehmann density. The other excess data will be taken as part of the continuum, that will peak around 115 GeV.

We start with the case $d = 5$. The delta-peak will be assumed to correspond to the peak at 98 GeV, with a fixed value of g_{98}^2. Ultimately we will vary the location of the peak between $95\,\text{GeV} < m_{peak} < 101\,\text{GeV}$ and $0.056 < g_{98}^2 < 0.144$. After fixing g_{98}^2 and m_{peak} we have one free variable, which we take to be μ_{lhd}. If we also take a fixed value for μ_{lhd} all parameters and thereby the spectral density is known. We can then numerically integrate the spectral density over selected ranges of s. The allowed range of μ_{lhd} is subsequently determined by the data at 115 GeV. Since the peak at 115 GeV is not very well constrained, we demand here only that the integrated spectral density from $s_{down} = (110\,\text{GeV})^2$ to $s_{up} = (120\,\text{GeV})^2$ is larger than 30%. This condition, together with formula (15), which implies:

$$\rho(s) < \frac{(s - m^2)^{1/2}}{\pi\,\mu_{lhd}^3}, \tag{17}$$

leads to the important analytical result:

$$\frac{2}{3\pi\,\mu_{lhd}^3}[\,(s_{up} - m_{peak}^2)^{3/2} - (s_{down} - m_{peak}^2)^{3/2}\,] > 0.3 \tag{18}$$

This implies $\mu_{lhd} < 53$ GeV. Using the constraint from the strength of the delta-peak, it follows that the continuum starts very close to the peak, the difference being less than 2.5 GeV. This allows for a natural explanation, why the CL for the fit in the whole range from 100 GeV to 110 GeV is somewhat less than what is expected by pure background. The enhancement can be due to a slight, spread-out Higgs signal. Actually when fitting the data

with the above conditions, one finds for small values of μ_{lhd}, that the integrated spectral density in the range 100 GeV to 110 GeV can become rather large, which would lead to problems with the 95% CL limits in this range. We therefore additionally demand that the integrated spectral density in this range is less than 30%. There is no problem fitting the data with these conditions. As allowed ranges we find:

$$95\,\text{GeV} < m < 101\,\text{GeV}$$
$$111\,\text{GeV} < M < 121\,\text{GeV}$$
$$26\,\text{GeV} < \mu_{lhd} < 49\,\text{GeV} \tag{19}$$

We now repeat the analysis for the case $d = 6$. The analytic argument gives the result:

$$\frac{s_{up} - s_{down}}{\pi^2\,\mu_{lhd}^2} > 0.3 \tag{20}$$

which implies $\mu_{lhd} < 28\,\text{GeV}$. Because of this low value of μ_{lhd} it is difficult to get enough spectral weight arond 115 GeV and one also tends to get too much density below 110 GeV. As a consequence the fit was only possible in a restricted range. Though not quite ruled out, the six-dimensional case therefore seems to be somewhat disfavoured compared to the five-dimensional case. As a consequence the fit was only possible in a restricted range. We found the following limits:

$$95\,\text{GeV} < m < 101\,\text{GeV}$$
$$106\,\text{GeV} < M < 111\,\text{GeV}$$
$$22\,\text{GeV} < \mu_{lhd} < 27\,\text{GeV} \tag{21}$$

5 Conclusion

We are now in a position to answer the following question. Is it possible to have a simple model that:

a) Is consistent with the precision data, even with the strong condition $m_H < 109\,\text{GeV}$?
b) explains the LEP-200 Higgs search data ?
c) has a dark matter candidate ?
d) gives no Higgs signal at the LHC ?

Given the above discussion, the answer is clearly yes, which leads to the question whether such a model is likely to be true. This is rather difficult to answer decisively. It depends on how significant the evidence in the data is, in particular in the LEP-200 Higgs search data. This significance is hard to estimate, since the data were not analyzed with this type of model in mind. If we take all present Higgs relevant data at face value and in combination, the standard model with a Higgs mass larger than 115 GeV would be ruled out at roughly the $3.7\,\sigma$ level. To come to a definite conclusion more evidence is therefore needed. It appears, that the Tevatron can provide further confirmation [32, 33]. In combination with the existing data, a $3\,\sigma$ Higgs signal at the Tevatron below 115 GeV would actually correspond to a $5\,\sigma$ discovery. At the same time one would thereby have proven that the Higgs field does not

correspond to a single particle peak. Given the fact that the LHC is essentially blind for this type of model, one can under circumstances argue for an extended running time of the Tevatron, in order to clarify the situation.

For a detailed study of this class of models however the ILC is essential. One needs to determine two functions, the Källén-Lehmann spectral density and the fraction of invisible decay. The Källén-Lehmann spectral density can be determined from the decay mode independent recoil spectrum in the $e^+e^- \to ZH$ process. The invisible decay fraction can be determined either directly or by comparison with the decay mode independent Higgs search and the direct $\bar{b}b$ mode. From the theory side there is no fundamental problem to calculate the relevant cross sections to the per mille level. From the experimental side one needs a precise knowledge of the incoming energy and of the luminosity. The beamstrahlung is probably the limiting factor here [34]. Altogether we conclude, that there is a strong scientific case to build the ILC, in particular if the LHC finds no sign of the Higgs particle.

Acknowledgments

6 Bibliography

References

[1] Slides: http://ilcagenda.linearcollider.org/contributionDisplay.py?contribId=243&sessionId=72&confId=1296

[2] M.S. Chanowitz, in *XXIII International Conference on High Energy Physics*, Berkeley, California (1986).

[3] J.J. van der Bij and M. Veltman, *Nucl. Phys.* B **231**, 205 (1984).

[4] J.J. van der Bij, *Nucl. Phys.* B **248**, 141 (1984).

[5] J.J. van der Bij, in *XIX Rencontre de Moriond* (1984).

[6] V. Borodulin and G. Jikia, *Nucl. Phys.* B **520**, 31 (1998).

[7] A. Ghinculov and J.J. van der Bij, *Nucl. Phys.* B **436**, 30 (1995).

[8] T. Binoth, A. Ghinculov and J.J. van der Bij, *Phys. Lett.* B **417**, 343 (1998).

[9] T. Binoth, A. Ghinculov and J.J. van der Bij, *Phys. Rev.* D **57**, 1487 (1998).

[10] R. Boughezal, J.B. Tausk and J.J. van der Bij, *Nucl. Phys.* B **713**, 278 (2005).

[11] R. Boughezal, J.B. Tausk and J.J. van der Bij, *Nucl. Phys.* B **725**, 3 (2005).

[12] B. Kastening and J.J. van der Bij, *Phys. Rev.* D **57**, 2903 (1998).

[13] R. Akhoury, J.J. van der Bij and H. Wang, *Eur. Phys. J.* C **20**, 497 (2001).

[14] S. Kyriazidou, *Nucl. Phys.* B **398**, 69 (1993).

[15] R. Casalbuoni, D. Dominici, R. Gatto, C. Giunti, *Phys. Lett.* B **178**, 235 (1986).

[16] R.S. Chivukula, M. Golden, *Phys. Lett.* B **267**, 233 (1991).

[17] R.S. Chivukula, M. Golden, D. Kominis, M.V. Ramana, *Phys. Lett.* B **293**, 400 (1992).

[18] J.D. Bjorken, *Int. J. Mod. Phys* A **7**, 4189 (1992).

[19] R. Akhoury, B. Haeri, *Phys. Rev.* D **48**, 1252 (1993).

[20] T. Binoth, J.J. van der Bij, *Z. Phys.* C **75**, 17 (1997).

[21] V. Silveira and A. Zee, *Phys. Lett.* B **161**, 136 (1985).

[22] J. McDonald, *Phys. Rev.* D **50**, 3637 (1994).

[23] M.C. Bento, O. Bertolami, R. Rosenfeld, *Phys. Lett.* B **518**, 276 (2001).

[24] C.P. Burgess, M. Pospelov, T. ter Veldhuis, NPB **619**, 709 (2001).

[25] H. Davoudiasl, R. Kitano, T. Li, H. Murayama, *Phys. Lett.* B **609**, 117 (2005).

[26] J.J. van der Bij, *Phys. Lett.* B **636**, 56 (2006).

[27] T. Ekelöf, *contribution to the XLII Rencontre de Moriond*, (2007).

[28] A. Hill and J.J. van der Bij, *Phys. Rev.* D **36**, 3463 (1987).

[29] J.R. Espinosa and J.F. Gunion, *Phys. Rev. Lett.* **82**, 1084 (1999).

[30] The LEP working group for Higgs boson searches, *Phys. Lett.* B **565**, 61 (2003).

[31] J. J. van der Bij and S. Dilcher, *Phys. Lett.* B **638**, 234 (2006).

[32] Slides:
`http://ilcagenda.linearcollider.org/contributionDisplay.py?contribId=149&sessionId=71&confId=1296`

[33] Slides:
`http://ilcagenda.linearcollider.org/contributionDisplay.py?contribId=156&sessionId=71&confId=1296`

[34] Slides:
`http://ilcagenda.linearcollider.org/contributionDisplay.py?contribId=232&sessionId=72&confId=1296`

Discovery and Identification of Contactlike Interactions in Fermion-pair Production at ILC

A. A. Pankov[1], N. Paver[2] and A. V. Tsytrinov[1]

1- ICTP Affiliated Centre, Pavel Sukhoi Technical University - Dept of Physics
Gomel 246746 - Belarus

2- University of Trieste and INFN-Trieste Section - Dept of Theoretical Physics
34100 Trieste - Italy

Non-standard scenarios described by effective contactlike interactions can be revealed only by searching for deviations of the measured observables from the Standard Model (SM) predictions. If deviations were indeed observed within the experimental uncertainty, the identification of their source among the different non-standard interactions should be needed. We here consider the example of the discrimination of gravity in compactified extra dimensions (ADD model) against the four-fermion contact interactions (CI). We present assessments of the identification reach on this scenario, that could be obtained from measurements of the differential cross sections for the fermionic processes $e^+e^- \to \bar{f}f$, with $f = e, \mu, \tau, c, b$, at the planned ILC.

1 Non-standard effective interactions

The non-standard contactlike local interactions we are going to consider are all characterized by corresponding large mass scales $\Lambda_{\alpha\beta}$ and Λ_H to some inverse power that specifically depends on the dimension of the relevant effective local operators:

a) The compositeness inspired dim-6 four-fermion contact interactions (CI):

$$\mathcal{L}^{\text{CI}} = 4\pi \sum_{\alpha,\beta} \frac{\eta_{\alpha\beta}}{\Lambda_{\alpha\beta}^2} \left(\bar{e}_\alpha \gamma_\mu e_\alpha\right) \left(\bar{f}_\beta \gamma^\mu f_\beta\right), \qquad \eta_{\alpha\beta} = \pm 1, 0, \tag{1}$$

with $\alpha, \beta = \text{L, R}$ the helicities of the incoming and outgoing fermions [1]. Generally, this kind of models can describe exchanges between SM particles of very heavy W', Z', leptoquarks, *etc.*

b) The ADD model of gravity in "large" compactified extra dimensions [2], that can be parameterized by the dim-8 contactlike interaction [3]:

$$\mathcal{L}^{\text{ADD}} = i\frac{4\lambda}{\Lambda_H^4} T^{\mu\nu} T_{\mu\nu}, \qquad \lambda = \pm 1. \tag{2}$$

Here, $T_{\mu\nu}$ is the energy-momentum of SM particles, and Λ_H essentially represents a cut-off on the exchange (in 4 dimensions) of a tower of Kaluza-Klein, spin-2, massive graviton excitations. For (sub)millimeter extra dimensions, the mass Λ_H scale may be expected to be of the TeV size.

In principle, in addition to the Planck mass M_D in $4 + n$ dimensions, such that $M_{\text{PL}} = M_D^{1+n/2} R^{n/2}$ with R the compactification radius, there can exist one independent mass scale we denote generically as Λ, that represents the relative strength of tree *vs.* loop virtual graviton exchanges. In the naive dimensional approximation (NDA), the relation of this

extra scale to Λ_H in Eq. (2) is [4]:

$$\frac{1}{\Lambda_H^4} = \frac{\pi^{n/2}}{8\Gamma(n/2)} \frac{\Lambda_{\rm NDA}^{n-2}}{M_D^{n+2}}. \tag{3}$$

Moreover, loops with virtual graviton exchanges can generate even 6-dimensional four-fermion interactions similar to the CI in Eq. (1). One example is the axial-axial operator:

$$\mathcal{L}_\Upsilon = \frac{1}{2} c_\Upsilon \left(\sum_f \bar{f}\gamma_\mu\gamma_5 f \right) \left(\sum_f \bar{f}\gamma^\mu\gamma_5 f \right), \tag{4}$$

with

$$c_\Upsilon = \frac{\pi^{n-2}}{16\Gamma^2(n/2)} \frac{\Lambda_{\rm NDA}^{2+2n}}{M_D^{4+2n}}. \tag{5}$$

The current experimental lower bounds on the mass scales in Eqs. (1) and (2), that parametrize the strength of the corresponding contactlike interactions, can be summarized qualitatively as follows [5]: $\Lambda_H > 1.3\,{\rm TeV}$; $\Lambda_{\alpha\beta} > 10 - 15\,{\rm TeV}$ [95% C.L.].

2   Discovery and identification of the ADD scenario

Clearly, constraints on $\Lambda_{\alpha\beta}$ and Λ_H are determined by the deviations of the observables, $\mathcal{O}$, from the SM expectations. We choose as basic observables the longitudinally polarized differential cross sections, $\mathcal{O} = \mathrm{d}\sigma/\mathrm{d}\cos\theta$, for the fermionic processes $e^+e^- \to \bar{f}f$ at ILC (f is limited to e, μ, τ, c, b). Obviously, the theoretical expressions of the cross sections including the novel physics (NP), to be compared to the data, are given by $\mathrm{d}\sigma \propto |{\rm SM} + {\rm NP}(\Lambda)|^2$, where Λ generically denotes $\Lambda_{\alpha\beta}$ or Λ_H. It has been strongly emphasized [6] that electron and positron beams polarization plays a crucial rôle in enhancing the sensitivity to the NP interactions and, indeed, this option is very seriously considered for the planned ILC.

The comparison between "theoretical" relative deviations, $\Delta\mathcal{O}$, and corresponding foreseen experimental relative uncertainties, $\delta\mathcal{O}$, can be performed by a simple χ^2 procedure combining the initial polarization configurations and the binning of the angular range for the measured reactions [7, 8]:

$$\Delta\mathcal{O} = \frac{\mathcal{O}({\rm SM} + {\rm NP}) - \mathcal{O}({\rm SM})}{\mathcal{O}({\rm SM})}, \qquad \chi^2(\mathcal{O}) = \sum_{\{P^-,\ P^+\}} \sum_{\rm bins} \left(\frac{\Delta(\mathcal{O})^{\rm bin}}{\delta\mathcal{O}^{\rm bin}} \right)^2. \tag{6}$$

The χ^2 in Eq. (6) will be a function of the mass scale Λ relevant to the contactlike interaction under consideration. The expected *discovery* reach on an individual interaction, i.e., the maximum value of the corresponding mass scale Λ for which a deviation caused by the interaction itself could be observed, can be assessed by assuming a situation where no deviation is observed and imposing, for 95% C.L., the constraint $\chi^2 \leq 3.84$. Basically, this is the way the current limits above have been obtained.

In Table 1, we give examples of discovery reaches expected for an ILC with the "reference" parameters: $\sqrt{s} = 0.5$ TeV; time-integrated luminosity $\mathcal{L}_{\rm int} = 500\,{\rm fb}^{-1}$, and electron and positron longitudinal polarizations $|P^-| = 0.8$, $|P^+| = 0.3$. While these luminosity and beams polarization seem guaranteed at the initial stage of ILC, $\mathcal{L}_{\rm int} = 1000\,{\rm fb}^{-1}$ and $|P^+|$ of

the order of 0.6 may be considered, eventually, for later runs of the machine. To obtain the results in Table 1, binning of the angular range by $\Delta \cos\theta = 0.2$ intervals has been used in (6), and the statistical uncertainties have been evaluated by the final fermions reconstruction efficiencies: 100% for electrons, 95% for μ and τ, 35% and 60% for c and b quarks, respectively. The dominant systematic uncertainties are found to originate from polarizations and luminosity, on which we have assumed the accuracies 0.1% and 0.5%, respectively. Earlier determinations, demonstrating the fundamental rôle of beams polarization for the discovery reaches on CI interactions, can be found, e.g., in Ref. [9]. The Table 1 shows the high sensitivity to $\Lambda_{\alpha\beta}$ allowed by polarization, and that Bhabha scattering is the process most sensitive to Λ_H.

Model	Processes			
	$e^+e^- \to e^+e^-$	$e^+e^- \to l^+l^-$	$e^+e^- \to \bar{b}b$	$e^+e^- \to \bar{c}c$
Λ_H	5.3; 5.5	3.7; 3.8	3.7; 4.0	3.7; 3.8
Λ_{VV}^{ef}	128.3; 136.7	136.4; 144.2	115.8; 137.4	128.3; 136.7
Λ_{AA}^{ef}	76.1; 90.3	122.4; 129.5	116.7; 139.5	116.9; 124.8
Λ_{LL}^{ef}	66.2; 82.7	81.9; 98.6	96.9; 105.7	84.1; 96.6
Λ_{RR}^{ef}	64.0; 81.5	78.4; 97.7	64.4; 98.0	71.5; 95.3
Λ_{LR}^{ef}	94.9; 100.1	74.1; 90.2	76.0; 95.9	54.5; 79.0
Λ_{RL}^{ef}	$\Lambda_{RL}^{ee} = \Lambda_{LR}^{ee}$	74.0; 90.6	70.9; 85.5	78.2; 86.5
M_C	20.5; 22.1	30.7; 32.5	9.7; 14.9	15.8; 17.3

Table 1: 95% C.L. discovery reaches (in TeV). Left and right entries in each column refer to the polarizations $(|P^-|, |P^+|)$=(0,0) and (0.8,0.3), respectively.

In principle, different interactions may cause similar deviations in (6), and one would need to identify, among the various contact interactions, the origin of the deviations, were they observed. In this regard, the *identification reach* on a given contact effective interaction can be defined as the maximum value of the characteristic mass scale Λ for which the considered interaction not only can cause observable deviations from the SM, but can also be discriminated as the source of the observed deviations against the other contact interactions for all values of *their* respective Λs.

Earlier attempts to estimate the *identification reaches* on ADD and CI models in high energy e^+e^- reactions have been presented in Ref. [10]. We here continue with the χ^2 analysis outlined above [7, 8].

To make an illustrative example, we assume that the ADD model (2) is found to be consistent with observed deviations. To assess the level at which this scenario can be distinguished from each of the CI models of Eq. (1), one can consider the "distances" in the $(\Lambda_H, \Lambda_{\alpha\beta})$ two-dimensional planes:

$$\tilde{\Delta}(\mathcal{O}) = \frac{\mathcal{O}(\text{CI}) - \mathcal{O}(\text{ADD})}{\mathcal{O}(\text{ADD})}, \qquad \tilde{\chi}^2(\mathcal{O}) = \sum_{\{P^-, P^+\}} \sum_{\text{bins}} \left(\frac{\tilde{\Delta}(\mathcal{O})^{\text{bin}}}{\tilde{\delta}\mathcal{O}^{\text{bin}}} \right)^2. \qquad (7)$$

In Eq. (7), symbols are analogous to Eq. (6), except that the statistical component of the uncertainty $\tilde{\delta}\mathcal{O}$ is now referred to the ADD model prediction. For each pair of α, β subscripts, we can find *confusion* regions in the above mentioned planes, where models cannot be distinguished from each other at the 95% C.L., by imposing the conditions $\tilde{\chi}^2(\Lambda_H, \Lambda_{\alpha\beta}) \leq 3.84$ for the pairs $\alpha\beta = \mathrm{LL}, \mathrm{RR}, \mathrm{RL}, \mathrm{LR}$. Each confusion region is enclosed by a contour that shows a minimum value of Λ_H, $\Lambda_H^{(\alpha\beta)}$, below which there is no confusion, namely, the "$\alpha\beta$" CI model can be *excluded* as the source of the

Figure 1: Exclusion and identification reaches on Λ_H at 95% C.L. obtained from Bhabha scattering.

observed deviations for all values of $\Lambda_{\alpha\beta}$. Clearly, the smallest of the $\Lambda_H^{(\alpha\beta)}$ determines the expected identification reach on the ADD model (2) [7]. This is exemplified in Figure 1, that refers to an ILC with $\sqrt{s} = 0.5\,\mathrm{TeV}$, $\mathcal{L}_{\mathrm{int}} = 500\,\mathrm{fb}^{-1}$ unpolarized (grey bars) and with polarized beams with $|P^-| = 0.8$, $|P^+| = 0.3$ (black bars). The Figure indicates $\Lambda_H^{\mathrm{ID}} = 3.2$ TeV (3.5 TeV) as the expected identification reach on (2) for unpolarized (polarized) beams. The beams polarization, when combined as in (7), play a rôle in substantially restricting the confusion regions. This is even more evident by repeating the same procedure for the identification reaches on the CI couplings [7].

3 Model-independent identification of the ADD scenario

In the previous section we compared *pairs* of individual contactlike interactions, (1) and (2). More generally, we can consider the possibility that, for a given final fermion flavour f, the CI interaction can be a linear combination of *all* the individual interactions in Eq. (1) with free, simultaneously non vanishing, independent coupling constants $\eta_{\alpha\beta}/\Lambda_{\alpha\beta}^2$. In this case, the corresponding identification reach on Λ_H would be defined as *model-independent*. The observables and their deviations in Ref. (7) now simultaneously depend on *all* mass scales $\Lambda_{\alpha\beta}$ and Λ_H as $\mathcal{O}(\mathrm{CI}) = \mathcal{O}(\Lambda_{\mathrm{LL}}, \Lambda_{\mathrm{RR}}, \Lambda_{\mathrm{RL}}, \Lambda_{\mathrm{LR}})$. The *confusion* region in the multi-parameter space $(\Lambda_H, \Lambda_{\alpha\beta})$ with $\alpha, \beta = \mathrm{L}, \mathrm{R}$, where the general CI model can mimic the ADD model and therefore cannot be discriminated, is determined by the condition $\bar{\chi}^2 \leq \bar{\chi}^2_{\mathrm{crit}}$. Here, for 95% C.L., $\bar{\chi}^2_{\mathrm{crit}} = 9.49$ for the annihilation channels $f = \mu, \tau, c, b$ and $\bar{\chi}^2_{\mathrm{crit}} = 7.82$ for Bhabha scattering ($f = e$), where the LR and RL couplings are equal. As an illustration, we show in Figure 2 examples of the two-dimensional projections of the four-dimensional surface enclosing the 95% C.L. confusion region, onto the planes $(\eta_{\mathrm{LL}}/\Lambda_{\mathrm{LL}}^2, \lambda/\Lambda_H^4)$ and $(\eta_{\mathrm{LR}}/\Lambda_{\mathrm{LR}}^2, \lambda/\Lambda_H^4)$ for the cases of unpolarized beams (dashed curves) and both beams polarized with $(|P^-|, |P^+|) = (0.8, 0.3)$ (solid lines). As one can see, the rôle of polarization in restricting the confusion region is dramatic.

As indicated by Figure 2, the contour of the confusion region identifies a minimal value of Λ_H for which the CI scenario can be excluded as the source of the deviations, and we take that value as the expected model-independent identification reach on the ADD scenario (2) [8]. The numerical results for such *model-independent identification reach* Λ_H^{ID} at the ILC, with parameters exposed in the caption, are shown in Table 2.

Using Eq. (3), we can turn the identification reach on Λ_H obtained above, into *allowed*

314   *LCWS/ILC 2007*
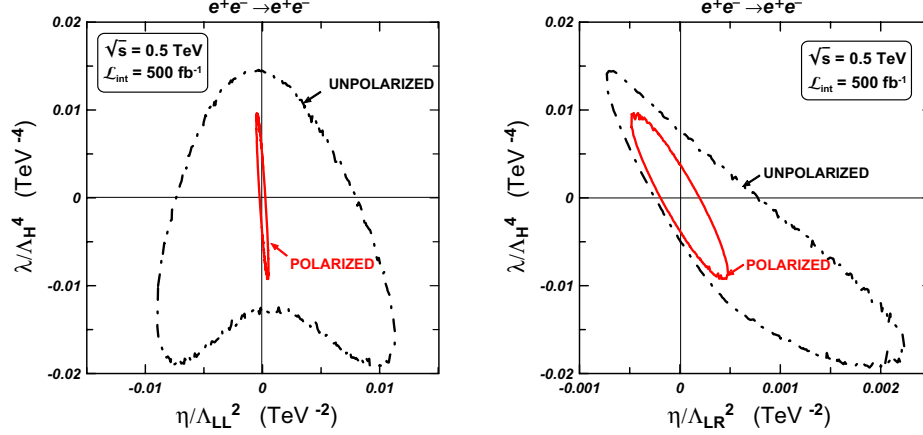
Figure 2: Two-dimensional projection of the 95% C.L. confusion region onto the planes $(\eta_{\mathrm{LL}}/\Lambda_{\mathrm{LL}}^2, \lambda/\Lambda_H^4)$ and $(\eta_{\mathrm{LR}}/\Lambda_{\mathrm{LR}}^2, \lambda/\Lambda_H^4)$ from Bhabha scattering .

Λ_H (TeV)	Process	
	$e^+e^- \to e^+e^-$	combined $e^+e^- \to \bar{f}f$
$\mathcal{L}_{\mathrm{int}} = 500 fb^{-1}$	3.2	4.8
$\mathcal{L}_{\mathrm{int}} = 1000 fb^{-1}$	3.9	5.2

Table 2: 95% C.L. model-independent identification reach on Λ_H obtained from Bhabha scattering and combination of all final fermions ($f = e, \mu, \tau, c, b$) at $\sqrt{s} = 0.5$ TeV, $\mathcal{L}_{\mathrm{int}} = 500 fb^{-1}$, ($|P^-|, |P^+|$)=(0.8, 0.3) and $\mathcal{L}_{\mathrm{int}} = 1000 fb^{-1}$, ($|P^-|, |P^+|$)=(0.8, 0.6), respectively.

and *excluded* regions in the two-dimensional $(M_D, \Lambda_{\mathrm{NDA}})$ plane at 95% C.L. An example, with $n = 5$ and using the constraints expected from combined fermionic processes e, μ, τ, c, b, is shown in Figure 3 by the lines "ILC, G-exchange" for the two options: $\mathcal{L}_{\mathrm{int}} = 500\,\mathrm{fb}^{-1}$, $|P^-| = 0.8$, $|P^+| = 0.3$ (thin solid curve) and $\mathcal{L}_{\mathrm{int}} = 1000\,\mathrm{fb}^{-1}$, $|P^-| = 0.8$, $|P^+| = 0.6$ (thick solid curve).

Analogously, one can derive the identification reach on the coupling constant c_Υ in Eq. (4), and then the corresponding 95% constraints in the $(M_D, \Lambda_{\mathrm{NDA}})$ plane *via* Eq. (5). The results, under the same conditions, are shown by the dashed lines "ILC, G-loops" in Figure 3. More details can be found in Ref. [8].

It should be interesting to compare our results on the M_D *v.s.* Λ_{NDA} allowed regions with the expectations from lepton-pair production $p+p \to l^+l^- + X$ ($l = e, \mu$) at the LHC (DY). We qualitatively assume that the same value of Λ enters into the different quark, antiquark and gluon subprocesses relevant to DY. Also, we attempt to assess the discrimination of deviations from the SM predictions caused by dimension-8 tree-level exchanges, Eqs. (2) and (3), from those due to the dimension-6 AA four-fermion interaction, Eqs. (4) and (5).

To this purpose, we utilize for the DY at the LHC the integrated angular "center-edge" asymmetry proposed in [11]. This observable has the property of being sensitive only to deviations from Eq. (2), but "transparent" to those from both Eq. (1) and Eq. (4). The identification reach obtained from DY at the LHC with $\mathcal{L}_{\text{int}} = 100 \, \text{fb}^{-1}$ (thick dot-dashed curve) is shown in Figure 3.

As Figure 3 shows, the limits on the tree-level graviton exchange parametrized by Eq. (2) and obtained from the LHC and ILC are complementary rather than competitive. Moreover, graviton-loop effects can dominate over tree-level exchange at larger M_D. In this regime, the identification of the effective operator c_Υ in fermion pair production at ILC provide the most efficient probe of theories with extra dimensions. In this case, the ILC(0.5 TeV) for chosen values of the luminosity and beams polarization could be definitely superior to the LHC.
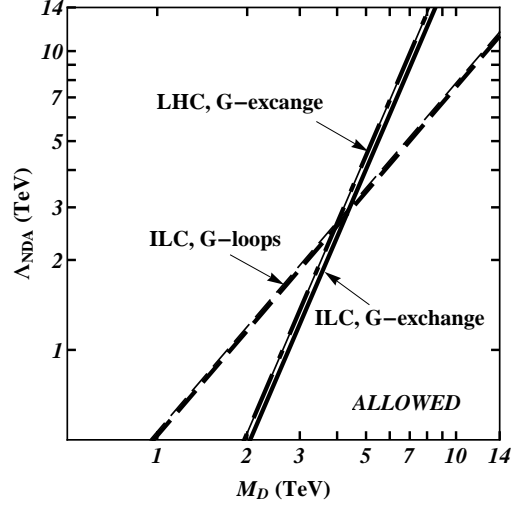
Figure 3: 95% C.L. identification reaches obtained at the polarized ILC(0.5 TeV) and LHC.

4 Acknowledgments

References

[1] E. Eichten, K. D. Lane and M. E. Peskin, Phys. Rev. Lett. **50** 811 (1983);
    R. Rückl, Phys. Lett. **B129** 363 (1983).

[2] N. Arkani-Hamed, S. Dimopoulos and G. R. Dvali, Phys. Lett. **B429** 263 (1998);
    I. Antoniadis, N. Arkani-Hamed, S. Dimopoulos and G. R. Dvali, Phys. Lett. **B436** 257 (1998).

[3] J. L. Hewett, Phys. Rev. Lett. **82** 4765 (1999).

[4] G. F. Giudice and A. Strumia, Nucl. Phys. **B663** 377 (2003);
    G. F. Giudice, T. Plehn and A. Strumia, Nucl. Phys. **B706** 455 (2005). [arXiv:hep-ph/0408320].

[5] W. M. Yao *et al.* [Particle Data Group], J. Phys. G **33** 1 (2006).

[6] G. Moortgat-Pick *et al.*, "The role of polarized positrons and electrons in revealing fundamental interactions at the linear collider", arXiv:hep-ph/0507011 (2005).

[7] A. A. Pankov, N. Paver and A. V. Tsytrinov, Phys. Rev. **D73** 115005 (2006).

[8] A. A. Pankov, A. V. Tsytrinov and N. Paver, Phys. Rev. **D75** 095004 (2007).

[9] S. Riemann, LC-TH-2001-007 (2001).

[10] G. Pasztor and M. Perelstein, in *APS/DPF/DPB Summer Study on the Future of ParticlePhysics* (Snowmass 2001), edited by N. Graf, hep-ph/0111471;
    T. G. Rizzo, JHEP **0210** 013 (2002);
    P. Osland, A. A. Pankov and N. Paver, Phys. Rev. **D68** 015007 (2003);
    A. A. Pankov and N. Paver, Phys. Rev. **D72** 035012 (2005).

[11] E. W. Dvergsnes, P. Osland, A. A. Pankov and N. Paver, Phys. Rev. **D69** 115001 (2004);
    E. W. Dvergsnes, P. Osland, A. A. Pankov and N. Paver, Int. J. Mod. Phys. **A20** 2232 (2005).

Top and QCD

Conveners: A. Juste, T. Teubner, R. Godbole

NNNLO correction to the toponium and bottomonium wave-functions at the origin [*]

M. Beneke[1], Y. Kiyo[2], A. Penin[3] and K. Schuller[1]

1- Institut für Theoretische Physik E, RWTH Aachen,
D-52056 Aachen, Germany
2- Institut für Theoretische Teilchenphysik, Universität Karlsruhe,
D-76128 Karlsruhe, Germany
3- Department of Physics, University Of Alberta,
Edmonton, AB T6G 2J1, Canada

We report new results on the NNNLO correction to the S-wave quarkonium wave-functions at the origin, which also provide an estimate of the resonance cross section in $t\bar{t}$ threshold production at the ILC.

1 Introduction

Top quark pair production near threshold will be an important process at the ILC to determine the top quark mass m_t, decay width Γ_t and the QCD coupling constant α_s. High precision is called for for these quantities, so the theoretical uncertainty for the cross section should be under control below the few percent level. For this purpose, the NNNLO QCD calculation of the cross section is mandatory.

Recently we computed the NNNLO correction [1, 2] to the quarkonium wave-functions at the origin, which governs height of the threshold cross section. In this proceedings we present an analysis of the combined result of the papers [1, 2]. For the details of the calculation we refer to the original papers.

The production cross section of a heavy quark pair $Q\bar{Q}$ is related to the two-point function of the vector current j^μ in QCD:

$$\left(q^\mu q^\nu - g^{\mu\nu}q^2\right)\Pi(q^2) = i\int d^d x e^{iqx}\langle\Omega|T\,j^\mu(x)j^\nu(0)|\Omega\rangle, \tag{1}$$

where $j^\mu = \bar{Q}\gamma^\mu Q$, $q^\mu \equiv (2m + E, \vec{0})$ in the center of mass frame of the $Q\bar{Q}$, and $d = 4 - 2\epsilon$. Near the $Q\bar{Q}$ threshold, the two-point function exhibits the bound-state contribution

$$\Pi(q^2) \overset{E\to E_n}{=} \frac{N_c}{2m^2}\frac{Z_n}{E_n - (E + i\,0)} + \text{non-pole}, \tag{2}$$

where E_n is energy of n-th resonance (n is principal quantum number of the quarkonium state, $i\,0$ specifies the physical sheet in the analytic continuation). The poles dominate the two-point function, therefore Z_n and E_n control the height and the pole position, respectively, of the threshold cross section.

The heavy quark threshold dynamics is non-relativistic (NR), so we utilize an effective field theory, non-relativistic QCD (NRQCD) for the quark (ψ) and anti-quark (χ). In

---

[*]Talk given by Y. Kiyo. SFB/CPP-07-68, TTP07-29, PITHA07/14.

NRQCD the vector current is mapped onto

$$j^i \quad = \quad c_v \psi^\dagger \sigma^i \chi + \frac{d_v}{6m^2} \psi^\dagger \sigma^i \mathbf{D}^2 \chi + \cdots, \tag{3}$$

where c_v, d_v are matching coefficients, having perturbative series expansion in α_s. Thus the two-point function reduces to the one in NRQCD, whose bound-state contribution is expressed by the quarkonium wave-function at the origin, $\psi_n(0)$,

$$i \int d^d x e^{iEt} \langle \Omega | T [\psi^\dagger \sigma^i \chi](x) [\chi^\dagger \sigma^i \psi](0) | \Omega \rangle \overset{E \to E_n}{=} 2N_c(d-1) \frac{|\psi_n(0)|^2}{E_n - (E + i\,0)} + \text{non-pole}. \tag{4}$$

The pre-factor $2N_c(d-1)$ is due to spin⊗color⊗space degrees of freedom. The relation between the residues of the QCD and NRQCD two-point functions is given by

$$Z_n \quad = \quad c_v \left[c_v - \frac{E_n}{m} \left(1 + \frac{d_v}{3} \right) + \cdots \right] \times |\psi_n(0)|^2, \tag{5}$$

where the $\mathbf{D}^2$ term in eq.(3) was replaced by $-mE$ using the equations of motion of the NRQCD fields. The wave-function as well as the matching coefficients possess scale dependence because of their UV and IR divergences characteristic to the effective theory calculations which we treat according to the threshold expansion [3]. The physical quantity measured in experiments is Z_n, a scale-invariant combination of the matching coefficients and the NR wave-function. In the next section we present semi-analytical formulae for all the building blocks needed to get Z_1, and discuss the importance of the NNNLO correction for stabilizing the perturbative result for the quarkonium wave-functions at the origin against scale variation.

2   NNNLO corrections to the wave-function at the origin

The wave-function at the origin to NNNLO consists of the Coulomb contribution, the non-Coulomb potential contribution, and the ultra-soft correction in NRQCD. The Coulomb contribution is finite and calculated analytically in [4, 5]. The non-Coulomb [1] and ultra-soft [2] computations require regularization and renormalization prescriptions, so that they are scheme-dependent quantities. We computed them with conventional dimensional regularization and divergences are renormalized in $\overline{\text{MS}}$ scheme. Combining all corrections we obtain the following numerical formula for the ground-state wave-function:

$$\frac{|\psi_1(0)|^2}{|\psi_1^{(0)}(0)|^2} \quad = \quad 1 + \alpha_s(\mu) \left[(5.25 - 0.32\,n_f)L + 0.21 - 0.13\,n_f \right] + \alpha_s^2(\mu) \left[(18.39 \right.$$

$$-2.23\,n_f + 0.07\,n_f^2)L^2 + (1.33 - 0.35\,n_f + 0.02\,n_f^2)L + 22.60 - 1.23\,n_f + 0.02\,n_f^2 \bigg]$$

$$+\alpha_s^3(\mu) \left[(53.7 - 9.8\,n_f + 0.6\,n_f^2 - 0.01\,n_f^3)\,L^3 + (-6.7 + 0.6\,n_f - 0.07\,n_f^2 + 0.002\,n_f^3)\,L^2 \right.$$

$$+(236.6 - 23.9\,n_f + 0.8\,n_f^2 - 0.01\,n_f^3 + 15.0\,l_m)\,L - 22.3\,L_{US} + 3.0\,l_m - 1.5\,l_m^2$$

$$+21.0 + 5.0\,n_f - 0.3\,n_f^2 + 0.004\,n_f^3 + 0.0015\,a_3 + \frac{\delta_\epsilon}{\pi} \bigg], \tag{6}$$

where $L = \ln\left(\mu/(mC_F\alpha_s(\mu))\right)$, $L_{US} = \ln\left(e^{5/6}\mu/(2m\alpha_s^2(\mu))\right)$, $l_m = \ln(\mu/m)$, and n_f is the number of light quark flavors, $a_3{}^{\text{a}}$ is the constant part of the three loop QCD potential, and δ_ϵ is a contribution from the $\mathcal{O}(\epsilon)$ terms of the non-Coulomb potentials given by

$$\delta_\epsilon = C_F^2 \left(\frac{v_m^{(1,\epsilon)}}{8} + \frac{v_q^{(1,\epsilon)}}{12} + \frac{v_p^{(1,\epsilon)}}{8} \right) - \frac{C_F}{6} b_2^{(\epsilon)}. \tag{7}$$

The effect of δ_ϵ is estimated to be an order of magnitude smaller compared to other constant terms [1], so we neglect it in our phenomenological analysis. The $\ln^2 \alpha_s$ [6, 7] and $\ln \alpha_s$ [8, 9] logarithmic terms in eq.(6) are already known.

From the divergent part of the wave-function calculation, the corresponding scale dependence of c_3 is extracted.[b] The matching coefficient c_v reads

$$c_v = 1 - \frac{8}{3\pi}\alpha_s(m) + \left[-\frac{35}{27}\ln\frac{\mu^2}{m^2} + \frac{11n_f}{27\pi^2} - \frac{125\,\zeta(3)}{9\pi^2} - \frac{14\ln 2}{9} - \frac{89}{54\pi^2} - \frac{511}{324} \right]\alpha_s(m)^2$$

$$+ \left[\left(\frac{43}{36\pi} - \frac{35n_f}{162\pi} \right) \ln^2\frac{\mu^2}{m^2} + \left(\frac{1399\,n_f}{1944\pi} - \frac{2818}{405\pi} - \frac{85\ln 2}{9\pi} \right) \ln\frac{\mu^2}{m^2} + \frac{\delta c_3}{\pi^3} \right]\alpha_s(m)^3. \tag{8}$$

The constant part of δc_3 is not fully known up to now, but the fermionic correction was calculated in [10],

$$\delta c_{3,\,n_f} = n_f\,C_F\,T_F \left[39.6\,C_A + 46.7\,C_F - n_f\,T_F\left(\frac{163}{162} + \frac{4\pi^2}{27} \right) - T_F\left(\frac{557}{162} - \frac{26\pi^2}{81} \right) \right]. \tag{9}$$

The coefficient d_v is known from [11], and given by

$$d_v = 1 - \left[\frac{16}{9\pi}\left(1 + 3\ln\frac{\mu^2}{m^2} \right) \right]\alpha_s(\mu) + \cdots. \tag{10}$$

3   Residue of the QCD two-point function

Now we combine all pieces and show numerical formulae for the residue of the QCD two-point function. We use the same coupling $\alpha_s(\mu)$ [c] for the matching coefficient and the NRQCD wave-function to construct the scale-invariant physical residue Z_n.

---

[a] Only a Padé estimate [12] $a_{3,\,\text{Pade}} = 6240$ (for $n_f = 4$), 3840 (for $n_f = 5$) is known.

[b] The result of [8] has been checked and one term (+ typos) of c_3 was corrected in [2].

[c] In eq.(8) $\alpha_s(m)$ is re-expressed by $\alpha_s(\mu)$ using $\alpha_s(m)/\alpha_s(\mu) = 1 + \frac{\alpha_s(\mu)}{4\pi}\beta_0 \ln\frac{\mu^2}{m^2} + \left(\frac{\alpha_s(\mu)}{4\pi} \right)^2 \left(\beta_0^2 \ln^2\frac{\mu^2}{m^2} + \beta_1 \ln\frac{\mu^2}{m^2} \right) + \cdots$ where β_i are the coefficients of the QCD β-function in $\overline{\text{MS}}$-scheme, and $\alpha_s \equiv \alpha_s^{(n_f=4,5)}$ for the bottom and top quarks, respectively.
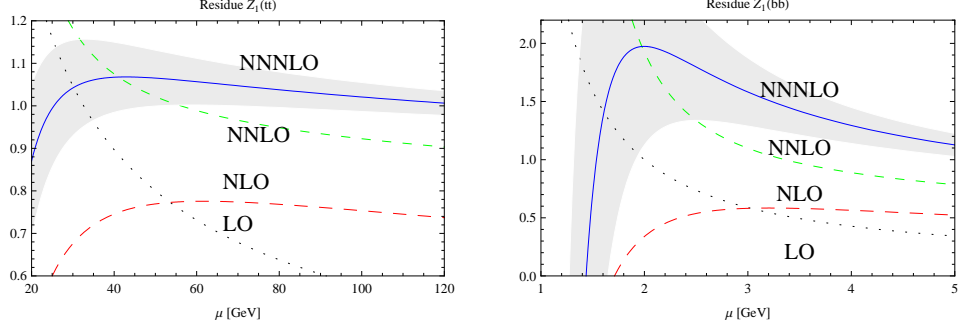
Figure 1: The scale dependence of the residue of the two-point function for the toponium (left) and bottomonium (right), normalized by its zeroth order value at $\mu = mC_F\alpha_s(\mu)$. The dotted line is LO and the solid line is NNNLO result.

For the ground state of top and bottom quarkonia, the residue is given by

$$Z_{1S(t\bar{t})} = \left\{ 1 + \left[3.66\,L - 2.13 \right]\alpha_s(\mu) + \left[8.93\,L^2 - 6.14\,L + 10.46 - 7.26\,l_m \right]\alpha_s^2(\mu) \right.$$

$$+ \left[18.17\,L^3 - 20.26\,L^2 + (110.82 - 11.57\,l_m)\,L - 22.27\,L_{US} - 16.35\,l_m^2 - 22.65\,l_m \right.$$

$$\left. \left. + (22.60 + 0.0015\,a_3 + 0.32\,\delta_\epsilon + 0.0645\,\delta c_3) \right]\alpha_s^3(\mu) \right\} \times |\psi_{1S(t\bar{t})}^{(0)}(0)|^2 , \qquad (11)$$

$$Z_{1S(b\bar{b})} = \left\{ 1 + \left[3.98\,L - 2.00 \right]\alpha_s(\mu) + \left[10.55\,L^2 - 6.51\,L + 11.19 - 7.44\,l_m \right]\alpha_s^2(\mu) \right.$$

$$+ \left[23.33\,L^3 - 23.12\,L^2 + (125.14 - 14.59\,l_m)\,L - 22.27\,L_{US} - 17.36\,l_m^2 - 26.61\,l_m \right.$$

$$\left. \left. + (17.44 + 0.0015\,a_3 + 0.32\,\delta_\epsilon + 0.0645\,\delta c_3) \right]\alpha_s^3(\mu) \right\} \times |\psi_{1S(b\bar{b})}^{(0)}(0)|^2 \qquad (12)$$

where $|\psi_{1S(Q\bar{Q})}^{(0)}(0)|^2 = (mC_F\alpha_s(\mu))^3/(8\pi)$ is the LO Coulomb wave-function. To see the numerical significance we plug the following values into the formulae: for the top quark, $m_t = 175$ GeV, $\mu = m_t\,C_F\,\alpha_s(\mu) = 32.62$ GeV; for the bottom quark, $m_b = 5$ GeV, $\mu = m_b\,C_F\,\alpha_s(\mu) = 2.02$ GeV. We use $a_3 = a_{3,\,\text{Pade}}$, and the unknown $\mathcal{O}(\epsilon)$ potentials as well as non-n_f term of δc_3 are set to zero. We obtain the following numbers for the toponium and bottomonium ground state at $\mu = mC_F\alpha_s(\mu)$,

$$Z_{1S(t\bar{t})} = \frac{(C_F\,m_t\,\alpha_s)^3}{8\pi}\left[1 - 2.13\,\alpha_s + 22.7\,\alpha_s^2 + \left(-38.8 + 5.8\,_{a3} + 37.6\,_{c3\,,nl} \right)\alpha_s^3 \right], \quad (13)$$

$$Z_{1S(b\bar{b})} = \frac{(C_F\,m_b\,\alpha_s)^3}{8\pi}\left[1 - 2.00\,\alpha_s + 17.9\,\alpha_s^2 + \left(-8.8 + 9.4\,_{a3} + 30.3\,_{c3\,,nl} \right)\alpha_s^3 \right], \quad (14)$$

where the coupling constant is $\alpha_s = 0.14,\ 0.304$ for the top and bottom quarkonia, respectively.

In Fig.1 we show the scale dependence of the ground-state pole residue for toponium and bottomonium. For the NNNLO lines δc_3 is set to zero, while the gray band indicates

the size of the contribution from the constant part of c_3; the upper/lower edge of the band is obtained by taking fermionic corrections $\delta c_{3,\,n_f}/-\delta c_{3,\,n_f}$ as an estimate of δc_3.[d] We observe that the scale dependence of the toponium wave-function is reduced significantly at NNNLO compared to NNLO as was also observed in renormalization group improved NNLO calculation [13, 14]. Its precise value will be fixed only once the third order matching coefficient is completely known. Since the threshold cross section is dominated by the ground-state contribution, we expect that the scale dependence of the $t\bar{t}$ threshold cross section will be also improved at NNLO. For the bottomonium wave-function, strong scale dependence remains even at NNNLO and the perturbative expansion may be out of control. Only if the constant part of the matching coefficient δc_3 is negative in total, the scale dependence of the bottomonium wave-function at the origin might be acceptable. The complete knowledge of c_3 is thus mandatory to draw the final conclusion on the size of NNNLO correction.

Acknowledgments

References

[1] M. Beneke, Y. Kiyo and K. Schuller, arXiv:0705.4518 [hep-ph].

[2] M. Beneke, Y. Kiyo and A. A. Penin, Phys. Lett. B **653** (2007) 53 [arXiv:0706.2733 [hep-ph]].

[3] M. Beneke and V. A. Smirnov, Nucl. Phys. B **522** (1998) 321 [arXiv:hep-ph/9711391].

[4] M. Beneke, Y. Kiyo and K. Schuller, Nucl. Phys. B **714** (2005) 67 [arXiv:hep-ph/0501289].

[5] A. A. Penin, V. A. Smirnov and M. Steinhauser, Nucl. Phys. B **716** (2005) 303 [arXiv:hep-ph/0501042].

[6] B. A. Kniehl and A. A. Penin, Nucl. Phys. B **577** (2000) 197 [arXiv:hep-ph/9911414].

[7] A. V. Manohar and I. W. Stewart, Phys. Rev. D **63** (2001) 054004 [arXiv:hep-ph/0003107].

[8] B. A. Kniehl, A. A. Penin, M. Steinhauser and V. A. Smirnov, Phys. Rev. Lett. **90** (2003) 212001; Erratum *ibid.* 91 (2003) 139903 [arXiv:hep-ph/0210161].

[9] A. H. Hoang, Phys. Rev. D **69** (2004) 034009 [arXiv:hep-ph/0307376].

[10] P. Marquard, J. H. Piclum, D. Seidel and M. Steinhauser, Nucl. Phys. B **758** (2006) 144 [arXiv:hep-ph/0607168].

[11] M. E. Luke and M. J. Savage, Phys. Rev. D **57** (1998) 413 [arXiv:hep-ph/9707313].

[12] F. A. Chishtie and V. Elias, Phys. Lett. B **521** (2001) 434 [arXiv:hep-ph/0107052].

[13] A. H. Hoang, A. V. Manohar, I. W. Stewart and T. Teubner, Phys. Rev. D **65** (2002) 014014 [arXiv:hep-ph/0107144].

[14] A. Pineda and A. Signer, Nucl. Phys. B **762** (2007) 67 [arXiv:hep-ph/0607239].

---

[d]By looking at constant part of the $c_v^{(2)}$, the non-fermionic correction is larger than the fermionic correction in magnitude and the sign is opposite. With this observation, a naive guess for c_3 is that the NNNLO line in the figure is most likely to be shifted down when the full constant part of c_3 is taken into account.

Towards a Monte Carlo Event Generator for $t\bar{t}$ production at threshold

Filimon Gournaris[1][*] and Stewart T. Boogert[2]

1- University College London, Department of Physics and Astronomy
Gower Street, London WC1E 6BT, UK

2- Royal Holloway University of London, Department of Physics
Egham, Surrey TW20 0EX, UK

One of the most important physics targets for the ILC will be the precision measurements of the top quark properties, and especially the top quark mass. Top-antitop production at threshold provides the ideal environment for making such measurements but is complicated by the machine's luminosity spectrum and thus needs to be carefully studied to understand the constraints involved and the potential precision reach. We present recent developments in the tools needed to make such studies, and in particular, progress towards a NNLO $t\bar{t}$ event generator at threshold with luminosity spectrum effects included.

1 Introduction

The measurement of top quark properties (mass, width, couplings) are some of the guaranteed highlights of the ILC physics program. The most promising method for these measurements is performing an energy scan around the $t\bar{t}$ production threshold ($\sqrt{s} \approx 350 GeV$). From the location and rise of the cross section lineshape, information about the top quark mass can be obtained, while from the shape and normalization one can extract information about the top quark width (Γ_t), the strong coupling constant (α_s) and the top-Yukawa coupling (y_t).

The main complication with such a measurement comes from the machine's luminosity spectrum. At the ILC, the distribution of luminosity as a function of real collision energy $d\mathcal{L}/dE$, called the luminosity spectrum, is a consequence of various energy loss mechanisms such as initial state radiation, beamstrahlung and machine energy spread. How the three components contribute to the luminosity spectrum can be seen in figure 1.

The luminosity spectrum directly affects the experimental cross section by the relation :

$$\sigma_{t\bar{t}}^{obs}(\sqrt{s}) = \int_0^1 dx_1 dx_2 \, \mathcal{L}(x_1, x_2, \sqrt{s}) \times \sigma_{t\bar{t}}^{th}(x_1, x_2, \sqrt{s}) \tag{1}$$

where $\sigma_{t\bar{t}^{obs}}$ is the experimental cross section, $\sigma_{t\bar{t}^{th}}$ is the theoretical cross section, $\mathcal{L}$ is the machine's luminosity spectrum and $x = \sqrt{s}/\sqrt{s_0}$ the scaled centre of mass energy.

The effect this has on the $t\bar{t}$ cross section can be seen in figure 1 where the three components of the luminosity spectrum have been simulated and applied to the theoretical cross section. The resonant-like structure that is present in the theoretical cross section curve flattens out in the observed one.

In order to make high precision top quark measurements using a threshold scan at the ILC, it is very important to have a precise understanding of both the theoretical quantities and the luminosity spectrum of the machine.

---

[*]fg@hep.ucl.ac.uk
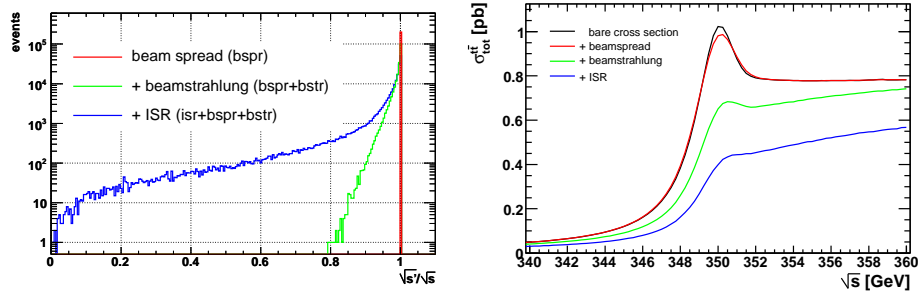
Figure 1: Left - The three components of the luminosity spectrum. Right - Smearing the $t\bar{t}$ cross section with the different components of the luminosity spectrum.

2   Threshold Simulations

In the past, a lot of effort has gone towards the understanding of the theoretical aspects [2, 3, 4, 5] of the top quark threshold at the ILC. On the experimental side, there have been studies [6, 7, 8] examining the impact of the luminosity spectrum on such a measurement. However, these studies were done in a naive way by smearing the theoretical cross section (using Eqn. 1) with a simulated luminosity spectrum or by moving on to a simpler form for the top threshold [9].

So far no studies have been done at the event by event level, examining the effect the luminosity spectrum could have on a detailed simulation of the measurement. The reason for this is that so far no event generator existed that could precisely describe the $t\bar{t}$ threshold. This is manifested in figure 2, where the cross section prediction for the threshold region from general purpose event generators (in this case Pandora [10] and Herwig [11]) are compared with a high precision (NNLO in QCD) calculation [3].

A further argument for going to fully differential event generator based simulations of the $t\bar{t}$ threshold is that for top quark studies, except from the total cross section, information also exist in the top quark momentum distributions [12]

Figure 2: Comparison of $t\bar{t}$ cross section predictions from Pandora, Herwig and NNLO QCD calculation by TOPPIK [3].

by using the forward-backward assymetry A_{FB} and the location of the peak in the top momentum distribution P_{peak}[6]. The top momentum distributions are sensitive to the top quark mass M_t and strong coupling constant α_s, but not on the top quark width Γ_t thus having different correlations of these three quantities than the cross section (which does depend on Γ_t). So they can provide another useful observable for disentangling the measured quantities and reducing the errors on the measurement. Also, the integral of Eqn. 1 does not include relativistic boost effects which will modify the experimental distributions and hence the sensitivity to observables such as A_{FB} and P_{peak}.

Furthermore, the process $e^+e^- \rightarrow t\bar{t}$ also contains information about the electroweak

sector through the sensitivity to the γ and Z couplings [12]. This would manifest itself in the angular distribution of the top quarks which would also require a fully differential study of the process. It is therefore fundamental for the $t\bar{t}$ threshold that a fully differential event generator based study that includes the effects of the luminosity spectrum is performed.

3 $t\bar{t}$ threshold event generator

The QCD NNLO code TOPPIK [3] was choosen as the calculation program of the generator due to its high order calculation, the simplicity and availability of the Fortran code and the availability of corrections (NNLL for total cross section [4], NLO for rescattering corrections [5]). TOPPIK performs a fully differential calculation by solving the Lippmann-Schwinger equation in momentum space resulting in two sets of Green functions, one for the S-wave and one for the P-wave contributions accounting for the vector and axial-vector current contributions to the process, which encode all the information about the $t\bar{t}$ system.

The problem with using TOPPIK as an event generator is that it is too slow[a] in calculating the quantities required by Eqn. 1 for any one phase space point ($\sqrt{s}, M_t, \Gamma_t, \alpha_s, M_H$). This makes it impossible to use in applications such as the variable energy system of Eqn. 1 as speed is essential both for large scale event generation and for fitting.

This problem is solved by the use of a multidimensional interpolation technique. By precalculating and storing a look up table of Green functions over the required phase space (i.e. $\sqrt{s}, M_t, \Gamma_t, \alpha_s$) and performing interpolations on these quantities for every future call to TOPPIK, a relative speed-up of $\times 5$ for interpolations in all parameters, and $\times 10^6$ for interpolations in only $\sqrt{s}$ is achieved.

For the generation procedure, the monte carlo integration is done using the general purpose adaptive simulator FOAM [15] by integrating over all phase space variables and weighting the generation by the integral of Eqn. 1.

This should result into events being produced according to the correct weight of the luminosity spectrum folded cross section. The top plot of figure 3 shows the average weight for 10^4 events at each point in $\sqrt{s}$ compared to the theoretical and experimental cross sections (beamstrahlung only). There is reasonable agreement between the smeared cross section and the generator based events upto the peak of the curve. The reason for disagreement beyond the peak is that FOAM is not optimized for integrating highly peaked distributions such as the luminosity spectrum. This problem has been encountered in the past and a
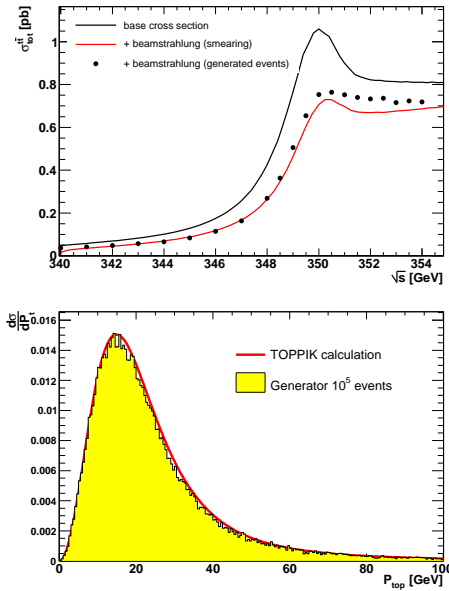
Figure 3: Top - Cross section with beamstrahlung using smearing and generator. Bottom - t Comparison of momentum distribution (no energy loss).

---

[a]More than 1.5sec per event calculation.

solution is possible by optimizing FOAM [15].

The generator produces $t\bar{t}$ pairs which are boosted according to any assymetry in beam energy and then decayed to b quarks and W's following a 2-body decay. The top momentum distribution for 10^5 generated events can be seen in the bottom plot of figure 3. There is good agreement between the calculated and generator based momentum distributions. This comparison was done by considering only the S-wave part of the process. Inclusion of the P-wave contribution and interference terms is trivial.

The resulting bW pairs will be given to a general purpose hadronization package (e.g. Pythia [14]) for further decays and hadronization. The interface of the NNLO calculation to QCD parton shower models should be simple because due to the large width of the top quark, its lifetime is very small thus suppressing QCD radiation which would complicate the interface of the different order calculations (double-counting etc.).

4   Summary

The effort towards a $t\bar{t}$ threshold event generator with luminosity spectrum effects included was presented. This is important both for a detailed study of the precision reach of the ILC at the $t\bar{t}$ threshold, but also to understand the effect of the luminosity spectrum on the event by event basis and the requirements on the luminosity spectrum and beam energy measurements for precision threshold physics ($t\bar{t}$, W^+W^-, SUSY thresholds etc.) at the ILC.

Acknowledgments

References

[1] Slides:
http://ilcagenda.linearcollider.org/contributionDisplay.py?contribId=187&sessionId=85&confId=1296

[2] M.J. Strassler and M.E. Peskin, Phys. Rev. **D43**, 1500 (1991)

[3] A.H. Hoang and T. Teubner, Phys. Rev. **D60**, 114067 (1999)

[4] A.H. Hoang et al., Phys. Rev. **D65**, 14014 (2002)

[5] R. Harlander et al., Z. Phys. **C73**, 477 (1996)

[6] M. Martinez and R. Miquel, Eur. Phys. J. **C27**, 49 (2003)

[7] D. Cinabro, *The ttbar Threshold and Machine Parameters at the NLC*, LCWS99 Proceedings, [arXiv: hep-ex/0005015] (2000)

[8] S.T. Boogert, talk given at the ECFA LC workshop, Durham, UK, Sept. 1-4, 2004

[9] K. Fujii, T. Matsui and Y. Sumino, Phys. Rev. **D50**, 4341 (1994)

[10] http://www.slac.stanford.edu/~mpeskin/LC/pandora.html

[11] G. Marchesini, B.R. Webber, G. Abbiendi, I.G. Knowles, M.H. Seymour and L. Stanco, Computer Physics Communications **67**, 465 (1992)

[12] A.H. Hoang, talk given at Workshop on Physics and Detectors for Future e^+e^- Linear Colliders, Keystone, Colorado, USA, Sept. 26-29, 1998

[13] S.T. Boogert and F. Gournaris, *Determination of $d\mathcal{L}/dE$ and total CM energy*, These proceedings.

[14] T. Sjöstrand et al. JHEP **05**, 026 (2006), [arXiv: hep-ph/0603175]

[15] S. Jadach, Comput. Phys. Commun. **152**, 55 (2003) [arXiv: physics/0203033]

Scalar Top Studies from Morioka'95 to DESY'07

A. Sopczak[1]*, A. Finch[1], A. Freitas[2], H. Nowak[3], C. Milsténe[4], M. Schmitt[5]

1- Lancaster U., 2- Zurich U., 3- DESY, 4- Fermilab, 5- Northwestern U.

Scalar top studies at the ILC are reviewed from initial sensitivity studies to a new precision mass determination method.

1   Introduction

Scalar top quarks have been studied in the framework of the ILC for more than a decade. In the following the developments since the International Linear Collider (ILC) workshop in Morioka 1995, where detection sensitivity was demonstrated, to recent precision mass determinations are presented. The interplay with accelerator and detector aspects is addressed through the importance of beam polarization for the accuracy of scalar top mass and mixing angle determination, and c-quark tagging for the vertex detector development. Different methods of scalar top mass determinations are addressed. Particular attention is given to the scenario of small stop-neutralino mass differences. The importance of scalar top studies at the ILC for the determination of the Cold Dark Matter (CDM) rate is emphasized. A new precision mass determination method, using two center-of-mass energies, one near the production threshold, improves significantly the scalar top mass, as well as the CDM prediction. The signal signature is two charm jets and missing energy from the process $e^+e^- \rightarrow \tilde{t}_1\bar{\tilde{t}}_1 \rightarrow c\tilde{\chi}_1^0\bar{c}\tilde{\chi}_1^0$.

2   Early Studies

A detection sensitivity with more than about 7σ ($\sigma = S/\sqrt{B}$), where S is the number of expected signal and B background events was demonstrated at the Linear Collider workshop in Morioka 1995 [1], as illustrated in Fig. 1.

3   Developments from Morioka'95 to Sitges'99 to Jeju'02

At Morioka'95 the initial sensitivity was demonstrated for a luminosity of 10 fb^{-1} and $\sqrt{s} = 500$ GeV using a LEP detector modeling. Higher luminosities (500 fb^{-1}) have been assumed based on the accelerator developments and presented at Sitges'99 [2]. In addition, an Iterative Discriminant (IDA) method was applied to separate expected signal and background events [2]. Figure 1 shows also the improvements in mass and mixing angle determination ($m_{\tilde{t}_1} = 180.0 \pm 1.0$ GeV) including e^- beam polarization and the SGV detector modeling. Subsequently, the SIMDET detector description was used. Slightly higher precision was obtained in the neutralino channel including e^- and e^+ beam polarization ($m_{\tilde{t}_1} = 180.0 \pm 0.8$ GeV), and the chargino decay mode was studied ($m_{\tilde{t}_1} = 180.0 \pm 0.5$ GeV) [3].

4   Major Challenge to Develop a Vertex Detector for the ILC

During the LEP era (1989-2000 data-taking) the tagging of b-quarks with a vertex detector was a major ingredient for many searches. The importance of c-quark tagging for scalar top studies was realized. Key aspects are the distance between the interaction point and the innermost layer of the vertex detector (radiation hardness, beam background) and the

---

*Email: andre.sopczak@cern.ch
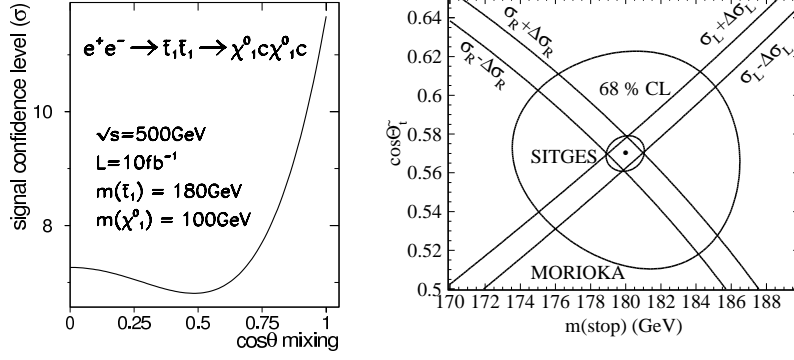
Figure 1: Left: initial sensitivity for scalar top quarks from the Morioka'95 workshop. Right: improvements of mass and mixing angle determination from Morioka'95 to Sitges'99.

material absorption length (multiple scattering). A realistic vertex detector concept from the LCFI collaboration was implemented for c-quark tagging in the scalar top studies. Such a detector could consist of 5 CCD layers at 15, 26, 37, 48 and 60 mm, each layer with $< 0.1\%$ absorption length.

The importance of the vertex detector was studied with two different vertex detector configurations, one with 4 layers (removing the innermost layer), and the other one with 5 layers. The study was performed at $\sqrt{s} = 500$ GeV for a scenario with large visible energy in the detector (Fig. 2) [4] ($m_{\tilde{t}_1} = 220.7$ GeV and $m_{\tilde{\chi}_1^0} = 120$ GeV), and one with small visible energy ($m_{\tilde{t}_1} = 122.5$ GeV and $m_{\tilde{\chi}_1^0} = 107.2$ GeV) leading to very similar results [5]. The innermost layer has a large effect on the c-tagging performance, while doubling the detector thickness has a small effect.
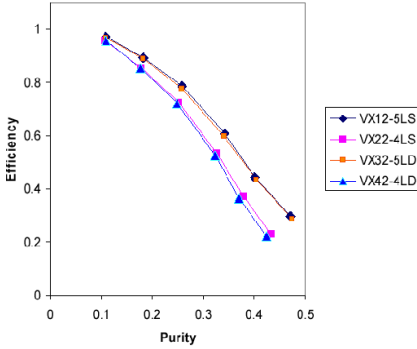
Figure 2: Scalar top c-tagging efficiency and purity with Weν background for different detector designs. The VX$_{12}$ curve is for a detector design with 5 layers (innermost at 15 mm) and single density, curve VX$_{22}$ is for a detector design with 4 layers (innermost at 26 mm). Curves VX$_{32}$ and VX$_{42}$ are for double density (0.128% absorption length per layer) with 4 and 5 layers, respectively.

5   Signal Scenarios

In order to investigate different detector scenarios and applying benchmark reactions for large and small visible energy three scalar top scenarios have been studied:

- For a comparison between different detector descriptions (SGV and SIMDET simulation packages) previous studies used $m_{\tilde{t}_1} = 180$ GeV and $m_{\tilde{\chi}_1^0} = 100$ GeV.

- At the Snowmass'01 workshop the SPS-5 benchmark was established using MSSM parameters yielding $m_{\tilde{t}_1} = 220.7$ GeV and $m_{\tilde{\chi}_1^0} = 120$ GeV.

- A cosmology motivated scenario has been studied in detail $m_{\tilde{t}_1} = 122.5$ GeV and $m_{\tilde{\chi}_1^0} = 107.2$ GeV, including a sequential-cut-based analysis and using the IDA method.

In the first two scenarios the stop-neutralino mass difference is large and thus large visible energy is expected in the detector, while in the third scenario small visible energy is expected [7]. The stop decay mode is always $\tilde{t}_1 \rightarrow \tilde{\chi}_1^0 c$.

6 Typical Analysis Strategy

Since the study for the Jeju'02 workshop the basic analysis strategy remained unchanged and signal and background processes have been generated for 500 fb^{-1} and $\sqrt{s} = 500$ GeV. A detector simulation (SIMDET) has been applied and a neural-network-based c-quark tagging algorithm has been used. The event selection has been performed with a sequential-cut-based analysis and an Iterative Discriminant Analysis (IDA).

7 Four Different Methods of Mass Determination

Four different methods of mass determination were studied. Two methods, which use the IDA for optimization of the signal to background ratio, are: a) stop cross-section determination with different beam polarizations (Fig. 3), and b) threshold dependence of production cross-section. Two cut-based selections were used in order to minimize the distortion of final state observables: c) endpoint of jet energy spectrum, and d) minimum mass of jets. These methods were discussed for the SPS-5 benchmark ($m_{\tilde{t}_1} = 220.7$ GeV) [6] and results are summarized also in Fig. 3.

Method	$\Delta m_{\tilde{t}_1}$ (GeV)	luminosity
Polarization	0.57	$2 \times 500\,\mathrm{fb}^{-1}$
Threshold scan	1.2	$300\,\mathrm{fb}^{-1}$
End point	1.7	$500\,\mathrm{fb}^{-1}$
Minimum mass	1.5	$500\,\mathrm{fb}^{-1}$
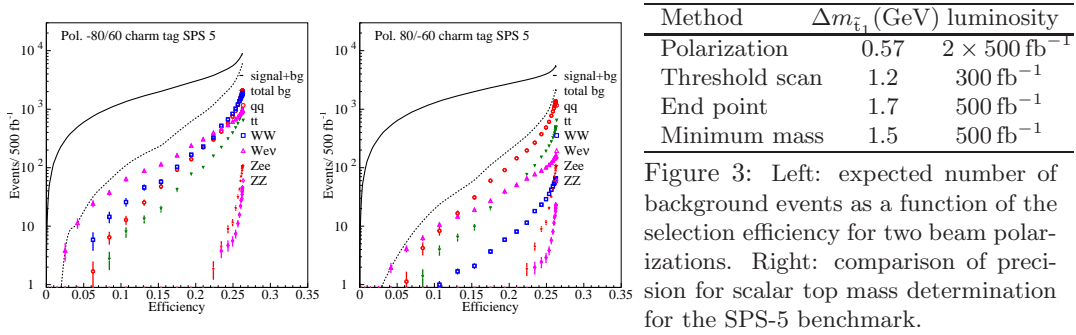
Figure 3: Left: expected number of background events as a function of the selection efficiency for two beam polarizations. Right: comparison of precision for scalar top mass determination for the SPS-5 benchmark.

8 Small Stop-Neutralino Mass Difference

A small stop-neutralino mass difference is motivated by cosmological aspects, baryogenesis $m_{\tilde{t}_1} < m_t$ and Dark Matter where $\tilde{\chi}_1^0$ is the Cold Dark Matter (CDM) candidate. A CDM rate consistent with observations is expected for a small $\tilde{t}_1 - \tilde{\chi}_1^0$ mass difference (co-annihilation). The discovery reach is shown for $m_{\tilde{t}_1} = 122.5$ GeV and $m_{\tilde{\chi}_1^0} = 107.2$ GeV [7] (Fig. 4).

For this small-mass-difference benchmark the determination of stop mass and mixing angle were performed as for the previously described large mass difference scenario. In the case of e^- and e^+ polarization $\Delta m_{\tilde{t}} = 1.0$ GeV and $|\cos\theta_{\tilde{t}}| < 0.074$ was obtained, while for e^- polarization only $\Delta m_{\tilde{t}} = 1.25$ GeV and $|\cos\theta_{\tilde{t}}| < 0.091$ was achieved [7].

For the CDM interpretation the following systematic uncertainties were taken into account: $\Delta m_{\tilde{\chi}_1^0} = 0.3$ GeV, polarization $\Delta P(e^{\pm})/P(e^{\pm}) = 0.5\%$, background rate $\Delta B/B = 0.3\%$, scalar top hadronization and fragmentation ($< 1\%$), c-quark tagging ($< 0.5\%$), detector calibration ($< 0.5\%$), and beamstrahlung: ($< 0.02\%$). The sum of the systematic uncertainties is 1.3% (left-handed beam polarization) and 1.2% (right-handed beam polarization) without the theory error on the cross-section. As the total systematic uncertainty is similar to the statistical uncertainty, a reduction to 0.8% was assumed being the same as
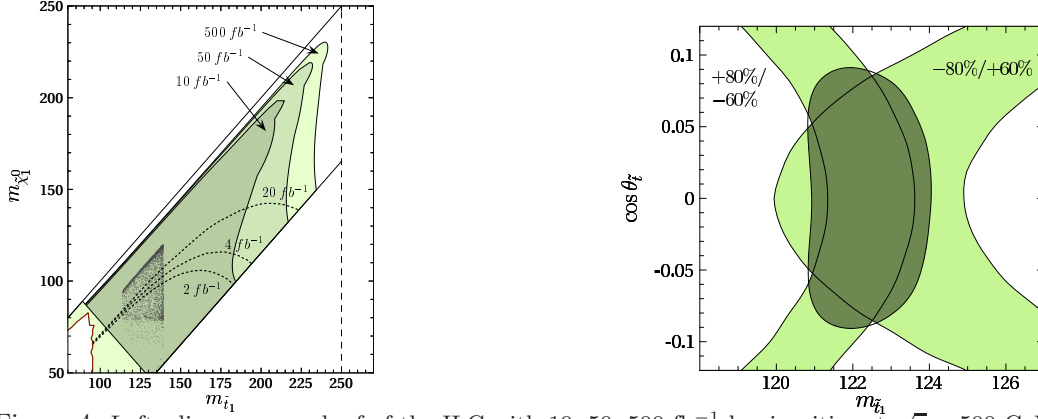
Figure 4: Left: discovery reach of of the ILC with 10, 50, 500 fb^{-1} luminosities at $\sqrt{s} = 500$ GeV for the reaction $e^+e^- \to \tilde{t}_1\bar{\tilde{t}}_1 \to c\tilde{\chi}_1^0\bar{c}\tilde{\chi}_1^0$. The results are given in the stop vs. neutralino mass plane. In the gray shaded region, a 5σ discovery is possible. The region $m_{\tilde{\chi}_1^0} > m_{\tilde{t}_1}$ is inconsistent with a neutralino as Lightest Supersymmetric Particle (LSP), while for $m_{\tilde{t}_1} > m_W + m_b + m_{\tilde{\chi}_1^0}$ the three-body decay $\tilde{t}_1 \to W^+\bar{b}\tilde{\chi}_1^0$ becomes accessible and dominant. In the light shaded corner to the lower left, the decay of the top quark into a light stop and neutralino is open. The dark gray dots indicate the region consistent with baryogenesis and dark matter. Also shown are the parameter region excluded by LEP searches (white area in the lower left corner) and the Tevatron light stop reach (dotted lines) for various integrated luminosities. Right: Determination of light stop mass $m_{\tilde{t}_1}$ and stop mixing angle $\theta_{\tilde{t}}$ from measurements of the cross-section $\sigma(e^+e^- \to \tilde{t}_1\bar{\tilde{t}}_1)$ for beam polarizations $P(e^-)/P(e^+) = -80\%/ + 60\%$ and $+80\%/ - 60\%$. Statistical and systematic errors are included.

the statistical uncertainty, taking into account the LEP experience. Including the expected theory uncertainty $m_{\tilde{t}_1} = 122.5 \pm 1.2$ GeV was achieved. The resulting CDM prediction included all parameters and their errors. The stop mass uncertainty is dominant for the CDM co-annihilation precision.

9   New Precision Mass Determination

In order to improve the mass resolution, a new method has been proposed to measure the stop cross-section at two center-of-mass energies, one of them near the kinematic threshold where the cross-section is very sensitive to the stop mass, and the other near the expected maximum production cross-section [8]. The center-of-mass energies $\sqrt{s} = 260$ GeV and $\sqrt{s} = 500$ GeV are chosen. This study also includes a more detailed description of the stop hadronization and fragmentation in the event simulation. Details are given in Ref [9]. For the event selection a sequential-cut-based analysis and the IDA method have been applied.

Both the sequential-cut-based analysis and the IDA method lead to small statistical uncertainties resulting in $\Delta m_{\tilde{t}_1} < 0.2$ GeV and thus systematic uncertainties are particularly important to evaluate. Three classes of systematic uncertainties are distinguished:

- instrumental uncertainties related to the detector and accelerator: detector calibration (energy scale), track reconstruction efficiency, charm-quark tagging efficiency, and integrated luminosity.

- Monte Carlo modeling uncertainty of the signal: charm and stop fragmentation effects. The Peterson fragmentation function in PYTHIA was used with $\epsilon_c = -0.031 \pm 0.011$ and $\epsilon_b = -0.0050 \pm 0.0015$, where $\epsilon_{\tilde{t}_1} = \epsilon_b(m_b/m_{m_{\tilde{t}_1}})$. Fragmentation effects increase the number of jets significantly and the importance of c-quark tagging is stressed in order to resolve the combinatorics.

- theoretical uncertainties on signal and background. Some improvement compared to the current loop calculation techniques is assumed, and an even larger reduction of this uncertainty is anticipated before the start of the ILC operation.

The systematic uncertainty using the IDA method from detector calibration (energy scale) is about twice as large (Table 1). This is because the sequential-cut-based analysis pays particular attention to cancellation of this uncertainty between the two analyses at the different center-of-mass energies. The uncertainties from other sources are about equal.

The assessment of the achievable stop mass precision is based on the statistical and systematic uncertainties on an observable Y which is constructed from ratios of luminosities, selection efficiencies and theoretical production cross-sections at the two center-of-mass energies. The IDA method has a smaller statistical uncertainty, and also a smaller background uncertainty due to a smaller number of expected background events. The expected stop mass uncertainty is inferred from the uncertainty on Y (Table 1), as given in Table 2.

Error source for Y	sequential cuts	IDA method
Statistical	3.1%	2.7%
Detector calibration	1.0%	2.1%
Charm fragmentation	0.5%	0.5%
Stop fragmentation	2.7%	2.8%
Sum of experimental systematics	3.0%	3.6%
Sum of experimental errors	4.3%	4.5%
Theory for signal cross-section	5.5%	5.5%
Theory for background cross-section	2.0%	1.1%
Total error ΔY	7.3%	7.2%

Table 1: Summary of statistical and systematic uncertainties on the observable Y.

	measurement error $\Delta m_{\tilde{t}_1}$ (GeV)	
Error category	sequential cuts	IDA method
Statistical	0.19	0.17
Sum of experimental systematics	0.18	0.22
Sum of experimental errors	0.26	0.28
Sum of all exp. and th. errors	0.45	0.45

Table 2: Estimated measurement errors (in GeV) on the stop quark mass.

10 Cold Dark Matter (CDM) Interpretation

The chosen benchmark parameters are compatible with the mechanism of electroweak baryogenesis [7]. They correspond to a value for the dark matter relic abundance within the WMAP bounds, $\Omega_{CDM}h^2 = 0.109$. The relic dark matter density has been computed as in Ref. [7][a]. In the investigated scenario, the stop and lightest neutralino masses are $m_{\tilde{t}_1} = 122.5$ GeV and $m_{\tilde{\chi}_1^0} = 107.2$ GeV, and the stop mixing angle is almost completely

---

[a]The assumed benchmark parameters changed slighty (larger slepton masses assumed) and thus $\Omega_{CDM}h^2$ changed from 0.1122 [7] to 0.109.
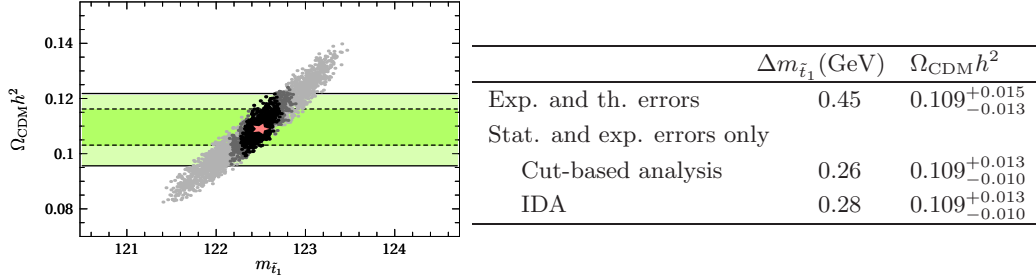
	$\Delta m_{\tilde{t}_1}$ (GeV)	$\Omega_{\mathrm{CDM}}h^2$
Exp. and th. errors	0.45	$0.109^{+0.015}_{-0.013}$
Stat. and exp. errors only		
Cut-based analysis	0.26	$0.109^{+0.013}_{-0.010}$
IDA	0.28	$0.109^{+0.013}_{-0.010}$

Figure 5: Left: expected dark matter relic abundance $\Omega_{\mathrm{CDM}}h^2$ taking into account detailed experimental errors for stop, chargino, neutralino sector measurements at the future ILC. The black dots correspond to a scan over the 1σ ($\Delta\chi^2 \leq 1$) region including the total expected experimental uncertainties (detector and simulation), the grey-dotted region includes also the theory uncertainty, and the light grey-dotted area are the previous results [7]. The red star indicates the best-fit point. The horizontal shaded bands show the 1σ and 2σ constraints on the relic density measured by WMAP. Right: estimated precision for the determination of stop mass and dark matter relic density for different assumptions about the systematic errors.

right-chiral. The improvement compared to Ref. [7] regarding the CDM precision determination is shown in Fig. 5 [8].

11   Conclusions

Over the last decade the studies on scalar top quarks evolved from first expected detection sensitivity (Morioka'95) to precision mass determination and Cold Dark Matter predictions. The e^- beam polarization is important for mass and mixing angle determination, and the e^+ polarization contributes in addition. Detector simulations include c-quark tagging as a benchmark for vertex detector design studies. Different detector descriptions (SIMDET and SGV) agree and dedicated simulations with SPS-5 parameters were performed. Simulations for small stop-neutralino mass difference have been performed including hadronization and fragmentation effects, leading to a larger number of jets. An important aspect of this cosmology-motivated benchmark scenario is to resolve the jet-combinatorics by identifying the c-quark jets. Precision mass determinations are possible with a method using two center-of-mass energies, e.g. $\sqrt{s} = 260$ and 500 GeV and the expected ILC precision on $\Omega_{\mathrm{CDM}}h^2$ is comparable to WMAP measurements. The ILC has a large potential to measure with precision scalar top quarks. Scalar top quark studies have addressed important questions related to accelerator and detector aspects. The proposed new method to measure the stop mass with higher precision can also be applied to many other searches for new particles.

References

[1] A. Sopczak, Talk "Supersymmetric Top Discovery Potential at a 500 GeV LC", Workshop on Physics and Experiments with Linear Colliders, Morioka, Japan, Proc. *Word Scientific* (1996) p. 571.

[2] A. Sopczak, Talk "Scalar Quark", Worldwide Workshop on the Future of e^+e^- Colliders, Sitges, Spain, Proc. *World Scientific* (2001) p. 347.

[3] A. Sopczak, Talk "Precision Measurements in the Scalar Top Sector of the MSSM", Worldwide Linear Collider Workshop, Jeju, Korea, Proc. *Sorim Press* (2003) p. 157.

[4] C. Milsténe and A. Sopczak, Econf C0508141:ALCPG1431, Snowmass'05 (2005).

[5] C. Milsténe and A. Sopczak, physics/0609017, Proc. LCWS'06, Bangalore, in press.

[6] A. Sopczak, SUSY'05, Durham, UK, published on-line, hep-ph/060213 (2006).

[7] M. Carena, A. Finch, A. Freitas, C. Milsténe, H. Nowak and A. Sopczak, Phys. Rev. **D72** (2005) 115008.

[8] A. Freitas, C. Milsténe, M. Schmitt and A. Sopczak, publication in preparation.

[9] C. Milsténe, A. Freitas, M. Schmitt and A. Sopczak, these proceedings.

Factorization Approach for Top Mass Reconstruction in the Continuum

Andre H. Hoang [1], Sean Fleming[2], Sonny Mantry[3], Iain W. Stewart[4]

1- Max-Planck-Institut für Physik, (Werner-Heisenberg-Institut)
Föhringer Ring 6, München, Germany, 80805 [*]

2- Department of Physics, University of Arizona, Tucson, AZ 85721, USA

3- California Institute of Technology, Pasadena, CA 91125, USA

4- Department of Physics, Massachusetts Institute of Technology, Boston, MA 02139, USA

Using effective theories for jets and heavy quarks it is possible to prove that the double differential top-antitop invariant mass distribution for the process $e^+e^- \to t\bar{t}$ in the resonance region for c.m. energies Q much larger than the top mass can factorized into perturbatively computable hard coefficients and jet functions and a non-perturbative soft function. For invariant mass prescriptions based on hemispheres defined with respect to the thrust axis the soft function can be extracted from massless jet event shape distributions. This approach allows in principle for top mass determinations without uncertainties from hadronization using the reconstruction method and to quantify the top mass scheme dependence of the measured top quark mass value.

1 Introduction

Precise measurements of the top quark mass are among the most important (standard) tasks of the ILC project as the top quark mass affects a number of interesting observables either directly or indirectly through quantum effects. To be useful such top mass measurements have to have small uncertainties, but also need to provide information to which mass scheme the measured number refers to. Both aims can be achieved from a threshold scan of the cross section $\sigma(e^+e^- \to t\bar{t})$ for $\sqrt{s} \approx 2m_t$, from which one expects measurements of the threshold masses, such as the 1S mass, with uncertainties of about 100 MeV [2, 3, 4, 5, 6]. Another method is based on mass reconstruction which relies on the idea that the peak of the invariant mass distribution of the top decay products is related to the top quark mass. This method can be applied at any c.m. energy and might also yield uncertainties well below 1 GeV [7]. However, until recently it was unknown for which mass scheme such measurements can be carried out with small theoretical uncertainties. This is because the naive relation between the observable peak of the invariant mass distribution and the perturbative top quark propagator pole is affected by hard (i.e. computable) as well as soft (i.e. non-perturbative) QCD effects and the present MC tools do not contain the required information in a systematic form. Obviously the top mass measurements at the LHC [9] suffer from the same problem, but the associated theoretical systematic uncertainty might be considerably larger than at the ILC.

2 Factorization Theorem

In Ref. [8] a theoretical formalism was presented which remedies this situation, as a first step, for the Linear Collider framework, where one does not need to account for QCD radiation

---

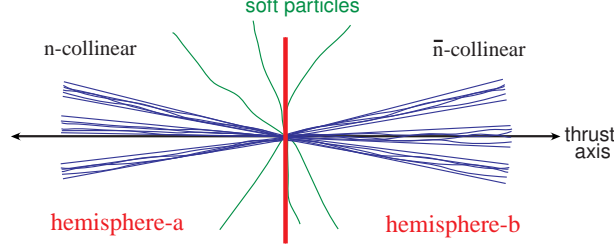[*]Electronic address: ahoang@mppmu.mpg.de

Figure 1: Six jet event initiated by a top quark pair, $t\bar{t} \to bW\bar{b}W \to bqq'\bar{b}qq'$. The plane separating the two hemispheres is perpendicular to the thrust axis and intersects the thrust axis at the interaction point. The total invariant mass inside each hemisphere is measured. Our analysis applies equally well to the lepton+jets and the dilepton channels (not shown).

arising from the initial state. Assuming a c.m. energy $Q \gg m_t$, m_t being the top quark mass, one can employ the hierarchy of scales

$$Q \gg m_t \gg \Gamma_t > \Lambda_{\mathrm{QCD}} \tag{1}$$

to establish a factorization theorem for the doubly differential top-antitop invariant mass distribution in the peak region around the top resonance:

$$\frac{d^2\sigma}{dM_t^2 \, dM_{\bar{t}}^2}\,, \qquad M_{t,\bar{t}}^2 - m^2 \sim m\,\Gamma \ll m^2\,. \tag{2}$$

The invariant masses $M_t^2 = (\sum_{i \in X_t} p_i^\mu)^2$, $M_{\bar{t}}^2 = (\sum_{i \in X_{\bar{t}}} p_i^\mu)^2$ depend on a prescription $X_{t,\bar{t}}$ which associates final state momenta p_i^μ to top and antitop invariant masses, respectively. For invariant masses in the resonance region the events are characterized by energy deposits predominantly contained in two back-to-back regions with opening angles m_t/Q associated with the energetic jets or leptons from the top decay plus collinear radiation, and by additional soft radiation populating the regions between the jets, see Fig. 1. We assume that the prescriptions $X_{t,\bar{t}}$ assign all soft radiation to either M_t^2 or $M_{\bar{t}}^2$ where the probability of radiation being assigned to X_t or $X_{\bar{t}}$ increases to unity when it approaches the top or antitop direction. The result for the double differential cross-section in the peak region at all orders in α_s and to leading order in the power expansion in $m_t \alpha_s/Q$, m_t^2/Q^2, Γ_t/m_t and $M_{t,\bar{t}} - m_t$ is given by [8]

$$
\begin{aligned}
\frac{d\sigma}{dM_t^2 \, dM_{\bar{t}}^2} &= \sigma_0 \, H_Q(Q, \mu_m) H_m\Big(m_J, \frac{Q}{m_J}, \mu_m, \mu\Big) \qquad\qquad \left[\hat{s}_{t,\bar{t}} = \frac{M_t^2 - m_J^2}{m_J}\right] \\
&\times \int d\ell^+ d\ell^- B_+\Big(\hat{s}_t - \frac{Q\ell^+}{m_J}, \Gamma_t, \mu\Big) \, B_-\Big(\hat{s}_{\bar{t}} - \frac{Q\ell^-}{m_J}, \Gamma_t, \mu\Big) S(\ell^+, \ell^-, \mu)\,. \tag{3}
\end{aligned}
$$

In Eq. (3) the normalization factor σ_0 is the total Born-level cross-section, the H_Q and H_m are perturbative coefficients describing hard effects at the scales Q and m_J, $B_\pm$ are perturbative jet functions that describe the evolution and decay of the the top and antitop close to the mass shell, and S is a nonperturbative soft function describing the soft radiation between the jets. The result was derived using the hierarchy of scales (1), matching QCD onto
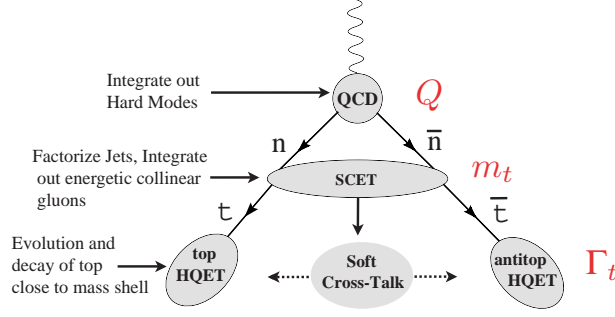
Figure 2: Sequence of effective field theories used to compute the invariant mass distribution.

(Soft-Collinear Effective Theory) SCET [10] at the scale $\mu = Q$, which in turn is matched onto (Heavy Quark Effective Theory) HQET [11] at a scale μ_m of order m_t generalized for unstable particle effects associated to the large top width Γ_t [12]. An illustration of this scheme is shown in Fig. 2. For details on the (admittedly non-trivial) derivation and on technical aspects of the factorization theorem we refer to Ref. [8]. In the following we will discuss the important ingredients of the factorization theorem and their physical interpretation and show what we can learn from them concerning the measurements of the top quark mass from the reconstruction method.

3   Jet Functions and Short-Distance Top Mass

The coefficients H_Q and H_m in Eq. (3) arise from matching and running in SCET and HQET down to the low energy scale μ where one evaluates the jet functions $B_\pm$ and the soft function S. These hard coefficients only affect the overall normalization of the invariant mass distribution and we will therefore not talk about them here. So let us concentrate on the jet and the soft functions, which determine the shape of the distribution and the location of the resonance peak. The jet functions describe the perturbative contributions of the shape of the invariant mass distribution and are defined by the imaginary part of a T-product vacuum matrix element. For the top quark it is

$$B_+(\hat{s}_t, \Gamma_t, \mu) \;\; = \;\; \mathrm{Im}\left[\,\frac{-i}{4\pi N_c m_J}\int d^4x\, e^{ir\cdot x}\,\big\langle 0\big|T\{\bar{h}_{v_+}(0)W_n(0)W_n^\dagger(x)h_{v_+}(x)\}\big|0\big\rangle\right]\,,\;\;(4)$$

where v_+ is the top four velocity ($v_+^2 = 1$) and $\hat{s}_t = 2v_+.r$ and h_{v_+} is the (HQET) heavy top quark field. The vacuum matrix element also contains Wilson lines of the form

$$W_n^\dagger(x) = \mathrm{P}\,\exp\left(ig\int_0^\infty ds\,\bar{n}\cdot A_+(\bar{n}s+x)\right),\;\; W_n(x) = \overline{\mathrm{P}}\,\exp\left(-ig\int_0^\infty ds\,\bar{n}\cdot A_+(\bar{n}s+x)\right),$$

where $\bar{n}$ is a light-like four vector pointing in the antitop direction and A_+ is field describing a gluon that is collinear to the quark. Up to the Wilson lines the vacuum matrix element is in fact a heavy quark propagator and, indeed, at tree-level it is just

$$B_\pm^{\mathrm{tree}}(\hat{s}, \Gamma_t) = \mathrm{Im}\left[\frac{-1}{\pi m_J}\,\frac{1}{\hat{s} - 2\delta m + i\Gamma_t}\right] = \frac{1}{\pi m_J}\,\frac{\Gamma_t}{(\hat{s} - 2\delta m)^2 + \Gamma_t^2}\,,$$

which is the imaginary part of the heavy quark propagator supplemented by a constant width term and describing a Breit-Wigner distribution having a width Γ_t. The residual mass term δm becomes relevant at higher orders and controls the mass scheme that is used. For the pole mass scheme $\delta m = 0$ to all order in α_s. It is the width term (which we can approximate as a constant since we are interested in the resonance region) that allows us to use perturbation theory for computing the jet function. To understand the role of the Wilson lines recall that the two-point function of simple heavy quark fields, evaluated off-shell, is not gauge invariant, a fact that becomes e.g. apparent from the gauge parameter dependence of the perturbative corrections. The jet functions $B_\pm$, however, are gauge-invariant due to the Wilson lines and well-defined *physical* objects. Physically the Wilson lines describe gluons radiated from the antitop (moving along the four vector $\bar{n}$) that are collinear to the top quark (moving along v_+), and it this additional radiation that renders the jet function gauge-invariant and physically meaningful. In momentum space the Wilson lines lead to additional Feynman diagrams having $1/(n \cdot k \pm i0)$ eikonal propagators.

Having defined the jet function it is now straightforward to address the question which mass scheme one might employ to have a good perturbative behavior of the jet function. At one-loop [8] one finds that the peak position is located at $\hat{s}_{\text{peak}} = 2\delta m - C_F \alpha_s(\mu)/2\Gamma_t[\ln(\frac{\mu}{\Gamma_t})+\frac{3}{2}]$. Recalling also that the pole mass contains a nasty $\mathcal{O}(\Lambda_{\text{QCD}})$ renormalon, it therefore natural to use a mass scheme different from the pole mass that is renormalon free and absorbs at least the major part of the higher order corrections to the peak position such that the resulting series is convergent. The definition of such a scheme is obviously not unique and can also be defined from moments of the distribution [13]. Generically we call such a mass a "jet mass" m_J and its perturbative relation to the pole mass reads

$$m_J = m_t^{\text{pole}} - \delta m, \tag{5}$$

where the HQET power counting requires that $\delta m \sim \alpha_s \Gamma$ in the resonance region. Using this relation one can relate the jet mass to other mass schemes. The jet mass m_J has already been used in the formulae shown before. From this examination we see that top mass one can measure from reconstruction is a jet mass. For sure, one cannot measure the $\overline{\text{MS}}$ mass from reconstruction because it has $\delta m \sim \alpha_s m_t \gg \Gamma_t$ and would invalidate the HQET power counting.

4   Soft Function

The soft function $S(\ell^+, \ell^-, \mu)$ describes the non-perturbative contributions of the invariant mass distribution in the resonance region. Its definition depends on the details of the prescription how soft radiation is associated to M_t and $M_{\bar{t}}$. One possible prescription is using a hemisphere mass definition, where X_t and $X_{\bar{t}}$ contain everything to the left or right of the plane perpendicular to the thrust axis of each event, see Fig. 1. It is easy to understand that such a (and any other) prescription is leading to a non-perturbative soft function since one cannot compute perturbatively how the soft particles are distributed around the hemisphere boundary. Other prescriptions are possible as long as they do not associate soft radiation going in the top direction to the antitop and vice-versa. This is in contrast to the jet functions which, according to the condition on X_t and $X_{\bar{t}}$ stated in Sec. 2 are prescription-independent since they describe energetic jets within a small cone with opening angle m_t/Q around the top direction. At leading order in the power counting

the allowed prescriptions do not affect these energetic jets. For the hemisphere prescription the soft function is defined by the vacuum matrix element

$$S_{\text{hemi}}(\ell^+, \ell^-) = \frac{1}{N_c} \sum_{X_s} \delta(\ell^+ - k_s^{+a}) \delta(\ell^- - k_s^{-b}) \langle 0 | (\overline{Y}_{\bar{n}})^{cd} (Y_n)^{ce}(0) | X_s \rangle \langle X_s | (Y_n^\dagger)^{ef} (\overline{Y}_{\bar{n}}^\dagger)^{df}(0) | 0 \rangle,$$

where c, d, e, f are color indices and the $Y's$ are Wilson lines with soft gluons of the form

$$Y_n(x) = \overline{\text{P}} \exp\left(-ig \int_0^\infty ds\, n \cdot A_s(ns+x) \right), \quad Y_n^\dagger(x) = \text{P} \exp\left(ig \int_0^\infty ds\, n \cdot A_s(ns+x) \right),$$

$$\overline{Y}_{\bar{n}}^\dagger(x) = \text{P} \exp\left(ig \int_0^\infty ds\, \bar{n} \cdot \overline{A}_s(\bar{n}s+x) \right), \quad \overline{Y}_{\bar{n}}(x) = \overline{\text{P}} \exp\left(-ig \int_0^\infty ds\, \bar{n} \cdot \overline{A}_s(\bar{n}s+x) \right). (6)$$

The k_s^{+a} and k_s^{-b} are operators that pick, according to the hemisphere mass prescription, the total $+$ and $-$ light-cone momentum of the gluons that are in hemisphere a and b, respectively, see Fig. 1. These Wilson lines describe soft radiation off the top and antitop quark and also render the soft function gauge-invariant.

The factorization theorem (3) shows that the soft function needs to be convoluted with the jet functions. This can be understood physically, since the way how the soft radiation is associated to M_t and $M_{\bar{t}}$ has to affect the observed invariant mass distribution. Field theoretically this convolution arises from the fact that the small components of light-cone momenta in the top and antitop jets fluctuate at the same length scales as the soft momenta described by the soft function. At this point it is also useful to note that S is a renormalized object and that its renormalization group evolution can be computed in perturbation theory. Nevertheless the actual form of the soft function (i.e. the initial condition for the soft function evolution at a low energy scale) is not computable with perturbative methods. So in practice the soft function needs to be modeled and eventually fixed by experimental data, similar to parton-distribution functions. How a soft model function can be constructed incorporating consistently the required higher order perturbative information has been discussed in Ref. [14].

Given that the soft function is nonperturbative and affects the invariant mass distribution at leading order, one might ask what one has gained from predicting the invariant mass distribution based on (3) and concerning a precise measurement of the top mass from the mass $M_{t,\bar{t}}$ where the resonance is located. The crucial aspect is that the soft function is universal and appears also in the factorization theorem for event shape distributions for jets originating from massless quarks [15] in the dijet region, where the thrust $T \approx 1$ [16]. This is related to the fact that the soft Y Wilson lines that arise from massless and from massive quark lines are identical. So our factorization theorem for the top invariant mass distribution in the resonance region becomes predictive after having determined a soft function from event shape distributions from e^+e^- data, which are already available from LEP [17]. Such a determination of the soft function was carried out by Korchemsky and Tafat in Ref. [18].

5 Numerical Analysis at LO

Using the factorization theorem it is straightforward to carry out a simple LO analysis using the tree-level result for the jet functions (i.e. one can set $\delta m = 0$) and the soft model
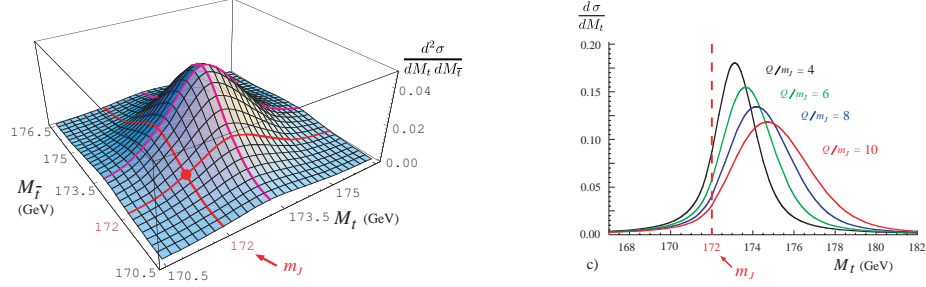
Figure 3: (a) Plot of the double differential hemisphere invariant mass cross-section $d^2\sigma/dM_t dM_{\bar{t}}$ in units of $4\sigma_0/\Gamma_t^2$ for $m_J = 172$, $Q = 4.33 m_J$ and $\Gamma_t = 1.43$ GeV. (b) Dependence of the single differential invariant mass distribution as described in the text on the c.m. energy Q with the same normalization.

function determined by Korchemsky and Tafat:

$$S_{\text{hemi}}^{\text{M1}}(\ell^+, \ell^-) = \theta(\ell^+)\theta(\ell^-)\frac{\mathcal{N}(a,b)}{\Lambda^2}\left(\frac{\ell^+\ell^-}{\Lambda^2}\right)^{a-1} \exp\left(\frac{-(\ell^+)^2 - (\ell^-)^2 - 2b\ell^+\ell^-}{\Lambda^2}\right), \quad (7)$$

where $\mathcal{N}$ is a normalization factor. From fits to e^+e^- heavy jet mass and thrust LEP data they obtained

$$a = 2, \qquad b = -0.4, \qquad \Lambda = 0.55\,\text{GeV}, \quad (8)$$

which we adopt in the following. The analysis illustrates a number of important features related to how the predictions by the factorization theorem depend on the c.m. energy Q.

In Fig. 3a the double differential invariant mass distribution is displayed for the input values $m_J = 172$, $Q = 4.33 m_J$ and $\Gamma_t = 1.43$ GeV. The conspicuous feature of the predicted distribution is that the observable resonance peak it shifted toward a higher value by about 1.5 GeV. This feature is one of the important properties of a invariant mass prescription that assigns all soft radiation to the masses. In the factorization theorem it arises from the Q/m factor involved in the convolution over the variables $\ell^\pm$. Intuitively it can be easily understood from the fact that the total invariant mass of a fast moving particle with mass m plus a soft momentum increases linearly with the soft momentum and the boost factor of the massive particle. This feature is also visible in Fig. 3b where the single differential invariant mass distribution

$$\frac{d\sigma}{dM_t} = \frac{2}{\Gamma} \int_{M_{\text{lower}}}^{M_{\text{upper}}} dM_{\bar{t}} \ \frac{d^2\sigma}{dM_t dM_{\bar{t}}}, \quad (9)$$

is plotted. Here the integration interval $[M_{\text{lower}}, M_{\text{upper}}]$ is twice the size of the measured peak mean half width and centered at the peak mass. For the single differential distribution one can relate the peak location approximately to the first moment of the soft function by

$$M_t^{\text{peak}} \simeq m_J + \frac{Q}{2m_J} S_{\text{hemi}}^{[1,0]}. \quad (10)$$

Interestingly this relation can also be used for fixed Q/m for invariant mass prescriptions that differ in the treatment of the soft radiation and lead to different first moments of the

soft function. When extrapolated to zero moment linearly one can obtain an estimate for the jet mass.

We also find that the distribution gets wider with Q/m. This is again a consequence of the Q/m factor occurring in the convolution over $\ell^{\pm}$ in the factorization theorem since for increasing Q the jet function gets effectively smeared over a wider distribution. The shift of the peak position as well as the widening of the invariant mass distribution have been observed in simulation studies at the ILC [7] and the LHC for large p_T events [9] and can now be better quantified using the factorization theorem.

6 Acknowledgments

References

[1] Slides:
http://ilcagenda.linearcollider.org/contributionDisplay.py?contribId=190&sessionId=85&confId=1296
http://ilcagenda.linearcollider.org/contributionDisplay.py?contribId=408&sessionId=73&confId=1296

[2] A. H. Hoang *et al.*, Eur. Phys. J. direct C **2**, 1 (2000) [arXiv:hep-ph/0001286]; A. H. Hoang, Acta Phys. Polon. B **34**, 4491 (2003) [arXiv:hep-ph/0310301].

[3] Y. Kiyo, these proceedings.

[4] A. H. Hoang, these proceedings.

[5] F. Gounaris, these proceedings.

[6] S. Boogert, these proceedings.

[7] S. V. Chekanov, arXiv:hep-ph/0206264; S. V. Chekanov and V. L. Morgunov, Phys. Rev. D **67**, 074011 (2003) [arXiv:hep-ex/0301014].

[8] S. Fleming, A. H. Hoang, S. Mantry and I. W. Stewart, arXiv:hep-ph/0703207.

[9] I. Borjanovic *et al.*, Eur. Phys. J. C **39S2**, 63 (2005) [arXiv:hep-ex/0403021].

[10] C. W. Bauer, S. Fleming and M. E. Luke, Phys. Rev. D **63**, 014006 (2001) [arXiv:hep-ph/0005275]; C. W. Bauer, S. Fleming, D. Pirjol and I. W. Stewart, Phys. Rev. D **63**, 114020 (2001) [arXiv:hep-ph/0011336]; C. W. Bauer, D. Pirjol and I. W. Stewart, Phys. Rev. D **65**, 054022 (2002) [arXiv:hep-ph/0109045]. C. W. Bauer, S. Fleming, D. Pirjol, I. Z. Rothstein and I. W. Stewart, Phys. Rev. D **66**, 014017 (2002) [arXiv:hep-ph/0202088].

[11] A. V. Manohar and M. B. Wise, Camb. Monogr. Part. Phys. Nucl. Phys. Cosmol. **10** (2000) 1.

[12] V. S. Fadin and V. A. Khoze, Sov. J. Nucl. Phys. **48**, 309 (1988) [Yad. Fiz. **48**, 487 (1988)]; M. Beneke, A. P. Chapovsky, A. Signer and G. Zanderighi, Phys. Rev. Lett. **93**, 011602 (2004) [arXiv:hep-ph/0312331]; A. H. Hoang and C. J. Reisser, Phys. Rev. D **71**, 074022 (2005) [arXiv:hep-ph/0412258].

[13] S. Fleming, A. H. Hoang, S. Mantry and I. W. Stewart, in preparation (2007)

[14] A. H. Hoang and I. W. Stewart, arXiv:0709.3519 [hep-ph].

[15] T. Gehrmann, these proceedings.

[16] G. P. Korchemsky and G. Sterman, Nucl. Phys. B **437**, 415 (1995) [arXiv:hep-ph/9411211]; C. W. Bauer, C. Lee, A. V. Manohar and M. B. Wise, Phys. Rev. D **70**, 034014 (2004) [arXiv:hep-ph/0309278].

[17] S. Kluth, Rept. Prog. Phys. **69**, 1771 (2006) [arXiv:hep-ex/0603011].

[18] G. P. Korchemsky and S. Tafat, JHEP **0010**, 010 (2000) [arXiv:hep-ph/0007005];

Probing CP properties of the Higgs Boson via
$e^+e^- \to t\bar{t}\phi$

R.M. Godbole[1], P.S. Bhupal Dev[1], A. Djouadi[2], M.M. Mühlleitner[3] and S.D. Rindani[4]

1- Center for High Energy Physics - Indian Institute of Science
Bangalore 560 012 - India

2- Laboratoire de Phyisque Théorique - U. Paris-Sud and CNRS
F-91405 Orsay - France

3- Theory Division, Department of Physics - CERN
CH-1211 Geneva 23 - Switzerland
Laboratoire de Physique Théorique - LAPTH
F-74941 Annecy-le-Vieux - France

4- Theoretical Physics Division - Physical Research Laboratory, Navrangpura
Ahmedabad 380 009 - India

One of the main endeavors at future high-energy colliders is the search for the Higgs boson(s) and, once found, the probe of the fundamental properties. In particular, the charge conjugation and parity (CP) quantum numbers have to be determined. We show that these are unambiguously accessible at future e^+e^- colliders through the measurement of the total cross section and the top polarization in associated Higgs production with top quark pairs.

1   Introduction

After the discovery of the Higgs boson - or several Higgs bosons in extensions beyond the Standard Model (SM) - we have to probe its properties in order to establish the Higgs mechanism [2] as responsible for the creation of particle masses without violating gauge symmetry. In the SM the Higgs mechanism is implemented by adding one isodoublet complex scalar field which leads after electroweak symmetry breaking to one single spin zero CP-even Higgs particle [2, 3]. In extensions beyond the SM the Higgs sector can be non-minimal, as *e.g.* in the Minimal Supersymmetric Standard Model (MSSM), which contains five physical Higgs states, *i.e.* two CP-even h and H, one CP-odd A and two charged $H^\pm$ Higgs bosons [3, 4]. To establish the Higgs mechanism experimentally we have to determine the Higgs spin, its behavior under charge and parity transformations, the couplings to gauge bosons and fermions, and finally the trilinear and quartic Higgs self-interactions must be measured to reconstruct the Higgs potential itself. To fulfill this program the Large Hadron Collider (LHC) analyses [5] must be complemented by the high-precision measurements at a future International Linear e^+e^- Collider (ILC) [6, 7, 8].

We address in this contribution the determination of the Higgs CP quantum numbers. To do so in an unambiguous way is somewhat problematic [9]. Observables sensitive to the Higgs spin-parity such as angular correlations in Higgs decays into $V = W, Z$ pairs [10, 11] or in Higgs production with or through these states [10, 12] only project out the CP-even component of the HVV coupling, even in the presence of CP violation. In addition, the purely pseudoscalar AVV coupling is zero at tree-level and is generated only through tiny loop corrections. In the Higgs couplings to fermions, however, the CP-even and CP-odd components can have the same magnitude. Here, the heaviest fermion discovered so far, the

top quark, plays a special role. The Htt coupling is largest being proportional to the top quark mass due to the Higgs mechanism. At a future ILC the Higgs boson can therefore be produced with sufficient rate in associated production with a $t\bar{t}$ pair, $e^+e^- \rightarrow t\bar{t}H$ [13, 14]. We propose a simple and straightforward way to determine the CP nature of a SM-like Higgs boson in this process, in an unambigious way, where we exploit that the cross section as well as the top quark polarization behave in a radically different way for CP-even and CP-odd Higgs production.

2   The total production cross section

The diagrams which contribute in the SM to the process $e^+e^- \rightarrow t\bar{t}H$ are shown in Fig.1. The bulk of the cross section is generated when the Higgs is radiated off the heavy top quarks [14], whereas the Higgs produced in association with a Z boson which then splits into a $t\bar{t}$ pair provides only a very small contribution, amounting to a few percent for $\sqrt{s} \leq 1$ TeV Detailed simulations have shown the cross section

Figure 1: Feynman diagrams for the associated production of Higgs bosons with a top quark pair.

to be measurable with an accuracy of order 10% [15]. We will discuss the case of a SM-like mixed CP Higgs state Φ and use the general form of the $t\bar{t}\Phi$ coupling

$$g_{\Phi tt} = -i\frac{e}{s_W}\frac{m_t}{2M_W}(a + ib\gamma_5) ,\tag{1}$$

where the coefficients a and b are assumed to be real and $s_W \equiv \sin\theta_W = \sqrt{1 - c_W^2}$. In the SM we have $a = 1, b = 0$ and for a purely pseudoscalar Higgs boson $a = 0, b \neq 0$. In the pseudoscalar case we take $b = 1$, consistent with a convenient normalization $a^2 + b^2 = 1$ chosen for the general case of a Higgs boson with an indefinite CP quantum number. A non–zero value for the product ab will hence signal CP violation in the Higgs sector. For the $ZZ\Phi$ coupling, we will use the form,

$$g_{ZZ\Phi}^{\mu\nu} = -ic(eM_Z/s_W c_W)g^{\mu\nu} .\tag{2}$$

And for the numerical analysis we chose $c = a$ [16] as $c = 1(0)$ in the case of a CP-even (odd) Higgs boson. We will thus have only one free parameter b. However, this simple parametrization for a SM–like Higgs need not be true in $e.g.$ a general 2HDM, where a, b and c are three independent parameters. We have calculated the cross section for the production of a mixed CP Higgs state including the polarization dependence of the final state top quarks. The lengthy result has been checked to agree with Ref. [14] for the unpolarized total cross section. In Fig. 2 left panel we show the production cross section for a purely scalar (H with $b = 0$) and a pseudoscalar (A with $b = 1$) Higgs as a function of the c.m. energy and for two mass values $M_\Phi = 120$ and 150 GeV. As can be inferred from the figure, the threshold rise of the cross section in the scalar and the pseudoscalar case is very different. Furthermore, for the same strength of the Φtt couplings, there is an order of magnitude difference between the H and A cross sections at moderate energies. Only at very high energies, $\sqrt{s} \gg 1$ TeV, the chiral limit is reached and the two cross sections become equal,

up to the small contribution due to the diagram including the $ZZ\Phi$ coupling. These two features hence provide an extremely powerful tool to discriminate the CP properties of the spin zero particle produced together with the top quark pair. The difference in the threshold behavior of the A and H case is strong enough so that the cross section measurement at only two different c.m. energies allows a clear determination of the CP properties of the Φ state. *e.g.* for $M_\Phi = 120$ GeV, the ratio of the cross sections at $\sqrt{s} = 800$ and 500 GeV is ~ 63 and ~ 7.5 for the scalar and pseudoscalar case, respectively. Finally, taking the ratio makes the conclusion robust with respect to the effect of the top Yukawa coupling, the higher order radiative corrections [17] or systematic errors in the measurement.

Figure 2: The production cross sections $\sigma(e^+e^- \to t\bar{t}\Phi)$ for a scalar and a pseudoscalar Higgs boson as a function of $\sqrt{s}$ for two masses $M_\Phi = 120$ and 150 GeV (left) and for unpolarized and polarized $e^\pm$ beams as a function of the parameter b at $\sqrt{s} = 800$ GeV with $M_\Phi = 120$ GeV (right).

We also studied the b dependence of the total $t\bar{t}\Phi$ production process at a given energy and for fixed M_Φ. Being a CP even quantity it only depends on b^2. Fig. 2 (right) shows the result for unpolarized and polarized $e^\pm$ beams. For the latter, we used the standard ILC values $P_{e^-} = -0.8$ and $P_{e^+} = 0.6$, which double the total rate.

3 Top quark polarization as a probe of the CP nature of Φ

Since the top quark, due to its large decay width $\Gamma_t \sim 1.5$ GeV, decays much before hadronization, its spin information is translated to the decay distribution before contamination through strong interaction effects. Furthermore, the lepton angular distribution of the decay $t \to bW \to b\bar{l}\nu$ is independent of any non-standard effects in the decay vertex, so that it is a pure probe of the physics of the top quark production process [18]. The net polarization of the top quark therefore provides an interesting tool for the probe of b, see also Ref.[19]. In Fig. 3 (left) we show as a function of $\sqrt{s}$ for $M_\Phi = 120$ and 150 GeV in the $H(b = 0)$ and $A(b = 1)$ case the expected degree of t-quark polarization P_t, given by

$$P_t = \frac{\sigma(t_L) - \sigma(t_R)}{\sigma(t_L) + \sigma(t_R)} \ . \tag{3}$$

As can be inferred from the figure, the degree of top polarization is again strikingly different for the CP even and CP odd case and shows a very different threshold dependence.

In addition, since P_t is constructed as a ratio of cross sections, the insights gained from this variable are not affected by a possibly model dependent normalization of the overall $tt\Phi$ coupling strength, higher order corrections etc. P_t is a parity odd quantity and receives contributions from the interferences between the γ and all Z exchange diagrams, with the one stemming from the diagram involving the $ZZ\Phi$ vertex being small. The parity violation effect for the emission of a (pseudo)scalar is controlled by the (vector) axial-vector $Zt\bar{t}$ coupling $(v_t = (2I_t^{3L} - 4Q_t s_W^2)/(4s_w c_W))$ $a_t = 2I_t^{3L}/(4s_W c_W)$, where I_t^{3L} denotes the top isospin and

Q_t the electric charge. Hence the ratios of the P_t values away from threshold are expected to be given by the $a_t/v_t \sim 3$, which indeed is confirmed by both Figs. 3 at $\sqrt{s} = 800$ GeV.

4 The sensitivity to CP mixing

We investigate how the behavior of the cross section and the measurement of the top polarization, which both are clear discriminators between a scalar and pseudoscalar Higgs state, can be used to get information on the CP mixing, *i.e.* the value of b. Ignoring systematical errors, the sensitivity of an observable $O(b)$ to the parameter b at $b = b_0$ is Δb, if $|O(b) - O(b_0)| = \Delta O(b_0)$ for $|b - b_0| < \Delta b$, where $\Delta O(b_0)$ is the statistical fluctuation in O at an integrated luminosity $\mathcal{L}$. For the cross section σ and the polarization P_t, the statistical fluctuation at a level of confidence f are given by $\Delta\sigma = f\sqrt{\sigma/\mathcal{L}}$ and $\Delta P_t = f/\sqrt{\sigma\mathcal{L}} \times \sqrt{1 - P_t^2}$. Fig. 4 (left) shows the sensitivity Δb from the cross section measurement for $M_\phi = 120$ GeV at $\sqrt{s} = 800$ GeV with $\mathcal{L} = 500$ fb^{-1}. For polarized $e^\pm$ beams it varies from 0.25 for $H(b = 0)$ to 0.01 for $A(b = 1)$, a rather precise determination obtained from a simple measurement. The top polarization is less sensitive to b, see Fig. 4 (right).

Figure 3: The top polarization in $e^+e^- \to t\bar{t}\Phi$ for a scalar and a pseudoscalar Higgs as a function of $\sqrt{s}$ for $M_\Phi = 120$, 150 GeV (left) and with unpolarized and polarized $e^\pm$ beams as a function of b at $\sqrt{s} = 800$ GeV for $M_\Phi = 120$ GeV (right).
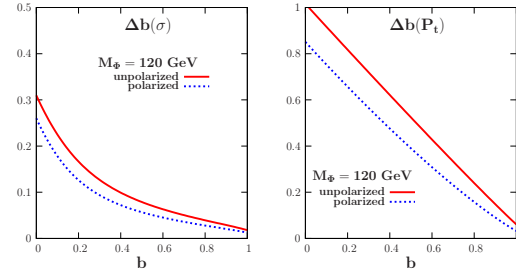
Figure 4: The sensitivity of the cross section (left) and the top polarization (right) to b for $M_\Phi = 120$ at $\sqrt{s} = 800$ with $\mathcal{L} = 500$ fb^{-1}.

Both σ and P_t are CP even quantities, they cannot depend linearly on b and hence not probe CP violation directly. Observables depending directly on the sine of the azimuthal angle (Φ) are linear in b. The updown asymmetry A_Φ of the antitop quark production with respect to the top-electron plane ($\Phi = 0$) is an example of such an observable:

$$A_\Phi = \frac{\sigma_{\text{partial}}(0 \leq \Phi < \pi) - \sigma_{\text{partial}}(\pi \leq \Phi < 2\pi)}{\sigma_{\text{partial}}(0 \leq \Phi < \pi) + \sigma_{\text{partial}}(\pi \leq \Phi < 2\pi)} \tag{4}$$

with $\sin\Phi = \frac{(\mathbf{p}_{e^-} - \mathbf{p}_{e^+}) \cdot (\mathbf{p}_t \times \mathbf{p}'_{\bar{t}})}{|\mathbf{p}_{e^-} - \mathbf{p}_{e^+}| \cdot |\mathbf{p}_t \times \mathbf{p}'_{\bar{t}}|}$, where $\mathbf{p}'_{\bar{t}}$ is the $\bar{t}$ momentum in the $\bar{t}$-Higgs rest frame. Fig. 5 shows the asymmetry A_Φ for a Higgs boson of 120 GeV and a c.m. energy of $\sqrt{s} = 800$ GeV as a function of b. It can reach values of order 5%. The non-zero value of the asymmetry arises from the channel which involves the $ZZ\Phi$ coupling
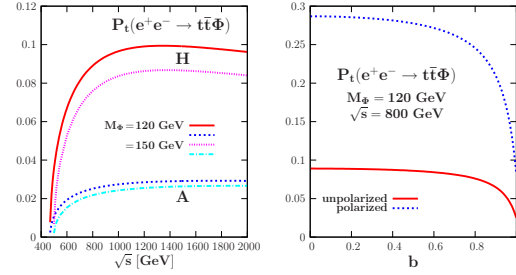
5 Summary

We have shown that the total cross section and the top polarization asymmetry for associated Higgs production with top quark pairs in e^+e^- collisions provide a very simple and unambiguous determination of the CP quantum numbers of a SM-like Higgs particle. Exploiting the up-down asymmetry of the anti-top with respect to the top-electron plane we further have a direct probe of CP violation at hand.
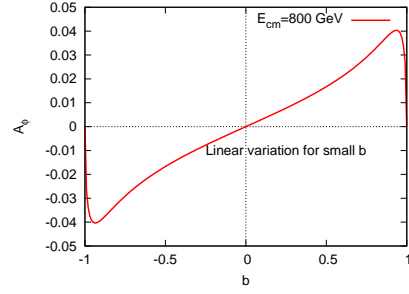
Figure 5: The up-down asymmetry of $\bar{t}$ in associated $t\bar{t}\Phi$ production for $M_\Phi = 120$ at $\sqrt{s} = 800$.

References

[1] Slides:
http://ilcagenda.linearcollider.org/contributionDisplay.py?contribId=193&sessionId=85&confId=1296

[2] P.W. Higgs, Phys. Rev. Lett. **13** 508 (1964); *ibid.* Phys. Rev. **145** 1156 (1966); F. Englert and R. Brout, Phys. Rev. Lett. **13** 321 (1964); G.S. Guralnik, C.R. Hagen and T. Kibble, Phys. Rev. Lett. **13** 585 (1965).

[3] J. Gunion, H. Haber, G. Kane, and S. Dawson, *The Higgs Hunter's Guide*, Addison–Wesley, Reading (USA), 1990; for recent reviews, see A. Djouadi, arXiv:hep-ph/0503172 and arXiv:hep-ph/0503173 to appear in Physics Reports; M. Gomez-Bock et al., arXiv:hep-ph/0509077.

[4] See e.g. M. Drees, R.M. Godbole and P. Roy, *Theory and phenomenology of sparticles*, World Scientific, 2005.

[5] ATLAS Collaboration, Technical Design Report, CERN–LHCC–99–14 and CERN–LHCC–99–15; CMS Collaboration, Technical Design Report, CMS–LHCC–2006–21.

[6] E. Accomando *et al.*, Phys. Rept. **299** 1 (1998); J. Aguilar-Saavedra *et al.*, arXiv:hep-ph/0106315; T. Abe *et al.*, arXiv:hep-ex/0106055-58; K. Abe *et al.*, arXiv:hep-ph/0109166.

[7] G. Weiglein *et al.*, Phys. Rept. **426** 47 (2006).

[8] A. Djouadi *et al.*, arXiv:0709.1893 (2007).

[9] R.M. Godbole *et al.*, in Ref. [7] and arXiv:hep-ph/0404024; E. Accomando *et al.*, arXiv:hep-ph/0608079.

[10] V. Barger *et al.*, Phys. Rev. **D49** 79 (1994).

[11] See for instance: S.Y. Choi *et al.*, Phys. Lett. **B553** 61 (2003); C. Buszello *et al.*, Eur. Phys. J. **C32** 209 (2004); R.M. Godbole *et al.*, arXiv:0708.0458.

[12] K. Hagiwara and M. Stong, Z. Phys. **C62** 99 (1994); T. Plehn, D. Rainwater and D. Zeppenfeld, Phys. Rev. Lett. **88** 051801 (2002); D. Miller *et al.*, Phys. Lett. **B505** 149 (2001); T. Han and J. Jiang, Phys. Rev. **D63** 096007 (2001); S. Biswal *et al.*, Phys. Rev. **D73** 035001 (2006).

[13] K. Gaemers and G. Gounaris, Phys. Lett. **B77** 379 (1978); A.Djouadi, J. Kalinowski and P.M. Zerwas, Mod. Phys. Lett. **A7** 1765 (1992).

[14] A. Djouadi, J. Kalinowski and P.M. Zerwas, Z. Phys. **C54** 255 (1992).

[15] A. Juste and G. Merino, arXiv:hep-ph/9910301; M. Martinez and R. Miquel, Eur. Phys. J. **C27** 49 (2003); A. Gay, LC–Note 2004; K. Desch and M.Schumacher in Ref. [7].

[16] B. Grzadkowski, J.F. Gunion and X. He, Phys. Rev. Lett. **77** 5172 (1996).

[17] S. Dittmaier *et al.*, Phys. Lett. **B441** 383 (1998); S. Dawson and L. Reina, Phys. Rev. **D57** 5851 (1998), **D59** 054012 (1999) and **D60** 015003 (1999); S. Dittmaier *et al.*, Phys. Lett. **B478** 247 (2000); G. Bélanger *et al.*, Phys. Lett. **B571** 163 (2003); A. Denner *et al.*, Phys. Lett. **B575** 290 (2003) and Nucl. Phys. **B680** 85 (2004).

[18] R.M. Godbole, S.D. Rindani and R.K. Singh, JHEP **12** 021 (2006).

[19] C.S. Huang and S.H. Zhu, Phys. Rev. **D65** 077702 (2002).

First results on $e^+e^- \to 3$ jets at NNLO

A. Gehrmann-De Ridder[1], T. Gehrmann[2], E.W.N. Glover[3], G. Heinrich[4]

1- Institute for Theoretical Physics, ETH, CH-8093 Zürich, Switzerland

2- Institut für Theoretische Physik, Universität Zürich, CH-8057 Zürich, Switzerland

3- Institute of Particle Physics Phenomenology, Department of Physics,
University of Durham, Durham, DH1 3LE, UK

4- School of Physics, The University of Edinburgh, Edinburgh EH9 3JZ, UK

Precision studies of QCD at e^+e^- colliders are based on measurements of event shapes and jet rates. To match the high experimental accuracy, theoretical predictions to next-to-next-to-leading order (NNLO) in QCD are needed for a reliable interpretation of the data. We report the first calculation of NNLO corrections ($\mathcal{O}(\alpha_s^3)$) to three-jet production and related event shapes, and discuss their phenomenological impact.

1 Introduction

Measurements at LEP and at earlier e^+e^- colliders have helped to establish QCD as the theory of strong interactions by directly observing gluon radiation through three-jet production events. The LEP measurements of three-jet production and related event shape observables are of a very high statistical precision. The extraction of α_s from these data sets relies on a comparison of the data with theoretical predictions. Comparing the different sources of error in this extraction, one finds that the experimental error is negligible compared to the theoretical uncertainty. There are two sources of theoretical uncertainty: the theoretical description of the parton-to-hadron transition (hadronisation uncertainty) and the uncertainty stemming from the truncation of the perturbative series at a certain order, as estimated by scale variations (perturbative or scale uncertainty). Although the precise size of the hadronisation uncertainty is debatable and perhaps often underestimated, it is certainly appropriate to consider the scale uncertainty as the dominant source of theoretical error on the precise determination of α_s from three-jet observables. From the planned luminosity of the ILC, one would expect measurements of event shapes comparable in statistical quality to what was obtained at LEP, thus allowing for precision QCD studies at ILC energies.

So far the three-jet rate and related event shapes have been calculated [1, 2] up to the next-to-leading order (NLO), improved by a resummation of leading and subleading infrared logarithms [3, 4] and by the inclusion of power corrections [5].

QCD studies of event shape observables at LEP [6] are based around the use of NLO parton-level event generator programs [7]. As expected, the current error on α_s from these observables [8] is dominated by the theoretical uncertainty. Clearly, to improve the determination of α_s, the calculation of the NNLO corrections to these observables becomes mandatory. We present here the first NNLO calculation of three-jet production and related event shape variables.

2 Calculation

Three-jet production at tree-level is induced by the decay of a virtual photon (or other neutral gauge boson) into a quark-antiquark-gluon final state. At higher orders, this process

receives corrections from extra real or virtual particles. The individual partonic channels that contribute through to NNLO are shown in Table 1. All of the tree-level and loop amplitudes associated with these channels are known in the literature [9–12].

For a given partonic final state, jets are reconstructed according to the same definition as in the experiment, which is applied to partons instead of hadrons. At leading order, all three final state partons must be well separated from each other. At NLO, up to four partons can be present in the final state, two of which can be clustered together, whereas at NNLO, the final state can consist of up to five partons, such that as many as three partons can be clustered together. The more partons in the final state, the better one expects the matching between theory and experiment to be.

LO	$\gamma^* \to q\,\bar{q}g$	tree level
NLO	$\gamma^* \to q\,\bar{q}g$	one loop
	$\gamma^* \to q\,\bar{q}\,gg$	tree level
	$\gamma^* \to q\,\bar{q}\,q\bar{q}$	tree level
NNLO	$\gamma^* \to q\,\bar{q}g$	two loop
	$\gamma^* \to q\,\bar{q}\,gg$	one loop
	$\gamma^* \to q\,\bar{q}\,q\,\bar{q}$	one loop
	$\gamma^* \to q\,\bar{q}\,q\,\bar{q}\,g$	tree level
	$\gamma^* \to q\,\bar{q}\,g\,g\,g$	tree level

Table 1: Partonic contributions to three-jet final states in perturbative QCD.

The two-loop $\gamma^* \to q\bar{q}g$ matrix elements were derived in [9] by reducing all relevant Feynman integrals to a small set of master integrals using integration-by-parts [13] and Lorentz invariance [14] identities, solved with the Laporta algorithm [15]. The master integrals [16] were computed from their differential equations [14] and expressed analytically in terms of one- and two-dimensional harmonic polylogarithms [17].

The one-loop four-parton matrix elements relevant here [11] were originally derived in the context of NLO corrections to four-jet production and related event shapes [18,19]. One of these four-jet parton-level event generator programs [19] is the starting point for our calculation, since it already contains all relevant four-parton and five-parton matrix elements.

The four-parton and five-parton contributions to three-jet-like final states at NNLO contain infrared real radiation singularities, which have to be extracted and combined with the infrared singularities [20] present in the virtual three-parton and four-parton contributions to yield a finite result. In our case, this is accomplished by introducing subtraction functions, which account for the infrared real radiation singularities, and are sufficiently simple to be integrated analytically. Schematically, this subtraction reads:

$$
\begin{aligned}
\mathrm{d}\sigma_{NNLO} = &\int_{\mathrm{d}\Phi_5} \left(\mathrm{d}\sigma^R_{NNLO} - \mathrm{d}\sigma^S_{NNLO}\right) \\
&+ \int_{\mathrm{d}\Phi_4} \left(\mathrm{d}\sigma^{V,1}_{NNLO} - \mathrm{d}\sigma^{VS,1}_{NNLO}\right) \\
&+ \int_{\mathrm{d}\Phi_5} \mathrm{d}\sigma^S_{NNLO} + \int_{\mathrm{d}\Phi_4} \mathrm{d}\sigma^{VS,1}_{NNLO} + \int_{\mathrm{d}\Phi_3} \mathrm{d}\sigma^{V,2}_{NNLO} \,,
\end{aligned}
$$

where $\mathrm{d}\sigma^S_{NNLO}$ denotes the real radiation subtraction term coinciding with the five-parton tree level cross section $\mathrm{d}\sigma^R_{NNLO}$ in all singular limits [21]. Likewise, $\mathrm{d}\sigma^{VS,1}_{NNLO}$ is the one-loop virtual subtraction term coinciding with the one-loop four-parton cross section $\mathrm{d}\sigma^{V,1}_{NNLO}$ in all singular limits [22]. Finally, the two-loop correction to the three-parton cross section is

denoted by $\mathrm{d}\sigma_{NNLO}^{V,2}$. With these, each line in the above equation is individually infrared finite, and can be integrated numerically.

Systematic methods to derive and integrate subtraction terms were available in the literature only to NLO [23, 24], with extension to NNLO in special cases [25]. In the context of this project, we fully developed an NNLO subtraction formalism [26], based on the antenna subtraction method originally proposed at NLO [19, 24]. The basic idea of the antenna subtraction approach is to construct the subtraction terms from antenna functions. Each antenna function encapsulates all singular limits due to the emission of one or two unresolved partons between two colour-connected hard partons. This construction exploits the universal factorisation of phase space and squared matrix elements in all unresolved limits. The individual antenna functions are obtained by normalising three-parton and four-parton tree-level matrix elements and three-parton one-loop matrix elements to the corresponding two-parton tree-level matrix elements. Three different types of antenna functions are required, corresponding to the different pairs of hard partons forming the antenna: quark-antiquark, quark-gluon and gluon-gluon antenna functions. All these can be derived systematically from matrix elements [27] for physical processes.

The factorisation of the final state phase space into antenna phase space and hard phase space requires a mapping of the antenna momenta onto reduced hard momenta. We use the mapping derived in [28] for the three-parton and four-parton antenna functions. To extract the infrared poles of the subtraction terms, the antenna functions must be integrated analytically over the appropriate antenna phase spaces, which is done by reduction [29] to known phase space master integrals [30].

A detailed description of the calculation will be given elsewhere [31].

3 Results

The resulting numerical programme, `EERAD3`, yields the full kinematical information on a given multi-parton final state. It can thus be used to compute any infrared-safe observable in e^+e^- annihilation related to three-particle final states at $\mathcal{O}(\alpha_s^3)$. As a first application, we derived results for the NNLO corrections to the thrust distribution [32].

In the numerical evaluation, we use $M_Z = 91.1876$ GeV and $\alpha_s(M_Z) = 0.1189$ [8]. Figure 1 displays the perturbative expression for the thrust distribution at LO, NLO and NNLO, evaluated for LEP and ILC energies. The error band indicates the variation of the prediction under shifts of the renormalisation scale in the range $\mu \in [Q/2; 2\,Q]$ around the e^+e^- centre-of-mass energy Q.

It can be seen that even at linear collider energies, inclusion of the NNLO corrections enhances the thrust distribution by around 10% over the range $0.03 < (1-T) < 0.33$, where relative scale uncertainty is reduced by about 30% between NLO and NNLO. Outside this range, one does not expect the perturbative fixed-order prediction to yield reliable results. For $(1-T) \to 0$, the convergence of the perturbative series is spoilt by powers of logarithms $\ln(1-T)$ appearing in higher perturbative orders, thus necessitating an all-order resummation of these logarithmic terms [3, 4], and a matching of fixed-order and resummed predictions [33].

The perturbative parton-level prediction is compared with the hadron-level data from the ALEPH collaboration [34] in Figure 1. Similar data are also available from the other LEP experiments [35]. The shape and normalisation of the parton-level NNLO prediction agrees better with the data than at NLO. We also see that the NNLO corrections account
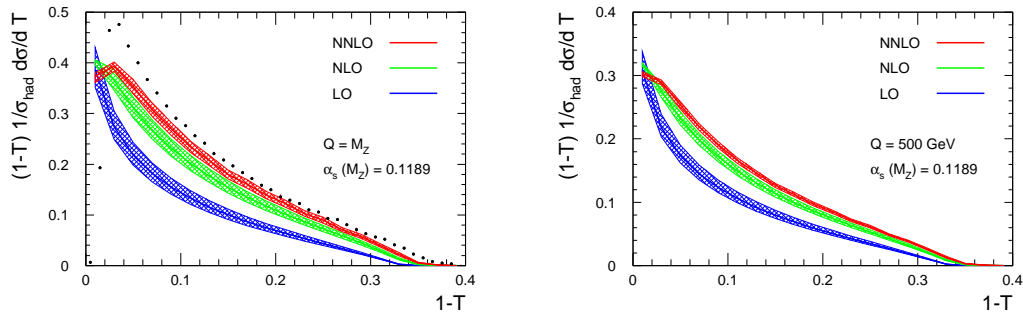
Figure 1: Thrust distribution at LEP and at the ILC with $Q = 500$ GeV.

for approximately half of the difference between the parton-level NLO prediction and the hadron-level data. A full study including resummation of infrared logarithms and hadronisation corrections is underway.

4   Conclusions

We developed a numerical programme which can compute any infrared-safe observable through to $\mathcal{O}(\alpha_s^3)$, which we applied here to determine the NNLO corrections to the thrust distribution. These corrections are moderate, indicating the convergence of the perturbative expansion. Their inclusion results in a considerable reduction of the theoretical error on the thrust distribution. Our results will allow a significantly improved determination of the strong coupling constant from jet observables from existing LEP data as well as from future ILC data.

Acknowledgements

References

[1] R.K. Ellis, D.A. Ross and A.E. Terrano, Nucl. Phys. B **178** (1981) 421.

[2] Z. Kunszt, Phys. Lett. B **99** (1981) 429; J.A.M. Vermaseren, K.J.F. Gaemers and S.J. Oldham, Nucl. Phys. B **187** (1981) 301; K. Fabricius, I. Schmitt, G. Kramer and G. Schierholz, Z. Phys. C **11** (1981) 315; L. Clavelli and D. Wyler, Phys. Lett. B **103** (1981) 383.

[3] S. Catani, G. Turnock, B.R. Webber and L. Trentadue, Phys. Lett. B **263** (1991) 491.

[4] S. Catani, L. Trentadue, G. Turnock and B.R. Webber, Nucl. Phys. B **407** (1993) 3.

[5] G.P. Korchemsky and G. Sterman, Nucl. Phys. B **437** (1995) 415; Y.L. Dokshitzer and B.R. Webber, Phys. Lett. B **352** (1995) 451; **404** (1997) 321; Y.L. Dokshitzer, A. Lucenti, G. Marchesini and G.P. Salam, JHEP **9805** (1998) 003.

[6] O. Biebel, Phys. Rept. **340** (2001) 165; S. Kluth, Rept. Prog. Phys. **69** (2006) 1771.

[7] Z. Kunszt and P. Nason, in *Z Physics at LEP 1*, CERN Yellow Report 89-08, Vol. 1, p. 373; S. Catani and M.H. Seymour, Phys. Lett. B **378** (1996) 287.

[8] S. Bethke, Prog. Part. Nucl. Phys. **58** (2007) 351.

[9] L.W. Garland, T. Gehrmann, E.W.N. Glover, A. Koukoutsakis and E. Remiddi, Nucl. Phys. B **627** (2002) 107 and **642** (2002) 227.

[10] S. Moch, P. Uwer and S. Weinzierl, Phys. Rev. D **66** (2002) 114001.

[11] E.W.N. Glover and D.J. Miller, Phys. Lett. B **396** (1997) 257; Z. Bern, L.J. Dixon, D.A. Kosower and S. Weinzierl, Nucl. Phys. B **489** (1997) 3; J.M. Campbell, E.W.N. Glover and D.J. Miller, Phys. Lett. B **409** (1997) 503; Z. Bern, L.J. Dixon and D.A. Kosower, Nucl. Phys. B **513** (1998) 3.

[12] K. Hagiwara and D. Zeppenfeld, Nucl. Phys. B **313** (1989) 560; F.A. Berends, W.T. Giele and H. Kuijf, Nucl. Phys. B **321** (1989) 39; N.K. Falck, D. Graudenz and G. Kramer, Nucl. Phys. B **328** (1989) 317.

[13] F.V. Tkachov, Phys. Lett. B **100** (1981) 65; K. Chetyrkin and F.V. Tkachov, Nucl. Phys. B **192** (1981) 159.

[14] T. Gehrmann and E. Remiddi, Nucl. Phys. B **580** (2000) 485.

[15] S. Laporta, Int. J. Mod. Phys. A **15** (2000) 5087.

[16] T. Gehrmann and E. Remiddi, Nucl. Phys. B **601** (2001) 248; **601** (2001) 287.

[17] E. Remiddi and J.A.M. Vermaseren, Int. J. Mod. Phys. A **15** (2000) 725; T. Gehrmann and E. Remiddi, Comput. Phys. Commun. **141** (2001) 296; **144** (2002) 200.

[18] L.J. Dixon and A. Signer, Phys. Rev. Lett. **78** (1997) 811; Phys. Rev. D **56** (1997) 4031; Z. Nagy and Z. Trocsanyi, Phys. Rev. Lett. **79** (1997) 3604; S. Weinzierl and D.A. Kosower, Phys. Rev. D **60** (1999) 054028.

[19] J. Campbell, M.A. Cullen and E.W.N. Glover, Eur. Phys. J. C **9** (1999) 245.

[20] S. Catani, Phys. Lett. B **427** (1998) 161; G. Sterman and M.E. Tejeda-Yeomans, Phys. Lett. B **552** (2003) 48.

[21] A. Gehrmann-De Ridder and E.W.N. Glover, Nucl. Phys. B **517** (1998) 269; J. Campbell and E.W.N. Glover, Nucl. Phys. B **527** (1998) 264; S. Catani and M. Grazzini, Phys. Lett. B **446** (1999) 143; Nucl. Phys. B **570** (2000) 287; F.A. Berends and W.T. Giele, Nucl. Phys. B **313** (1989) 595; V. Del Duca, A. Frizzo and F. Maltoni, Nucl. Phys. B **568** (2000) 211.

[22] Z. Bern, L.J. Dixon, D.C. Dunbar and D.A. Kosower, Nucl. Phys. B **425** (1994) 217; D.A. Kosower, Nucl. Phys. B **552** (1999) 319; D.A. Kosower and P. Uwer, Nucl. Phys. B **563** (1999) 477; Z. Bern, V. Del Duca and C.R. Schmidt, Phys. Lett. B **445** (1998) 168; Z. Bern, V. Del Duca, W.B. Kilgore and C.R. Schmidt, Phys. Rev. D **60** (1999) 116001.

[23] Z. Kunszt and D.E. Soper, Phys. Rev. D **46** (1992) 192; S. Frixione, Z. Kunszt and A. Signer, Nucl. Phys. B **467** (1996) 399; S. Catani and M.H. Seymour, Nucl. Phys. B **485** (1997) 291.

[24] D.A. Kosower, Phys. Rev. D **57** (1998) 5410; **71** (2005) 045016.

[25] S. Catani and M. Grazzini, Phys. Rev. Lett. **98** (2007) 222002.

[26] A. Gehrmann-De Ridder, T. Gehrmann and E.W.N. Glover, JHEP **0509** (2005) 056.

[27] A. Gehrmann-De Ridder, T. Gehrmann and E.W.N. Glover, Nucl. Phys. B **691** (2004) 195; Phys. Lett. B **612** (2005) 36; **612** (2005) 49.

[28] D.A. Kosower, Phys. Rev. D **67** (2003) 116003.

[29] C. Anastasiou and K. Melnikov, Nucl. Phys. B **646** (2002) 220.

[30] A. Gehrmann-De Ridder, T. Gehrmann and G. Heinrich, Nucl. Phys. B **682** (2004) 265.

[31] A. Gehrmann-De Ridder, T. Gehrmann, E.W.N. Glover and G. Heinrich, in preparation.

[32] A. Gehrmann-De Ridder, T. Gehrmann, E.W.N. Glover and G. Heinrich, arXiv:0707.1285 [hep-ph].

[33] R.W.L. Jones, M. Ford, G.P. Salam, H. Stenzel and D. Wicke, JHEP **0312** (2003) 007.

[34] A. Heister *et al.* [ALEPH Collaboration], Eur. Phys. J. C **35** (2004) 457.

[35] G. Abbiendi *et al.* [OPAL Collaboration], Eur. Phys. J. C **40** (2005) 287;
P. Achard *et al.* [L3 Collaboration], Phys. Rept. **399** (2004) 71;
J. Abdallah *et al.* [DELPHI Collaboration], Eur. Phys. J. C **29** (2003) 285.

BFKL resummation effects in exclusive production of rho meson pairs at the ILC

M. Segond[1,*], L. Szymanowski[2,3], S. Wallon[1]

1- Université Paris-Sud- LPT[†]
91405-Orsay- France

2- Université de Liège
B4000 Liège-Belgium

3- Sołtan Institute for Nuclear Studies
Hoża 69, 00-681 Warsaw- Poland

We calculate the Born order cross-section for the exclusive production of rho meson pairs in e^+e^- scattering in the Regge limit of QCD and we show the feasibility of the measurement of this process at the ILC. We also investigate the leading and next-to-leading order BFKL evolution, making this process a very clean test of the BFKL resummation effects.

1 Impact factor representation in the Regge limit of QCD

We are focusing on the high-energy (Regge) limit, when the cm energy $s_{\gamma^*\gamma^*}$ is much larger than all other scales of the process, in which $t-$channel gluonic exchanges dominate [1]. The highly virtual photons (the virtualities $Q_i^2 = -q_i^2$, supply the hard scale which justifies the use of perturbation theory) provide small transverse size objects ($q\bar{q}$ color dipoles) whose scattering by pairs is the cleanest place to study the typical Regge behaviour with $t-$channel BFKL Pomeron exchange [2], in perturbative QCD. If one selects the events with comparable photon virtualities, the BFKL resummation effects dominate with respect to the conventional partonic evolution of DGLAP [3] type. Several studies of BFKL dynamics have been performed at the level of the total cross-section [4]. At high energy, the impact factor representation of the scattering amplitude has the form of a convolution in the transverse momentum $\underline{k}$ space between the two impact

Figure 1: The amplitude of the process $\gamma^*_{L,T}(q_1)\gamma^*_{L,T}(q_2) \to \rho^0_L(k_1)\rho^0_L(k_2)$ in the impact representation.

factors, corresponding to the transition of $\gamma^*_{L,T}(q_i) \to \rho^0_L(k_i)$, via the $t-$channel exchange of two reggeized gluons (with momenta $\underline{k}$ and $\underline{r} - \underline{k}$). The final states ρ mesons are described in the collinear factorization by their distribution amplitudes (DA) in a similar way as in the classical work of Brodsky-Lepage [5].
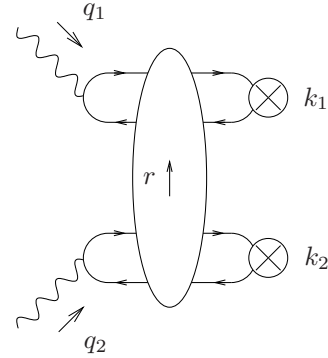
---

[*] speaker
[†] Unité mixte 8627 du CNRS

2 Non-forward Born order cross-section at ILC for $e^+e^- \to e^+e^-\rho_L^0 \rho_L^0$

Our purpose is to evaluate at Born order and in the non-forward case the cross-section of the process $e^+e^- \to e^+e^-\rho_L^0 \rho_L^0$ in the planned experimental conditions of the International Linear Collider (ILC).

We focus on the LDC detector project and we use the potential of the very forward region accessible through the electromagnetic calorimeter BeamCal which may be installed around the beampipe at 3.65 m from the vertex. This calorimeter allows to
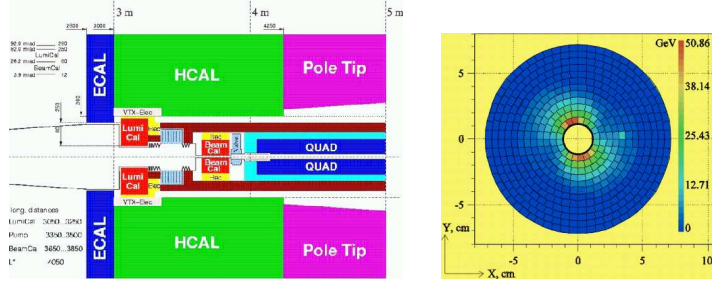

Figure 2: LDC (a). Beamstrahlung in BeamCal (b).

detect (high energetic) particles down to 4 mrad. This important technological step was not feasible a few years ago. The foreseen energy of the collider is $\sqrt{s} = 500$ GeV. Moreover we impose that $s_{\gamma^*\gamma^*} > c\,Q_1\,Q_2$ (where c is an arbitrary constant): it is required by the Regge kinematics for which the impact representation is valid. We choose $Q_{i\,min} = 1$ GeV and $Q_{i\,max} = 4$ GeV: indeed the various amplitudes involved are completely negligible for higher values of virtualities.
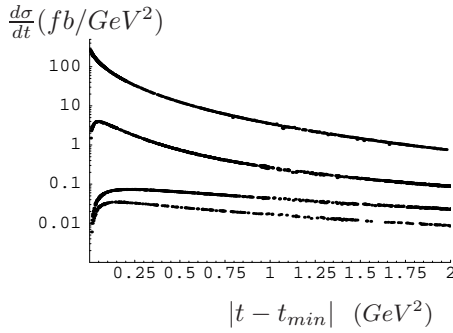
Figure 3: Cross-sections for $e^+e^- \to e^+e^-\rho_L^0 \rho_L^0$ process. Starting from above, we display the cross-sections corresponding to the $\gamma_L^*\gamma_L^*$ mode, to the $\gamma_L^*\gamma_T^*$ modes, to the $\gamma_T^*\gamma_{T'}^*$ modes with different $T \neq T'$ and finally to the $\gamma_T^*\gamma_{T'}^*$ modes with $T = T'$.

Figure 4: Cross-sections for $e^+e^- \to e^+e^-\rho_L^0 \rho_L^0$ at $t = t_{min}$ for different values of the parameter c: the red curves correspond to $c = 1$, the green curves to $c = 2$ and and the yellow curves to $c = 3$. For each value of c, by decreasing order the curves correspond to gluon-exchange, quark-exchange with γ_L^* and quark-exchange with γ_T^* .

We now display in Fig.3 the cross-sections as a function of the momentum transfer t for the different γ^* polarizations. For that we performed analytically the integrations over $\underline{k}$ (using conformal transformations to reduce the number of massless propagators) and numerically the integration over the accessible phase space. We assume the QCD coupling constant to be $\alpha_s(\sqrt{Q_1Q_2})$ running at three loops, the parameter $c = 1$ which enters in the Regge limit condition and the energy of the beam $\sqrt{s} = 500$ GeV. We see that all the differential cross-sections which involve at least one transverse photon vanish in the forward case when $t = t_{min}$, due to the s-channel helicity conservation. We finally display in the

Table.1 the results for the total cross-section integrated over t for various values of c. With the foreseen nominal integrated luminosity of $125\,\mathrm{fb}^{-1}$, this will yield $4.26\,10^3$ events per year with $c = 1$. By looking into the upper curve in the Fig.3 related to the longitudinal polarizations, one sees that the point $t = t_{min}$ gives the maximum of the total cross-section (since the transverse polarization case vanishes at t_{min}) and then practically dictates the trend of the total cross-section which is strongly peaked in the forward direction (for the longitudinal case) and strongly decreases w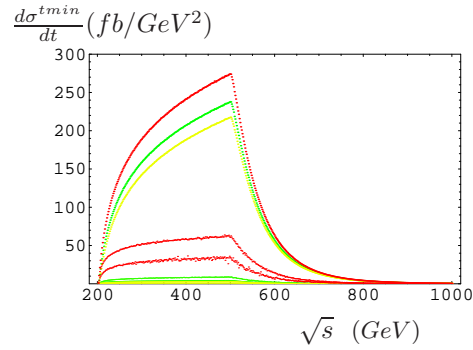ith t (for all polarizations). From now we only consider the forward dynamics. The Fig.4 shows the cross-section (for both gluons and quarks exchanges) at t_{min} for different values of

c	$\sigma^{Total}\,(fb)$
1	34.1
2	29.6
10	20.3

Table 1: σ^{Total} for various c.

the parameter c which enters in the Regge limit condition: the increase of c leads to the suppression of quarks exchanges (studied in [6]) and supplies us an argument to fix the value of c on the gluon exchange dominance over the quark exchange contribution. The ILC collider is expected to run at a cm nominal energy of 500 GeV, though it might be extended in order to cover a range between 200 GeV and 1 TeV. Although the Born order cross-sections do not depend on s, the triggering effects introduce an s-dependence that explains the peculiar ('fin of shark' like) shape of the cross sections displayed in Fig.4: because we chose $Q_{i\,min} = 1\mathrm{GeV}$ (as hard cut required by the perturbative analysis), the corresponding minimal angle of the scattered leptons (that behaves like $2\,Q_{i\,min}/\sqrt{s}$) will cross over the experimental cut imposed by the resolution of the calorimeter as soon as $\sqrt{s}$ will be bigger than 500 GeV, explaining why the cross-sections fall down between 500 GeV and 1 TeV. The measurability is then optimal for $\sqrt{s} = 500$ GeV.

3 Forward differential cross-section with BFKL evolution

The results obtained at Born approximation can be considered as a lower limit of the cross-sections for ρ-mesons pairs production with complete BFKL evolution taken into account. We also consider below only the forward case and we first evaluate the leading order (LO) BFKL evolution (in the saddle point approximation) of our process. The comparison of Fig.4 with Fig.5 leads to the conclusion that the LO BFKL evolution dramatically enhances the shape of the cross-section when increasing $\sqrt{s}$, though it is not very fruitful to make precise predictions: indeed, the Pomeron intercept (which corresponds to the leading pole in the ω plane and then controls the power like growth of the amplitude) takes quite large values mainly because it is proportional to the strong coupling $\alpha_s(\sqrt{Q_1 Q_2})$ whose scale dependence is arbitrarily prescribed at LO, and causes severe instabilities (since its running starts at 1GeV with our choice of the hard cut). It is well-known that the next-to-leading order (NLO) contribution is expected to be between the LO and Born order cross-sections since the value of the intercept is widely reduced when considering NLO BFKL evolution. To study these effects we use the renormalization group improved BFKL kernel [7]. Our results are in accordance with the ones made from the full NLO kernel used in [8]. In this approach developed in [9], we must find the solutions (the NLL Pomeron intercept ω_s and the anomalous dimension γ_s) of a set of two coupled equations. Although this approach needs a fixed strong coupling, we reconstruct in ω_s and γ_s a scale dependence by fitting with polynomials of Q_i a large range of solutions obtained for various values of $\alpha_s(\sqrt{Q_1 Q_2})$. Moreover, the results are much less sensitive to the choice of the scale dependence of the strong coupling than the ones obtained at LO. We display in the Fig.6 the curves (with $c = 1$) at Born order obtained previously with the one obtained after NLO BFKL resummation.
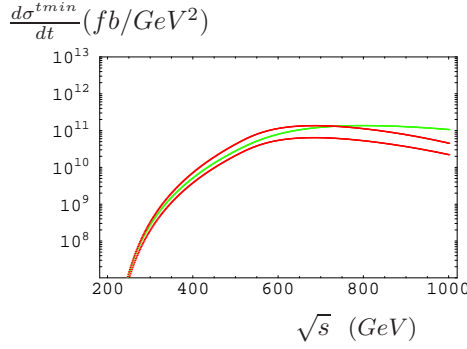
$$\frac{d\sigma^{tmin}}{dt}(fb/GeV^2)$$

$$\frac{d\sigma^{tmin}}{dt}(fb/GeV^2)$$

Figure 5: Cross-sections at $t = t_{min}$ for $e^+e^- \to e^+e^- \rho_L^0 \, \rho_L^0$ with LO BFKL evolution for different α_s : the upper and lower red curves for α_s running respectively at one and three loops and the green one for $\alpha_s = 0.46$.
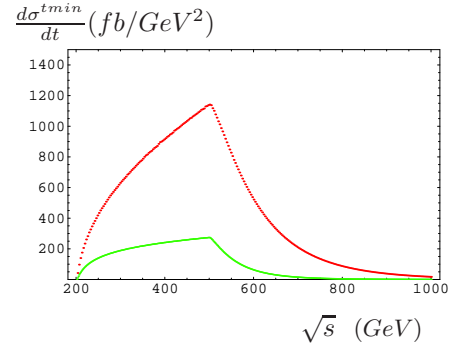
Figure 6: Cross-sections at $t = t_{min}$ for $e^+e^- \to e^+e^- \rho_L^0 \, \rho_L^0$ with NLO BFKL evolution (red curve) and at Born order (green curve) .

4 Acknowledgments

5 Bibliography

References

[1] M. Segond, L. Szymanowski and S. Wallon, Eur. Phys. J. C **52** (2007) 93.

[2] E.A. Kuraev, L.N. Lipatov and V.S. Fadin, Phys. Lett. **B60** (1975) 50-52; Sov. Phys. JETP **44** (1976) 443-451; Sov. Phys. JETP **45** (1977) 199-204; Ya.Ya. Balitskii and L.N. Lipatov, Sov. J. Nucl. Phys. **28** (1978) 822-829.

[3] V. N. Gribov and L. N. Lipatov, Yad. Fiz. **15** (1972) 781 [Sov. J. Nucl. Phys. **15** (1972) 438]; G. Altarelli and G. Parisi, Nucl. Phys. B **126** (1977) 298 ; Y. L. Dokshitzer, Sov. Phys. JETP **46** (1977) 641 [Zh. Eksp. Teor. Fiz. **73** (1977) 1216].

[4] J. Bartels, A. De Roeck and H. Lotter, Phys. Lett. B **389** (1996) 742 ; S. J. Brodsky, F. Hautmann and D. E. Soper, Phys. Rev. Lett. **78** (1997) 803 [Erratum-ibid. **79** (1997) 3544]; J. Kwiecinski and L. Motyka, Phys. Lett. B **462** (1999) 203 ; M. Boonekamp, A. De Roeck, C. Royon and S. Wallon, Nucl. Phys. B **555** (1999) 540 ; J. Bartels, C. Ewerz and R. Staritzbichler, Phys. Lett. B **492** (2000) 56; J. Kwiecinski and L. Motyka, Eur. Phys. J. C **18** (2000) 343 .

[5] S. J. Brodsky and G. P. Lepage, Phys. Lett. **B87** (1979) 359 and Phys. Rev. D **24** (1981) 1808; A.V. Efremov and A.V. Radyushkin, Phys. Lett. **B94** (1980) 245.

[6] B. Pire, M. Segond, L. Szymanowski and S. Wallon, Phys.Lett.B **639** (2006) 642-651.

[7] G. P. Salam, JHEP **9807** (1998) 019 ; M. Ciafaloni and D. Colferai, Phys. Lett. B **452** (1999) 372 ; M. Ciafaloni, D. Colferai and G. P. Salam, Phys. Rev. D **60** (1999) 114036 ; V. A. Khoze, A. D. Martin, M. G. Ryskin and W. J. Stirling, Phys. Rev. D **70** (2004) 074013 .

[8] D. Y. Ivanov and A. Papa, Nucl. Phys. B **732** (2006) 183 and Eur. Phys. J. C **49** (2007) 947.

[9] R. Enberg, B. Pire, L. Szymanowski and S. Wallon, Eur. Phys. J. C **45** (2006) 759 [Erratum-ibid. C **51** (2007) 1015].

[10] Slides:
http://ilcagenda.linearcollider.org/contributionDisplay.py?contribId=195&sessionId=85&confId=1296

$\gamma\gamma$, $e - \gamma$, $e^- e^-$ Physics and Technology

Conveners: J. Gronberg, M. Velasco, M. Krawczyk, V. Telnov, E. Asakawa, K. Cheung

H and A Discrimination using Linear Polarization of Photons at the PLC

A.F.Żarnecki[1], P.Nieżurawski[1], M.Krawczyk[2*]

1- Institute of Experimental Physics, University of Warsaw
Hoża 69, 00-681 Warszawa, Poland

2- Institute of Theoretical Physics, University of Warsaw
Hoża 69, 00-681 Warszawa, Poland

First realistic estimate of the usefulness of the Photon Linear Collider with linearly polarized photons as analyzer of the CP-parity of Higgs bosons is presented. MSSM Higgs bosons H and A with 300 GeV mass, for the model parameters corresponding to the so called "LHC wedge" region, are considered. When switching from circular to linear photon polarization a significant increase in heavy quark production background, which is no longer suppressed by helicity conservation, and decrease of the Higgs boson production cross sections by a factor of two is expected. Nevertheless, after three years of Photon Linear Collider running heavy scalar and pseudoscalar Higgs bosons in MSSM can be distinguished at a 4.5 σ level.

1 Introduction

The physics potential of a Photon Linear Collider (PLC) is very rich and complementary to the physics program of the e^+e^- and hadron-hadron colliders. It is an ideal place to study the mechanism of the electroweak symmetry breaking (EWSB) and the properties of the Higgs sector, as it allows for a resonant production of the Higgs particles. In our previous studies we have performed realistic simulations of the Higgs boson production at PLC within the Standard Model [2, 3], Two Higgs Doublet Model (2HDM) [4], MSSM [5] and a generic model with the CP violating Higgs boson couplings [6]. In all cases we have assumed circular polarization of colliding photon beams, which is favourable from the point of view of production cross section and background suppression. However, it does not allow to disentangle between production of heavy MSSM Higgs bosons H and A [5]. It was suggested that for studies of the CP-parity of Higgs particles and search for a potential violation of the CP-invariance in the Higgs sector linear photon polarization should be used [7]. In the presented study [1] we have made the first realistic estimate of the Higgs measurement at PLC running with linearly polarized beams.

2 Luminosity spectra

In order to perform this analysis, parametrization of the PLC luminosity spectra CompAZ [8] has to be extended to linear photon polarization. As pointed out in [9], there are significant correlations between polarizations of colliding photons, resulting in sizable increase of the effective polarization. They are of special importance at high beam energies, where average beam polarizations are low. Only due to this phenomena measurements with linear polarization are possible at all in this energy region. CAIN [10] program was used to simulate

---
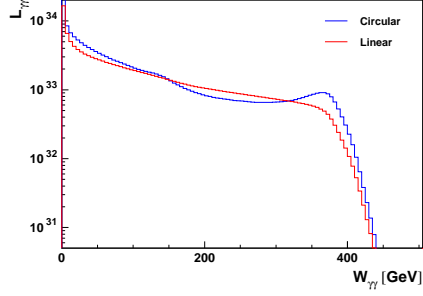
Figure 1: Expected luminosity spectra at the PLC for circular and linear photon beam polarizations, as obtained from CAIN simulation. Parameters of the TESLA Photon Collider were used with electron beam energy of 250 GeV and electron circular polarization of 85%.
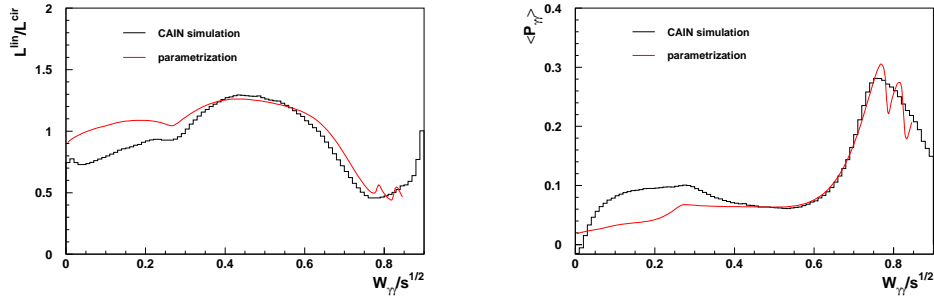
Figure 2: Comparison of the CAIN simulation results for linear photon beam polarization with new luminosity spectra parametrization based on CompAZ. Ratio of $\gamma\gamma$ luminosities for linear and circular polarization (left plot) and the average product of polarizations for colliding photons (right plot) are considered.

Compton backscattering process with linearly polarized laser photons at the PLC, taking into account all correlations. Based on this simulation we derive expected luminosity and polarization in $\gamma\gamma$ collisions. Figure 1 shows the comparison of the expected PLC luminosity spectra for circular and linear beam polarizations. For linear polarization luminosity spectra is no longer peaked at high energies and the luminosity in the region of high energy $W_{\gamma\gamma}$ decreases. Simulation results were used to constrain parameters describing polarization gain in $\gamma\gamma$ collisions. As shown in Figure 2 the obtained parametrization properly describes modification of the luminosity spectra due to change of beam polarization, especially in the high energy domain. Also the average product of photon polarizations, $\langle P_{\gamma\gamma} \rangle$, is well described. In the region of large $W_{\gamma\gamma}$, $\langle P_{\gamma\gamma} \rangle$ of up to about 30% can be obtained.

3   Cross section measurement

Parametrized luminosity spectra are used to simulate Higgs boson production with linearly polarized beams. We considered production of the MSSM Higgs bosons H and A for the parameter values corresponding to the "LHC wedge" region: $M_A = 300$ GeV, $\tan\beta = 7$, $M_2 = \mu = 200$ GeV. For these parameter values, bosons H and A are almost degenerate
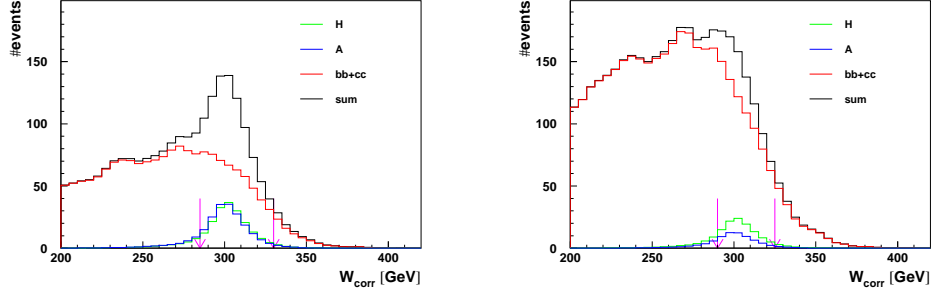
Figure 3: Reconstructed invariant mass distributions expected after one year of PLC running, for circular (left) and linear (right) photon beam polarizations.

in mass and can not be distinguished on the detector level. Analysis follows our previous study described in [5]. However, here only the background from heavy quark production $(\gamma\gamma \to Q\bar{Q}(g)$, $Q = b, c)$ is taken into account. Figure 3 shows the reconstructed invariant mass distributions expected after one year of PLC running, for circular and linear beam polarizations. We observe that with linear polarization signal (H and A production) decreases by about factor of two. This is because of the luminosity drop at high $W_{\gamma\gamma}$, but also due to the reduced circular polarization of the photon beam (even with 100% linear laser polarization, some degree of the circular polarization is expected due to the polarization of the incident electron beam). Smaller degree of circular polarization results also in significant increase in heavy quark production background, which is no longer suppressed by the helicity conservation. After independent cut optimization, signal to background ratio for linear polarization is about factor of 3 smaller than for the circular polarization. Precision of the cross section measurement, for H and A production, changes from about 8% for circular beam polarization to about 18% for linear one, after one year of PLC running.

4   Discrimination between H and A

For linear photon polarization we observe a clear difference between production of scalar and pseudo-scalar Higgs bosons, as shown in Figure 3 (right). By selecting parallel or perpendicular orientation of linear polarizations of two beams, we enhance production of scalar or pseudo-scalar state, respectively. By combining measurements with different polarization orientations, cross sections for H and A production can be disentangled. After three years of PLC running (one year with each orientation of linear polarization and one year with circular polarisation) cross section determination precision of 22% can be obtained. Hypothesis of pure scalar or pure pseudo-scalar production (assuming that the total production cross section for unpolarized beam is the same as in the considered MSSM scenario) can be distinguished at 4.5 σ level, see Figure 4. Polarization of the photon beam obtained in the process of Compton backscattering is determined by polarizations of the incident laser and electron beams. Circular and linear polarization configurations considered so far correspond to the laser light with 100% circular or 100% linear polarization, and 85% circular polarization for electrons. However, one could also consider laser with mixed polarization. In fact, highest $\langle P_{\gamma\gamma} \rangle$ can be obtained by using 95% linear laser polarization with additional contribution of 30% circular laser polarization. However, the corresponding polarization configuration
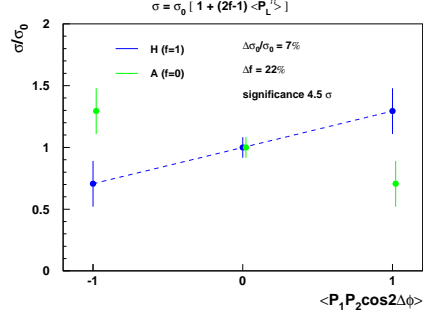
Figure 4: Expected precision of Higgs boson production cross section measurements after three years of PLC running with circular and two linear laser beam polarizations.

results also in sizable decrease of luminosity at high $W_{\gamma\gamma}$ so that the final measurement precision is significantly worse. Therefore we can conclude that the best separation between H and A states can be obtained with 100% linear laser polarization.

5 Conclusions

We presented the first realistic estimate of the Higgs boson CP-parity determination at the PLC with linear beam polarization. Heavy MSSM Higgs bosons H and A, for model parameters corresponding to the so called "LHC wedge", were considered. Significant increase in heavy quark production background, which is no longer suppressed by helicity conservation, and decrease of the Higgs boson production rate result in the cross section measurement precision much lower than for the circular beam polarization. Nevertheless, after three years of PLC running cross sections for H and A production can be separately measured with precision of about 20%. Hypotheses of pure scalar or pure pseudo-scalar nature of the Higgs boson (assuming the same value for the total production cross section) can be distinguished at 4.5 σ level.

References

[1] Slides:
http://ilcagenda.linearcollider.org/contributionDisplay.py?contribId=441&sessionId=79&confId=1296

[2] P. Nieżurawski, A. Żarnecki, M. Krawczyk, Acta Phys. Pol. **B 34**, 177 (2003);
P. Nieżurawski, arXiv:hep-ph/0507004, arXiv:hep-ph/0503295.

[3] P.Nieżurawski, A.F.Żarnecki, M.Krawczyk, JHEP 0211, 034 (2002).

[4] P. Nieżurawski, A.F. Żarnecki, M. Krawczyk, JHEP 0502, 041 (2005).

[5] P. Nieżurawski, A.F. Żarnecki, M. Krawczyk, arXiv:hep-ph/0507006;
P. Nieżurawski, A.F. Żarnecki, M. Krawczyk, Acta Phys. Pol. **B37**, 1187 (2006).

[6] P. Nieżurawski, A.F. Żarnecki, M. Krawczyk, Acta Phys. Pol. **B36**, 833 2005.

[7] K. Hagiwara, Nucl. Instrum. Meth. **A472**, 12 (2001).

[8] A.F. Żarnecki, Acta Phys. Polon. **B34** 2741 (2003).

[9] V. Telnov, *Nontrivial effects in linear polarization at photon colliders*, ECFA workshop, Montepellier, France (2003).

[10] K. Yokoya, KEK-Report-85-9.

Charge Asymmetry in $\gamma\gamma \rightarrow \mu^+\mu^- + \nu$'s/ $\gamma\gamma \rightarrow W^\pm\mu^\mp + \nu$'s, effect of photon non-monochromaticity and $p_\perp$ dependence

D. A. Anipko[1], I. F. Ginzburg[1], K.A. Kanishev[1], A. V. Pak[1], *
M. Cannoni[2], O. Panella[2]

1 - Sobolev Institute of Mathematics and Novosibirsk State University,
Novosibirsk, Russia

2 - Istituto Nazionale di Fisica Nucleare,
Sezione di Perugia, Via A. Pascoli, I-06123, Perugia, Italy

The momentum distributions of positively and negatively charged leptons ($\ell^\pm = \mu^\pm$, $e^\pm$) in the reactions of type $\gamma\gamma \rightarrow \ell^+\ell^- + N\nu$, $\gamma\gamma \rightarrow W^\pm\ell^\mp + N\nu$ at $\sqrt{s} > 200$ GeV with polarized photons demonstrates a considerable charge asymmetry. We discuss the influence of photon non-monochromaticity on this effect and its dependence on transverse momentum, which will be essential for the study of New Physics effects.

Photon colliders with high energy highly polarized photon beams [1] provide very effective field for the study of new effects of both SM and New Physics. In particularly, it is naturally to expect that the charge asymmetry of leptons, produced in the collision of neutral but highly polarized colliding particles $\gamma\gamma \rightarrow \ell^+\ell^- + neutrals$ (where $\ell = \mu$, e), can be a good tool for the discovery of New Physics effects [2].

In this report we study most important background process of this type – the SM process, in which *neutrals* are ν's and main mechanism is given by $\gamma\gamma \rightarrow W^+W^-$ process with subsequent lepton decay of W. The latter process (+ other SM processes) will ensure very high event rate at the anticipated luminosity of ILC. The charge asymmetry here appears due to transformation of initial photon helicity into distribution of final leptons via P-violating but CP-preserving leptonic decay of W. Indeed, it was found earlier that the charge asymmetry in distributions of charged leptons in $\gamma\gamma \rightarrow \mu^+\mu^-\nu_\mu\bar{\nu}_\mu$ processes is a very strong effect [3]. The same observable final state can be produced in processes with more neutrinos: $\gamma\gamma \rightarrow W^\pm\mu^\mp + N\nu$. Contribution of such processes with intermediate τ-lepton was taken into account in [4]. It was shown that this cascade processes changes the asymmetry only weakly. In this report we discuss additionally two new points.

First, the photon beams at the Photon Colliders will be non-monochromatic. How it influence for charge asymmetry?

Second, we present most of results, applying cuts on the muons scattering angles given by $\pi - \theta_0 > \theta > \theta_0$, with $\theta_0 = 10$ mrad, and a cut on muons transverse momentum $p_\perp^c > 10$ GeV, both on each muon or W and on the couple of muons. These simultaneous cuts reduce many backgrounds. We expect that the New Physics effects will be more important at high $p_\perp$. How discussed SM charge asymmetry depend on cut value $p_\perp^c$?

Our numerical results have been obtained with the CompHEP/CalcHEP packages [5], [6] in a version which allows one to take into account the circular polarization of the initial photons and choose different random seed numbers for Monte Carlo (MC) [6].

$\gamma\gamma \to \mu^+\mu^-\nu\bar{\nu}$, monochromatic photons.

Fig. 1. presents the distributions of muons in the $p_\parallel$, $p_\perp$ plane, $\partial^2\sigma/(\partial p_\parallel \partial p_\perp)$ at different photon polarizations for monochromatic beams and without cascade processes.

These figures show explicitly strong difference in the distributions of negative and positive muons as well as strong dependence of distributions on photon polarizations. Therefore, the charge asymmetry in the process is a strong effect.

To obtain quantitative description, we consider normalized mean values of longitudinal $p_\parallel^\mp$ and transverse $p_\perp^\mp$ momenta of μ^- or μ^+, in the forward hemisphere ($p_\parallel > 0$, subscript $+$), and take their relative difference as a measure of the longitudinal Δ_L and transverse Δ_T charge asymmetry:

$$P_{L,T+}^\pm = \frac{\int p_{\parallel,\perp}^\pm d\sigma}{E_\gamma^{max}\int d\sigma}, \quad \Delta_{L,T} = \frac{P_{L,T+}^- - P_{L,T+}^+}{P_{L,T+}^- + P_{L,T+}^+}$$

MC calculations simulate experiment and have statistical uncertainty similar to that in the future experiment. We find it useful to obtain statistical uncertainties $\delta_{L,T}$ of the considered integral characteristics at given expected number of events (about 10^6) by repeating our calculation 5 times with different seed number inputs for MC (with CalcHEP [6]). Also we consider as an independent set of observations data obtained by simultaneous change λ_1, $\lambda_2 \to -\lambda_1$, $-\lambda_2$, $\mu^- \leftrightarrow \mu^+$ (this change should not change distributions due to CP conservation in SM).

Table I presents obtained average momenta for the positive and negative muons and corresponding asymmetry quantities together with their statistical uncertainties (in percents).

Fig.1 *Muon distribution in* $\gamma_-\gamma_- \to W\mu + \nu's$ *(upper plots) and* $\gamma_+\gamma_- \to W\mu + \nu's$ *(lower plots), left – μ^-, right – μ^+*

$\gamma_{\lambda_1}\gamma_{\lambda_2}$	N	P_N^- δP_N^-	P_N^+ δP_N^+	Δ_N $\delta\Delta_N$
$\gamma_-\gamma_-$	L	0.606 0.29%	0.201 0.55%	0.501 0.57%
	T	0.333 0.61%	0.159 0.28%	0.335 0.44%
$\gamma_+\gamma_-$	L	0.223 0.74%	0.609 0.19%	-0.463 0.47%
	T	0.164 0.08%	0.262 0.31%	-0.231 2.76%

Table I. *Charge asymmetry quantities and statistical uncertainties for* $\gamma_{\lambda_1}\gamma_{\lambda_2} \to W\mu\nu$ *process, N=T or L.*

Cascade process contribution.

The final state $\mu\mu$ (or $W\mu$) + *missing* $p_\perp$ mainly arises through the process $\gamma\gamma \to \mu^+\mu^-\nu_\mu\bar{\nu}_\mu$ ($\gamma\gamma \to W\mu\nu$). In addition, *cascade processes* such as $\gamma\gamma \to \tau^+\mu^-\nu_\tau\bar{\nu}_\mu$ ($\gamma\gamma \to W\tau\nu$), $\tau \to \mu\nu_\mu\nu_\tau$, contribute at the level 37% (17%) relative to the leading contribution. The straightforward calculation of such processes is out of potential of known packages. The good way give here *double-resonant (DRD) approximation*, in which one consider only diagrams $\gamma\gamma \to W^+W^-$ (DRD diagrams) with subsequent decay of W to leptons. Direct calculation shows these DRD-diagrams are responsible for about 98% of the total $\gamma\gamma \to W\mu\nu$ cross-section. The same is valid for the momentum distributions. Therefore the
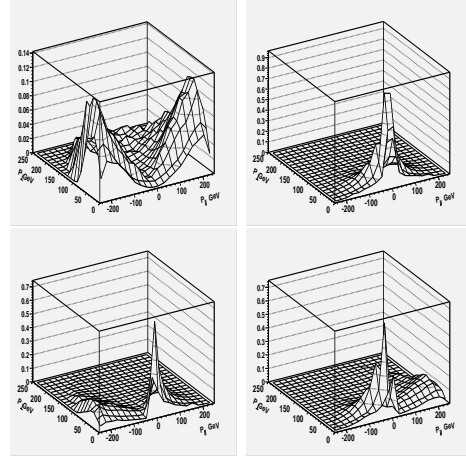
inaccuracy implemented by the using of DRD approximation for cascade process is no more than $2\% \cdot Br(\tau \to \mu) \approx 0.3\%$. That is within statistical uncertainty shown in the Table I.

In the framework of DRD approximation, the polarization of τ in the rest frame of W is collinear with the known momentum of corresponding neutrino, and the momentum distribution of muons from the decay of τ in this system is calculated easily. The distribution of final muons in our process is given by the convolution of the mentioned accurate distribution of μ in τ decay with the CompHEP-generated distribution [4].

Note that the decay $\tau \to \mu \nu_\tau \nu_\mu$ involves three particles. The effective mass of the neutrino pair $m_{\nu\nu}$ varies from 0 to almost m_τ. Hence, in the collision frame $E_\mu \leq E_\tau(1 - m_{\nu\nu}^2/m_\tau^2)$. Therefore, the distribution of muons in the cascade process is similar in the main features to that of incident τ, but it is strongly contracted to the origin of coordinates. Therefore, cascade processes change the asymmetry only weakly, and their contribution to the asymmetry reduces even more with the growth of applied cuts (see [4]).

Effect of photon non-monochromaticity

At the Photon Collider photons will be non-monochromatic with spectra peaked near the high energy limit E_γ^{max}. Moreover, due to the finite distance between conversion point (CP) and interaction point (IP) and also due to rescatterings of laser photons on electrons after first collision with laser photon, photon spectra even non-factorizable. Fortunately in the high energy part of spectra $(E_\gamma > E_\gamma^{max}/\sqrt{2})$ these spectra are factorizable with high precision and these photons have high degree of polarization. Moreover, the form of effective spectra in this region is described with high accuracy with the aid of one additional parameter only, independent on details of organization of experimental set up [7]. The luminosity of Photon Collider is normalized for this very region only.

As for low energetic tail of effective photon spectrum it depends strongly on details of experimental set-up which will vary in the process of construction of ILC.

Fig.2 *The distributions of muons calculated with "realistic" spectra distribution. Upper plots - $\gamma_-\gamma_-$. Lower plots – $\gamma_+\gamma_-$. Left – μ^-, right – μ^+*

So, in our simulations for the high energy part of the spectrum $E_\gamma > E_\gamma^{max}/\sqrt{2}$ we used the approximation from [7] with $\rho = 1$ and $x = 4.8$ with polarization for ideal Compton effect [1]. To imitate low energy part of spectrum we used spectra from [1] for the case when IP and CP coincide ($\rho = 0$) and consider these photons to be unpolarized. The resulting distributions of muons are presented on Fig. 2. These distributions resemble the distributions presented on Fig. 1. with additional wide peak at low energies. Table II shows the corresponding asymmetry quantities. These values are slightly smaller in comparison to monochromatic case. But they are still large enough and replicate in main

$\gamma_{\lambda_1}\gamma_{\lambda_2}$	N	P_N^-	P_N^+	Δ_N
$\gamma_-\gamma_-$	L	0.365	0.157	0.398
	T	0.284	0.179	0.228
$\gamma_+\gamma_-$	L	0.174	0.338	-0.321
	T	0.200	0.236	-0.082

Table II. *Charge asymmetry quantities for "realistic" photon spectra.*

features the values in Table I (with approximately the same statistical uncertainties).

Dependence on $p^c_{\perp\mu}$ cut

New Physics effects are expected to be switched on at the relatively large transverse momenta. That is why we study the dependence of observed effects on the cut value $p^c_{\perp\mu}$.
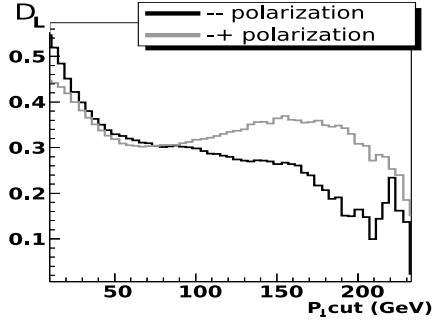
Fig.3 *The $p^c_{\perp\mu}$ dependence of asymmetry.*
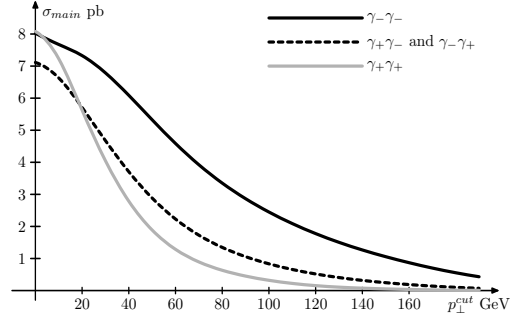
Fig.4 *The smoothed $\gamma\gamma \to W^+\mu^-\bar{\nu}$ cross section dependence on $p^c_{\perp\mu}$.*

Figs. 3 and 4 show the $p^c_{\perp\mu}$ dependence of the asymmetry quantity Δ_L and the cross section of the $\gamma\gamma \to W^+\mu^-\bar{\nu}$ process. One can see that the asymmetry remains large even with large cuts, while the cross section quickly reduces.

Conclusions

- The asymmetry effect is huge and easily observable.
- Cascade process weakly affect the asymmetry.
- Introduced quantities (especially Δ_L) are large even with large $p^c_{\perp\mu}$ cuts (but the number of events reduces strong at large $p^c_{\perp\mu}$).
- Taking into account same effects for e^+e^-, $e^+\mu^-$, μ^+e^- enhance effective cross section for $\gamma\gamma \to \ell^+\ell^-\nu\bar{\nu}$ from 1.2 to 4.8 pb and for $\gamma\gamma \to W^+\ell^-\bar{\nu}$, etc. to 30 pb.
- The statistical uncertainty is at the level of radiative corrections, so the tree-level approximation is sufficient
- Non-monochromaticity of photon spectra decreases the considered asymmetries but retain them large enough.

References

[1] I. F. Ginzburg, G. L. Kotkin, V. G. Serbo and V. I. Telnov, Nucl. Instrum. Meth. 205 (1983) 47; I. F. Ginzburg, G. L. Kotkin, S. L. Panfil, V. G. Serbo and V. I. Telnov, Nucl. Instrum. Meth. A 219 (1984) 5.

[2] I. F. Ginzburg, hep-ph/0211099.

[3] D. A. Anipko, M. Cannoni, I. F. Ginzburg, A. V. Pak, O.Panella, *Nucl. Phys.* **B** *Proc. Suppl.* **126** (2004) 354–359; hep-ph/0306138; hep-ph/0410123.

[4] D. A. Anipko, M. Cannoni, I. F. Ginzburg, K. A. Kanishev, O. Panella, A. V. Pak. *Acta Phys. Polonica,* **B37** (2006) 1193-1200

[5] E. Boos et al. Nucl. Instr. Meth. **A534** (2004) 250; hep-ph/0403113

[6] A. Pukhov, hep-ph/0412191

[7] I.F. Ginzburg, G.L. Kotkin. *Eur. Phys. J.* **C 13** (2000) 295–300

Anomalous Gamma Gamma Interaction

Philip Yock

University of Auckland - Department of Physics
Auckland - New Zealand

Data from LEP2 on hadron production in $\gamma\gamma$ interactions at high p_T exceed the predictions of QCD by about an order of magnitude. The amplitude for the process is asymptotically proportional to the sum of the squares of the charges of quarks. The data are suggestive of models where quarks have unit charges, or larger. Unequivocal tests could be made with the ILC or CLIC, but a plasma wakefield e^-e^- collider might provide the most affordable option [1].

1   The anomaly

Hints of anomalous hadron production in $\gamma\gamma$ interactions were first reported from studies made at SLAC and DESY [2]. The first evidence for a large anomaly was reported by the L3 group from studies carried out at LEP2 at 200 GeV [3]. L3 reported data on inclusive π^0 production at values of p_T approaching 20 GeV/c. The data, shown in Figure 1, exceed the QCD prediction by about an order of magnitude at the highest transverse momenta.

The $\gamma\gamma$ interactions observed by L3 occurred in the process $e^-e^+ \rightarrow e^-e^+\pi^0 X$ where $\gamma's$ were radiated by the incoming e^- and e^+. The radiative process was known to be a copious source of $\gamma\gamma$ interactions [4]. Events were selected by L3 in which the outgoing e^- and e^+ emerged in the beam pipe of the collider and, although undetected, were known to produce almost real γ's. The $\gamma\gamma$ events were identified by calorimeter measurements in which the total energy of emerging hadrons was significantly less than 200 GeV.

Figure 1: Differential cross-section for inclusive π^0 production in $\gamma\gamma$ interactions measured at LEP2 and the prediction by QCD

Observations of π^0 production at LEP2 have not been reported by other groups. However, data on $\pi^\pm$ production have been reported by both L3 and OPAL [3, 5]. They are comparable to the π^0 data. Both L3 and OPAL found significant excesses over the QCD prediction at $p_T \sim 17$ GeV/c. The excess reported by L3 is slightly greater than that shown in Figure 1 for π^0 production, whereas for OPAL the excess is slightly less.

Data have also been reported by L3 and OPAL on inclusive jet production [3, 5]. The data by L3 extend to higher values of p_T than those of OPAL, and they show a greater excess over the QCD prediction, reaching nearly an order of magnitude at 45 GeV/c. Most of the above datasets are displayed in [1].
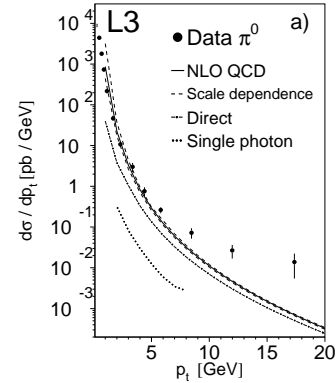
2   Experimental remarks

The main source of background in the above experiments results from $e^-e^+ \to Z\gamma$ where initial state radiation reduces the invariant mass of the e^-e^+ system to that of the Z, and the γ emerges in the beam pipe and is undetected. Hadronic decays of the Z in these events can mimic $\gamma\gamma$ interactions. However, Z's produced as above are boosted to an energy of $\sim 0.65\sqrt{s}$. Both L3 and OPAL made cuts on the total energy observed in their calorimeters to remove the background. The high-precision calorimeters employed by L3 enabled them to place the cut at $0.4\sqrt{s}$ and maintain the background below 1% [1]. In the case of OPAL, the cut was placed at a lower level, and/or extra conditions applied, resulting in analyses of greater complexity.

3   Physics implications

The measurements by L3 and OPAL are significant. According to the Standard Model (SM), the Feynman diagram shown in Figure 2 applies when $p_T \geq$ few GeV/c [2]. The amplitude was therefore predicted to be proportional to the sum of the squares of the charges of quarks accessible at 200 GeV, and the cross section expected to provide a simple but sensitive constraint on these basic charges [6]. The data are, however, inconsistent with the SM expectation. If valid, they suggest alternative models with larger charges.
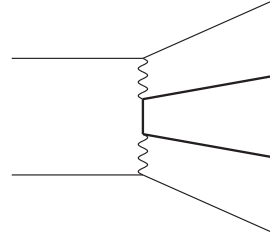
Figure 2: Feynman diagram for hadron production at asymptotically high p_T in $\gamma\gamma$ interactions as observed with e^-e^+ colliders. Thin lines denote leptons, heavy lines quarks.

3.1   Unit charges

Ferreira [7] considered a Han-Nambu model with unit charges and found improved agreement with the data, although the p_T dependence was not perfectly fitted. He reviewed the extensive literature that exists on quarks of unit charges, and considered the production of b hadrons in $\gamma\gamma$ interactions where a possible excess of data over theory was reported. He found this excess could be accounted for by unit charges. We note, however, that the ALEPH group subsequently reported a lower cross section for the production of b hadrons [8].

3.2   High charges

Before QCD was proposed, two theories of highly charged quarks were proposed, independently. In one, quarks were proposed by Schwinger [9] to be magnetic monopoles, in the other they were proposed by the author [10] to be highly electrically charged particles. In both cases it was assumed that strong electromagnetic forces between quarks accounted for quark binding, and that strong nuclear interactions between composite states occurred as residual interactions. Colour charges were not included. Both theories were based on eigenvalue equations for charge. In [9] a modified version of Dirac's eigenvalue equation for magnetic charge was assumed. In [10] a physical solution to a Gell-Mann-Low equation was assumed. In both theories, little progress was made in solving the field equations, because of the strong couplings involved.

A generalized Yukawa model [11] was proposed for [10], as shown in Figure 3. Bare mesons and nucleons were assumed to act as partons of unit charge at low energies, thus avoiding the hadronization puzzle of the SM. Large electromagnetic effects were anticipated to occur at the shorter scale shown in the figure. The possibility arises that the LEP2 data are exhibiting the onset of large electromagnetic effects, because the $\gamma\gamma$ amplitude is proportional to the square of the charges of the participating particles. Measurements at higher energies would provide a clear test of this model.

The data shown in Figure 1 are similar to Rutherford's old α-particle scattering data, here reproduced in [1]. Both cross-sections fall in similar fashion through ~ 5.5 orders of magnitude. It was, of course, Rutherford's data that supplanted J.J. Thomson's model of the atom in which low-mass electrons swarmed in a cloud of massless, positive charge, a model that bears some resemblance to today's SM of the nucleon. In contrast, Rutherford's nuclear atom bears more resemblance to particle models with highly charged quarks. We note that the latter require multiple generations of quarks that are not replications of one another [9, 10]. They thus possess inbuilt symmetry breaking. Current searches for the Higgs boson may therefore be viewed as null tests of these models [12].

Figure 3: Generalized Yukawa model of the nucleon. The dots represent highly charged quarks clustered to form bare mesons and nucleons. The larger scale is the π Compton wavelength, i.e. the observed size of the nucleon. The smaller scale represents the fundamental separation between quarks in bound states, assumed in [11] to be $\sim 1,000\times$ smaller.

4   Future experiments

As remarked above, the $\gamma\gamma$ interaction probes fundamental parameters of the SM, sensitively. Existing data from LEP2 by L3 and OPAL, whilst in approximate agreement with one other, are in serious disagreement with the SM. It would clearly be useful if the remaining LEP2 groups (ALEPH and DELPHI) subjected their data to similar analyses. Studies of $\gamma\gamma$ interactions at higher energies would, however, be of greater interest, because neither the L3 nor the OPAL datasets reached asymptotic limits.

The International Linear Collider (ILC) and the Compact Linear Collider (CLIC) would both be ideal machines for this purpose. Plans for the former are more advanced, but both could be used to study $\gamma\gamma$ interactions. Purpose-built $\gamma\gamma$ colliders would not be required. This has been amply demonstrated by the L3 and OPAL experiments. Moreover, both ILC and CLIC could be operated as e^-e^- colliders. In this mode, background from e^-e^+ annihilation would be absent. The cuts on $\sqrt{s}$ described in Section 2 would not be required, and the full beam energy of the colliders could be utilised, thereby accessing significantly higher values of $p_T \sim 100$ GeV/c given sufficient luminosity.

A plasma wakefield collider [13] could offer a more affordable means for carrying out the above program, especially if the Higgs boson fails to materialize at Fermilab and at the LHC. Both electrons and positrons can be accelerated in plasma wakefields. However, an e^-e^- configuration would greatly reduce the cost. Moreover, as remarked above, it would
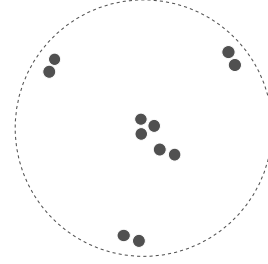
be subject to greatly reduced background.

5 Conclusions

Despite often-made claims to the contrary, e.g. [14], the SM has not withstood every challenge. For example, Yukawa's meson theory, confirmed by the discovery of the π-meson in 1947, appears to lie outside the model[a]. Similarly, the lifetimes of the strange particles, also discovered in 1947, lie outside the model [16]. A raison d'être for the strange particles has yet to be provided, and, conversely, glueballs have yet to be confirmed. The $\gamma\gamma$ results present additional challenges. They are suggestive of alternative models with quarks of unit or larger charges, but further data at higher energies are needed. Three machines would be capable of providing such data - ILC, CLIC, and a plasma wakefield collider. Of these, plans for the first are most advanced, but the last could eventually prove most affordable.

Acknowledgements

Pablo Achard, Barry Barish, Bob Bingham, John Campbell, Francis Collins, Pedro Ferreira, Brian Foster, Philippe Gavillet, Chan Joshi, Maria Kienzle-Focacci, Paolo Palazzi, Francois Richard, Valery Telnov and Thorsten Wengler are thanked for correspondence.

References

[1] Slides:
http://ilcagenda.linearcollider.org/contributionDisplay.py?contribId=443&sessionId=79&confId=1296

[2] J. Binnewies, B.A. Kniehl and G. Kramer, Phys. Rev. **D53** 6110 (1996).

[3] P. Achard *et al.*, L3 Collaboration, Phys. Lett. **B524** 44 (2002);
P. Achard *et al.*, L3 Collaboration, Phys. Lett. **B554** 105 (2003);
P. Achard *et al.*, L3 Collaboration, Phys. Lett. **B602** 157 (2004).

[4] S.J. Brodsky, T. Kinoshita and H. Terezawa, Phys. Rev. Lett. **25** 972 (1970).

[5] G. Abbiendi *et al.*, OPAL Collaboration, Phys. Lett. **B651** 92 (2007);
G. Abbiendi *et al.*, OPAL Collaboration, arXiv:0706.4382 (2007).

[6] E. Witten, Nucl. Phys. **B120** 189 (1977).

[7] P.M. Ferreira, arXiv:hep-ph/0209156 (2002).

[8] S. Schael *et al.*, ALEPH Collaboration, arXiv:0706.3150 (2007).

[9] J. Schwinger, Science **165** 757 (1969).

[10] P.C.M. Yock, Int. J. Theor. Phys. **2** 247 (1969).

[11] P.C.M. Yock, Int. J. Theor. Phys. **41** 1591 (2002).

[12] P.C.M. Yock, CERN Courier **43** 1 56 (2003).

[13] I. Blumenthal, C.E. Clayton, F-J. Decker, M.J. Hogan, C. Huang *et al.*, Nature **445** 741 (2007);
C. Joshi, CERN Courier **47** 5 28 (2007).

[14] A. Wright and R. Webb, Nature **448** 269 (2007).

[15] M. Derrick *et al.*, ZEUS Collaboration, Phys. Lett. **B384** 388 (1996);
J. Breitweg *at al.*, ZEUS Collaboration, Nucl. Phys. **B596** 3 (2001).

[16] H.Y. Cheng, Int. J. Mod. Phys. **A4** 495 (1989);
S.D. Bass and A. de Roeck, Nucl. Phys. Proc. Supp. **105** 1 (2002).

---

[a]In [15] a pion term was clearly required but added 'by hand'.

Using JetWeb to tune Monte Carlo for hadronic backgrounds from $\gamma\gamma$ events at a linear collider

A. Buckley[1], J. M. Butterworth[2], J. W. Monk[2], E. Nurse[2], M. R. Whalley[1] and M. Wing[2]

1- University of Durham - IPPP
South Road, Durham - England

2- University College London - Dept. of Physics & Astronomy
Gower Street, London - England

We demonstrate the JetWeb system for validating and tuning Monte Carlo simulations and show how it can be applied to Monte Carlo simulations for hadronic backgrounds at a linear lepton collider.

1 Introduction

Collisions at a future linear lepton collider will exist inside a background of a very large number of photons. These photons arise from both bremsstrahlung and beamstrahlung [2]. Due to the hadronic content of the photon, these photons lead to an important QCD background. Accurately simulating this background with Monte Carlo will therefore be useful in understanding its effect.

$\gamma\gamma$ interactions in which the partonic structure of the photon is revealed are similar to resolved photoproduction at the HERA lepton-proton collider, the difference being that one of the photons is replaced by a proton. $\gamma\gamma$ events at LEP also resolve the structure of the photon, although the collision energy is lower than at either HERA or a future linear collider. Monte Carlo simulations can therefore be tuned to best fit the photon data from these two colliders and then extrapolated to the higher energies of a linear collider.

2 JetWeb

JetWeb [3] is a web application and database of Monte Carlo results that has been developed by the CEDAR [4] collaboration. JetWeb allows a user to supply a set of Monte Carlo parameters (either input by hand into the web interface or uploaded in a HepML XML file) and perform a search for models that match those parameters. If a matching model already exists within JetWeb's database then a comparison between the Monte Carlo and experimental results can immediately be made across a wide range of datasets from many experiments. The comparison allows a simple visual inspection of the plots or the χ^2 can be calculated between the Monte Carlo and experimental data for all or a subset of the plots. The latter is important because it allows one to determine if the Monte Carlo is valid for all interactions, not just those of immediate interest.

If JetWeb's database does not already contain a model that matches the search then results are not returned immediately. Instead, the user is given the opportunity to request generation of Monte Carlo data to match the new model. The data is generated on a computing grid using scripts written out by JetWeb that steer either HZTool or Rivet (section 4).

Although its primary intended use is validation of existing Monte Carlo tunings, JetWeb can be used in this case to provide a simple way of comparing tunings to photon data.

3 HepData

HepData [3] is used by JetWeb as the source of the comparison plots against which Monte Carlos are validated. The original HepData [5] has been maintained as a hierarchical database at Durham for around thirty years. However, this legacy database, which is usually accessed via Fortran routines, lacks many of the features required for a more modern Java application such as JetWeb. For this reason, the CEDAR collaboration is migrating HepData to a relational MySQL database.

The new HepData allows the data to be represented not only as a database, which can be accessed using remote SQL queries if necessary, but also as a Java object model. The Java object model is a set of Java objects that represent structures from the data, and these objects are automatically filled from the database using the Hibernate system [6]. Hibernate protects the object model from needing to know the details of the underlying database.

4 Rivet

Rivet [7, 8] has been developed by the CEDAR collaboration as a C++ replacement for HZTool [9], which was originally written in Fortran by the H1 and Zeus collaborations. The initial purpose of HZTool was to allow analyses by one experiment to be easily reproduced in Monte Carlo by the other, however it can more generally be used by anyone to reproduce any analysis that is implemented within the HZTool framework.

One of the main ways in which Rivet improves upon HZTool is by the use of what are called *projections*. A projection is a C++ object that acts on a Monte Carlo event to project out a quantity or quantities from that event. For example, a projection might do something as simple as project out only the stable final state particles from the full HepMC record, or it may do something more complicated such as run the jet finding algorithm of a particular experiment. To construct an analysis, all one needs to do is therefore chain together the appropriate set of projections. Once a projection has been applied to an event, Rivet caches the results, which are then available to all analyses. In this way, each projection need only be run once per event, even if many analyses are run as is the case with JetWeb.

Rivet provides histogram booking routines for the AIDA and ROOT histogram formats and also a generator steering package called RivetGun. RivetGun provides a simple interface that allows many different generators to be steered from the command line.

JetWeb runs HZTool or Rivet on a computing grid in order to reproduce all of the analyses that are relevant to the Monte Carlo that is requested by a user.

5 Comparison data and tuneable parameters

For this demonstration we vary the parameters `PTJIM` and the photon radius from the Jimmy [10] multiple interactions model used with Herwig [11]. In these proceedings we show only a small number of the available plots comparing values of `PTJIM` of 2 GeV and 3 GeV and photon radii of 0.47 GeV^{-1} and 0.19 GeV^{-1} (figure 1). All other parameters are set at their default values. A much larger set of plots is available from the relevant pages of the online JetWeb server for models 8, 9, 11 and 14 [12]. The data shown here are taken from two H1 photoproduction papers [13, 14] that show the dependence of the cross section on the fraction x_γ of the photon's momentum carried by the parton and the transverse energy, E_T, of the jets. Data from [13] shows the x_γ dependence above a give jet E_T, while data from

PHRAD	PTJIM	χ^2		
		data from [13]	data from [14]	total
0.47 GeV^{-1}	2 GeV	7.6	0.35	5.4
0.47 GeV^{-1}	3 GeV	0.90	0.93	0.91
0.19 GeV^{-1}	2 GeV	6.8	0.39	4.876
0.19 GeV^{-1}	3 GeV	0.86	0.83	0.85

Table 1: The χ^2 per degree of freedom from JetWeb models 8, 9, 11 and 14 with data shown in figure 1. Where `PHRAD`=0.19 GeV^{-1}, `PTJIM`, is set to 2 GeV.

[14] shows the E_T dependence in a given x_γ range. The χ^2 per degree of freedom for the plots shown is given in table 1. Note that Herwig is a leading order Monte Carlo, and as such the shape of the distributions produced is more important than the overall normalisation.

An important difference between the two papers is that in [13] the outgoing lepton is tagged, which allows the fraction of the beam lepton's momentum carried by the photon (y) to be determined. In [14], the lepton is not tagged and y must be estimated using calorimeter information. `PTJIM` is a cut-off scale below which there can be no radiation, so a lower value of `PTJIM` leads to a higher simulated calorimeter activity. This means that while the values of y determined in [13] are not sensitive to `PTJIM`, in [14] they are. There is a $1/y$ dependence in x_γ, so the sensitivity to changes in the underlying event model is not the same in both papers.

The analysis in [13] requires the jet E_T to be greater than 4 GeV, whereas in [14] the E_T starts at 7 GeV. This makes the top row of plots from [13] more sensitive to the underlying event, which has a greater effect on lower E_T jets. Indeed, the extent to which the underlying event is dominating the simulated jet can be seen in the second row, in which a jet pedestal for the underlying event has been removed leading to an underestimation of the data by the simulation.

6   Acknowledgments

7   Bibliography

References

[1] Slides:
http://ilcagenda.linearcollider.org/contributionDisplay.py?contribId=444&sessionId=79&confId=1296

[2] D. Schulte, Thesis and TESLA Note 97-08, Study of Electromagnetic and Hadronic Background in the Interaction Region of the TESLA Collider (1996).

[3] A. Buckley, W. J. Stirling, M. R. Whalley, J. M. Butterworth, J. Monk, E. Nurse and B. Waugh, arXiv:hep-ph/0605048.

[4] A. Buckley, arXiv:0708.2655 [hep-ph].

[5] HepData reaction database: http://durpdg.dur.ac.uk/hepdata/reac.html
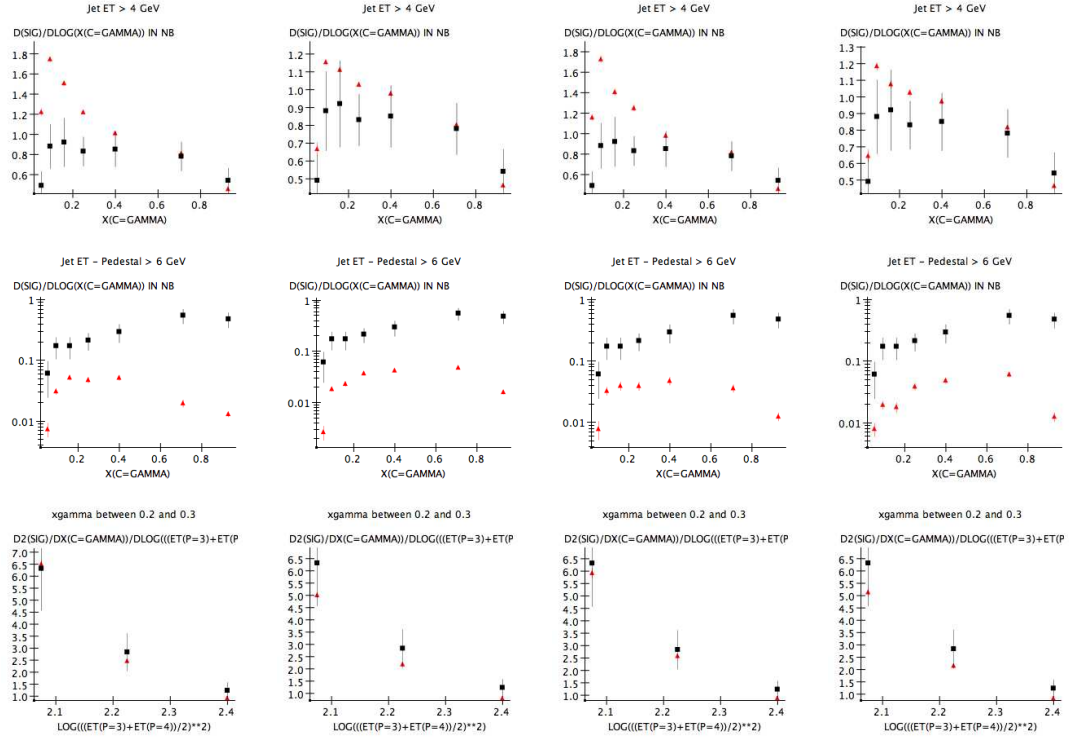
Figure 1: Plots taken from JetWeb comparing Herwig simulation to data from [13](top two rows) and [14] (bottom row) for PTJIM values of 2 GeV (first and third columns) or 3 GeV (second and fourth columns) and photon radii of 0.47 GeV^{-1} (left two columns) or 0.19 GeV^{-1} (right two columns).

[6] Hibernate: http://www.hibernate.org/

[7] B. M. Waugh, H. Jung, A. Buckley, L. Lonnblad, J. M. Butterworth and E. Nurse, arXiv:hep-ph/0605034.

[8] Rivet project: http://projects.hepforge.org/rivet/

[9] J. Bromley *et al.*, *Prepared for Workshop on Future Physics at HERA (Preceded by meetings 25-26 Sep 1995 and 7-9 Feb 1996 at DESY), Hamburg, Germany, 30-31 May 1996*

[10] J. M. Butterworth, J. R. Forshaw and M. H. Seymour, "Multiparton interactions in photoproduction at HERA," Z. Phys. C **72** (1996) 637 [arXiv:hep-ph/9601371].

[11] G. Corcella, I. G. Knowles, G. Marchesini, S. Moretti, K. Odagiri, P. Richardson, M. H. Seymour and B. R. Webber, JHEP **0101** (2001) 010 [arXiv:hep-ph/0011363]; hep-ph/0210213.

[12] http://jetweb.cedar.ac.uk/jetweb-webapp/JWSearch/

[13] C. Adloff *et al.* [H1 Collaboration], Phys. Lett. B **483** (2000) 36 [arXiv:hep-ex/0003011].

[14] C. Adloff *et al.* [H1 Collaboration], Eur. Phys. J. C **1** (1998) 97 [arXiv:hep-ex/9709004].

Heavy neutral MSSM Higgs bosons at the Photon Collider - a comparison of two analyses

M. Krawczyk[1], M. Spira[2], P. Nieżurawski[3], A. F. Żarnecki[3]

1- Institute of Theoretical Physics, Warsaw University, ul. Hoża 69, 00-681 Warsaw, Poland

2- Paul-Scherrer-Institut, CH–5232 Villigen PSI, Switzerland

3- Institute of Experimental Physics, Warsaw University, ul. Hoża 69, 00-681 Warsaw, Poland

Measurement of the cross section for the process $\gamma\gamma \to A/H \to b\bar{b}$ at the Photon Linear Collider has been considered in two independent analyses [2, 3] for the parameter range corresponding to the so-called "LHC wedge". Significantly different expectations for signal to background ratio were obtained (36 vs. 2). After detailed comparison we have found that differences in the final results are mainly due to different assumptions on $\gamma\gamma$-luminosity spectra, jet definitions and selection cuts.

In this contribution [1] two analyses [2, 3] are compared which estimate the precision of the cross section measurement for the production of heavy neutral MSSM Higgs bosons in the process $\gamma\gamma \to A/H \to b\bar{b}$. Both analyses were focused on the so-called "LHC wedge", *i.e.* the region of intermediate values of $\tan\beta$, $\tan\beta \approx 4$–10, and masses $M_{A/H}$ above 200 GeV, where the heavy bosons A and H may not be discovered at the LHC and at the first stage of the e^+e^- linear collider. In each of these analyses NLO corrections to signal and background processes were taken into account. As the results of the two approaches seem to differ significantly, we undertook the task of comparing them, focusing on the case of $M_A = 300$ GeV with MSSM parameters $\text{tg}\beta = 7$ and $M_2 = \mu = 200$ GeV.

In the first analysis [2] the NLO corrections to the background process $\gamma\gamma \to b\bar{b}$ have been calculated according to Ref. [4]. Resummation of large Sudakov and non-Sudakov logarithms due to soft gluon radiation and soft gluon and bottom-quark exchange in the virtual corrections has been taken into account [5]. The NLO-α_s was normalized to $\alpha_s(M_Z) = 0.119$ and the scale given by the $\gamma\gamma$ invariant mass was used. Jets were defined within the Sterman–Weinberg criterion and slim two-jet configurations in the final state were selected: if the radiated gluon energy was larger than 10% of the total $\gamma\gamma$ invariant energy and if the angles between all 3 partons in the final state were larger than $20°$, the event was rejected. The interference between the signal and background processes has been taken into account. The NLO QCD corrections of the interference terms to quark final states including the resummation of the large (non-)Sudakov logarithms were calculated. The description of the $\gamma\gamma$-luminosity was based on the LO cross section formula for the Compton process. The beam energy was tuned to obtain maximum luminosity at the value of the pseudoscalar Higgs mass M_A. The background was reduced with a cut on the polar angle of the bottom quark only, $|\cos\theta_b| < 0.5$. Events were collected within the invariant-mass window $M_A \pm 3$ GeV. The results for the peak cross section are shown in Fig. 1.

The second analysis [3] was based on realistic simulations of the $\gamma\gamma$-luminosity for the PLC [6, 7]. One-year run of PLC was assumed with beam energy optimized for the production of the pseudoscalar Higgs bosons. The distribution of the primary vertex and the beam crossing angle were taken into account. The total widths and branching ratios of the Higgs bosons and the H mass were calculated with HDECAY [8]. These results were used

to generate events and to calculate the signal cross section in the resonance approximation with Pythia. As the main background to Higgs-boson production the heavy-quark pair production was considered; the event samples were generated using the program by G. Jikia [9] which includes exact one-loop QCD corrections to the lowest order processes $\gamma\gamma \to q\bar{q}(g)$ [10], and the non-Sudakov form factor in the double-logarithmic approximation, calculated up to 4 loops [11]. The JADE jet definition with $y_{cut}^{J} = 0.01$ is used to define 2- and 3-parton final states. The resummation of Sudakov logarithms due to soft gluon bremsstrahlung is omitted. The LO-α_s normalized to $\alpha_s(M_Z) = 0.119$ was used at the scale given by the average of the squared transverse masses of the quark and anti-quark. Other background processes were also studied. As about two $\gamma\gamma \to hadrons$ events (*overlaying events*) are expected per bunch crossing, they were generated with Pythia, and have been overlaid on signal and background events according to the Poisson distribution. On the detector level (simulated with Simdet) jets were reconstructed using the Durham algorithm with $y_{cut}^{D} = 0.02$. Events with 2 or 3 jets were accepted. To reduce the background a cut on the polar angle for each jet was imposed, $|\cos\theta_{jet}| < 0.65$, and the ratio of the total longitudinal momentum to the total measured energy was required to be small, $|P_z|/E < 0.06$. Cuts to suppress the influence of overlaying events and the $\gamma\gamma \to W^+W^-$ background were also applied. A realistic b-tagging algorithm was used. All cuts were optimized (see [12]). The result of the analysis is shown in Fig. 2 where the distribution of the corrected invariant mass, W_{corr} (see [13]), after imposing all cuts is presented for the signal and individual background contributions.

The results of both analyses differ significantly. In the first analysis the background contribution is negligible: the signal to background ratio is $S/B \approx 36$ in the invariant mass window 297-303 GeV. In the second analysis $S/B \approx 2$ was obtained in the window 295-305 GeV if only the process $\gamma\gamma \to b\bar{b}$ is taken into account as the background. In order to understand the sources of those differences the cross sections for the background process $\gamma\gamma \to b\bar{b}$ and signal process $\gamma\gamma \to A/H \to b\bar{b}$ were recalculated within both approaches with the same cuts and the same $\gamma\gamma$-luminosity spectrum.

The following conclusions emerged after investigation of the two calculations of the heavy quark background. With the polar angle cut imposed only on the quark b the 3-jet part is larger than the 2-jet part by more than an order of magnitude. However, if the cut on the anti-quark angle is added, the 2-jet and 3-jet cross sections differ only by a factor 2-3. Thus, requiring only 2-jet events is less essential if the angular cut is applied for both quarks. This corresponds to the common cut on the jet polar angle which is usually applied on the detector level. The 2-jet cross sections obtained in the two approaches agree within a factor of 2. Moreover, the full resummation of Sudakov and non-Sudakov logarithms does not modify the 2-jet numbers too much compared to the 4-loop expansion of the non-Sudakov logarithms. If the JADE algorithm is applied in both analyses then the obtained cross sections agree within 15%.

The comparison for the signal process was performed for $M_A = 300$ GeV. The same MSSM parameter set was used, *i.e.* $\tan\beta = 7$, $\mu = 200$ GeV, $M_2 = 200$ GeV, trilinear couplings equal to 1500 GeV, and common sfermion mass equal to 1 TeV. Decays to supersymmetric particles and loops with them were taken into account. With JADE jet definitions the results of both approaches agree within 5% for the total cross section, and within 30% for the 2-jet and 3-jet classes separately. The differences in the separation of 2-jet and 3-jet classes originate mainly from the different approaches used in the two analyses. The second analysis used the resonance approximation and generated gluon radiation by parton show-

ers, while the first analysis used a full NLO calculation for the signal process including soft gluon resummation for the 2-jet part.

Finally, we have compared the results for the invariant-mass window 297-303 GeV taking into account the assumed $\gamma\gamma$-luminosity spectra with the same normalization. Our first conclusion is that if the JADE jet definition were used in both analyses, the difference in the signal to background ratio between our analyses would be mainly due to the different contributions of $J_z = 0$ and $|J_z| = 2$ parts to the $\gamma\gamma$-luminosity. The $J_z = 0$ luminosity component of the realistic luminosity distribution used in the second analysis amounts only to 94% of the same component of the ideal spectrum used in the first analysis. What is more important, in the realistic spectrum about 5.5 times more of the $|J_z| = 2$ component is taken into account relative to the same component in the ideal spectrum. If the JADE algorithm with $y_{cut}^J = 0.01$ is used, the signal to background ratio is around 12 in case of the first approach with angular cuts $|\cos\theta_{b/\bar{b}}| < 0.5$ and if 2- and 3-jet events are taken into account. In the second approach the ratio is around 6. However, if a correction accounting for the differences in the luminosity spectra is applied, the rescaled result of the second analysis is around 10, thus only 17% less than in the first analysis.

Our second observation is that the use of the Sterman-Weinberg jet definition leads to much higher rates of 2-jet events for the signal than for the background. This results in nearly 2 times higher signal to background ratios in comparison to results obtained with the JADE jet definition if only 2-jet events are taken into account.

The measurement of the process $\gamma\gamma \to A/H \to b\bar{b}$ at the PLC is very promising, even for the realistic $\gamma\gamma$-luminosity spectrum, which is less advantageous than the ideal one. Use of the clustering algorithm based on the Sterman-Weinberg jet definition would lead to much higher signal to background ratios, if only 2-jet events were taken into account.

References

[1] Slides:
http://ilcagenda.linearcollider.org/contributionDisplay.py?contribId=505&sessionId=79&confId=1296

[2] M. Mühlleitner, M. Krämer, M. Spira, P. Zerwas, Phys. Lett. B 508 (2001) 311.

[3] P. Nieżurawski, A.F. Żarnecki, M. Krawczyk, Acta Phys. Pol. B 37 (2006) 1187.

[4] B. Kamal, Z. Merebashvili, A.P. Contogouris, Phys. Rev. D51 (1995) 4808 and (E) *ibid.* D55 (1997) 3229.

[5] V.S. Fadin, V.A. Khoze, A.D. Martin, Phys. Rev. D56 (1997) 484; M. Melles, W.J. Stirling, Phys. Rev. D59 (1999) 094009, Eur. Phys. J. C9 (1999) 101, Nucl. Phys. B564 (2000) 325.

[6] V. I. Telnov, http://www.desy.de/~telnov/ggtesla/spectra/.

[7] A. F. Żarnecki, Acta Phys. Polon. B 34 (2003) 2741, hep-ex/0207021.

[8] A. Djouadi, J. Kalinowski, M. Spira, Comput. Phys. Commun. 108 (1998) 56.

[9] G. Jikia, S. Söldner-Rembold, Nucl. Instrum. Meth. A 472 (2001) 133.

[10] G. Jikia, A. Tkabladze, Nucl. Instrum. Meth. A 355 (1995) 81; Phys. Rev. D 54 (1996) 2030.

[11] M. Melles, W. J. Stirling, Phys. Rev. D 59 (1999) 94009; Eur. Phys. J. C 9 (1999) 101; M. Melles, W. J. Stirling, V. A. Khoze, Phys. Rev. D 61 (2000) 54015; M. Melles, Nucl. Instrum. Meth. A 472 (2001) 128.

[12] P. Nieżurawski, hep-ph/0507004; hep-ph/0503295; P. Nieżurawski, A.F. Żarnecki, M. Krawczyk, hep-ph/0507006.

[13] P. Nieżurawski, A. Żarnecki, M. Krawczyk, Acta Phys. Pol. B 34 (2003) 177.
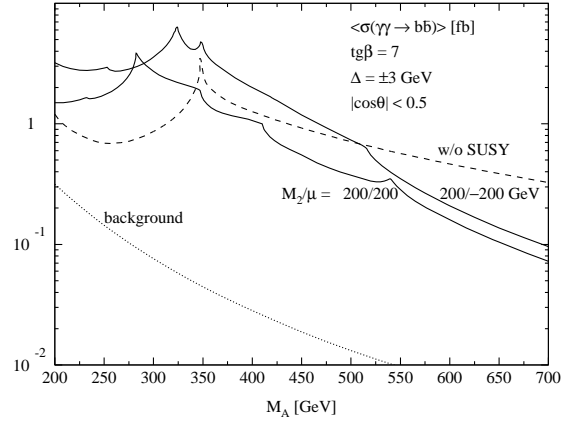
Figure 1: *Average cross sections in the invariant mass window ± 3 GeV for resonant heavy Higgs boson H, A production in $\gamma\gamma$ collisions as a function of the pseudoscalar Higgs mass M_A with final decays into $b\bar{b}$ pairs, and the corresponding background cross section. From Ref. [2].*
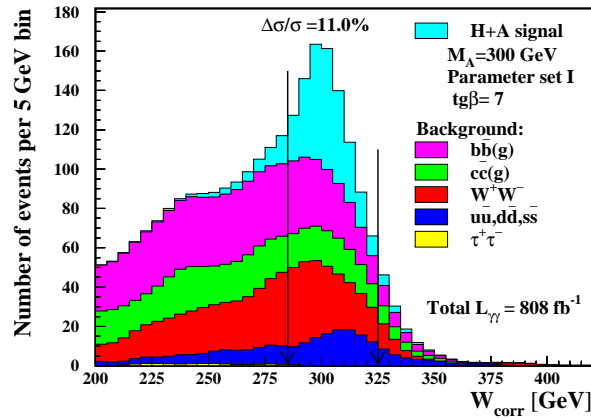
Figure 2: *Distributions of the corrected invariant mass, W_{corr}, for signal and all considered background contributions, with overlaying events included. The best precision of 11% for $\gamma\gamma \rightarrow A/H \rightarrow b\bar{b}$ cross section measurement is achieved in the W_{corr} window between 285 and 325 GeV. From Ref. [3].*

Present status of the photon collider, what next?

V.I. Telnov

Institute of Nuclear Physics
630090, Novosibirsk, Russia

Please, see my review talk on this subject in proceedings of the conference PHOTON2007 which was held in one month after LCWS07 [1]. Here I would like to give only one remark.

Although the photon collider is the "option" (or the ILC second stage) but it is extremely important now to make the baseline ILC design which allows rather easy transition between e^+e^- and $\gamma\gamma$, γe modes of operation. Unfortunately, the ILC configuration in the Reference Design Report [2] with one IP at 14 mrad crossing angle is not compatible with the photon collider, because the photon collider needs 25 mrad. Any upgrade needs additional excavation in the IR region which is practically impossible. Moreover, the accelerator part of the Reference Design Report does not include any options (e^-e^-, $\gamma\gamma$, γe, fixed target) and consider only basic e^+e^- mode. The GDE management were not against the options but motivated this very strange design decision by necessity to reduce the initial ILC cost (political reasons).

Now a good news. The GDE agreed that ILC Engeenering Design should include the photon collider. At IRENG07 [3] it was agreed to redesign the interaction region area in order to make it compatible with $\gamma\gamma$ collisions. So, the photon collider has returned to the track after two years uncertainties (and a struggle for existence)!

References

[1] PHOTON2007: International Conference on the Structure and Interactions of the Photon including the 17th International Workshop on Photon-Photon Collisions and the International Workshop on High Energy Photon Linear Colliders, July 17, 2007, Paris. http://lpnhe-lc.in2p3.fr/photon2007/

[2] International linear collider Reference Design Report, ILC-Report-2007-001, August 2007.

[3] ILC Interaction Region Engineering Design Workshop (IRENG07), September 17-21, 2007, SLAC, Stanford, USA. http://www-conf.slac.stanford.edu/ireng07/

Loop Calculations

Conveners: D. Wackeroth, S. Dittmaier, Y. Yasui

New results for 5-point functions

J. Gluza[1] and T. Riemann[2*]

1 – Institute of Physics, Univ. of Silesia, Universytecka 4, 40007 Katowice, Poland

2 – Deutsches Elektronen-Synchrotron DESY
Platanenallee 6, D–15738 Zeuthen, Germany

Bhabha scattering is one of the processes at the ILC where high precision data will be expected. The complete NNLO corrections include radiative loop corrections, with contributions from Feynman diagrams with five external legs. We take these diagrams as an example and discuss several features of the evaluation of pentagon diagrams. The tensor functions are usually reduced to simpler scalar functions. Here we study, as an alternative, the application of Mellin-Barnes representations to 5-point functions. There is no evidence for an improved numerical evaluation of their finite, physical parts. However, the approach gives interesting insights into the treatment of the IR-singularities.

1 Introduction

Bhabha scattering,

$$e^+ + e^- \rightarrow e^+ + e^-, \tag{1}$$

is one of the most important reactions at e^+e^- colliders.[a] At ILC energies, small angle Bhabha scattering is dominated by pure photonic contributions and is foreseen as a luminosity monitor, and large angle Bhabha scattering is also one of the reactions with an expected jigh event statistics and with a very clean theoretical Standard Model prediction. For these reasons, a NNLO (next-to-next-to leading order) prediction of the complete QED contributions and a NNLLO (next-to-next-to leading logarithmic order) prediction in the Standard Model are needed. The virtual QED corrections at NNLO accuracy have been determined in a series of articles quite recently [3–11]. A complete evaluation of the photonic corrections covers additionally the real photon emission contributions and fermion pair production.

In this talk, we discuss one class of Feynman diagrams for real photon emission, namely radiative loop corrections,

$$e^+ + e^- \rightarrow e^+ + e^- + \gamma, \tag{2}$$

which are contributing at NNLO to reaction (1). Their evaluation includes 5-point functions. Usually, the scalar, vector, and tensor functions of this type will be reduced to simpler one-loop functions. We also discuss an alternative approach, based on Mellin-Barnes representations of Feynman parameter integrals.

---

*Presented by T.R.
[a]A link to the slides of this contribution is [1]. See also [2].

2 Reduction of 5-point functions

A critical point in an algebraic reduction of vector or higher tensor 5-point functions to scalar 2-point, 3-point, and 4-point functions (in four dimensions) is the appearance of inverse Gram determinants. It is known that these inverse Gram determinants are spurious [12–14] and that they may be canceled out in the final analytical expressions. For the approach proposed in [15], we have demonstrated this cancellation quite recently. Because that part of the presentation was decribed in some detail in other contexts [16, 17], we don't repeat the material in these proceedings again.

The focus will be on two questions:

- Is the MB-approach useful for the numerical evaluation of the finite parts of scalar, vector, and tensor 5-point functions?

- How to treat the infrared divergencies of these functions?

3 Mellin-Barnes representation for massive 5-point functions

The use of Mellin-Barnes (MB) integrals for the representation and evaluation of Feynman integrals has a long history, although a systematic use of it became possible quite recently. The replacement of massive propagators by MB-integrals was proposed in [18] for a finite 3-point function. It was worked out for one-loop n-point functions with arbitrary indices (powers of propagators) in $d = 4 - 2\epsilon$ dimensions in [19–21], where also some of the related earlier literature is discussed, as well as the applicability to tensor integrals and to multi-loop problems. The aim was a replacement of massive by massless propagators. In [22], the Feynman parameter representation (or α-parameter representation, the difference plays no role here) was derived and then for the characteristic function of the diagrams an MB-representation was applied. Along this line, a systematic approach to MB-presentations for divergent multi-loop integrals was derived and solved for non-trivial massless and massive cases [23–29]. Since software packages like AMBRE.m [30] (in Mathematica, for the derivation of MB-representations), MB.m [31] (in Mathematica, for their analytical and series expansion in ϵ), and XSUMMER [32] (in FORM [33], for taking sums of their residues) became publicly available, quite involved integrals may be treated, see e.g. [34].

Of course, such a complicated task like the evaluation of – ideally – arbitrary Feynman integrals will not be finally solved with using one or the other method. In fact, already quite simple problems may be used to demonstrate the limitations of some approach. We will study here, with MB-integrals, some one-loop functions of massive QED as occurring in Bhabha scattering, with focussing on the 5-point function shown in Figure 1.

We define

$$I_5[A(q)] \;\;=\;\; e^{\epsilon\gamma_E} \int \frac{d^d q}{i\pi^{d/2}} \frac{A(q)}{d_1 d_2 d_3 d_4 d_5}, \tag{3}$$

with the chords Q_i,

$$d_i = (q - Q_i)^2 - m_i^2. \tag{4}$$

This representation becomes unique after choosing one of the chords (and the direction of the loop momentum), e.g.:

$$Q_5^\mu = 0, \quad Q_1^\mu = p_1^\mu. \tag{5}$$
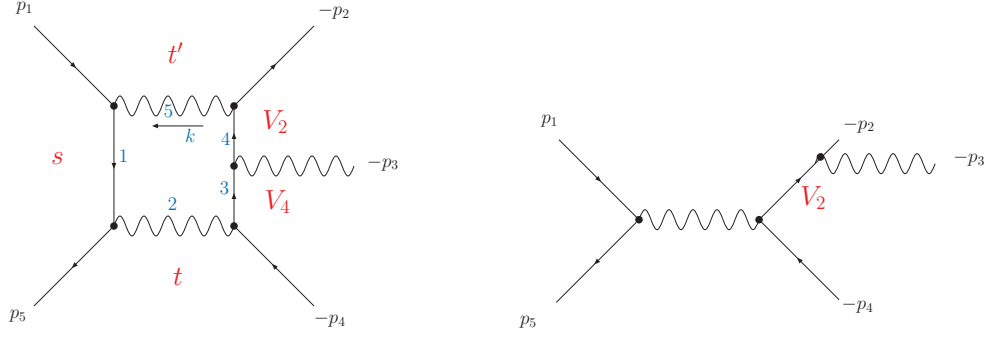
Figure 1: A pentagon topology and a Born topology

The numerator $A(q)$ contains the tensor structure,

$$A(q) = \{1, q^\mu, q^\mu q^\nu, q^\mu q^\nu q^\rho, \cdots\}, \tag{6}$$

or may be used to define pinched diagrams; e.g. a shrinking of line 5 leads to a box diagram corresponding to

$$I_5[d_5] = e^{\epsilon \gamma_E} \int \frac{d^d q}{i\pi^{d/2}} \frac{1}{d_1 d_2 d_3 d_4}. \tag{7}$$

For details of the derivation of Feynman parameter integrals we refer to any textbook on perturbative quantum field theory or to [35]. A Feynman parameter representation for Fig. 1 is:

$$I_5[A(q)] = -e^{\epsilon \gamma_E} \int_0^1 \prod_{j=1}^5 dx_j \, \delta\left(1 - \sum_{i=1}^5 x_i\right) \frac{\Gamma(3+\epsilon)}{F(x)^{3+\epsilon}} \, B(q), \tag{8}$$

with $B(1) = 1, B(q^\mu) = Q^\mu, B(q^\mu q^\nu) = Q^\mu Q^\nu - \frac{1}{2}g^{\mu\nu}F(x)/(2+\epsilon)$, and $Q^\mu = \sum x_i Q_i^\mu$. The diagram depends on five kinematical invariants and the F-form in (8) is:

$$F(x) = m_e^2(x_2 + x_4 + x_5)^2 + [-s]x_1 x_3 + [-V_4]x_3 x_5 + [-t]x_2 x_4 + [-t']x_2 x_5 + [-V_2]x_1 x_4. \tag{9}$$

Henceforth, $m_e = 1$. It is evident that the F-form cannot be made more compact. After the introduction of seven subsequent Mellin-Barnes representations,

$$\frac{1}{[A(x) + Bx_i x_j]^R} = \frac{1}{2\pi i} \int_C dz [A(x)]^z [Bx_i x_j]^{-R-z} \frac{\Gamma(R+z)\Gamma(-z)}{\Gamma(R)}, \tag{10}$$

one for each additive term in F, we may perform the x-integrations using a generalization of the integral representation of the Beta function:

$$\int_0^1 \prod_{j=1}^N dx_j \, x_j^{\alpha_j - 1} \, \delta\left(1 - x_1 - \cdots - x_N\right) = \frac{\Gamma(\alpha_1) \cdots \Gamma(\alpha_N)}{\Gamma(\alpha_1 + \cdots + \alpha_N)}. \tag{11}$$

The final MB-integral may be easily derived using our Mathematica package AMBRE.m [30] (see also example1.nb and example2.nb of the package). The representation is five-dimensional after twice applying Barnes' first lemma. The integrals are well-defined on integration strips parallel to the imaginary axis, for a finite value of $\epsilon = d/2 - 2$. After an analytical continuation in ϵ, preferably done by MB.m [31], one gets a sequence of finite, multi-dimensional MB-integrals. We performed these steps and met the following situation for the terms proportional to $1/\epsilon$ and $O(1)$:

- scalar integrals: the MB-integrals are up to three-fold;

- vector integrals: the MB-integrals are up to three-fold;

- tensor integrals: the MB-integrals are up to five-fold.

We performed some experimental calculations, but there is no need to go into more detail: A numerical evaluation of these integrals, especially of the five-dimensional ones, in the Minkowskian region, is not competative to the old-fashioned numerical packages like FF [36], or LoopTools [36–38], which rely on the preceding algebraic reduction of all the 5-point functions to well-known scalar 2- to 4-point functions.

For this reason, we restrict the discussion now to the infrared divergent parts only. As is well-known, they have a lower dimensionality, and here the MB-presentations are well-suited. As examples we will use the scalar and vector 5-point functions.

4 Infrared singularities

Let us consider first the scalar function. A set of five independent invariants may be read off from (9):

$$
\begin{aligned}
s &= (p_1 + p_5)^2, \\
t &= (p_4 + p_5)^2, \\
t' &= (p_1 + p_2)^2, \\
V_2 &= 2p_2 p_3 \quad \sim E_3, \\
V_4 &= 2p_4 p_3 \quad \sim E_3,
\end{aligned}
$$

and the two massless propagators are $d_5 = q^2$ and $d_2 = (q + p_1 + p_5)^2$. In the IR-limit, where $E_3 \to 0$, it will be $t' \approx t$ and $0 \leq V_2, V_4 << s, |t|$. The leading IR-singularities are easily found algebraically from the following decomposition:

$$
\frac{1}{d_1 d_2 d_3 d_4 d_5} = \frac{-1}{s} \left[\frac{2(q - Q_5)(q - Q_2)}{d_1 d_2 d_3 d_4 d_5} + \frac{1}{V_2} \left(\frac{2(q - Q_5)(q - Q_3)}{d_1 d_3 d_4 d_5} - \frac{1}{d_1 d_3 d_4} - \frac{1}{d_1 d_4 d_5} \right) \right.
$$
$$
\left. + \frac{1}{V_4} \left(\frac{2(q - Q_2)(q - Q_4)}{d_1 d_2 d_3 d_4} - \frac{1}{d_1 d_2 d_3} - \frac{1}{d_1 d_3 d_4} \right) \right]. \tag{12}
$$

The 4-point functions depend on the variables (t, t', V_2) and (t, t', V_4), respectively, and the leading IR-singularities of I_5 trace back, by construction, to the two IR-divergent 3-point

functions:

$$\int \frac{d^d k}{d_1 d_2 d_3 d_4 d_5} = \frac{1}{sV_2} \int \frac{d^d k}{d_1 d_4 d_5} + \frac{1}{sV_4} \int \frac{d^d k}{d_1 d_2 d_3} + \cdots = \frac{1}{\epsilon} \left[\frac{F(t')}{sV_2} + \frac{F(t)}{sV_4} \right] + \cdots$$

(13)

The integrals with numerators are constructed such that they are free of IR-singularities arising from the virtual photon lines. It is of importance here to observe that the denominators V_2 and V_4 are proportional to the photon energy E_3 and thus give rise to additional IR-problems, stemming from the photon phase space integral over the squared sum of matrix elements; e.g.:

$$\int \frac{d^3 p_3}{2E_3} \frac{A}{E_3} \frac{B(E_3)}{E_3} \rightarrow \int_0^\omega \frac{dE_3}{E_3} = \ln(E_3)|_0^\omega.$$

(14)

Here, one term (A/E_3) comes from the real photon emission Born diagram, and the other one $(B(E_3)/E_3)$ from our pentagon diagram. After dimensional regularisation, this becomes evaluable and contributes also to the Laurent series in ϵ. We learn from (14) that a complete treatment of the IR-problem includes a careful control of the subleading (and in 4 dimensions non-integrable) terms like $1/V_i$ and $\ln(V_i)/V_j$. This leads to phase space integrals with a behaviour like:

$$\int_0^\omega \frac{dE_3}{E_3^{5-d}} \left(\frac{a}{\epsilon} + b \ln(E_3) + c \right) = -\frac{2a+b}{4\epsilon^2} - \frac{c - 2a \ln(\omega)}{2\epsilon}$$
$$+ c \ln(\omega) + \frac{1}{2}(2a+b) \ln^2(\omega) + O(\epsilon).$$

(15)

Evidently, one separates with the 3-point functions in (13) only a leading singularity, while we expect expressions like

$$\int \frac{d^d k}{d_1 d_2 d_3 d_4 d_5} = \frac{A_2}{sV_2 \epsilon} + \frac{A_4}{sV_4 \epsilon} + \frac{B_2}{sV_2} \ln(V_2) + \frac{B_4}{sV_4} \ln(V_4) + \frac{C_2}{sV_2} + \frac{C_4}{sV_4} + \cdots$$

(16)

Subleading singuarities may arise from the ϵ-finite 4- and 3-point functions with pre-factors $1/V_i$.

It is also evident that the whole above discussion immediately transfers over to vector and tensor integrals.

Concentrating now on the IR-divergent parts, we may safely assume now the validity of the Born kinematics, including

$$t' = t,$$

(17)

which is justified bcause of the vanishing photon momentum in this limit. This 'eats' another MB-integration (in the F-form (9) one additive term vanishes), and the starting point of further discussions are four-dimensional MB-integrals. For the scalar pentagon:

$$I_5 = \frac{-e^{\epsilon \gamma_E}}{(2\pi i)^4} \prod_{i=1}^4 \int_{-i\infty+u_i}^{+i\infty+u_i} dz_i (-s)^{z_2} (-t)^{z_4} (-V_2)^{z_3} (-V_4)^{-3-\epsilon-z_1-z_2-z_3-z_4} \frac{\prod_{j=1}^{12} \Gamma_j}{\Gamma_0 \Gamma_{13} \Gamma_{14}},$$

(18)

with a normalization $\Gamma_0 = \Gamma[-1 - 2\epsilon]$, and the other Γ-functions are:

$$
\begin{aligned}
\Gamma_1 &= \Gamma[-z_1], \quad \Gamma_2 = \Gamma[-z_2], \quad \Gamma_3 = \Gamma[-z_3], \quad \Gamma_4 = \Gamma[1 + z_3], \\
\Gamma_5 &= \Gamma[1 + z_2 + z_3], \quad \Gamma_6 = \Gamma[-z_4], \quad \Gamma_7 = \Gamma[1 + z_4], \quad \Gamma_8 = \Gamma[-1 - \epsilon - z_1 - z_2], \\
\Gamma_9 &= \Gamma[-2 - \epsilon - z_1 - z_2 - z_3 - z_4], \quad \Gamma_{10} = \Gamma[-2 - \epsilon - z_1 - z_3 - z_4], \\
\Gamma_{11} &= \Gamma[-\epsilon + z_1 - z_2 + z_4], \quad \Gamma_{12} = \Gamma[3 + \epsilon + z_1 + z_2 + z_3 + z_4],
\end{aligned}
$$

and, in the denominator:

$$
\Gamma_{13} = \Gamma[-1 - \epsilon - z_1 - z_2 - z_4], \quad \Gamma_{14} = \Gamma[-\epsilon - z_1 - z_2 + z_4]. \tag{19}
$$

The I_5 is finite if all Γ-functions in the numerator have positive real parts of the arguments; this may be fulfilled for finite ϵ (here we follow the method invented in [25]):

$$
\epsilon = -\frac{3}{4}. \tag{20}
$$

The real shifts u_i of the integration strips r_i may be chosen to be:

$$
\begin{aligned}
u_1 &= -5/8, \\
u_2 &= -7/8, \\
u_3 &= -1/16, \\
u_4 &= -5/8, \\
u_5 &= -1/32. \tag{21}
\end{aligned}
$$

The further discussion of the scalar case is very similar to that of the QED vertex function given in [39], so we may concentrate here on the results for the IR-divergent part:

$$
I_5^{IR} = I_5^{IR}(V_2) + I_5^{IR}(V_4), \tag{22}
$$

$$
I_5^{IR}(V_i) = \frac{I_{-1}^s(V_i)}{\epsilon} + I_0^s(V_i). \tag{23}
$$

The explicit expressions for the inverse binomial sums solving the MB-integrals are obtained by applying the residue theorem (closing the integration contours to the left):

$$
\frac{I_{-1}(V_i)^s}{\epsilon} = \frac{1}{2sV_i\epsilon} \sum_{n=0}^{\infty} \frac{(t)^n}{\binom{2n}{n}(2n+1)}, \tag{24}
$$

with I_{-1}^s being in accordance with (13), and:

$$
I_0(V_i)^s = \frac{1}{2sV_i} \sum_{n=0}^{\infty} \frac{(t)^n}{\binom{2n}{n}(2n+1)} [-2\ln(-V_i) - 3S_1(n) + 2S_1(2n+1)], \tag{25}
$$

where we introduce the harmonic numbers $S_k(n) = \sum_{i=1}^{n} 1/i^k$, and have to understand $\ln(-V_i) = \ln(V_i/s) + \ln[-(s + i\delta)/m_e^2]$.

The series may be summed up in terms of polylogarithmic functions with the aid of Table 1 of Appendix D of [40]:

$$\sum_{n=0}^{\infty} \frac{t^n}{\binom{2n}{n}(2n+1)} = \frac{y}{y^2-1} 2\ln(y), \tag{26}$$

$$\sum_{n=0}^{\infty} \frac{t^n}{\binom{2n}{n}(2n+1)} S_1(n) = \frac{y}{y^2-1}\left[-4\text{Li}_2(-y) - 4\ln(y)\ln(1+y)\right.$$

$$\left. + \ln^2(y) - 2\zeta_2\right], \tag{27}$$

$$\sum_{n=0}^{\infty} \frac{t^n}{\binom{2n}{n}(2n+1)} S_1(2n+1) = \frac{y}{y^2-1}\left[2\text{Li}_2(y) - 4\text{Li}_2(-y) - 4\ln(y)\ln(1+y)\right.$$

$$\left. + 2\ln(y)\ln(1-y) + \frac{1}{2}\ln^2(y) - 4\zeta_2\right], \tag{28}$$

with

$$y \equiv y(t) = \frac{\sqrt{1-4/t}-1}{\sqrt{1-4/t}+1}. \tag{29}$$

For the vector and higher tensor 5-point functions one gets quite similar results. The IR-divergent pieces arise only from those contributions, which are proportional to the chords Q_2 and Q_5 of the massless internal lines (one of them is set to zero here, $Q_5 = 0$):

$$I_5^{IR}[q^\mu] = Q_2^\mu\left(\frac{I_{-1}^v(V_2, V_4)}{\epsilon} + I_0^v(V_2, V_4)\right). \tag{30}$$

The MB-integrals introduced in (8) will not get modified by the additional factors $B(q^\mu)$ etc., but the subsequent x-integrations will. For the vector integrals, we obtain:

$$I_5[q^\mu]|_{t'=t} = \sum_{i=1}^{5} Q_i^\mu I_5(i), \tag{31}$$

and

$$I_5(2) = \frac{-e^{\epsilon\gamma_E}}{(2\pi i)^4}\prod_{i=1}^{4}\int_{-i\infty+u_i}^{+i\infty+u_i} dz_i(-s)^{z_2}(-t)^{z_4}(-V_2)^{z_3}(-V_4)^{-3-\epsilon-z_1-z_2-z_3-z_4}\frac{\prod_{j=1}^{12}\Gamma_j^v}{\Gamma_0^v\Gamma_{13}^v\Gamma_{14}^v}, \tag{32}$$

where it is $\Gamma_j^v = \Gamma_j$ with two exceptions:

$$\Gamma_{10}^v = \Gamma[-1-\epsilon-z_1-z_3-z_4],$$
$$\Gamma_0^v = \Gamma[-2\epsilon]. \tag{33}$$

After similar manipulations as described above, we obtain finally for the IR-divergent part of the vector pentagon (and, not discussed at all, the tensor pentagon):

$$I_5^{IR}[q^\mu] \;=\; Q_2^\mu \; I_5^{IR}(V_4) + Q_5^\mu \; I_5^{IR}(V_2), \tag{34}$$

and

$$I_5^{IR}[q^{\mu\nu}] \;=\; Q_2^\mu Q_2^\nu \; I_5^{IR}(V_4) + Q_5^\mu Q_5^\nu \; I_5^{IR}(V_2). \tag{35}$$

In the above derivations, we chose arbitrarily $Q_5 = 0$. The leading and non-leading IR-divergent parts of the tensor functions are contained in those terms of the tensor decomposition, which are proportional to the chords of the massless internal lines, and they agree with the corresponding scalar functions.

In conclusion, we have demonstrated, by analysing the loop functions without squaring matrix elements, that IR divergencies of scalar and tensor one-loop pentagon diagrams can be treated in a systematic, efficient way by using Mellin-Barnes representations. The leading singularities of the ϵ expansion of MB-integrals are obtained straightforwardly and have the same IR-structure as the vertex functions obtained by quenching. Both the leading and non-leading singular parts (the latter being kinematical end point singularities) can be expressed by a few well-known inverse binomial sums or, equivalently, polylogarithmic functions. The IR-structure of vector and tensor functions is completely reducible to that of the scalar function.

Acknowledgements

References

[1] Slides:
http://ilcagenda.linearcollider.org/contributionDisplay.py?contribId=414&sessionId=73&confId=1296.

[2] S. Actis, M. Czakon, J. Gluza, and T. Riemann, DESY 07-192, Contribution to these Proceedings, Session of Working Group on "New Physics at TeV Scale and Precision Electroweak Studies".

[3] Z. Bern, L. Dixon, and A. Ghinculov, *Phys. Rev.* **D63** (2001) 053007, hep-ph/0010075.

[4] N. Glover, B. Tausk, and J. van der Bij, *Phys. Lett.* **B516** (2001) 33–38, hep-ph/0106052.

[5] A. Penin, *Phys. Rev. Lett.* **95** (2005) 010408, hep-ph/0501120.

[6] R. Bonciani, A. Ferroglia, P. Mastrolia, E. Remiddi, and J. van der Bij, *Nucl. Phys.* **B716** (2005) 280–302, hep-ph/0411321.

[7] S. Actis, M. Czakon, J. Gluza, and T. Riemann, *Nucl. Phys.* **B786** (2007) 26–51, arXiv:0704.2400v.2 [hep-ph].

[8] T. Becher and K. Melnikov, *JHEP* **06** (2007) 084, arXiv:0704.3582 [hep-ph].

[9] R. Bonciani, A. Ferroglia, and A. Penin, arXiv:0710.4775 [hep-ph].

[10] S. Actis, M. Czakon, J. Gluza, and T. Riemann, *Acta Phys. Polon.* **B38** (2007) 3517, arXiv:0710.5111 [hep-ph].

[11] S. Actis, M. Czakon, J. Gluza, and T. Riemann, arXiv:0711.3847 [hep-ph].

[12] Z. Bern, L. Dixon, and D. Kosower, *Nucl. Phys.* **B412** (1994) 751–816, hep-ph/9306240.

[13] T. Binoth, J. Guillet, G. Heinrich, E. Pilon, and C. Schubert, *JHEP* **10** (2005) 015, hep-ph/0504267.

[14] A. Denner and S. Dittmaier, *Nucl. Phys.* **B734** (2006) 62–115, hep-ph/0509141.

[15] J. Fleischer, F. Jegerlehner, and O. Tarasov, *Nucl. Phys.* **B566** (2000) 423–440, hep-ph/9907327.

[16] J. Fleischer, *Application of Mellin-Barnes representation to the calculation of massive five-point functions in Bhabha scattering*, talk given at the Conference on Frontiers in Perturbative Quantum Field Theory, June 14-16 2007, ZiF, Bielefeld.

[17] J. Fleischer, J. Gluza, K. Kajda, and T. Riemann, *Acta Phys. Polon.* **B38** (2007) 3529, arXiv:0710.5100 [hep-ph].

[18] N. Usyukina, *Teor. Mat. Fiz.* **22** (1975) 300–306 (in Russian).

[19] E. Boos and A. Davydychev, *Theor. Math. Phys.* **89** (1991) 1052–1063.

[20] A. Davydychev, *J. Math. Phys.* **32** (1991) 1052–1060.

[21] A. Davydychev, *J. Math. Phys.* **33** (1992) 358–369.

[22] N. Usyukina and A. Davydychev, *Phys. Lett.* **B298** (1993) 363–370.

[23] V. Smirnov, *Phys. Lett.* **B460** (1999) 397–404, hep-ph/9905323.

[24] V. Smirnov and O. Veretin, *Nucl. Phys.* **B566** (2000) 469–485, hep-ph/9907385.

[25] B. Tausk, *Phys. Lett.* **B469** (1999) 225–234, hep-ph/9909506.

[26] V. Smirnov, *Phys. Lett.* **B524** (2002) 129–136, hep-ph/0111160.

[27] V. Smirnov, "Evaluating Feynman Integrals" (Springer Verlag, Berlin, 2004).

[28] V. Smirnov, *Springer Tracts Mod. Phys.* **211** (2004) 1–244.

[29] G. Heinrich and V. Smirnov, *Phys. Lett.* **B598** (2004) 55–66, hep-ph/0406053.

[30] J. Gluza, K. Kajda, and T. Riemann, *Comput. Phys. Commun.* **177** (2007) 879–893, arXiv:0704.2423 [hep-ph].

[31] M. Czakon, *Comput. Phys. Commun.* **175** (2006) 559–571, hep-ph/0511200.

[32] S. Moch and P. Uwer, *Comput. Phys. Commun.* **174** (2006) 759–770, math-ph/0508008.

[33] J. Vermaseren, *Nucl. Phys. Proc. Suppl.* **116** (2003) 343–347, hep-ph/0211297.

[34] M. Czakon, J. Gluza, and T. Riemann, *Nucl. Phys.* **B751** (2006) 1–17, hep-ph/0604101.

[35] J. Gluza and T. Riemann, "Feynman Integrals and Mellin-Barnes Representations", lectures held at Int. School on Computer Algebra and Particle Physics, CAPP, 25-30 March 2007, DESY, Zeuthen, Germany,
https://indico.desy.de/getFile.py/access?contribId=1&sessionId=14&resId=0&
materialId=slides&confId=157.

[36] G. van Oldenborgh, *Comput. Phys. Commun.* **66** (1991) 1.

[37] T. Hahn and M. Perez-Victoria, *Comput. Phys. Commun.* **118** (1999) 153–165, hep-ph/9807565.

[38] T. Hahn and M. Rauch, *Nucl. Phys. Proc. Suppl.* **157** (2006) 236–240, hep-ph/0601248.

[39] J. Gluza, F. Haas, K. Kajda, and T. Riemann, *PoS (ACAT)* (2007) 081, arXiv:0707.3567 [hep-ph].

[40] A. Davydychev and M. Kalmykov, *Nucl. Phys.* **B699** (2004) 3–64, hep-th/0303162.

Two-Loop Electroweak NLL Corrections: from Massless to Massive Fermions

Bernd Jantzen[*]

Paul Scherrer Institut (PSI)
5232 Villigen PSI - Switzerland

Recently the two-loop next-to-leading logarithmic (NLL) virtual corrections to arbitrary processes with massless external fermions have been calculated. Within the spontaneously broken electroweak theory the one- and two-loop mass singularities have been derived to NLL accuracy and expressed as universal correction factors depending only on the quantum numbers of the external particles. This talk summarizes the results for massless fermionic processes and presents new aspects arising in the extension of the corresponding loop calculations to massive external fermions. As a preliminary result, the Abelian form factor for massive fermions is given.

1 Electroweak corrections at high energies

Past and present collider experiments have explored high-energy processes at energy scales at the order of or below the masses M_W and M_Z of the weak gauge bosons. But the Large Hadron Collider (LHC) and the proposed International Linear Collider (ILC) will reach scattering energies in the TeV regime. For the first time, the characteristic energy Q of the reactions will be very large compared to M_W. At these high energies $Q \gg M_W$, electroweak radiative corrections are enhanced by large logarithms $\ln(Q^2/M_W^2)$, which start to be sizable at energies of a few hundred GeV and increase with energy. At LHC and ILC, logarithmic electroweak effects can amount to tens of per cent at one loop and several per cent at two loops. In view of the expected experimental precision especially at ILC, theoretical predictions with an accuracy of about 1% are required, so the two-loop corrections are crucial.

For sufficiently high Q, mass-suppressed terms of $\mathcal{O}(M_W^2/Q^2)$ become negligible and the electroweak corrections assume the form of a tower of logarithms with terms $\alpha^l \ln^j(Q^2/M_W^2)$, $0 \le j \le 2l$, at l loops. The leading logarithms (LLs) with power $j = 2l$ are known as Sudakov logarithms [2]. The subleading logarithms with $j = 2l - 1, 2l - 2, \ldots$ are denoted as next-to-leading logarithmic (NLL), next-to-next-to-leading logarithmic (N²LL) terms, and so on. The experience with four-fermion processes [3, 4] shows that the subleading logarithmic contributions may be of the same size as the leading ones. In addition, large cancellations occur between the individual logarithmic terms, so the restriction to the LL approximation is not sufficient, and the NLL corrections or even further subleading terms are required.

1.1 Origin of electroweak logarithms

Logarithms $\ln(Q^2/M_W^2)$ arise from mass singularities, when a virtual gauge boson (photon γ, Z or $W^\pm$ boson) couples to an on-shell external leg and to any other (internal or external) line of the diagram. The region where the gauge boson momentum is collinear to the momentum of the external particle yields a single-logarithmic one-loop contribution. In the

---

[*]Talk based on work done in collaboration with A. Denner and S. Pozzorini.

special case that the gauge boson is exchanged between two different external legs, a double-logarithmic contribution arises from the regions where the gauge boson momentum is soft and collinear to one of the external momenta. In addition, ultraviolet (UV) singularities lead to single-logarithmic contributions.

In the case of photons, the mass singularities are not regulated by a finite gauge boson mass. In $D = 4 - 2\epsilon$ space–time dimensions, the singularities appear as poles $1/\epsilon$ and $1/\epsilon^2$ per loop. For a consistent treatment of leading and subleading logarithmic contributions, each pole in ϵ has to be counted like a logarithm $\ln(Q^2/M_W^2)$. Finite masses of the external particles regularize the collinear singularities and lead to logarithms involving these masses.

It has been shown at one loop for arbitrary processes [5] and at two loops for massless fermionic processes [6] that the electroweak LL and NLL corrections are universal: they depend only on the quantum numbers of the external particles and can be written in terms of universal correction factors which factorize from the Born matrix element.

1.2   Approaches for virtual two-loop electroweak corrections at high energies

Two-loop electroweak corrections at high energies have been studied in recent years with two complementary approaches. On the one hand, evolution equations known from QCD have been applied to the electroweak theory by splitting the latter into a symmetric $SU(2) \times U(1)$ regime above the weak scale M_W and a QED regime below the weak scale. Then the evolution equations permit to resum the one-loop result to all orders in perturbation theory. From this approach the LL [7] and NLL [8] corrections for arbitrary processes as well as the N^{2}LL approximation for massless four-fermion processes $f\bar{f} \to f'\bar{f}'$ [9] are known, where the NLL and N^{2}LL terms are valid in the equal mass approximation $M_Z = M_W$.

On the other hand, various calculations have checked and extended the resummation predictions by explicit diagrammatic two-loop calculations. At first, the LLs for the fermionic form factor [10] were obtained, then the LLs for arbitrary processes [11], the angular-dependent NLLs for arbitrary processes [12] and the complete NLLs for the massless fermionic form factor [13]. Finally, the N^{3}LL approximation for the massless fermionic form factor was calculated for $M_Z = M_W$ and combined with the evolution equations, yielding the N^{3}LL corrections for massless neutral-current four-fermion processes in an expansion $M_Z \approx M_W$ around the equal mass case [3, 4].

2   Two-loop next-to-leading logarithmic corrections

In order to complete the missing diagrammatic NLL calculations, the goal of this project is to derive virtual two-loop electroweak corrections for arbitrary processes in NLL accuracy. In contrast to the resummation approaches, we rely on the complete spontaneously broken electroweak theory. We consider processes with external momenta p_i, where all kinematical invariants, $r_{ij} = (p_i + p_j)^2$, are of the order of the large scale $Q^2 \gg M_W^2$. We implement the particle masses M_W, M_Z, m_t and M_{Higgs}, which are different, but of the same order. In particular, we consider a massive top quark and neglect the masses of the other fermions. We thus get combinations of large logarithms $L = \ln(Q^2/M_W^2)$ and poles in ϵ from virtual photons. At l loops, terms $\alpha^l L^n \epsilon^{-j+n}$ are LLs if $j = 2l$, and NLLs if $j = 2l-1$ $(n = 0, 1, \ldots)$. The NLL coefficients involve angular-dependent logarithms, $\ln(-r_{ij}/Q^2)$, and logarithms of mass ratios, $\ln(M_Z^2/M_W^2)$ and $\ln(m_t^2/M_W^2)$.

We have completed the calculation for processes with massless external fermions [6] and are about to extend our results to massive fermionic processes.

2.1 Extraction of NLL mass singularities

In order to extract the mass singularities from the loop diagrams, we first isolate the so-called factorizable contributions: These are diagrams where the gauge bosons couple only to external legs, not to internal legs of the tree subdiagram, and where the gauge boson momenta have been set to zero in the tree subdiagram. For these factorizable contributions we use a soft–collinear approximation which eliminates the Dirac structure of the loop corrections and factorizes the loop integrals from the Born matrix element. This approximation is an extension of the eikonal approximation and reproduces the correct NLL result not only for soft, but also for collinear gauge bosons.

The remaining non-factorizable contributions are obtained by subtracting from all diagrams yielding mass singularities the factorizable contributions. We have shown that the non-factorizable contributions vanish due to the collinear Ward identities proven in [5].

Therefore only the factorizable contributions need to be evaluated explicitly. For the LL and NLL terms at two loops, we need a double-logarithmic contribution from a soft and collinear gauge boson which is exchanged between two different external legs, and another, at least single-logarithmic, loop correction. The two-loop factorizable contributions in the case of massless external fermions are depicted in Figure 1.
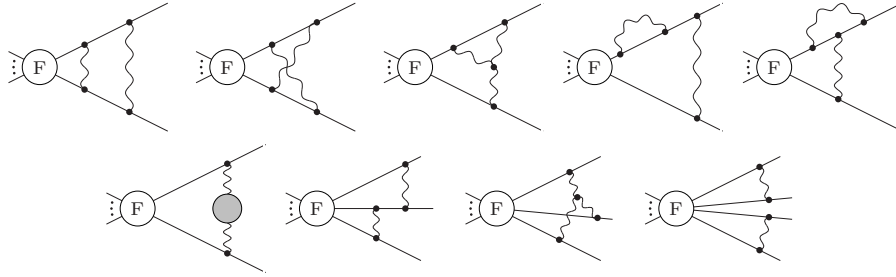
Figure 1: Two-loop factorizable contributions for massless external fermions. "F" denotes the factorized tree subdiagram, in which the gauge boson momenta are set to zero. The grey blob in the gauge boson propagator stands for all possible self-energy insertions.

The factorizable diagrams also include NLL contributions from UV momentum regions. When a subdiagram with a small characteristic scale of the order M_W^2 yields UV singularities which are renormalized at the scale Q^2, large logarithms $\ln(Q^2/M_W^2)$ arise. The soft–collinear approximation mentioned above is not valid for UV momenta, so we cannot use it for subdiagrams of this type and employ projection techniques instead.

2.2 Results for massless fermionic processes

We have evaluated the loop integrals of the factorizable contributions with two independent methods: An automatized algorithm which is based on the sector decomposition technique [14], and the method of expansion by regions combined with Mellin–Barnes representations (see [4] and references therein). The NLL result for massless fermionic processes

$f_1 f_2 \to f_3 \cdots f_n$ has been published in [6]. It allows to write the combined one- and two-loop result in the factorized form $\mathcal{M} = \mathcal{M}_0 F^{\mathrm{sew}} F^Z F^{\mathrm{em}}$, where $\mathcal{M}_0$ is the Born matrix element, and the correction terms read $F^{\mathrm{sew}} = \exp\!\big[\frac{\alpha}{4\pi}F_1^{\mathrm{sew}} + \big(\frac{\alpha}{4\pi}\big)^2 G_2^{\mathrm{sew}}\big]$, $F^Z = 1 + \frac{\alpha}{4\pi}\Delta F_1^Z$ and $F^{\mathrm{em}} = \exp\!\big[\frac{\alpha}{4\pi}\Delta F_1^{\mathrm{em}} + \big(\frac{\alpha}{4\pi}\big)^2 \Delta G_2^{\mathrm{em}}\big]$. The symmetric-electroweak factor F^{sew} equals the result from a symmetric $SU(2) \times U(1)$ theory where all gauge boson masses are equal to M_W. The factor F^Z incorporates the terms from the mass difference $M_Z \neq M_W$. And the electromagnetic terms in F^{em} factorize and exponentiate separately, such that a separation of the singularities due to the massless photon is possible. The one-loop terms F_1^{sew} and ΔF_1^{em} get exponentiated, and the additional two-loop terms G_2^{sew} and ΔG_2^{em} are proportional to β-function coefficients. For details of the correction terms, we refer to [6].

Our results confirm the resummation predictions based on the evolution equations. By applying our general correction factors to the case of massless four-fermion scattering, we have found agreement with the neutral-current results in [3, 9], and we have obtained a new NLL result for the charged-current processes.

3 From massless to massive fermions

For massive external fermions, the diagrams from the factorizable contributions have to be reevaluated, additional diagrams with Yukawa interactions have to be considered and the cancellation of the non-factorizable contributions must be verified. This section deals with new complications which arise from massive external fermions in the loop integrals.

3.1 Expansion by regions with massive external particles

Expansion by regions [15, 16] is a powerful method for the asymptotic expansion of loop integrals. It is based on the following recipe: Divide the integration domain of the loop momenta into regions corresponding to the asymptotic limit considered. In every region, expand the integrand appropriately. Integrate each of the expanded terms over the whole integration domain.

The integrand is expanded before integration, and each expanded term has a unique order in powers of the large scale Q and the small scale M_W. But on-shell momenta p_i of massive external particles involve two scales, as their momentum squared is $p_i^2 = m_i^2 \sim M_W^2$ and their combinations with other external momenta are $r_{ij} = (p_i + p_j)^2 \sim Q^2$. In order to separate these two scales, the external momenta are reparametrized in terms of light-like momenta $\tilde{p}_i$ as $p_i = \tilde{p}_i + (p_i^2/\tilde{r}_{ij})\tilde{p}_j$, with some other external leg $j \neq i$ and $\tilde{p}_i^2 = \tilde{p}_j^2 = 0$, $\tilde{r}_{ij} = 2\tilde{p}_i\tilde{p}_j$ [16]. Through this shift, all contractions of external momenta with loop momenta can now be divided into parts of distinct scales, and the expansion is done in inverse powers of the new large scales $\tilde{r}_{ij} = r_{ij} + \mathcal{O}(M_W^2)$.

With respect to any pair of external light-like momenta $\tilde{p}_i, \tilde{p}_j$, the loop momenta can be expressed in Sudakov components parallel and perpendicular to these external momenta: $k = k_i^{(i,j)}\tilde{p}_i/Q + k_j^{(i,j)}\tilde{p}_j/Q + k_\perp^{(i,j)}$, with $k_i^{(i,j)} = 2\tilde{p}_j k\, Q/\tilde{r}_{ij}$, $k_j^{(i,j)} = 2\tilde{p}_i k\, Q/\tilde{r}_{ij}$ and $\tilde{p}_i k_\perp^{(i,j)} = \tilde{p}_j k_\perp^{(i,j)} = 0$. In each region, the components of the loop momenta are assigned specific sizes in powers of Q and M_W. Typical regions are listed in Table 1. While the hard, soft, collinear and ultrasoft regions are already present for massless external particles, the two ultracollinear regions are only relevant for massive external particles.

Region	hard	soft	i-collinear	j-collinear	ultrasoft	i-ultracoll.	j-ultracoll.
$k_i^{(i,j)}$	Q	M_W	Q	M_W^2/Q	M_W^2/Q	M_W^2/Q	M_W^4/Q^3
$k_j^{(i,j)}$	Q	M_W	M_W^2/Q	Q	M_W^2/Q	M_W^4/Q^3	M_W^2/Q
$k_\perp^{(i,j)}$	Q	M_W	M_W	M_W	M_W^2/Q	M_W^3/Q^2	M_W^3/Q^2

Table 1: Typical regions with the corresponding sizes of loop momentum components

3.2 Power singularities and fermion masses

Asymptotic expansions with small masses and large kinematical scales not only produce logarithmic mass singularities, but also power singularities $Q^2/M_{W,Z}^2$ and Q^2/m_t^2. These are generated at two loops by subdiagrams with a small scale of the order M_W^2. The method of expansion by regions predicts, for the contribution of each region, where power singularities can appear, by means of a simple power counting in the expanded integrals.

When complete Feynman diagrams are considered, the terms in the numerator ensure the cancellation of the power singularities. In diagrams where power singularities are present for individual scalar integrals, care must be taken to keep all the mass factors in the numerator which ensure the cancellations. In particular, the masses in the numerator of fermion propagators and in the Dirac equation of the spinors may not be neglected. Therefore we are not allowed to use the soft–collinear approximation for small-scale subdiagrams. However, these are exactly the same diagrams where we have employed alternative projection techniques already in the massless case in order to get the UV contributions right.

Additional complications originate from fermion masses in the numerator due to the chiral structure of the electroweak theory. With each mass factor along a fermion line, the chirality of the fermion in its interactions with the weak gauge bosons changes. We have found, though, that fermion masses in the numerator are relevant exclusively in pure QED diagrams where the chirality changes do not matter.

3.3 Preliminary results

We have completed the calculation of all factorizable contributions involving two massive or massless external fermion legs. This permits to determine the two-loop form factor in an Abelian model with both a massive gauge boson (mass M_W, coupling α) and a massless one (coupling α'). The one-loop form factor as a function of the two external fermion masses is given by $F_1(m_1, m_2) = \frac{\alpha}{4\pi} F_1^M + \frac{\alpha'}{4\pi} \left[F_1^0(0,0) + \Delta F_1^0(m_1) + \Delta F_1^0(m_2) \right]$. The NLL contribution (up to the order ϵ^2) from the massive gauge boson is independent of the fermion masses,

$$F_1^M = -L^2 - \frac{2}{3}L^3\epsilon - \frac{1}{4}L^4\epsilon^2 + 3L + \frac{3}{2}L^2\epsilon + \frac{1}{2}L^3\epsilon^2, \tag{1}$$

with $L = \ln(Q^2/M_W^2)$, while the contribution from the massless gauge boson is split into a completely massless part and corrections for each of the fermion masses:

$$F_1^0(0,0) = -2\epsilon^{-2} - 3\epsilon^{-1}, \quad \Delta F_1^0(0) = 0,$$

$$\Delta F_1^0(m_i) = \epsilon^{-2} + L_i\epsilon^{-1} + \frac{1}{2}L_i^2 + \frac{1}{6}L_i^3\epsilon + \frac{1}{24}L_i^4\epsilon^2 + \frac{1}{2}\epsilon^{-1} + \frac{1}{2}L_i + \frac{1}{4}L_i^2\epsilon + \frac{1}{12}L_i^3\epsilon^2, \tag{2}$$

with $L_i = \ln(Q^2/m_i^2)$. We have found that the NLL two-loop form factor (without closed fermion loops) simply exponentiates the one-loop result, $F_2(m_1, m_2) = \frac{1}{2}\left[F_1(m_1, m_2)\right]^2$.

4 Conclusions

We evaluate two-loop electroweak corrections in NLL accuracy for arbitrary processes with massive and massless external fermions. The methods which we have successfully applied for massless fermions work well also in the massive case, and the complications arising from fermion masses are under control. Preliminary results are already available for the form factor, they factorize and exponentiate like in the massless case. The calculation for processes with external fermions will soon be completed, and our method can be extended to arbitrary processes involving external gauge bosons or scalar particles.

Acknowledgments

The author gratefully acknowledges the pleasant collaboration with A. Denner and S. Pozzorini in the project presented in this talk.

References

[1] Slides:
http://ilcagenda.linearcollider.org/contributionDisplay.py?contribId=400&sessionId=73&confId=1296

[2] V. V. Sudakov, Sov. Phys. JETP **3** 65 (1956).

[3] B. Feucht, J. H. Kühn and S. Moch, Phys. Lett. **B561** 111 (2003);
B. Feucht, J. H. Kühn, A. A. Penin and V. A. Smirnov, Phys. Rev. Lett. **93** 101802 (2004);
B. Jantzen, J. H. Kühn, A. A. Penin and V. A. Smirnov, Phys. Rev. **D72** 051301 (2005) [Erratum-ibid. **D74** 019901 (2006)]; Nucl. Phys. **B731** 188 (2005) [Erratum-ibid. **B752** 327 (2006)].

[4] B. Jantzen and V. A. Smirnov, Eur. Phys. J. **C47** 671 (2006).

[5] A. Denner and S. Pozzorini, Eur. Phys. J. **C18** 461 (2001); Eur. Phys. J. **C21** 63 (2001).

[6] A. Denner, B. Jantzen and S. Pozzorini, Nucl. Phys. **B761** 1 (2007).

[7] V. S. Fadin, L. N. Lipatov, A. D. Martin and M. Melles, Phys. Rev. **D61** 094002 (2000).

[8] M. Melles, Phys. Rev. **D63** 034003 (2001); Phys. Rev. **D64** 014011 (2001); Phys. Rev. **D64** 054003 (2001); Phys. Rept. **375** 219 (2003); Eur. Phys. J. **C24** 193 (2002).

[9] J. H. Kühn, A. A. Penin and V. A. Smirnov, Eur. Phys. J. **C17** 97 (2000);
J. H. Kühn, S. Moch, A. A. Penin and V. A. Smirnov, Nucl. Phys. **B616** 286 (2001) [Erratum-ibid. **B648** 455 (2003)].

[10] M. Melles, Phys. Lett. **B495** 81 (2000);
M. Hori, H. Kawamura and J. Kodaira, Phys. Lett. **B491** 275 (2000).

[11] W. Beenakker and A. Werthenbach, Phys. Lett. **B489** 148 (2000); Nucl. Phys. **B630** 3 (2002).

[12] A. Denner, M. Melles and S. Pozzorini, Nucl. Phys. **B662** 299 (2003).

[13] S. Pozzorini, Nucl. Phys. **B692** 135 (2004).

[14] A. Denner and S. Pozzorini, Nucl. Phys. **B717** 48 (2005).

[15] M. Beneke and V. A. Smirnov, Nucl. Phys. **B522** 321 (1998);
V. A. Smirnov and E. R. Rakhmetov, Theor. Math. Phys. **120** 870 (1999);
V. A. Smirnov, Phys. Lett. **B465** 226 (1999).

[16] V. A. Smirnov, *Applied asymptotic expansions in momenta and masses*, Springer Tracts Mod. Phys. **177** 1 (2002).

Effective Theory Approach to
W-Pair Production near Threshold

Christian Schwinn

RWTH Aachen - Institut für Theoretische Physik E
D–52056 Aachen - Germany

In this talk, I review the effective theory approach to unstable particle production and present results of a calculation of the process $e^-e^+ \to \mu^- \bar{\nu}_\mu u \bar{d} X$ near the W-pair production threshold up to next-to-leading order in $\Gamma_W/M_W \sim \alpha \sim v^2$. The remaining theoretical uncertainty and the impact on the measurement of the W mass is discussed.

1 Introduction

The masses of particles like the top quark, the W boson or yet undiscovered particles like supersymmetric partners can be measured precisely using threshold scans at an e^-e^+ collider. In particular the error of the W mass could be reduced to $6\,\mathrm{MeV}$ by measuring the four fermion production cross section near the W-pair threshold [2], provided theoretical uncertainties are reduced well below 1%. In such precise calculations one has to treat finite width effects systematically and without violating gauge invariance. The next-to-leading order (NLO) calculations of W-pair production [3] available at LEP2 were done in the pole scheme [4] and were supposed to break down near threshold. The recent computation of the complete NLO corrections to $e^-e^+ \to 4f$ processes in the complex mass scheme [5] is valid near threshold and in the continuum, but is technically demanding and required to compute one loop six-point functions.

In this talk [1], I report on the NLO corrections to the total cross section of the process

$$e^-e^+ \to \mu^- \bar{\nu}_\mu u \bar{d} X \tag{1}$$

near the W-pair threshold [6] obtained using effective field theory (EFT) methods [7, 8, 9]. This calculation is simpler than the one of [5] and results in an almost analytical expression of the result that allows for a detailed investigation of theoretical uncertainties. However, the method is not easily extended to differential cross sections. Section 2 contains the leading order (LO) EFT description while the NLO approximation of the tree and the radiative corrections are described in Sections 3 and 4, respectively. Results are presented in Section 5 together with an estimate of the remaining theoretical uncertainties and a comparison to [5].

2 Unstable particle effective theory

To provide a systematic treatment of finite width effects, in [7, 8] EFT methods were used to expand the cross section simultaneously in the coupling constant α, the ratio Γ/M and the virtuality of the resonant particle $(k^2 - M^2)/M^2$, denoted collectively by δ. The modes at the small scale δ (the resonance, soft or Coulomb photons, ...) and the external particles are described by an effective Lagrangian $\mathcal{L}_\mathrm{eff}$ that contains elements of heavy quark effective theory or non-relativistic QED and soft-collinear effective theory (SCET) (for reviews of the various EFTs see e.g [11]). "Hard" fluctuations with virtualities $\sim M^2$ are not part

of the EFT and are integrated out. Their effect is included in short-distance coefficients in $\mathcal{L}_{\text{eff}}$ that can be computed in fixed-order perturbation theory without resummations of self-energies. Finite width effects are relevant for the modes at the small scale and are incorporated through complex short-distance coefficients in $\mathcal{L}_{\text{eff}}$ [8, 10].

It might be useful to compare the EFT approach to the pole scheme for the example of the production of a single resonance Φ in the inclusive process $f_1 \bar{f}_2 \to X$. The pole scheme provides a decomposition of the amplitude into resonant and non-resonant pieces [4]:

$$\mathcal{A}(s)|_{s \sim M^2} = \frac{\mathcal{R}(\bar{s})}{s - \bar{s}} + \mathcal{N}(s), \tag{2}$$

where both $\bar{s}$, the complex pole of the propagator defined by $\bar{s} - M^2 - \Pi(\bar{s}) = 0$, and $\mathcal{R}(\bar{s})$, the residue of $\mathcal{A}(s)$ at $\bar{s}$, are gauge independent. In the EFT, it is convenient to obtain the cross section from the imaginary part of the forward-scattering amplitude that reads [8]

$$i\mathcal{A}(s)|_{s \sim M^2} = \int d^4x \, \langle f_1 \bar{f}_2 | T \left[i\mathcal{O}^{\dagger}_{\Phi f_1 \bar{f}_2}(0) i\mathcal{O}_{f_1 \bar{f}_1 \Phi}(x) \right] |f_1 \bar{f}_2 \rangle + \langle f_1 \bar{f}_2 | i\mathcal{O}_{4f}(0) |f_1 \bar{f}_2 \rangle. \tag{3}$$

Here $\mathcal{O}_{f_1 \bar{f}_2 \Phi}$ describes the production of Φ while $\mathcal{O}_{4f}$ describes non-resonant contributions. The matching coefficients of these operators are gauge independent since they are computed from on-shell scattering amplitudes in the underlying theory, where for unstable particles "on-shell" implies $k^2 = \bar{s}$. The structure of (3) is similar to (2), but the EFT provides a field theoretic definition of the several terms. Higher order corrections to the matching coefficients correspond to the *factorizable corrections* in the pole scheme. Loop corrections to the matrix elements in the EFT correspond to the *non-factorizable corrections* [7].

Turning to W-pair production near threshold, the appropriate effective Lagrangian to describe the two non-relativistic W bosons with $k^2 - M_W^2 \sim M_W^2 v^2 \sim M_W^2 \delta$ is given by [9]

$$\mathcal{L}_{\text{NRQED}} = \sum_{a=\mp} \left[\Omega_a^{\dagger i} \left(iD^0 + \frac{\vec{D}^2}{2M_W} - \frac{\Delta}{2} \right) \Omega_a^i + \Omega_a^{\dagger i} \frac{(\vec{D}^2 - M_W \Delta)^2}{8M_W^3} \Omega_a^i \right] \tag{4}$$

with the matching coefficient [8] $\Delta \equiv (\bar{s} - M_W^2)/M_W$. If M_W is the pole mass, this becomes $\Delta = -i\Gamma_W$. The fields $\Omega_{\pm}^i \equiv \sqrt{2M_W} W_{\pm}^i$ describe the three physical polarizations of the Ws; the unphysical modes are not part of the EFT [9]. The covariant derivative $D_\mu \Omega_{\pm}^i \equiv (\partial_\mu \mp ieA_\mu)\Omega_{\pm}^i$ includes interactions with those photon fluctuations that keep the virtualities of the Ωs at the order δ. These are *soft* photons with $(q^0, \vec{q}) \sim (\delta, \delta)$ and *potential* (Coulomb) photons with $(q^0, \vec{q}) \sim (\delta, \sqrt{\delta})$. Collinear photons are also part of the EFT but do not contribute at NLO. The Lagrangian (4) reproduces the expansion of the resummed transverse W propagator in δ, as can be seen by writing the W four-momenta as $k^\mu = M_W v^\mu + r^\mu$ with $v^\mu \equiv (1, \vec{0})$ and a potential residual momentum $(r^0, |\vec{r}|) \sim M_W (v^2, v) \sim (\delta, \sqrt{\delta})$:

$$\frac{i}{k^2 - M_W^2 - \Pi_T^W(k^2)} \left(-g_{\mu\nu} + \frac{k_\mu k_\nu}{k^2} \right) \quad \Rightarrow \quad \frac{i(-g_{\mu\nu} + v_\mu v_\nu)}{2M_W(r^0 - \frac{\vec{r}^2}{2M_W} + \frac{\Delta}{2})}. \tag{5}$$

Higher orders in the expansion of the propagator are reproduced by the higher order kinetic terms in (4) and residue factors included in the production operators [6].

The production of a pair of non-relativistic W bosons is described by the operator [9]

$$\mathcal{O}_p^{(0)} = \frac{\pi\alpha}{s_w^2 M_W^2} \left(\bar{e}_{c_2,L} \left(\gamma^i n^j + \gamma^j n^i \right) e_{c_1,L} \right) \left(\Omega_-^{\dagger i} \Omega_+^{\dagger j} \right) \tag{6}$$

that is determined from the on-shell tree-level scattering amplitude $e^- e^+ \to W^+ W^-$:

$$
\begin{array}{c}\text{(diagrams)}\end{array} \qquad (7)
$$

At threshold, only the t-channel diagram and the $e_L^- e_R^+$ helicity contribute at leading order in δ. Similar to (3), the LO $e^- e^+$ forward-scattering amplitude in the EFT is given by the expectation value of a time ordered product of the operators (6), evaluated using (4):

$$
i\mathcal{A}^{(0)} = \int d^4 x \, \langle e^- e^+ | \mathrm{T}[i\mathcal{O}_p^{(0)\dagger}(0) i\mathcal{O}_p^{(0)}(x)] | e^- e^+ \rangle = \mathcal{O}_p^{(0)} \quad \mathcal{O}_p^{\dagger(0)} . \qquad (8)
$$

One estimates $\mathcal{A}^{(0)} \sim \alpha^2 \sqrt{\delta}$, noting that each Ω propagator (5) contributes δ^{-1} and counting the potential loop integral as $dk^0 d^3 k_i \sim \delta^{5/2}$. The total cross section for the process (1) is obtained from appropriate cuts of $\mathcal{A}^{(0)}$, where cutting an $\Omega_\pm$ line has to be interpreted as cutting the self-energies resummed in the EFT propagator. At LO, the cuts contributing to the flavour-specific final state are correctly extracted by multiplying the imaginary part of $\mathcal{A}^{(0)}$ by the leading-order branching fractions. In terms of $E = \sqrt{s} - 2M_W$ one obtains [6]

$$
\sigma^{(0)}(e^- e^+ \to \mu^- \bar{\nu}_\mu u \bar{d}) = \frac{\pi \alpha^2}{27 s_w^4 s} \mathrm{Im} \left[-i \sqrt{-\frac{E + i\Gamma_W}{M_W}} \right] . \qquad (9)
$$

3 NLO EFT approximation to the born cross section

Some parts of the NLO EFT calculation of the process (1) are included in a Born calculation in the full theory with a fixed width prescription. One contribution arises from *four-electron operators* $\mathcal{O}_{4e}^{(k)}$ analogous to those in (3). Their matching coefficients $C_{4e}^{(k)}$ are obtained from the forward-scattering amplitude in the full electroweak theory. The leading imaginary parts of $C_{4e}^{(k)}$ are of order α^3 and arise from cut two-loop diagrams corresponding to all squared tree diagrams of the processes $e^- e^+ \to W^- u \bar{d}$ and $e^- e^+ \to W^+ \mu^- \bar{\nu}_\mu$, calculated in dimensional regularization without self-energy resummations, but expanded near threshold:

$$
\begin{array}{c}\text{(diagrams)}\end{array} \qquad (10)
$$

Since these corrections to the amplitude are of order α^3, and counting $\alpha \sim \delta$, they are suppressed by $\delta^{1/2}$ compared to $\mathcal{A}^{(0)} \sim \alpha^2 \delta^{1/2}$ and are denoted as "$\sqrt{\mathrm{N}}$LO" corrections.

The second class of contributions arises from *production-operator and propagator corrections*. Performing the tree-level matching (7) up to order $\sim v$ and v^2 leads to higher order production operators $\mathcal{O}_p^{(1/2)}$ and $\mathcal{O}_p^{(1)}$. The operators $\mathcal{O}_p^{(1/2)}$ like $\left(\bar{e}_L \gamma^j e_L \right) \left(\Omega_-^i (-i) D^j \Omega_+^i \right)$ are given in [9]. At NLO one needs diagrams with two insertions of an $\mathcal{O}_p^{(1/2)}$ operator, one

insertion of an $\mathcal{O}_p^{(1)}$ operator and insertions of kinetic corrections from (4):

$$i\mathcal{A}_{\rm born}^{(1)} = \mathcal{O}_p^{(1/2)} \!\!\!\!\underset{\Omega}{\overset{\Omega}{\bigcirc}}\!\!\!\! \mathcal{O}_p^{\dagger(1/2)} + \mathcal{O}_p^{(1)} \!\!\!\!\underset{\Omega}{\overset{\Omega}{\bigcirc}}\!\!\!\! \mathcal{O}_p^{\dagger(0)} + \mathcal{O}_p^{(0)} \!\!\!\!\overset{(\vec{k}^2-M\Delta)^2}{\bigcirc}\!\!\!\! \mathcal{O}_p^{\dagger(0)}$$

Equivalently one can directly expand the spin averaged squared matrix elements [6].

As seen in Figure 1, the EFT approximations converge to the full Born result but it turns out that a partial inclusion of $N^{3/2}LO$ corrections is required to get an agreement of $\sim 0.1\%$ at 170 GeV and $\sim 10\%$ at 155 GeV [6]. For higher-order initial state radiation (ISR) improvement by a convolution with radiator functions, one needs $\sigma_{\rm Born}$ at energies far below threshold, where the EFT is not valid. For the numerical results in Section 5 the ISR-improved Born cross section from Whizard [12] was used, but one could also match the EFT to the full theory below, say, $\sqrt{s} = 155$ GeV.
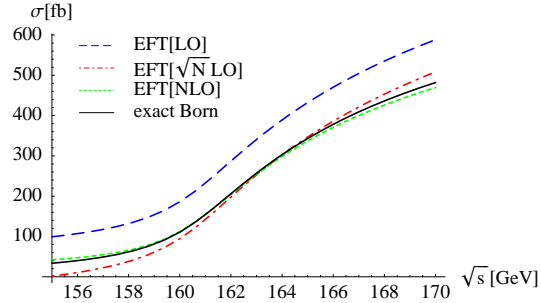

Figure 1: Convergence of EFT approximations to the born cross section from Whizard

4 Radiative corrections

The radiative corrections needed up to NLO are given by higher order calculations of short distance coefficients and by loop calculations in the EFT. Counting the QCD coupling constant as $\alpha_s^2 \sim \alpha_{ew} \sim \delta$, the corrections to Γ_W up to order $\alpha_{ew}\alpha_s$ ($\sqrt{\text{NLO}}$), α_{ew}^2 and $\alpha_{ew}\alpha_s^2$ (NLO) have to be included. The flavour-specific NLO *decay corrections* are correctly taken into account by multiplying the imaginary part of the LO forward-scattering amplitude with the one-loop corrected branching ratios. For the NLO *renormalization of the production operator* (6) one has to calculate the one-loop corrections to the on-shell scattering $e^-e^+ \to W^+W^-$ at leading order in the non-relativistic expansion:

Due to the threshold kinematics, many of the 180 one-loop diagrams do not contribute, consistent with the vanishing of the tree-level s-channel diagrams at leading order in v. In terms of a finite coefficient $c_p^{(1,\rm fin)}$ given in [6], the matching coefficient reads

$$C_p^{(1)} = \frac{\alpha}{2\pi}\left[\left(-\frac{1}{\varepsilon^2} - \frac{3}{2\varepsilon}\right)\left(-\frac{4M_W^2}{\mu^2}\right)^{-\varepsilon} + c_p^{(1,\rm fin)}\right]. \tag{11}$$

The *first and second Coulomb correction* arise from the exchange of potential photons. Their magnitude can be estimated counting the loop-integral measure in the potential region

as $d^4 q \sim \delta^{5/2}$, the Ω propagator and the potential photon propagator $i/|\vec{q}|^2$ as δ^{-1}. One finds that single Coulomb exchange is a $\sqrt{\text{NLO}}$ correction compared to the LO amplitude:

$$\raisebox{-1em}{\includegraphics[]{}} \quad \sim \alpha^3 \int d^4 k \, d^4 q \, \frac{1}{|\vec{q}|^2} \, \delta^{-4} \sim \alpha^3 \sim \mathcal{A}^{(0)} \sqrt{\delta} \tag{12}$$

At threshold the one-photon exchange is of the order of 5% of the LO amplitude while two-photon exchange is only a few-permille correction [13] and no resummation is necessary.

Soft photon corrections correspond to two-loop diagrams in the EFT containing a photon with momentum $(q_0, |\vec{q}|) \sim (\delta, \delta)$. They give rise to $\mathcal{O}(\alpha)$ corrections as can be seen from a power-counting argument similar to the one for Coulomb-exchange but counting the soft-photon propagator $-i/q^2$ as δ^{-2} and the soft loop-integral as δ^4. In agreement with gauge invariance arguments and earlier calculations [14], the sum of all diagrams where a soft photon couples to an Ω line vanishes. The only remaining diagrams give

$$\raisebox{-1em}{\includegraphics[]{}} \quad = \frac{4\pi^2 \alpha^2}{s_w^4 M_W^2} \frac{\alpha}{\pi} \int \frac{d^d r}{(2\pi)^d} \frac{1}{\eta_- \eta_+} \left[\left(\frac{1}{\varepsilon^2} + \frac{5}{12}\pi^2 \right) \left(-\frac{2\eta_-}{\mu} \right)^{-2\varepsilon} \right] \tag{13}$$

with $\eta_- = r_0 - \frac{|\vec{r}|^2}{2M_W} + i\frac{\Gamma^{(0)}}{2}$ and $\eta_+ = E - r_0 - \frac{|\vec{r}|^2}{2M_W} + i\frac{\Gamma^{(0)}}{2}$. The ϵ^{-2} poles cancel between (13) and diagrams with an insertion of the NLO production operator (11) while the remaining ϵ^{-1} poles proportional to $(2\log(\eta_-/M_W) + 3/2)$ are discussed below.

5   Results and estimate of remaining uncertainties

The radiative corrections in Section 4 were calculated for $m_e = 0$ so the result is not infrared safe. It should be convoluted with electron distribution functions in the $\overline{\text{MS}}$ scheme after minimal subtraction of the IR poles. However, the available distribution functions assume m_e as IR regulator. Our result can be converted to this scheme by adding contributions from the hard-collinear region where $k^\mu \sim M_W$, $k^2 \sim m_e^2$, and the soft-collinear region where $k^\mu \sim \Gamma_W$, $k^2 \sim m_e^2 \frac{\Gamma_W}{M_W}$. These cancel the ϵ-poles but introduce large logs of M_W/m_e:

$$\sigma^{(1)}(s) = \frac{\alpha^3}{27 s_w^4 s} \text{Im} \left\{ (-1) \sqrt{-\frac{E + i\Gamma_W}{M_W}} \left(4 \ln \left(-\frac{4(E + i\Gamma_W)}{M_W} \right) \ln \left(\frac{2M_W}{m_e} \right) \right. \right.$$

$$\left. \left. - 5 \ln \left(\frac{2M_W}{m_e} \right) + \text{Re} \left[c_p^{(1,\text{fin})} \right] + \frac{\pi^2}{4} + 3 \right) \right\} + \Delta\sigma_{\text{Coulomb}}^{(1)} + \Delta\sigma_{\text{decay}}^{(1)}. \tag{14}$$

At this stage, one can compare to the results of [5] for the strict $\mathcal{O}(\alpha_{ew})$ corrections without higher order ISR improvement, $\sigma_{4\text{f}}(161\text{GeV}) = 105.71(7)$ fb and $\sigma_{4\text{f}}(170\text{GeV}) = 377.1(2)$. From (14) one obtains $\sigma_{\text{EFT}}(161\text{GeV}) = 104.97(6)$ fb and $\sigma_{\text{EFT}}(170\text{GeV}) = 373.74(2)$ so the difference between the EFT and [5] is only about $0.7\% - 1\%$.

The large logs in (14) can be resummed by convoluting the NLO cross section with the structure functions used e.g. in [3], after appropriate subtractions to avoid double-counting. The solid line in Figure 2 shows the resulting corrections relative to σ_{Born}. Compared to the large correction from ISR improvement of σ_{Born} alone (blue/dashed), the size of the genuine radiative correction is about $+8\%$.

The largest remaining uncertainty is due to the treatment of ISR that is accurate only at leading-log level. It is formally equivalent to improve only σ_{Born} by higher order ISR [3, 5], but not the radiative corrections. The results of this approach are shown in the red (dash-dotted) line in Figure 2 and differ by almost 2% at threshold from the treatment discussed above. This translates to an uncertainty of $\delta M_W \sim 31$ MeV [6]. The remaining theory uncertainty comes from the uncalculated $N^{3/2}LO$ corrections in the EFT. The $O(\alpha)$ corrections to the the four-electron operators (10) lead to an estimated uncertainty of $\delta M_W \sim 8$ MeV [6].

Figure 2: Size of the relative NLO corrections for different treatments of ISR

These corrections are included in [5]. The effect of diagrams with single-Coulomb exchange together with a soft photon or a hard correction to the production vertex is estimated as $\delta M_W \sim 5$ MeV. Therefore it should be possible to reach the theoretical accuracy required for the M_W measurement since the largest remaining uncertainties can be eliminated by an improved treatment of ISR and with input of the full four fermion calculation.
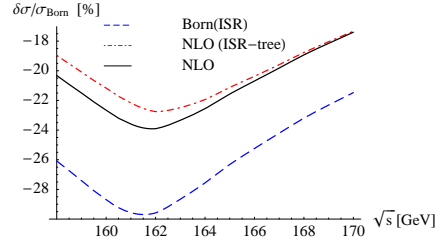
Acknowledgments

References

[1] http://ilcagenda.linearcollider.org/contributionDisplay.py?contribId=401&sessionId=73&confId=1296

[2] G. Wilson in *2nd ECFA/DESY Study*, pp. 1498–1505. Desy LC note LC-PHSM-2001-009

[3] A. Denner, S. Dittmaier, M. Roth, and D. Wackeroth *Phys. Lett.* **B475** (2000) 127–134, [hep-ph/9912261]; *Nucl. Phys.* **B587** (2000) 67–117, [hep-ph/0006307]; W. Beenakker, F. A. Berends, and A. P. Chapovsky *Nucl. Phys.* **B548** (1999) 3–59, [hep-ph/9811481]

[4] R. G. Stuart *Phys. Lett.* **B262** (1991) 113–119; A. Aeppli, G. J. van Oldenborgh, and D. Wyler *Nucl. Phys.* **B428** (1994) 126–146, [hep-ph/9312212]

[5] A. Denner, S. Dittmaier, M. Roth, and L. H. Wieders *Phys. Lett.* **B612** (2005) 223–232, [hep-ph/0502063]; *Nucl. Phys.* **B724** (2005) 247–294, [hep-ph/0505042]

[6] M. Beneke, P. Falgari, C. Schwinn, A. Signer, and G. Zanderighi arXiv:0707.0773 [hep-ph]

[7] A. P. Chapovsky, V. A. Khoze, A. Signer, and W. J. Stirling *Nucl. Phys.* **B621** (2002) 257–302, [hep-ph/0108190]

[8] M. Beneke, A. P. Chapovsky, A. Signer, and G. Zanderighi *Phys. Rev. Lett.* **93** (2004) 011602, [hep-ph/0312331]; *Nucl. Phys.* **B686** (2004) 205–247, [hep-ph/0401002]

[9] M. Beneke, N. Kauer, A. Signer, and G. Zanderighi *Nucl. Phys. Proc. Suppl.* **152** (2006) 162–167, [hep-ph/0411008]

[10] A. H. Hoang and C. J. Reisser *Phys. Rev.* **D71** (2005) 074022, [hep-ph/0412258]

[11] I. Z. Rothstein, TASI lectures 2002, hep-ph/0308266; M. Neubert, TASI lectures 2004, hep-ph/0512222

[12] W. Kilian in *2nd ECFA/DESY Study*, pp. 1924–1980. DESY LC-Note LC-TOOL-2001-039

[13] V. S. Fadin, V. A. Khoze, and A. D. Martin *Phys. Lett.* **B311** (1993) 311–316; V. S. Fadin, V. A. Khoze, A. D. Martin, and W. J. Stirling *Phys. Lett.* **B363** (1995) 112–117, [hep-ph/9507422]

[14] V. S. Fadin, V. A. Khoze, and A. D. Martin *Phys. Rev.* **D49** (1994) 2247–2256; K. Melnikov and O. I. Yakovlev *Phys. Lett.* **B324** (1994) 217–223, [hep-ph/9302311]

Status reports from the GRACE Group

Y. Yasui[1], T. Ueda[2], E. de Doncker[3], J. Fujimoto[2],
N. Hamaguchi[4], T. Ishikawa[2], Y. Shimizu[5] and F. Yuasa[2]

1- Tokyo Management College
Ichikawa, Chiba 272-0001, Japan

2- High Energy Accelerator Research Organization (KEK)
1-1 OHO Tsukuba, Ibaraki 305-0801, Japan

3- Western Michigan University
Kalamazoo, MI 49008-5371, USA

4- Hitachi, Ltd., Software Division
Totsuka-ku, Yokohama, 244-0801, Japan

5- The Graduate University for Advanced Studies, Sokendai
Shonan Village, Hayama, Kanagawa 240-0193, Japan

We discuss a new approach for the numerical evaluation of loop integrals. The fully numerical calculations of an infrared one-loop vertex and a box diagram are demonstrated. To perform these calculations, we apply an extrapolation method based on the ϵ-algorithm. In our approach, the super high precision control in the numerical manipulation is essential to handle the infrared singularity. We adopt a multi-precision library named `HMLib` for the precision control in the calculations.

1   Introduction

Measurements of fundamental parameters with high precision will be one of the important issues at the ILC experiment. We suppose to determine the masses and couplings for the standard model (SM) and some of the beyond the standard models like the minimal supersymmetric model(MSSM) within a few percent precision [1]. These precision measurements require the knowledge of high precision theoretical predictions, especially the computation of higher loop corrections. Since,the vast number of Feynman diagrams appear in the loop calculations, performing such computation is absolutely beyond the human power if it should be done by hand. The procedure of a perturbation calculation is well established, thus computers must be able to take the place of human hand. In this purpose several groups have developed computer programs which generate Feynman diagrams and calculate cross sections automatically, like `GRACE` [2], `FeynArts-FormCalc` [3] and `CompHEP` [4].

The `GRACE` system, developed by Minamitateya group, is one of the systems to calculate Feynman amplitudes including loop diagrams. Our final goal of the `GRACE` system is to construct the fully automatic computation system of multi-loop integrals. In this stage, it is successfully working for one-loop calculations in both the SM [5] and the MSSM [6]. However, the fully automatic way to compute multi-loop integrals is not established, thus the system is still semi-automatic. Especially, since infrared singularities require the analytic manipulations, it makes difficult to handle the singularity in the automatic way. To avoid such a difficulty, we really need to treat loop integrals in a fully numerical way.

In this paper, we discuss the fully numerical computation of one-loop integrals with existing infrared singularities. First, we demonstrate the calculations of an one-loop vertex

and a box diagram in QED case. We put a fictitious photon mass as a regulator of the infrared singularities. For the calculations, we adopt the very brute force way as the numerical extrapolation method. In our approach, the ϵ-algorithm is efficient. We also introduce a precision control technique to handle the numerical calculation with extremely small photon masses.

In QCD, one can not avoid to use the dimensional regularization to treat the infrared singularity. The sector decomposition technique [7] is useful to pick up the singularities but in general, the numerical integration of each term is not trivial because the denominators of the integrands can be zero in the integral region. Therefore, the extrapolation method should be effective in this case, too.

The layout of this paper is as follows. In section 2, we show the basic idea and formula of the loop integrals. Numerical results of the infrared one-loop vertex and box diagram are shown in section 3. The case for the dimensional regularization is discussed in section 4. In section 5 we will summarize this paper.

2   Basic idea

The basic idea of our numerical method is the combination of an efficient multi-dimensional integration routine and an extrapolation method. Here, we consider a scalar one-loop n-point integral given by

$$I(\epsilon) = \int \frac{d^4 l}{(2\pi)^4 i} \frac{1}{(l^2 - m_1^2 + i\epsilon)((l+p_1)^2 - m_2^2 + i\epsilon) \cdots ((l + \sum_{j=1}^{n-1} p_j)^2 - m_n^2 + i\epsilon)}, \quad (1)$$

where l is the loop momentum, p_j is the momentum of the jth external particle and m_j is the mass carried by the jth internal line. Putting $\epsilon > 0$ in the denominator of Feynman integrals to prevent the integral from diverging, we can get the numerical results of $I(\epsilon)$ for a given ϵ. Calculating a sequence of $I(\epsilon_l)$ with various value of $\epsilon_l = \epsilon_0 \times (const.)^{-l}$ $(l = 0, 1, 2, \cdots)$ and extrapolating into the limit of $\epsilon \to 0$, we can get the final result of the integration which appears in a physical amplitude.

In this approach, we use `DQAGE` routine in the multi-dimensional integration. It is included in the package `QUADPACK` [8] and it is a globally adaptive integration routine. We also apply the ϵ-algorithm introduced by P.Wynn[9]. The algorithm accelerates the conversion of the sequences. Our approach is very efficient for massive one-loop and two-loop integrals including non-scalar type integrals [10, 11, 12, 13].
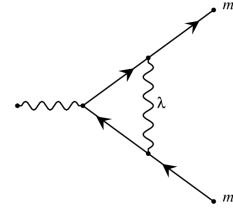
produced by GRACEFIG

Figure 1: One-loop vertex diagram

λ [GeV]	Average lost-bits	Maximum lost-bits
10^{-20}	88	92
10^{-21}	98	102
10^{-22}	108	112

Table 1: Lost-bits information from `HMLib` with the quadruple precision arithmetic. λ is a fictitious photon mass.

In the above massive cases, the results are consistent with analytic ones very well, even in the double precision arithmetic or quadruple precision arithmetic. On the other hand, for massless cases, we need much more careful treatments to handle the infrared singularities. For the infrared divergent diagram, it becomes harder to get a result with an enough accuracy even in the quadruple precision arithmetic. Thus, the precision control of the numerical integration becomes another important elements in our approach [14].

For the precision control, we use `HMlib`[15] as the multi-precision library. The advantage of this library is that it gives an information of the lost-bits during the calculation, thus we can guarantee the precision of the results. In Table 1, we show an example of the lost-bits information supplied by `HMLib`. Here, we demonstrated the calculation of one-loop vertex diagram (Fig.1). The diagram includes the infrared singularity due to the photon exchange. We put a fictitious photon mass λ as a regulator of the infrared singularity. In P-precision presentation implemented in `HMlib`, a sign bit is 1 bit and an exponent bit is 15 bits and a mantissa is $(32 \times P - 16)$ bits with based on IEEE754 FP. When $P = 4$ (quadruple precision), the mantissa becomes 112 bits. In the Table when λ is 10^{-23} GeV, the maximum number of lost-bits is the same as the number of bits of the mantissa. This means quadruple-precision is not enough and we have to perform the calculation within octuple or higher precision.
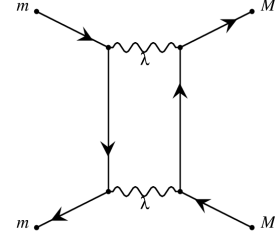
produced by GRACEFIG

Figure 2: One-loop box diagram in QED

3 Numerical results

For the one-loop vertex diagram shown in Fig. 1, the loop integral we consider in this paper is

$$I = \int_0^1 dx \int_0^{1-x} dy \frac{1}{D}, \qquad (2)$$

where

$$D = -xys + (x+y)^2 m^2 + (1-x-y)\lambda^2. \qquad (3)$$

Here s denotes squared central mass energy and m and λ are a mass of external particles and a fictitious photon mass respectively. Replacing s by $s+i\epsilon$ in (3) and applying extrapolation method, we obtain the numerical results which are shown in Table 2 [14]. Results are compared to analytic results evaluated by the formula in [16]. The combination of the extrapolation method and multi precision control with `HMLib` works very well and we get stable results even though the photon mass becomes much smaller as 10^{-160} GeV.

We also demonstrate the calculation of the one-loop box diagram shown in Fig.2. Here, we consider the following integral,

$$I = \int_0^1 dx \int_0^{1-x} dy \int_0^{1-x-y} dz \frac{1}{D^2}, \qquad (4)$$

where

$$
\begin{aligned}
D & = & -xys - tz(1-x-y-z) + (x+y)\lambda^2 & \qquad (5) \\
& + & (1-x-y-z)(1-x-y)m^2 + z(1-x-y)M^2. & \qquad (6)
\end{aligned}
$$

n	Numerical Results	P	Analytical Results [P=4]
-30	-0.150899286980769753D-01 $\pm$ 0.771D-26	8	-0.150899286980482291E-01
	0.189229839615898822D-02 $\pm$ 0.124D-25	8	0.189229839615525389E-02
-80	-0.405390396284235075D-01 $\pm$ 0.580D-15	16	-0.405390396283445396E-01
	0.478581216125478532D-02 $\pm$ 0.401D-12	16	0.478581216112143981E-02
-120	-0.608983283726997427D-01 $\pm$ 0.556D-15	32	-0.608983283725815879E-01
	0.710062317325786663D-02 $\pm$ 0.415D-12	32	0.710062317309438855E-02
-160	-0.812576170752810666D-01 $\pm$ 0.549D-10	32	-0.812576183472699269E-01
	0.941543418501223556D-02 $\pm$ 0.109D-11	32	0.941543432496722442E-02

Table 2: Numerical results of the one-loop vertex diagram with $\sqrt{s} = 500$ GeV, $t = -150^2$ GeV^2, $m = m_e = 0.5 \times 10^{-3}$ GeV. Photon mas $\lambda = 10^n$[GeV] and P denotes P-precision. The upper is the result of Real part and the lower is one of Imaginary part.

s denotes squared central mass energy and m and M are external masses of particles. Again, replacing s by $s + i\epsilon$ in eq.(6) and applying extrapolation method, we obtain the numerical results. We show the real part of the numerical results with the analytic ones in Table 3 as an example [14]. The results are almost consistent each other. However, since high precision computation costs huge CPU time, we only have done the quadruple precision arithmetic. Thus the results are not reliable when the photon mass is smaller as 10^{-30} GeV.

4 Dimensional Regularization

We next consider the diagram contains two massive and two massless external legs, and internal lines are all massless with the dimensional regularization, where $D = \varepsilon + 2$ (Fig. 3). In order to pick up the singularities, we apply the sector decomposition technique. The loop integral is expressed as follows:

$$I_4 = \int \prod_{i=1}^{4} dx_i \frac{\delta(1 - \sum x_i)}{(-sx_1x_3 - tx_2x_4 - m_3^2 x_3 x_4 - m_4^2 x_1 x_4)^{2-\varepsilon}}, \quad (7)$$

$$= \sum_{n=-2,-1,0,\cdots} C_n \times \varepsilon^n. \quad (8)$$

Figure 3: One-loop box diagram with two massive external legs, so called "hard" case.

In the case of $s = 123$ GeV^2, $t = -200$ GeV^2, $m_3^2 = 50$ GeV^2 and $m_4^2 = 60$ GeV^2, the denominator of each integrand corresponding to $1/\varepsilon$ and the finite term can be zero. Again, $+i\epsilon$ is introduced in the denominator of eq.(8) to specify the analyticity of it and the extrapolation method does work to perform the numerical integration. Table 4 shows the complete numerical integration can reconstruct the results with the analytical expressions [17].
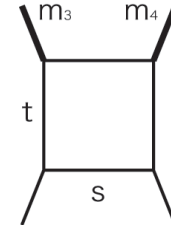
5 Summary

We discussed a new approach of the numerical method for multi-loop integrals. The combination of an efficient multi-dimensional integration routine and an extrapolation method is

n	Numerical Results	P	Numerical Results [P=4]
-15	-0.1927861102670278D-06 $\pm$ 0.314D-14	4,4,2	-0.1927861122439641E-06
-20	-0.2472486348234972D-06 $\pm$ 0.586D-15	4,4,2	-0.2472486352599175E-06
-25	-0.3017111253761463D-06 $\pm$ 0.111D-13	4,4,2	-0.3017111582758710E-06
-30	-0.3562028882831722D-06 $\pm$ 0.867D-10	4,4,2	-0.3561736812918245E-06

Table 3: Numerical results of the loop integral of one-loop box diagram with $\sqrt{s} = 500$ GeV, $t = -150^2 GeV^2$, $m = 0.5 \times 10^{-5}$ GeV, $M = 150$ GeV. Photon mas $\lambda = 10^n$[GeV] and P denotes P-precision. This is results of Real part.

n	Numerical Results	Analytic Results
-2	-0.40650406505E-04	-0.40650406504E-04
-1	-0.34156307031E-03	-0.34156306995E-03
0	-0.14929502492E-02	-0.14929502456E-02

Table 4: Numerical v.s. Analytical results in the double precision arithmetic. Real part of C_n of Fig. 3 with $s = 123$ GeV^2, $t = -200$ GeV^2, $m_3^2 = 50$ GeV^2 and m_4^2=60 GeV^2.

applicable to the one-loop integral even though it includes infrared singularities both with the introduction of the fictitious mass and the dimensional regularization. We demonstrated the fully numerical calculations for one-loop vertex and box diagram with infrared singularities. To handle the infrared singularities, high precision control is essential and in some case quadruple precision is not enough to obtain the stable results. In our calculations, we applied the multi-precision library `HMLib` which has the high performance of the precision control . Our method is efficient and we obtain reliable results for one-loop vertex and box diagrams with infrared singularities.

Acknowledgments

References

[1] see for example, ILC Reference Design Report volume 2:"Physics at the ILC", eds A. Djouadi *et al.*, ILC Global Design Effort and World Wide Study (2007)

[2] G. Belanger, F. Boudjema, J. Fujimoto, T. Ishikawa, T. Kaneko, K. Kato, Y. Shimizu, Phys.Rept. **430** 117 (2006);
J. Fujimoto, T. Ishikawa, M. Jimbo, T. Kaneko, K. Kato, S. Kawabata, T. Kon, M. Kuroda, Y. Kurihara, Y. Shimizu and H. Tanaka, Comput. Phys. Commun. **153** 106 (2003); Program package `GRACE/SUSY` (`GRACE v2.2.0`) is available from `http://minami-home.kek.jp/` .

[3] T. Hahn, Nucl. Phys. Proc. Suppl. **89** 231 (2000) ; T. Hahn, Comput. Phys. Commun. **140** 418(2001) ; T. Hahn and C. Schappacher, Comput. Phys. Commun. **143** 54 (2002).

[4] A.Pukhov *et al.*, arXiv:hep-ph/9908288; A. Semenov, Nucl. Instrum. Meth. A502 558 (2003).

[5] F.Boudjema, J.Fujimoto, T.Ishikawa, T.Kaneko, K.Kato, Y.Kurihara, Y.Shimizu, Y.Yasui, *Electroweak Corrections for the Study of the Higgs Potential at the LC* LCWS05, Stanford (2005).

[6] J. Fujimoto, T. Ishikawa, M. Jimbo, T. Kon, Y. Kurihara, M. Kuroda, Phys. Rev. **D75**, 113002 (2007).

[7] T. Binoth, G. Heinrich, Nucl.Phys. **B585**, 741 (2000), T. Binoth, G. Heinrich, Nucl.Phys. **B680**, 375 (2004).

[8] R. Piessens, E. de Doncker, C. W. Ubelhuber and D. K. Kahaner, *QUADPACK, A Subroutine Package for Automatic Integration*, Springer Series in Computational Mathematics. Springer-Verlag, (1983).

[9] P.Wynn, Math. Tables Automat. Computing 10 91(1956):
P.Wynn, SIAM J. Numer. Anal. **3** 91(1966).

[10] E. de Doncker, Y. Shimizu, J. Fujimoto and F. Yuasa, Comput. Phys. Commun. **159** 145 (2004).

[11] E. de Doncker, J. Fujimoto and F. Yuasa, Nucl. Instr. and Meth **A534** 269 (2004).

[12] E. de Doncker, S. Li, Y. Shimizu, J. Fujimoto and F. Yuasa, Lecture Notes in Computer Science **3514**,151 (2005).

[13] E. de Doncker, Y. Shimizu, J. Fujimoto and F. Yuasa, A talk in LoopFest V, June 19-21, 2006. SLAC, USA,
http://www-conf.slac.stanford.edu/loopfestv/proc/proceedings.htm.

[14] F. Yuasa, E. de Doncker, J. Fujimoto, N. Hamaguchi, T. Ishikawa and Y. Shimizu, *Precise Numerical Evaluation of the Scalar One-Loop Integrals with the Infrared Divergence*, ACAT workshop, Amsterdam, (2007);arXiv:0709.0777.

[15] N. Hamaguchi, IPSJ SIG Technical Report 2007-ARC-172 (22)/ 2007-HPC-109 (22) pp. 127-132.
N. Hamaguchi, IPSJ SIG Technical Report 2007-ARC-172 (23)/ 2007-HPC-109 (23) pp. 133-138.

[16] J. Fujimoto, Y. Shimizu, K. Kato and Y. Oyanagi, Progress of Theoretical Physics **Vol.87** No. 5 1232 (1992).

[17] G. Duplanžić, B. Nižić, Eur. Phys. J. C **20**, 357 (2001), Y. Kurihara, Eur.Phys. **J.C45**, 427 (2006).

Tools for NNLO QCD Calculations

T. Gehrmann

Institut für Theoretische Physik, Universität Zürich, CH-8057 Zürich, Switzerland

For precision studies with QCD observables at colliders, higher order perturbative corrections are often mandatory. For exclusive observables, like jet cross sections or differential distributions, these corrections were until recently only known to next-to-leading order (NLO) in perturbation theory. Owing to many new technical developments, first next-to-next-to-leading order (NNLO) QCD calculations are now becoming available. We review the recent progress in this field.

1 Introduction

At present-day colliders, a number of benchmark reactions is measured to a very high experimental accuracy. These reactions allow for a very precise determination of the parameters of the Standard Model, and may reveal minute deviations, hinting towards new physics effects. For many of these benchmark reactions, one faces the problem that the observables [1] are inherently exclusive (like jet cross sections), or differential in several variables (if kinematical cuts are involved). While fully inclusive quantities are often known to third order in perturbation theory, the perturbative expression for those exclusive observables is much less well known. Consequently, the precision of many benchmark reactions is limited not by the quality of the experimental data, but by the error on the theoretical (next-to-leading order, NLO) calculations used for the extraction of the Standard Model parameters. To improve upon this situation, an extension of the theoretical calculations to next-to-next-to-leading order (NNLO) is therefore mandatory.

2 Ingredients to NNLO calculations

At next-to-next-to-leading order, three types of processes contribute to an observable with m hard particles in the final state:

1. the two-loop corrections to the m-particle process, where all particles are hard.

2. the one-loop corrections to the $(m+1)$-particle process, where one particle can become unresolved (collinear or soft).

3. the tree-level $(m+2)$-particle process, where up to two particles can become unresolved.

Each contribution contains infrared singularities, which cancel only in the sum. Since the definition of the observable final state (jet algorithm or kinematical cuts) acts differently on each of these processes, it is mandatory to compute all of them individually. This is in variance with calculations of fully inclusive quantities (total cross sections, sum rules), where all contributions can be added before evaluation using the optical theorem.

QCD infrared factorisation predicts that the behaviour of cross sections in soft or collinear limits is process-independent. At NNLO, the corresponding universal tree-level double unresolved [2] and one-loop single unresolved [3] factors are known. Based on this universal

behaviour, one aims to develop process-independent techniques for NNLO calculations of exclusive observables.

The first calculations combining elements of this type are the derivations of the NNLO corrections to the deep inelastic structure functions [4], and to the coefficient functions for vector boson [5] and Higgs boson production [6,7] at hadron colliders. Although these observables are fully inclusive, one still has to consider the individual parton-level contributions separately, since they include collinear radiation associated with the incoming partons.

NNLO calculations for hadron colliders also require parton distributions accurate to this order. Following the derivation of the three-loop splitting functions [8], global NNLO fits [9] are now becoming available. These are however still somewhat limited by the fact that not all observables included in the fit are known to NNLO.

3   Techniques and applications

The derivation of the individual ingredients to NNLO calculations, and their combination into a parton-level event generator, are posing a variety of computational challenges. Many new techniques have been developed in this context.

3.1   Sector decomposition

In computing the various contributions to perturbative corrections at NNLO and beyond, one frequently encounters the problem of overlapping singularities. These appear if one particular term develops a singular behaviour in more than one region of phase space. The technique of sector decomposition offers an elegant solution to this problem. Originally proposed as a tool in formal proofs of renormalisability [10], and only used occasionally afterwards [11], this technique was fully formulated first for multi-loop integrals [12] and subsequently extended to phase space integrations [13,14].

Starting from a parameter representation of the (virtual or real) integral under consideration, the space of integrations is decomposed iteratively into non-overlapping sectors. At the end of this iteration each sector contains only a single type of singularity. In each sector, after expanding all regulators in distributions, the Laurent series of the integral is well-defined, and its coefficients can be obtained by numerical integration.

This technique has been used in the calculation of virtual two-loop and three-loop multi-leg integrals [12,15], often ahead of or in timely coincidence with analytical results. For loop integrals involving mass thresholds inside the physical region, sector decomposition must be combined with contour deformation to avoid pinch singularities [16,17].

Concerning the calculation of real radiation corrections at NNLO, the first-ever results for fully differential observables were obtained using sector decomposition for $e^+e^- \to 2$ jets [18], $pp \to H + X$ [19], muon decay [20] and $pp \to V + X$ [21].

3.2   Integral reduction

Within dimensional regularisation, the large number of different integrals appearing in multi-loop calculations can be reduced to a small number of so-called *master integrals* by using integration-by-parts (IBP) identities [22]. These identities exploit the fact that the integral over the total derivative of any of the loop momenta vanishes in dimensional regularisation.

For integrals involving more than two external legs, another class of identities exists due to Lorentz invariance. These Lorentz invariance identities [23] rely on the fact that an infinitesimal Lorentz transformation commutes with the loop integrations, thus relating different integrals. The common origin of IBP and LI identities is the Poincare invariance of loop integrals within dimensional regularisation.

In principle, the identities for all loop integrals of a given topology can be solved in a closed symbolic form [22]. In practise, this solution is often overly complex, and can not be found in an automated manner. Instead, one pursues another approach, the so-called Laporta algorithm [24], which solves the system of identities for a given topology by assigning a weight to each integral according to its complexity. In turn, the very large system of interconnected identities is solved by elimination, thereby reducing each integral in the system to master integrals. Several computer implementations of the Laporta algorithm are available [23–25].

Originally formulated only for loop integrals, these reduction techniques can also be applied to multi-particle phase space integrals by expressing on-shell conditions and kinematic constraints in the form of generalised propagators [7, 14].

3.3 Mellin-Barnes integration

The techniques described in the previous section allow to reduce the hundreds to thousands of different integrals appearing in an actual calculation to a small set of master integrals. The reduction equations do not yield any information on the master integrals, which have to be determined using some other technique. Unlike in the one-loop case, where a direct integration using Feynman parameters is usually sufficient, master integrals at two or more loops pose a considerable computational challenge.

A commonly used analytical approach is to replace the product of loop propagators by multiple Mellin-Barnes integrations [26]. This replacement can be performed in an automated manner using computer algebra [27]. After integration over the loop momenta in dimensional regularisation, the Mellin-Barnes integrals are normally not yet well-defined around $d = 4$, where the Laurent expansion is desired. To arrive at this limit, one must first perform analytic continuations, which can again be done using computer algebra [28, 29], thereby transforming each single Mellin-Barnes integral into a sum of integrals and residues. After analytic continuation, the Laurent coefficients can be determined by carrying out the Mellin-Barnes integrals numerically [28]. Analytical results for Mellin-Barnes integrals can often be obtained (especially if they can be expressed as multiple harmonic sums [30–32]), and systematic methods for them are under development.

Using Mellin-Barnes integration techniques, analytical results were obtained for two-loop four-point functions with massless [33–35] and massive [36] internal propagators.

3.4 Differential equations

A method for the analytic computation of master integrals avoiding the explicit integration over the loop momenta is to derive differential equations in internal propagator masses or in external momenta for the master integral, and to solve these with appropriate boundary conditions. This method has first been suggested [37] to relate loop integrals with internal masses to massless loop integrals.

It has been worked out detail and generalised to differential equations in external momenta in [23, 38]. Differentiation of a master integral with respect to an external invariant

or to a mass yields a combination of integrals of the same topology. Using the integral reduction techniques described above, these can be reexpressed by the master integral itself, plus simpler integrals. As a result, one obtains an inhomogeneous differential equation for the master integral. Solving this equation and matching the solution onto an appropriate boundary condition (obtained in a special kinematical point) then yields the desired master integral, very often in a closed form containing hypergeometric functions and their generalisations. The Laurent expansion of the integral then amounts to expansion of these functions [39]. A detailed review of the method can be found in [40].

Using the differential equation technique, master integrals were derived for massless two-loop four-point functions [41–43], for massive two-loop vertex functions [44, 45] and for parts of the master integrals required for Bhabha scattering [46].

3.5 Virtual corrections and infrared structure

Using the IBP and LI equations for the reduction to master integrals, which were then computed with various of the above-mentioned techniques, results for a variety of two-loop corrections were obtained for $1 \to 2$, $1 \to 3$ and $2 \to 2$ reactions. These include all massless parton-parton scattering amplitudes [47], processes yielding two-photon final states [48], light-by-light scattering [49] and vector boson decay into three massless partons [50, 51] and its crossings [52]. For amplitudes involving external masses, all two-loop form factors [53] of a heavy quark were derived, and large parts of the virtual two-loop corrections to Bhabha scattering [54] are completed.

These results are usually expressed in terms of harmonic polylogarithms [55], which are a generalisation of the well-established Nielsen's polylogarithms [56]. If several scales are involved in a process, the set of functions needs to be further extended to include multidimensional harmonic polylogarithms [50, 57, 58].

After ultraviolet renormalisation, these two-loop amplitudes still contain poles of infrared origin. This infrared pole structure is universal for massless amplitudes, and can be predicted from resummation formulae [59]. Exploiting the fact that a particle mass can also act as an infrared regulator, the universality of infrared singularities can be extended to massive amplitudes [60], where not only the divergent terms but also logarithmically enhanced terms are universal. Knowing the corresponding massless scattering amplitudes, it is therefore possible to construct massive amplitudes up to corrections of order m^2/s, which was recently accomplished for heavy quark production [61] and Bhabha scattering [62, 63].

3.6 Subtraction methods

To build exclusive final states at a given order, a jet algorithm or event shape definition has to be applied separately to each partonic channel contributing at this order and all partonic channels have to be summed. However, each partonic channel contains infrared singularities which, after summation, cancel among each other. Consequently, these infrared singularities have to be extracted before the jet algorithm can be applied. While explicit infrared singularities from purely virtual contributions are obtained immediately after integration over the loop momenta, their extraction is more involved for real radiation. The singularities associated with the real emission of soft and/or collinear partons in the final state become only explicit after integrating the real radiation matrix elements over the appropriate phase space.

In the sector decomposition method described above, the full matrix elements are integrated numerically, after expansion as a Laurent series (which amounts to subtraction of residues in each sector). A different approach is pursued by subtraction methods, which extract infrared singularities of the real radiation contributions using infrared subtraction terms. These terms are constructed such that they approximate the full real radiation matrix elements in all singular limits while still being integrable analytically.

Several methods for constructing NLO subtraction terms systematically were proposed in the literature [64–68]. For some of these methods, extension to NNLO was discussed [69] and worked out for special cases [70]. Up to now, the only method worked out in full detail to NNLO is antenna subtraction [71].

The basic idea of the antenna subtraction approach is to construct the subtraction terms from antenna functions. Each antenna function encapsulates all singular limits due to the emission of unresolved partons between two colour-connected hard partons. All antenna functions can be derived systematically from matrix elements [72] for physical processes. The antenna subtraction method was used recently in the derivation of the NNLO QCD corrections to $e^+e^- \to 3$ jets and related event shapes [73].

4   Results and outlook

The computational challenges of NNLO QCD calculations required for precision phenomenology have led to the development of a variety of new technical methods. Using these methods, many ingredients to NNLO QCD calculations were assembled in recent times. Many core results were derived more than once using independent, different methods.

These ingredients are now assembled into complete NNLO QCD calculations, which are usually carried out in the form of a parton-level event generator. In such a program, the full kinematical information is available for each event, and cross sections are obtained by adding all events relevant to the observable under consideration. This setup allows a great flexibility in the implementation of experimental cuts, and in the simultaneous evaluation of numerous kinematical distributions.

Up to now, fully exclusive NNLO QCD calculations were performed for $e^+e^- \to 2j$ [18, 72, 74], $e^+e^- \to 3j$ [73, 75], the forward-backward asymmetry in e^+e^- annihilation [76], Higgs production [19, 70] and vector boson production [21] at hadron colliders, as well as muon decay in QED [20].

Virtual two-loop corrections are available for a number of further $2 \to 2$ reactions, including jet production and vector-boson-plus-jet production at hadron colliders, jet production in deep inelastic scattering, and heavy quark production observables. The full calculation of these observables may require further improvements to existing tools, but further results of NNLO calculations are clearly within reach in the near future.

Acknowledgement

References

[1] R.K. Ellis, W.J. Stirling and B.R. Webber, *QCD and Collider Physics*, Cambridge University Press (Cambridge, 1996);
G. Dissertori, I.G. Knowles and M. Schmelling, *Quantum Chromodynamics: High Energy Experiments and Theory*, Oxford University Press (Oxford, 2003).

[2] A. Gehrmann-De Ridder and E.W.N. Glover, Nucl. Phys. B **517** (1998) 269;
J. Campbell and E.W.N. Glover, Nucl. Phys. B **527** (1998) 264;
S. Catani and M. Grazzini, Phys. Lett. B **446** (1999) 143; Nucl. Phys. B **570** (2000) 287.

[3] Z. Bern, L.J. Dixon, D.C. Dunbar and D.A. Kosower, Nucl. Phys. B **425** (1994) 217;
D.A. Kosower, Nucl. Phys. B **552** (1999) 319;
D.A. Kosower and P. Uwer, Nucl. Phys. B **563** (1999) 477;
Z. Bern, V. Del Duca and C.R. Schmidt, Phys. Lett. B **445** (1998) 168;
Z. Bern, V. Del Duca, W.B. Kilgore and C.R. Schmidt, Phys. Rev. D **60** (1999) 116001.

[4] E.B. Zijlstra and W.L. van Neerven, Nucl. Phys. B **383** (1992) 525; Phys. Lett. B **297** (1992) 377.

[5] R. Hamberg, W.L. van Neerven and T. Matsuura, Nucl. Phys. B **359** (1991) 343; **644** (2002) 403 (E).

[6] R.V. Harlander and W.B. Kilgore, Phys. Rev. Lett. **88** (2002) 201801;
S. Catani, D. de Florian and M. Grazzini, JHEP **0105** (2001) 025;
V. Ravindran, J. Smith and W.L. van Neerven, Nucl. Phys. B **665** (2003) 325;
O. Brein, A. Djouadi and R. Harlander, Phys. Lett. B **579** (2004) 149;
R.V. Harlander and W.B. Kilgore, Phys. Rev. D **68** (2003) 013001.

[7] C. Anastasiou and K. Melnikov, Nucl. Phys. B **646** (2002) 220;
C. Anastasiou, L.J. Dixon, K. Melnikov and F. Petriello, Phys. Rev. D **69** (2004) 094008.

[8] S. Moch, J.A.M. Vermaseren and A. Vogt, Nucl. Phys. B **688** (2004) 101;
A. Vogt, S. Moch and J.A.M. Vermaseren, Nucl. Phys. B **691** (2004) 129.

[9] S. Alekhin, K. Melnikov and F. Petriello, Phys. Rev. D **74** (2006) 054033;
A.D. Martin, W.J. Stirling, R.S. Thorne and G. Watt, arXiv:0706.0459 [hep-ph].

[10] K. Hepp, Commun. Math. Phys. **2** (1966) 301.

[11] M. Roth and A. Denner, Nucl. Phys. B **479** (1996) 495.

[12] T. Binoth and G. Heinrich, Nucl. Phys. B **585** (2000) 741; **680** (2004) 375.

[13] G. Heinrich, Nucl. Phys. Proc. Suppl. **116** (2003) 368; **135** (2004) 290; Eur. Phys. J. C **48** (2006) 25;
C. Anastasiou, K. Melnikov and F. Petriello, Phys. Rev. D **69** (2004) 076010;
T. Binoth and G. Heinrich, Nucl. Phys. B **693** (2004) 134.

[14] A. Gehrmann-De Ridder, T. Gehrmann and G. Heinrich, Nucl. Phys. B **682** (2004) 265.

[15] T. Gehrmann, G. Heinrich, T. Huber and C. Studerus, Phys. Lett. B **640** (2006) 252.

[16] A. Lazopoulos, K. Melnikov and F. Petriello, Phys. Rev. D **76** (2007) 014001.

[17] C. Anastasiou, S. Beerli and A. Daleo, JHEP **0705** (2007) 071.

[18] C. Anastasiou, K. Melnikov and F. Petriello, Phys. Rev. Lett. **93** (2004) 032002.

[19] C. Anastasiou, K. Melnikov and F. Petriello, Phys. Rev. Lett. **93** (2004) 262002; Nucl. Phys. B **724** (2005) 197;
C. Anastasiou, G. Dissertori and F. Stöckli, arXiv:0707.2373 [hep-ph].

[20] C. Anastasiou, K. Melnikov and F. Petriello, hep-ph/0505069.

[21] K. Melnikov and F. Petriello, Phys. Rev. Lett. **96** (2006) 231803; Phys. Rev. D **74** (2006) 114017.

[22] F.V. Tkachov, Phys. Lett. **100B** (1981) 65;
K.G. Chetyrkin and F.V. Tkachov, Nucl. Phys. **B192** (1981) 159.

[23] T. Gehrmann and E. Remiddi, Nucl. Phys. B **580** (2000) 485.

[24] S. Laporta, Int. J. Mod. Phys. A **15** (2000) 5087.

[25] C. Anastasiou and A. Lazopoulos, JHEP **0407** (2004) 046.

[26] V.A. Smirnov, *Evaluating Feynman Integrals*, Springer Tracts of Modern Physics (Heidelberg, 2004).

[27] J. Gluza, K. Kajda and T. Riemann, arXiv:0704.2423 [hep-ph].

[28] C. Anastasiou and A. Daleo, JHEP **0610** (2006) 031.

[29] M. Czakon, Comput. Phys. Commun. **175** (2006) 559.

[30] S. Moch, P. Uwer and S. Weinzierl, J. Math. Phys. **43** (2002) 3363;
S. Weinzierl, Comput. Phys. Commun. **145** (2002) 357.

[31] S. Moch and P. Uwer, Comput. Phys. Commun. **174** (2006) 759.

[32] J. Blümlein, Comput. Phys. Commun. **159** (2004) 19.

[33] V. A. Smirnov, Phys. Lett. B **460** (1999) 397; **491** (2000) 130; **500** (2001) 330; **524** (2002) 129; **567** (2003) 193;
V.A. Smirnov and O.L. Veretin, Nucl. Phys. B **566** (2000) 469;
G. Heinrich and V.A. Smirnov, Phys. Lett. B **598** (2004) 55.

[34] J.B. Tausk, Phys. Lett. B **469** (1999) 225.

[35] C. Anastasiou, J.B. Tausk and M.E. Tejeda-Yeomans, Nucl. Phys. B (Proc. Suppl.) **89** (2000) 262.

[36] M. Czakon, J. Gluza and T. Riemann, Phys. Rev. D **71** (2005) 073009; Nucl. Phys. B **751** (2006) 1;
S. Actis, M. Czakon, J. Gluza and T. Riemann, arXiv:0704.2400 [hep-ph].

[37] A.V. Kotikov, Phys. Lett. B **254** (1991) 158.

[38] E. Remiddi, Nuovo Cim. A **110** (1997) 1435;
M. Caffo, H. Czyz, S. Laporta and E. Remiddi, Nuovo Cim. A **111** (1998) 365.

[39] T. Huber and D. Maître, Comput. Phys. Commun. **175** (2006) 122.

[40] M. Argeri and P. Mastrolia, arXiv:0707.4037 [hep-ph].

[41] C. Anastasiou, T. Gehrmann, C. Oleari, E. Remiddi and J.B. Tausk, Nucl. Phys. B **580** (2000) 577.

[42] T. Gehrmann and E. Remiddi, Nucl. Phys. B (Proc. Suppl.) **89** (2000) 251.

[43] T. Gehrmann and E. Remiddi, Nucl. Phys. B **601** (2001) 248; **601** (2001) 287.

[44] R. Bonciani, P. Mastrolia and E. Remiddi, Nucl. Phys. B **661** (2003) 289; **702** (2004) 359 (E); Nucl. Phys. B **690** (2004) 138.

[45] C. Anastasiou, S. Beerli, S. Bucherer, A. Daleo and Z. Kunszt, JHEP **0701** (2007) 082;
U. Aglietti, R. Bonciani, G. Degrassi and A. Vicini, JHEP **0701** (2007) 021.

[46] R. Bonciani, A. Ferroglia, P. Mastrolia, E. Remiddi and J.J. van der Bij, Nucl. Phys. B **701** (2004) 121.

[47] C. Anastasiou, E.W.N. Glover, C. Oleari and M.E. Tejeda-Yeomans, Nucl. Phys. B **601** (2001) 318; **601** (2001) 347; **605** (2001) 486;
E.W.N. Glover, C. Oleari and M.E. Tejeda-Yeomans, Nucl. Phys. **605** (2001) 467;
C. Anastasiou, E.W.N. Glover and M.E. Tejeda-Yeomans, Nucl. Phys. B **629** (2002) 255;
E.W.N. Glover and M.E. Tejeda-Yeomans, JHEP **0306** (2003) 033;
E.W.N. Glover, JHEP **0404** (2004) 021;
Z. Bern, A. De Freitas and L.J. Dixon, JHEP **0203** (2002) 018; JHEP **0306** (2003) 028;
A. De Freitas and Z. Bern, JHEP **0409** (2004) 039.

[48] Z. Bern, A. De Freitas and L.J. Dixon, JHEP **0109** (2001) 037.

[49] Z. Bern, A. De Freitas, L.J. Dixon, A. Ghinculov and H.L. Wong, JHEP **0111** (2001) 031;
T. Binoth, E.W.N. Glover, P. Marquard and J.J. van der Bij, JHEP **0205** (2002) 060.

[50] L.W. Garland, T. Gehrmann, E.W.N. Glover, A. Koukoutsakis and E. Remiddi, Nucl. Phys. B **627** (2002) 107; **642** (2002) 227.

[51] S. Moch, P. Uwer and S. Weinzierl, Phys. Rev. D **66** (2002) 114001.

[52] T. Gehrmann and E. Remiddi, Nucl. Phys. B **640** (2002) 379.

[53] W. Bernreuther, R. Bonciani, T. Gehrmann, R. Heinesch, T. Leineweber, P. Mastrolia and E. Remiddi, Nucl. Phys. B **706** (2005) 245; **712** (2005) 229; Phys. Rev. Lett. **95** (2005) 261802; Nucl. Phys. B **750** (2006) 83;
W. Bernreuther, R. Bonciani, T. Gehrmann, R. Heinesch, T. Leineweber and E. Remiddi, Nucl. Phys. B **723** (2005) 91;
W. Bernreuther, R. Bonciani, T. Gehrmann, R. Heinesch, P. Mastrolia and E. Remiddi, Phys. Rev. D **72** (2005) 096002.

[54] R. Bonciani and A. Ferroglia, Phys. Rev. D **72** (2005) 056004.

[55] E. Remiddi and J.A.M. Vermaseren, Int. J. Mod. Phys. A **15** (2000) 725;
T. Gehrmann and E. Remiddi, Comput. Phys. Commun. **141** (2001) 296;
D. Maître, Comput. Phys. Commun. **174** (2006) 222; hep-ph/0703052.

[56] N. Nielsen, Nova Acta Leopoldiana (Halle) **90** (1909) 123;
K.S. Kölbig, J.A. Mignaco and E. Remiddi, BIT **10** (1970) 38.

[57] T. Gehrmann and E. Remiddi, Comput. Phys. Commun. **144** (2002) 200.

[58] J. Vollinga and S. Weinzierl, Comput. Phys. Commun. **167** (2005) 177.

[59] S. Catani, Phys. Lett. B **427** (1998) 161;
G. Sterman and M.E. Tejeda-Yeomans, Phys. Lett. B **552** (2003) 48.

[60] A. Mitov and S. Moch, JHEP **0705** (2007) 001.

[61] M. Czakon, A. Mitov and S. Moch, Phys. Lett. B **651** (2007) 147; arXiv:0707.4139 [hep-ph].

[62] A.A. Penin, Phys. Rev. Lett. **95** (2005) 010408; Nucl. Phys. B **734** (2006) 185.

[63] T. Becher and K. Melnikov, JHEP **0706** (2007) 084.

[64] Z. Kunszt and D.E. Soper, Phys. Rev. D **46** (1992) 192.

[65] S. Catani and M.H. Seymour, Nucl. Phys. B **485** (1997) 291; **510** (1997) 503(E).

[66] S. Frixione, Z. Kunszt and A. Signer, Nucl. Phys. B **467**, 399 (1996);
G. Somogyi and Z. Trocsanyi, Acta Phys. Chim. Debr. **XL** (2006) 101;
Z. Nagy, G. Somogyi and Z. Trocsanyi, hep-ph/0702273.

[67] D.A. Kosower, Phys. Rev. D **57** (1998) 5410; **71** (2005) 045016.

[68] A. Daleo, T. Gehrmann and D. Maître, JHEP **0704** (2007) 016.

[69] S. Weinzierl, JHEP **0303** (2003) 062;
D.A. Kosower, Phys. Rev. D **67** (2003) 116003;
W.B. Kilgore, Phys. Rev. D **70** (2004) 031501;
M. Grazzini and S. Frixione, JHEP **0506** (2005) 010;
G. Somogyi, Z. Trocsanyi and V. Del Duca, JHEP **0506** (2005) 024; **0701** (2007) 070;
G. Somogyi and Z. Trocsanyi, JHEP **0701** (2007) 052.

[70] S. Catani and M. Grazzini, Phys. Rev. Lett. **98** (2007) 222002.

[71] A. Gehrmann-De Ridder, T. Gehrmann and E.W.N. Glover, JHEP **0509** (2005) 056.

[72] A. Gehrmann-De Ridder, T. Gehrmann and E.W.N. Glover, Nucl. Phys. B **691** (2004) 195; Phys. Lett. B **612** (2005) 36; **612** (2005) 49.

[73] A. Gehrmann-De Ridder, T. Gehrmann, E.W.N. Glover and G. Heinrich, arXiv:0707.1285 [hep-ph] and these proceedings.

[74] S. Weinzierl, Phys. Rev. D **74** (2006) 014020.

[75] A. Gehrmann-De Ridder, T. Gehrmann and E.W.N. Glover, Nucl. Phys. Proc. Suppl. **135** (2004) 97;
A. Gehrmann-De Ridder, T. Gehrmann, E.W.N. Glover and G. Heinrich, Nucl. Phys. Proc. Suppl. **160** (2006) 190.

[76] S. Catani and M.H. Seymour, JHEP **9907** (1999) 023;
S. Weinzierl, Phys. Lett. B **644** (2007) 331.

Higgs Production by Gluon initiated Weak Boson Fusion

M. M. Weber

Department of Physics, University at Buffalo
The State University of New York, Buffalo, NY 14260-1500, USA

The gluon-gluon induced terms for Higgs production through weak-boson fusion are calculated. They form a finite and gauge-invariant subset of the NNLO corrections in the strong coupling constant. This is also the lowest order with sizeable t-channel colour exchange contributions, leading to additional hadronic activity between the outgoing jets.

1 Introduction

The weak-boson-fusion (WBF) process $qq' \to qq'H$ is one of the major Higgs-boson production processes at the LHC. With a cross section of up to 20% of the leading gluon fusion process for low Higgs masses it allows a discovery of the Higgs boson in the intermediate mass range as well as for high masses [2, 3]. Furthermore it allows for precise measurements of the Higgs couplings.

Weak-boson fusion has a characteristic signature that can be used to separate it well from the background processes [4]. Since the LO diagrams do not contain t-channel exchange of coloured particles the final-state quarks appear as jets in opposite hemispheres at high rapidities. In the central region between the jets there is very little hadronic activity, only the Higgs decay products are found here.

At NLO the QCD corrections to total rates [5, 6] and the differential cross section [7, 8] have been calculated. They increase the cross section at the LHC by about 10% while reducing the residual scale dependence to about 3%. Colour exchange contributions are strongly suppressed at NLO since diagrams with t-channel gluon exchange contribute only through their interference with u-channel Born diagrams. Since the interference between t- and u-channel diagrams is very small it is usually neglected. In this approximation there are no colour exchange contributions even at NLO and the corrections can be expressed in terms of the structure functions of deep inelastic scattering. Recently also the NLO electroweak corrections and the QCD corrections to the interference terms and have been calculated [9].

Contributions with sizeable t-channel colour exchange can first appear at NNLO. Although at this order gluon or quark pairs can be exchanged between the quark lines, the non-colour-singlet part contributes only in the interference with u-channel diagrams and can therefore be expected to be tiny. Another part of the NNLO corrections is the square of the $\mathcal{O}(\alpha_s)$ amplitudes. In this contribution non-suppressed diagrams with net colour exchange may appear leading to a possible deviation from the characteristic signature of WBF. Furthermore the NNLO corrections might be larger than could be expected from a naive extrapolation of the NNLO DIS results.

In order to assess the size of these effects we have studied the process $gg \to q\bar{q}H$ and the crossed processes $q\bar{q} \to ggH$, $qg \to qgH$ and $\bar{q}g \to \bar{q}gH$ [10]. The amplitude is of $\mathcal{O}(\alpha_s)$ and its square therefore contributes to WBF at NNLO. Since these are loop induced processes appearing first in this order, they are a UV-finite and gauge-invariant subset of the full
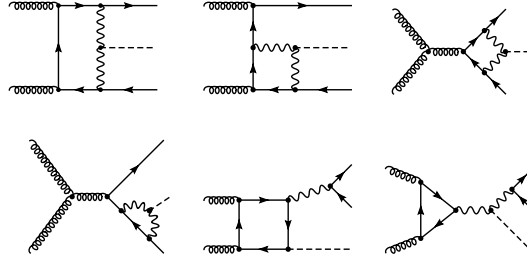
Figure 1: Sample diagrams for the process $gg \to q\bar{q}H$.

NNLO corrections. Due to the large gluon luminosity at the LHC they can also be expected to constitute a sizeable part of the complete NNLO corrections.

The same process also appears in the real-emission corrections to Higgs production in gluon fusion at NNLO. The production of the resulting H+2jet final states has been studied in [11]. However, since these diagrams are of a different order in the coupling constant we will not consider them in this work.

2   Calculational Framework

An overwiev of the calculation using the process $gg \to q\bar{q}H$ as an example is given in the following. A full description of the complete calculation can be found in Ref. [10]. Some sample 1-loop diagrams are shown in Figure 1. We treat the quarks including the b-quark as massless, and always sum over all 5 light flavours. With this approximation the Higgs boson couples only to the weak gauge bosons and to closed top-quark loops.

The last two diagrams belong to a class containing a virtual Z-boson splitting into a final state $q\bar{q}$ pair. These diagrams form a gauge-invariant subset. The Z-boson may become resonant and this class then describes HZ production with a subsequent $Z \to q\bar{q}$ decay. Consequently these diagrams belong to the NNLO corrections to the Higgsstrahlung process $q\bar{q} \to HZ$ and have to be taken into account there. Since we are only interested in WBF this diagram class is discarded in the following.

Furthermore some diagrams are part of real corrections to lower order Higgs-production processes. Since these are singular in the soft and collinear parts of the phase space we require the two final-state quarks to form two well-resolved jets. With this restriction all diagrams are IR finite over the whole remaining phase space and one obtains a well-defined total rate.

Technically the most challenging part of the calculation are the 5-point diagrams like the first one in Figure 1. These diagrams are similar to the ones appearing in the recent calculation of the electroweak corrections to the process $e^+e^- \to \nu\bar{\nu}H$ [12] and the same techniques can also be applied in this case.

The actual calculation of the diagrams has been performed using the 't Hooft–Feynman gauge. The graphs were generated by *FeynArts* [13] and the evaluation of the amplitudes performed using *FormCalc* [14]. The analytical results of *FormCalc* in terms of Weyl-spinor chains and coefficients containing the tensor loop integrals have been translated to *C++* code for the numerical evaluation. The tensor and scalar 5-point functions are reduced to 4-point functions following Ref. [15], where a method for a direct reduction is described that avoids

leading inverse Gram determinants which can cause numerical instabilities. The remaining tensor coefficients of the one-loop integrals are recursively reduced to scalar integrals with the Passarino–Veltman algorithm [16] for non-exceptional phase-space points. In the exceptional phase-space regions the reduction of the 3- and 4-point tensor integrals is performed using the methods of Ref. [17] which allow for a numerically stable evaluation.

The phase-space integration is performed with Monte Carlo techniques using the adaptive multi-dimensional integration program VEGAS [18].

3 Numerical Results

To study the impact of the contribution calculated here we compare the total cross section to the LO result for WBF. In order to get a well defined total rate we always employ a minimal set of cuts. These minimal cuts ensure two well-separated jets in the final state and are given by

$$p_{T_j} > 20 \, \text{GeV}, \quad |\eta_j| < 5, \quad R > 0.6,$$

where p_{T_j} and η_j are the transverse momenta and the pseudorapidities of the final state jets emerging from the quarks and gluons and

$$R = \sqrt{(\Delta\eta)^2 + (\Delta\phi)^2}$$

with $\Delta\eta = \eta_1 - \eta_2$ and $\Delta\phi = \phi_1 - \phi_2$ is the separation of the jets in the pseudorapidity–azimuthal angle plane.

A much improved signal-to-background ratio for weak-boson fusion can be obtained by further cuts [4]. These additional WBF cuts require that the two jets are well separated, reside in opposite detector hemispheres and have a large dijet invariant mass

$$|\Delta\eta| > 4.2, \quad \eta_1 \cdot \eta_2 < 0, \quad m_{jj} > 600 \, \text{GeV}.$$

The total cross section summed over all crossed processes is shown on the l.h.s of Figure 2 as a function of the Higgs-boson mass. With only the minimal cuts employed the total rate is about 70 fb for low Higgs masses and falls off steeply towards higher masses. At $m_H = 100 \, \text{GeV}$ this amounts to about 2% of the LO cross section for WBF which is in accordance with the naive expectation for the order of magnitude of the NNLO corrections. The decrease of the cross section toward higher m_H is however much steeper for the $gg \to q\bar{q}H$ process than the rather moderate decrease of the LO result.

The effect of the additional WBF cuts is a strong suppression of the cross section by roughly a factor 30. This strong suppression is in contrast to the LO and NLO WBF rates which only show a suppression by about a factor of $2 - 3$. As the WBF cuts are designed to take advantage of the characteristic signature of weak-boson fusion, this indicates that the kinematics of the contribution investigated here is rather different than the normal WBF kinematics.

The cross sections for the separate processes using WBF cuts are shown on the r.h.s of Figure 2. The largest contribution comes from the process $qg \to qgH$ while all other processes are at least a factor of 3 smaller.

In order to shed more light on the origin of the strong suppression caused by the WBF cuts the behaviour of the quantities appearing in the cuts has to be investigated. Therefore the distributions in the pseudorapidity separation $\Delta\eta$ and the jet-jet invariant mass m_{jj} are
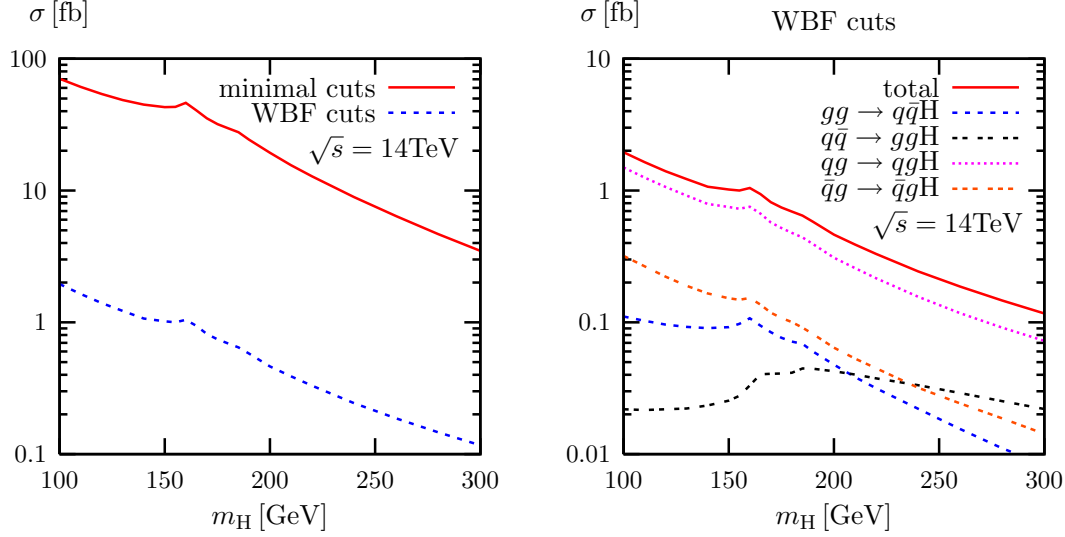
Figure 2: Total cross section summed over all processes with minimal cuts and WBF cuts applied (l.h.s) and separate contributions of all processes using WBF cuts (r.h.s).

shown in Figure 3 for a Higgs mass of $m_H = 120\,\text{GeV}$. The pseudorapidity-separation is peaked at low values of about 1 which is much lower than the corresponding peak for the LO result located at $\Delta\eta \simeq 4$ [7, 8]. The invariant mass distribution falls off fast with increasing m_{jj}. This falloff is stronger than for WBF at leading order. This shows that the jets are less well separated than for the LO WBF and therefore suffer a stronger suppression by the additional WBF cuts.

4 Summary

We have performed a calculation of the loop-induced process $gg \to q\bar{q}H$ and the crossed processes. These are a gauge-invariant and finite part of the NNLO corrections to weak-boson fusion featuring t-channel colour exchange, which is strongly suppressed at lower orders. The total cross section is about 70 fb at $m_H = 100\,\text{GeV}$ and falls off towards higher Higgs masses. Imposing further cuts commonly used to separate the weak-boson-fusion signal from background leads to a strong suppression of the total rates by about a factor of 30. An investigation of distributions has shown this to be caused by different kinematics than for the leading-order weak-boson-fusion process.
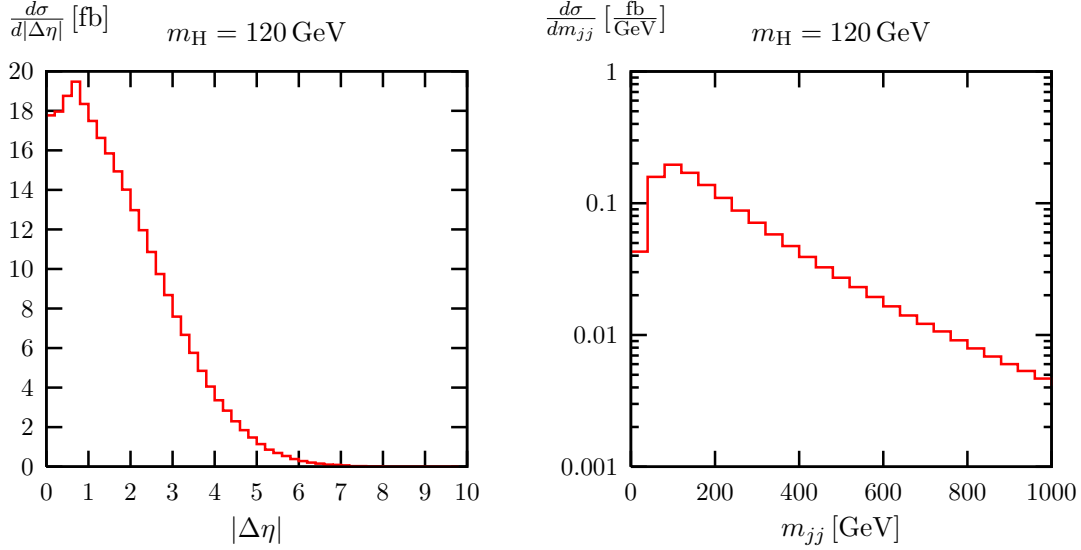
Acknowledgements

Figure 3: Distribution in the pseudorapidity separation of the quark jets (l.h.s) and the jet-jet invariant mass (r.h.s) for a Higgs mass $m_H = 120\,\text{GeV}$.

References

[1] Slides:
http://ilcagenda.linearcollider.org/contributionDisplay.py?contribId=409&sessionId=73&confId=1296

[2] S. Asai *et al.*, Eur. Phys. J. C **32S2** (2004) 19 [arXiv:hep-ph/0402254].

[3] S. Abdullin *et al.*, Eur. Phys. J. C **39S2** (2005) 41.

[4] D. L. Rainwater, R. Szalapski and D. Zeppenfeld, Phys. Rev. D **54** (1996) 6680 [arXiv:hep-ph/9605444]; D. L. Rainwater and D. Zeppenfeld, Phys. Rev. D **60** (1999) 113004 [Erratum-ibid. D **61** (2000) 099901] [arXiv:hep-ph/9906218]; T. Plehn, D. L. Rainwater and D. Zeppenfeld, Phys. Rev. D **61** (2000) 093005 [arXiv:hep-ph/9911385].

[5] T. Han, G. Valencia and S. Willenbrock, Phys. Rev. Lett. **69** (1992) 3274 [arXiv:hep-ph/9206246].

[6] A. Djouadi and M. Spira, Phys. Rev. D **62** (2000) 014004 [arXiv:hep-ph/9912476].

[7] T. Figy, C. Oleari and D. Zeppenfeld, Phys. Rev. D **68** (2003) 073005 [arXiv:hep-ph/0306109].

[8] E. L. Berger and J. Campbell, Phys. Rev. D **70** (2004) 073011 [arXiv:hep-ph/0403194].

[9] M. Ciccolini, A. Denner and S. Dittmaier, arXiv:0707.0381 [hep-ph].

[10] R. Harlander, J. Vollinga and M. M. Weber, in preparation.

[11] V. Del Duca, W. Kilgore, C. Oleari, C. Schmidt and D. Zeppenfeld, Nucl. Phys. B **616** (2001) 367 [arXiv:hep-ph/0108030] and Phys. Rev. Lett. **87** (2001) 122001 [arXiv:hep-ph/0105129].

[12] A. Denner, S. Dittmaier, M. Roth and M. M. Weber, Phys. Lett. B **560** (2003) 196 [hep-ph/0301189] and Nucl. Phys. B **660** (2003) 289 [hep-ph/0302198].

[13] T. Hahn, Comput. Phys. Commun. **140** (2001) 418 [hep-ph/0012260].

[14] T. Hahn and M. Perez-Victoria, Comput. Phys. Commun. **118** (1999) 153 [hep-ph/9807565]; T. Hahn, Nucl. Phys. Proc. Suppl. **89** (2000) 231 [hep-ph/0005029].

[15] A. Denner and S. Dittmaier, Nucl. Phys. B **658** (2003) 175 [hep-ph/0212259].

[16] G. Passarino and M. Veltman, Nucl. Phys. B **160** (1979) 151.

[17] A. Denner and S. Dittmaier, Nucl. Phys. B **734** (2006) 62 [arXiv:hep-ph/0509141].

[18] G. P. Lepage, J. Comput. Phys. **27** (1978) 192 and CLNS-80/447.

Four-Loop QCD Corrections and Master Integrals for the ρ-Parameter

M. Faisst[1], P. Maierhöfer[1] and C. Sturm[2] *

1- Institut für Theoretische Teilchenphysik, Universität Karlsruhe,
D-76128 Karlsruhe - Germany

2- Dipartimento di Fisica Teorica, Università di Torino &
INFN, Sezione di Torino - Italy

The calculation of the four-loop QCD corrections to the electroweak ρ-parameter arising from top- and bottom-quarks of the order $\mathcal{O}(G_F m_t^2 \alpha_s^3)$ is discussed. In particular the computation of the numerous master integrals in the standard and ε-finite basis is addressed.

1 Introduction

The ρ-parameter measures the relative strength of the charged and the neutral current and is equal one at lowest order perturbation theory in the Standard Model. Higher order corrections induce a shift in the lowest order value, which can be related to the transversal parts of the W- and Z-boson self-energies at zero momentum transfer

$$\delta\rho = \frac{\Pi_T^Z(0)}{M_Z^2} - \frac{\Pi_T^W(0)}{M_W^2}, \tag{1}$$

where M_Z and M_W are the $Z-$ and $W-$boson masses, respectively. The one-loop correction has first been evaluated in Ref. [2] and was used in order to establish a limit on the mass splitting within one fermion doublet. For a top-bottom fermion-doublet the dominant shift to the ρ-parameter is given by

$$\delta\rho_1 = 3 \frac{G_F m_t^2}{8\sqrt{2}\,\pi^2} = 3\,x_t, \tag{2}$$

where the bottom quark mass has been neglected, hence it is quadratic in the top-quark mass m_t. The symbol G_F denotes the Fermi coupling constant.
The ρ-parameter enters in numerous physical quantities, e.g. it is related to the indirect prediction of the W-boson mass and to the weak mixing angle.
The perturbative expansion in the strong coupling constant α_s defined in the $\overline{\text{MS}}$-scheme for six flavors is given by:

$$\delta\rho^{\overline{\text{MS}}} = 3x_t \sum_{i=0}^{3} \left(\frac{\alpha_s}{\pi}\right)^i \delta\rho_i^{\overline{\text{MS}}}. \tag{3}$$

Here x_t is expressed in terms of the $\overline{\text{MS}}$ quark mass $m_t \equiv m_t(\mu)$ at the scale $\mu = m_t$ and α_s at the same scale. The two-loop QCD corrections [3–5] to the ρ-parameter have been calculated about 20 years ago and the three-loop QCD corrections [6,7] more than ten years ago. Also important are two-loop [8–12] and three-loop electroweak effects proportional to

---

*Talk given at the International Linear Collider Workshop, Hamburg, 2007 [1].

x_t^2 and x_t^3, which have been determined in Refs. [13, 14] as well as three-loop mixed electroweak/QCD corrections of order $\alpha_s\, x_t^2$, which have been calculated in Ref. [14].

In a first step at four-loop order in perturbative QCD the singlet contributions have been computed in Ref. [15]. They are characterized by the fact that the external current couples to two different closed fermion loops, whereas for the non-singlet contributions the external current couples to the same closed fermion loop. Sample diagrams for both types of contributions are shown in Fig. 1.
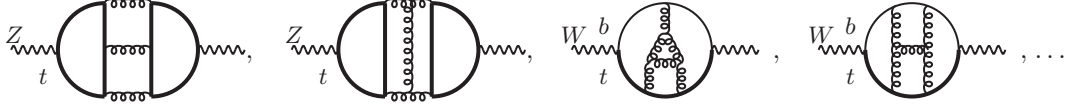

Figure 1: The first two diagrams are sample diagrams for the singlet contribution, whereas the third and fourth diagram are non-singlet type diagrams.

In the following Section 2 the calculation of the four-loop QCD corrections to the ρ-parameter from top- and bottom-quarks, in particular the non-singlet contribution, shall be discussed and we outline our computation of the appearing master integrals. In Section 3 we present the result and close with the summary and conclusions in Section 4.

2   Methods of calculation

The calculation of the transversal parts of the W- and Z-boson self-energies at zero momentum leads to the determination of four-loop tadpoles. In order to reduce all appearing integrals to a smaller set of master integrals the traditional Integration-by-parts(IBP) method has been employed in combination with Laporta's algorithm [16, 17], which has been implemented in a FORM [18–20] based program, which uses Fermat [21] for the simplification of the polynomials in the space-time dimension d. The number of surviving master integrals is however with 63 quite sizable. The master integrals in the standard basis are shown in Fig. 2.

2.1   The master integrals in the standard basis

These master integrals can be classified into three groups. The first group of 13 integrals $\{T_{4,1}, T_{5,1}, T_{5,2}, T_{5,3}, T_{5,4}, T_{6,3}, T_{6,4}, T_{6,1}, T_{6,2}, T_{7,1}, T_{7,2}, T_{8,1}, T_{9,1}\}$ have already been used in previous calculations, e.g. in the determination of moments of the vacuum polarization function [22, 23] or the decoupling relations [24–26]. All of them have been determined with the help of the method of difference equations [16, 17, 27–29] in Ref. [30] and subsequently in Ref. [31], where the method of ε-finite basis has been employed. Some of these master integrals or particular orders in the ε-expansion have also been found in Refs. [15, 29, 32–38] analytically or numerically.

The second set of 12 master integrals $\{T_{5,5}, T_{5,6}, T_{5,7}, T_{6,5}, T_{6,6}, T_{6,7}, T_{6,8}, T_{7,3}, T_{7,4}, T_{9,2}, T_{5,10}, T_{7,16}\}$ is "simple" in the sense, that they are factorized and can be found via a repeated application of the well-known analytical formulas for a one-loop massless propagator and a one-loop massive tadpole. Less simpler diagrams like $T_{7,4}$ can be extracted from [39–41] while the most complicated non-planar one $T_{9,2}$ can be obtained from [42, 43].
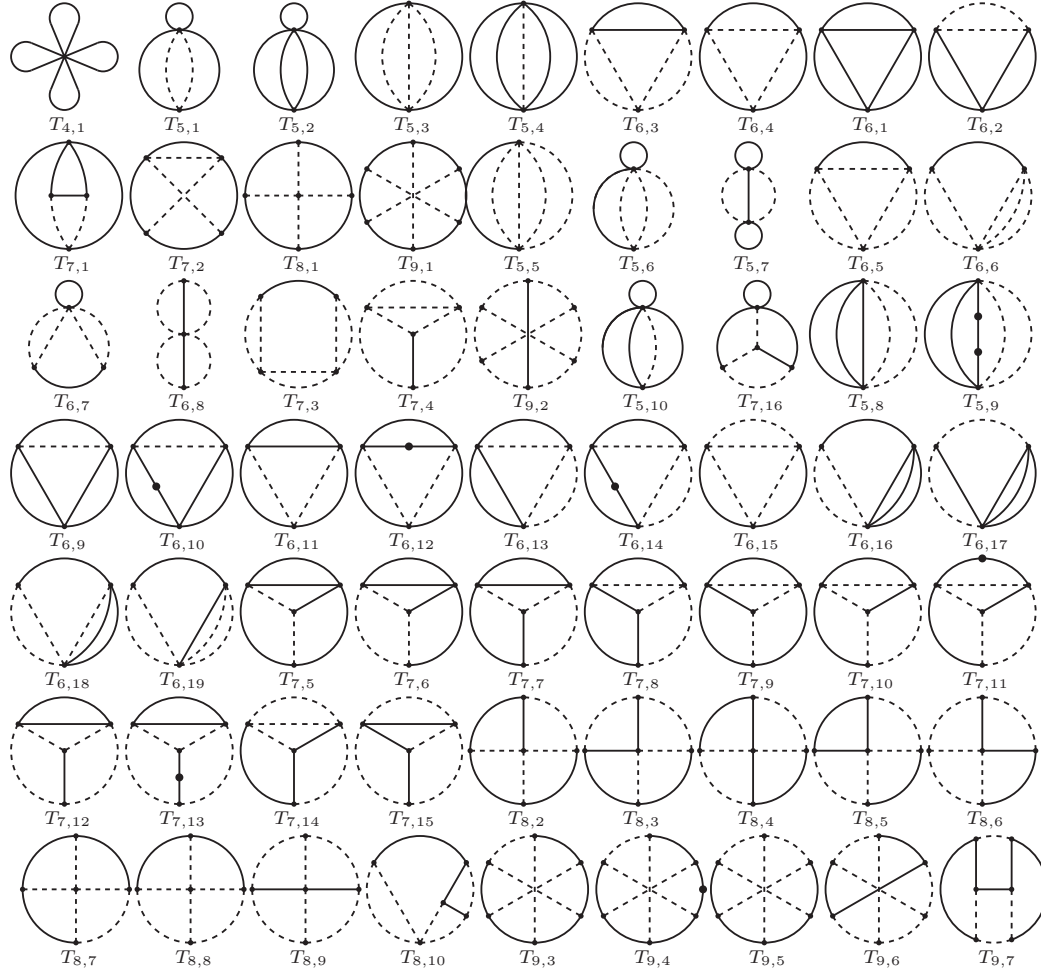
Figure 2: The master integrals in the standard basis, which come out naturally while solving the linear system of IBP equations with the help of Laporta's Algorithm and which have a minimal number of lines, a minimal number of dots and irreducible scalar products. Solid (dashed) lines denote massive (massless) propagators. The first index i of the topologies $T_{i,j}$ denotes the number of lines, whereas the second one j enumerates the topologies with the same number of lines.

The last group of remaining 38 master integrals we solved in Ref. [44] with the help of Padé approximations in the ε-finite basis or by means of the method of difference equations; results for the master integrals in the standard basis have also been determined in Ref. [50].

2.2 The master integrals in the ε-finite basis

One problem, which in general arises while solving the linear system of IBP-equations is, that a division by $(d-4)$ can occur. This can lead to spurious poles in front of a master integral. Each master integral which has a spurious pole as coefficient needs to be evaluated

deeper in its ε-expansion, which is increasingly tedious. As a result of this it can be useful to select a new ε-finite basis of master integrals [31], whose coefficients in the space-time dimension $d = 4 - 2\varepsilon$ are finite in the limit $\varepsilon \to 0$. The ε-finite basis has the advantage, that the members only need to be evaluated up to the finite order in the ε-expansion.

Following the prescription of Ref. [31] an ε-finite basis has been constructed in Ref. [44] for the master integrals of Fig. 2, where the integrals $\{T_{4,1}, T_{5,1}, T_{5,3}, T_{6,3}, T_{5,5}, T_{5,6}, T_{5,7}, T_{6,5}, T_{6,6}, T_{6,7}, T_{6,8}, T_{7,3}, T_{7,4}, T_{9,2}\}$ have been excluded from the construction, since they are known to sufficiently high order in the ε-expansion. In order to remove spurious poles in front of the remaining master integrals the integrals $\{T_{5,2}, T_{5,4}, T_{6,4}, T_{6,1}, T_{6,2}, T_{7,1}, T_{7,2}, T_{5,10}, T_{5,8}, T_{5,9}, T_{6,9}, T_{6,10}, T_{6,12}, T_{6,13}, T_{6,14}, T_{6,15}, T_{6,16}, T_{6,17}, T_{6,18}, T_{6,19}, T_{7,6}, T_{7,11}, T_{7,14}, T_{7,15}, T_{9,4}\}$ needed to be replaced. The master integrals in the ε-finite basis have been computed with a semi-numerical method based on Padé-approximations [31, 45–48]. The pole-part could be extracted completely analytically. The relations between the two bases can be used in order to compute master integrals in the standard basis from the results of the ε-finite one. This allows also to obtain analytical information for the master integrals in the standard basis from the ε-finite one. In addition one can also derive special relations among particular orders of different master integrals, e.g.

$$\frac{45\zeta_4}{2} - \frac{166\zeta_3}{9} + \frac{1685\zeta_2}{48} - \frac{9\sqrt{3}s_2}{2} + \frac{11561}{128} = T_{6,18}^{(0)} - T_{6,13}^{(0)}, \tag{4}$$

which are given in Ref. [44]. They are important, if one wants to compute further orders of the master integrals in the ε-expansion analytically. In Eq. (4) $T_{i,j}^{(0)}$ denotes the constant order in the ε-expansion, ζ_n is the Riemann zeta-function and s_2 is the Clausen-function $\mathrm{Cl}_2(\frac{\pi}{3})$.

3 Result

After having inserted the results for the master integrals into the parameter $\delta\rho$ and having performed renormalization in $\overline{\mathrm{MS}}$-scheme, one obtains the following result [49]:

$$\delta\rho^{\overline{\mathrm{MS}}} = 3x_t\left(1 - \frac{\alpha_s}{\pi}0.19325 + \left(\frac{\alpha_s}{\pi}\right)^2(\underset{\sim\sim\sim\sim}{-4.2072}\underline{+0.23764}) + \left(\frac{\alpha_s}{\pi}\right)^3(\underset{\sim\sim\sim\sim}{-3.2866}\underline{+1.6067})\right). \tag{5}$$

This result has been confirmed in the completely independent work of Ref. [50]. Starting from three-loop order there arise the singlet type diagrams, whose numerical value is shown separately in Eq. (5). The singlet contribution is underlined by the wavy line, whereas the non-singlet contribution is underlined by the solid line. At three-loop order the singlet-diagrams completely dominate the numerical correction, if the $\overline{\mathrm{MS}}$-definition is adopted for the top-quark mass. At four-loop order the dominance is less pronounced. If the result is expressed in terms of the top-quark pole-mass one obtains for the four-loop contribution $\delta\rho_3^{\mathrm{pole}} = -93.1501$, which corresponds to a small shift of around 2 MeV in the W-boson mass. This is well below the expected precision of future experiments and the result based on the three-loop calculation is stabilized.

4 Summary and conclusion

The four-loop QCD corrections from top- and bottom-quarks of order $\mathcal{O}(G_F m_t^2 \alpha_s^3)$ to the ρ-parameter have been computed. All appearing loop-integrals have been reduced to master

integrals. These have been computed with the help of the method of difference equations in the standard basis or by means of Padé-approximations in the ε-finite basis. At least the pole-part of all the master integrals has been determined analytically. The four-loop contribution leads to a small shift in the W-boson mass of around 2 MeV, which is well below the anticipated precision of future experiments.

Acknowledgments

References

[1] Slides:
    http://ilcagenda.linearcollider.org/contributionDisplay.py?contribId=411&sessionId=73&confId=1296.

[2] M. J. G. Veltman, Nucl. Phys. **B123** 89 (1977).

[3] A. Djouadi and C. Verzegnassi, Phys. Lett. **B195** 265 (1987).

[4] A. Djouadi, Nuovo Cim. **A100** 357 (1988).

[5] B. A. Kniehl, J. H. Kühn and R. G. Stuart, Phys. Lett. **B214** 621 (1988).

[6] L. Avdeev, J. Fleischer, S. Mikhailov and O. Tarasov, Phys. Lett. **B336** 560 (1994).

[7] K. G. Chetyrkin, J. H. Kühn and M. Steinhauser, Phys. Lett. **B351** 331 (1995).

[8] J. J. van der Bij and F. Hoogeveen, Nucl. Phys. **B283** 477 (1987).

[9] R. Barbieri, M. Beccaria, P. Ciafaloni, G. Curci and A. Vicere, Phys. Lett. **B288** 95 (1992).

[10] R. Barbieri, M. Beccaria, P. Ciafaloni, G. Curci and A. Vicere, Nucl. Phys. **B409** 105 (1993).

[11] J. Fleischer, O. V. Tarasov and F. Jegerlehner, Phys. Lett. **B319** 249 (1993).

[12] J. Fleischer, O. V. Tarasov and F. Jegerlehner, Phys. Rev. **D51** 3820 (1995).

[13] J. J. van der Bij, K. G. Chetyrkin, M. Faisst, G. Jikia and T. Seidensticker, Phys. Lett. **B498** 156 (2001).

[14] M. Faisst, J. H. Kühn, T. Seidensticker and O. Veretin, Nucl. Phys. **B665** 649 (2003).

[15] Y. Schröder and M. Steinhauser, Phys. Lett. **B622** 124 (2005).

[16] S. Laporta and E. Remiddi, Phys. Lett. **B379** 283 (1996).

[17] S. Laporta, Int. J. Mod. Phys. **A15** 5087 (2000).

[18] J. A. M. Vermaseren, "New features of FORM", math-ph/0010025.

[19] J. A. M. Vermaseren, Nucl. Phys. Proc. Suppl. **116** 343 (2003).

[20] M. Tentyukov and J. A. M. Vermaseren, Comput.Phys.Commun. **176** 385 (2007).

[21] R. H. Lewis, Fermat's User Guide, http://www.bway.net/~lewis/ .

[22] K. G. Chetyrkin, J. H. Kühn and C. Sturm, Eur. Phys. J. **C48** 107 (2006).

[23] R. Boughezal, M. Czakon and T. Schutzmeier, Phys. Rev. **D74** 074006 (2006).

[24] K. G. Chetyrkin, J. H. Kühn and C. Sturm, Nucl. Phys. Proc. Suppl. **164** 203 (2007).

[25] K. G. Chetyrkin, J. H. Kühn and C. Sturm, Nucl. Phys. **B744** 121 (2006).

[26] Y. Schröder and M. Steinhauser, JHEP **01** 051 (2006).

[27] S. Laporta, Phys. Lett. **B504** 188 (2001).

[28] S. Laporta, Phys. Lett. **B523** 95 (2001).

[29] S. Laporta, Phys. Lett. **B549** 115 (2002).

[30] Y. Schröder and A. Vuorinen, JHEP **06** 051 (2005).

[31] K. G. Chetyrkin, M. Faisst, C. Sturm and M. Tentyukov, Nucl. Phys. **B742** 208 (2006).

[32] D. J. Broadhurst, Z. Phys. **C54** 599 (1992).

[33] D. J. Broadhurst, "On the enumeration of irreducible k-fold Euler sums and their roles in knot theory and field theory", hep-th/9604128.

[34] K. G. Chetyrkin, J. H. Kühn, P. Mastrolia and C. Sturm, Eur. Phys. J. **C40** 361 (2005).

[35] B. A. Kniehl and A. V. Kotikov, Phys. Lett. **B638** 531 (2006).

[36] E. Bejdakic and Y. Schröder, Nucl. Phys. Proc. Suppl. **160** 155 (2006).

[37] B. A. Kniehl and A. V. Kotikov, Phys. Lett. **B642** 68 (2006).

[38] B. A. Kniehl, A. V. Kotikov, A. I. Onishchenko and O. L. Veretin, Phys. Rev. Lett. **97** 042001 (2006).

[39] D. J. Broadhurst, Z. Phys. **C32** 249 (1986).

[40] D. I. Kazakov, Theor. Math. Phys. **58** 223 (1984).

[41] I. Bierenbaum and S. Weinzierl, Eur. Phys. J. **C32** 67 (2003).

[42] K. G. Chetyrkin and P. B. Baikov, in preparation; see also the transparency of the talk by K.G. Chetyrkin delivered at the 7-th Workshop on Elementary Particle Theory Loops and Legs in Quantum Field Theory, April, 2004, http://www-zeuthen.desy.de/∼lldesy/talks/chetyrkin.pdf .

[43] S. Bekavac, Comput. Phys. Commun. **175** 180 (2006).

[44] M. Faisst, P. Maierhöfer and C. Sturm, Nucl. Phys. **B766** 246 (2007).

[45] J. Fleischer and O. V. Tarasov, Z. Phys. **C64** 413 (1994).

[46] P. A. Baikov and D. J. Broadhurst, "Three-loop QED vacuum polarization and the four-loop muon anomalous magnetic moment", hep-ph/9504398.

[47] M. Faisst, K. G. Chetyrkin and J. H. Kühn, Nucl. Phys. Proc. Suppl. **135** 307 (2004).

[48] M. Faisst, PhD thesis, Cuvillier Verlag, Goettingen **ISBN 3-86537-506-5**.

[49] K. G. Chetyrkin, M. Faisst, J. H. Kühn, P. Maierhöfer and C. Sturm, Phys. Rev. Lett. **97** 102003 (2006).

[50] R. Boughezal and M. Czakon, Nucl. Phys. **B755** 221 (2006).

Precise quark masses from sum rules

Matthias Steinhauser

Institut für Theoretische Teilchenphysik, Universität Karlsruhe (TH)
76128 Karlsruhe, Germany

In this contribution an improved analysis is described to extract precise charm and bottom quark masses from experimental and theoretical moments of the photon polarization function. The obtained $\overline{\text{MS}}$ mass values read $m_c(3 \text{ GeV}) = 0.986(13)$ GeV and $m_b(10 \text{ GeV}) = 3.609(25)$ GeV.

1 Introduction

The theory of strong interaction has the strong coupling constant and the quark masses as fundamental input parameters. The latter constitute an essential input for the evaluation of weak decay rates of heavy mesons and for quarkonium spectroscopy. Furthermore, decay rates and branching ratios of a light Higgs boson — as suggested by electroweak precision measurements — depend critically on the masses of the charm and bottom quarks. Last not least, confronting the predictions for these masses with experiment is an important task for all variants of Grand Unified Theories. To deduce the values in a consistent way from different experimental investigations and with utmost precision is thus a must for current phenomenology.

The method described in this contribution goes back to 1977 [1] and was applied to next-to-next-to-leading order (NNLO) in Ref. [2]. The NNNLO analysis, including updated experimental input, was presented in Ref. [3].

2 Moments

The basic object which enters our analysis is the photon polarization function defined through

$$\left(-q^2 g_{\mu\nu} + q_\mu q_\nu\right) \Pi(q^2) \quad = \quad i \int \mathrm{d}x\, e^{iqx} \langle 0|T j_\mu(x) j_\nu^\dagger(0)|0\rangle \,, \tag{1}$$

with j_μ being the electromagnetic current. The normalized total cross section for hadron production in e^+e^- annihilation is then given by

$$R(s) \quad = \quad \frac{\sigma(e^+e^- \to \text{hadrons})}{\sigma_{\text{pt}}} \quad = \quad 12\pi \operatorname{Im}\left[\Pi(q^2 = s + i\epsilon)\right] \,, \tag{2}$$

where $\sigma_{\text{pt}} = 4\pi\alpha^2/(3s)$. In the following we add a subscript Q to indicate the contribution from the heavy quark Q.

The idea for extracting a quark mass value m_Q is based on moments constructed from Π_Q. On one hand one can compute the Taylor expansion of $\Pi_Q(q^2)$ around $q^2 = 0$ and obtain the so-called "theory-moments" from

$$\mathcal{M}_n \quad = \quad \frac{12\pi^2}{n!} \left(\frac{\mathrm{d}}{\mathrm{d}q^2}\right)^n \Pi_Q(q^2)\bigg|_{q^2=0} . \tag{3}$$

The three-loop contribution to $\Pi_Q(q^2)$ up to $n = 8$ within QCD has been computed in Refs. [4, 5] and the four-loop calculation for $n = 0$ and $n = 1$ has been performed in Refs. [6, 7]. In the analysis of Ref. [3] also two-loop QED corrections and non-perturbative contributions have been considered. The latter shows a visible effect only in the case of the charm quark.

From dimensional considerations we have $m_Q \sim (\mathcal{M}_n)^{\frac{1}{2n}}$ which implies a stronger dependence of m_Q on variations of $\mathcal{M}_n$ for smaller values of n. Furthermore, higher values of n require a careful theoretical treatment of the threshold region and the construction of an effective theory. The analysis performed in Ref. [3] is restricted to $n = 1, 2, 3$ and 4. Note that precise mass values can only be obtained for the three lowest moments since the non-perturbative contributions become too big already for $n = 4$.

One of the major advantages of the method discussed in this paper is that we can adopt the $\overline{\text{MS}}$ scheme for the quark mass entering Eq. (3) and thus directly extract the corresponding value for the mass.

In order to extract experimental moments one exploits the analyticity of Π_Q and arrives at

$$\mathcal{M}_n = \int \frac{\mathrm{d}s}{s^{n+1}} R_Q(s), \tag{4}$$

where R_Q naturally divides into three parts: At lower energies one has the narrow resonances which are the J/Ψ and Ψ' for charm the $\Upsilon(nS)$ ($n = 1, \ldots, 4$) in the case of the bottom quark. The corresponding contributions to $\mathcal{M}_n$ are obtained with the help of the narrow width approximation for $R(s)$

$$R^{\text{res}}(s) = \frac{9\pi M_R \Gamma_{ee}}{\alpha^2} \left(\frac{\alpha}{\alpha(s)} \right)^2 \delta(s - M_R^2), \tag{5}$$

where the electronic widths Γ_{ee} are known at the 1-2% level.

The second part is called threshold region and extends in the case of the charm quark from 3.73 GeV to about 5 GeV. In this region the cross section shows a rapid variation and can not be described by perturbation theory. Measurements from the BES collaboration from 2001 [8] and 2006 [9] provide excellent data for $R(s)$ with an uncertainty of about 4%. In order to obtain R_c one has to subtract the contribution from the light quarks which is explained in detail in Ref. [3].

The treatment of the bottom threshold region is quite similar. Measurements of R from threshold up to 11.24 GeV have been performed by the CLEO Collaboration more than 20 years ago [10], with a systematic error of 6%. No radiative corrections were applied. The average value derived from the four data points below threshold amounts to $\bar{R} = 4.559 \pm 0.034$(stat.) which is 28% larger than the prediction from perturbative QCD (pQCD). However, a later result of CLEO [11] at practically the same energy, $R(10.52\ \text{GeV}) = 3.56 \pm 0.01 \pm 0.07$, is significantly more precise and in perfect agreement with theory. Applying a rescaling factor of $1/1.28$ to the old CLEO data not only enforces agreement between old and new CLEO data and pQCD in the region below the $\Upsilon(4S)$, it leads, in addition, also to excellent agreement between theory and experiment above threshold around 11.2 GeV where pQCD should be applicable also to bottom production. Further support to our approach is provided by the CLEO measurement of the cross section for bottom quark production at $\sqrt{s} = 10.865$ GeV which is given by $\sigma_b(\sqrt{s} = 10.865\ \text{GeV}) = 0.301 \pm 0.002 \pm 0.039$ nb [12].
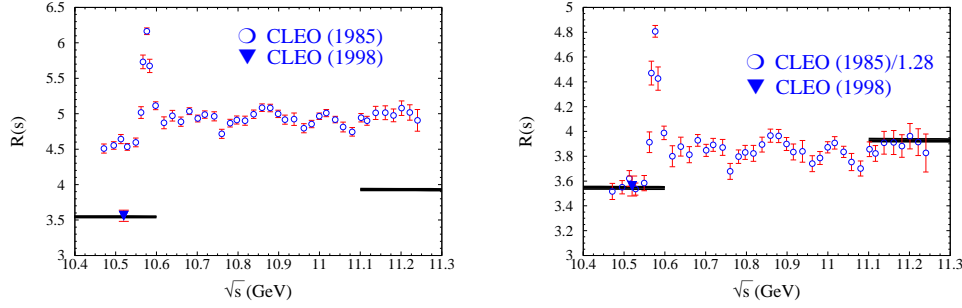
Figure 1: In the left plot the data for $R(s)$ are shown as published in Refs. [10] (circles) and [11] (triangle). The black curves are the predictions from pQCD outside the resonance region. In the right plot the older data from [10] are rescaled by a factor $1/1.28$.

The central value can be converted to $R_b(10.865 \text{ GeV}) = 0.409$. On the other hand, if one extracts $R_b(10.865 \text{ GeV})$ from the rescaled CLEO data from 1984 [10] one obtains $R_b(10.865 \text{ GeV}) = 0.425$ which deviates by less than 4% from the recent result [12].

In Fig. 1 the original and the rescaled data from [10] is shown and compared to pQCD and data point from [11]. We thus extract the threshold contribution to the moments from the interval $10.62 \text{ GeV} \leq \sqrt{s} \leq 11.24 \text{ GeV}$ by applying the rescaling factor to the data, subtract the "background" from u, d, s and c quarks and attribute a systematic error of 10% to the result.

The third contribution to the experimental moment is provided by the so-called continuum region which for the charm and bottom quark starts above 4.8 GeV and 11.24 GeV, respectively. In both cases there is no precise experimental data available. On the other hand, pQCD is supposed to work very well in these energy regions, in particular since $R_Q(s)$ is known to order α_s^2 including the full quark mass dependence and to order α_s^3 including quartic mass effects. For recent compilations we refer to Refs. [13, 14, 15] and would like to mention the `Fortran` program `rhad` [15] which provides a convenient platform to access easily the various radiative corrections.

3 Quark masses

Equating the theoretical and experimental moments of Eqs. (3) and (4), adopting $\mu = 3 \text{ GeV}$ ($\mu = 10 \text{ GeV}$) for the charm (bottom) quark and solving for the quark mass leads to the results which are shown in Fig. 2 in graphical form.[a] It is nicely seen that the results for m_Q further stabilize when going from three to four loops. At the same time the uncertainty is considerably reduced. Furthermore, the preference for the first three moments is clearly visible. Also the analysis for $n = 2$ and $n = 3$ leads to small errors, even if we include the uncertainty from the yet uncalculated four-loop contributions.[b] We emphasize the remarkable consistency between the three results which we consider as additional confirmation of our approach.

---

[a]The numerical results including a detailed error analysis can be found in Ref. [3].
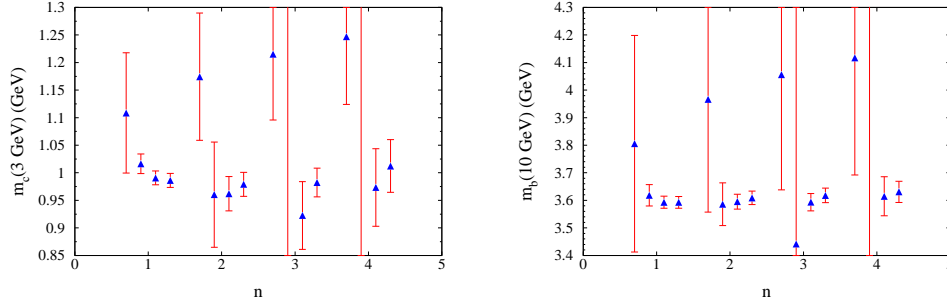[b]See Ref. [3] for details.

Figure 2: $m_c(3 \text{ GeV})$ (left) and $m_b(10 \text{ GeV})$ (right) for $n = 1, 2, 3$ and 4. For each value of n the results from left to right correspond the inclusion of terms of order α_s^0, α_s^1, α_s^2 and α_s^3 to the theory-moments. Note, that for $n = 3$ and $n = 4$ the uncertainties can not be determined in those cases where only the two-loop corrections of order α_s are included into the coefficients $\bar{C}_n$ as the equation cannot be solved for the quark mass.

The final result for the $\overline{\text{MS}}$-masses read $m_c(3 \text{ GeV}) = 0.986(13)$ GeV and $m_b(10 \text{ GeV}) = 3.609(25)$ GeV. They can be translated into $m_c(m_c) = 1.286(13)$ GeV and $m_b(m_b) = 4.164(25)$ GeV. This analysis is consistent with but significantly more precise than a similar previous study.

Acknowledgments

References

[1] V. A. Novikov, L. B. Okun, M. A. Shifman, A. I. Vainshtein, M. B. Voloshin and V. I. Zakharov, Phys. Rept. **41** (1978) 1.

[2] J. H. Kühn and M. Steinhauser, Nucl. Phys. B **619** (2001) 588 [Erratum-ibid. B **640** (2002) 415] [arXiv:hep-ph/0109084].

[3] J. H. Kühn, M. Steinhauser and C. Sturm, Nucl. Phys. B **778** (2007) 192 [arXiv:hep-ph/0702103].

[4] K. G. Chetyrkin, J. H. Kühn and M. Steinhauser, Phys. Lett. B **371** (1996) 93 [arXiv:hep-ph/9511430].

[5] K. G. Chetyrkin, J. H. Kühn and M. Steinhauser, Nucl. Phys. B **505** (1997) 40 [arXiv:hep-ph/9705254].

[6] K. G. Chetyrkin, J. H. Kühn and C. Sturm, Eur. Phys. J. C **48** (2006) 107 [arXiv:hep-ph/0604234].

[7] R. Boughezal, M. Czakon and T. Schutzmeier, Phys. Rev. D **74** (2006) 074006 [arXiv:hep-ph/0605023].

[8] J. Z. Bai *et al.* [BES Collaboration], Phys. Rev. Lett. **88** (2002) 101802 [arXiv:hep-ex/0102003].

[9] M. Ablikim *et al.* [BES Collaboration], arXiv:hep-ex/0612054.

[10] D. Besson *et al.* [CLEO Collaboration], Phys. Rev. Lett. **54** (1985) 381.

[11] R. Ammar *et al.* [CLEO Collaboration], Phys. Rev. D **57** (1998) 1350 [arXiv:hep-ex/9707018].

[12] G. S. Huang *et al.* [CLEO Collaboration], Phys. Rev. D **75** (2007) 012002 [arXiv:hep-ex/0610035].

[13] K. G. Chetyrkin, J. H. Kühn and A. Kwiatkowski, Phys. Rept. **277** (1996) 189.

[14] K. G. Chetyrkin, A. H. Hoang, J. H. Kühn, M. Steinhauser and T. Teubner, Eur. Phys. J. C **2** (1998) 137 [arXiv:hep-ph/9711327].

[15] R. V. Harlander and M. Steinhauser, Comput. Phys. Commun. **153** (2003) 244 [arXiv:hep-ph/0212294].

On-shell renormalisation constants including two different nonzero masses

S. Bekavac, D. Seidel

Institut für Theoretische Teilchenphysik, Universität Karlsruhe (TH)
76128 Karlsruhe, Germany

We present results for the effect of a second massive quark in the relation between the pole and the minimal subtracted quark mass at the three loop level. We also consider the analogous effect for the wave function renormalisation constant. Some technical details of the calculation are given. Our result is phenomenologically relevant for the bottom quark including virtual charm effects.

1 Introduction

Quark masses are fundamental parameters of the Standard Model (SM) and thus it is desirable to determine their numerical values with the highest possible precision. In order to do so it is necessary to fix a renormalisation scheme which defines the quark mass. Often physical observables are expressed through some "short distance" mass [1] to obtain predictions which are free of the renormalon problem. To do so, one frequently needs the relation between the on-shell and the $\overline{\text{MS}}$ mass. Many authors contributed to the latter task [2, 3, 4]. In this contribution we present the recently published calculation [5], where we have included the effect of a second nonzero quark mass to the relation between the quarks in those two schemes at the three loop level. After having reduced the problem to the calculation of master integrals we use two different ways to solve them, namely the differential equation and the Mellin-Barnes method. From the phenomenological point of view this result is important for the bottom-quark including effects from virtual charm-quarks. As a byproduct we also obtain the corresponding contribution to the wave function renormalisation constant.

2 Renormalisation constants

Introducing the decomposition of the quark self-energy

$$\Sigma(q, m_q) \;=\; m_q\, \Sigma_1(q^2, m_q) + (\slashed{q} - m_q)\, \Sigma_2(q^2, m_q)\,, \tag{1}$$

we can express the renormalisation constants, which are defined through

$$m_{q,0} = Z_m^{\text{OS}}\, M_q\,, \qquad \psi_0 = \sqrt{Z_2^{\text{OS}}}\, \psi\,, \tag{2}$$

by [6, 4]

$$Z_m^{\text{OS}} \;=\; 1 + \Sigma_1(M_q^2, M_q)\,, \tag{3}$$

$$\left(Z_2^{\text{OS}}\right)^{-1} \;=\; 1 + 2M_q^2 \frac{\partial}{\partial q^2}\Sigma_1(q^2, M_q)\Big|_{q^2=M_q^2} + \Sigma_2(M_q^2, M_q)\,. \tag{4}$$

ψ is the quark field renormalised in the on-shell scheme with mass m_q, M_q is the on-shell mass and bare quantities are denoted by a subscript 0. Thus, to obtain Z_m^{OS} one only needs
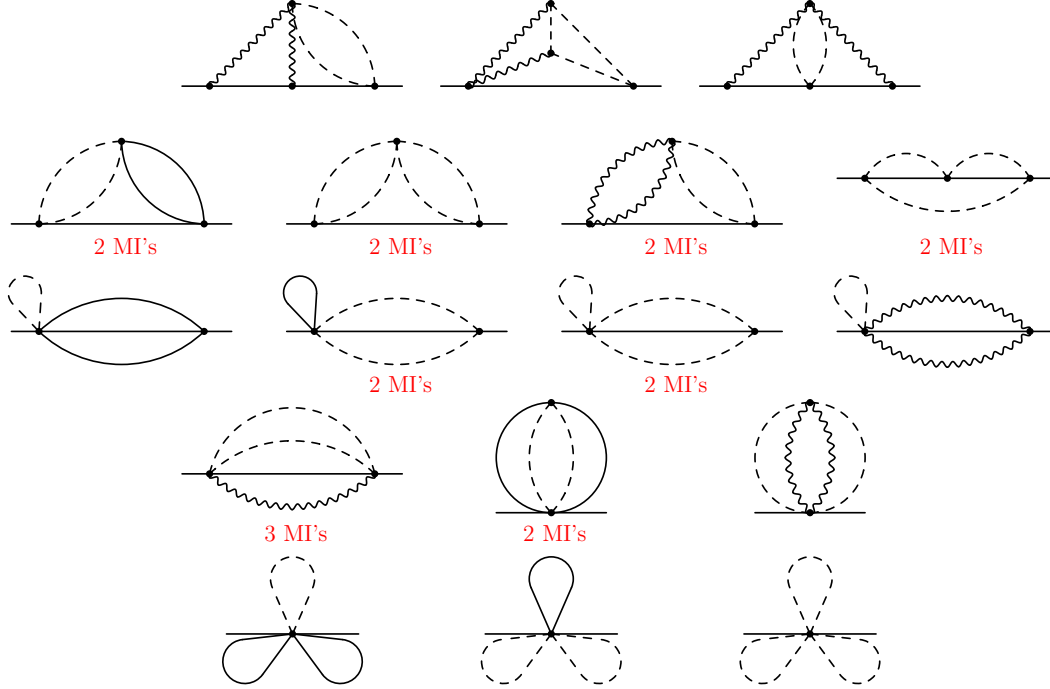
Figure 1: Master integrals. The solid/wavy lines correspond to particles with mass $M_q/0$, the dashed lines denote the quark with the second nonzero mass.

to calculate Σ_1 for $q^2 = M_q^2$. To calculate Z_2^{OS}, one has to compute the first derivative of the self-energy diagrams. The mass renormalisation is taken into account iteratively by calculating one- and two-loop diagrams with zero-momentum insertions.

In the case of the mass renormalisation it is convenient to consider the ratio between the on-shell and $\overline{\text{MS}}$ renormalisation constants

$$ z_m = \frac{Z_m^{\text{OS}}}{Z_m^{\overline{\text{MS}}}} = \frac{m_q(\mu)}{M_q} \tag{5} $$

which is finite. Here we have introduced the renormalisation dependent $\overline{\text{MS}}$-mass $m_q(\mu)$.

In contrast to Z_m^{OS} the wave function renormalisation constant contains next to ultra-violet also infrared divergences. Thus it is not possible to construct a finite quantity by considering the ratio between the on-shell and $\overline{\text{MS}}$ renormalisation constant.

3 Computational techniques

In order to compute the on shell self energy we use `QGRAF` [7] to generate the feynman diagrams and the various topologies are identified with the help of `q2e` and `exp` [8, 9]. In a next step the reduction of the various functions to so-called master integrals (MI's) has to be achieved. For this step we use the so-called Laporta method [10, 11] which reduces the

three-loop integrals to 26 MI's. We use the implementation of Laporta's algorithm in the program `Crusher` [12]. It is written in `C++` and uses `GiNaC` [13] for simple manipulations like taking derivatives of polynomial quantities. In the practical implementation of the Laporta algorithm one of the most time-consuming operations is the simplification of the coefficients appearing in front of the individual integrals. This task is performed with the help of `Fermat` [14] where a special interface has been used (see Ref. [15]). The main features of the implementation are the automated generation of the integration-by-parts (IBP) identities [16], a complete symmetrisation of the diagrams and the possibility to use multiprocessor environments.

In Fig. 1 a graphical representation of the master integrals can be found. As indicated in the figure, many topologies contain more than one master integral. We have chosen two independent ways to compute the ε-expansion of the master integrals. The first one relies on the differential equation method [17]. With this method we were able to evaluate all but four master integrals in analytic form. With the help of our second method, based on the Mellin-Barnes technique (see, e.g., Ref. [18]) we can get numerical results for all master integrals. Here we have used the `Mathematica` package `MB.m` [19].

3.1 Differential-Equation-Method

First we set up differential equations in $z = M_f/M_q$, where M_f is the second nonzero quark mass, for each of the individual integrals. Each equation will contain the master integral itself and integrals belonging to the corresponding topology. The latter can again be reduced to the set of master integrals. For all the topologies which contain only one master integral (e.g. all six-propagator integrals in Fig. 1) this gives a "simple" equation whereas for the other topologies we get two or three coupled equations, respectively. In the next step we expand the differential equations in ε. Choosing an appropriate basis for the master integrals, all equations decouple order by order in ε. We can now solve for all integrals by repeated use of Euler's variation of the constant method. The initial conditions we need are all known from the literature [20, 21, 22, 6].

We were able to get analytical results for all master integrals in terms of Harmonic Polylogarithms (HPL's [23]) up to order ε^{-1}. Unfortunately we were not yet able to get analytical results in higher orders in ε for the four integrals belonging to the two topologies depicted as the leftmost ones in the second row of Fig. 1. For all other integrals we provide analytical results up to the order we need in our calculation. To calculate the MI's in terms of HPL's it is necessary that the (pseudo)poles in the corresponding differential equations are all of the form $1/z$, $1/(z+1)$ and $1/(z-1)$, were these poles can occur up to arbitrary order. This is the case in all topologies except for the ones mentioned above. We have not found a proper change of variables to bring the differential equation into this form. As a consequence we only managed to integrate the integrals in these topologies up to the order ε^{-1}. The remaining parts can e.g. be integrated numerically with Mathematica.

To evaluate our results numerically and for general algebraic manipulations of terms involving HPL's we use the Mathematica package HPL [24, 25].

3.2 Mellin-Barnes-Method

The Mellin-Barnes method as a tool for the evaluation of Feynman integrals has become very popular in the recent years. The basic formula is [18]

$$\frac{1}{(X+Y)^\lambda} = \frac{1}{\Gamma(\lambda)} \frac{1}{2\pi i} \int_{-i\infty}^{i\infty} dz\, \Gamma(1+z)\Gamma(-z)\frac{Y^z}{X^{\lambda+z}}, \tag{6}$$

which transforms a propagator like term into a complex contour integral. A common recipe to evaluate Feynman integrals is the following: First one introduces Feynman parameters for a loop variable. Then one can perform the corresponding momentum integration. After that one applies formula (6) to the denominators containing the Feynman parameters. Finally the Feynman parameters can be integrated yielding the Mellin-Barnes representation of the original integral. This procedure has recently been automatised [26].

The Mellin-Barnes integration is to be performed along a contour which reaches from $-\infty$ to ∞ on the imaginary axis with indentations such that the poles of $\Gamma(\ldots + z)$ and those of $\Gamma(\ldots - z)$ are separated by the contour.

Mellin-Barnes integrals usually have singularities for certain values of their parameters. If there are for example Gamma functions of the form $\Gamma(\varepsilon + z)\,\Gamma(-z)$, it is not possible to find an appropriate integration contour when $\varepsilon \to 0$. The integral is therefore singular in ε and this is how UV poles of Feynman integrals manifest themselves in their Mellin-Barnes representation. One has thus to regularise the integral, that is, identify the ε poles. This can be done by shifting the integration contour using the residue theorem. Prescriptions to do so have been given in Refs. [27] and [28], the latter has been automatised, see Refs. [29, 19].

Finally the regularised integrals can be expanded in ε and evaluated by numerical integration, which is also implemented in the package `MB.m` [19], or by application of the residue theorem and summing up the residues. Depending on the dimension of the integrals and the complexity of the integrand this can be done numerically or analytically.

To calculate the master integrals for this work we first simplified the Mellin-Barnes integrals by inserting the representations of known subtopologies. The regularisation has been done partly using `MB.m` and the approach of Ref. [27]. One- and two-dimensional MB-integrals were calculated via their sum representation, higher dimensional integrals using `MB.m`.

The 4-line integrals can all be represented as Mellin-Barnes-integrals of maximal dimension 1, which can be evaluated as single sums. For the 5 line master integrals we find representations of dimension 2 to 5. The integrals with 6 lines have 3 to 5 dimensional representations. We find good agreement with the results obtained from the differential equation method.

Inserting the results for the master integrals into the final result we observe large numerical cancellations near $M_f = 0$ between the contributions originating from different master integrals. On the other hand, the expansion for $M_f/M_q \ll 1$ converges very fast, which is relevant for $M_f = m_c$ and $M_q = m_b$. For this reason we decided to derive an expansion of our result including eighth order terms. The coefficients that could not be obtained analytically can be evaluated numerically from their Mellin-Barnes-representation, which is in our case at most two-dimensional.

4 Results and applications

As an application of our result we want to discuss the charm quark effects in the relations between the pole, the $\overline{\text{MS}}$ and the $1S$ quark mass. For illustration we use $m_b(m_b) = 4.2$ GeV, $m_c(m_c) = 1.3$ GeV, $\mu = m_b$ and $\alpha_s^{(4)}(m_b) = 0.2247$. The relation between the on-shell and the $\overline{\text{MS}}$ mass leads to

$$M_b = \left[4.2 + 0.401 + \left(0.199 + 0.0094 \Big|_{m_c} \right) + \left(0.145 + 0.0182 \Big|_{m_c} \right) \right] \text{GeV}, \quad (7)$$

where the tree-level, one-, two- and three-loop results are shown separately. The contributions from the charm quark mass which vanish for $m_c \to 0$ are marked by a subscript m_c. One observes that the higher order contributions are significant. In particular, the two-loop charm quark effects amount to 9 MeV and the three-loop ones to 18 MeV. A similar bad convergence is observed in the relation between the $1S$ mass [30] M_b^{1S} and the pole mass M_b. For $M_b = 4.8$ GeV, $m_c(m_c) = 1.3$ GeV, $\mu = M_b$ and $\alpha_s^{(4)}(M_b) = 0.2150$ it is given by

$$M_b^{1S} = \left[4.8 - 0.049 - \left(0.073 + 0.0041 \Big|_{m_c} \right) - \left(0.098 + 0.0112 \Big|_{m_c} \right) \right] \text{GeV}. \quad (8)$$

However, the relation between the $1S$ and the $\overline{\text{MS}}$ quark mass is much better behaved as can be seen in the following example where we have chosen $M_b^{1S} = 4.69$ GeV, $m_c(m_c) = 1.3$ GeV, $\mu = M_b^{1S}$ and $\alpha_s^{(4)}(M_b^{1S}) = 0.2167$

$$m_b = \left[4.69 - 0.382 - \left(0.098 + 0.0047 \Big|_{m_c} \right) - \left(0.030 + 0.0051 \Big|_{m_c} \right) \right] \text{GeV}. \quad (9)$$

The two-loop charm effects amount to only 4.7 MeV and three-loop ones to 5.1 MeV. We want to mention that in case only the linear approximation [3] of the charm quark mass effects is used the corresponding three-loop results in Eqs. (7) and (9) read 0.0167 and 0.0037, respectively.

Acknowledgements

References

[1] M. Beneke, Phys. Lett. B **434** (1998) 115 [arXiv:hep-ph/9804241]. K. Melnikov and A. Yelkhovsky, Phys. Rev. D **59** (1999) 114009 [arXiv:hep-ph/9805270]. A. H. Hoang, Phys. Rev. D **61** (2000) 034005 [arXiv:hep-ph/9905550].

[2] R. Tarrach, Nucl. Phys. B **183** (1981) 384. N. Gray, D. J. Broadhurst, W. Grafe and K. Schilcher, Z. Phys. C **48** (1990) 673. D. J. Broadhurst, N. Gray and K. Schilcher, Z. Phys. C **52** (1991) 111. K. G. Chetyrkin and M. Steinhauser, Phys. Rev. Lett. **83** (1999) 4001 [arXiv:hep-ph/9907509]. K. G. Chetyrkin and M. Steinhauser, Nucl. Phys. B **573** (2000) 617 [arXiv:hep-ph/9911434]. K. Melnikov and T. van Ritbergen, Phys. Lett. B **482** (2000) 99 [arXiv:hep-ph/9912391]. K. Melnikov and T. van Ritbergen, Nucl. Phys. B **591** (2000) 515 [arXiv:hep-ph/0005131].

[3] A. H. Hoang, arXiv:hep-ph/0008102.

[4] P. Marquard, L. Mihaila, J. H. Piclum and M. Steinhauser, Nucl. Phys. B **773** (2007) 1 [arXiv:hep-ph/0702185].

[5] S. Bekavac, A. Grozin, D. Seidel and M. Steinhauser, arXiv:0708.1729 [hep-ph].

[6] K. Melnikov and T. van Ritbergen, Nucl. Phys. B **591** (2000) 515 [arXiv:hep-ph/0005131].

[7] P. Nogueira, J. Comput. Phys. **105** (1993) 279.

[8] R. Harlander, T. Seidensticker and M. Steinhauser, Phys. Lett. B **426** (1998) 125 [hep-ph/9712228].

[9] T. Seidensticker, hep-ph/9905298.

[10] S. Laporta and E. Remiddi, Phys. Lett. B **379** (1996) 283 [arXiv:hep-ph/9602417].

[11] S. Laporta, Int. J. Mod. Phys. A **15** (2000) 5087 [arXiv:hep-ph/0102033].

[12] P. Marquard and D. Seidel, unpublished.

[13] C. Bauer, A. Frink and R. Kreckel, arXiv:cs.sc/0004015.

[14] R. H. Lewis, Fermat's User Guide, http://www.bway.net/~lewis.

[15] M. Tentyukov and J. A. M. Vermaseren, arXiv:cs.sc/0604052.

[16] K. G. Chetyrkin and F. V. Tkachov, Nucl. Phys. B **192** (1981) 159.

[17] A. V. Kotikov, Phys. Lett. B **254** (1991) 158.

[18] V. A. Smirnov, Springer Tracts Mod. Phys. **211** (2004) 1.

[19] M. Czakon, Comput. Phys. Commun. **175** (2006) 559 [arXiv:hep-ph/0511200].

[20] M. Argeri, P. Mastrolia and E. Remiddi, Nucl. Phys. B **631**, 388 (2002) [arXiv:hep-ph/0202123].

[21] P. Mastrolia and E. Remiddi, Nucl. Phys. B **657** (2003) 397 [arXiv:hep-ph/0211451].

[22] P. Marquard, J. H. Piclum, D. Seidel and M. Steinhauser, Nucl. Phys. B **758** (2006) 144 [arXiv:hep-ph/0607168].

[23] E. Remiddi and J. A. M. Vermaseren, Int. J. Mod. Phys. A **15** (2000) 725 [arXiv:hep-ph/9905237].

[24] D. Maitre, Comput. Phys. Commun. **174** (2006) 222 [arXiv:hep-ph/0507152].

[25] D. Maitre, arXiv:hep-ph/0703052.

[26] J. Gluza, K. Kajda and T. Riemann, arXiv:0704.2423 [hep-ph].

[27] V. A. Smirnov, Phys. Lett. B **460** (1999) 397 [arXiv:hep-ph/9905323].

[28] J. B. Tausk, Phys. Lett. B **469** (1999) 225 [arXiv:hep-ph/9909506].

[29] C. Anastasiou and A. Daleo, JHEP **0610** (2006) 031 [arXiv:hep-ph/0511176].

[30] A. H. Hoang, M. C. Smith, T. Stelzer and S. Willenbrock, Phys. Rev. D **59** (1999) 114014 [arXiv:hep-ph/9804227].

Cosmological Connections

Conveners: M. Battaglia, Z. Zhang, N. Okada

Heavy Dirac Neutrino Dark Matter

G. Bélanger[1], A. Pukhov[2] and G. Servant[3]

1- Laboratoire de Physique Theorique LAPTH, CNRS - U. de Savoie
B.P.110, F-74941 Annecy-le-Vieux, France

2- Skobeltsyn Inst. of Nuclear Physics, Moscow State University
Moscow 119992, Russia

3- CERN Physics Department, Theory Division, CH-1211 Geneva 23, Switzerland
& Service de Physique Théorique, CEA Saclay, F91191 Gif-sur-Yvette, France

Heavy Dirac neutrinos are viable dark matter candidates provided their coupling to the standard model Z is suppressed to satisfy constraints from direct detection experiments.

1   Introduction

Although evidence for dark matter has become very convincing, we still have few clues on what this dark matter could be. On the theoretical side, many candidates have been proposed, in particular weakly interacting massive particles (WIMPS) provide naturally the right amount of relic abundance.

We reexamine the case of a Dirac neutrino with a mass at the electroweak scale but that does not come from the Higgs vev. An example is a vector-like fermion with a Kaluza-Klein mass. In addition, our candidate does not have standard neutrino interactions. Indeed, a heavy fourth-generation purely Dirac neutrino with Standard Model (SM) interactions is excluded as dark matter because it leads to a large cross-ection for scattering on nucleons and a very small value for the relic abundance [2]. Besides, there are strong constraints from EW precision tests if the neutrino mass comes from EW symmetry breaking.

We consider a generic extension of the SM containing a stable heavy neutrino, ν' [3]. We assume that this neutrino is an $SU(2)_L$ singlet but charged under $SU(2)_R$. Electroweak symmetry breaking typically induces a mixing between the Z and the Z', leading to a small effective coupling of ν' to the Z. Examples of this type were studied in warped extra dimensions [4, 5] and in universal extra dimensions [6]. We further assume a discrete symmetry under which all SM fields are neutral and ν' is the lightest new charged particle.

The low energy constraints on additional neutral or charged gauge bosons (Z',W') that might be present in this generic model can be avoided simply by assuming that the new gauge bosons couple only to the fermions of the third generation. Typical mass limits are then $M_{Z'}, M_{W'} > 500$ GeV [3]. We introduce effective couplings of ν' to Z, Z' and H, denoted g_Z, $g_{Z'}$ and g_H respectively:

$$g_Z \overline{\nu'} \gamma^\mu \frac{1+\gamma_5}{2} \nu' Z_\mu \ , \qquad g_{Z'} \overline{\nu'} \gamma^\mu \frac{1+\gamma_5}{2} \nu' Z'_\mu \ , \qquad g_H \overline{\nu'} \nu' H \tag{1}$$

As motivated in higher-dimensional models, only one chirality has non-suppressed couplings to the gauge bosons. However, our results essentially do not depend on the presence or not of the projector. We assume that the remaining new physics which makes the model more complete does not interfere much with our dark matter analysis.

2 Direct detection

The cross section for elastic scattering of a Dirac neutrino on nucleons is dominated by Z exchange and in contrast with Majorana dark matter, the Z exchange contributes to the spin-independent scattering cross section [4]. In order to satisfy limits from direct detection experiments, in particular those of Xenon [7], the ν' coupling to the Z must be suppressed. This means that $g_Z \lesssim 10^{-2} g (g = e/\sin\theta_W)$ for $M_{\nu'} \sim 100$ GeV while for a ν' in the TeV range larger values of g_Z are allowed due to the reduced experimental sensitivity. Suppressed couplings are quite natural in models where the coupling arise from mixing effects and in fact low energy constraints on the Z–Z' mixing can be even more severe than the ones from direct detection [3]. When the ν' has a sizable coupling to the Higgs, the Higgs exchange contributes significantly to the spin independent cross section. The constraints from both Xenon [7] and CDMS [8] in the g/g_Z-$M_{\nu'}$ plane are displayed in Fig. 1 with and without the Higgs contribution (with $m_H = 120$ GeV, $g_H = 0.25$).

3 Relic abundance

The parameter that determines the elastic scattering of Dirac neutrino dark matter on nucleus is the same parameter that drives the annihilation of neutrinos and determines the relic density. The suppressed coupling g_Z that is required from direct detection constraints is nevertheless sufficient to guarantee an annihilation rateresulting in $\Omega_{\nu'} h^2 \approx 0.1$ for three different ranges of neutrino masses. This is illustrated in Fig. 1. First, when $M_{\nu'} \approx M_Z/2$ neutrinos annihilate very efficiently into fermion pairs through Z exchange even if g_Z is small. Second when $M_{\nu'} \approx M_H/2$ the annihilation cross section through Higgs exchange is enhanced significantly provided the ν' couples to the Higgs. Third, for heavier neutrinos, $M_{\nu'} > 700$ GeV, the WW annihilation channel increases significantly, while satisfying unitarity limits. Furthermore, for this range of masses the experimental constraint from direct detection is less severe.

The presence of a Z' will in general enhance the annihilation cross section opening the possibility of satisfying both direct de-
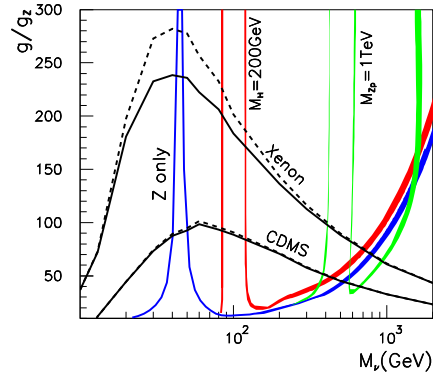

Figure 1: WMAP region, $0.097 < \Omega_{\nu'} h^2 < 0.113$, in the $g/g_Z - M_{\nu'}$ plane including Z-exchange only (blue band), also the Higgs exchange (red band), and the Z' exchange (green band) and region allowed by direct detection (full or dotted). The region above the CDMS/Xenon lines and below the WMAP band is allowed.

tection and relic abundance constraints for $M_{\nu'} \approx M_{Z'}/2$. In particular, a Z' of 1TeV gives quite naturally a viable dark matter candidate in the few hundred GeV range, see Fig. 1. Other new particles introduced in addition to the ν' can also increase the annihilation cross section and make the ν' a viable dark matter candidate in the few hundred GeV range. For example, a W' can contribute via t-channel exchange of a new charged lepton or coan-

nihilation with new heavy leptons or quarks could increase the annihilation cross section without affecting the direct detection rate [3]. The latter mechanism is of course very much dependent on the mass of the new fermions. In summary, the Dirac neutrino is expected to be rather heavy, thus with a limited potential for discovery at colliders, except for small windows around the mass of resonances or when coannihilation effects are important.

4   Collider signatures

Like in other WIMP models, the standard searches rely on pair production of the heavier exotic particles which ultimately decay into the WIMP, leading to signals with energetic leptons and/or jets and missing E_T. Some signatures that are more specific to the neutrino WIMP model include invisible Higgs decay into ν', production of a long-lived charged lepton and production of new colored fermion. The latter is of course model dependent and has been studied for the LHC within the context of a model with warped extra dimensions [9]. Production of long-lived charged leptons, for example a τ' nearly degenerate with ν', is a very distinctive signature of new physics at colliders and has been searched for at LEP and Tevatron. For such a signature to be relevant however requires very special conditions on the parameters of the model, for example a weak $\tau'\nu'W$ coupling and/or a small $\tau' - \nu'$ mass splitting [3]. The invisible Higgs can be probed at LHC via the weak boson fusion process [10]. Sensitivity is best when the Higgs is too light to decay into W pairs. Then, for $g_H > 0.01 - 0.1$ a signal should be observed at LHC [3]. The ILC has however a greater potential to probe the invisible Higgs.

5   Conclusion

A Dirac neutrino is a viable dark matter candidate in the mass range from 40 GeV to a few TeV however special mechanisms such as resonance annihilation or coannihilation are required if the neutrino mass is below 700 GeV. A signal is expected in direct detection experiments in the near future especially in the mass range relevant for searches at the ILC.

6   Acknowledgments

References

[1] Slides:
    http://ilcagenda.linearcollider.org/contributionDisplay.py?contribId=80&sessionId=80&confId=1296
[2] K. Enqvist, K. Kainulainen and J. Maalampi, Nucl. Phys. B **317**, 647 (1989).
[3] G. Belanger, A. Pukhov and G. Servant, arXiv:0706.0526 [hep-ph], and refereces therein.
[4] K. Agashe and G. Servant, Phys. Rev. Lett. **93**, 231805 (2004) [arXiv:hep-ph/0403143].
[5] K. Agashe and G. Servant, JCAP **0502** (2005) 002 [arXiv:hep-ph/0411254].
[6] K. Hsieh, R. N. Mohapatra and S. Nasri, JHEP **0612** (2006) 067 [arXiv:hep-ph/0610155].
[7] J. Angle *et al.* [XENON Collaboration], arXiv:0706.0039 [astro-ph].
[8] D. S. Akerib *et al.* [CDMS Collaboration], Phys. Rev. Lett. **93** (2004) 211301 [arXiv:astro-ph/0405033].
[9] C. Dennis, M. Karagoz Unel, G. Servant and J. Tseng, arXiv:hep-ph/0701158.
[10] D. Cavalli *et al.*, arXiv:hep-ph/0203056.

Model-independent WIMP Searches at the ILC

Christoph Bartels[1,2] and Jenny List[1]

1- DESY - FLC
Notkestr. 85, 22607 Hamburg - Germany

2- Universität Hamburg - Inst. f. Experimentalphysik
Luruper Chaussee 149, 22761 Hamburg - Germany

We investigate the possibility to detect WIMPs at the ILC in a model-independent way using events with single photons. The study is done with a full detector simulation of the LDC detector and MarlinReco. It turns out that WIMPs are observable this way at the ILC if their coupling to electrons is not too small. Beam polarisation can increase the accessible phase space significantly.

1   Introduction

Weakly interacting massive particles (WIMPs) are currently favoured as candidates for Dark Matter, which makes up about 20% percent of the total matter-energy content of the universe. Although the lightest supersymmetric particle, which is the lightest neutralino in many SUSY models, would make a very good WIMP if SUSY with R-Parity conservation is realised in nature, most extensions of the Standard Model of particle physics contain WIMPs. In fact the more general requirement is that some new conserved quantum number makes the lightest of the new particles stable. The International Linear Collider (ILC) offers the possibility to look for WIMPs in a rather model-independent way, which first has been pointed out in [2]. Here, the expected sensitivity to such a WIMP signal, the achievable mass resolution and the influence of beam polarisation are studied using a full detector simulation.

Assuming that the cosmic relic density of WIMPs is determined by pair annihilation of WIMPs, and that an unknown branching fraction κ_e of these annihilations proceeds into an e^+e^- pair($XX \to e^+e^-$), crossing relations can be used to derive an expected cross-section for the reverse process, i.e. $e^+e^- \to XX$. This cross-section contains as free parameters:

- the e^+e^- branching fraction κ_e

- the mass of the WIMP M_X

- the spin of the WIMP S_X

- the angular momentum of the annihilation's dominant partial wave J.

In order that this process be observable in a collider detector, where the WIMPs themselves leave no signature, an additional photon from initial state radiation is required: $e^+e^- \to XX\gamma$.

The main Standard Model background process for this reaction is neutrino pair production, again with an ISR photon: $e^+e^- \to \nu\bar{\nu}\gamma$. At energies significantly above the Z^0 pole, this reaction is dominantly mediated by t-channel W-exchange and can thus be reduced significantly by choosing the appropriate polarisations for the electron and position beams. Therefore we consider three possible scenarios for the helicity structure of the WIMP coupling to electrons:

- the same as the SM charged current weak interaction, i.e. only $\kappa(e_L^- e_R^+)$ is nonzero

- parity and helicity conserving, i.e. $\kappa(e_L^- e_R^+) = \kappa(e_R^- e_L^+)$

- opposite to SM charged current weak interaction, i.e. only $\kappa_e = \kappa(e_R^- e_L^+)$ is nonzero.

Especially in the last case a significant enhancement of the signal over background ratio is expected.

2 Software and Reconstrucion Tools

The neutrino background has been generated with NUNUGPV [3], which is a dedicated generator for neutrino pair production with up to three photons $e^+ e^- \to \nu \bar{\nu} \gamma (\gamma \gamma)$. $1.2 \cdot 10^6$ events with at least one photon with an energy E_γ 8 GeV $< E_\gamma <$ 250 GeV and a polar angle θ_γ $15° < \theta_\gamma < 165°$ were generated at a center-of-mass energy of $\sqrt{s} = 500$, corresponding to an integrated luminosity of 500 fb^{-1}. These events serve not only to describe the irreducible Standard Model background, but are also reweighted w.r.t. energy and polar angle of the photon according to the WIMP cross-section. The benefit of the is method is that in this way a signal sample can be obtained for all mass and spin hypotheses to be tested without applying the detector simulation again, which reduces the processing time tremendously.

This sample has been subjected to the full LDC detector simulation, using the detector model LDC01Sc with a 4 T magnetic field and Mokka 6.1 [4]. The events were then reconstructed with MarlinReco [5], using the WOLF [6] algorithm for particle flow and a simple selection demanding $E_\gamma <$ 10 GeV and $20° < \theta_\gamma < 180°$. For the energy resolution studies described in the following, also an angular match to the generated photon was required.

3 Energy Resolution Studies

The influence of the detector's energy resolution has been studied at two levels: besides the full reconstruction, the so called cheated reconstruction makes use of the simulation information for associating calorimeter clusters with particles. This way the pure detector resolution and calibration can be disentangled from confusion effects, noise and so on. Figure 1 shows the generated (left) as well as the cheated and fully reconstructed (right) energy spectra of the most energetic photon candidate of the events.

While the peak at $E_\gamma = 240$ GeV from radiative returns to the Z^0 resonance is extremely clear at the generator level, it his heavily smeared after reconstruction, even for the cheated case. The full reconstruction yields even less photons at high energies. The reason for this effect can be seen in the left plot of figure 2, which shows the mean number of photon candiates per generated photon as a function of the generated photon's energy.

It is clearly visible that at high photon energies the WOLF algorithm tends to split clusters stemming from one photon into several photon candidates. Therefore we apply a merging procedure to neighboring photon candidates, after which the fully reconstructed photon energy distribution is practically identical to the cheated spectrum shown in the right hand plot of figure 1.

The energy resolution obtained after the recombination procedure is shown in right plot of figure 2 as a function of $1/\sqrt{E}$. With being roughly constant at about 6%, it seems to be significantly worse than the $14.4\%\sqrt{E} + 0.5\%$ aimed for at the ILC. This effect has been meanwhile tracked down to an imperfect calibration, which means that the results presented
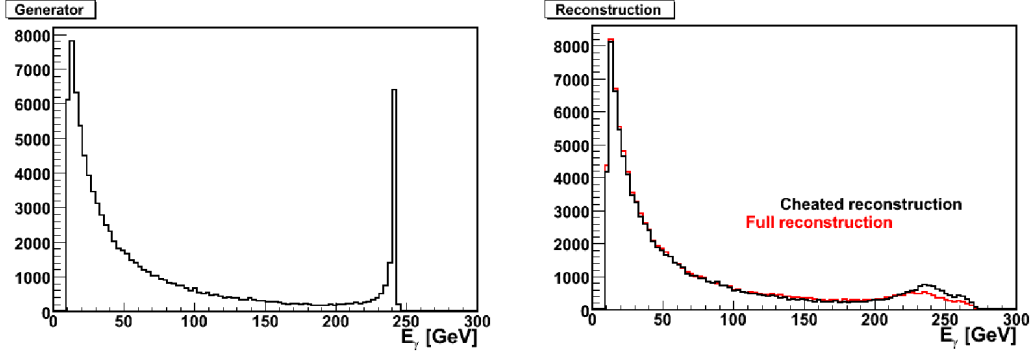
Figure 1: Energy spectra of the event's most energetic photon at generator level (left) as well as cheated and fully reconstructed (right)

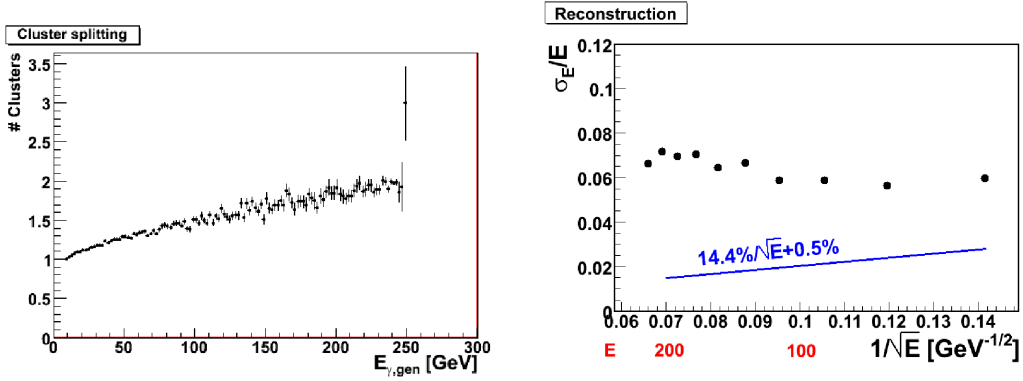in the next section are expected to improve further once a better calibration procedure is applied.

Figure 2: Left: Mean number of reconstructed photon candidates per generated photon vs the generated photon's energy.
Right: Photon energy resolution after the recombination procedure vs $1/\sqrt{E}$.

4   Preliminary Analysis Results

Currently, the following scenarios have been investigated:

- WIMP spin: P-wave annihilation (J=1) for $S_X = 1$ and $S_X = \frac{1}{2}$

- WIMP couplings: $\kappa(e_L^- e_R^+) > 0$, $\kappa(e_R^- e_L^+) > 0$ and $\kappa(e_L^- e_R^+) = \kappa(e_R^- e_L^+) > 0$

- polarisation: unpolarised beams, e^- polarisation only ($P_{e^-} = 0.8$) and additional e^+ polarisation ($P_{e^-} = 0.8$ and $P_{e^+} = 0.6$).

Observation reach

For each combination of these parameters, the reach of the ILC with an integrated luminosity of 500 fb^{-1} at $\sqrt{s} = 500$ GeV for a 3σ observation of WIMPs has been determined as a function of the WIMP mass. Due to the high irreducible background from Standard Model neutrino production, the sensitivity has been obtained statistically by using fractional event counting [7] as implemented in the RooT class TLimit.
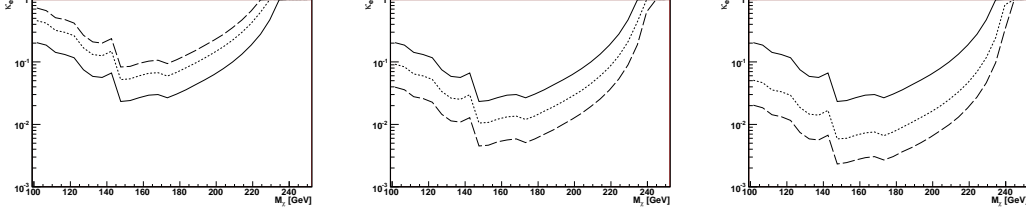

Figure 3: 3σ observation reach of the ILC for a Spin-1 WIMP in terms of WIMP mass and κ_e for three different assumptions on the chirality of the electron-WIMP coupling, see text. Full line: $P_{e^-} = P_{e^+} = 0$, dotted line: $P_{e^-} = 0.8, P_{e^+} = 0$, dashed line : $P_{e^-} = 0.8, P_{e^+} = 0.6$. Regions above the curves are accessible.

Figure 3 shows the expected ILC sensitivity for Spin-1 WIMPs in terms of the minimal observable branching fraction to electrons κ_e as a function of the WIMP mass. The leftmost plot shows the case where the WIMPs couple only to lefthanded electrons and righthanded positrons ($\kappa(e_L^- e_R^+)$), the middle plot shows the parity and helicity conserving case ($\kappa(e_L^- e_R^+) = \kappa(e_R^- e_L^+)$), while the right plot is dedicated to the case that the WIMPs couple to righthanded electrons and lefthanded positrons ($\kappa(e_R^- e_L^+)$). The regions above the curves are accessible, where the full line gives the result for unpolarised beams, the dotted line for $P_{e^-} = 0.8$ and the dashed line for $P_{e^-} = 0.8$ and $P_{e^+} = 0.6$. In the latter two coupling scenarios polarised beams increase the reach significantly, especially the additional positron polarisation increases the accessible range in κ_e by about a factor of 2. Figure 4 shows the same for a Spin-$\frac{1}{2}$ WIMP. Here the sensitivity is somewhat worse, but again beam polarisation extends the observable part of the parameter space significantly.
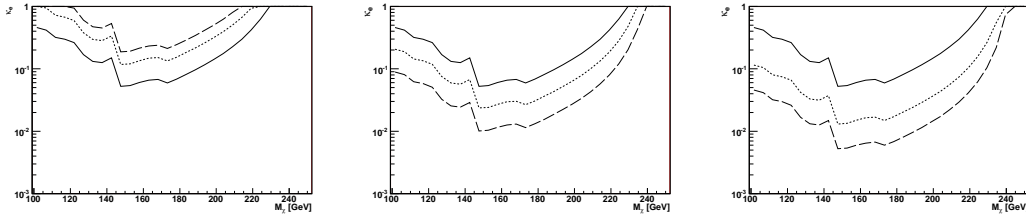

Figure 4: 3σ observation reach of the ILC for a Spin-$\frac{1}{2}$ WIMP in terms of WIMP mass and κ_e for three different assumptions on the chirality of the electron-WIMP coupling, see text. Full line: $P_{e^-} = P_{e^+} = 0$, dotted line: $P_{e^-} = 0.8, P_{e^+} = 0$, dashed line : $P_{e^-} = 0.8, P_{e^+} = 0.6$. Regions above the curves are accessible.

Mass resolution

If WIMPs are observed at the ILC, their mass can be determined from the recoil mass distribution of the photons:

$$M_{\mathrm{recoil}}^2 = s - 2\sqrt{s}E_\gamma \tag{1}$$

Figure 5 shows an example for the recoil mass distribution for a 150 GeV Spin-1 WIMP with both beams polarised. The WIMP signal shown in dark grey kicks in at $M_{\mathrm{recoil}} = 316$ GeV.

From this distribution, the WIMP mass can be reconstructed for example by a template method. For this procedure, only 200 fb^{-1} of the available MC sample have been analysed as dataset, the rest is used for the templates. Figure 6 shows the obtained $\Delta\chi^2$ as function of the reconstructed WIMP mass for a 150 GeV Spin-1 WIMP for $\kappa_e = 0.3$. The left plot shows the helicity and parity conserving case, the right plot the case that the WIMPs couple to righthanded electrons and lefthanded positrons ($\kappa(e_R^-e_L^+)$). Again the full line gives the result for unpolarised beams, the dotted line for $P_{e^-} = 0.8$ and the dashed line for $P_{e^-} = 0.8$ and $P_{e^+} = 0.6$. Without any beam polarisation,

Figure 5: Recoil mass distribution for a 150 GeV Spin-1 WIMP

the mass resolution is about 4 GeV, which is reduced to about 1.2 GeV by switching on the electron polarisation. Positron polarisation improves the resolution by another factor 2 to about 0.6 GeV.
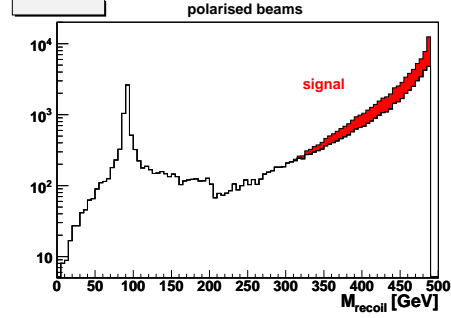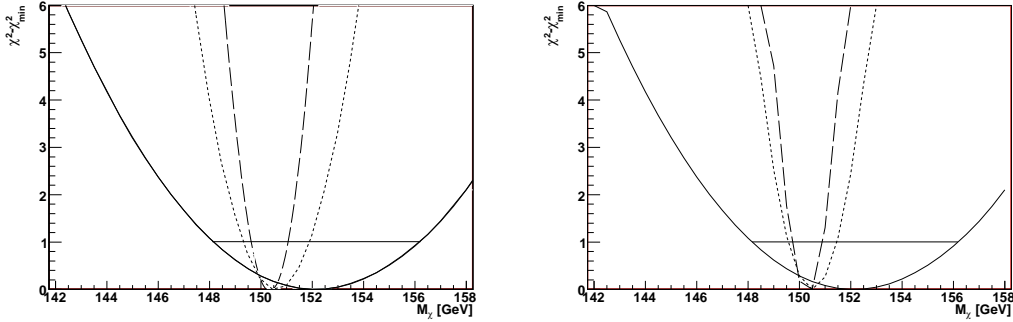

Figure 6: $\Delta\chi^2$ from mass determination by a template method for a Spin-1 WIMP with $M_X = 150$ GeV. Left: parity and helicity conserving couplings, right:$\kappa(e_R^-e_L^+)$. Full line: $P_{e^-} = P_{e^+} = 0$, dotted line: $P_{e^-} = 0.8, P_{e^+} = 0$, dashed line : $P_{e^-} = 0.8, P_{e^+} = 0.6$.

Figure 7 shows the analoguos results for a 180 GeV Spin-$\frac{1}{2}$ WIMP. As for the observation reach, the situation is slightly worse than in the Spin-1 case, but again the use of beam polarisation leads to a significant gain in resolution.
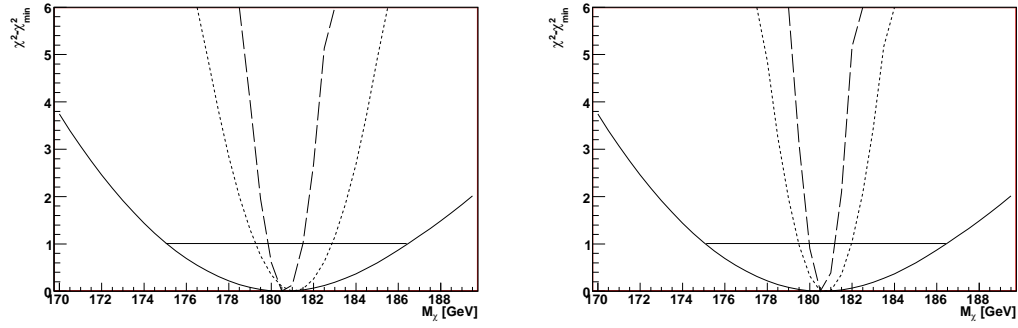
448

Figure 7: $\Delta\chi^2$ from mass determination by a template method for a Spin-$\frac{1}{2}$ WIMP with M_X=150 GeV. Left: parity and helicity conserving couplings, right:$\kappa(e_R^- e_L^+)$. Full line: $P_{e^-} = P_{e^+} = 0$, dotted line: $P_{e^-} = 0.8, P_{e^+} = 0$, dashed line : $P_{e^-} = 0.8, P_{e^+} = 0.6$.

5   Conclusions and Outlook

The study of model-independent WIMP production at the ILC presented here is one of the first examples of analyses performed using the full simulation of the LDC detector. A reconstruction for these fully simulated events exists and usable for analysis, but needs further improvements in parallel to the optimization of the detector concept. Already with the current level of sophistication this study shows that there is a good chance to detect WIMPs in this model-independent way at the ILC and to measure their mass with a precision of about 1 GeV. Both the range in phase space as well as the mass resolution improve significantly when polarised beams are assumed. Typically the use of 80% electron polarisation gives improvements of a factor of two over unpolarised beams, whereas an additional positron polarisation of 60% yields another factor of two.

The results presented here will be improved in the near future by applying a more appropriate detector calibration and by using other particle flow algorithms and photon finders. Furthermore reducible backgrounds as well as beamstrahlung have to be included in the study, before finally different detector concepts can be compared.

Acknowledgments

References

[1] Slides:
     http://ilcagenda.linearcollider.org/contributionDisplay.py?contribId=81&sessionId=80&confId=1296

[2] A. Birkedal, K. Matchev and M. Perelstein, Phys. Rev. D **70** (2004) 077701 [arXiv:hep-ph/0403004].

[3] G. Montagna, O. Nicrosini and F. Piccinini, Comput. Phys. Commun. **98**, 206 (1996).

[4] http://polywww.in2p3.fr/activites/physique/geant4/tesla/www/mokka/mokka.html

[5] http://ilcsoft.desy.de/marlin

[6] A. Raspereza, "Clustering Algorithm for Highly Granular Calorimeter," Talk at LCWS 2005, Snowmass.

[7] T. Junk, Nucl. Instrum. Meth. A **434** (1999) 435 [arXiv:hep-ex/9902006].

New Analysis of SUSY Dark Matter Scenarios at ILC

Zhiqing Zhang

Laboratoire de l'Accélérateur Linéaire
Univ. Paris-Sud and IN2P3-CNRS

Applying realistic veto efficiencies for the low angle electromagnetic calorimeter located in the very forward direction of the future international linear collider, we revisited the Standard Model background contributions studied previously in stau analyses with supersymmetrical dark matter scenarios.

In supersymmetry (SUSY) models with R-parity conservation, the lightest SUSY particle neutralino, $\tilde{\chi}_1^0$, is often considered as the best candidate to satisfy the cosmological constraints on cold Dark Matter (DM) of the universe.

In two previous studies [1, 2], one of the most challenging scenarios analyzed concerns the benchmark point D' [3] in the so-called co-annihilation region. In the mSUGRA model, the mass spectrum depends on two parameters m_0 and $M_{1/2}$, the common masses of scalars and gauginos superpartners at the unification scale. The parameter μ, defining the higgsino mass, is derived, in absolute value, by imposing the electroweak symmetry breaking condition in terms of these two parameters and of $\tan\beta$, the ratio of the vacuum expectations which appear in the two Higgs doublets of SUSY. In scenario D', these parameters take the value $m_0 = 101\,\text{GeV}$, $M_{1/2} = 525\,\text{GeV}$, $\tan\beta = 10$ and $\text{sign}(\mu) < 0$. The resulting $\tilde{\chi}_1^0$ has a mass value of 212 GeV and the next lightest SUSY particle stau, $\tilde{\tau}$, has a mass value of 217 GeV. The mass difference is only 5 GeV. When the mass difference is small, the co-annihilation process $\tilde{\chi}_1^0\tilde{\tau} \to \tau\gamma$ becomes the dominant process for regulating the relic DM density of the universe. It is therefore crucial to measure precisely the mass values of $\tilde{\chi}_1^0$ and $\tilde{\tau}$.

The $\tilde{\chi}_1^0$ mass can be measured [2] using the end-point method with a precision down to 170 MeV (80 MeV) relying on $e^+e^- \to \tilde{\mu}^+\tilde{\mu}^- \to \mu^+\tilde{\chi}_1^0\mu^-\tilde{\chi}_1^0$ ($\tilde{e}^+\tilde{e}^- \to e^+\tilde{\chi}_1^0 e^-\tilde{\chi}_1^0$) for the modified SPS 1a scenario with a mass value of $\tilde{\mu}$ or $\tilde{e}$ of 143 GeV and $\tilde{\chi}_1^0$ of 135 GeV under the following experimental conditions: a center-of-mass energy (Ecm) of 400 GeV, an integrated luminosity ($\mathcal{L}$) of $200\,\text{fb}^{-1}$ and a polarized electron (positron) beam at 0.8 (0.6).

The stau analyses are more challenging not only because the final state particle of the tau decay is very soft with missing energy due to undetected neutrino(s) in addition to $\tilde{\chi}_1^0$ but also because the Standard Model (SM) background processes have rates which are many orders of magnitude larger than that of the signal. The cross section values of the signal and the dominant SM background processes are given in Table 1. The signal row with Ecm= 442 GeV corresponds to the optimal center-of-mass energy method (referred to hereafter as *method one* using the cross section measurement or event counting near threshold) proposed in [1] whereas the other signal rows correspond to cases studied in another method (*method two* relying on the measured energy spectra of the tau decay final state, the first and other rows are respectively studied in [2] and [4]).

The suppression of the dominant SM background processes $e^+e^- \to \tau^+\tau^-e^+e^-$, $c\bar{c}e^+e^-$ depends critically on whether the spectator e^+ and/or e^- can be found in the low angle calorimeter (BeamCal) located at 370 cm from the interaction point in the very forward

---

Ecm (GeV)	Beam polarization (P_{e^-}/P_{e^+})	σ (fb)
Signal		
600	0.8/0.6	50
600	unpolarized	20
500	0.8/0.6	25
500	unpolarized	10
442	unpolarized	0.456
Dominant SM backgrounds		
500	unpolarized	$4.3 \cdot 10^5 (e^+e^- \to \tau^+\tau^- e^+e^-)$
		$8.2 \cdot 10^5 (e^+e^- \to c\bar{c}e^+e^-)$

Table 1: Cross section values of the signal ($e^+e^- \to \tilde{\tau}^+\tilde{\tau}^-$) and the dominant SM background processes for different Ecm and beam polarizations.

direction around the beam pipe. In the previous studies [1, 2], either an ideal veto or an old realistic veto [5] was assumed.

In this analysis, we revisit the SM background suppression using realistic veto efficiencies obtained in a recent study [6]. In this study, the BeamCal design is different for the small (0 or 2 mrad) or large (20 mrad) crossing angle beam configuration. In the small crossing angle case, the BeamCal has an inner (outer) radius of 1.5 cm (16.5 cm).

In order to identify an energetic spectator e^+ or e^- out of several TeV energy deposit from huge number of low energy e^+e^- pairs stemming from beamstrahlung photon conversions, the BeamCal is designed to have fine granularity and large longitudinal segmentation. The resulting veto efficiency is about 100% for high energy electrons close to the beam energy (250 GeV), decreases down to 20% for a 75 GeV electron near the inner side of the calorimeter and is assumed to be fully inefficient for electrons below 75 GeV.

Taking the background process $e^+e^- \to \tau^+\tau^- e^+e^-$ as an example, after applying all analysis cuts of *method one* defined in [1], the remaining background amounts to 0.08 fb (561 fb) when the forward veto is included (excluded). This is illustrated in Fig. 1. This should be compared with the final signal cross section of $0.456 \times 5.7\% = 0.026$ fb taking into account of the efficiency of the analysis. The corresponding numbers for *method two* are 0.26 fb(168 fb without the veto) for the two-photon $\tau^+\tau^-$ back-
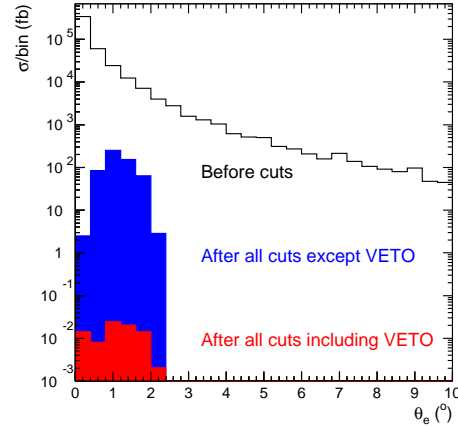

Figure 1: Angular distribution of the spectator electrons from $e^+e^- \to \tau^+\tau^- e^+e^-$ expressed in fb/bin. The blue shaded distribution corresponds to the distribution obtained after all the selections described in [1] with the exception of the forward veto and the red shaded distribution corresponds to the distribution when the veto is further included.
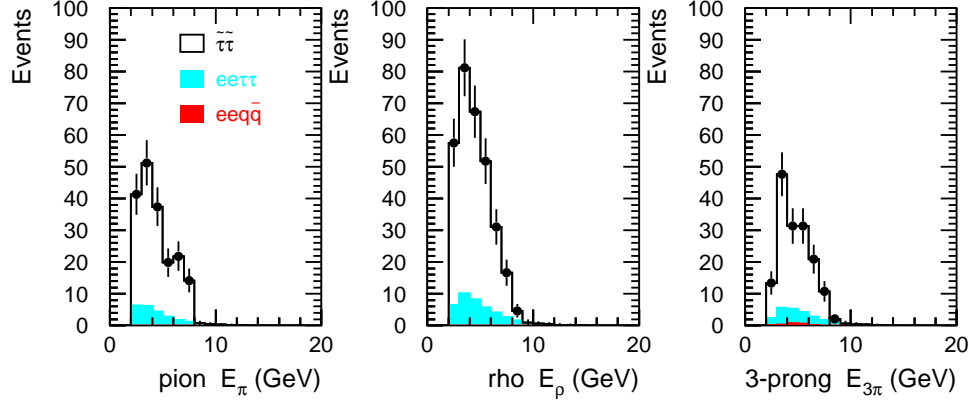
ground and $10 \times 6.4\% = 0.64$ fb for the signal at Ecm= 500 GeV and also with unpolarized

Figure 2: The energy spectra of the hadronic final state in $\tau \to \pi\nu_\tau$, $\tau \to \rho\nu_\tau$ and $\tau \to 3\pi\nu_\tau$ decays from the signal reaction $e^+e^- \to \tilde{\tau}^+\tilde{\tau}^- \to \tau^+\tilde{\chi}_1^0\tau^-\tilde{\chi}_1^0$ and two-photon production assuming head-on collision and Ecm= 500 GeV, $\mathcal{L} = 300\,\mathrm{fb}^{-1}$ and $P_{e^-} = 0.8$ and $P_{e^+} = 0.6$.

Ecm (GeV)	P_{e^-}/P_{e^+}	$\mathcal{L}\,(\mathrm{fb}^{-1})$	σ (fb)	Efficiency (%)	$\delta m_{\tilde{\tau}}$ (GeV)	$\delta\Omega h^2$ (%)
600	0.8/0.6	300	50	7.6	$0.11 - 0.13$	$1.4 - 1.7$
600	unpolarized	300	20	7.7	$0.14 - 0.17$	$1.8 - 2.2$
500	0.8/0.6	300	25	6.4	$0.13 - 0.20$	$1.7 - 2.6$
500	unpolarized	500	10	6.5	0.15	1.9
442	unpolarized	500	0.456	5.7	0.54	6.9

Table 2: Experimental conditions (Ecm, the beam polarizations and the integrated luminosity) and the corresponding results (the analysis efficiency, the stau mass uncertainty and the relative uncertainty on the DM density determination).

beams. The signal over background ratios for *method one* and *method two* are respectively 0.3 and 2.5. Therefore for *method one* where one is aiming for a background free selection, the current veto and analysis selections are not good enough and need further improvement.

For *method two*, although the absolute remaining background is larger than that from *method one*, the background level is already acceptable, given the much bigger signal production cross section for an Ecm well beyond the mass threshold. In particular the signal over background ratio can substantially improve when the beams are polarized. This is shown in Fig. 2.

Experimentally, the maximum τ energy ($E_{\max}$) can be determined from the upper endpoint of the spectra, after having subtracted the small SM background contribution, from a fit using for instance a polynomial function. Since the maximum τ energy depends on Ecm, the mass values of $\tilde{\tau}$, $\tilde{\chi}_1^0$ and τ, knowing $E_{\max}$, Ecm, $m_{\tilde{\chi}_1^0}$ and m_τ will thus allow one to derive the mass value of $\tilde{\tau}$. Assuming conservatively a precision of 100 MeV for the $\tilde{\chi}_1^0$ mass measurement, the $\tilde{\tau}$ mass is expected to be measured in the range of $0.13 - 0.2$ GeV. This in turn will result in an uncertainty of the DM density of $1.7 - 2.6\%$ based on the microMegas program [7].

The results for the benchmark scenario D' are summarized in Table 2. For the result of *method one*, we have assumed that the background-free selection could be eventually achieved. The methods can also be applied to other co-annihilation scenarios. In general, the larger the mass difference between $\tilde{\tau}$ and $\tilde{\chi}_1^0$ is, the better the precision on the DM density will be [1, 2].

In summary, we have revisited the SM background contributions to the challenging stau scenarios using the realistic veto efficiencies obtained recently. If these scenarios are close to the one realized in nature, the uncertainty on the relic DM density obtained in linear collider can well match the precision to be expected from the Planck mission.

Acknowledgments

References

[1] P. Bambade, M. Berggren, F. Richard and Z. Zhang, hep-ph/0406010; Z. Zhang, hep-ph/0411035.

[2] H.-U. Martyn, hep-ph/0408226.

[3] M. Battaglia *it al.*, Eur. Phys. J. **C33** (2004) 273, hep-ph/0306219.

[4] Z. Zhang, contribution to ILC-ECFA and GDE Joint Meeting, Valencia, 6-10 Nov., 2006.

[5] A. Stahl, private communication.

[6] P. Bambade, V. Drugakov and W. Lohmann, physics/0610145.

[7] G. Bélanger *et al.*, Comput. Phys. Commun. **149** (2002) 103-120, hep-ph/0112278.